Studying Turbulence Using Numerical Simulation Databases - V

Proceedings of the 1994 Summer Program

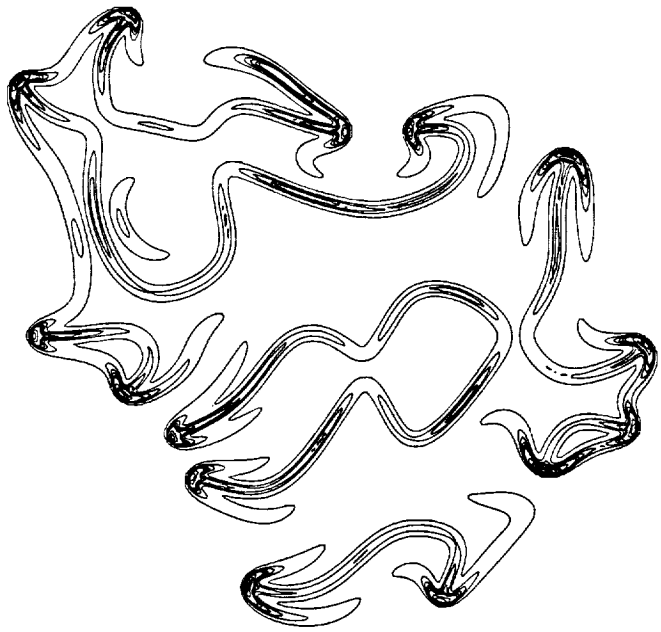

Center for Turbulence Research

December 1994

Ames Research Center

Stanford University

ORIGINAL PAGE
BLACK AND WHITE PHOTOGRAPH

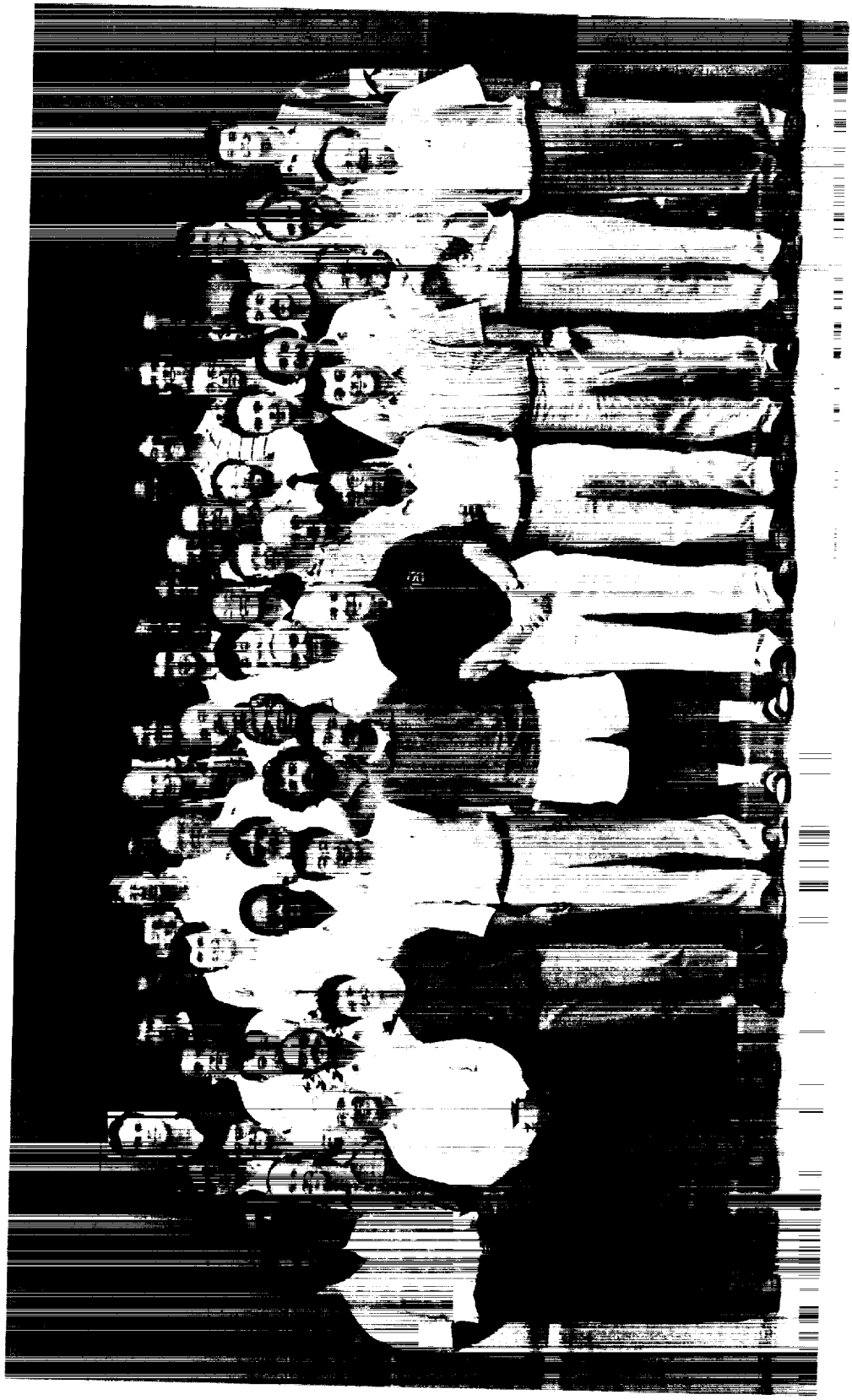

CONTENTS

Preface

The fifth Summer Program of the Center for Turbulence Research was held during the four-week period July 5 to July 29, 1994. As in the past summer programs, direct numerical simulation databases were used to study turbulence physics and modeling issues. Thirty participants from nine countries were selected based on their research proposals. They joined eighteen local participants from Stanford and NASA-Ames Research Center who devoted virtually all of their time during the Program to this activity.

Once again the largest group, comprising more than half of the participants, was the turbulent reacting flows and combustion group. We are indeed very pleased to see that the activities and the results from the CTR Summer Programs have made a positive impact on the international combustion community which is reflected in the increased number and caliber of the participants each year. The remaining participants were in three groups: Fundamentals, Modeling & LES, and Rotating turbulence. They made important progress on a variety of problems using a combination of theory and simulation.

For the first time in the CTR Summer Programs, participants included engineers from the U. S. aerospace industry. These participants were exposed to a variety of problems involving turbulence, and were able to incorporate the models developed at CTR in their company codes. They were exposed to new ideas on turbulence prediction, methods which already appear to have had an impact on their capabilities at their laboratories. We believe that such interactions among the practitioners in the government, academia, and industry are the most meaningful way of transferring new technology to industry and of applying new ideas beneficial to industry.

As part of the program, four review tutorials were given on *Physical Models of Turbulent Fine Scales* (Dale Pullin), *Turbulence Issues and Problems Facing the Engine Industries* (Andreja Brankovic), *Small-Scale Behavior in Distorted Boundary Layers* (Seyed Saddoughi), and *Turbulent Combustion* (Kenneth Bray). A number of colleagues from around the world attended the final presentations on July 29 and participated in discussions of the work.

This report contains twenty-five papers that resulted from the 1994 Summer Program. The papers are divided into four groups; each is preceded by an overview. Early reporting of eleven of the projects occurred at the Forty-Seventh Meeting of the Fluid Dynamics Division of the American Physical Society in Atlanta, Georgia, November 20-22, 1994.

We are grateful to Ms. Debra Spinks for the compilation of this report and her invaluable assistance in the organization of the Summer Program.

Parviz Moin
William C. Reynolds

The combustion group

The combustion group was the largest group at the 1994 Summer workshop. This reflects the importance of the area, the complexity of the physics involved, and the arriving maturity of simulation methods. Members of the group included visitors W. Ashurst, K. N. C. Bray, R. S. Cant, J. Card, J. H. Chen, F. J. Higuera, W. Kollmann, A. Liñán, S. Mahalingam, P. Orlandi, T. Poinsot, C. J. Rutland, A. Trouvé, L. Vervisch, R. Verzicco, and D. Veynante. Local hosts were K. Akselvoll, G. Bruneaux, M. Day, J. H. Ferziger, T. Mantel, R. D. Moser, and G. Ruetsch.

Simulation of turbulent combusting flows is made difficult by the thinness of most flames relative to turbulence length scales, the large number of dependent variables (some introduced by the chemistry), the fact that flame properties cannot be determined from external conditions alone, and the large number of parameters required to completely define a turbulent reacting flow. These obstacles also make experiments difficult, thus placing a premium on any contribution that simulation can make. Also, there are a number of approaches to the prediction of turbulent combustion for practical applications that need to be validated and/or improved. These include Reynolds-averaged methods, methods based on probability distribution functions (PDFs), and flamelet models.

The 1994 Summer Program had the ambition of making a contribution to each of these areas. Nine reports are included in these proceedings. The first paper concerns flames in non-turbulent flows but investigates issues that have a direct bearing on the properties of flames in turbulent flows. The next five present simulations of flames in various turbulent flows. The final three papers are primarily concerned with issues related to models for turbulent flows.

An important issue in turbulent combustion is flame stabilization. This is the process by which the flame is anchored so that it is not blown away by the flow of fresh gases. If the reactants are not premixed, the process involves diffusive mixing of reactants followed by a small premixed flame normal to the principal flow direction followed by a diffusion flame. The stability of these triple flames is investigated by Veynante *et al.* who show that there are two modes of triple flame stabilization; they also look at the interaction of these flames with a vortex.

Since complete flame chemistry models involve hundreds of reactions and dozens of species, it is important to know which effects can be treated with simpler chemistry models. Card *et al.* compare methane diffusion flames computed with one step and four step approximations to the chemistry and show that there are significant differences. A by-product of this work is a demonstration of just how difficult it is to include realistic chemistry in simulations from the numerical point of view.

Taking another tack, Ashurst *et al.* investigate the propagation of a flame whose properties do not change along the flame surface, which means that effects of the flow on flame structure are not considered. This case can be handled with a simplified model equation. They use this approach to study the geometric properties of the flame surface.

PRECEDING PAGE BLANK NOT FILMED PAGE 2 INTENTIONALLY

The ratio of the diffusivities for heat and chemical species (the Lewis number) has an important effect on the properties of flames. Most studies of this issue have dealt with laminar flames. The paper by Liñán *et al.* considers the effect of non-unity Lewis number on a diffusion flame in a mixing layer; the results, which show an important influence of Lewis numbers, are in general accord with laminar flame theory.

The effect of heat release, which other than the variation of transport properties with temperature is the principal effect of chemical reaction on the flow, is difficult to simulate because the incompressible equations cannot be used even though the fluid velocities are very low. Higuera and Moser consider a two-dimensional mixing layer with infinitely fast chemistry and find that, although similar phenomena are found in both the reacting and non-reacting flows, the quantitative differences are significant.

Flames may be quenched by heat transfer to solid surfaces; this phenomenon has important consequences in internal combustion engines. Bruneaux *et al* did simulations of turbulent flames in channel flow with constant temperature walls (using single step chemistry and ignoring heat release) and found significant quenching. An existing model for the quenching is inadequate, but an improved developed model fits the data very well.

Rutland and Cant investigated Reynolds averaged models for turbulent flames. In particular, the model of Bray, Moss, and Libby (BML), which obtains considerable simplification by assuming a bimodal PDF, was looked at in considerable detail and found to agree very well with simulation results for statistics up to third order. They also looked at the flux of chemical species and found it to be counter-gradient in the flame region, largely due to the effects of pressure.

Flamelet mean reaction rate models, which can be used in conjunction with Reynolds averaged flow field models, have seen increased popularity in the past few years and were looked at by Trouvé *et al.* To close the equation for flame surface density, a model is required for the turbulent flux of flame surface density. This quantity and the species flux are investigated. It is found that the species flux is co-gradient in a flow generated by the authors but counter-gradient (see preceding paragraph) in the flow of Rutland and Cant. This is believed to be a consequence of the different parameter ranges in the two flows, but further study is required.

As noted above, two principal models for turbulent flames have been of the surface density function (SDF) of PDF types. The two types of models have important advantages and disadvantages that are largely complementary. This suggests that a combination might have the best of both worlds. Vervisch *et al* made an interesting and potentially very important step towards the construction of such a model and used simulation results to test it.

As we have demonstrated, important progress in a number of directions was made at the Summer Workshop. Perhaps as importantly, the workshop has stimulated work that the participants are continuing and which should yield important results in the near future.

Joel Ferziger & Ken Bray

51-25
34721
N95-21036

Effects of non-unity Lewis numbers in diffusion flames

By A. Liñán[1], P. Orlandi[2], R. Verzicco[2] AND F. J. Higuera[1]

The purpose of this work is to carry out direct numerical simulations of diffusion controlled combustion with non-unity Lewis numbers for the reactants and products, thus accounting for the differential diffusion effects of the temperature and concentration fields. We use a formulation (Liñán (1991a)) based on combining the conservation equations in a way to eliminate the reaction terms similar to the method used by Burke and Schumann (1928) for unity Lewis numbers. We present calculations for an axisymmetric fuel jet and for a planar, time evolving mixing layer, leaving out the effects of thermal expansion and variations of the transport coefficients due to the heat release. Our results show that the front of the flame shifts toward the fuel or oxygen sides owing to the effect of the differential diffusion and that the location of maximum temperature may not coincide with the flame. The dependence of the distribution of the reaction products on their Lewis number has been investigated.

1. Introduction

In many practical combustion systems reactions between fuel and oxidizer take place in thin reaction layers where the reactants meet at stoichiometric proportions, arriving by diffusion from opposite sides of the flame. In these systems the rate of burning is controlled by diffusion and not by the kinetics of the reaction, when the reaction is sufficiently fast. The turbulent character of the flow is an unavoidable requirement when we want to obtain large burning rates. The distorted and strongly corrugated form of the flames, when the flow is turbulent or even transitional, makes direct numerical simulation (DNS) of these flows very difficult.

The problem simplifies if we can assume that the Lewis numbers of the species, i.e. the ratios of their thermal to their mass diffusivities, are equal to unity. In this case we find combinations of species concentrations and temperature that are conserved in the reaction and are transported and diffuse like inert species. The assumptions of equal diffusivities and infinitely fast reaction have, therefore, been widely used for the description of diffusion controlled combustion after the pioneering work of Burke and Schumann (1928). See, for example, Delhaye *et al.* (1994) for a recent two-dimensional simulation of a spatially evolving mixing layer.

1 Escuela T. S. Ingenieros Aeronáuticos, Pza. Cardenal Cisneros 3, 28040 Madrid, Spain

2 Università di Roma, "La Sapienza", Dipartimento di Meccanica e Aeronautica, Via Eudossiana 18, 00184 Roma Italy

The purpose of the work described here has been to show how DNS of diffusion controlled combustion can be carried out for transitional flows with non-unity Lewis numbers using a generalization, given in Liñán (1991a) and Liñán and Williams (1993), of the Burke-Shumann procedure. Preliminary calculations have been made for an axisymmetric fuel jet in a stagnant oxidizer atmosphere and for a temporally evolving plane mixing layer, leaving aside in both cases the effect of thermal expansion. The results show some of the effects of the Lewis numbers on the flame location and on the temperature and product concentration.

Experimental work on reacting shear layers with nearly constant gas density has been performed by Mungal and Dimotakis (1984), Mungal, Hermanson and Dimotakis (1985), Masutani and Bowman (1986), and Mungal and Frieler (1988). Riley, Metcalfe and Orszag (1986) carried out three-dimensional simulations of a temporally evolving mixing layer with a single-step reaction whose rate does not depend on temperature, and much numerical work has been done subsequently on different aspects of reacting shear flows (see, for example, the Proceedings of previous Summer Programs). Models of scalar mixing and chemical reactions in turbulent mixing layers and jets have been proposed by Marble and Broadwell (1977), Broadwell and Breidenthal (1982), and Broadwell and Mungal (1991). See also the review by Bilger (1989)

2. Formulation

We assume that an infinitely fast reaction, with the overall stoichiometry

$$F + rO_2 \rightarrow (1+r)P + (q) \tag{1}$$

is taking place in the thin reaction zone so that a mass of oxygen, r, is consumed and a mass of products, $(1+r)$, is generated together with a thermal energy per unit mass of fuel consumption, q.

If D_T, D_T/L_F, D_T/L_O, and D_T/L_P are the thermal and mass diffusivities of the fuel, oxygen, and products (written in terms of the corresponding Lewis numbers), we can form combinations of the conservation equations for the species and the energy where the reaction terms are eliminated. Thus, if Y_F and Y_O are the mass fractions of the fuel and of the oxygen, we can derive the conservation equation

$$\rho\frac{D}{Dt}(rY_F - Y_O) - \nabla\cdot\rho D_T\nabla(rY_F/L_F - Y_O/L_O) = 0, \tag{2}$$

where the reaction term is absent. This equation can be written in the form

$$L_m\rho\frac{D}{Dt}Z - \nabla\cdot(\rho D_T\nabla\tilde{Z}) = 0, \tag{3}$$

which uses the traditional mixture fraction

$$Z = (S\hat{Y}_F - \hat{Y}_O + 1)/(1+S), \tag{4a}$$

based on the Schvab-Zeldovich coupling function appearing in the material derivative term of Eq. (2) and the modified mixture fraction $\widetilde{Z}$, defined by

$$\widetilde{Z} = (\widetilde{S}\widehat{Y}_F - \widehat{Y}_O + 1)/(1 + \widetilde{S}), \tag{4b}$$

based on the coupling function appearing in the diffusion term of Eq. (2), where the mean Lewis number is defined as $L_m = L_O(1 + S)/(1 + \widetilde{S})$. In these relations $\widehat{Y}_F = Y_F/Y_{F0}$, $\widehat{Y}_O = Y_O/Y_{O0}$ are the mass fractions scaled by their free-stream values, and $S = rY_{F0}/Y_{O0}$ and $\widetilde{S} = SL_O/L_F$ are air/fuel mass stoichiometric ratios. Notice that the combination $(rY_F/L_F - Y_O/L_O)$ and its gradient, and therefore $\widetilde{Z}$ and grad $\widetilde{Z}$, are continuous in the thin flame, where we have a reaction-diffusion balance. The gradient of Z, on the other hand, has a jump in the reaction sheet.

In a similar fashion to the conservation equation for the mixture fraction, we can write a conservation equation

$$\rho L_P \frac{DY}{Dt} - \nabla \cdot (\rho D_T \nabla Y) = (L_P - L_F)\rho \frac{DY_F}{Dt} + (L_P - L_O)\rho \frac{DY_O}{Dt} \tag{5}$$

for the 'potential' product mass fraction

$$Y = \widehat{Y}_F + \widehat{Y}_O + \frac{1 + \widetilde{S}}{1 + r} \frac{L_F}{L_P} \frac{Y_P}{Y_{F0}}, \tag{6}$$

and the conservation equation

$$\rho \frac{DH}{Dt} - \nabla \cdot (\rho D_T \nabla H) = (1 - L_F)\rho \frac{D\widehat{Y}_F}{Dt} + (1 - L_O)\rho \frac{D\widehat{Y}_O}{Dt} \tag{7}$$

for the reduced total enthalpy

$$H = \widehat{Y}_F + \widehat{Y}_O + c_p(T - T_0)L_F \frac{1 + \widetilde{S}}{qY_{F0}}. \tag{8}$$

Here we have assumed a constant specific heat c_p and used the low Mach number approximation for the energy equation. Eqs. (3), (5)m and (7) must be complemented by the equations of state, continuity and momentum conservation, in addition to the Burke-Schumann equilibrium condition: $\widehat{Y}_F = 0$ on the air side of the flame and $\widehat{Y}_O = 0$ on the fuel side. Namely, by the relations

$$\widehat{Y}_F = 0, \quad 1 - \widehat{Y}_O = Z/Z_S = \widetilde{Z}/\widetilde{Z}_S \tag{9a}$$

where $Z < Z_S = 1/(1 + S)$ or $\widetilde{Z} < \widetilde{Z}_S = 1/(1 + \widetilde{S})$, and

$$\widehat{Y}_O = 0, \quad \widehat{Y}_F = (Z - Z_S)/(1 - Z_S) = (\widetilde{Z} - \widetilde{Z}_S)/(1 - \widetilde{Z}_S) \tag{9b}$$

where $\widetilde{Z} > \widetilde{Z}_S$. The flame lies on the stoichiometric mixture fraction level surface where $\widetilde{Z} = \widetilde{Z}_S$. Thus $\widetilde{Z}$ is given by Eq. (3) complemented by the piecewise linear relation $Z(\widetilde{Z})$ given by Eqs. (9). If $L_F = L_O$ then $Z \equiv \widetilde{Z}$.

The temperature and product concentrations are given, using Eqs. (9), by H and $\widetilde{Z}$, and Y and $\widetilde{Z}$, according to Eqs. (6) and (8). H and Y are given by eqs. (5) and (7), where the differential diffusion effects, represented by the terms in the right hand side of the equations, can be written in terms of $\widetilde{Z}$.

The boundary conditions to be used include $Z = H - 1 = Y - 1 = 0$ on the air feed stream and $Z - 1 = H - H_F = Y - 1 = 0$ on the fuel feed stream, with $H_F = 1 + c_p(T_F - T_O)(1 + \widetilde{S})/qY_{F0}$ in terms of the fuel and air feed stream temperatures T_F and T_O.

We have carried out calculations of the flow field without taking into account the effects of variable density or variable transport coefficients associated with the exothermicity of the reaction. The emphasis here has been placed on non-unity Lewis number effects, while the companion paper by Higuera and Moser (this issue) deals with the effects of thermal expansion and variable diffusivity for the equi-diffusional case.

The mixture fraction field, as well as the concentration fields of the fuel and oxygen, given in terms of $\widetilde{Z}$ by relations (9a) and (9b), are dependent on the parameters L_F, L_O and $\widetilde{S} = SL_F/L_O$. In all of our calculations we have used the reasonable assumption $L_O = 1$ and have considered $T_F = T_O$ and some representative values of L_F and of the mass stoichiometric ratio $S = rY_{F0}/Y_{O0}$.

Eqs. (5) and (7), giving the reduced total enthalpy H and the potential product concentration Y, are identical if the Lewis number L_P of the product is 1. If the initial temperature of the fuel is equal to that of the ambient air, then, the boundary conditions are also identical and the values of $c_p(T-T_0)/q$ and $Y_P/(1+r)$ are equal.

We have determined the product concentration for values of $L_P \neq 1$. The product concentration has been scaled with the constant value, $Y_{F0}(1 + r)/(1 + S)$, of the product mass fraction along the flame sheet when all the Lewis numbers are equal to the unity; in this equi-diffusional case, the flame temperature is constant and equal to the adiabatic flame temperature $T_e = T_0 + qY_{F0}/[c_p(1 + S)]$.

Due to the so called differential diffusion effects (effects of non-unity Lewis numbers) we may expect the flame temperature to vary in the range between T_e and $T_d = T_0 + qY_{F0}/[c_pL_F(1 + \widetilde{S})]$; the last value corresponding to cases where diffusion is dominant over convection and local accumulation. Similarly, the product mass fraction along the flame sheet should vary between $Y_{F0}(1 + r)/(1 + S)$ and $Y_{F0}(1 + r)(L_P/L_F)/(1 + \widetilde{S})$. Notice, however, that the total product generation in the flame will not be dependent on the diffusivity of the product, but on $\widetilde{S}$ and L_F, because in these constant density calculations the product generation is controlled by the diffusion of the reactants to the flame sheet.

3. Simulations of jet diffusion flames

Before performing the simulation of a space developing axisymmetric jet, the

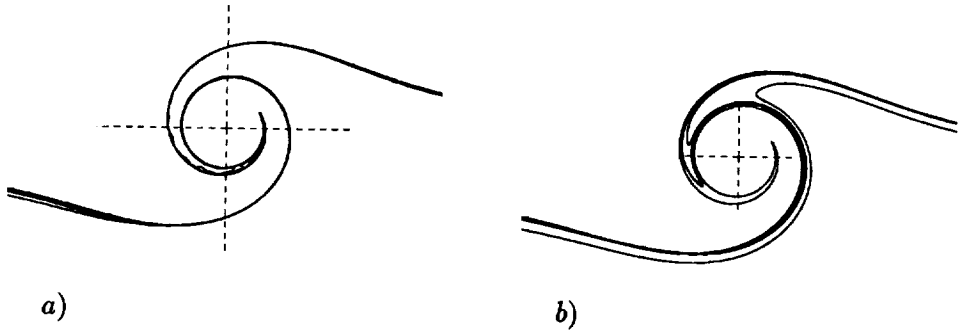

a) *b)*

FIGURE 1. Contour plots of the stoichiometric mixture fraction $Z_S = 0.272$ ($L_O = 0.8$, $L_F = 1.2$, and $r = 5$) for the Marble problem: *a*) $Pe = 5000$ lines are superimposed for $t = 4$, $t = 8$, $t = 12$, $t = 16$, and $t = 20$, *b*) solutions at $t = 20$ for $Pe = 100$, $Pe = 500$, $Pe = 1000$, and $Pe = 5000$. $Pr = 0.72$ in all cases. The crossing of —·— lines indicates the center of the vortex.

numerics related to the solution of Eqs. (3) and (5) have been checked by investigating whether the numerical solution reproduces the self-similar behavior of the mixture fraction Z when it is advected and diffused by a point vortex of circulation Γ (Marble problem). This problem has been theoretically studied by Liñán (1991b) for non-unity Lewis numbers. Since in the numerical simulation we could not use a point vortex, we considered a Rankine vortex (i.e. a vortex with $\omega = const$ for $r \leq \sigma$ and $\omega = 0$ for $r > \sigma$) of core size $\sigma = 0.1$ and unity circulation. It is clear that with this approximation the self-similar solution does not hold for $t = 0^+$ but only after a certain transient. This simulation was necessary to investigate whether our finite difference scheme could handle different variables in the right-hand and the left-hand sides of Eq. (3) ($\widetilde{Z}$ and Z respectively) since due to stability reasons an implicit discretization of the right-hand side of Eq. (3) has been used. Numerical difficulties could arise from the fact that in the reaction sheet there is a jump in the grad Z. In our numerical resolution a variable χ was introduced ($Z = \widetilde{Z}/\chi$) with χ given by the comparison of Eq. (4*a*) and (4*b*) with the Burke-Schumann condition in the oxygen and fuel regions. By this transformation in the left-hand side, the time derivative $\partial Z/\partial t$ is substituted by $\partial(\widetilde{Z}/\chi)\partial t$ and the equation is thus discretized as for the momentum equations.

In Fig. 1a the distributions of the line $Z_S = 0.25$ are given for a value of $Pe \equiv \Gamma/D_T = 5000$ at different times in terms of the coordinates $x = \eta\cos(\theta)$ and $y = \eta\sin(\theta)$ with $\eta = r/\sqrt{(\Gamma t/2\pi)}$ the similarity variable, r and θ being radial and azimuthal coordinates in the physical domain. The oscillations inside the spiral of Fig. 1*a*, observed at $t = 4$, are due to the grid (129×129) which is not fine enough to represent the very sharp gradients at this Pe. These oscillations disappear due to diffusivity, and the solution reaches a self-similar distribution where advection is balanced by diffusivity. In Fig. 1b the self-similar solutions at different Pe are shown and these solutions compare well with the theoretical results obtained by Liñán.

Having verified that the numerical method can satisfactorily deal with non-unity Lewis numbers, we move on to more realistic computations of a fuel jet exhausting into stagnant air. In what follows we use the mean exhaust velocity and the radius a of the exhaust pipe as units of velocity and length. The Reynolds number based on these quantities is $Re = 2500$ for the simulations presented in this section, this value being a limit fixed by the present computer's limitations. The injection velocity is uniform except for a thin boundary layer with a momentum thickness of roughly $a/60$. This inlet velocity profile is very similar to the one of the Longmire & Eaton experiment, which produced a vortex shedding with a Strouhall number $St = 0.5$. Several simulations were performed without combustion in order to find under what conditions the jet can sustain the continuous formation of vortex rings without any inlet perturbation. It was observed that the outer boundary should be located at a certain minimum distance from the symmetry axis to have a Strouhall number in agreement with that in the experiments of Longmire & Eaton (1992).

Fig. 2 shows the results of three simulations of a methane jet in air for which $r = 4$, $Y_{O0} = 0.23$, and $L_F = 0.8$ at a time $t = 70$ after the onset of injection. The figure includes the vorticity field, common to all the simulations, and the position of the flame for $\widetilde{Z}_S = 0.46$, 0.166, and 0.044, corresponding to $\widetilde{S} = 0.92$, 4, and 17.4, which in turn are obtained by setting Y_{F0} equal to 0.053, 0.23, and 1. Notice how with increasing value of the stoichiometric ratio $\widetilde{S}$ the flame moves toward the air side, out of the region of strong shear.

In these simulations there are source terms in the right hand sides of Eqs. (5)-(7) which arise due to the effect of the differential diffusion. These terms can not be checked by theoretical considerations as done before for the Z equation; however, an obvious physical requirement is that no negative values of $\widehat{Y}_F$ and of $\widehat{Y}_O$ should occur. Negative concentrations did indeed appear in our preliminary computations during the early stages of the flow (not displayed) when the front of the jet is moving into the air and the gradients are very steep. However, these unphysical transient oscillations disappear when the round jet is formed.

In Fig. 3 the variation of the fuel flux, scaled with its inlet value, is given for the three cases mentioned before, showing as expected that in the case of very diluted fuel the flux decreases faster than in the other cases. This figure shows that the fuel is mainly accumulated within the vortices and depleted in the braid regions. We observe furthermore the large accumulation of fuel in the last vortex formed by pairing of previous vortices. This means that as a result of the combustion the cores of the vortices run out of oxygen, and large quantities of unburned fuel are transported far from the injection place due to the convection of the vortices themselves. We did not observe complete fuel consumption in these simulations because of the limited extension of the domain in the downstream direction. Simulations will be carried out in the future with a longer domain to investigate this issue. Plots of the corresponding scaled product concentration for $L_p = 1$ are shown in Fig. 4, showing that the location of the maximum generation of products coincides with the location of maximum fuel consumption. We have also evaluated but not plotted here the mixture fraction gradient, and we observe that it has the largest values

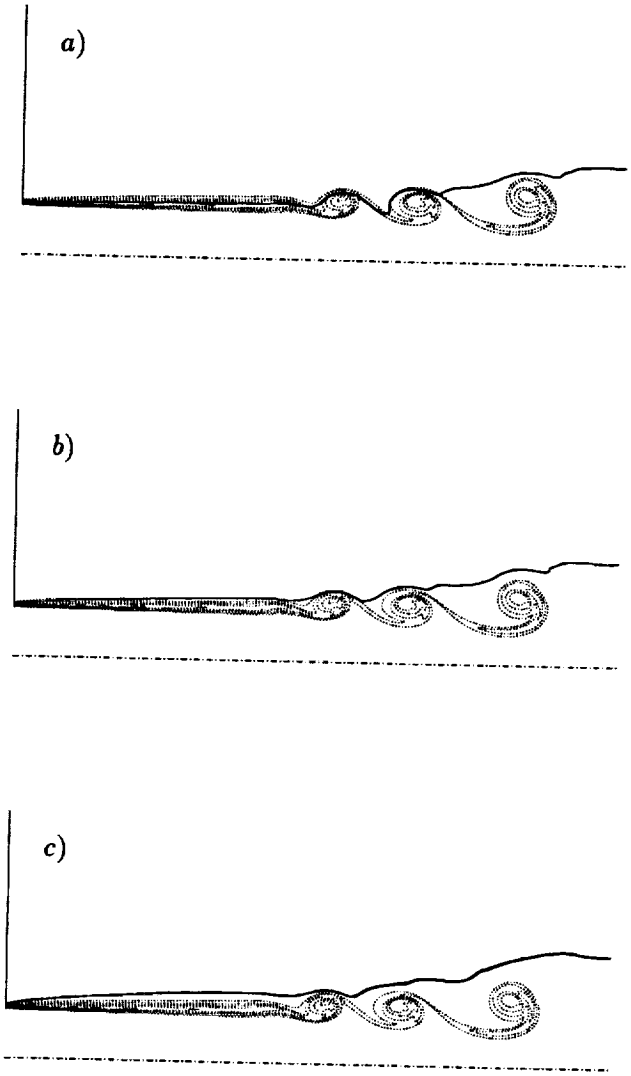

FIGURE 2. Countour plots of the azimuthal vorticity (·····)for the jet at $t = 70$ and $Re = 2500$, $Pr = 0.72$. Contour increment $\Delta = 0.5$. Thick solid line is the flame position: *a*) $\widetilde{Z}_S = 0.46$, *b*) $\widetilde{Z}_S = 0.166$, *c*) $\widetilde{Z}_S = 0.044$.

in the braid regions where we find also the largest values of the concentration of the products. The gradient of Z evaluated at the flame sheet measures the burning rate per unit flame flame surface. If it exceeds a critical value, the flame would be locally extinguished according to the analysis of Liñán (1974). (See Givi, Jou and Metcalfe (1986) for numerical work on flame extinction in a temporally evolving

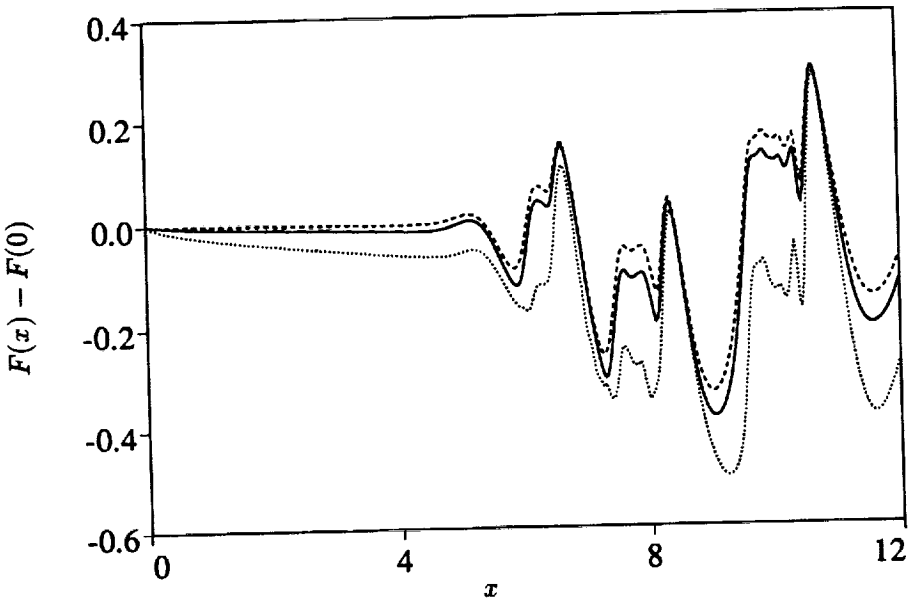

FIGURE 3. Axial profile of the fuel flux (reduced by its value at the inlet) for the simulations shown in Fig. 2: ---- $S = 17.4$, —— $S = 4$, ····· $S = 0.92$.

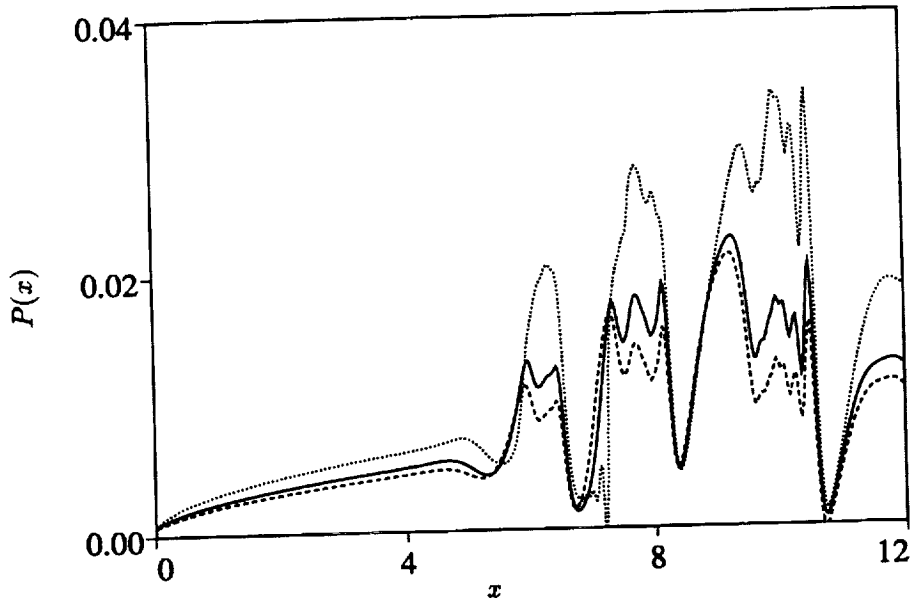

FIGURE 4. Axial profile of the products flux for the simulations shown in Fig. 2: ---- $S = 17.4$, —— $S = 4$, ····· $S = 0.92$.

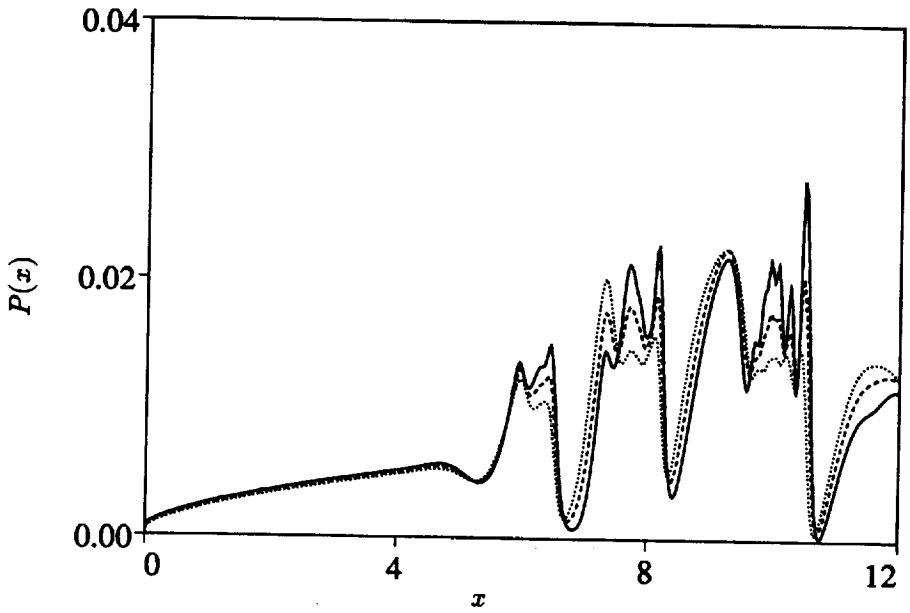

FIGURE 5. Axial profile of the products flux for $\widetilde{S} = 4$. —— $L_P = 0.8$, ---- $L_P = 1$, ····· $L_P = 1.2$.

mixing layer.)

To investigate the effect of the products Lewis number on the distribution of the concentration of the products we have performed simulations with $L_P = 0.8$ and with $L_P = 1.2$. As indicated before, the contour levels of the product concentration for $L_P = 1$ also give the temperature levels. Fig. 5 shows for the case $Y_{F0} = 0.23 = Y_{O0}$ that the products, which are mainly generated in the braid regions at a rate independent of their diffusivity, are more concentrated in the eddies when L_P is larger, thus leading to stronger variations of the product flux when the eddies travel past a given station.

4. Temporally evolving mixing layer

Two-dimensional simulations of a temporally evolving mixing layer have been carried out using as initial conditions the base profiles

$$u = \mathrm{erf}(\sqrt{\pi}y) \quad \text{and} \quad \begin{cases} \dfrac{\widetilde{Z}}{\widetilde{Z}_S} = \dfrac{\mathrm{erfc}(\sqrt{\pi Pr L_O}\, y)}{\mathrm{erfc}(\sqrt{\pi Pr L_O}\, y_f)} & \text{for } \widetilde{Z} < \widetilde{Z}_S \\ \dfrac{1-\widetilde{Z}}{1-\widetilde{Z}_S} = \dfrac{1+\mathrm{erf}(\sqrt{\pi Pr L_F}\, y)}{1+\mathrm{erf}(\sqrt{\pi Pr L_F}\, y_f)} & \text{for } \widetilde{Z} > \widetilde{Z}_S \end{cases} \qquad (10a-b)$$

plus initial perturbations proportional to the eigenfunctions of the most unstable small perturbation of the error function velocity profile and its subharmonic. Here y_f, the position of the flame, verifies

$$1 + \mathrm{erf}(\sqrt{\pi Pr L_F}\, y_f) = \left(\frac{L_F}{L_O}\right)^{1/2} \frac{1-\widetilde{Z}_S}{\widetilde{Z}_S} \mathrm{erfc}(\sqrt{\pi Pr L_O}\, y_f) e^{-\pi Pr (L_F - L_O) y_f^2}$$

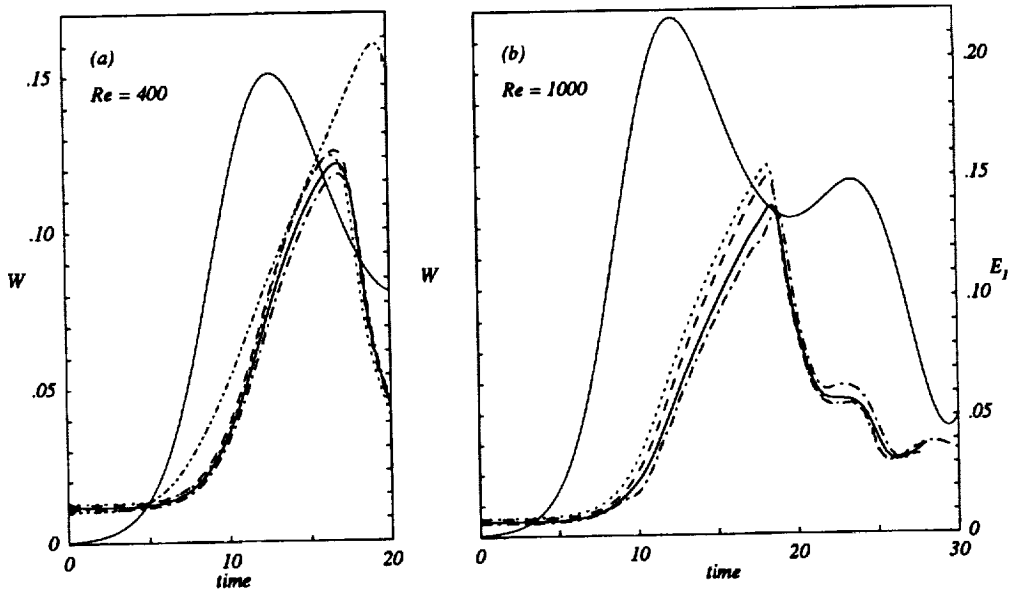

FIGURE 6. Overall rate of product generation for: (*a*) $Re = 400$. ——— : $L_F = 1$, $S = 9$ ($\widetilde{S} = 9$). ---- : $L_F = 0.8$, $S = 7.2$ ($\widetilde{S} = 9$). ····· : $L_F = 0.8$, $S = 9$ ($\widetilde{S} = 11.25$). —·— : $L_F = 1.2$, $S = 10.8$ ($\widetilde{S} = 9$). —··— : $L_F = 1$, $S = 1$ ($\widetilde{S} = 1$). (*b*) $Re = 1000$. ——— : $L_F = 1$, $S = 9$ ($\widetilde{S} = 9$). ---- : $L_F = 0.5$, $S = 4.5$ ($\widetilde{S} = 9$). —·— : $L_F = 1.5$, $S = 13.5$ ($\widetilde{S} = 9$). ····· : $L_F = 0.5$, $S = 4.5$ ($\widetilde{S} = 9$) with the initial conditions of $L_F = 1$. The thin curves to be read off the scales to the right represent the first mode of the kinetic energy spectrum.

which, for $\widetilde{Z}_S \gg 1$, yields

$$y_f \approx \frac{1}{\sqrt{\pi Pr L_F}} \left\{ \ln \left[\frac{S}{2\sqrt{\pi}} \frac{1}{\sqrt{\ln \frac{S}{2\sqrt{\pi}}}} \right] \right\}^{1/2}$$

Eqs. (10) and similar expressions for the total enthalpy and the potential product mass fraction correspond to the parallel flow resulting from the evolution of a half-space ($y < 0$) filled with $\widehat{Y}_O = 0$, $\widehat{Y}_F = 1$ and a half-space ($y > 0$) filled with $\widehat{Y}_O = 1$, $\widehat{Y}_F = 0$, moving initially with opposite velocities. Hereafter velocities are scaled with half this velocity difference, and distances with the vorticity thickness of the basic flow (10a). $Pr = 1$ in the simulations.

Fig. 6a shows the overall rate of product generation,

$$W = \frac{1}{L} \frac{d}{dt} \int \widehat{Y}_P \, dx \, dy$$

where $\widehat{Y}_P$ is the scaled product concentration and L is the streamwise length of the computational domain for a number of simulations with $Re = 400$ and a time interval covering a vortex roll-up. To establish a common basis for comparison, the same initial $\widetilde{Z}$ was used in all the simulations, corresponding to the base profile (10b) with $Pr = L_F = L_O = 1$. As can be seen, the rate of product generation peaks after roll-up in all the cases computed, the peak value being the highest in the only case displayed with $\widetilde{S} = 1$ (and similar to those of other cases not displayed with $L_F \neq 1$ and $\widetilde{S}$ about 1). This is because the flame sheet then lies inside the region of high vorticity and, in the absence of density changes that might alter the flow, large portions of the flame are subject to high strain rates that increase its surface and the fluxes of the reactants toward it. The other curves in Fig. 6a correspond to higher values of $\widetilde{S}$, for which the peak values increase with decreasing L_F or decreasing S. In the following we give some tentative explanations of these results.

The weak dependence of the rate of product generation on the Lewis number of the fuel when $\widetilde{S}$ is kept constant can be understood by noticing that, in the absence of molecular transport, each material particle would conserve its initial temperature and mass fractions of fuel and oxygen so that the fields of these variables as well as the position and shape of the flame would not change. In particular, the values of $\nabla\widehat{Y}_O$ and $\nabla\widehat{Y}_F$ at the flame would not depend on L_F, but the diffusion flux of fuel, $-L_F^{-1}\nabla\widehat{Y}_F$, would. What happens is that the stoichiometric ratio S is changing with L_F to keep $\widetilde{S}$ constant; S decreases when L_F decreases, and the flame then requires more fuel to consume the same amount of oxygen, generating more products. The variation, however, is small if S is large because the product generation is then essentially determined by the consumption of oxygen.

Similarly, to understand the weak dependence of the rate of product generation on the stoichiometric ratio, notice that for large values of S, the flame sits in a region where the modified mixture fraction is decaying exponentially, and according to (10b), a $|\nabla\widetilde{Z}|_{flame} = O(y_f\widetilde{Z}_S)$, with $y_f = O(\ln\widetilde{Z}_S^{-1})$ and $\widetilde{Z}_S = 1/(1+\widetilde{S})$, should be expected. Hence a decrease of S at constant L_F is accomodated with only a small shift of the flame, whereas $\nabla\widehat{Y}_O = -(1+\widetilde{S})\nabla\widetilde{Z}$ remains practically constant and $\nabla\widehat{Y}_F \approx \nabla\widetilde{Z}$ increases. As before, this implies a weak increase of the rate of product generation.

Further computations were carried out with $Re = 1000$ and a time interval covering the first pairing to assess the influence of the molecular transport on the previous results and to study the evolution after the roll-up of the vortices. Rather extreme values of L_F were chosen to exaggerate the effect of this parameter, and initial conditions (10b) with both $L_F = 1$ and L_F equal to the values actually used in the computations were considered in an attempt to describe the influence of this factor. The results, in Fig. 6b, have the same appearance as cases with the smaller Reynolds number, with slightly lower peak values of the rate of product generation. No further peaks appear during the pairing process.

Fig. 7 shows the temperatures for $L_F = 0.5$ and 1.5 as well as the vorticity and the flame positions during the first pairing of the vortices. The maximum temperature

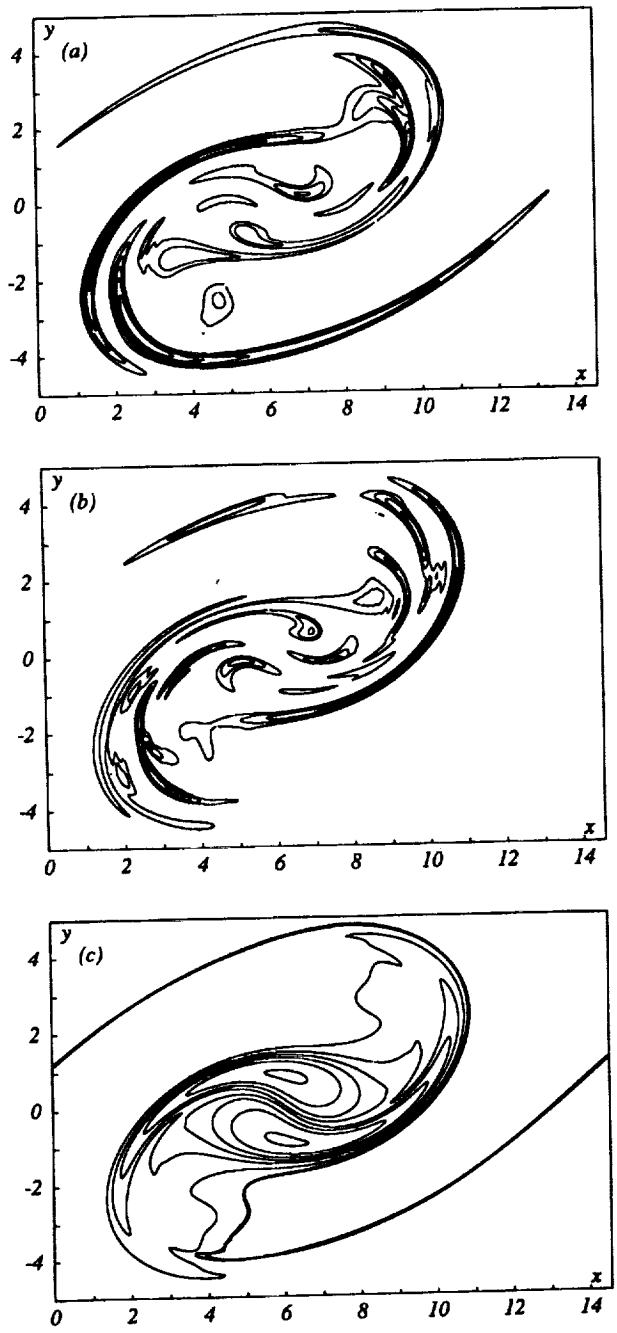

FIGURE 7. Results for $Re = 1000$ at $t = 38$. (*a.*) Temperature field for $L_F = 0.5$. (*b.*) Temperature field for $L_F = 1.5$. (*c.*) Vorticity field and position of the practically coinciding flames for $L_F = 0.5$ and 1.5.

in these pictures is attained at points separated from the flame, a consequence of the differential diffusion acting in thin layers that were around the flame at earlier times.

5. Conclusions

The work carried out has shown the feasibility of direct numerical simulations of diffusion controlled combustion with non-unity Lewis numbers of reactants and products. In the calculations we have left out the effects of thermal expansion and variations of the transport coefficients due to heat release. The preliminary calculations should be extended in the future to include effects of heat release, and a more systematic analysis should be carried out to verify or extend the tentative conclusions presented here.

REFERENCES

BILGER, R. W. 1989 Turbulent diffusion flames. *Ann. Rev. Fluid Mech.* **21,** 101–135.

BROADWELL, J. E. & BREIDENTHAL, R. E. 1982 A simple model of mixing and chemical reaction in a turbulent shear layer. *J. Fluid Mech.* **125,** 397–410.

BROADWELL, J. E. & MUNGAL, M. G. 1991 Large-scale structures and molecular mixing. *Phys. Fluids A.* **3,** 1193–1206.

BURKE, S. P. & SCHUMANN, T. E. W. 1928 Diffusion flames. *Industr. Eng. Chem.* **20,** 998–1004.

DELHAYE, B., VEYNANTE, D. & CANDEL, S. M. 1994 Simulation and modeling of reactive shear layers. *Theoret. Comput. Fluid Dynamics.* **6,** 67–87.

GIVI, P., JOU, W.-H. & METCALFE, R. W. 1986 Flame extinction in a temporally developing mixing layer. Proc. 21nd. Int. Symp. Combustion, 1251–1261. The Combustion Institute, Pittsburgh.

KATTA, V. R., GOSS, L. P. & ROQUEMORE, W. H. 1994 Effect of non-unity Lewis number and finite rate chemistry of a H_2/air jet diffusion flame. *Comb. & Flame.* **96,** 60–74.

LIÑÁN, A. 1974 The asymptotic structure of laminar diffusion flames for large activation energies. *Astronautica Acta.* **1,** 1007-1031.

LIÑÁN, A. 1991a The structure of diffusion flames. In Fluid Dynamical Aspects of Combustion theory. Ed. by Onofri, M. & Tesev, A. Longman Scientific & Technical, 11-29.

LIÑÁN, A. 1991b El papel de la Mecánica de Fluidos en los Procesos de Combustión. (In Spanish). Real Academia de Ciencias, Madrid, Spain.

LIÑÁN, A. & WILLIAMS, F. A. 1993 Fundamental Aspects of Combustion. Oxford Univ. Press.

LONGMIRE, E. K. & EATON, J. K. 1992 Structure of a particle-laden round jet. *J. Fluid Mech.* **236,** 217–257.

MAHALINGAM, S., CANTWELL, B. J. & FERZIGER J. H. 1990 Full numerical simulation of co-flowing axisymmetric jet diffusion flames. *Phys. Fluids A.* **2,** 720-728.

MARBLE, F. & BROADWELL, J. E. 1977 The coherent flame model for turbulent chemical reaction. Report No. TRW-9-PU. Project SQUID.

MASUTANI, S. M. & BOWMAN, C. T. 1986 The structure of a chemically reacting plane mixing layer. *J. Fluid Mech.* **172,** 93–126.

MUNGAL, M. G. & DIMOTAKIS, P. E. 1984 Mixing and combustion with low heat release in a turbulent shear flow. *J. Fluid Mech.* **148,** 349–382.

MUNGAL, M. G. & FRIELER, C. E. 1988 The effects of Damköhler number in a turbulent shear layer. *Comb. Flame.* **71,** 23–34.

MUNGAL, M. G., HERMANSON, J. C. & DIMOTAKIS, P. E. 1985 Reynolds number effects on mixing and combustion in a reacting shear layer. *AIAA J.* **23,** 1418–1423.

RILEY, J. J., METCALFE, R. W. & ORSZAG, S. A. 1986 Direct numerical simulations of chemically reacting turbulent mixing layers. *Phys. Fluids.* **29,** 406–422.

52-25
39732
N95-21037

Effect of chemical heat release in a temporally evolving mixing layer

By F. J. Higuera[1] AND R. D. Moser[2]

Two-dimensional numerical simulations of a temporally evolving mixing layer with an exothermic infinitely fast diffusion flame between two unmixed reactants have been carried out in the limit of zero Mach number to study the effect of the heat release on the early stages of the evolution of the flow. Attention has been directed to relatively large values of the oxidizer-to-fuel mass stoichiometric ratio typical of hydrocarbon flames, and initial vorticity distributions thicker than the temperature and species distributions have been chosen to mimic the situation at the outlet of a jet. The results show that, during the stages of the evolution covered by the present simulations, enhancement of combustion occurs by local stretching of the flame without much augmentation of its area. The rate of product generation depends strongly on the initial conditions, which suggests the possibility of controlling the combustion by acting on the flow. Rollup and vortex amalgamation still occur in these reacting flows but are very much affected by the production of new vorticity by baroclinic torques. These torques lead to counter rotating vortex pairs around the flame and, more importantly, in thin layers of light fluid that leave the vicinity of the flame when the Kelvin-Helmholtz instability begins to develop. Propelled by the vortex pairs, these layers wind around, split on reaching high pressure regions, and originate new vortex pairs in a process that ends up building large-scale vortices with a vorticity distribution more complex than for a constant density fluid.

1. Introduction

Combustion typically involves large amounts of energy release that very often result in strong couplings of the molecular transport and chemical reactions with the motion of the gas where such processes occur. A fast chemical reaction between two initially unmixed reactants in a mixing layer is a prototype of many practical situations. In this case reaction occurs in a very thin flame controlled by the diffusion of the reactants from the carrying streams. Furthermore, the diffusion fluxes reaching the flame depend on the nature of the flow through the action of large-scale mixing and by the stretching and wrinkling that the flow imposes on the flame. Conversely, the flow may be very much affected by the gas expansion and baroclinic torques due to the chemical heat release. The coupled problem rapidly becomes very complicated and much work is required to analyze the elements of the coupling separately.

1 E.T.S. Ingenieros Aeronáuticos, Pza. Cardenal Cisneros 3, 28040 Madrid, Spain

2 NASA Ames Research Center

Experimental investigations of gas-phase reacting shear flows under conditions of low heat release, with no apparent coupling between heat release and the fluid mechanics, have been conducted by Mungal & Dimotakis (1984), Mungal, Hermanson & Dimotakis (1985) and Mungal & Frieler (1988) using the hydrogen-fluorine reaction, and by Masutani & Bowman (1986) using the nitric oxide-ozone reaction. The amount of mixing and product formation, the effects of the Reynolds number and chemical reaction rate, and the structure of the reacting layer prior to the mixing transition are some of the issues addressed in these investigations. Models of the mixing and chemical reaction under these conditions were proposed by Marble & Broadwell (1977) and by Broadwell & Breidenthal (1982) and Broadwell & Mungal (1991). On the numerical side, Riley, Metcalfe & Orszag (1986) carried out three-dimensional simulations of a temporally-evolving constant density flow with a single-step temperature-independent chemical reaction and showed that their results agree with similarity theory and compare well with the experimental data of Mungal & Dimotakis. Givi, Jou & Metcalfe (1986) addressed the problem of local extinction of a single-step irreversible Arrhenius reaction by means of two-dimensional temporally evolving simulations, and Ghoniem & Givi (1988) used the same kinetics in a two-dimensional spatially evolving simulation. A simulation of the spatially evolving flow with an infinitely fast reaction was performed by Delhaye *et al.* (1994), who also proposed a model based on an equation for the mean flame surface density and a description of the strained flame elements.

The effect of heat release on the flow was investigated by Wallace (1981), using the nitric oxide-ozone reaction with adiabatic temperatures up to 700 K and, more thoroughly, by Hermanson & Dimotakis (1989). They used the hydrogen-fluorine reaction with adiabatic temperatures ranging from 486 to 1240 K and showed that the growth rate of the layer, the turbulent shear stresses, and the overall entrainment are reduced as a consequence of the heat release. They also found that large-scale structures persisted in their experiment, but the mean structure space scaled with the layer width decreased with increasing heat release, which led these authors to suggest that the mechanisms of large-structure coalescence are inhibited by heat release. A review of further experimental work can be found in Dimotakis (1991).

McMurtry *et al.* (1986) studied the coupling between chemical heat release and fluid dynamics by means of direct numerical simulations of a two-dimensional, temporally evolving mixing layer with a single-step, irreversible exothermic reaction independent of the temperature. Using a zero Mach number formulation, they found that the rate of product generation, the thickness of the mixing layer, and the vorticity at the center of the vortex structures all decrease with increasing rates of heat release. They analyzed the influence of the baroclinic torque, pointing out that it changes sign across the flame because the direction of the pressure gradient in the high temperature region is roughly radially outward from the centers of the vortices, while the density gradient changes sign across the reaction front. As the flow evolves, this results in the generation of vorticity that alternately opposes and enhances the original vorticity, leading to several local extremas and to a vorticity distribution more diffuse than for a constant density fluid. McMurtry,

Riley & Metcalfe (1989) confirmed these results in a three-dimensional simulation and found that the Reynolds stresses, the turbulent kinetic energy, and the three-dimensionality of the flow also decrease with increasing heat release, in agreement with the experimental results of Hermanson & Dimotakis. Similar results were obtained by Grinstein & Kailasanath (1992) in a two-dimensional simulation of a compressible subsonic spatially evolving mixing layer.

Extensive simulations of compressible and/or reacting mixing layers have been carried out by Planché & Reynolds (1992) using an exothermic Arrhenius kinetics and values of the equivalence ratio such that the flame is near the center of the layer. They found that this flow behaves as two independent colayers separated by an approximately plane flame. Mixing occurs only between fuel and combustion products on one side of the layer and between oxidizer and products on the other side, but no roll-up or pairing was seen. Instead, the authors propose that the modification of the mean flow by the structures of each colayer causes the decay of these structures and the emergence of new ones of larger scale, which results in a slow growth of the layer.

The purpose of this work is to investigate in further detail the effect of chemical heat release on the first stages of the development of a plane mixing layer at zero Mach number. As in much previous work, we restrict ourselves to two-dimensional numerical simulations, which should provide valuable information since it is abundantly clear that these early stages are dominated by the dynamics of large-scale two-dimensional structures. The chemical reaction takes place between two unmixed species and the reaction time is supposed to be much shorter than the shortest time scale of the flow, so that the molecular mixing of the reactants is confined to a continuous infinitely thin diffusion flame. This assumption leaves out many important phenomena related to ignition and extinction but, in its broad range of applicability, gives results independent of any specific reaction law and renders the numerical resolution of the reaction zone unnecessary. A further limitation comes from the temporally evolving nature of the computations, which leaves out the effects of entrainment asymmetry (see, e.g., Dimotakis 1986 for a discussion of entrainment) and feedback from the downstream flow. While both effects are very important for a real reacting mixing layer, we expect that the temporally evolving flow still contains the essential ingredients of the internal dynamics of the mixing layer. As for the results, while a drastic reduction of the efficiency of the large-scale mixing seems to be unavoidable for non-small Mach numbers or when the flame sits near the center of the mixing layer, we find that this is not necessarily the case for the relatively high values of the effective stoichiometric ratio (or equivalence ratio) and initial vorticity distributions typical of many practical combustion systems. In this case, the mean location of the flame is displaced toward the oxidizer side and the presence of low density fluid modifies the evolution of the vorticity without suppressing the roll-up and pairing processes typical of constant density mixing layers.

2. Formulation and numerical method

Consider a plane two-dimensional temporally evolving unconfined mixing layer between a gas stream of velocity U and temperature T_o carrying a mass fraction $y_{o\infty}$

of an oxidizer and another gas stream of velocity $-U$ and temperature T_f carrying a mass fraction $y_{f\infty}$ of a fuel. The two species react in an exothermic infinitely fast chemical reaction so that a diffusion flame exists in the mixing layer where an amount of heat Q is released per unit mass of burned fuel. The velocity U is much smaller than the speeds of sound in either stream so that compressibility effects are negligible, but the density and temperature of the gas change due to the heat release (and to the temperature difference between the two streams if $T_f \neq T_o$).

In what follows the velocities and lengths are scaled with U and $\delta_\omega = 2U/\max(\partial\overline{u}/\partial y)_0$, the vorticity thickness of the initial mean flow, the temperatures and densities with the fuel-stream values T_f and ρ_f, and the pressure with $\rho_f U^2$.

The mass and momentum conservation equations are

$$\frac{\partial \rho}{\partial t} + \nabla \cdot (\rho \mathbf{v}) = 0 \ , \tag{1}$$

$$\frac{\partial}{\partial t}(\rho \mathbf{v}) + \nabla \cdot (\rho \mathbf{v}\mathbf{v}) = -\nabla p + \frac{1}{Re}\{\nabla \cdot (\tilde{\mu}\nabla \mathbf{v}) + \mathbf{N}\} \ , \tag{2}$$

where $Re = \rho_f U \delta_\omega / \mu_f$ is the Reynolds number, $\tilde{\mu} = \mu/\mu_f$ depends only on the temperature: $\tilde{\mu} = T^\sigma$,

$$\mathbf{N} = \begin{pmatrix} \tilde{\mu}_y v_x - \tilde{\mu}_x v_y \\ \tilde{\mu}_x u_y - \tilde{\mu}_y u_x \end{pmatrix} \ ,$$

and the normal viscous stress $Re^{-1}(\tilde{\mu}_v + \tilde{\mu}/3)\nabla \cdot \mathbf{v}$ is included in the pressure.

In the limit of zero Mach number, and neglecting the variations of the mean molecular mass of the gas mixture, the equation of state is

$$\rho T = 1 \ . \tag{3}$$

The velocity and pressure are L-periodic functions of the streamwise coordinate x (the choice of the period is discussed later) and satisfy

$$u \to \pm 1 \ , \qquad \rho v \to \alpha_\pm \phi \ , \qquad \frac{\partial p}{\partial y} \to \mp \alpha_\pm \frac{\partial \phi}{\partial t} \qquad \text{for} \qquad y \to \pm\infty \ , \tag{4}$$

where $\phi = \frac{1}{L}\int_0^L \int_{-\infty}^{\infty} \frac{\partial \rho}{\partial t}\, dx\, dy$ is the outflow due to the gas expansion, which is split between the two sides of the mixing layer by means of the factors $\alpha_+ = 1/(1+T_o^{1/2})$ and $\alpha_- = \alpha_+ - 1$. These values result from matching the mixing layer to outer wave regions where acoustic effects would be important.

Assuming that the Lewis numbers of the two species are equal to unity, the energy and species conservation equations are

$$L(T) = \frac{Q}{c_p T_f} w \ , \qquad L(y_f) = -w \ , \qquad L(y_o) = -sw \ , \tag{5a,b,c}$$

where

$$L(*) = \frac{\partial}{\partial t}(\rho *) + \nabla \cdot (\rho \mathbf{v} *) - \frac{1}{RePr}\nabla \cdot (\tilde{\mu}\nabla *) \ , \tag{6}$$

y_f and y_o are the mass fractions of fuel and oxidizer, $\rho_f U w/\delta_\omega$ is the mass of fuel consumed per unit volume per unit time, s is the mass of oxidizer required to burn the unit mass of fuel ($s = \mathrm{M}_o\nu/\mathrm{M}_f$ for the overall reaction $F + \nu O \rightarrow products$, where M_f and M_o are the molecular masses of the two species), and c_p and Pr are the specific heat at constant pressure and the Prandtl number, both assumed constant.

As can be seen by combining (5b)–(5c) and (5a)–(5b), the mixture fraction and the modified enthalpy, $(SY_f - Y_o + 1)/(1 + S)$ and $(T - T_o + qY_f)/(1 - T_o + q)$ respectively, satisfy transport equations similar to (5) but without reaction terms in the right hand sides (Williams 1985). Here $Y_f = y_f/y_{f\infty}$ and $Y_o = y_o/y_{o\infty}$, $S = sy_{f\infty}/y_{o\infty}$ is the effective stoichiometric ratio, and $q = Qy_{f\infty}/c_pT_f$. In addition, both variables satisfy the same boundary conditions and, assuming that the initial conditions are also the same, we find that

$$\frac{SY_f - Y_o + 1}{1 + S} = \frac{T - T_o + qY_f}{1 - T_o + q} \equiv Z(x, y, t) \tag{7}$$

satisfies

$$L(Z) = 0 \ , \tag{8}$$

and

$$\begin{aligned} Z &= 0 \quad \text{for} \quad y \rightarrow \infty \\ Z &= 1 \quad \text{for} \quad y \rightarrow -\infty \\ Z(x, y, t) &= Z(x + L, y, t). \end{aligned} \tag{9}$$

In the Burke-Schumann limit of diffusion-controlled flames eqs. (5a-c) yield $w = 0$ to leading order (see Williams 1985 for details). The precise form of the consumption rate need not by specified in this limit other than requiring that $w = 0$ implies

$$Y_fY_o = 0 \ , \tag{10}$$

which means that the two reactants do not coexist, being separated by an infinitely thin flame where both concentrations vanish. Eqs. (7) and (10) suffice then to determine the temperature and species concentrations in terms of the mixture fraction Z. At the flame the mixture fraction and temperature take the values

$$Z_{st} = \frac{1}{1 + S} \qquad \text{and} \qquad T_{ad} = T_o + \frac{1 - T_o + q}{1 + S} \ , \tag{11}$$

and

$$\begin{aligned} Y_f &= \tfrac{Z/Z_{st} - 1}{S} \ , \quad Y_o = 0 \ , \quad T = 1 + (T_{ad} - 1)\tfrac{1 - Z}{SZ_{st}} \quad \text{for} \quad Z > Z_{st} \\ Y_f &= 0 \ , \quad Y_o = 1 - \tfrac{Z}{Z_{st}} \ , \quad T = T_o + (1 - T_o + q)Z \quad \text{for} \quad Z < Z_{st} \end{aligned} \tag{12}$$

Notice that since Z and its first derivatives are continuous across the flame, the gradients of oxidizer and fuel concentrations and the gradients of temperature on either side of the flame verify

$$\left.\frac{\partial Y_o}{\partial n}\right|_+ = -S \left.\frac{\partial Y_f}{\partial n}\right|_- \qquad \text{and} \qquad \left.\frac{\partial T}{\partial n}\right|_+ = \left.\frac{\partial T}{\partial n}\right|_- + q \left.\frac{\partial Y_f}{\partial n}\right|_- , \tag{13a,b}$$

where n is the normal to the flame.

The problem (1)–(4), (8), (9), and (12) is to be solved subject to the initial conditions discussed in the following section.

For the numerical treatment, a second order finite volume method on a staggered grid is used for eqs. (1), (2), and (8). The time integration, which is also second order accurate, is explicit for the convection terms, implicit for the transport terms, and uses a time splitting for the pressure correction. This amounts to the standard decomposition $(\rho\mathbf{v})^{(n+1)} - (\rho\mathbf{v})^{(n)} = \delta_1(\rho\mathbf{v}) - \Delta t \nabla \delta p$, and (1) yields

$$\Delta t \nabla^2 \delta p = \left(\frac{\partial \rho}{\partial t}\right)^{(n+1)} + \nabla \cdot \left[(\rho\mathbf{v})^{(n)} + \delta_1(\rho\mathbf{v})\right] . \tag{14}$$

The only difference with respect to a constant density fluid is the presence of $(\partial\rho/\partial t)^{(n+1)}$ in the right hand side of (14). Since $\rho = \rho(Z)$, by (3) and (12), this term can be computed by evaluating (8) at the time level $(n+1)$. However $(\rho\mathbf{v}Z)^{(n+1)}$ in the convection term of this equation gives the unknown contribution

$$\Delta t \frac{\nabla \cdot (Z^{(n+1)} \delta p)}{\left(\frac{\rho}{d\rho/dZ} + Z\right)^{(n+1)}}$$

along with others already known ($Z^{(n+1)}$ is already known from the solution of (8), which can be computed before solving (14)). Thus, when this $(\partial\rho/\partial t)^{(n+1)}$ is carried into (14) and into the boundary condition (4) for v, an elliptic problem results for δp which differs from the usual one for a liquid. This problem is solved iteratively at each time step.

Eq. (12) implies $dT/dZ = (1 - T_o + q) - (q/SZ_{st})H(Z - Z_{st})$, where $H(\zeta)$ is the Heaviside step function. In the numerical simulations, the discontinuity of the temperature derivative at the flame was smoothed out replacing $H(\zeta)$ by $H_\beta(\zeta) = [\tanh(\beta\zeta) + 1]/2$ and then, to the same approximation, $T(Z) = T_{ad} - (q/\beta S Z_{st}) \ln 2^{1/2} + \int_{Z_{st}}^{Z} (dT/dZ')\, dZ'$, which becomes exact when $\beta \to \infty$. This approximation amounts to assigning a finite thickness to the flame, measured by β^{-1}. It was checked that the results do not depend on β provided it is sufficiently large for the transport effects to dominate in the scale of this artificial thickness. Typically $\beta = 20$ in the computations presented below.

3. Initial conditions and linear stability

The initial conditions are the superposition of a base flow independent of x and small perturbations proportional to the eigenfunctions of the most unstable mode and its subharmonic, as given by a linear stability analysis of the base flow.

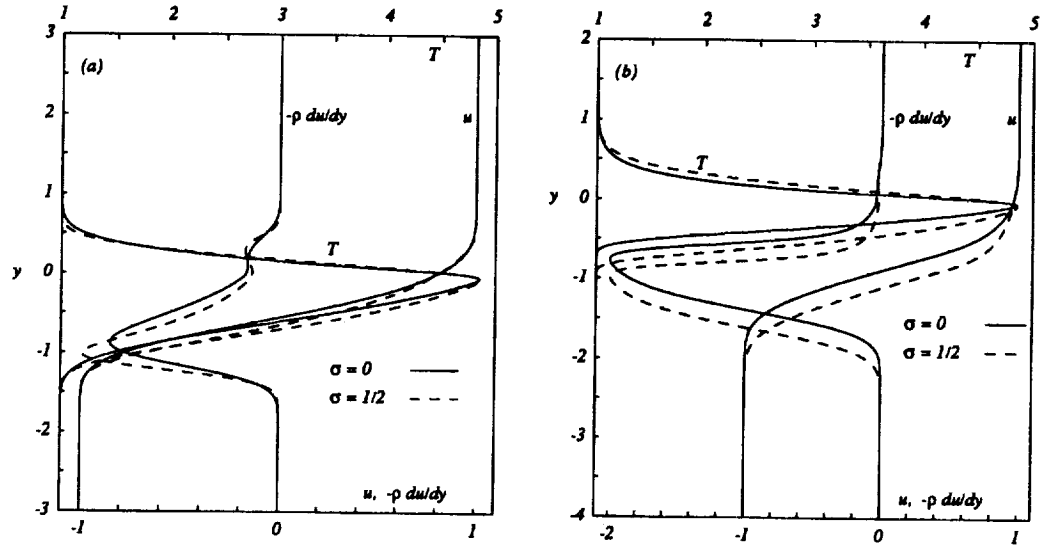

FIGURE 1. Temperature, velocity, and density-weighted vorticity for: (*a*) first type of base flow, and (*b*) second type of base flow.

Two kinds of base flows are considered. The first is the result of letting an initial state consisting of a halfspace with $Z = 0$ and another with $Z = 1$, each moving with opposite velocities parallel to their common boundary evolve for a finite time t. This leads to a self-similar flow in which the mixture fraction and the streamwise velocity are of the form $Z = Z(\eta)$ and $u = U(\eta)$ with $\eta = \xi/t^{1/2}$ and $\xi = \int^y \rho\, dy$, and satisfy

$$[F(Z)Z_\eta] + \frac{Pr}{2}\eta Z_\eta = 0 \ , \tag{15a}$$

$$[F(Z)U_\eta] + \frac{1}{2}\eta U_\eta = 0 \ , \tag{15b}$$

$$Z = 0 \ , \quad U = 1 \qquad \text{for} \quad \eta \to \infty \ , \tag{15c}$$

$$Z = 1 \ , \quad U = -1 \qquad \text{for} \quad \eta \to -\infty \ , \tag{15d}$$

where $F(Z) = T^{\sigma-1}$ with $T(Z)$ given by (12), rounded as commented at the end of the previous section. The extra condition $Z(0) = Z_{st}$ is used to fix the origin; it amounts to measuring transverse distances from the flame. The transverse velocity, $O(1/\sqrt{Re\, t})$, due to the gas expansion, and the pressure are computed afterward from the equations of motion and the boundary conditions (4). The nondimensional vorticity thickness of this flow is $\delta_\omega = 2(t/Re)^{1/2}/\max_\eta(\rho U_\eta)$, and the condition $\delta_\omega = 1$ determines the value of t in the previous expressions. The resulting profiles for $q = 40$, $S = 9$, and $Pr = 1$ are plotted in Fig. 1a. Notice that the flame (at $y = 0$) is displaced toward the oxidizer side of the mixing layer. This is because the oxidizer and fuel diffusion fluxes must satisfy (13a) and, for the present moderately large S, this is possible only if the flame is in a region of small fuel concentration.

The previous solutions give vorticity and mixture fraction profiles of similar thickness when $Pr = O(1)$. This, however, is not a realistic representation of situations in which one or the two streams have been flowing parallel to a splitter plate or channel wall before forming the mixing layer. Then the vorticity at a short distance downstream the edge of the plate spreads over a boundary layer whose thickness depends on the length of the solid wall, whereas the diffusion of the species and the heat begins only around the trailing edge of the plate and extends therefore to a thinner sublayer. Assuming that the flow is laminar upstream, the thickness of this sublayer is $O(\epsilon^{1/3})$ in the nondimensional variables of the previous section, where $\epsilon = x/Re$ and x is the distance to the edge of the plate (Goldstein 1930). The structure of the laminar mixing layer for $Re \gg x \gg Re^{-1/2}$ (if only one of the fluids move) or for $Re \gg x \gg Re^{-1/4}$ (if the two fluids move) consists of a self-similar flow in this sublayer and one or two thicker layers of cold vortical flow. This solution can be computed by using asymptotic matching. Here, with a view to mimic the flow in the case of a stream of fuel discharging into stagnant oxidizer without having to construct a uniformly valid solution out of the different asymptotic expansions, we consider a base flow with velocity $u = 1 - 2df/d\xi$, where $f(\xi)$ and $Z(\xi)$ satisfy

$$\epsilon[F(Z)Z_\xi]_\xi + \frac{2}{3}PrfZ_\xi = 0 \ , \tag{16a}$$

$$\epsilon[F(Z)f_{\xi\xi}]_\xi + \left[\frac{2}{3}G + \frac{1}{2}\epsilon(1-G)\right]ff_\xi - \frac{1}{3}Gf_\xi{}^2 = 0 \ , \tag{16b}$$

$$Z = f_\xi = 0 \qquad \text{for} \quad \xi \to \infty \ , \tag{16c}$$

$$Z = f_\xi = 1 \qquad \text{for} \quad \xi \to -\infty \ , \tag{16d}$$

with

$$G = \frac{1}{2}\left\{1 + \tanh\left[\gamma\left(\xi_c^{3/2} + \frac{f}{f_\xi^{1/2}}\right)\right]\right\} \ ,$$

$1 \gg \xi_c \gg \epsilon^{1/3}$ and γ constants, and the condition $Z(0) = Z_{st}$ to fix the origin. Eqs. (16a,b) reduce to the ones describing Goldstein's self-similar flow in the distinguished limit $[f = \epsilon^{2/3}f_i, \xi = \epsilon^{1/3}\xi_i, (f_i, \xi_i) = O(1)]$ for $\epsilon \to 0$, in which $G \to 1$, and to Blasius' equation for an isothermal flow ($Z = 0$) in the distinguished limit $(f, \xi) = O(1)$ for $\epsilon \to 0$, in which $G \to 0$. Thus, in an approximate sense, the solution of (16) for small values of ϵ describes the whole flow. The artificial parameters $-\xi_c$ and γ control the position and abruptness of the transition between the two regions. Fig. 1b shows the solution of (16) for $q = 40$, $S = 9$, $Pr = 1$, $\epsilon = 2.2\text{x}10^{-3}$, $\xi_c = 0.33$, and $\gamma = 1$, normalized to have $\delta_\omega = 1$.

A linear stability analysis of both types of flows is carried out using the parallel flow approximation and neglecting transport effects for the perturbations. Squire's theorem holds for these zero Mach number flows and, therefore, it suffices to consider planar perturbations of the form $u = u_s(y) + \Delta u(x, y)$, etc., where the subscript s denotes here the base flow and $\Delta u(x, y) = \hat{u}(y)\exp[i\alpha(x - ct)] \ll 1$, with α real

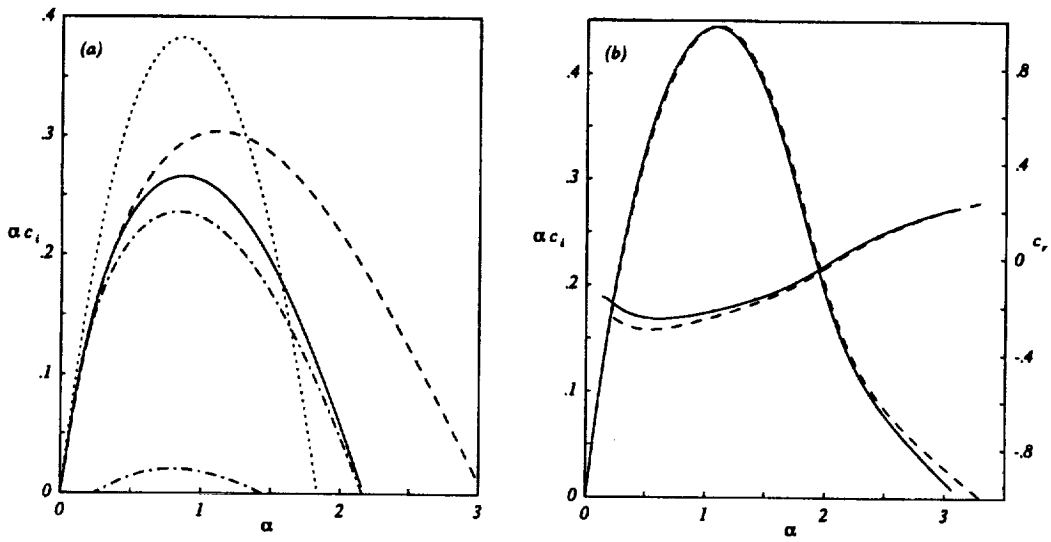

FIGURE 2. Growth rate as a function of the wave number for (*a*) the first type of base flow and (*b*) the second type of base flow. In (*a*), the cases depicted are ——— , $q = 40$, $S = 9$, $\sigma = 0$; - - - - , $q = 40$, $S = 9$, $\sigma = 1/2$; —·— , $q = 20$, $S = 4$, $\sigma = 0$; and ····· , $q = 0$. In (*b*) the cases depicted are ——— , $q = 40$, $S = 9$, $\sigma = 0$; and - - - - : $q = 40$, $S = 9$, $\sigma = 1/2$, and the phase speed is on the right-hand scale.

and c complex. After standard manipulations of the linearized equations, we end up with the eigenvalue problem

$$\begin{aligned} &(u_s - c)\left[(\rho_s \hat{v}')' - \rho_s \alpha^2 \hat{v}\right] - (\rho_s u_s')' \hat{v} = 0 \ , \\ &\hat{v} \to 0 \qquad \text{for} \quad y \to \pm\infty \ , \end{aligned} \tag{17}$$

where $\hat{v}$ is the transverse velocity perturbation. The resulting growth rate (αc_i) as a function of the wave number is plotted in Fig. 2a for several base flows of the first type discussed above and in Fig. 2b for base flows of the second type.

It was pointed out by Shin & Ferziger (1991) and Planché & Reynolds (1992) that the density-weighted vorticity $-\rho_s u_s'$ plays to a large extent the same role as the vorticity for a constant density flow. This quantity has two distinct peaks for sufficiently exothermic reactions with values of S not far from one, leading to two different unstable modes for a range of α bounded away from zero. Each mode is associated with one of the peaks and has a phase velocity closer to the velocity of the stream nearer to that peak. A remnant of the two peaks can be seen in Fig. 1a, and two unstable modes still exist for $q = 20$, $S = 4$ (Fig. 2a). However, the lower peak dominates for higher values of S, leaving only one unstable mode for each wave number. The corresponding eigenfunctions have their extremes around the flame position and around the peak of the weighted vorticity.

Another important feature is that the phase velocity of the perturbations depends on the wave number; it is negative for the cases of Fig. 2a and, contrarily to what

Case	σ ($\mu \propto T^\sigma$)	A_1	A_2	φ_1	Re	Base Flow
(a)	0.0	0.05	0.05	0	1000	1
(b)	0.0	0.15	0.05	0	1000	1
(c)	0.5	0.05	0.05	0	1000	1
(d)	0.5	0.15	0.05	0	1000	1
(e)	0.5	0.15	0.05	$\pi/2$	1000	1
(f)	0.5	0.15	0.05	0	2000	1
(C)	0.5	0.05	0.05	0	1000	2
(D)	0.5	0.15	0.05	0	1000	2

Table 1. Conditions for the various cases run. A_1 and A_2 are the subharmonic and fundamental amplitudes (see text) and φ_1 is the relative phase of the subharmonic. Base flow types (1 and 2) are described in §3.

can be seen in Fig. 2b, its absolute value increases with α. In general, the maximum growth rate increases by decreasing q or increasing S.

4. Numerical results and discussion

In all the cases discussed in this section the temperature of the two streams are equal ($T_o = 1$) and, unless otherwise specified, $q = 40$ and $S = 9$, leading to an adiabatic temperature of 5 times the free-stream temperature. This relatively high value of S is typical of many real situations; e.g., $S \sim 15$ for hydrocarbons burning in air. The Reynolds number is 1000 in all the computations except case (f) below, and $Pr = 1$. The length L of the computational domain is twice the wavelength of the most amplified small perturbation for the corresponding base flow. The initial perturbation is given by the eigenfunction of this mode normalized so that $\max|\hat{u}| = 1$ and multiplied by the amplitude $A_2 = 0.05$ plus that of its subharmonic taken with various amplitudes (A_1) and phases (φ_1). The specific conditions of each case are listed in the Table. The cross-stream boundary conditions are applied at $y = \pm 8$ in computations with the first type of initial conditions and at $y = -9$ and $y = 7$ in computations with the second type of initial conditions.

4.1. Global results

Global results for a number of simulations carried out with the first type of initial conditions are displayed in Fig. 3. Fig. 3a shows the time evolution of the mean momentum thickness ($\delta_m = \int_{-\infty}^{\infty}(1 - \overline{\rho}\,\overline{u}^2)\,dy$, the overbar meaning streamwise average) scaled with its initial value. As can be seen, the growth rate of the mixing layer is similar for all the cases displayed, and smaller than for a constant density fluid. Fig. 3b shows the overall rate of product generation (W),

$$W = \frac{1}{L}\int w\,dx\,dy = \frac{1}{L}\frac{d}{dt}\int \rho\tilde{Y}_p\,dx\,dy,$$

where

$$\tilde{Y}_p = \begin{cases} (1-Z)/(1-Z_{st}) & \text{if } Z > Z_{st}; \\ Z/Z_{st} & \text{if } Z < Z_{st}; \end{cases}$$

is proportional to the product mass fraction. Figs. 3c and 3d show the first two Fourier modes of the transversely averaged kinetic energy

$$E_k = \frac{1}{2}\int_{-\infty}^{\infty} \left\{ \left(\widehat{\rho^{1/2}u}\right)^2(k,y) + \left(\widehat{\rho^{1/2}v}\right)^2(k,y) \right\} dy \ ,$$

where the hat denotes streamwise Fourier transform. The modes in Figs. 3c-d correspond to the wave numbers of the most amplified perturbation ($k = 2$) and its subharmonic ($k = 1$).

The first peaks of the curves of Fig. 3c represent the roll-up of the vortices, which is accompanied by a first maximum of the product generation, and the first peaks of the curves of Fig. 3d represent the amalgamation of pairs of vortices. Cases (a) and (b) correspond to a constant viscosity fluid ($\sigma = 0$) with the amplitude of the subharmonic $A_1 = 0.05$ and 0.15, respectively. The amalgamation occurs earlier and the reaction rate has a tall peak shortly after the maximum of E_1 when the amplitude of the subharmonic is larger. Cases (c) and (d) are the analogs of (a) and (b) with a variable viscosity fluid ($\sigma = 0.5$), whereas case (e) differs from (d) only by a $\pi/2$ shift in the phase of the subharmonic. The effect of the initial phase shift is less obvious here than for a constant density fluid because the phase speed of the perturbations depends on the wave number and, therefore, the phase shift changes with time. However, a strong influence remains, as the change in phase results in a delay in the amalgamation and suppresses the tall peak of the rate of product generation. Case (f) has the same initial conditions as (d) but $Re = 2000$. The differences between the two reflect the influence of the viscosity, which may be strong at $Re = 1000$, especially when the viscosity increases with temperature.

In none of the cases presented does the flame sheet enter the cores of the vortices, and its surface never increases very much. This is because the relation (13a) implies that the flame must always be in regions of small fuel concentration since S is moderately large, and such regions are not easily ingested by the vortices when cushioned by a layer of low density fluid (see next subsection). Similarly, owing to (13b), the temperature gradient on the oxidizer side must be much larger than on the fuel side when q is large, a fact that is confirmed in Figs. 5 and 6 below. Under these conditions, the peaks along the flame in the product generation rate are due to the enhancement of the diffusion fluxes in regions of high strain on the flame surface. The strong dependence of this strain (and therefore the rate of product generation) on the amplitude and phase of the initial perturbations suggests that it is possible to control the combustion by manipulating the flow.

Further computations were carried out decreasing q (hence the flame temperature) at constant S, and decreasing q and S simultaneously to bring the flame closer to the center of the mixing layer while keeping the flame temperature constant. The results of the first series of computations, similar to (a) but with q equal to 20 and 30, show features approaching those of an incompressible flow as q decreases: the

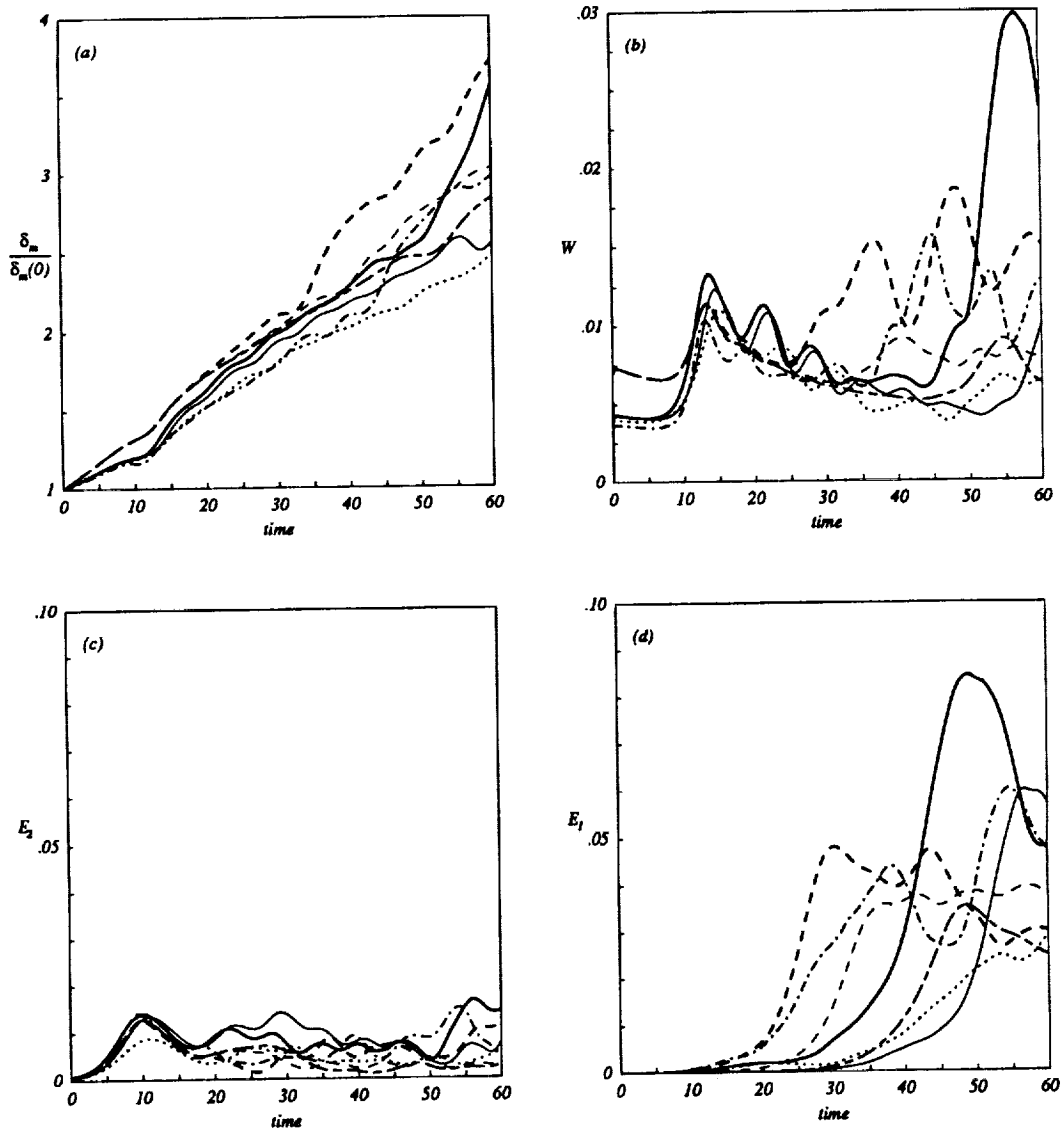

FIGURE 3. Evolution of (a) the scaled momentum thickness, (b) the overall rate of product generation, (c) the kinetic energy in the second Fourier mode, and (d) the kinetic energy in the first Fourier mode, for cases: —— (a); —— (b); ---- (c); ---- (d); —-— (e); —·— (f); ····· (g).

vortices get rounder than in Fig. 5 below, the layer grows faster, and the fuel lean region containing the flame is more easily wrinkled and stretched by the flow, which results in higher rates of product generation. The second series of computations, $(q, S) = (20, 4)$, $(12, 2)$, and $(8, 1)$, show that the amalgamation is retarded or suppressed and the rate of product generation decays with oscillations after peaking at

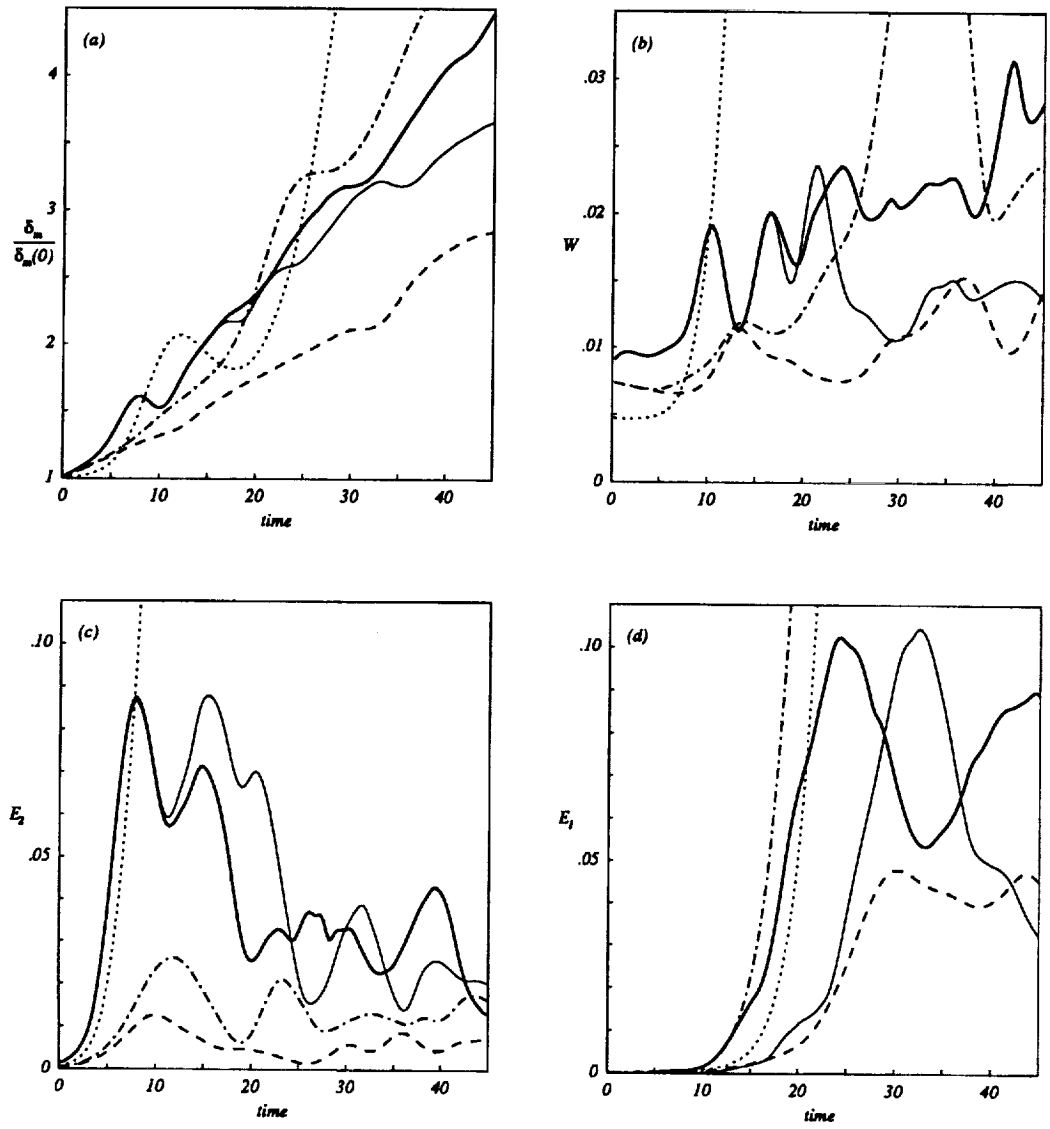

FIGURE 4. Evolution of (a) the scaled momentum thickness, (b) the overall rate of product generation, (c) the kinetic energy in the second Fourier mode, and (d) the kinetic energy in the first Fourier mode, for cases: —— (C); —— (D); ---- (d); —·— (d'); and ····· a constant density flow.

roll-up when S begins to decrease (case (g) in Fig. 3b is the first case of this series; for still smaller values of S the roll-up also disappears, apparently giving way to the two-colayers regime discussed by Planché & Reynolds (1992)).

Fig. 4 shows the same quantities as Fig. 3 for two runs carried out with initial conditions of the second type: cases (C) and (D) are analogous to (c) and (d); i.e.,

$\sigma = 1/2$ and the amplitude of the subharmonic equal to 0.05 and 0.15, respectively. For comparison, the results of case (d) have been repeated in this figure (dashed lines), and the results for a constant density fluid ($q = 0$, $S = 9$) have also been included (dotted lines). Finally the dash-and-dot lines correspond to case (d') discussed below. As can be seen, the growth of the mixing layer is faster than for the first type of initial conditions, and similar to that of a constant density fluid for times up to about 20. The amplitude of the second mode of the kinetic energy (E_2) is also higher, of the order of the amplitude of the first mode (E_1), reflecting a more efficient roll-up and the presence of round vortices at least during part of the evolution. The two peaks of E_2 reflect another characteristic feature of this flow that will be commented on below.

4.2. Mechanics of the flow

Fig. 5 shows the evolution of the vorticity and the temperature for case (f), which is typical of the first type of initial conditions. In accordance with the results of the linear analysis, the vortices move with a velocity closer to that of the fuel stream (the lower stream in Fig. 5) than to that of the oxidizer stream (the structures move to the left). Furthermore, the interaction of the vortical region of the layer with the fuel side (lower) is typical of the constant density flow, with large excursions of free-stream fluid into the layer, whereas on the oxidizer side (where the flame is), these large-scale incursions are not so pronounced. The hydrodynamic mixing layer grows by entraining free-stream fluid as the vortices roll-up and amalgamate. On the oxidizer side, however, the heat release of the flame and the associated volumetric expansion of the surrounding fluid acts as a source of fluid volume to be entrained. Thus this low-density fluid below the flame, which is easier to entrain than the free-stream cold fluid, acts as a buffer between the mixing layer and the flame, inhibiting the entrainment of the flame and free-stream fluid.

The light fluid enters each vortex in the form of a jet to its upper right, turns around the vortex to the left on the lower side, and splits into a recirculating flow around the vortex core and a blob of light fluid that leaves the vortex to the lower left ($t = 9$ to 15). The heavy fluid entering a vortex at its lower left turns over the top to the right and tends to escape as a tongue by its upper right ($t = 15$). The light fluid appears to be more easily turned and engulfed by the vortices than the heavy fluid, as might be expected given the difference in density. The right-ward moving tongue at the top throttles the ingestion of new light fluid from the upper right ($t = 15$), and similarly, the left-ward moving blob of light fluid temporarily suspends the ingestion of new heavy fluid.

The general effect of these combined motions of light and heavy fluid is to make the temperature field structures more elongated than for a constant density fluid. The numerical results show a variety of situations depending on the order in which the supplies of light and heavy fluid to a given vortex are interrupted and restored, which in turn depends on the initial conditions and on the Reynolds number. The supply of light fluid can be interrupted more than once before two neighboring vortices amalgamate. Thus, in case (b) (not displayed), a tongue of heavy fluid separates completely from a vortex, restoring the ingestion of light fluid, but it

remains cold on leaping over the next vortex to the right (which is undergoing a similar evolution), so that, along with some newly ingested fluid from the lower stream, it throttles the supply of light fluid to this vortex for a second time. For their part, the blobs of light fluid in the lower part of the layer cool down while moving toward the left and undergo a further splitting in this case, being partially ingested by the next vortex to the left of that which shed the blob.

The right-ward motion of the tongues of heavy fluid over the vortices also determines the end of the roll-up process, and when this happens sections of the original vorticity layer are left unrolled between the tongues and the flame. It seems likely that through this mechanism the phase of the subharmonic in the initial condition may induce differences in the amount of vorticity rolled in each vortex and, thereby, in the subsequent evolution of the mixing layer. The unrolled vorticity patches correspond to regions of strong shear that move toward the right relative to the vortices, leap from vortex to vortex, and are selectively reinforced by the baroclinic torque. At sufficiently high Reynolds numbers some of these patches eventually roll up into secondary vortices located one or more periods to the right of the vortex to which they were initially tied (upper left of Fig. 5b at $t = 18$ to 21).

The evolution leading to the premature termination of the roll-up and the disruption of the rolled and unrolled vorticity can also be described in terms of the vorticity; see comments on Fig. 6 below. Here we note that in general the distributions of both $\nabla \times \mathbf{v}$ and $\nabla \cdot \mathbf{v}$ are required to reconstruct the velocity field. The vorticity is initially present in the flow, and its dynamics are essentially inviscid through convection and the baroclinic torque. In contrast, in the absence of compressibility effects, the changes in the density of a fluid particle are due to temperature changes, which are brought about by heat conduction. Thus at sufficiently high Reynolds numbers, heat conduction, and hence $\nabla \cdot \mathbf{v} = -\frac{1}{\rho}\frac{D\rho}{Dt}$, should be confined to very thin layers (which can only have a small effect on the large-scale dynamics of the flow) and, in a fully developed flow, to the smallest scales (which cannot influence the large-scale dynamics by this means because the net change of volume is negligible). This points toward a decreasing importance of $\nabla \cdot \mathbf{v}$ as the Reynolds number increases. Though $Re = 2000$ is probably not sufficiently high to claim independence of $\nabla \cdot \mathbf{v}$, the evolution depicted in Fig. 5 is probably more affected by the motion of the counterrotating vortex pairs that appear in the flow than by the dilatation or contraction of the fluid particles. Such pairs arise due to the baroclinic torque ($-\nabla T \times \nabla p$ in the vorticity equation), which, owing to the low pressure at the vortex centers, is positive in the lower halves of the light fluid jets entering the vortices and in most of the heated region above the flame, and negative in the upper halves of the jets and below the flame. This leads to production of positive vorticity in the former regions, which forms left-ward moving pairs with the rolled vorticity of the layer and, to a lesser extent, right-ward moving pairs with the unrolled vorticity.

It seems that in some cases, though not in the one displayed in Fig. 5, the unrolled layers of vorticity act as precursors to the amalgamation by establishing bridges

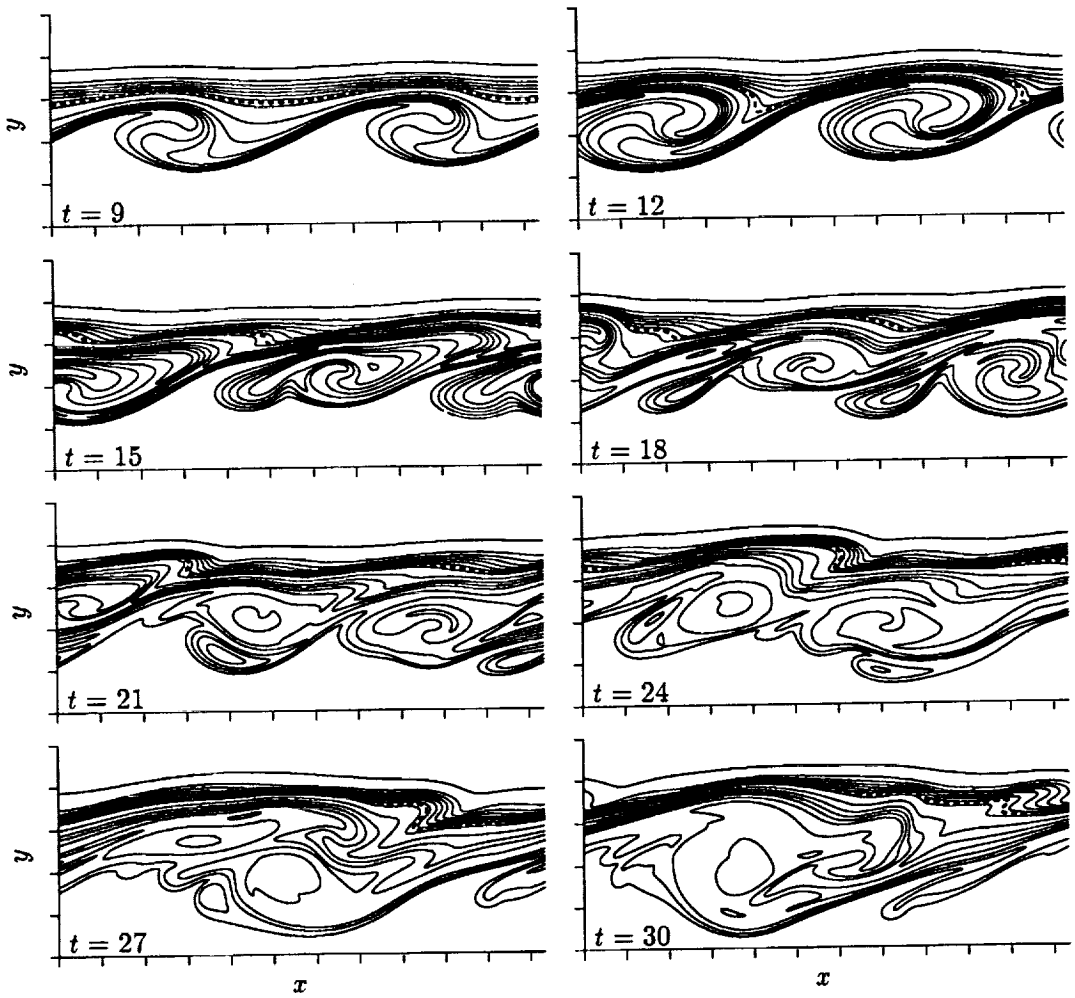

FIGURE 5(*a*). Evolution of the temperature in case (*f*). The contour increment is 0.5 and the free-stream temperature is 1. The flame location is indicated by the heavy dashed line.

between adjacent vortices with the right end of a bridge rolling around the vortex that will come to the bottom of the pair while the left end is still connected to the vortex that will come to the top. Any nearby secondary vortex that might have formed as well as the remnants of warm fluid blobs shed by other vortices are typically ingested in the amalgamation process.

The result of the amalgamation is a vortex much less organized than for a constant density fluid. It contains several vorticity peaks and layers of positive vorticity left over by the secondary vortices and vortex pairs that existed at earlier times ($t = 27$ to 30). However, the large-scale behavior of the new vortex does not differ qualitatively from that of the previous ones: as far as it can be followed in the

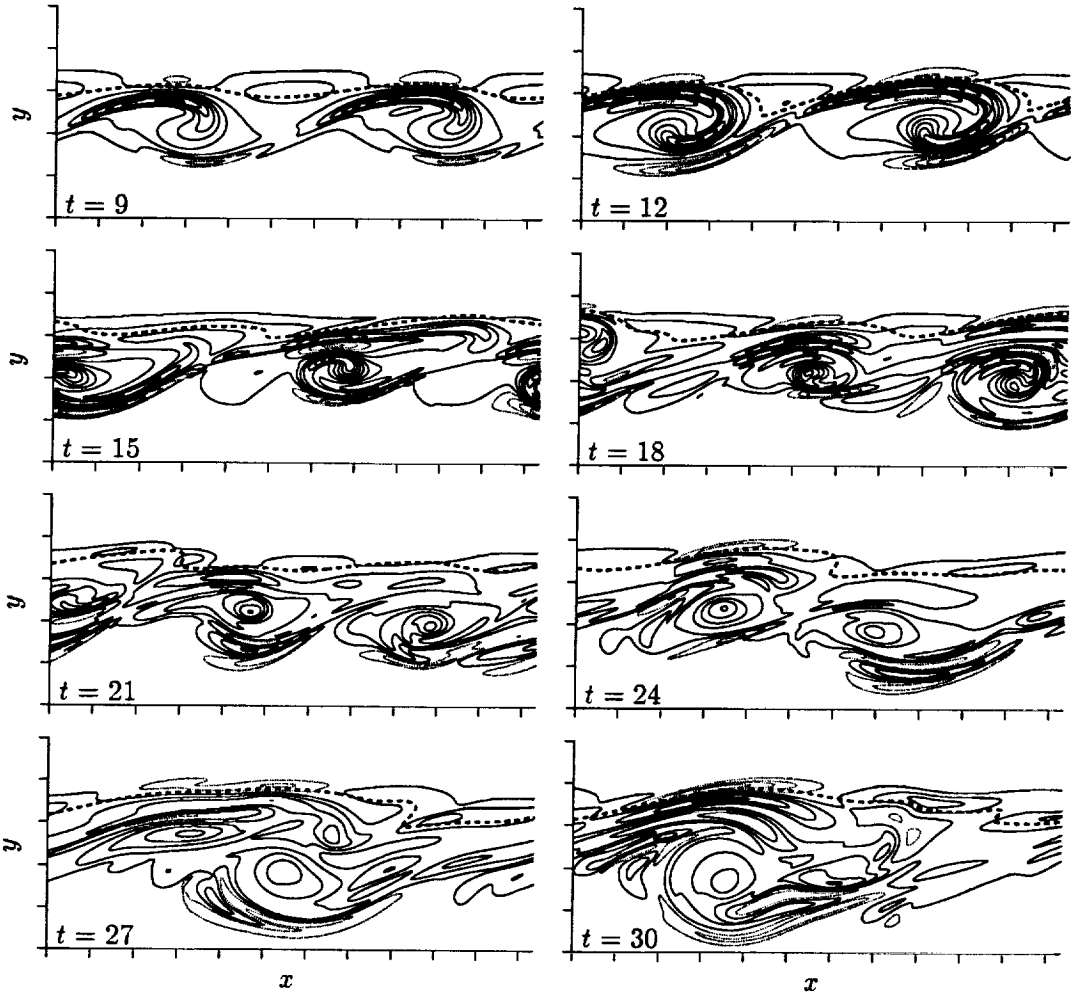

FIGURE 5(*b*). Evolution of the vorticity in case (*f*). The contour increment is 0.6 and positive contours are dotted. The flame location is indicated by the heavy dashed line.

present simulations, the vortex grows by ingesting light and heavy fluid until it ends up filling the computational domain.

To try to ascertain the importance of the baroclinic torque, the momentum Eq. (2) was artificially modified, replacing the pressure gradient term by $-\rho\nabla p$. This amounts to having a constant density fluid insofar as the pressure forces are concerned. No baroclinic term appears then in the vorticity equation (obtained by taking the curl of the modified momentum equation), but the term $-\omega\nabla\cdot\mathbf{v}$ due to the gas expansion is left unaltered, as well as the effect of $\nabla\cdot\mathbf{v}$ in the other conservation equations. Case (*d*) was rerun with this modification (it is denoted by (*d'*) in what follows) and some results are shown in Fig. 4 (dash-and-dot lines; the

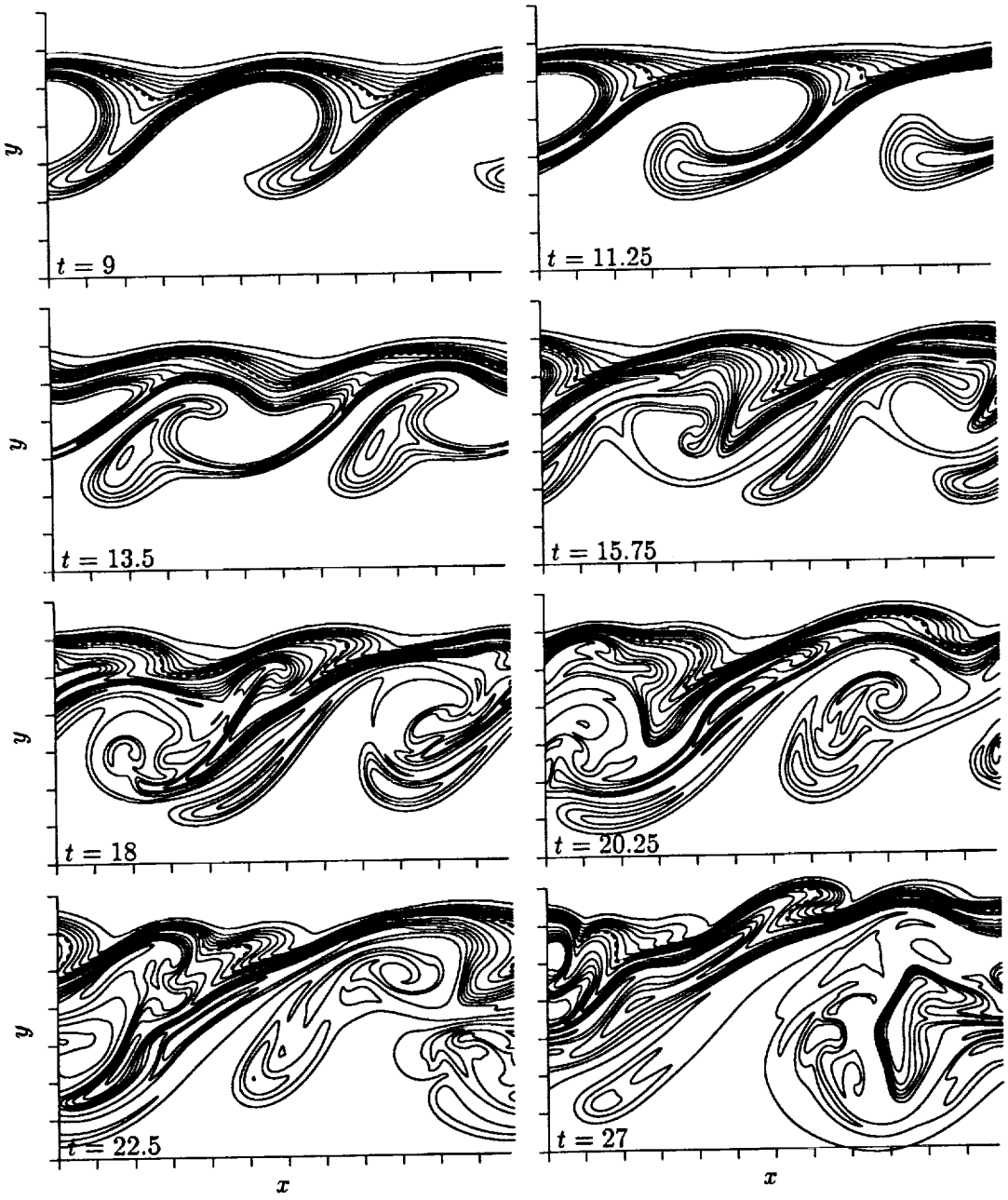

FIGURE 6(*a*). Evolution of the temperature in case (*D*). The contour increment is 0.5 and the free-stream temperature is 1. The flame location is indicated by the heavy dashed line.

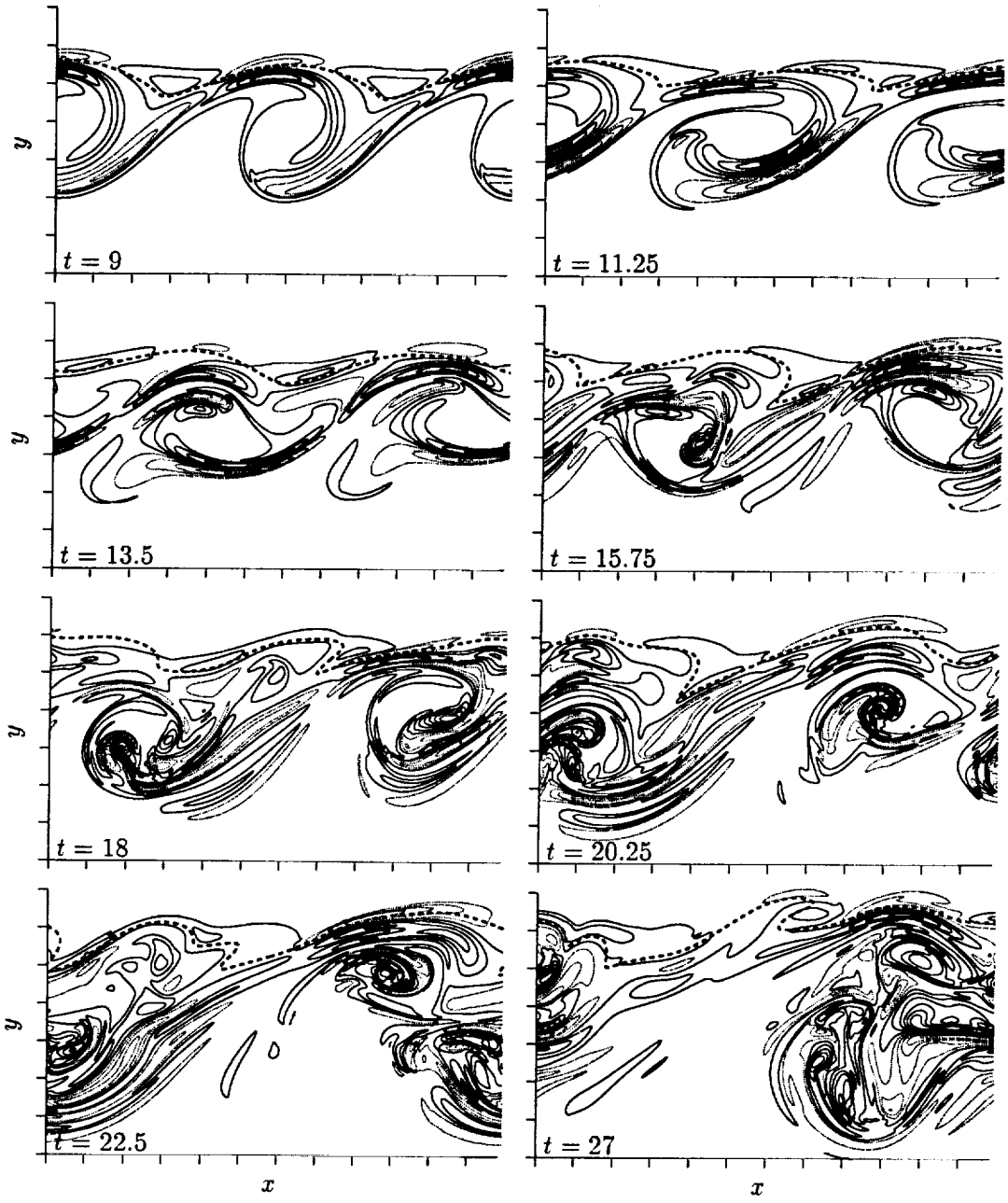

FIGURE 6(*b*). Evolution of the vorticity in case (*D*). The contour increment is 0.8 and positive contours are dotted. The flame location is indicated by the heavy dashed line.

dashed lines correspond to case (d)). As can be seen, the growth rate of the layer and the rate of product formation increase very much due to the modification, and inspection of the vorticity fields reveals that the vortices and the general appearance of the flow are closer to a constant density fluid than to case (d).

Fig. 6 shows the evolution of the vorticity and the temperature for case (D), the analog of (d) with an initial condition of the second type. Contrary to Fig. 5, the bulk of the initial vorticity is now in the low temperature fuel. The Kelvin-Helmholtz instability begins to develop as for a constant density fluid, leading to relatively round structures (for $t = 9$ and before) that are responsible for the first peak of E_2 in Fig. 4c. Very soon, however, the deflection of the light fluid around the flame leads to tongues where new vorticity is generated by the baroclinic torques in the form of counterrotating pairs. It is worth noting that this occurs in regions that would be relatively free of vorticity in a constant density fluid. The vortex pairs are more prominent than in Fig. 5 and clearly dominate the flow. They travel toward the left deep in the fuel stream ($t = 11.25$) before the dominant negative vorticity brings them back toward the shear layer, and in so doing, they make the elongated structures responsible for the dip of E_2 and engulf large amounts of cold fuel that are subsequently incorporated into the mixing layer. On returning to the shear layer, each of the regions of light fluid has the appearance of a mushroom with a very thin stalk. The high pressure above the cap of the mushroom splits it into a recirculating tongue and a shed blob, each with its associated vortex pair. The high pressure also squeezes substantial parts of the high temperature strip around the flame, increasing the diffusion fluxes and the burning rate while the parts of the strip between two pressure maxima get compressed and sucked by the depressions at the centers of the forming vortices. This leads to secondary tongues of light fluid (that begin forming at about $t = 13.5$ in Fig. 6a) where the baroclinic torques generate new counterrotating vortex pairs. Between $t = 15.75$ and $t = 18$, each secondary tongue is pinched off by a high pressure region and the recirculating part of one of the primary tongues, which splits again in this process into a layer leaving the vortex by its upper right and another that winds around along with the segmented secondary tongue. The process of formation of a secondary tongue and splitting of the recirculating flow occurs once again during this computation, and since there are several vortex pairs winding around, the vortex cores in Fig. 6b have for some time a multilayered structure until diffusion cancels vorticity of opposite signs (and temperature differences) leaving cores of predominantly negative vorticity ($t = 27$).

Finally these cores undergo a pairing, during which one or two more counterrotating vortex pairs are formed and ingested from the upper right of the forming vortex. At later times (not shown) these new pairs will become the front of a new tongue that heads toward the lower core moving toward the lower left while light fluid comes in behind and rolls around the surviving upper vortex. The result is an elongated structure with an associated decrease of E_1 in Fig. 4d.

Parts of the high temperature strip around the flame are alternatively strained and compressed by the evolving flow, and patches of fluid separate from this strip to form the tongues, but as was mentioned before, the flame itself remains outside

the vortex cores at least in the part of the evolution covered by these computations. This fact makes the flow in the vortices below the flame similar to a mixing layer between two fluids of different densities. To assess the extent of the similarity, further computations were carried out for an inert flow: $q = 0$ in the formulation of sec. 2 but $T_o = 5$, so that the maximum temperature of the fluid equals the flame temperature of the previous reacting flow simulation. Except for the absence of baroclinic vorticity production around the flame, the results of this simulation (not displayed) have the same general appearance as those of Fig. 6, though minor differences do occur.

Acknowledgments

We are indebted to Prof. A. Liñán for his continuous guide and advice and to Prof. J. Jiménez for enlightening discussions during the summer program.

REFERENCES

BROADWELL, J. E. & BREIDENTHAL, R. E. 1982 A simple model of mixing and chemical reaction in a turbulent shear layer. *J. Fluid Mech.* **125,** 397–410.

BROADWELL, J. E. & MUNGAL, M. G. 1991 Large-scale structures and molecular mixing. *Phys. Fluids A.* **3,** 1193–1206.

DELHAYE, B., VEYNANTE, D. & CANDEL, S. M. 1994 Simulation and modeling of reactive shear layers. *Theoret. Comput. Fluid Dynamics.* **6,** 67–87.

DIMOTAKIS, P.E. 1986 Two-dimensional shear-layer entrainment . *AIAA J.* **24,** 1791–1796.

DIMOTAKIS, P. E. 1991 Turbulent free shear layer mixing and combustion. In High-Speed Flight Propulsion Systems, Murthy, S. N. B., and Curran, E. T., eds, AIAA Inc.. *Progress in Astronautics and Aeronautics.* **137,** 265–340.

GHONIEM, A. F. & GIVI, P. 1988 Lagrangian simulation of a reacting mixing layer at low heat release. *AIAA J.* **26,** 690–697.

GIVI, P., JOU, W.-H. & METCALFE, R. W. 1986 Flame extinction in a temporally developing mixing layer. *Proc. 21nd. Int. Symp. Combustion.* The Combustion Institute, Pittsburgh. 1251–1261.

GRINSTEIN, F. F. & KAILASANATH, K. 1992 Chemical heat release and dynamics of transitional reactive shear flows. *Phys. Fluids A.* **4,** 2207–2221.

GOLDSTEIN, S. 1930 Concerning some solutions of the boundary layer equations in hydrodynamics. *Proc. Camb. Phil. Soc.* **26,** 1–30.

HERMANSON, J. C. & DIMOTAKIS, P. E. 1989 Effects of heat release in a turbulent, reactive shear layer. *J. Fluid Mech.* **199,** 333–375.

MARBLE, F. & BROADWELL, J. E. 1977 The coherent flame model for turbulent chemical reaction. Report No. TRW-9-PU. Project SQUID.

MASUTANI, S. M. & BOWMAN, C. T. 1986 The structure of a chemically reacting plane mixing layer. *J. Fluid Mech.* **172,** 93–126.

McMURTRY, P. A., JOU, W.-H., RILEY, J. J. & METCALFE, R. W. 1986 Direct numerical simulation of a reacting mixing layer with chemical heat release. *AIAA J.* **24,** 962–970.

McMURTRY, P. A., RILEY, J. J. & METCALFE, R. W. 1989 Effects of heat release on the large-scale structure in a turbulent mixing layer. *J. Fluid Mech.* **199,** 297–332.

MUNGAL, M. G. & DIMOTAKIS, P. E. 1984 Mixing and combustion with low heat release in a turbulent shear flow. *J. Fluid Mech.* **148,** 349–382.

MUNGAL, M. G. & FRIELER, C. E. 1988 The effects of Damkóhler number in a turbulent shear layer. *Comb. Flame.* **71,** 23–34.

MUNGAL, M. G., HERMANSON, J. C. & DIMOTAKIS, P. E. 1985 Reynolds number effects on mixing and combustion in a reacting shear layer. *AIAA J.* **23,** 1418–1423.

PLANCHÉ, O. H. & REYNOLDS, W. C. 1992 A numerical investigation of the compressible reacting mixing layer. Report TF-56. Dept. Mech. Engn. Stanford University, CA.

RILEY, J. J., METCALFE, R. W. & ORSZAG, S. A. 1986 Direct numerical simulations of chemically reacting turbulent mixing layers. *Phys. Fluids.* **29,** 406–422.

SHIN, D. S. & FERZIGER, J. H. 1991 Linear stability of the reacting mixing layer. *AIAA J.* **29,** 1634–1642.

WALLACE, A. K. 1981 Experimental investigation on the effects of chemical heat release in the reacting turbulent plane shear layer. Ph. D. Thesis. U. Adelaide.

WILLIAMS, F. A. 1985 *Combustion Theory,* 2nd ed. Benjamin/Cummings, Menlo Park CA.

53-25
29773
N95-21038

Direct numerical simulations of turbulent non-premixed methane-air flames modeled with reduced kinetics

By J. M. Card[1], J. H. Chen[1], M. Day[2], AND S. Mahalingam[3]

Turbulent non-premixed stoichiometric methane-air flames modeled with reduced kinetics have been studied using the direct numerical simulation approach. The simulations include realistic chemical kinetics, and the molecular transport is modeled with constant Lewis numbers for individual species. The effect of turbulence on the internal flame structure and extinction characteristics of methane-air flames is evaluated. Consistent with earlier DNS with simple one-step chemistry, the flame is wrinkled and in some regions extinguished by the turbulence, while the turbulence is weakened in the vicinity of the flame due to a combination of dilatation and an increase in kinematic viscosity. Unlike previous results, reignition is observed in the present simulations. Lewis number effects are important in determining the local stoichiometry of the flame. The results presented in this work are preliminary but demonstrate the feasibility of incorporating reduced kinetics for the oxidation of methane with direct numerical simulations of homogeneous turbulence to evaluate the limitations of various levels of reduction in the kinetics and to address the formation of thermal and prompt NO_x.

1. Introduction

During the 1992 CTR summer program we studied the influence of finite-rate chemistry and transient effects on the structure of a turbulent non-premixed flame using DNS (Chen et al. 1992a, 1992b, Mahalingam et al. 1994). In this DNS, the combustion chemistry was approximated by an Arrhenius single- and two-step model. While these simple mechanisms provide useful insights for modeling under conditions ranging from near equilibrium to near extinction, they do not, however, relate the flame structure and extinction characteristics to the underlying elementary chemical-kinetic steps (typically more than 100 reactions) necessary to describe the combustion process in hydrocarbons. But the incorporation of such detailed chemistry for simulations at turbulent Reynolds numbers of practical interest is technologically infeasible at the present time. Thus, it is desirable to introduce reduced chemical-kinetic mechanisms for the description of the combustion chemistry (Smooke 1991). These mechanisms are deduced from a detailed mechanism by

1 Sandia National Laboratories
2 Stanford University
3 University of Colorado at Boulder

the systematic application of steady-state approximations for intermediate species. The combustion kinetics are then described by a few (two to five) global reactions, in which only the most elementary kinetic steps are retained and the concentrations of various intermediate species are represented by algebraic relations.

Computations employing reduced mechanisms have successfully been accomplished for laminar, planar hydrocarbon, and hydrogen flames (Peters and Rogg 1993). Recent progress has also been made using reduced kinetics in simulations of reacting flows of $H_2 - O_2$ systems (Baum *et al.* 1992, and Montgomery *et al.* 1993).

The primary objective of this study is to evaluate the effect of different levels of reduction of fuel oxidation kinetics on methane-air turbulent diffusion flame structure and extinction characteristics.

2. Reduced chemistry for flame structure

The oxidation of methane can be described by the following reduced mechanism (Seshadri and Peters 1988):

$$\mathrm{CH_4 + 2H + H_2O \rightleftharpoons CO + 4H_2}, \qquad \mathrm{I'}$$

$$\mathrm{CO + H_2O \rightleftharpoons CO_2 + H_2}, \qquad \mathrm{II'}$$

$$\mathrm{2H + M \rightleftharpoons H_2 + M}, \qquad \mathrm{III'}$$

$$\mathrm{O_2 + 3H_2 \rightleftharpoons 2H + 2H_2O}. \qquad \mathrm{IV'}$$

These global reactions were deduced from a 40-some-step starting mechanism by the systematic application of steady-state assumptions for the intermediate species. The global rates for the above reaction can be expressed in terms of the elementary rates shown in Table 1, namely

$$\omega_{\mathrm{I'}} = \omega_{\mathrm{I}} = k_{38f}[\mathrm{CH_4}][\mathrm{H}], \qquad (1)$$

$$\omega_{\mathrm{II'}} = \omega_{\mathrm{II}} = (k_{18f}/K_3)[\mathrm{H}]([\mathrm{CO}][\mathrm{H_2O}]/[\mathrm{H_2}] - [\mathrm{CO_2}]/(K_{18}/K_3)), \qquad (2)$$

$$\omega_{\mathrm{III'}} = \omega_{\mathrm{III}} = k_{5f}[\mathrm{H}][\mathrm{O_2}][M], \qquad (3)$$

$$\omega_{\mathrm{IV}} = k_{1f}[\mathrm{H}]([\mathrm{O_2}] - [\mathrm{H}]^2[\mathrm{H_2O}]^2/[\mathrm{H_2}]^3 K_1 K_2 K_3^2), \qquad (4)$$

where partial equilibria were assumed for elementary steps (2) and (3). In the above rates, the K's are equilibrium constants, the k's are the elementary rate constants, in which the numbering is selected to agree with Peters and Rogg (1993), and where i is the concentration of species i. Moreover, the concentration of the third body is $[M] = 6.5[\mathrm{CH_4}] + 6.5[\mathrm{H_2O}] + 1.5[\mathrm{CO_2}] + 0.75[\mathrm{CO}] + 0.4[\mathrm{O_2}] + 0.4[\mathrm{N_2}] + 1.0[\mathrm{other}]$.

If we further assume that the H atom is in steady state, we get

$$\omega_{\mathrm{IV'}} = \omega_{\mathrm{I'}} + \omega_{\mathrm{III'}},$$

and the four-step mechanism reduces to the three-step approximation

$$\mathrm{CH_4 + O_2 \rightleftharpoons CO + H_2 + H_2O}, \qquad \mathrm{I}$$

$$CO + H_2O \rightleftharpoons CO_2 + H_2, \qquad \text{II}$$

$$O_2 + 2H_2 \rightleftharpoons 2H_2O, \qquad \text{III}$$

with rates for steps I, II, and II given by Eqs. (1-3), respectively.

Equations (1),(3), and (4) may be employed to show that

$$[H] = (1 - k_{38f}[CH_4]/(k_{1f}[O_2]) - k_{5f}[M]/k_{1f})^{1/2}\,[O_2]^{1/2}[H_2]^{3/2}(K_1K_2)^{1/2}K_3/[H_2O].$$

Assuming partial equilibrium for the water-gas shift (eq. II) results in a two-step mechanism, and a one-step mechanism may be obtained by assuming H_2 (and hence, CO also) to be in steady state. The rate for the global step $CH_4 + 2O_2 \rightarrow CO_2 + 2H_2O$ is taken from Bui-Pham (1992), namely, $k = 5.2 \times 10^{13}\exp(-14906/T)$ (units are moles, cm, s , degK, and KJ/mole). For comparative purposes, future calculations will consider the rate constant determined by Puri (1987).

The four-, three-, and 1-step kinetic mechanisms and the corresponding global rates are the basis for the present study.

3. Governing equations and numerical method

The governing equations are the continuity, momentum, species, and energy equations written in Cartesian tensor notation as follows:

$$\frac{\partial \rho}{\partial t} + \frac{\partial \rho u_j}{\partial x_j} = 0\,, \tag{5}$$

$$\frac{\partial \rho u_i}{\partial t} + \frac{\partial \rho u_i u_j}{\partial x_j} = -\frac{\partial p}{\partial x_i} + \frac{\partial \tau_{ij}}{\partial x_j}\,, \tag{6}$$

$$\frac{\partial \rho Y_\alpha}{\partial t} + \frac{\partial \rho Y_\alpha u_j}{\partial x_j} = -\frac{\partial}{\partial x_j}(\rho Y_\alpha V_{\alpha j}) + \dot{\omega}_\alpha \tag{7}$$

$$\frac{\partial \rho e_t}{\partial t} + \frac{\partial (\rho e_t + p) u_j}{\partial x_j} = \frac{\partial (u_i \tau_{ij})}{\partial x_j} - \frac{\partial q_j}{\partial x_j} \tag{8}$$

where

$$\tau_{ij} = \mu\Big(\frac{\partial u_i}{\partial x_j} + \frac{\partial u_j}{\partial x_i} - \frac{2}{3}\delta_{ij}\frac{\partial u_k}{\partial x_k}\Big)\,, \tag{9}$$

is the stress tensor,

$$e_t = e + \frac{1}{2}\sum_{k=1}^{3} u_k^2, \quad e = \sum_{\alpha=1}^{N} Y_\alpha h_\alpha - \frac{p}{\rho} \tag{10}$$

is the total energy per unit mass of the mixture, e is the internal energy per unit mass, h_α is the enthalpy of species α given by,

$$h_\alpha = h_\alpha^0 + \int_{T^0}^{T} C_{p\alpha}(T')dT', \quad \alpha = 1, \cdots, N \tag{11}$$

where h_α^0 and $C_{p\alpha}$ are the corresponding enthalpy of formation and specific heat at constant pressure respectively. The heat flux vector is given by

$$q_j = -\lambda \frac{\partial T}{\partial x_j} + \rho \sum_{\alpha=1}^{N} h_\alpha Y_\alpha V_{\alpha j} \tag{12}$$

and the species diffusion velocity is

$$V_{\alpha j} = -D_{\alpha N} \frac{1}{Y_\alpha} \frac{\partial Y_\alpha}{\partial x_j}, \quad \alpha = 1, \cdots N-1 \tag{13}$$

where $D_{\alpha N}$ is the binary diffusion coefficient between species α and the N-th species taken to be nitrogen. To ensure that the net diffusion velocity is zero, the constraint $\sum_{\alpha=1}^{N} Y_\alpha V_{\alpha j} = 0$ is enforced to obtain V_{Nj}. The equation of state is

$$p = \rho R T \tag{14}$$

where R is the mixture gas constant given by

$$R = R^0/\bar{W}, \quad \bar{W} = \left[\sum_{\alpha=1}^{N} \left(\frac{Y_\alpha}{W_\alpha} \right) \right]^{-1} \tag{15}$$

where R^0 is the universal gas constant, $\bar{W}$ is the average molecular weight of the mixture, and W_α is the species molecular weight. The mixture averaged thermal conductivity is modeled through the approximation suggested by Smooke and Giovangigli (1991),

$$\lambda = \bar{C}_p A \left(\frac{T}{T_0} \right)^r \quad \bar{C}_p(T) = \sum_{\alpha=1}^{N} Y_\alpha C_{p\alpha}(T) \tag{16}$$

where $A = 2.58 \times 10^{-4}$ g/cm-sec, $r = 0.7$, and $\bar{C}_p$ is the specific heat of the gaseous mixture. The individual species specific heats are obtained as polynomial functions of temperature using the Chemkin thermodynamic database (Kee *et al.* 1987). The diffusion coefficients are obtained by prescription of Lewis numbers for individual species through

$$D_{\alpha N} = \frac{\lambda}{\bar{C}_p \rho L e_\alpha}. \tag{17}$$

The Lewis number data is obtained from Smooke and Giovangigli (1991). For the one-step mechanism, the Lewis numbers for CH_4, O_2, CO_2, and H_2O are 0.97, 1.11, 1.39, and 0.83, respectively, for the three-step mechanism, the additional Lewis numbers for H_2 and CO (0.3 and 1.1, respectively) were employed, and for the four-step mechanism, the Lewis number for H is 0.18. The other symbols in these equations have the usual meaning.

For the three-step reduced mechanism, conservation equations for six reacting species is considered (CH_4, O_2, CO_2, CO, H_2, and H_2O) and the mass fraction of

N_2 is obtained through the relationship $\sum_{\alpha=1}^{N} Y_\alpha = 1$, where $N = 7$. Based on the discussion in the previous section, the reaction rates for the six species is computed through the following expressions:

$$\dot{\omega}_{CH_4} = -W_{CH_4}\dot{\omega}_I, \quad \dot{\omega}_{O_2} = -W_{O_2}[\dot{\omega}_I + \dot{\omega}_{III}], \quad \dot{\omega}_{CO_2} = W_{CO_2}\dot{\omega}_{II},$$

$$\dot{\omega}_{CO} = W_{CO}[\dot{\omega}_I - \dot{\omega}_{II}], \quad \dot{\omega}_{H_2} = W_{H_2}[\dot{\omega}_I + \dot{\omega}_{II} - 2\dot{\omega}_{III}], \tag{18}$$

and,

$$\dot{\omega}_{H_2O} = W_{H_2O}[\dot{\omega}_I - \dot{\omega}_{II} + 2\dot{\omega}_{III}].$$

For the four-step mechanism, $N = 8$, and seven reacting species (CH_4, O_2, CO_2, CO, H_2, H_2O, and H) are considered. The reaction rate for these species is given by:

$$\dot{\omega}_{CH_4} = -W_{CH_4}\dot{\omega}_I, \quad \dot{\omega}_{O_2} = -W_{O_2}\dot{\omega}_{IV}, \quad \dot{\omega}_{CO_2} = W_{CO_2}\dot{\omega}_{II},$$

$$\dot{\omega}_{CO} = W_{CO}[\dot{\omega}_I - \dot{\omega}_{II}], \quad \dot{\omega}_{H_2} = W_{H_2}[4\dot{\omega}_I + \dot{\omega}_{II} + \dot{\omega}_{III} - 3\dot{\omega}_{IV}], \tag{19}$$

and,

$$\dot{\omega}_{H_2O} = W_{H_2O}[2\dot{\omega}_{IV} - \dot{\omega}_{II} - \dot{\omega}_I], \quad \dot{\omega}_H = 2\dot{\omega}_{IV} - 2\dot{\omega}_I - 2\dot{\omega}_{III}.$$

The dimensionless form of the governing equations is obtained through definition of appropriate reference quantities based on the air stream properties. The sound speed at infinity a_∞, corresponding density ρ_∞, and the dynamic pressure $\rho_\infty a_\infty^2$ are used for the velocity, density, and pressure reference quantities. The reference temperature is $(\gamma_\infty - 1)T_\infty$ where γ_∞ is the ratio of specific heats at temperature T_∞ of the air stream. The reference fluid properties used are μ_∞, λ_∞, and $C_{p\infty}$ corresponding to air at temperature T_∞. A reference length scale L_{ref} is chosen to be the distance between the fuel and oxidizer jets in the opposed diffusion flame used to initialize all the dependent variables in the computational domain. The equations are solved using a standard sixth-order accurate compact finite differencing scheme (Lele, 1992) for approximating spatial derivatives, and a third-order Runge-Kutta scheme for time advancement. A modified version of the Navier-Stokes Characteristic Boundary Condition (NSCBC) procedure originally developed by Poinsot and Lele (1992), and suitably modified to account for variable specific heats is implemented. The boundary conditions are periodic in the y direction and non-reflecting in the x direction (see Chen *et al.*, 1992a).

The turbulence field is prescribed by an initial two-dimensional turbulent kinetic energy spectrum function

$$E(k) = C_0 \frac{u_0^2}{k_0} \left(\frac{k}{k_0}\right)^4 \exp\left[-2\left(\frac{k}{k_0}\right)^2\right], \tag{20}$$

where k is the wavenumber, k_0 is the wavenumber corresponding to the most energetic eddies, and u_0 is the rms velocity.

4. Initial conditions and flame parameters

The reacting flow field in a steady opposed jet diffusion flame configuration including a full 40 step chemical kinetic mechanism was obtained using the Sandia code OPPDIF. Pure methane and air at 1 atmosphere, 300°K with a strain rate of approximately 20 sec^{-1} are the conditions imposed at the fuel and oxidizer jet separated by a distance of 1 cm. These correspond to low strain rate conditions. The strained laminar flame solution from OPPDIF was then allowed to relax to an unstrained condition in the DNS code. The unstrained laminar flame profile was used to initialize all of the species mass fractions, temperature, and density fields in the turbulence simulations.

The DNS was initialized in a two-dimensional computational domain with a plane laminar diffusion flame in the center of the domain. The fuel stream is on the left half of the domain while the oxidizer stream is on the right half of the domain. The velocity field was initialized with the turbulent kinetic energy spectrum given in (20). The turbulence Reynolds number was taken to be 57 based on the turbulence microscale. The flame is thicker than the turbulence microscale but smaller than the turbulence integral scale. Two-dimensional simulations were performed on a 129 by 129 grid.

5. Results and discussion

5.1 Laminar flamelet results

To initialize the direct simulations, the structure for laminar counterflow flamelets were calculated for low strain rates (< 100 sec^{-1}). The details for such calculations may be found in Smooke (1991). Shown in Figs. 1 and 2 are the flamelet structure in mixture fraction space for a global one-step reaction and a three-step mechanism, respectively.

A distinctive qualitative difference between the one-step and three-step mechanism is the broadness of the reaction zone. In Fig. 1c, it can be seen that the consumption of the fuel extends over a much wider range of mixture fraction for the one-step mechanism. The thinness of the fuel-consumption layer in multi-step mechanisms is one of the primary causes of resolution difficulties in direct simulations of turbulent combustion flames. In addition, it can readily be seen in Figs. 1b and 2b that the fuel and oxygen profiles are quite different. In the one-step approximation, fuel leaks through the reaction zone. However, for the three-step mechanism, only oxygen leaks through the reaction layer, which is in agreement with experiments and numerical calculations employing full detailed mechanisms.

Preliminary calculations using the four-step mechanism indicate that the qualitative features of the flamelet agree with previous studies. The major expected difference between the three- and four-step mechanisms is the H atom profile. In the three-step mechanism, all the H is produced on the fuel-lean side of the flamelet and is consumed entirely in the fuel-consumption layer. For the four-step approximation, the H atom profile is broader, in which the fuel-consumption layer is within the H nonequilibrium layer. The monograph by Smooke (1991) may be consulted for

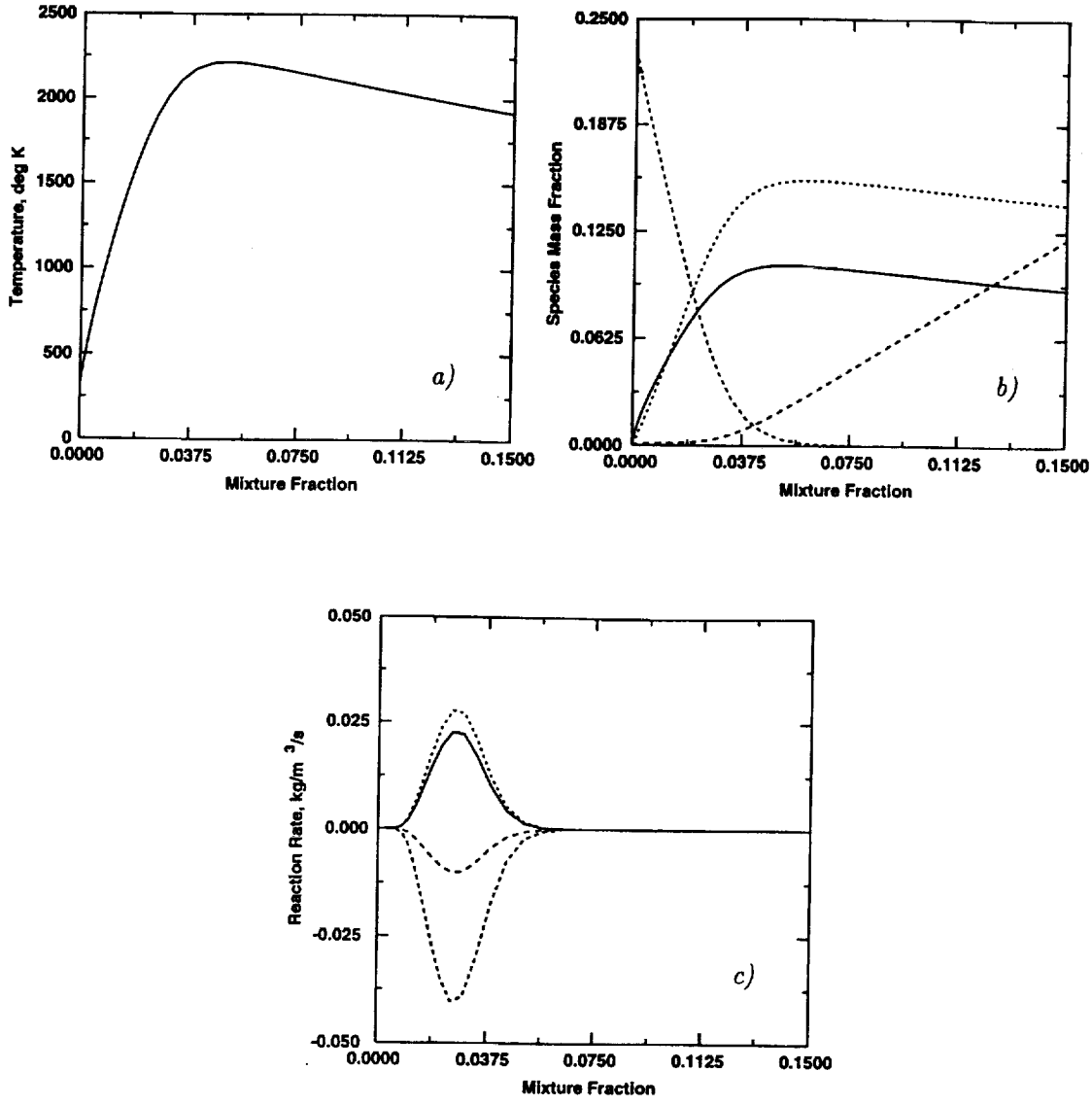

FIGURE 1. One-dimensional unstrained laminar flame for methane-air one-step mechanism: a) temperature, b) species mass fractions, c) species reaction rates. (—— H_2O, ····· CO_2, ····· O_2, ---- CH_4).

more detailed discussion on the structure of laminar methane flames using reduced chemistries.

5.2 Turbulent flame structure

Preliminary results are presented here for the DNS using the global one-step mechanism described in section 2. Simulations are currently underway for the three- and four-step mechanisms. In order to resolve the fuel consumption layer the resolution

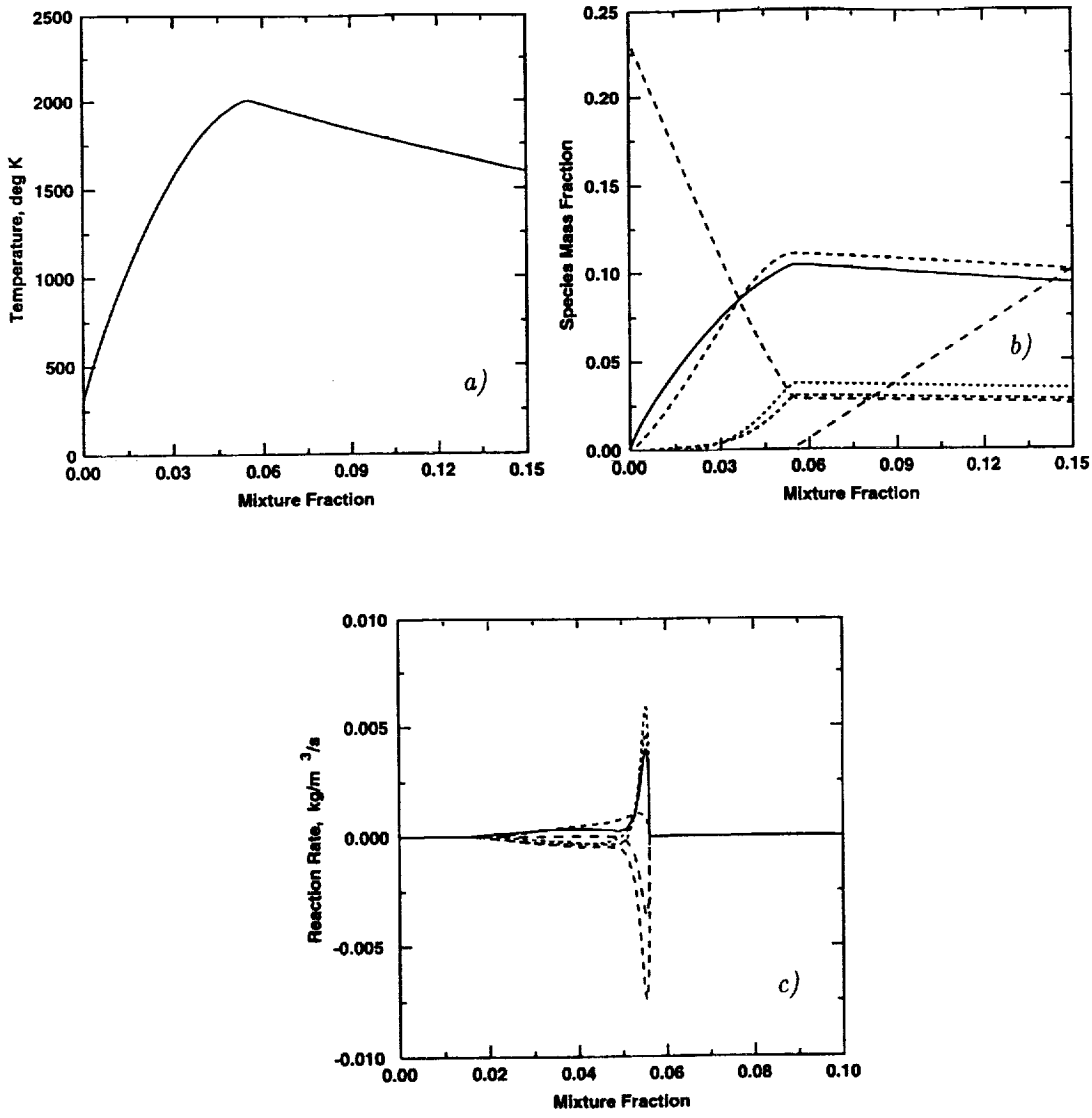

FIGURE 2. One-dimensional strained laminar flame for methane-air three-step mechanism: a) temperature, b) species mass fractions, c) species reaction rates. (—— H_2O, ····· $H_2 * 40$, ····· CO, ---- CO_2, ---- O_2, ---- CH_4).

requirements are much greater for the three- and four-step mechanisms than for the one-step mechanism.

The turbulent two-dimensional DNS was postprocessed at 1.0 and 1.5 turbulent eddy turn times. This is sufficient time for the initial adjustment to occur between the imposed turbulence spectrum and the laminar flame. Instantaneous images of the vorticity magnitude, temperature, reaction rate, and species concentrations at $t = 1.0$ eddy turn time are shown in Fig. 3. It is evident from Fig. 3a that the

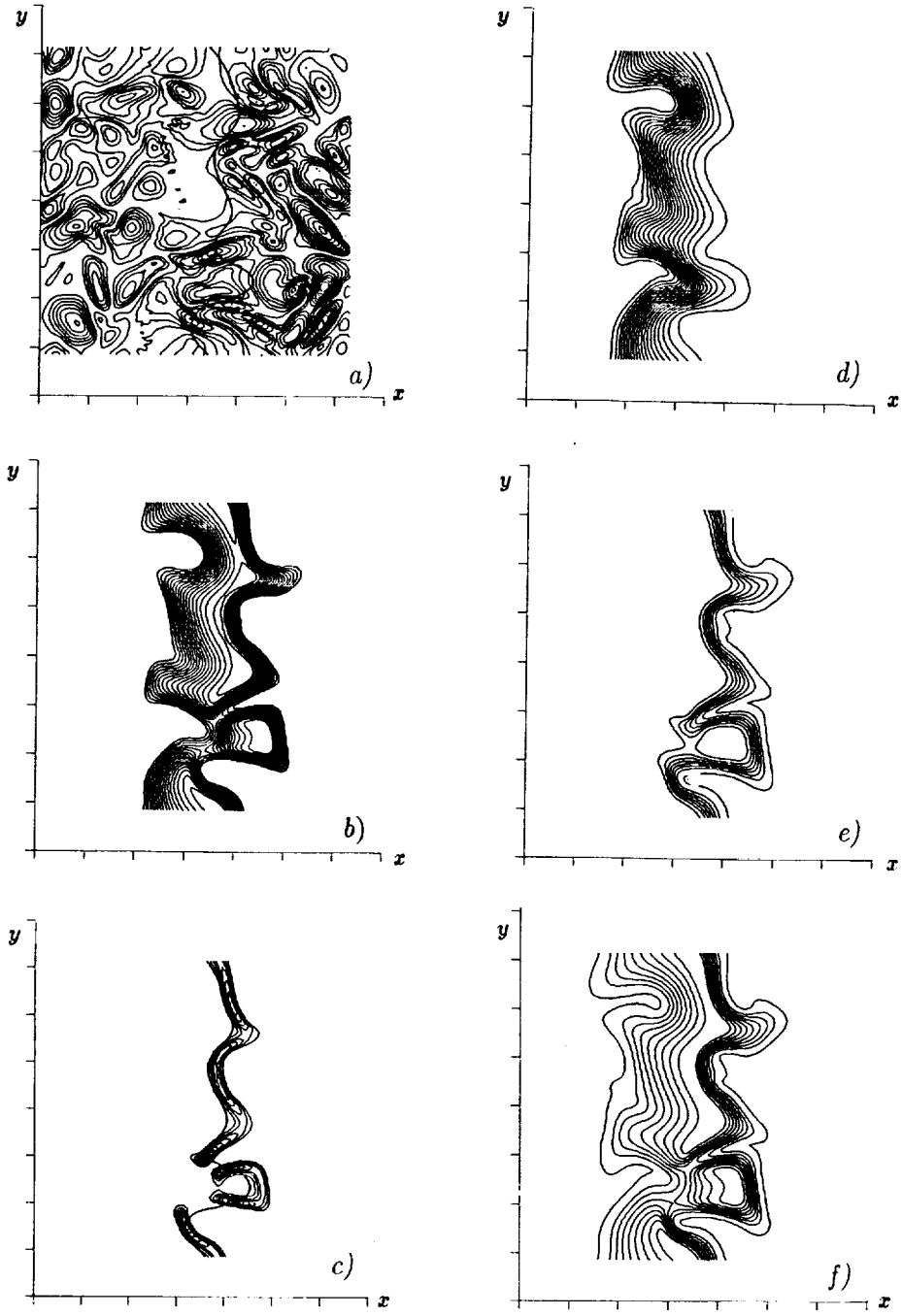

FIGURE 3. Computed fields at 1.0 eddy turn time for the one-step mechanism: a) vorticity magnitude contours with stoichiometric mixture fraction,$f = 0.057$, b) temperature, c) CH_4 reaction rate with $f = 0.057$, d) CH_4 mass fraction, e) O_2 mass fraction, f) CO_2 mass fraction.

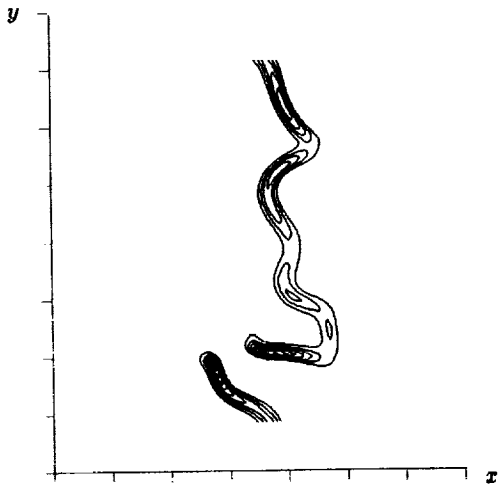

FIGURE 4. CH_4 reaction rate at 1.5 eddy turn times.

vorticity is greatly dampened in the vicinity of the reaction zone. The turbulence was initialized at all locations in the computational domain except near the outflow boundaries normal to the flame. Due to a combination of dilatational effects and a substantial increase in the kinematic viscosity with temperature, vorticity in the vicinity of the flame is dampened. Note in Fig. 3c that the vorticity is dampened more on the fuel side than on the oxidizer side. This is due to the lower density (higher temperature) that exists on the rich side of the flame which results in a higher kinematic viscosity on that side.

While the effect of the heat release is to weaken the turbulence, the effect of the turbulence is to wrinkle the flame. There are regions where the flame is locally extinguished as shown by the discontinuities in the reaction rate contour lines shown in Fig. 3c. At a later time in the simulation, $t = 1.5$ eddy turn times, the conditions are such that locally the strain rate is reduced in regions with hot products due to the heat release. The hot products act as an ignition source and in locations where fuel and oxidizer are present, the flame starts to burn once again. A comparison of Fig. 4 and Fig. 3c shows a region where reignition occurs. Previous simulations with simple chemistry (Chen 1992a, 1992b) did not report the occurrence of reignition.

It is also observed from the reaction rate contours and the stoichiometric mixture fraction line (Fig. 3c) that the flame does not always burn at the stoichiometric mixture fraction. Near the peak reaction rates the flame is stoichiometric; however, in regions that are curved toward the oxidizer stream the flame tends to burn lean, whereas in regions that are curved toward the fuel stream the flame tends to burn rich. We suspect that this is a Lewis number effect and that it is particularly pronounced in regions having the largest curvature. In regions that are curved toward

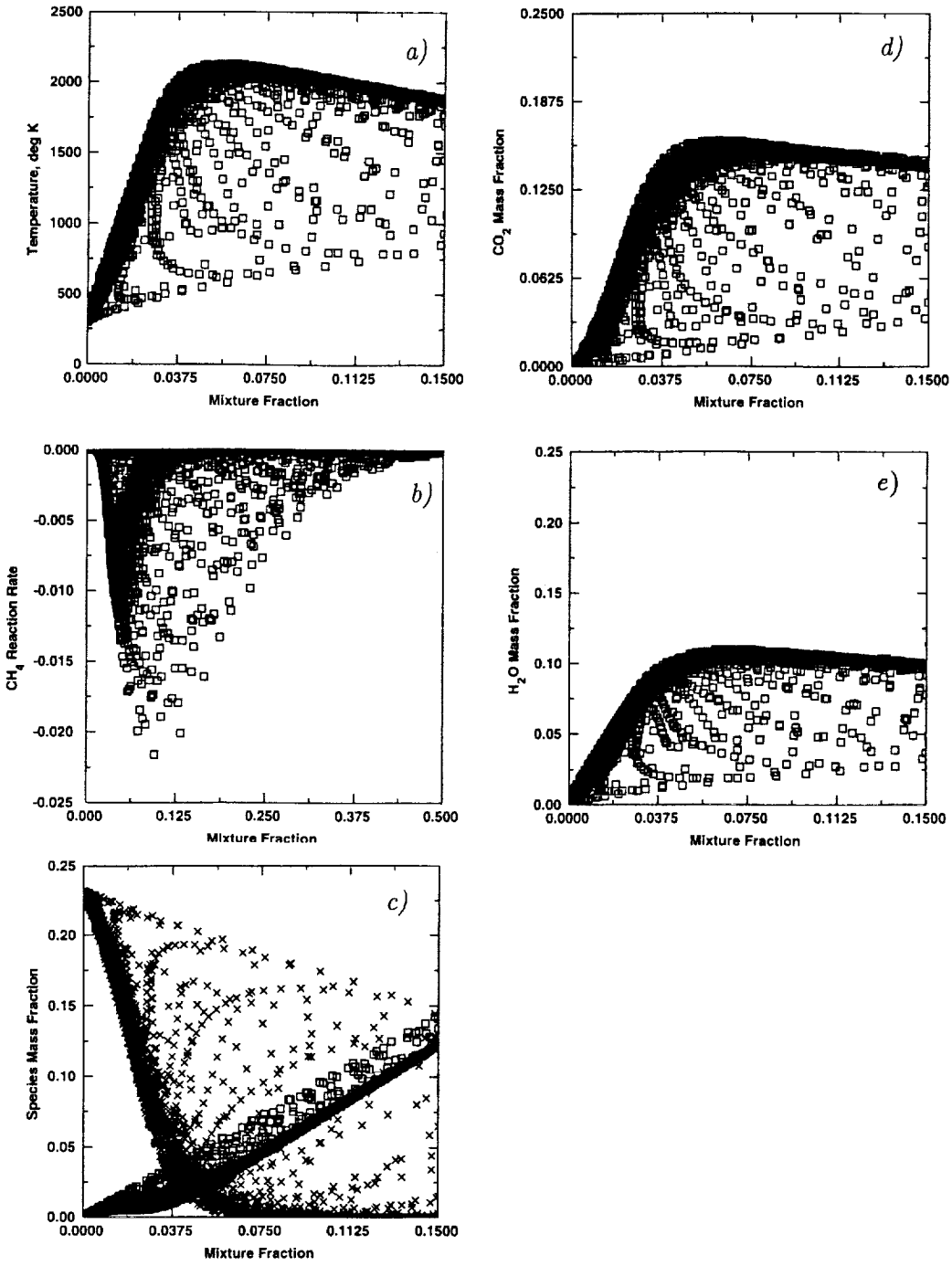

FIGURE 5. Scatter plots at 1.0 eddy turn time for one-step mechanism: a) temperature, b) CH_4 reaction rate, c) CH_4 and O_2 mass fraction (□ CH_4, × O_2), d) CO_2 mass fraction, and e) H_2O mass fraction.

the oxidizer, the defocusing of methane overcomes the greater mass diffusivity of methane ($Le = 0.97$) over oxygen ($Le = 1.11$). Hence, the flame tends to burn lean. On the other hand, in regions that are curved towards the fuel, the additive effect of focusing the methane combined with its larger mass diffusivity leads to a situation where there is an abundance of methane at the reaction zone. Hence, in this situation the flame tends to burn rich, and eventually, as the curvature becomes too large, the flame becomes too rich to burn, at which point local extinction occurs first at the flame tip. Since the reactant Lewis numbers in the DNS can readily be interchanged, these influences will be studied in greater detail in future simulations.

The reactant and product concentrations are presented in Figs. 3d-3f. Note that CH_4 is more diffusive than O_2. The products CO_2 and H_2O follow the temperature (Fig. 3b) quite closely; hence, for the sake of brevity, only CO_2 is presented in Fig. 3f.

Scatter plots of the temperature, CH_4 reaction rate, and species concentrations in mixture fraction space are shown in Fig. 5. The mixture fraction, f, is defined to be zero in the oxidizer stream and unity in the fuel stream. The maximum temperature occurs near the stoichiometric mixture fraction, $f = 0.057$. The CH_4 reaction rate peak is shifted slightly toward the fuel side. Consistent with the physical representation of the flame, the presence of both high and low values of the temperature and reaction rate in Figs. 5a and 5b suggests that there are regions in the flame that are fully burning as well as other regions that are being extinguished by the local strain-rate field. From Fig. 5c, note that there is leakage of both CH_4 and O_2 in this one-step model. Also, a significant portion of the flame is undergoing various stages of extinction as indicated by the spread of points between the equilibrium and frozen flow limits.

6. Concluding remarks

Preliminary results from DNS demonstrate that two-dimensional simulations of turbulent non-premixed methane-air flames modeled with reduced chemistry are feasible. The global one-step simulation required 50 cpu hours on a Cray-YMP. Extensions to three- and four-step mechanisms requires resolving the fuel consumption layer of the flame, a region that is approximately an order of magnitude smaller than the overall flame thickness. Simulations on a uniform grid will have enormous resolution requirements if the internal flame structure is to be fully resolved. This suggests a real need for a local adaptive mesh refinement capability for simulations of hydrocarbon flames.

Once the three- and four-step simulations are completed, detailed comparisons of the internal flame structure and extinction characteristics will be made. In particular, strain-rate and curvature statistics will be obtained and comparisons of the turbulence simulations with steady one-dimensional strained laminar flame predictions will be made. Finally, reduced mechanisms for the formation of thermal and prompt NO_x will be evaluated from the major species concentrations and the temperature.

Acknowledgements

This research was supported by the Center for Turbulence Research and the

Department of Energy, Division of Basic Energy Sciences. One of us (SM) acknowledges partial funding through the AWU-DOE faculty fellowship program. The authors are grateful to their CTR hosts T. Mantel, G. Reutsch, and J. M. Samaniego for their excellent arrangements. We would also like to thank A. Liñán, T. Poinsot, A. Trouvé, and T. Echekki for many insightful discussions.

REFERENCES

BAUM, M., POINSOT, T., & HAWORTH, D. 1992 Numerical simulations of turbulent premixed $H_2/O_2/N_2$ flames with chemistry. *Proceedings of the 1992 Summer Program.* Center for Turbulence Research, NASA Ames/Stanford Univ., 345-366.

CHEN, J., MAHALINGAM, S., PURI, I., & VERVISCH, L. 1992a Effect of finite-rate chemistry and unequal Schmidt numbers on turbulent non-premixed flames modeled with single-step chemistry. *Proceedings of the 1992 Summer Program.* Center for Turbulence Research, NASA Ames/Stanford Univ., 367-387.

CHEN, J., MAHALINGAM. S., PURI, I., & VERVISCH, L. 1992b Non-premixed flames modeled with two-step chemistry. *Proceedings of the 1992 Summer Program.* Center for Turbulence Research, NASA Ames/Stanford Univ., 389-402.

BUI-PHAM, M. N. 1992 Studies in structures of laminar hydrocarbon flames. Ph.D. Dissertation, University of California, San Diego.

KEE, R. J., RUPLEY, F. M., & MILLER, J. A. 1987 The Chemkin Thermodynamic Database. *SAND-8215B.*

LELE, S. 1992 Compact finite difference schemes with spectral-like resolution. *J. Comput. Phys.,* (to appear).

MAHALINGAM, S., CHEN, J., & VERVISCH, L. 1994 Finite-rate chemistry and transient effects in direct numerical simulations of turbulent non-premixed flames. *Comb. & Flame* (submitted).

MONTGOMERY, C. J., KOSALY, G. & RILEY, J. J. 1992 Direct numerical simulations of turbulent H_2-O_2 combustion using reduced chemistry. Submitted for presentation at the 31st AIAA Aerospace Sciences Meeting to be held at Reno, NV, January, 1993.

PETERS, N. 1985 Numerical and Asymptotic Analysis of Systematically Reduced Reaction Schemes for Hydrocarbon Flames. *Numerical Simulation of Combustion Phenomena.* Lecture Notes in Physics, **241,** 90-109.

PETERS, N. 1986 Laminar flamelet concepts in turbulent combustion. *Twenty-First Symposium (International) on Combustion.* The Combustion Institute. 1231-1250.

PETERS, N. & ROGG, B. (ED.) 1993 Reduced kinetic mechanisms for applications in combustion systems. *Lecture Notes in Physics m15,* Springer-Verlag, New York.

PETERS, N. & WILLIAMS, F. A. 1987 The asymptotic structure of stoichiometric methane-air flames. *Comb. & Flame.* **68,** 185.

POINSOT, T., AND LELE, S. 1991 Boundary conditions for direct simulations of compressible viscous flows. *J. Comput. Phys.* **101,** No 1.

PURI, I. K., SESHADRI, K., SMOOKE, M. D. AND KEYES, D. E. 1987 A comparison between numerical calculations and experimental measurements of the structure of a counterflow methane-air diffusion flame. *Comb. Science and Tech.* **56,** 1.

SESHADRI, K. AND PETERS, N. 1988 Asymptotic structure and extinction of methane-air diffusion flames. *Comb. & Flame.* **73,** 23.

SMOOKE, M. D. (ED.) 1991 in Reduced kinetic mechanisms and asymptotic approximation for methane-air flames. *Lecture Notes in Physics 384,* Springer-Verlag, New York.

WILLIAMS, F. A. 1985 Combustion theory, second edition. Addison/Welsly.

19734
N95-21039

Triple flame structure and diffusion flame stabilization

By D. Veynante,[1] L. Vervisch,[2] T. Poinsot,[3] A. Liñán[4] AND G. Ruetsch[5]

The stabilization of diffusion flames is studied using asymptotic techniques and numerical tools. The configuration studied corresponds to parallel streams of cold oxidizer and fuel initially separated by a splitter plate. It is shown that stabilization of a diffusion flame may only occur in this situation by two processes. First, the flame may be stabilized behind the flame holder in the wake of the splitter plate. For this case, numerical simulations confirm scalings previously predicted by asymptotic analysis. Second, the flame may be lifted. In this case a triple flame is found at longer distances downstream of the flame holder. The structure and propagation speed of this flame are studied by using an actively controlled numerical technique in which the triple flame is tracked in its own reference frame. It is then possible to investigate the triple flame structure and velocity. It is shown, as suggested from asymptotic analysis, that heat release may induce displacement speeds of the triple flame larger than the laminar flame speed corresponding to the stoichiometric conditions prevailing in the mixture approaching the triple flame. In addition to studying the characteristics of triple flames in a uniform flow, their resistance to turbulence is investigated by subjecting triple flames to different vortical configurations.

1. Introduction

The structure and the stabilization of diffusion flames is a topic of intense research which has numerous practical applications in jet flames, aircraft engines, diesel car engines, torches, etc. At the same time, it is a complex phenomenon which has generated much theoretical and experimental work in the last years (Takahashi *et al.* 1990, Liñán 1994, Dold 1989, Kioni *et al.* 1993).

Our goal in the present work is to investigate two aspects of diffusion flame stabilization as suggested from asymptotic theory: (1) stabilization of a diffusion flame in the viscous region immediately downstream of the flame holder, and (2) stabilization of the diffusion flame as a triple flame far downstream.

These two computations are performed for laminar flows only: the triple flame is considered in Section 4 while the stabilization at the splitter plate is studied

1 Laboratoire EM2C, Ecole Centrale Paris, France
2 LMFN/INSA CORIA/URA CNRS230 Rouen France
3 Institut de Mecanique des Fluides de Toulouse and CERFACS, France
4 E.T.S.I. Aeronáuticos, Universida Politecnica de Madrid
5 Center for Turbulence Research

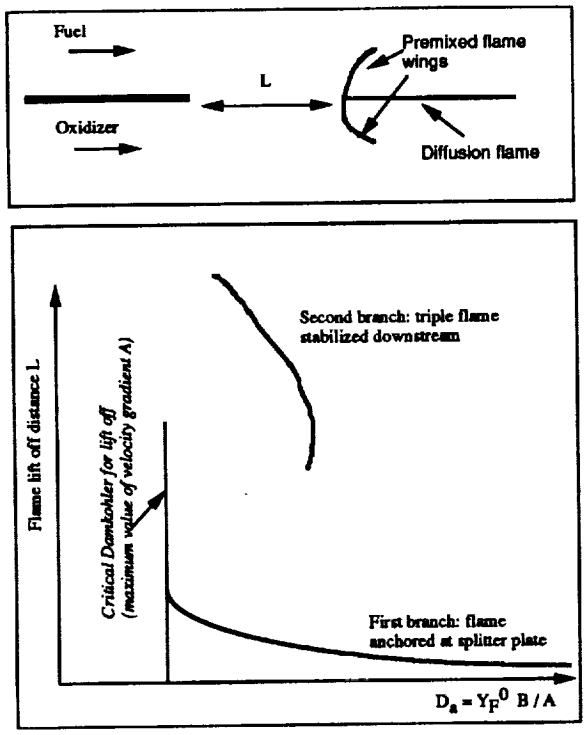

FIGURE 1. Asymptotic results for diffusion flame stabilization and lift-off.

in Section 5. The influence of turbulence is investigated later in Section 6 by using a technique developed previously for premixed flames both experimentally and numerically (Roberts *et al.* 1993, Samaniego 1993, Poinsot *et al.* 1991): vortices are generated upstream of the flame and interact with the flame front. Although these isolated vortices are too crude to represent real turbulence, they provide useful estimates of the effects of hydrodynamic excitation on the flame and of the flame's capacity to resist these excitations.

2. Regimes of flame stabilization

Classical results concerning triple flame studies may be found in Dold 1989, Liñán 1988, Dold *et al.* 1991, and Liñán and Crespo 1976. For the present study we have chosen to focus on two aspects of triple flame stabilization: stabilization in the wake of the splitter plate (anchored case) or stabilization far downstream (lifted flame). These two aspects correspond to the two stable branches of the curve proposed by Liñán (1994) and given in Fig. 1. The x coordinate corresponds to the Damköhler number defined by $D_a = Y_O^0 B/A$ where B is the pre-exponential constant and A is the velocity gradient at the splitter plate. The y coordinate is the distance between the flame holder and the flame.

The lower branch of Fig. 1 corresponds to flames stabilized in the wake of the splitter plate. When the velocity gradient in the wake increases, the flame moves

slightly downstream until a critical value of the velocity gradient, A_{lo}, is reached. At that point, flame stabilization is no longer possible near the splitter plate and the flame is lifted off. The critical value at which lift off occurs is estimated by Liñán as

$$Y_O^0 B/A_{lo} = \Phi^3 \exp(\Phi) \tag{1}$$

where Φ is a nondimensional parameter defined by

$$\Phi = \frac{T_a}{T_0}\left(1 + \frac{QY_F^0}{c_P T_0(1 + rY_F^0/Y_O^0)}\right)^{-1}$$

In these equations, T_a is the activation temperature, Q is the heat released per unit mass of fuel, and $r = (W_O\nu_O)/(W_F\nu_F)$ or the mass ratio of oxidizer to fuel in the reaction. We will check in Section 5 whether numerical simulations confirm this analysis.

If lift-off occurs, then stabilization may occur downstream of the splitter plate (on the upper branch of Fig. 1) if the local flow speed decreases enough to be equal to or less than the characteristic triple-flame speed which may exist at that point. In this case, the local velocity profile upstream of the flame is essentially constant (initial shear has been dissipated), and the problem may be viewed as an eigenvalue problem in which a triple flame propagates at a constant speed in a flow which is moving in the opposite direction at the same absolute speed. Numerically, it is essential to be able to track in real time the value of this velocity to keep the flame inside the computational box. When the triple flame is stabilized, it is possible to study its structure and propagation speed. Asymptotic studies suggest that triple flames may propagate at a speed U_F larger than the premixed flame speed S_L^0 corresponding to the conditions encountered at the tip of the triple flame.

3. Numerical method and configurations

For all computations presented here, the fully-compressible reacting Navier Stokes equations were solved in two dimensions. The chemistry used corresponds to a simple irreversible reaction:

$$\nu_F F + \nu_O O \rightarrow \nu_P P$$

and the mass reaction rate for the fuel F is written following Williams (1985):

$$\dot{\omega}_F = D\nu_F W_F/Y_F^0 \rho^{ex}(Y_F/W_F)^{\nu_F}(Y_O/W_O)^{\nu_O}\exp(-T_a/T) \tag{2}$$

where T_a is the activation temperature.

For simplicity, the stoichiometric coefficients ν_O and ν_F have been set to unity in this study. Two values of ex have been used (1 and 2). For both cases, to allow comparison with asymptotic results, Eq. (2) may be written

$$\dot{\omega}_F = B\rho^{ex} Y_F Y_O exp(-T_{act}/T) \tag{3}$$

where B has the dimension s^{-1} if $ex = 1$ and $m^3/(kgs)$ if $ex = 2$.

Using this formulation for the reaction rate, the conservation equations to be solved are:

$$\frac{\partial \rho}{\partial t} + \frac{\partial}{\partial x_i}(\rho u_i) = 0$$

$$\frac{\partial \rho u_i}{\partial t} + \frac{\partial}{\partial x_j}(\rho u_i u_j) = -\frac{\partial P}{\partial x_i} + \frac{\partial \tau_{ij}}{\partial x_j}$$

$$\frac{\partial \rho E}{\partial t} + \frac{\partial}{\partial x_i}[(\rho E + P)\, u_i] = \frac{\partial}{\partial x_i}(\tau_{ij} u_j) + \frac{\partial}{\partial x_i}\left(\lambda \frac{\partial T}{\partial x_i}\right) + Q\dot{\omega}_F$$

$$\frac{\partial \rho Y_F}{\partial t} + \frac{\partial}{\partial x_j}(\rho Y_F u_j) = \frac{\partial}{\partial x_i}\left(\rho \mathcal{D}_F \frac{\partial Y_F}{\partial x_i}\right) - \dot{\omega}_F$$

$$\frac{\partial \rho Y_O}{\partial t} + \frac{\partial}{\partial x_j}(\rho Y_O u_j) = \frac{\partial}{\partial x_i}\left(\rho \mathcal{D}_O \frac{\partial Y_O}{\partial x_i}\right) - r\dot{\omega}_F$$

where the total energy density and deviatoric stress tensor are given by:

$$\rho E = \frac{1}{2}\rho u_i^2 + \frac{P}{\gamma - 1}$$

$$\tau_{ij} = \mu\left(\frac{\partial u_i}{\partial x_j} + \frac{\partial u_j}{\partial x_i} - \frac{2}{3}\delta_{ij}\frac{\partial u_k}{\partial x_k}\right)$$

We assume that the mixture has a specific heat ratio of $\gamma = 1.4$ and the dynamic viscosity is a function on temperature, $\mu = \mu_0(T/T_0)^b$, with $b = 0.76$. We also assume that the Prandtl and Schmidt numbers,

$$Pr = \frac{\mu c_p}{\lambda}; Sc = \frac{\mu}{\rho \mathcal{D}},$$

remain constant, and $\mathcal{D} = \mathcal{D}_F = \mathcal{D}_O$. As a result, the Lewis number $Le = Sc/Pr$ is constant and is taken as unity throughout this study. We can also define the heat release parameter and Zel'dovich numbers as:

$$\alpha = \frac{T_f - T_0}{T_f}; \beta = \alpha \frac{T_a}{T_f}$$

where T_f is the adiabatic flame temperature.

The governing equations are solved using direct numerical simulations. Spatial derivatives are taken using sixth-order compact difference algorithm of Lele 1990, and time advancement is performed using a third-order Runge Kutta scheme (Wray 1990). Boundary conditions are specified using the Navier-Stokes characteristic boundary condition method of Poinsot and Lele 1990.

4. Characteristics of a lifted triple flame

We begin the analysis of triple flames by considering a lifted triple flame stabilized in the far field with a uniform inflowing velocity. In addition to describing the stabilization in the lifted case, this approach can be viewed as a first step in understanding the behavior of triple flames in more complicated flow scenarios, such as in the wake of a splitter plate (section 5) and in response to vortices (section 6).

We initialize the computations of the triple flame by first stabilizing a planar premixed flame in the computation domain. In doing so, the mixture fraction is uniform throughout the domain with the stoichiometric value $Z = Z_S = 0.5$. Associated with this flame are the planar flame speed S_L^0 and the planar flame thickness δ_L^0. We then change the inflow mixture fraction profile from uniform to a hyperbolic tangent profile varying from $Z = 0$ to 1 while maintaining the same uniform inlet velocity profile. The response of the flame to the mixture fraction gradient is shown in the time sequence of Fig. 2. For this case the heat release corresponds to $\alpha = 0.75$ and the Zel'dovich number is $\beta = 8.0$. With the uniform flow approaching from the left, as the mixture fraction gradient reaches the flame surface only the centerline is exposed to the stoichiometric mixture fraction and locally maintains the planar flame speed and reaction rate. Above this point the mixture is fuel rich, and below fuel lean. As a result, these regions of non-unity equivalence ratio burn less, the reaction rate drops, and the local flame speed is reduced. The excess fuel and oxidizer then combine behind the premixed flame along the stoichiometric surface and burn in a trailing diffusion flame. Thus the "triple" flame refers to the fuel-rich premixed flame, the fuel-lean premixed flame, and the trailing diffusion flame.

4.1 Flame stabilization

In addition to the change in structure that occurs when the planar premixed flame is subjected to a mixture fraction gradient, the propagation velocity of the flame increases, as observed in Fig. 2. In order to study the triple-flame in further detail, a method of stabilizing the flame in the computational domain is needed. We accomplish this by calculating the relative progression velocity of iso-scalar surfaces. This method, also used in Vervisch *et al.* 1994, results from equating the transport equation for a scalar variable Y:

$$\rho \frac{DY}{Dt} = \frac{\partial}{\partial x_i}\left(\rho \mathcal{D} \frac{\partial Y}{\partial x_i}\right) + \dot{w}_Y$$

with the Hamilton-Jacobi equation for the scalar field (Kerstein *et al.* 1988):

$$\rho \frac{DY}{Dt} = \rho V |\nabla Y|.$$

Solving for the relative progression velocity, V, we obtain:

$$V = \frac{1}{\rho|\nabla Y|}\frac{\partial}{\partial x_i}\left(\rho \mathcal{D} \frac{\partial Y}{\partial x_i}\right) + \frac{1}{\rho|\nabla Y|}\dot{w}_Y$$

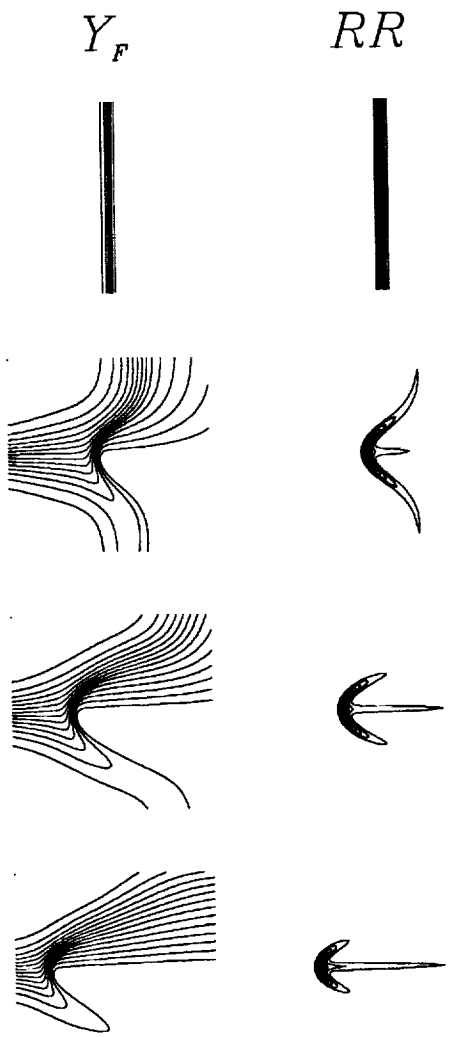

FIGURE 2. Response of a planar premixed flame to a mixture fraction gradient. The top row shows the flame under premixed conditions, with a uniform flow approaching from the left. As the mixture fraction gradient reaches the flame surface, the flame shape changes from a premixed planar flame to one with fuel-rich and fuel-lean premixed curved fames followed by a trailing diffusion flame. In addition to the change in shape, the flame propagates faster relative to the premixed case.

This relation is evaluated on the centerline in the preheat zone and subtracted from the local fluid velocity, giving the correction to be applied at the inlet. If one were to apply this correction at the inlet alone, then changes to the flame would only

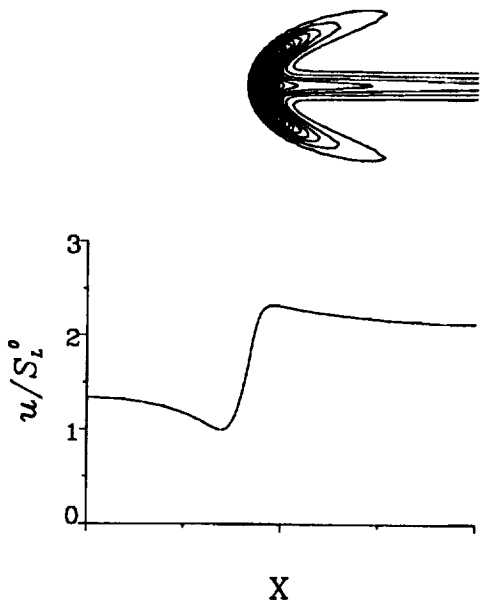

FIGURE 3. Reaction rate and horizontal velocity along the centerline.

occur after the convective time required to reach the flame, which is both time consuming and can also introduce stability problems. A more efficient method is to apply the correction to all points in the flow, as a Gallilean transformation, such that the steady state situation is quickly reached.

4.2 Effect of heat release

We now turn our attention to studying the effect of heat release on the triple flame and, in particular, how this affects the propagation velocity. The analytical work of Dold 1989 and Hartley and Dold 1991 provide estimates of the triple-flame speed for weak ($\beta\partial Z/\partial y \to 0$) and moderate ($\beta\partial Z/\partial y \sim O(1)$) values of the mixture fraction gradient under the assumption of zero heat release. They find that the flame speed is greatest for zero mixture fraction gradient, corresponding to a planar flame, and then decreases as the mixture fraction gradient increases. This is in contrast to the change in flame speed we observe in Fig. 2. The discrepancy lies in the assumptions concerning heat release. To investigate this further, we examine the velocity field along the centerline of the triple flame in Fig. 3. Here we observe that, in addition to the rise in velocity through the flame, the horizontal component of the velocity reaches a minimum before the flame. The velocity at this minimum is close to the planar laminar flame speed, and far upstream the velocity is larger. Therefore it is necessary to distinguish these two velocities. The local flame speed is important in terms of chemical reaction, where the far-field flame speed is identified with the propagation of the entire structure, U_F.

The mechanism responsible for this velocity difference can be seen in the sketch of Fig. 4. Here we examine the velocity vectors before and after they pass through

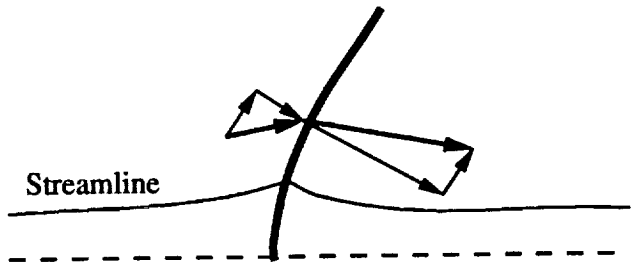

FIGURE 4. Mechanism responsible for creating triple-flame speeds larger than the planar-flame speeds. Heat release causes an increase in the normal component of flow, and the flow redirection causes an upstream divergence of flow.

the flame surface. In cases where there is heat release, the component of the velocity perpendicular to the flame increases across the surface, whereas the tangential component remains unchanged. The jump in the perpendicular velocity component results in a bending of the velocity vector towards the centerline. This redirection of the flow is accommodated by the divergence of the stream lines ahead of the flame, resulting in the decrease of the velocity observed in Fig. 3. Since the local flame speed along the stoichiometric line is S_L^0, the flame can be stabilized only if the flow speed at this point remains near S_L^0, which requires an increase in the upstream velocity. Note than in absence of heat release, there is no flow redirection across the flame and therefore the far-field and local flame speeds are equal.

4.3 Effect of the mixture fraction gradient

In their previous analytical work, Dold 1989 and Hartley and Dold 1991 observed a large effect of the mixture fraction on the triple-flame speed. Due to the effects of flame curvature, they observed a decrease in the flame speed as the mixture fraction gradient increases and thus radius of curvature decreases. In cases with heat release, we observe qualitatively the same behavior although the quantitative aspects are very different. For zero heat release cases the planar premixed flame is an upper limit for the flame speed; however, for finite heat release the flame speed is always observed to be greater than S_L^0. This is depicted in Fig. 5, where the far-field flame speed, U_F/S_L^0, and the local flame speed are plotted versus the inverse of the mixture fraction gradient taken at the flame location, $(\delta_L^0 \partial Z/\partial y)^{-1}$, representing a mixing layer thickness or alternatively a Damköhler number. Here we see that, in agreement with the zero heat release analysis, the local flame speeds remain of the order of S_L^0, decreasing slightly below this value for small values of the mixing thickness.

For small values of the mixing thickness, one might expect quenching to occur. However, in agreement with the analysis of Dold 1989 and Hartley and Dold 1991, quenching is not observed. Under the assumption of zero heat release, quenching was observed only when the flame was subjected to an external strain(Dold *et al.* 1990). In cases with heat release, the resistance to quenching is further strengthened. The

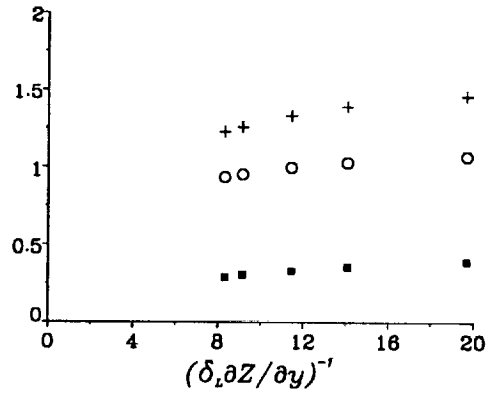

FIGURE 5. Far-field flame speed(+), local flame speed(o), and their differences(■) as a function of the mixing thickness. All speeds are normalized by S_L^0, and for all cases $\alpha = 0.75$ and $\beta = 8.0$. The mixture fraction gradient is evaluated along a line passing through the maximum reaction rate.

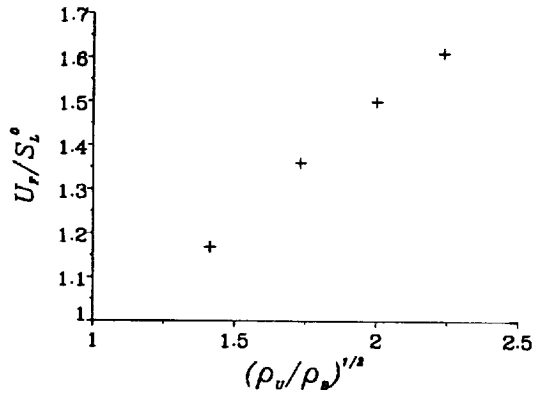

FIGURE 6. Ratio of triple-flame to planar-flame speeds for various heat releases.

strain field which creates the reduction in the horizontal velocity also decreases the effective mixture fraction gradient in front of the flame, and therefore limits how small the effective Damköhler number can become in Fig. 5. The only way to continue this graph to smaller thicknesses is to apply a strain of opposite sense externally, (*cf.* Section 6 where the response of triple flames to vortices is examined).

As the mixing thickness increases, not only do the far-field and local flame speeds increase, but also the difference between the two, indicating that heat release effects become more important as the mixture thickness increases. This trend can be understood by applying the mechanism in Fig. 3 to different mixing thicknesses. Since the difference between the far-field and local flame speeds depends on the flow redirection through the flame, which *locally* depends on the reaction rate along

the premixed wings, then the distribution of the reaction rate along the premixed wings becomes an important characteristic. As the mixing thickness becomes larger, the reaction rate is stronger along the premixed wings as one moves away from stoichiometric conditions. This causes the flow to be deflected more and thus the difference in the velocities to increase.

In the limit of large mixing thickness, one expects from asymptotic results that the flame speed reaches a constant value for a given heat release. This value is related to the jump in density by:

$$\frac{U_F}{S_L^0} \sim \sqrt{\frac{\rho_u}{\rho_b}}$$

A comparison of data from numerical simulations with this result is shown in Fig. 6, where overall good agreement is observed.

5. Diffusion flame stabilized in the wake of a splitter plate

5.1 Configuration and parameters

In the region immediately downstream of the splitter plate, the velocity profile exhibits a wake which has a strong influence on flame stabilization. For this work, we assume that both streams have the same speed and vorticity thickness so that the velocity gradient at the splitter plate, A, is the same on both sides of the plate. Inlet profiles for temperature, species, and velocities are given in Fig. 7; the temperature is imposed everywhere and equal to the splitter plate temperature, and species profiles correspond to step functions.

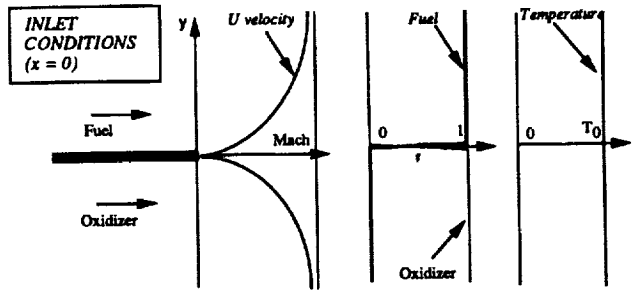

FIGURE 7. Configuration for simulations of diffusion flame stabilization lift-off

For these computations it is important to control inlet temperature; asymptotic analysis shows that flame stabilization is obtained not only from the existence of a low velocity region in the wake, but also from the presence of heat losses from the flame to the splitter plate.

The parameters controlling the flow are the Mach number at infinity (equal on both sides) $M_a = U_o/c$ and the width of the shear layers δ. The characteristic velocity gradient A is $A = U_o/\delta$. The velocity profile at the inlet was chosen in different ways depending on the runs: (1) a *tanh* profile was first used, where $u(y) = U_o tanh(y/\delta)$. This profile leads to a singular point at $y = 0$ and sometimes to numerical instabilities; (2) an *exp* profile was also tested where $u(y) = U_o(1 - exp(-y^2/\delta^2))$. Corresponding runs will be labeled as 'tanh' or 'exp' cases. For all cases, the reference Reynolds number cL/ν is 1000 where L is the reference length of the problem, ν is the kinematic viscosity in the fuel at infinity, and c is the sound speed in the fresh gases. The parameters controlling the chemistry for these runs are given in Table 1.

Table 1. Chemistry parameters for DNS of triple flame in a wake

Case	T_{act}/T_0	T_a/T_0	D_{fuel}	b	Pr	Le	S_L^0/c	d/L	δ_l^0/L
Flame 1	18	5	53	0.76	0.75	1.0	0.022	0.046	0.4
Flame 2	12	5	53.	0.76	0.75	1.0	0.08	0.013	0.16

The adiabatic temperature T_a and the laminar flame speed S_L^0 given above correspond to a premixed laminar flame speed where the premixed gases would have a fuel mass fraction equal to $Y_F^0/2$ and an oxidizer mass fraction of $Y_O^0/2$. These levels are the maximum levels which may be obtained in the wake of the splitter plate, and therefore this velocity is the maximum premixed flame speed which may exist in the wake. The Lewis number is the same for oxidizer and fuel, and the problem is symmetric ($Y_F^0 = Y_O^0 = 1$). Molecular weights are also supposed to be equal, and in the expression of the reaction rate, ex is 2. The reduced pre-exponential constant D_{fuel} is defined by $D_{fuel} = \nu_F LB\rho_0 Y_O^0/(cW)$ where W is the molecular weight of fuel or reactant. The two flame thicknesses indicated are $d = \nu/S_L^0$ and $\delta_l^0 = (T_a - T_0)/Max(\frac{\partial T}{\partial x})$.

5.2 Structure of stabilized diffusion flames

Let us first consider a stabilized triple flame in a wake. For this case, the parameters are a Mach number of 0.2, a vorticity thickness of 0.05 with an *exp* profile, and chemistry parameters corresponding to Flame 2 (see Table 1). In this case, a stabilized flame is found in the wake at a distance D which is given by $D/L = 0.95$ (or $D/d = 73$ or $D/\delta_l^0 = 5.9$). The density field (similar to the temperature field) and the reaction rate field are given in Fig. 8. The influence of the cold splitter plate is clearly seen from the density field. The flame is losing energy towards the plate, and this phenomenon produces flame stabilization. Without the plate the flame would propagate even more upstream and eventually get stabilized on the

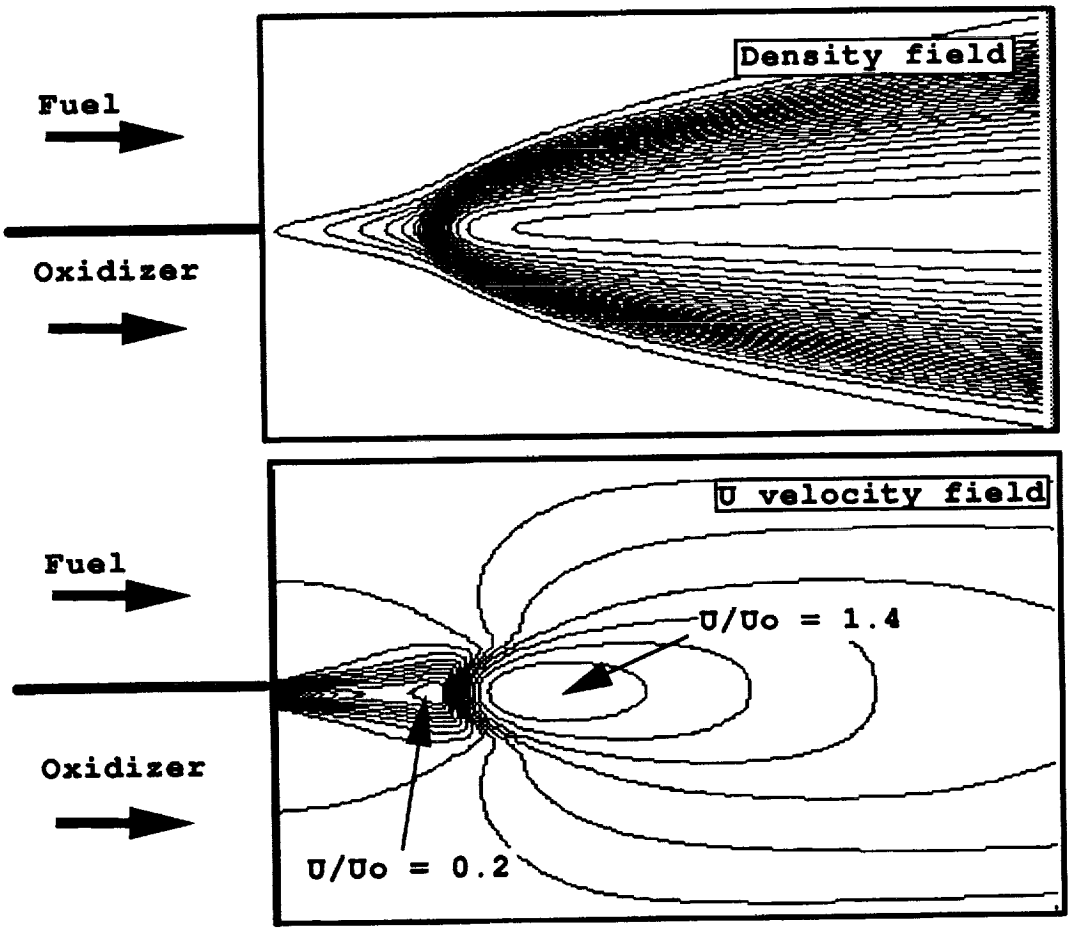

FIGURE 8. Triple flame stabilized in a wake.

splitter plate. This situation would not be unusual but we wanted to avoid it for the first test cases.

Different cuts along the centerline axis of the flame (Case 15) are presented in Fig. 9. The axial velocity profile is plotted along with the same profile in the case without the flame (wake only). It is seen that for small values of x, both profiles are essentially similar (close to the splitter plate). For larger x values, the influence of the triple flame on the flow divergence is first felt and the velocity decreases for the triple flame while the cold flow velocity keeps increasing. Finally closer to the flame front, a second effect due to the flame appears: temperature starts increasing, the density decreases, and the velocity increases to a value of the order of $1.4U_o$.

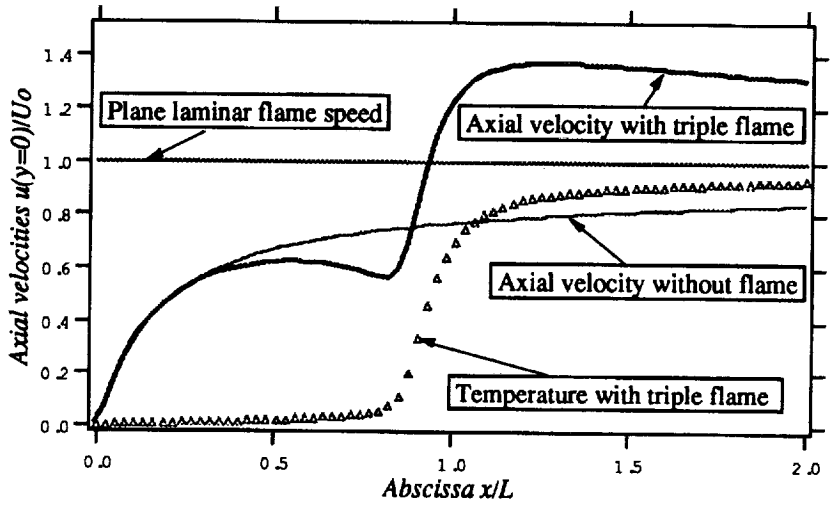

FIGURE 9. Axial velocity and temperature profiles along wake axis.

5.3 Stability domain of the diffusion flame in a wake flow

An important question for practical applications is the possibility of predicting flame stabilization. For triple flames, the usual technique used for this prediction is to compare the local flow speed and the triple flame speed. Stabilization may be obtained if the local flow speed is smaller than the flame speed.

DNS results as well as asymptotic theory provides a slightly more complex picture. Fig. 10 compares plots of axial velocity along the wake axis for three stabilized triple flames (Cases 13, 15, and 16) and one lifted flame (Case 19) with the propagation speed of the triple flame. When doing this exercise, one has to take into account the decrease of the flame speed to zero when the flame comes too close to the splitter plate. This phenomenon explains how a 'stable' stabilization point may be obtained in a triple flame. If heat losses towards the splitter plate are not accounted for, the local flow speed will always be less than the flame speed near the splitter plate, and this theory will always predict stabilization close to the splitter plate. It is therefore crucial to include heat losses effect into the evaluation of the flame speed U_F. This was done here in a crude way using the following formula:

$$U_F = U_P(1 - exp(-\frac{D - P_1 d}{P_2 d})) \tag{4}$$

where P_1 and P_2 are two Peclet numbers and D is the stand-off distance between splitter plate and flame. When $D < P_1 d$, no flame can exist. Furthermore, the influence of the wall is felt down to a distance of the order of $(P_1 + P_2)d$ (such relations may be found in studies of flame wall interaction and they were used here as a first guess of splitter plate effects). Typical values for P_1 and P_2 are 4. The quantity U_P is the triple flame speed determined in the previous section. It is proportional to S_L^0 but is larger due to flow divergence. For the present computation,

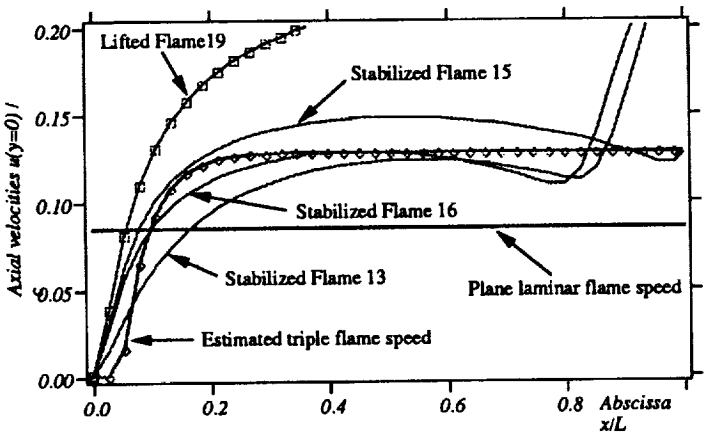

FIGURE 10. Velocity and temperature profiles along wake axis for different stabilized diffusion flames.

the following formula was used: $U_P = 1.5S_L^0$ as suggested from the study of the freely propagating triple flame studied above.

Fig. 10 shows that stabilization is indeed obtained if the flow speed on the wake axis U is at some point equal to U_F. For the lifted flame (Case 19), this is satisfied nowhere; the flame cannot find a stable location in the wake and it is lifted. Note that at the flame location itself, the local flow speed reaches a minimum as for free triple flames. However, this value of velocity is larger than the laminar unstrained flame speed. This is different from the "free" triple flame described above.

As for the freely propagating triple flame, the flow speed itself is strongly influenced by the flame. This influence may be evidenced by plotting the velocity difference on the wake axis between the reacting case and the cold flow case (Fig. 11). The triple flame induces a flow deceleration ahead of it. This deceleration scales with the laminar flame speed and may be compared to the result obtained for freely propagating flames in the previous sections.

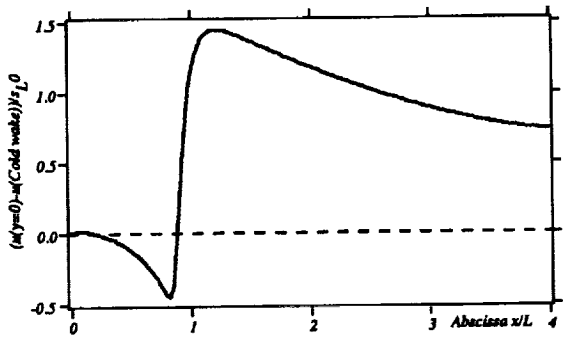

FIGURE 11. Velocity difference along wake axis between stabilized flame and cold flow cases.

From the above results, it is clear that in the configuration studied here, the velocity gradient is not the only controlling parameter for flame stabilization as suggested by asymptotic analysis. The velocity at infinity U_0 is also important. If this velocity is too small, we are too far from the assumptions of asymptotic analysis (where the velocity gradient is supposed to be maintained from $y = 0$ to $y = \infty$). For example, in the extreme case where the velocity U_0 is less than the flame speed S_L^0, the flame will always be stabilized independently of the velocity gradient A. However, for sufficiently large values of U_0, the velocity gradient A is indeed the controlling parameter. Lift off values of A were determined in these conditions for the two flames studied here by a process of trial and error. Results are given below. Since the asymptotic theory was developed with $ex = 1$, there is some uncertainty due to a slightly different expression of the reaction rate. Values of the parameters required to obtain lift off are also indicated (subscript $_{lo}$) both in code units and in flame units.

Table 2. Values of velocity gradient at liftoff

Flame	$A_{lo}L/c$	$A_{lo}L/c$	$\frac{S_L^0/\delta_l^0}{L/c}$	$\frac{A_{lo}}{(S_L^0/\delta_l^0)}$	$\frac{U_{o(lo)}}{c}$	$\frac{\delta_{lo}}{L}$	$\frac{U_{o(lo)}}{S_L^0}$	$\frac{\delta_{lo}}{\delta_l^0}$
	DNS	Asymp						
1	0.17	0.3	0.055	3.1	0.1	0.6	4.54	1.5
2	8	3.4	0.5	16	0.3	0.04	3.75	0.08

It appears that the trends provided by asymptotic analysis are correct but that the exact numbers are not right as expected from the differences between the asymptotic model and the actual computation. Flame 2 which has a lower activation temperature is much more difficult to lift than Flame 1. The normalized velocity gradient $A_{lo}L/c$ for lift off of Flame 2 is 47 times larger than the velocity gradient necessary to lift Flame 1. Asymptotic theory (developed in the limiting case of high activation energies) predicted an increase of 11 (instead of 47).

6. Interaction between vortical structures and triple flames

The triple-flame structure certainly plays an important role in turbulent combustion systems, for instance in the case of ignition of non-uniform mixtures it has been observed, through direct numerical simulation (Réveillon *et al* 1994), that triple flames traveling along the stoichiometric line may strongly contribute to the success of ignition. The triple flame then propagates in a turbulent environment, the stoichiometric line is distorted by the turbulence, and the flame is subjected to multiple interactions with vortical structures.

In this section, attention is focused on the interaction between the stabilized triple flame in the "far field" and a single vortex or a pair of vortices. Vortices are

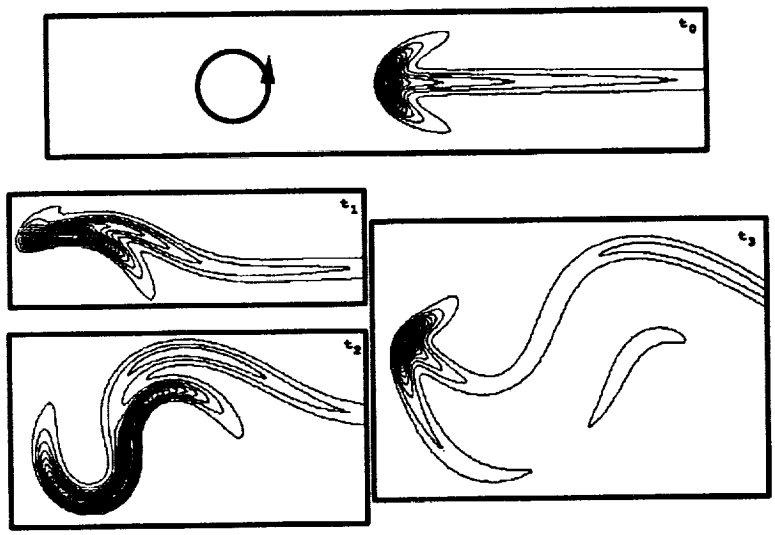

FIGURE 12. Triple flame interacting with a single vortex. Isocontours of the reaction rate are shown at three different times.

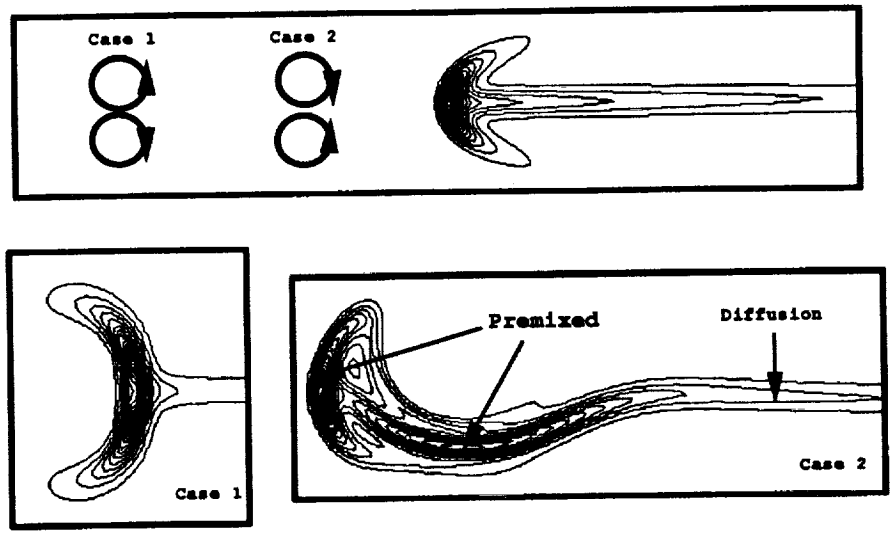

FIGURE 13. Triple flame interaction with two vortex pairs.

characterized by their maximum velocity, u_{vort}, and a length scale, δ_{vort}, chosen equal to the diameter of the single vortex or to the sum of the diameter and of the distance between the core of the vortices. Calculations have been realized for $u_{vort}/S_L^0 = 10$ and $\delta_{vort}/\delta_L^0 = 5$.

When either a single vortex or a pair of vortices proceed towards the triple flame, the mixture fraction field is convected by this vortical structure. Moreover, a distribution of strain rate is imposed to the diffusive and reactive layers and the resulting

velocity and species fields may strongly differ from those required to stabilize the flame. However, it is observed in Figs. 12 and 13 that the triple flame maintains the stabilization process by adjusting its structure to this new and unsteady environment. Also, because of their triple structure, these flames are much more robust than pure non-premixed flames. Indeed, to complete extinction it is required to extinguish both premixed wings and the diffusive part. It has been observed that even when, because of intense vorticity (i.e. strain rate), one of the wings is quenched the others reactive zones are able to sustain the combustion.

From Fig. 13 we observe that the triple-flame is responding to the modification of the chemical species field by a deformation of its internal structure following the location of the stoichiometric value of the mixture fraction. In the case of a single vortex (Fig. 12), the triple point and its wings are convected by the vortex, then eventually the trailing diffusion flame can be locally quenched and a certain amount of premixing is reached. From this local premixed zone, two triple flames facing each other may emerge. During these processes, the local consumption speed of the flame is increased or decreased depending on the position of the vortex with respect to the axis of symmetry.

By inducing a concave shape for the iso-mixture fraction line, a pair of vortices can even reverse the curvature of the wings, as seen in Fig. 13. This "reversible flame" is then convected by the mean velocity of the vortex pair.

When two kernels of premixing are created during the interaction, these two flames propagate, and if in a turbulent environment an iso-stoichiometric line is issued from both of the these premixed flames, two propagating triple-flames will emerge with their trailing diffusion flames.

These observations illustrate how non-premixed combustion can propagate through a turbulent non-uniform mixture, and one may speculate that these generic situations may also be observed in stabilization of turbulent jet flames in open air.

7. Conclusions

Triple flames correspond to the stabilization zone of a diffusion flame between two parallel streams of cold oxidizer and fuel, initially separated by a splitter plate. Such a flame is stabilized in a flow when its propagation speed is able to be sustained by the local flow velocity. As shown from asymptotic theory, two locations where this criterion is satisfied exist. First, the flame may be anchored in the wake of the splitter plate. If the upstream flow velocity is too high, the triple flame may also be lifted and stabilized far from the splitter plate in a zone where the flow velocity is lower. Of course, a too high upstream velocity leads to a complete blow-off of the flame. Numerical simulations of the two situations have been reported and quantitative results have been compared to asymptotic predictions. The flow field upstream of the triple flame is strongly modified by the heat release, and the flame is in fact able to sustain higher free-stream velocities than expected. The agreement with asymptotic theory is found to be qualitatively good. Interactions of the triple flame with a pair of vortices have also been studied. These flames are able to sustain strong vortex interactions by modification of its structure. This mechanism allows us to understand how a diffusion flame may be stabilized in a vortex street.

REFERENCES

DOLD, J. W. 1989 Flame propagation in a nonuniform mixture: analysis of a slowly varying triple flame. *Combust. & Flame.* **76,** 71.

DOLD, J. W., HARTLEY, L. J. & GREEN, D. 1991 Dynamics of laminar triple-flamelet structures in non-premixed turbulent combustion. *Dynamical Issues in Combustion Theory.* Springer-Verlag, 83.

HARTLEY, L. J. & DOLD, W. 1991 Flame propagation in a nonuniform mixture: analysis of a propagating triple-flame. *Combust. Sci. & Tech.* **80,** 23.

KERSTEIN, A. R., ASHURST, WM. T., & WILLIAMS, A. 1988 Field equations for interface propagation in an unsteady homogeneous flow field. *Phys. Rev. A.* **37,** 2728.

KIONI, P. N., ROGG, B., BRAY, K. N. C. & LIÑÁN, A. 1993 Flame spread in laminar mixing layers: the triple flame. *Combust. & Flame.* **95,** 276.

LELE, S. 1992 Compact finite difference schemes with spectral-like resolution. *J. Comp. Phys.* **103,** 16.

LIÑÁN, A. 1974 The asymptotic structure of counterflow diffusion flames for large activation energies. *Acta Astronaitica.* **1,** 1007.

LIÑÁN, A. 1994 Ignition and flame spread in laminar mixing layers. *Combustion in high speed flows.* ed. Buckmaster, Jackson, and Kumar. Kluwer Acad. Pub., 461.

LIÑÁN, A. 1988 Diffusion flame attachment and flame front propagation along mixing layers. *Combust. Sci. & Tech.* **57,** 129.

LIÑÁN, A. & CRESPO, A. 1976 Asymptotic analysis of unsteady diffusion flames for large activation energies. *Combust. Sci. & Tech.* **14,** 95.

POINSOT, T., VEYNANTE, D., & CANDEL, S. 1991 Quenching processes and premixed turbulent combustion diagrams. *J. Fluid Mech.* **228,** 561.

POINSOT, T. & LELE, S. 1992 Boundary conditions for direct simulations of compressible viscous flows. *J. Comp. Phys.* **101,** 104.

RÉVEILLON, J., DOMINGO, P., & VERVISCH, L. 1994 Autoignition in non-uniform mixture. To be published.

ROBERTS, W. L., DRISCOLL, J. F., DRAKE, M. C. & GOSS, L. P. 1993 Images of the quenching of a flame by a vortex – to quantify regions of turbulent combustion. *Combust. & Flame.* **94,** 58.

SAMANIEGO, J. M. 1993 Stretched induced quenching in flame-vortex interactions. *Annual Research Briefs.* Center for Turbulence Research, NASA Ames/Stanford U. 219.

TAKAHASI, F. & SCHMOLL, W. J. 1990 Lifting criteria of jet diffusion flames. *23rd Symposium (International) on Combustion.* The Combustion Institute, Pittsburgh, 677.

VERVISCH, L., KOLLMANN, W., & BRAY K. N. C. 1994 Pdf modeling for premixed turbulent combustion based on the properties of iso-concentration surfaces. *Proceedings of the 1994 Summer Program.* Center for Turbulence Research, NASA Ames/Stanford Univ.

WRAY, A. A. Private communication.

55-25
39735

Center for Turbulence Research
Proceedings of the Summer Program 1994

N95-21040

Turbulent transport in premixed flames

By C. J. Rutland[1] AND R. S. Cant[2]

Simulations of planar, premixed turbulent flames with heat release were used to study turbulent transport. Reynolds stress and Reynolds flux budgets were obtained and used to guide the investigation of important physical effects. Essentially all pressure terms in the transport equations were found to be significant. In the Reynolds flux equations, these terms are the major source of counter-gradient transport. Viscous and molecular terms were also found to be significant, with both dilatational and solenoidal terms contributing to the Reynolds stress dissipation. The BML theory of premixed turbulent combustion was critically examined in detail. The BML bimodal pdf was found to agree well with the DNS data. All BML decompositions, through the third moments, show very good agreement with the DNS results. Several BML models for conditional terms were checked using the DNS data and were found to require more extensive development.

1. Introduction

The use of DNS to study turbulent premixed flames has proved to be very successful. Most of the previous work in this area has focused on turbulence effects on the flame structure and statistics. This has provided invaluable information and insight for formulating turbulent combustion models for the mean reaction rate (Bray & Cant, 1991, Trouvé & Poinsot, 1993).

As combustion models have advanced it is apparent that turbulence models require more attention. Most modern turbulent combustion models rely heavily on mixing and time-scale (strain rate) information from the turbulence models. Thus, it is critical to understand how turbulent transport is affected by premixed combustion.

A model formalism developed by Bray, Moss, and Libby (1985) provides a highly developed theoretical basis for turbulent premixed flames. It is based on a presumed, bi-modal pdf of the reaction progress variable that is readily obtained using DNS simulations. The BML theory has proved successful in predicting several properties of premixed flames including counter-gradient transport (Libby & Bray, 1981).

The purpose of the current work is to study the major physical effects of premixed flames on turbulent transport in the context of the BML formalism. The BML theory results in decompositions of higher moments in terms of conditional lower moments. This approach simplifies closure and is examined in detail. A variety

1 Department of Mechanical Engineering,University of Wisconsin-Madison
2 Department of Mechanical Engineering, UMIST, Manchester M60 1QD, United Kingdom

PRECEDING PAGE BLANK NOT FILMED
PAGE 74 INTENTIONALLY BLANK

of terms in the BML theory require modeling approximations and these were also investigated. To provide data for this study, a direct simulation was made of a planar, turbulent premixed flame with heat release.

1.1. Simulation method and parameters

The flow configuration represents a planar turbulent flame shown schematically in Fig. 1. Turbulent flow enters at the left, passes through the flame brush, and exits at the right. The spanwise boundaries (y, z) are periodic and the flow is considered to be homogeneous in these directions. This configuration simplifies analysis of the results because most of the statistical information varies only in the streamwise direction.

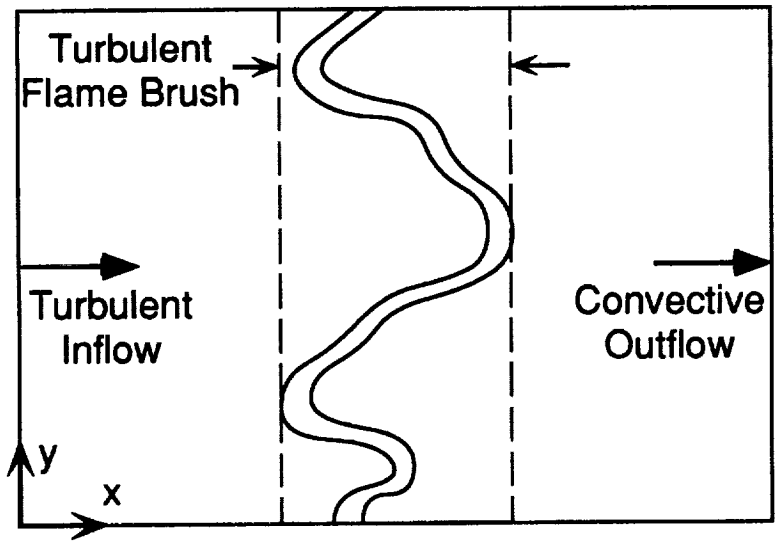

FIGURE 1. Schematic drawing of the computational domain and turbulent flame brush. The domain size is 5 x 2π x 2π and the grid size is 251 x 128 x 128.

The flame is considered to be premixed with a simple, single step, global reaction rate controlled by Arrhenius kinetics. Since the issues of interest concern only flame-turbulence interaction, acoustic energy is assumed to be unimportant and is removed from the equations using the low Mach number approximation (McMurtry *et al.*, 1986). However, the reaction is exothermic and heat release effects are retained through density variations in both time and space. It is also assumed that the Lewis number is unity and that Soret and Dufour effects are negligible. This results in the following set of equations:

$$\frac{\partial \rho}{\partial t} + \frac{\partial \rho u_i}{\partial x_i} = 0 \tag{1}$$

$$\frac{\partial \rho u_i}{\partial t} + \frac{\partial \rho u_j u_i}{\partial x_j} = -\frac{\partial p}{\partial x_i} + \frac{\partial \tau_{ij}}{\partial x_j} \tag{2}$$

$$\frac{\partial \rho T}{\partial t} + \frac{\partial \rho u_j T}{\partial x_j} = \frac{1}{RePr}\frac{\partial^2 T}{\partial x_j \partial x_j} + \dot{\omega} \tag{3}$$

where

$$\tau_{ij} = \frac{1}{Re}\left[\left(\frac{\partial u_i}{\partial x_j} + \frac{\partial u_j}{\partial x_i}\right) - \frac{2}{3}\frac{\partial u_k}{\partial x_k}\delta_{ij}\right] \tag{4}$$

$$\rho\left[\left(\frac{\alpha}{1-\alpha}\right)T + 1\right] = 1 \tag{5}$$

$$\dot{\omega} = B^* \rho (1-T) exp\left(\frac{-\beta(1-T)}{1-\alpha(1-T)}\right) \tag{6}$$

The equations have been non-dimensionalized using the laminar flame speed, the domain size in the spanwise direction, the inlet density, and the inlet and adiabatic flame temperatures. The non-dimensional temperature varies between 0 and 1. Thus, for these unity Lewis number simulations, temperature is equivalent to the reaction progress variable, c.

The equations are solved using Fourier pseudo-spectral methods for the spanwise derivatives and a sixth order, compact finite difference scheme (Lele, 1990) for the streamwise derivatives. Heat release in the flame precludes the use of Fourier methods in the streamwise direction.

The low Mach number approximation results in an elliptic aspect to the problem that is satisfied using a Poisson equation derived from the pressure gradient and the continuity equation. The solution is obtained on a pressure grid that is staggered only in the streamwise direction to avoid difficulties with pressure boundary conditions. Time integration is carried out using a combination of explicit 3rd-order compact Runge-Kutta and implicit Crank-Nicolson methods. The viscous and diffusion terms are treated primarily with the implicit method, and the non-linear terms are integrated with the explicit method.

The turbulent inflow boundary is simulated by a pre-computed isotropic turbulent field. This turbulent field is generated using a specified energy spectrum, continuity, and random phases. The energy spectrum for the current work is given by (Schumann & Patterson, 1978):

$$E(k) = C_o \frac{k}{k_o^2} exp\left(-\frac{k}{k_o}\right) \tag{7}$$

where $C_o = 3.0$ and $k_o = 5.0$. Using an approach developed by Lee *et al.* (1991), velocities are interpolated onto a plane moving through the isotropic field. This plane is used as the inflow boundary in the flame calculations. The outflow boundary uses a convection condition with corrections for global mass conservation (Rutland *et al.*, 1989). Additional information about the numerical methods can be found in Zhang (1994).

The problem parameters were chosen to satisfy several constraints. The primary consideration was to remain in the thin flame regime in which local, internal

flame structure is not significantly affected by the turbulence. From previous work (Rutland *et al.*, 1989), it was determined that the simulated flames are thin if the Karlovitz number, Ka, is approximately one or less, where:

$$Ka = \frac{\delta / S_L}{\lambda / u'} \tag{8}$$

Since at least 15 grid points are required to resolve the laminar flame structure, the thin flame requirement sets the basic grid spacing. In other words, grid resolution of the flame is more stringent than grid resolution of the turbulence. The flame was initiated as a laminar flame in a laminar flow field at the midpoint of the domain in the x-direction. At the start of the simulations, the turbulence at the inlet was rapidly, but smoothly, ramped-up to the inlet values reported in Table 1. As the calculation proceeded in time, the turbulence and flame interacted until a fairly stationary turbulent flame developed.

Table 1: Simulation and data set parameters

Problem parameters :	
α, heat release parameter, Eq. (5)	$0.7; (\tau = 2.3)$
β, activation energy parameter, Eq. (6)	6.0
B^*, pre − exponential parameter, Eq. (6)	1225.9
Re, scaling Reynolds number, Eq. (3)	30
Pr, Prandtl number	0.7
Inlet turbulence parameters :	
κ, kinetic energy	3.0
λ, Taylor microscale	0.18
L, integral length scale	1.35
Re_L, integral scale Reynolds number	56.7
Integral time scale	0.964
Data set information	
time (non − dimensional)	4.57
time (turn over)	4.73
laminar flame thickness	0.173
turbulent flame speed	2.03
turbulent flame brush location	$x \approx 1.0$ *to* 4.4

2. Reynolds stress budget

In the one-dimensional turbulent flame configuration being studied, spanwise derivatives of mean quantities are zero. The primary Reynolds stress transport equation is for the $(i,j) = (1,1)$ term:

$$\frac{\partial \overline{\rho u_1'' u_1''}}{\partial t} + \frac{\partial \tilde{u} \overline{\rho u_1'' u_1''}}{\partial x_1} = -2\overline{\rho u_1'' u_1''} \frac{\partial \tilde{u}_1}{\partial x_1} - \frac{\partial \overline{\rho u_1'' u_1'' u_1''}}{\partial x_1} - 2\overline{u_1'' \frac{\partial p}{\partial x_1}} + 2\overline{u_1'' \frac{\partial \tau_{1k}}{\partial x_k}} \tag{9}$$

In this basic form of the equation, the pressure and viscous terms have not been decomposed. Fig. 2 shows how the terms vary through the flame brush. We have adopted the convention that terms are plotted with their signs. Thus, terms from the right hand side of an equation are positive in the plots when the term is a source of the conserved quantity on the left hand side of the equation.

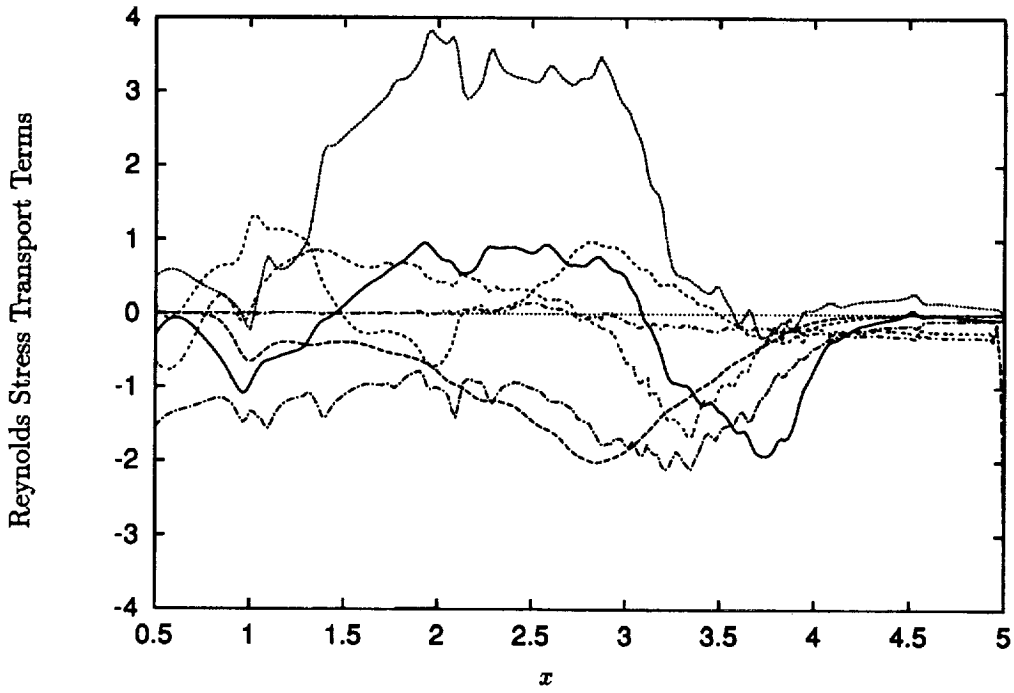

FIGURE 2. Reynolds stress budget, Eq. (9): convection term (———), production term (-----), triple correlation (- - - - -), velocity-pressure gradient (·····), viscous term (—·—·—), unsteady term (- - - -), unclosed term (- - - - -).

The Reynolds stress budget in Fig. 2 includes the unsteady term and the 'unclosed' amount in the budget. The magnitude of the unclosed quantity is negligible except in the latter part of the flame brush. This comes from errors in estimating the unsteady term via a simple finite difference when density changes. The unsteady term is still significant, indicating that there is some growth in the flame brush as it moves towards higher turbulence levels. Despite the relatively large unsteady term, it is believed that the Reynolds stress budget accurately reflects the relative importance and magnitudes of the various terms.

Fig. 2 shows that the pressure term is the dominate source of turbulence. The major sinks are the dissipation and 'production' terms. Note that in this context the production term actually represents mean dilatation since there is no mean shear. In the following paragraphs, the pressure and viscous terms are decomposed following conventional procedures in second moment modeling (Jones, 1980). While there

is some indication that this approach could be revised for reacting flows (Strahle, 1983), we follow the convention of Bray *et al.* (1985).

The pressure terms are dominant sources of turbulence in the flame brush. Standard decomposition first separates the mean and fluctuating pressure. Then, the fluctuating term is rewritten as a transport term, a pressure-strain term, and a pressure dilatation term:

$$-2\overline{u_1''\frac{\partial p}{\partial x_1}} = -2\overline{u_1''}\frac{\partial \bar{p}}{\partial x_1} - 2\frac{\partial \overline{u_1''p'}}{\partial x_1} + \Phi_{11} + \frac{2}{3}\overline{p'\frac{\partial u_k''}{\partial x_k}} \tag{10}$$

where

$$\Phi_{ij} = \overline{p'\left(\frac{\partial u_i''}{\partial x_j} + \frac{\partial u_j''}{\partial x_i}\right)} - \frac{2}{3}\overline{p'\frac{\partial u_k''}{\partial x_k}}\delta_{ij} \tag{11}$$

Fig. 3 shows the variation of the pressure terms through the flame brush. The dominant terms appear to be the mean pressure term and the pressure transport term. The mean pressure gradient is always positive and increases turbulence. The pressure transport term changes sign from positive in the leading half of the flame brush to negative in the trailing half. The pressure dilatation is also an important source of turbulence throughout the flame brush. The pressure strain is fairly small and oscillates around zero through the flame.

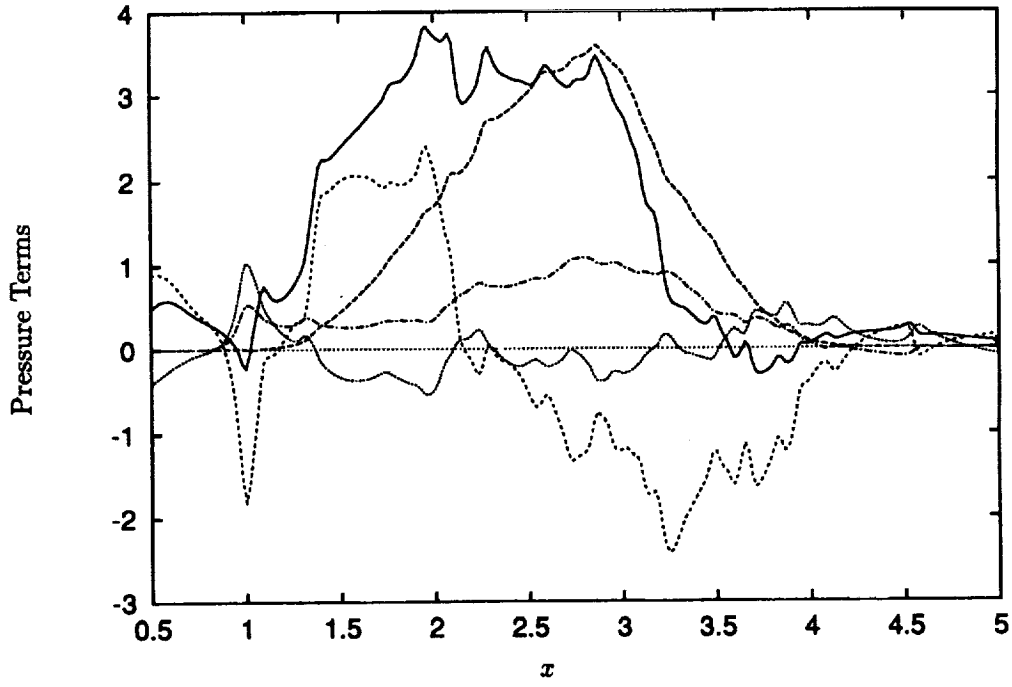

FIGURE 3. Pressure terms in the Reynolds stress budget, Eq. (10): total velocity-pressure gradient (———), mean pressure gradient (- - - - -), pressure transport (- - - - -), pressure strain (·····), pressure dilatation (—·—·—).

In general, these results justify the standard decomposition for the pressure term. The mean pressure gradient is significant and can be obtained directly in second moment models. The pressure strain is small so that its modeling should be less critical in the flame zone. Pressure dilatation is important and new models have been suggested from other DNS results (Zhang & Rutland, 1994). The most troublesome term is the pressure transport term. It is unlikely that combining this term with other transport terms in a gradient diffusion model will be satisfactory in premixed flames.

The major sinks for turbulence are the mean dilatation and the viscous terms. Since the mean dilatation is readily obtained in second moment models, we will focus only on the viscous term. Conventional decomposition similar to that used for the pressure term leads to

$$\overline{2u_1''\frac{\partial \tau_{1k}}{\partial x_k}} = 2\frac{\partial \overline{u_1''\tau_{1k}}}{\partial x_k} - 2\overline{\tau_{1k}}\frac{\partial \overline{u_1''}}{\partial x_k} - \Pi_{11} - \frac{2}{3}\overline{\tau'_{mk}\frac{\partial u''_m}{\partial x_k}} \tag{12}$$

where

$$\Pi_{ij} = \overline{\tau'_{ik}\frac{\partial u''_j}{\partial x_k} + \tau'_{jk}\frac{\partial u''_i}{\partial x_k} - \frac{2}{3}\tau'_{mk}\frac{\partial u''_m}{\partial x_k}\delta_{ij}} \tag{13}$$

This gives a turbulent transport term, a mean viscous term, a deviatoric term (Π_{ij}), and the dissipation function. Note that in the viscous stress, τ_{ij} is separated into a mean and fluctuating term using standard averaging instead of Favre averaging. This facilitates the separation of terms used in Eq. (12).

The variation of viscous terms through the flame brush are plotted in Fig. 4. This shows that the dissipation function dominates and the mean term is small, as expected. Interestingly, the transport term and the deviatoric term tend to have opposite signs and nearly balance each other in the leading half of the flame. It is unclear why this occurs. Recent work by Antonia *et al.* (1994) indicate that the anisotropy tensor for the dissipation function varies as the Reynolds stress anisotropy. This suggests that Π_{ij} might follow the Reynolds stress anisotropy. However, this was not found in the current reacting flow dataset since the Reynolds stress anisotropy increases through the flame brush while Π_{ij} decreases slightly.

Since the dissipation function dominates the viscous term, it is examined in more detail. This is facilitated by separating the term into solenoidal and dilatational terms as follows:

$$\overline{\frac{2}{3}\tau'_{ij}\frac{\partial u''_i}{\partial x_j}} = \frac{2}{3Re}\left[\overline{2\hat{S}'_{ij}\hat{S}'_{ij}} + \frac{4}{3}\overline{\theta'\theta'}\right] \tag{14}$$

where

$$\hat{S}'_{ij} = \frac{1}{2}\left(\frac{\partial u'_i}{\partial x_j} + \frac{\partial u'_j}{\partial x_i}\right) - \frac{1}{3}\theta'\delta_{ij} \tag{15}$$

$$\theta' = \frac{\partial u'_k}{\partial x_k} \tag{16}$$

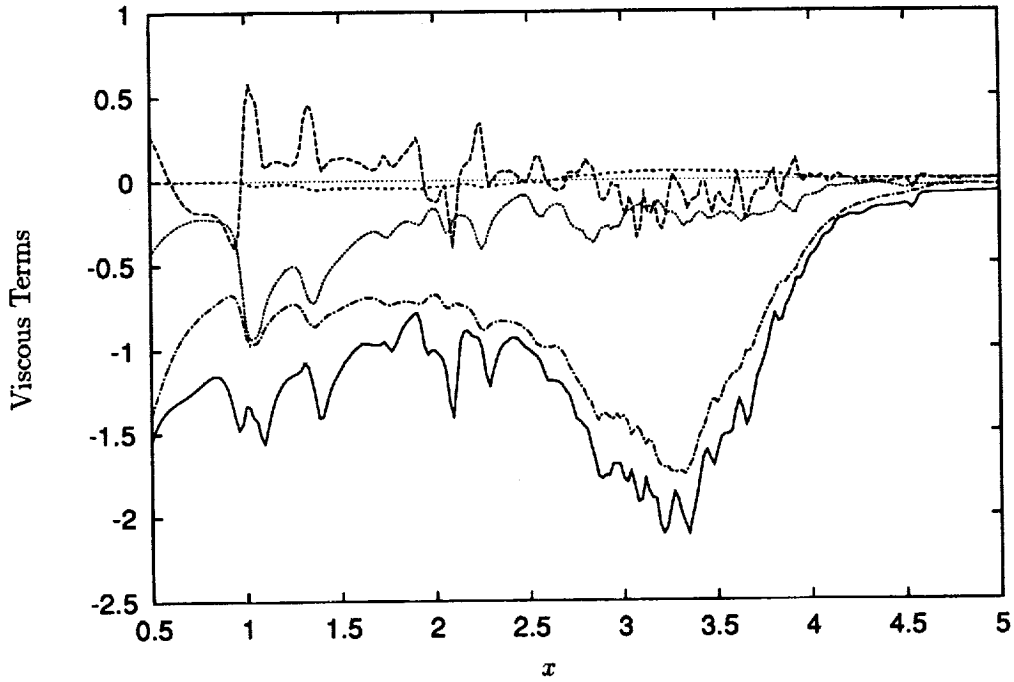

FIGURE 4. Viscous terms in the Reynolds stress budget, Eq. (12): total viscous term (———), viscous stress transport (– – – – –), mean viscous stress gradient term (- - - - -), deviatoric term (·····), dissipation function (—·—·—).

This result uses the symmetry of τ'_{ij} and the relationship:

$$\overline{g'h''} = \overline{g'h'} \tag{17}$$

Note that the solenoidal term is not purely homogeneous. However, comparisons with the homogeneous dissipation calculated using enstrophy have shown the non-homogenous contributions to be small in the current data set. Thus, the main contribution to the solenoidal term is from vorticity.

Fig. 5 shows the variation of the dissipation terms through the flame brush. The dilatational dissipation is significant throughout and dominates in the leading half of the flame brush. The solenoidal dissipation becomes significant in the latter half of the flame brush. This was found to coincide with increasing vorticity generation by baroclinic torque.

Since the only dilatation in the flow occurs at the local flame sheet, the dilatational dissipation comes exclusively from this region. This was confirmed by evaluating the dilatational dissipation conditioned on the progress variable so that contributions from the reactants, flame zone, and products could be determined. This is important since the modeling of terms that are due to the local flame sheet can be fairly straightforward provided the mean reaction rate (or flame sheet density) is known.

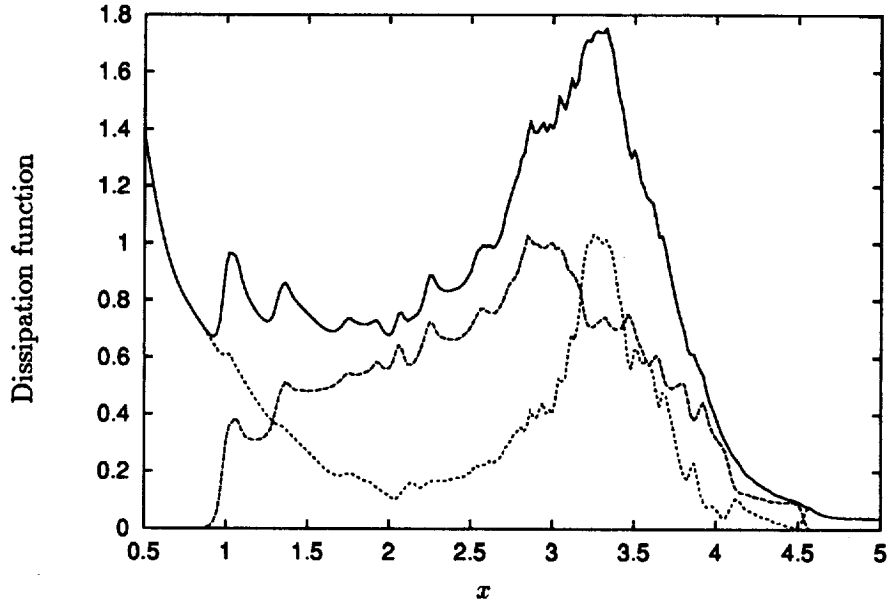

FIGURE 5. Dissipation function in the Reynolds stress budget, Eq. (14): total dissipation function (———), dilatational dissipation (-----), solenoidal dissipation (-----).

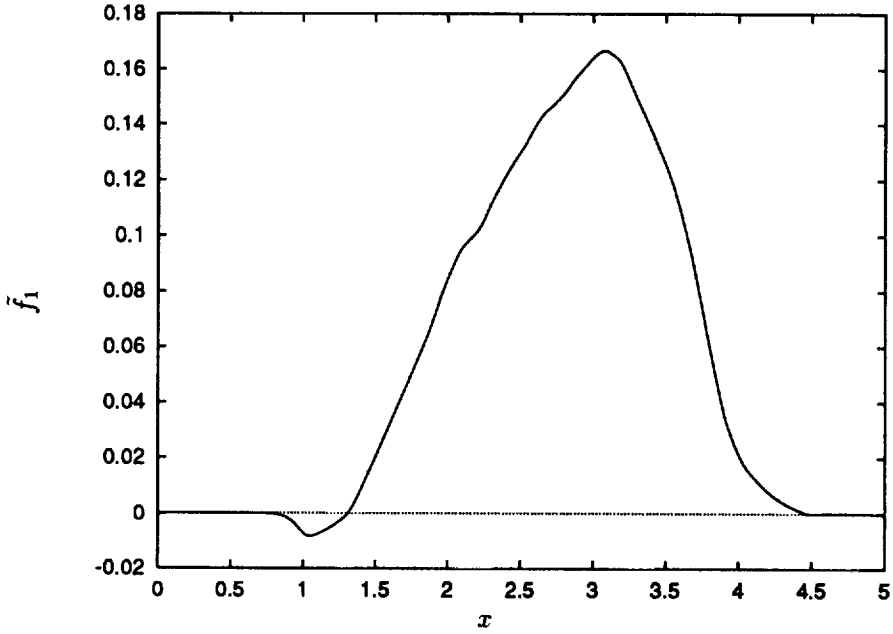

FIGURE 6. Reynolds flux $\tilde{f}_1 = \overline{\rho u_1'' c''}$ vs. distance x through the flame. Positive values indicate the presence of counter-gradient transport.

3. Scalar flux budget

The existence of counter-gradient transport in turbulent premixed flames has been confirmed both by experiment (Moss, 1980) and by theoretical analysis (Libby & Bray, 1981). Turbulent transport of heat and mass is found to occur in a direction opposite to that indicated by the sign of the mean gradient. In the present simulations this is equivalent to counter-gradient transport of the reaction progress variable c, whose mean gradient is positive in the x-direction and identically zero in the other two directions. Thus counter-gradient transport corresponds to positive values of the x-wise component of the turbulent Reynolds flux of reaction progress variable $\tilde{f}_1 = \overline{\rho u_1'' c''}/\bar{\rho}$.

A plot of this quantity is shown in Fig. 6, where it is evident that strong counter-gradient transport is indeed present throughout almost the entire flame brush, except for a small region at the leading edge in which gradient transport prevails. This result is consistent with previous findings (Libby, 1985).

It is possible to investigate the mechanisms behind the occurrence of counter-gradient transport by examining the budget of the Reynolds flux $\tilde{f}_1$. The balance equation for $\tilde{f}_1$ may be written as

$$\begin{array}{ccccccccc} \dfrac{\partial \bar{\rho}\tilde{f}_1}{\partial t} & + & \dfrac{\partial\, \bar{\rho}\tilde{u}_k\tilde{f}_1}{\partial\, x_k} & = & -\overline{\rho u_k'' u_1''}\dfrac{\partial\, \tilde{c}}{\partial\, x_k} & - \bar{\rho}\tilde{f}_k\dfrac{\partial\, \tilde{u}_1}{\partial\, x_k} & + \overline{u_1'' w} & - \dfrac{\partial \overline{\rho u_k'' u_1'' c''}}{\partial\, x_k} \\ (x) & & (ix) & & (i) & & (ii) & (iii) & (iv) \end{array}$$

$$\begin{array}{ccccccc} -\overline{c''}\dfrac{\partial\, \bar{p}}{\partial\, x_1} & - \overline{c''\dfrac{\partial\, p'}{\partial\, x_1}} & + \left(\overline{c''\dfrac{\partial\, \tau_{1k}}{\partial\, x_k}}\right. & \left. - \overline{u_1''\dfrac{\partial\, J_k}{\partial\, x_k}}\right) \\ (v) & (vi) & (vii) & (viii) \end{array} \qquad (18)$$

Each term in this equation was evaluated individually from the DNS dataset and all are plotted in Fig. 7, with signs included as they appear in the equation. It should be noted that the simulated flame is not yet statistically stationary, but the budget is balanced within statistical error by the inclusion of the non-stationary term. It is clear from the figure that the dominant terms in the budget are those involving the pressure. The mean pressure term (v) is largest over more than half of the flame brush while the fluctuating pressure term (vi) is also significant, particularly over the forward portion of the flame brush. Both tend to promote counter-gradient transport by contributing towards positive values of the Reynolds flux. These results lend support to the theory that counter-gradient transport is produced by the local pressure gradient acting preferentially to accelerate the light, low-density burned gas more than the heavier unburned gas. In the present case the mean pressure gradient is negative, i.e. decreasing in the positive x-direction. Thus the burned gas is accelerated in the same direction and counter to the gradient of mean product mass fraction (and progress variable). It is worth noting that this mechanism would operate even in the absence of a contribution from the fluctuating pressure term.

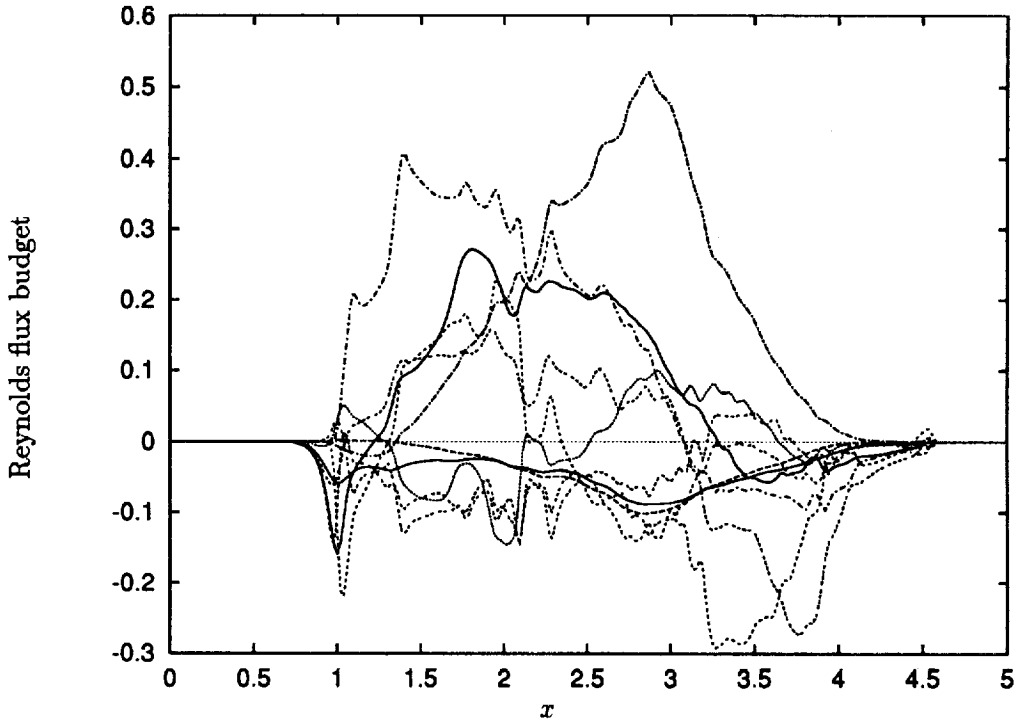

FIGURE 7. Reynolds flux budget, Eq. (18): production term (*i*) (——— , lower), production term (*ii*) (– – – – –), velocity-reaction rate term (*iii*) (– – – – –), third-moment term (*iv*) (·····), mean pressure term (*v*) (— — —), fluctuating pressure term (*vi*) (– – – – –), viscous term (*vii*) (– – – –), molecular diffusion term (*viii*) (– – – – – –), convective term (*ix*) (– – – – – – – –), non-stationary term (*x*) (——— , upper).

The role of this term in further promoting counter-gradient transport is clear from the present results and indicates that this term is not negligible in this context.

None of the other source terms in the budget of Reynolds flux appears individually to exert a major influence on turbulent transport. The pressure terms are balanced by a combination of the other terms and there is no other dominant effect. Nevertheless it is interesting to examine the velocity-reaction rate term (*iii*) and the dissipation rate of the scalar flux (terms *vii* and *viii*). Both of these terms are driven by direct molecular effects in the presence of reacting gas and both are subject to the need for closure modeling. The velocity-reaction rate term is plotted in Fig.8. This term is non-zero only within the flame brush and appears noisy due to the relative lack of statistical sample associated with the presence of reaction. The correlation becomes negative towards the rear of the flame, reflecting the tendency of the velocity fluctuation magnitude to increase even as the reaction rate is falling.

The dissipation terms account for the removal of Reynolds flux due to viscous effects (term *vii*) and to molecular diffusion (term *viii*) and are plotted in Fig. 9. Both are non-zero only in the presence of reaction and are noisy for reasons given

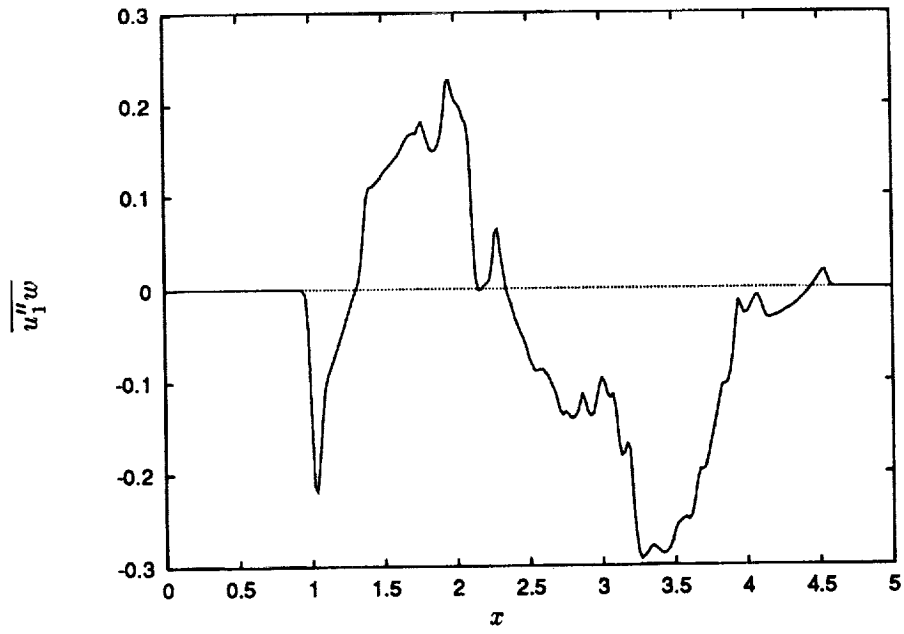

FIGURE 8. The velocity-reaction rate correlation $\overline{u_1''w}$ (term *iii*) vs. distance x through the flame.

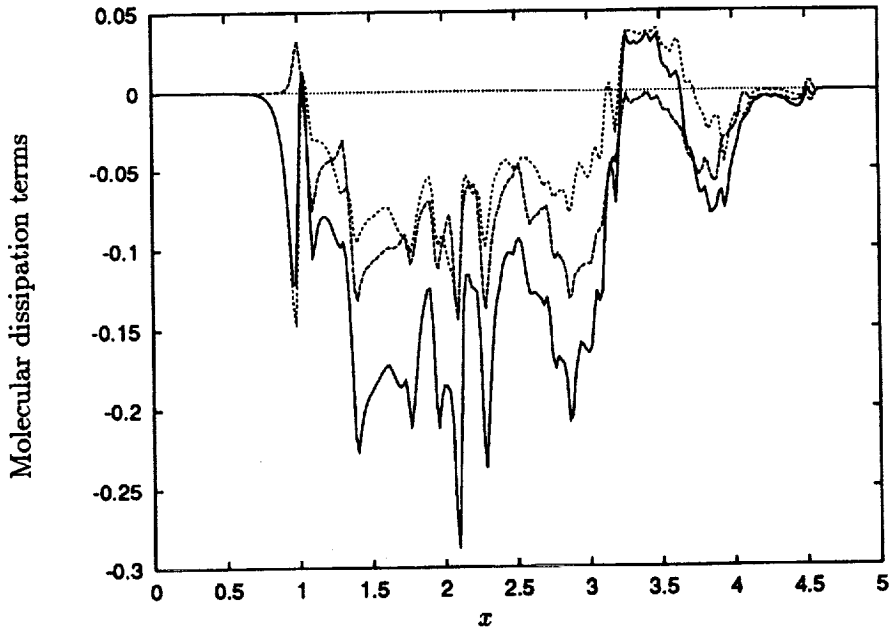

FIGURE 9. Dissipation terms in the Reynolds flux balance Eq. (18), plotted vs. distance x through the flame. Viscous term (*vii*) (-----), molecular diffusion term (*viii*) (- - - - -), total dissipation (*vii* + *viii*) (——).

above. Each has a predominantly negative sign and acts as a mild sink throughout the flame brush. In the present case their magnitudes are very similar indicating that viscous and diffusional effects are of roughly equal importance in this flame.

4. BML Decompositions

The BML formalism is based on the premise that the laminar flamelets occurring within the turbulent flame brush are thin in the sense that the pdf of the progress variable is dominated by the entries at zero and unity, with little contribution from the interior part of the distribution. This has been checked using DNS by evaluating the weight functions α, β and γ corresponding respectively to unburned reactants, fully-burned products and material undergoing reaction. Results for these quantities are shown in Fig. 10. It is clear that γ is very much smaller than α and β throughout almost the entire flame brush, providing emphatic confirmation that the BML assumption is indeed valid in this flame.

The only exceptions occur near to the leading edge of the flame brush where it is clear that $\beta \to 0$ faster than γ, and at the trailing edge where $\alpha \to 0$ faster than γ. The maximum value of γ is about 0.15, attained near the center of the flame brush. Terms multiplying γ in several of the key BML expressions have been evaluated also and are generally found to be small.

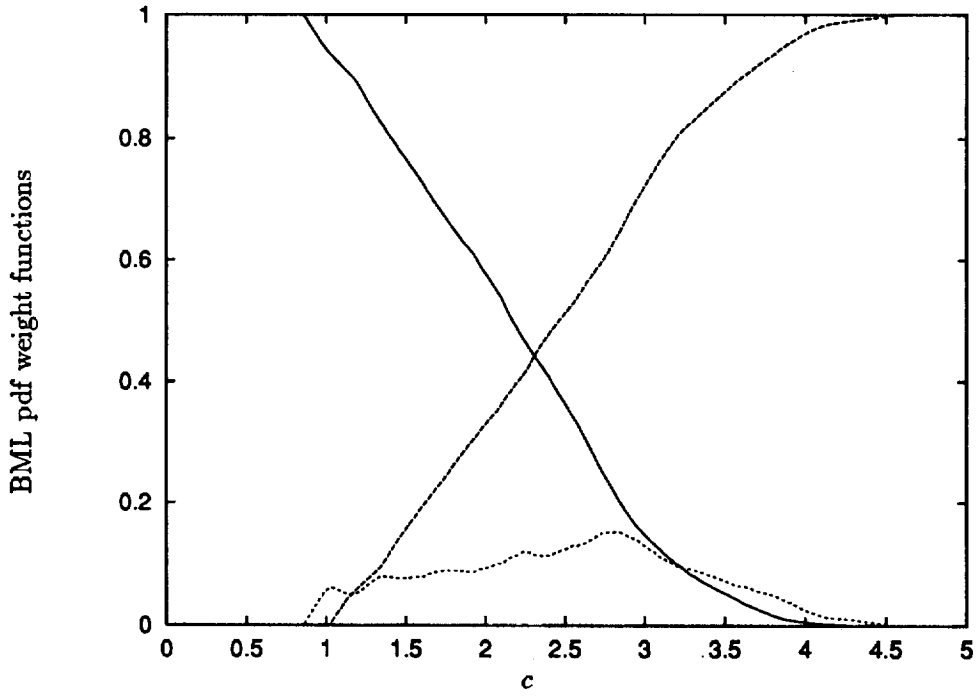

FIGURE 10. The weight functions α, β and γ in the BML pdf of progress variable c plotted against distance x through the flame. Reactant weight function α (———), product weight function β (-----), reacting material weight function γ (- - - - -).

The BML formalism may be used to decompose all of the second- and third-moment unconditional statistics of interest in terms of conditional statistics of lower order. For example, a covariance such as the Reynolds flux $\tilde{f}_1$ may be expressed in terms of a difference of conditional means:

$$\tilde{f}_1 = \overline{\rho u_1'' c''} \Big/ \bar{\rho} = \tilde{c}(1-\tilde{c})(\bar{u}_{1P} - \bar{u}_{1R}) \tag{19}$$

where subscripts P and R indicate product and reactant, respectively. The conditional reactant and product mean velocities are shown in Fig. 11. The abrupt fall to zero at the ends is due to a lack of statistical sample: there is no more reactant (product) on which to condition as $c \to 1(0)$. It is interesting to note that there is no tendency of the conditional velocities or their difference to approach some asymptotic value at either limit. Checks were carried out to ensure that the results were insensitive to the choice of conditioning levels: this was confirmed for threshold values of c set at (0.01, 0.99), (0.05, 0.95) and (0.10, 0.90). Sample sizes were also checked and found to be adequate for the evaluation of the conditional means. Clearly the conditional difference $\bar{u}_{1P} - \bar{u}_{1R}$ is positive throughout most of the flame brush, implying through Eq.(19) that the Reynolds flux is positive and that counter-gradient diffusion is to be expected.

The BML formalism becomes particularly valuable in treating the unclosed third-moment correlations which appear in the balance equations for the Reynolds stresses and fluxes. Expressions for these terms are given in Bray *et al.* (1985) as

$$\begin{aligned}\overline{\rho u_i'' u_j'' u_m''} \Big/ \bar{\rho} = \tilde{c}(1-\tilde{c}) \big[&(1-2\tilde{c})(\bar{u}_{iP} - \bar{u}_{iR})(\bar{u}_{jP} - \bar{u}_{jR})(\bar{u}_{kP} - \bar{u}_{kR}) \\ &+ \left(\overline{u_i' u_j'}_P - \overline{u_i' u_j'}_R\right)(\bar{u}_{kP} - \bar{u}_{kR}) \\ &+ \left(\overline{u_j' u_k'}_P - \overline{u_j' u_k'}_R\right)(\bar{u}_{iP} - \bar{u}_{iR}) \\ &+ \left(\overline{u_i' u_k'}_P - \overline{u_i' u_k'}_R\right)(\bar{u}_{jP} - \bar{u}_{jR}) \big] \\ &+ (1-\tilde{c})\overline{u_i' u_j' u_k'}_R + \tilde{c}\overline{u_i' u_j' u_k'}_P + O(\gamma)\end{aligned} \tag{20}$$

and

$$\begin{aligned}\overline{\rho u_i'' u_j'' c''} \Big/ \bar{\rho} = \tilde{c}(1-\tilde{c}) \big[&(1-2\tilde{c})(\bar{u}_{iP} - \bar{u}_{iR})(\bar{u}_{jP} - \bar{u}_{jR}) \\ &+ \left(\overline{u_i' u_j'}_P - \overline{u_i' u_j'}_R\right) \big] + O(\gamma)\end{aligned} \tag{21}$$

In each case the third-moment quantity is decomposed as a series of terms involving mainly first- and second-moment conditional differences. This decomposition is central to the BML closure approach since only the conditional quantities need to be modeled, and these contain no contribution arising from density change. In order to check the decomposition, every quantity in each of these expressions was evaluated from the DNS database, and comparisons between the exact and the decomposed

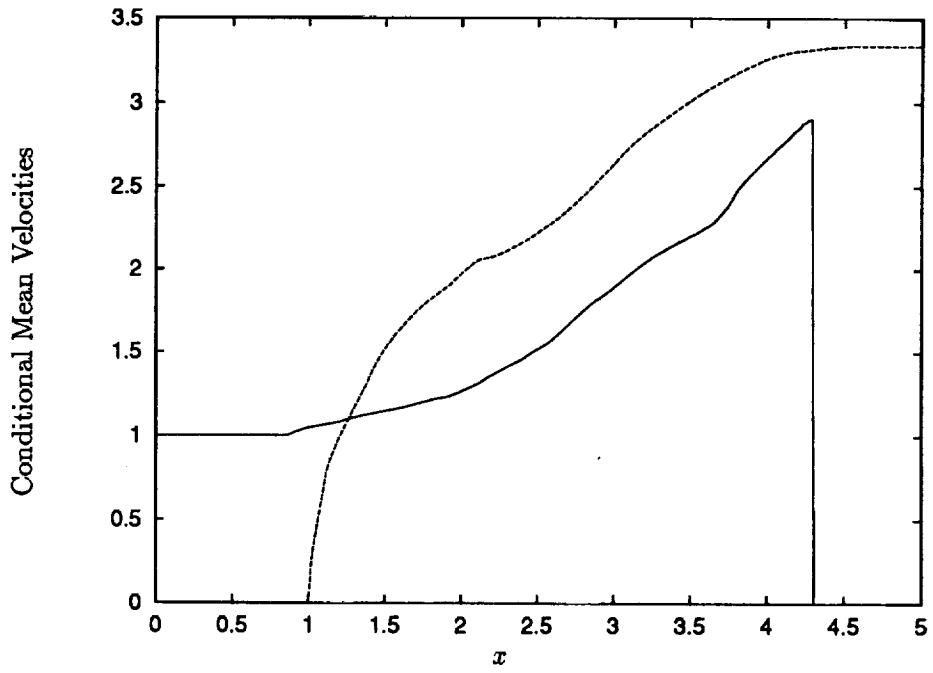

FIGURE 11. Conditional reactant and product mean velocities $\tilde{u}_{1R}$ (———) and $\tilde{u}_{1P}$ (-----) plotted against x distance x through the flame.

results are shown in Fig. 12a for the Reynolds stress component $\overline{\rho u_1'' u_1'' u_1''}/\bar{\rho}$ and in Fig. 12b for the flux component $\overline{\rho u_1'' u_1'' c''}/\bar{\rho}$. Agreement is very good in each case over almost the entire flame brush, and the accuracy of the BML decomposition is verified. The third-moment stress remains non-zero outside the flame brush due to contributions from the conditional third moments. The third- moment flux by contrast is non-zero only within the flame brush, and there are discrepancies between exact and decomposed values at the leading and trailing edges. These are due once again to a lack of conditional sample as $c \to 0, 1$. All ten independent components of the third-moment stress were evaluated and compared, as were all six independent components of the third-moment flux, and the same degree of agreement was apparent in all cases.

5. BML Modeling

BML closure modeling is based on balance equations for the second-moment Reynolds stresses and fluxes. These balance equations contain divergences of the third-moment terms as decomposed in Eqs. (20) and (21) above, and hence closure models are required for the unknown conditional differences. The conditional velocity differences $(\tilde{u}_{1P} - \tilde{u}_{1R})$ may be evaluated from the Reynolds fluxes $\tilde{f}_i$ using Eq. (19), and hence require no modeling.

The only terms remaining to be modeled are the differences of the conditional

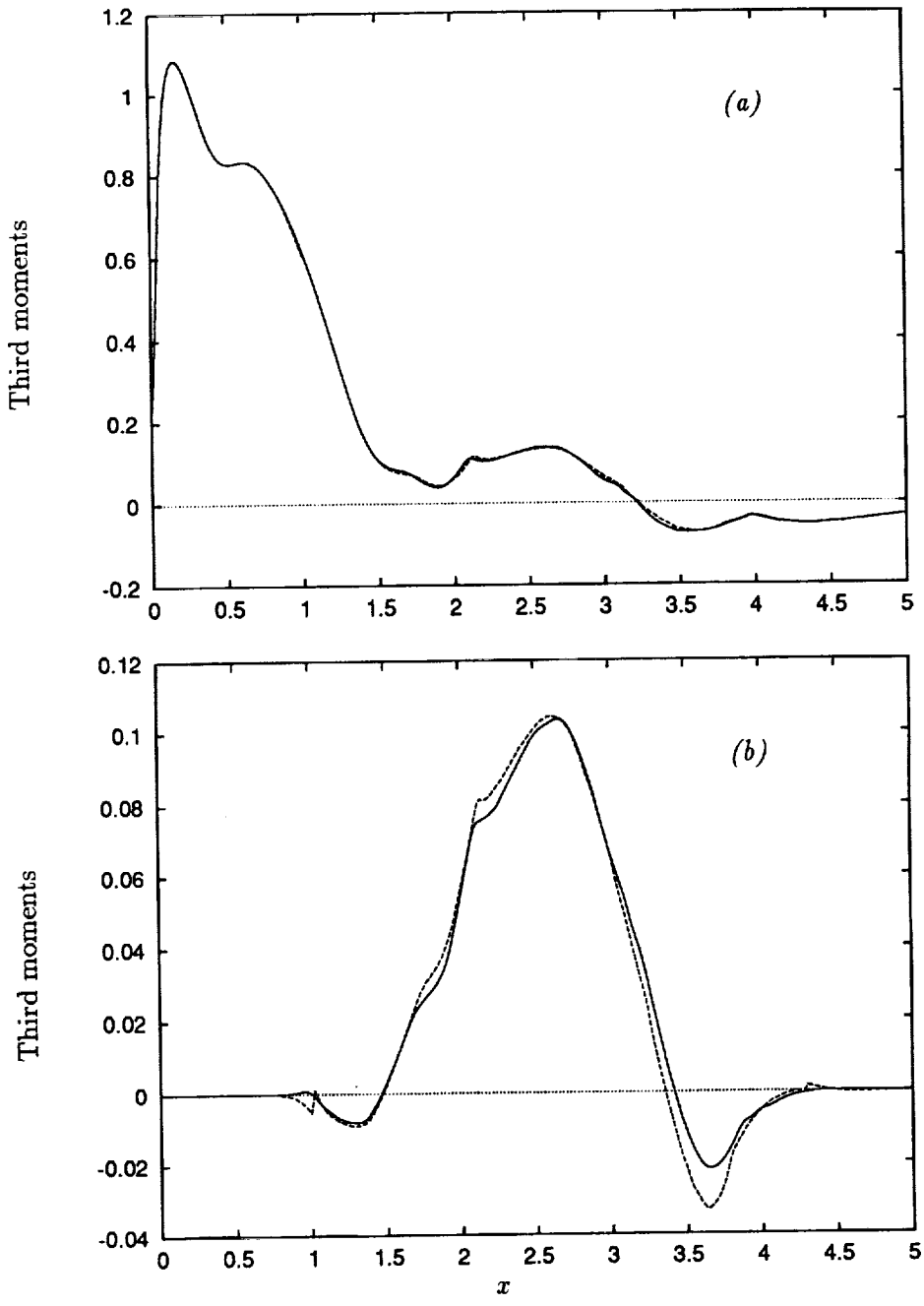

FIGURE 12. Decomposition of third-moment terms. Exact (———) and BML-decomposed (-----) forms plotted together for comparison. *(a)* Third-moment stress component $\overline{\rho u_1'' u_1'' u_1''}/\bar{\rho}$. *(b)* Third-moment flux component $\overline{\rho u_1'' u_1'' c''}/\bar{\rho}$

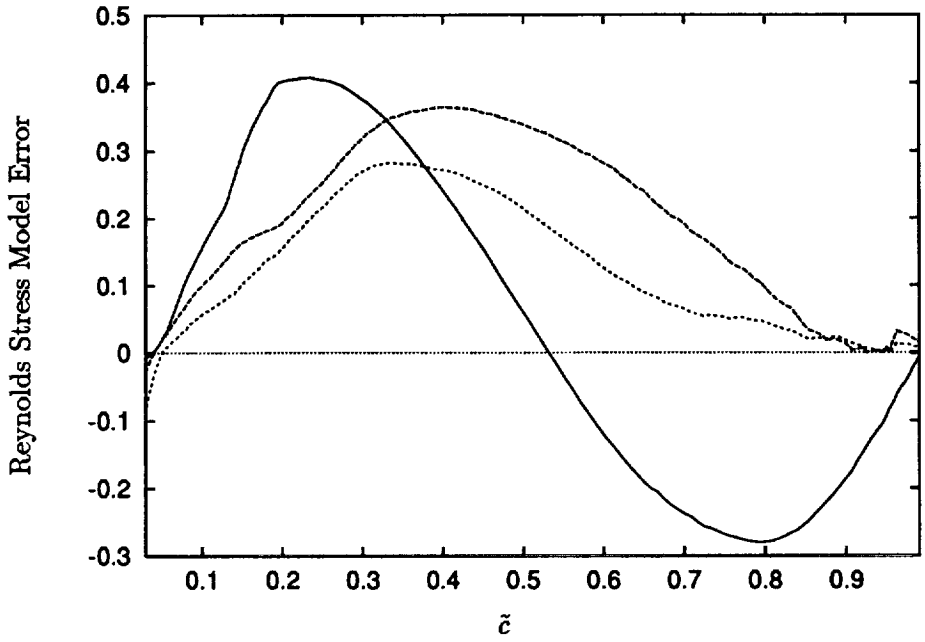

FIGURE 13. Errors in the modeled differences in conditional Reynolds stresses, Eq. (22): 11 (———), 22 (-----), 33 (- - - - -). The errors are normalized by the difference between the maximum and minimum value over the whole range.

second-moment and third-moment stresses. A simple linear fit to model the difference in second moment stress has been proposed by Bray *et al.* (1985):

$$\left(\overline{u_i'u_j'}_P - \overline{u_i'u_j'}_R\right) \approx \left[(1-\kappa_1)\,\tilde{c} + (\kappa_0 - 1)\,(1-\tilde{c})\right] \frac{\overline{\rho u_i'' u_j''}}{\bar{\rho}} \tag{22}$$

where the constants κ_0 and κ_1 are allowed to vary with (i,j). This model was motivated by the requirement that the total Favre-averaged Reynolds stresses reduce to the conditional stresses at the edges of the flame brush: $\tilde{c} \to 0, 1$. This requirement also provides a means to evaluate the κ terms.

The κ terms were evaluated using the DNS data and the results are shown in Fig. 13. The figure shows the error of the modeled terms for the three normal stresses. By construction, the errors go to zero near the boundaries of the flame. The exact limits $\tilde{c} \to 0, 1$ could not be used to find the κ terms since the sample rates were too low. However, at least for the normal stresses, the κ values approached the limits fairly smoothly and were readily estimated. The errors plotted in Fig. 13 show that a linear fit is not very accurate. The terms would be better modeled by a second order fit for the tangential stresses and a third order fit for the normal stresses. However, further theoretical work is needed before such ad-hoc models are developed.

A generalized gradient-transport model has been proposed for modeling the differences of the conditional third-moment stresses (Bray *et al.* 1985):

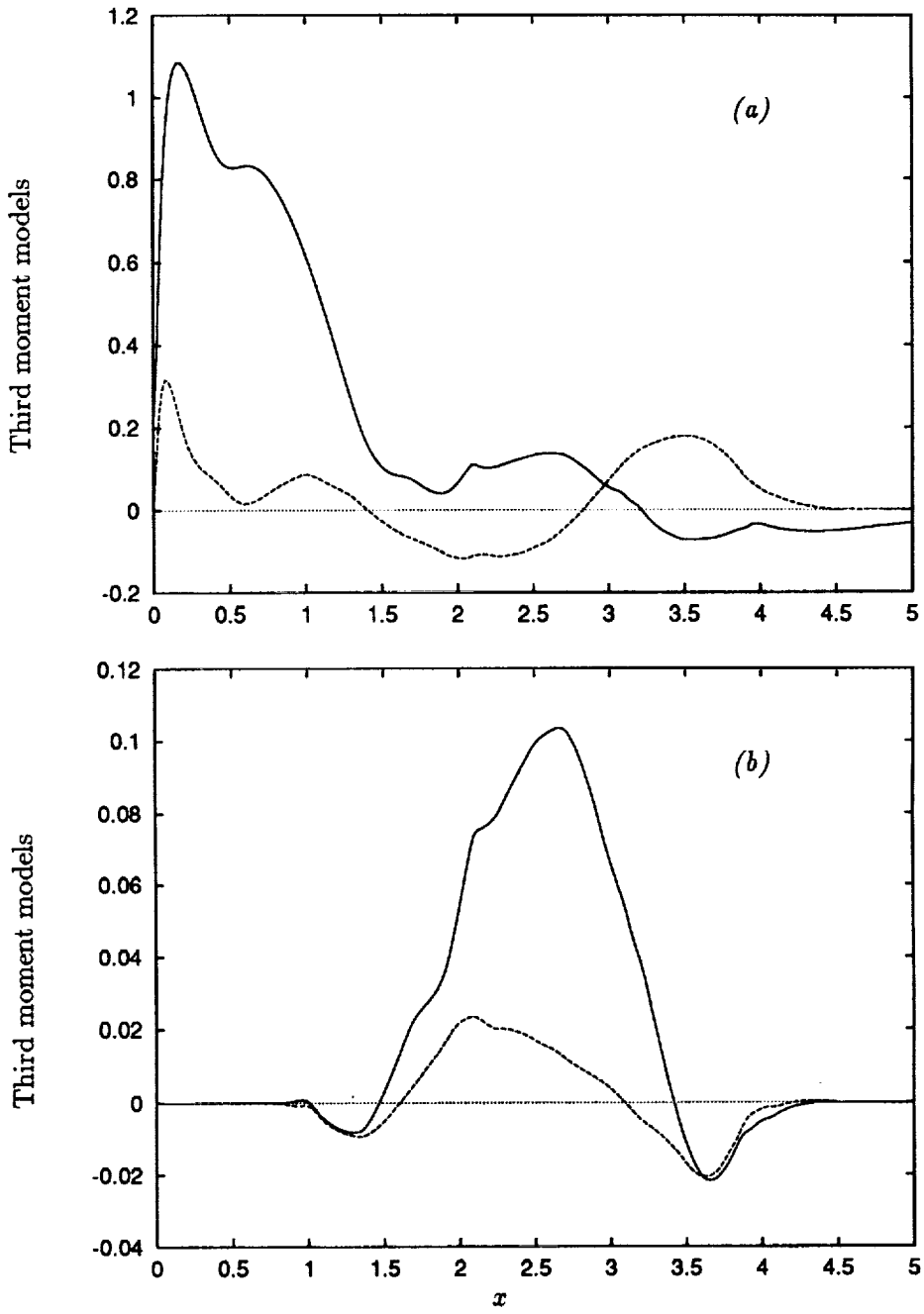

FIGURE 14. Modeling of third-moment terms. Exact (———) and modeled (-----) forms plotted together for comparison. *(a)* Third-moment stress component $\overline{\rho u_1'' u_1'' u_1''}/\bar{\rho}$. *(b)* Third-moment flux component $\overline{\rho u_1'' u_1'' c''}/\bar{\rho}$.

$$(1-\tilde{c})\,\overline{u_i'u_j'u_k'}_R + \tilde{c}\,\overline{u_i'u_j'u_k'}_P \approx -c_s\frac{\tilde{k}}{\tilde{\varepsilon}}\frac{\overline{\rho u_k''u_m''}}{\bar{\rho}}\frac{\partial}{\partial x_m}\left(\frac{\overline{\rho u_i''u_j''}}{\bar{\rho}}\right) \tag{23}$$

All of the terms in Eqs. (20) and (21) which require modeling according to eqs.(22) and (23) have been evaluated from the DNS data and assembled to yield modeled third-moment stress and flux components $\overline{\rho u_1''u_1''u_1''}/\bar{\rho}$ and $\overline{\rho u_1''u_1''c''}/\bar{\rho}$, and the results are plotted in Fig. 14. The agreement of the modeled terms with their exact equivalents is poor and contrasts strongly with the excellent agreement obtained using the BML decomposition only. Both the conditional stress sub-model and the third-moment gradient diffusion sub-model are seen to be seriously deficient, failing to capture even the qualitative trends of the exact third-moment stress. Some evidence of the correct trend is present in the comparison for the third-moment flux, but quantitative agreement is not achieved. Again, all ten independent third-moment stresses and all six independent third- moment fluxes were evaluated, but the agreement remained comparably poor in all cases. Clearly the present sub-models are in need of considerable improvement.

6. Conclusions

The DNS data have been used to identify several important physical effects regarding turbulent transport occurring in premixed flames. Probably the most significant is counter gradient transport of the scalar flux. This was found previously in experiments (Moss, 1980) and predicted by theoretical analysis (Libby & Bray, 1981). The DNS results help confirm that pressure effects are the major contribution to counter gradient transport.

The DNS results also revealed the importance of pressure terms in Reynolds stress transport. The mean pressure gradient term dominates, but pressure transport and pressure dilatation are also very important. Dissipation, which is a major sink in the Reynolds stress budget, was found to be composed of both solenoidal and dilatational terms. The DNS data showed both terms to be significant.

Results have been obtained from the DNS which allow thorough validation of the BML model formalism in a statistically planar turbulent premixed flame. The principal assumption of BML - that the pdf of the progress variable is strongly bimodal - has been checked and found to be valid throughout the simulated flame. All of the second-moment and third-moment Reynolds stress and Reynolds flux components have been evaluated and compared with their equivalents obtained using the BML formalism. Very good agreement is observed where terms obtained through the BML decomposition are themselves evaluated from the DNS. This confirms that BML provides a valid theoretical framework for the treatment of premixed turbulent flames.

By contrast, agreement is poor where the decomposed terms are evaluated using currently available model expressions. Thus, while the framework has been found to be satisfactory, the modeling itself must be improved. Much of the information which will be required to underpin the necessary model development is contained within the present DNS dataset. Its exploitation will form the next major task.

REFERENCES

ANTONIA, R. A., DJENIDI, L., & SPALART, P. R. 1994 Anisotropy of the dissipation tensor in a turbulent boundary layer. *Physics of Fluids.* **6-7,** 2475-2479.

BRAY, K. N. C. & CANT, R. S. 1991 Some Applications of Kolmogorov's Turbulence Research in the Field of Combustion. *Proc. R. Soc. Lond. A.* **434,** 217-240.

BRAY, K. N. C., LIBBY, P. A. & MOSS. J. B. 1985 Unified Modeling Approach for Premixed Turbulent Combustion - Part I: General Formulation. *Combust. Flame.* **61,** 87-102.

JONES, W. P. 1980 Models for Turbulent Flows with Variable Density and Combustion *Prediction Methods for Turbulent Flows*, W. Kollmann, Ed., Hemisphere Publishing Corp.

LEE, S., LELE, S. K. & MOIN, P. 1991 Simulations of Spatially Decaying Compressible Turbulence. Center for Turbulence Research, NASA Ames/Stanford Univ., Manuscript 126.

LELE, S. K. 1992 Compact Finite Difference Schemes with Spectral-like Resolution. *J. of Comp. Physics.* **103,** 16-42.

LIBBY, P. A. & BRAY, K. N. C. 1981 Countergradeint Diffusion in Premixed Turbulent Flames. *AIAA Journal.* **19-2,** 205-213.

LIBBY, P. A. 1985 Theory of Normal Premixed Turbulent Flames Revisited. *Prog. Energy. Combust. Sci..* **11,** 83-96.

MCMURTRY, P. A., JOU, W.-H., RILEY, J. J.& METCALFE, R. W. 1986 Direct Numerical Simulations of a Reacting Mixing Layer with Chemical Heat Release. *AIAA Journal.* **24-6,** 962-970.

MOSS, J. B. 1980 Simultaneous measurements of concentrations and velocity in an open premixed turbulent flame. *Combust. Sci. Tech.* **22,** 119-129.

RUTLAND, C. J., FERZIGER, J. H.& CANTWELL, B. J. 1989 Effects of Strain, Vorticity, and Turbulence on Premixed Flames. *Report No. TF-44.* Thermosciences Division, Dept. of Mechanical Engineering, Stanford University.

SCHUMANN, U. & PATTERSON, G. S. 1978 Numerical study of pressure and velocity fluctuations in nearly isotropic turbulence. *J. Fluid Mech.* **88-4,** 685-709.

STRAHLE, W. C. 1983 Velocity-Pressure Gradient Correlation in Reactive Turbulent Flows. *Combust. Sci. Tech.* **32,** 289-305.

TROUVÉ, A. & POINSOT, T. 1993 The Evolution Equation for the Flame Surface Density in Turbulent Premixed Combustion, Center for Turbulence Research, NASA Ames/Stanford Univ., Manuscript 140.

ZHANG, S. & RUTLAND, C. J. 1994 Pressure Effects in Turbulent Trasnport of Premixed Flames. *Submitted to Comb. and Flame.*

ZHANG, S. 1994 Simulations of Premixed Flames with Heat Release, Ph.D. Thesis, Dept. of Mech. Engr., Univ. of Wisconsin.

39736
N95-21041

Center for Turbulence Research
Proceedings of the Summer Program 1994

The coupling between flame surface dynamics and species mass conservation in premixed turbulent combustion

By A. Trouvé[1], D. Veynante[2], K. N. C. Bray[3] AND T. Mantel[4]

Current flamelet models based on a description of the flame surface dynamics require the closure of two inter-related equations: a transport equation for the mean reaction progress variable, $\widetilde{c}$, and a transport equation for the flame surface density, Σ. The coupling between these two equations is investigated using direct numerical simulations (DNS) with emphasis on the correlation between the turbulent fluxes of $\widetilde{c}$, $\overline{\rho u'' c''}$, and Σ, $\langle u'' \rangle_S \Sigma$. Two different DNS databases are used in the present work: a database developed at CTR by A. Trouvé and a database developed by C. J. Rutland using a different code. Both databases correspond to statistically one-dimensional premixed flames in isotropic turbulent flow. The run parameters, however, are significantly different, and the two databases correspond to different combustion regimes. It is found that in all simulated flames, the correlation between $\overline{\rho u'' c''}$ and $\langle u'' \rangle_S \Sigma$ is always strong. The sign, however, of the turbulent flux of $\widetilde{c}$ or Σ with respect to the mean gradients, $\partial \widetilde{c}/\partial x$ or $\partial \Sigma/\partial x$, is case-dependent. The CTR database is found to exhibit gradient turbulent transport of $\widetilde{c}$ and Σ, whereas the Rutland DNS features counter-gradient diffusion. The two databases are analyzed and compared using various tools (a local analysis of the flow field near the flame, a classical analysis of the conservation equation for $\widetilde{u'' c''}$, and a thin flame theoretical analysis). A mechanism is then proposed to explain the discrepancies between the two databases and a preliminary simple criterion is derived to predict the occurrence of gradient/counter-gradient turbulent diffusion.

1. Flame surface density and species mass evolution equations

The objective of theoretical descriptions of turbulent reacting flows is to provide tractable expressions for unclosed terms appearing in the conservation equations for mass, momentum, and energy. In the following, we focus our attention on mass conservation. In the classical theory of turbulent premixed flames, under the assumption of simple chemistry, the mass fractions of the reactive species are all linearly related and may be expressed in terms of a single reduced mass fraction called the reaction progress variable, $c = 1 - (Y_R/Y_{R,u})$, where Y_R is the fuel mass

1 Institut Francais du Pétrole, France
2 Laboratoire E.M2.C., C.N.R.S. and Ecole Centrale Paris, France
3 Cambridge University, U.K.
4 Center for Turbulence Research

fraction and $Y_{R,u}$ its value in the unburnt gas. The ensemble-averaged species mass balance is then written as:

$$\frac{\partial(\overline{\rho}\widetilde{c})}{\partial t} + \nabla.(\overline{\rho}\widetilde{\mathbf{U}}\widetilde{c}) + \nabla.(\overline{\rho\mathbf{u}''c''}) = \nabla.(\overline{\rho D\nabla c}) + \overline{\dot{\omega}}_R/Y_{R,u}, \tag{1}$$

where the tilde superscript denotes a Favre (density-weighted) average $\widetilde{Q} \equiv \overline{\rho Q}/\overline{\rho}$, the double prime symbol denotes the instantaneous deviation from the Favre average, $Q'' = Q - \widetilde{Q}$, D is the fuel mass diffusivity, and $\dot{\omega}_R$ represents the mass of fuel consumed by chemical reaction, per unit time and per unit volume.

In the flamelet theory for turbulent premixed combustion, the reaction zone is assumed to be a thin surface separating fresh and burnt gases. The local reaction rate may be expressed in terms of the local flame surface-to-volume ratio, Σ', and the ensemble-averaged reaction rate may be expressed in terms of the mean flame surface-to-volume ratio, also called the flame surface density, $\Sigma = \overline{\Sigma'}$ (Bray 1980, Williams 1985, Peters 1986):

$$\overline{\dot{\omega}_R} = \rho_u Y_{R,u} \langle S_C \rangle_S \, \Sigma, \tag{2}$$

where ρ_u is the density in the unburnt gas and $\langle S_C \rangle_S$ is the mean fuel consumption speed. The mean consumption speed accounts for local variations of the reaction rate along the flame surface while the flame surface density, Σ, characterizes the flame wrinkling due to the turbulent motions. For flames with Lewis numbers close to unity, $\langle S_C \rangle_S$ remains close to the laminar burning velocity s_L and to first order the mean reaction rate is proportional to Σ (Haworth & Poinsot 1992; Rutland & Trouvé 1993; Trouvé & Poinsot 1994). The $\widetilde{c}$-equation is then re-written as:

$$\frac{\partial(\overline{\rho}\widetilde{c})}{\partial t} + \nabla.(\overline{\rho}\widetilde{\mathbf{U}}\widetilde{c}) + \nabla.(\overline{\rho\mathbf{u}''c''}) = \nabla.(\overline{\rho D\nabla c}) + \rho_u s_L \Sigma. \tag{3}$$

In (3), the contribution of molecular diffusion is usually neglected for high Reynolds number flows and closure is only required to describe the turbulent flux of $\widetilde{c}$, $\overline{\rho\mathbf{u}''c''}$ and the flame surface density, Σ. A variety of modeling choices may be made for those terms ranging from standard gradient transport approximations for $\overline{\rho\mathbf{u}''c''}$ or simple algebraic closures for Σ, to full transport equations for both $\overline{\rho\mathbf{u}''c''}$ and Σ.

For instance, in the Coherent Flame Model (Marble & Broadwell 1977; Darabiha *et al.* 1987; Maistret *et al.* 1989; Candel *et al.* 1990) the flame surface density is obtained via a modeled formulation of an exact evolution equation called the Σ-equation (Pope 1988; Candel & Poinsot 1990):

$$\frac{\partial\Sigma}{\partial t} + \nabla.\widetilde{\mathbf{U}}\Sigma + \nabla.\langle\mathbf{u}''\rangle_S\Sigma + \nabla.\langle w\mathbf{n}\rangle_S\Sigma = \langle\kappa\rangle_S \, \Sigma, \tag{4}$$

where w is the flame front propagation speed, $\mathbf{n}$ is the flame normal vector pointing towards the fresh gases, κ is the flame stretch, and $\langle\ \rangle_S$ denotes a flame surface mean defined as an area-weighted ensemble-average (Pope 1988), $\langle Q\rangle_S \equiv \overline{Q\Sigma'}/\overline{\Sigma'} = \overline{Q\Sigma'}/\Sigma$. The three convective terms on the left-hand side of (4) are transport terms that correspond respectively to convection by the mean flow, turbulent diffusion,

and flame propagation. The term on the right-hand side of the equation is the source/sink term for flame surface density and accounts for production of flame surface area due to hydrodynamic straining and dissipation due to combined effects of flame propagation and flame surface curvature (Trouvé & Poinsot 1994). Different closure assumptions are required in the Σ-equation, in particular to calculate: the turbulent diffusion velocity, $\langle \mathbf{u}'' \rangle_S$, the transport due to flame propagation, $\langle w\mathbf{n} \rangle_S$, and the turbulent flame stretch, $\langle \kappa \rangle_S$ (see Duclos *et al.* (1993) for a critical review of the different formulations of the modeled Σ-equation that can be found in the literature).

While the need to model Σ through a transport equation has become increasingly recognized in recent years, the modeling of the turbulent flux of $\widetilde{c}$, $\overline{\rho \mathbf{u}'' c''}$, remains in comparison somewhat controversial. Using a standard gradient diffusion approximation (GD), one may write:

$$\overline{\rho u_i'' c''} = -\mu_t \frac{\partial \widetilde{c}}{\partial x_i}, \tag{5}$$

where μ_t is the turbulent viscosity.

Premixed flames, however, are known to exhibit counter-gradient diffusion (CGD) of mass reactant (Libby & Bray 1981; Bray *et al.* 1981). CGD is related to the differential effect of mean pressure gradients on cold, heavy reactants and hot, light products. This effect may be shown very simply under the classical Bray-Moss-Libby assumption of fresh reactants ($c = 0$) and fully burnt products ($c = 1$) separated by a thin flame sheet, leading to a bimodal probability density function of c. The x-component of the turbulent flux may then be written as (Bray 1980):

$$\overline{\rho u'' c''} = \overline{\rho} \widetilde{u'' c''} = \overline{\rho} \widetilde{c}(1 - \widetilde{c}) \left(\overline{U}_b - \overline{U}_u \right), \tag{6}$$

where $\overline{U}_b$ and $\overline{U}_u$ are respectively the x-component of the conditional mean velocity within burnt and unburnt gases. Thermal expansion and the associated flow acceleration through the flame will tend to make $\overline{U}_b$ greater than $\overline{U}_u$, thereby promoting counter-gradient turbulent diffusion of $\widetilde{c}$ ($\overline{\rho u'' c''} / \partial \widetilde{c} / \partial x > 0$, contrary to the predictions from Eq. (5)). Note that counter-gradient diffusion has been observed in a number of experiments (Moss 1980; Shepherd *et al.* 1982; Cheng & Shepherd 1991; Armstrong & Bray 1992).

While CGD has been extensively studied in the past ten years, the implications of this non-gradient transport phenomenon on the distribution of flame surface densities and the overall mean reaction rate remains unknown. In fact, a variety of conflicting modeling assumptions are still used in the current literature ranging from assumptions that simply neglect CGD and use standard gradient transport approximations as displayed in (5) (Darabiha *et al.* 1987; Maistret *et al.* 1989; Candel *et al.* 1990; Cant *et al.* 1990) to formulations where such approximations are carefully avoided and where closure is achieved by writing a transport equation for $\overline{\rho \mathbf{u}'' c''}$ (for instance in the Bray-Moss-Libby model: Bray 1980; Bray *et al.* 1989; Bray 1990).

It is important to realize that the closure assumptions required in the Σ-equation cannot be made independently of those required in the equation for $\widetilde{c}$. This may be best understood by considering the interdependence of Σ and $\widetilde{c}$. As seen in Eq. (3), Σ is a source term for $\widetilde{c}$ and the mean reaction progress variable will depend strongly on the distribution of flame surface densities. In addition, following Pope (1988), Σ may be expressed in terms of statistical properties of the c-field. For instance, the flame surface density is expressed as the product of the expected value for the magnitude of the gradient of c, conditioned on the flame surface, times the probability of being on that surface:

$$\Sigma = \langle |\nabla c| \mid c = c_f \rangle \; p(c_f), \tag{7}$$

where the flame is viewed as a surface-contour, $c = c_f$, and where $p(c_f)$ is the probability of $c = c_f$.

This theoretical coupling between Σ and $\widetilde{c}$ must have implications for models. Some of those implications are already well-known. For instance, in current models of the Σ-equation, while the turbulent transport, $\langle \mathbf{u}'' \rangle_S$, is described exclusively in terms of statistics of the turbulent flow field, the realizability of the combustion model is ensured by using a modeled expression for the flame stretch, $\langle \kappa \rangle_S$, that is $\widetilde{c}$-dependent. For instance, the closure model for $\langle \kappa \rangle_S$ leads to a vanishing Σ when the reaction reaches completion and $\widetilde{c}$ approaches unity.

The objective of the present work is to study further the exact implications of the coupling between the equations for Σ and $\widetilde{c}$. More specifically, direct numerical simulation (DNS) is used to determine: (1) if and under what conditions gradient-diffusion (GD) or counter-gradient diffusion (CGD) is observed in the $\widetilde{c}$-equation; (2) if there is any correlation between the turbulent flux of $\widetilde{c}$ and the turbulent flux of Σ, and in particular whether CGD (GD) in the $\widetilde{c}$-equation occurs with CGD (GD) in the Σ-equation.

2. Two different DNS databases

In the present work, two different direct numerical simulation databases are used. The first one, referenced as the CTR database, was developed at CTR by A. Trouvé and was previously used to study the statistics of the turbulent flame stretch, $\langle \kappa \rangle_S$, across the turbulent flame brush (Trouvé & Poinsot 1994). The CTR database was developed using a fully compressible, 3D, Navier-Stokes solver with one step irreversible chemistry. The numerical configuration corresponds to a premixed flame propagating in decaying isotropic turbulence. The ratio between the turbulent rms velocity and the laminar flame speed, u'/s_L, is set to an initial value of 10 and decreases to about 3 after four turbulent eddy turnover times. The second database was recently developed by C. J. Rutland (see Rutland & Cant 1994) using a low Mach number, 3D code. The Rutland code assumes a constant viscosity, whereas the CTR code features temperature-dependent transport coefficients. The numerical configuration corresponds to a premixed flame propagating in approximately stationary, weak turbulence, $u'/s_L \approx 1$. In the Rutland configuration, like in the CTR one, the simulated turbulent flame is statistically 1D. Comparisons between

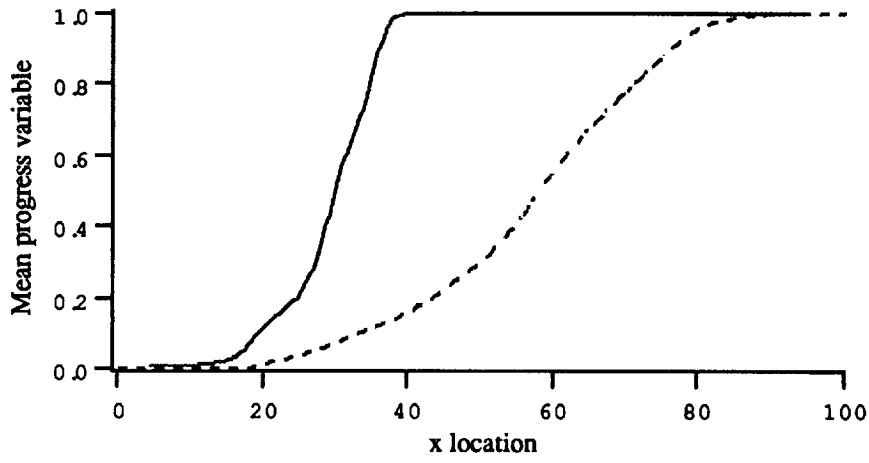

FIGURE 1. Comparison of the CTR and the Rutland DNS. The mean progress variable $\widetilde{c}$ is plotted as a function of x-location along the direction of mean propagation. The comparison is performed at a time selected so that the turbulent flame speed is approximately the same in both cases. Length scales are made non-dimensional by the laminar flame thickness, δ_L. ——— : CTR database; ---- : Rutland database.

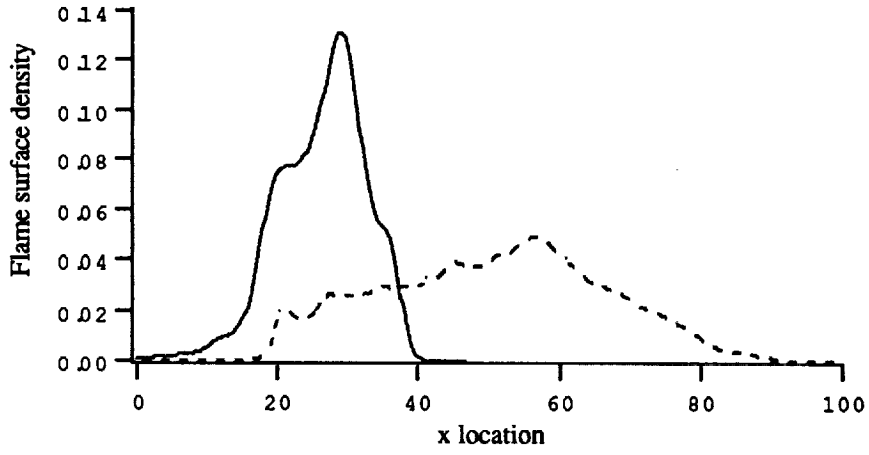

FIGURE 2. Comparison of the CTR and the Rutland DNS. The flame surface density Σ is plotted as a function of x-location along the direction of mean propagation. ——— : CTR database; ---- : Rutland database.

the two databases are performed assuming that the different computations correspond to the same laminar flame (same laminar flame thickness, δ_L, same laminar flame speed, s_L, and same molecular transport coefficients).

While the two databases feature turbulent flames with similar values of the turbulent flame speed, S_T, they also correspond to turbulent flames with significantly different structure. Fig. 1 shows two instantaneous profiles of the Favre-averaged progress variable $\widetilde{c}$ as a function of x-location along the direction of mean propagation. Fig. 2 presents a similar comparison for the flame surface density profiles. It is seen that the flame brush is about three times thicker in Rutland's database compared to the CTR case. Also, the flame front wrinkling, as measured by the magnitude of the flame surface density, is much greater in the CTR database. As seen in Fig. 3, the two DNS lie at different locations in the classical turbulent combustion diagram due to Borghi and Barrère (see Borghi 1985) and therefore correspond to different turbulent combustion regimes. The CTR database corresponds to flames that are more turbulent and feature smaller length scales. The box plotted in Fig. 3 corresponds to a zone where counter-gradient diffusion has been experimentally observed. Rutland's simulation lies in this zone, the CTR database lies outside. Note also that according to the Klimov-Williams criterion, the CTR database corresponds to non-flamelet combustion. Recent work by Poinsot *et al.* (1991) has shown that the domain of flamelet combustion is in fact significantly larger and the CTR database is within that domain according to the Poinsot *et al.* criterion (see Fig. 3).

The most interesting result is that the two databases display striking differences in their turbulent transport properties. Fig. 4 shows the turbulent flux $\widetilde{\overline{\rho}u''c''}$ as a function of the mean progress variable $\widetilde{c}$. Rutland's database exhibits counter-gradient turbulent diffusion of $\widetilde{c}$ ($\widetilde{\overline{\rho}u''c''} > 0$), whereas gradient diffusion transport is found in the CTR database ($\widetilde{\overline{\rho}u''c''} < 0$). These differences can be related to differences between the two codes (compressible/incompressible and variable/constant molecular transport coefficients), differences due to different initial and boundary conditions, or differences due to different values of the run parameters corresponding to different combustion regimes.

Figs. 5a and 5b present the spatial variations of different relevant mean flow velocities, $\widetilde{U}$, $\overline{U}_u$, $\overline{U}_b$, and $\langle u \rangle_S$, across the turbulent flame brush. In the Rutland simulation, the mean velocity within the products, $\overline{U}_b$, is always greater than the mean velocity within the reactants, $\overline{U}_u$, which according to (6) corresponds to counter-gradient turbulent diffusion of $\widetilde{c}$. In the CTR database, however, $\overline{U}_u$ is greater than $\overline{U}_b$, which again according to (6) corresponds to gradient turbulent diffusion. This last result may seem surprising since it is expected that the thermal expansion will induce a burnt gas velocity larger than the fresh gas velocity. It is worth emphasizing that conditional velocities may be difficult to interpret because the sampling is quite different for $\overline{U}_u$ and for $\overline{U}_b$. For example, at the leading edge of the turbulent flame brush, the flow field corresponds mainly to values of the progress variable $c = 0$, and the fresh gas conditional velocity, $\overline{U}_u$, is computed from a large number of samples. At that location, a few pockets have a value of

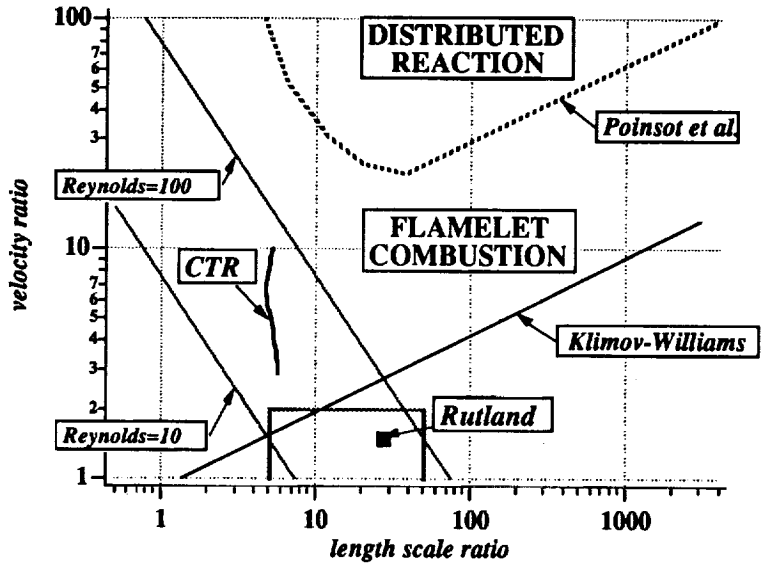

FIGURE 3. Premixed turbulent combustion diagram showing the different combustion regimes (from Borghi 1985; and Poinsot *et al.* 1991). The coordinates are the ratio of the turbulent length scale, l_t, and the laminar flame thickness, δ_l, and the ratio of the turbulent fluctuation, u', divided by the laminar flame speed, s_L. The parameters of the two DNS databases are plotted in the diagram.

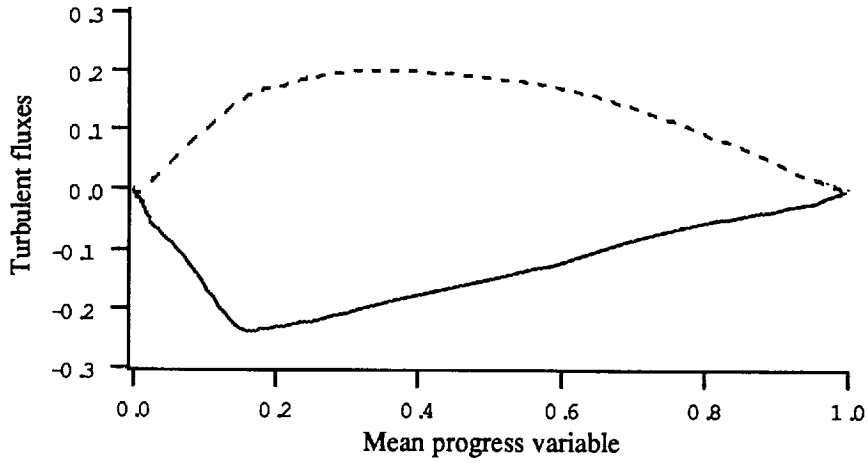

FIGURE 4. Comparison of the CTR and the Rutland DNS. The turbulent $\widetilde{c}$-flux, $\overline{\rho}\widetilde{u''c''}$, is plotted as a function of the mean reaction progress variable, $\widetilde{c}$. Velocities are made non-dimensional by the laminar burning velocity, s_L. —— : CTR database; ---- ; Rutland database

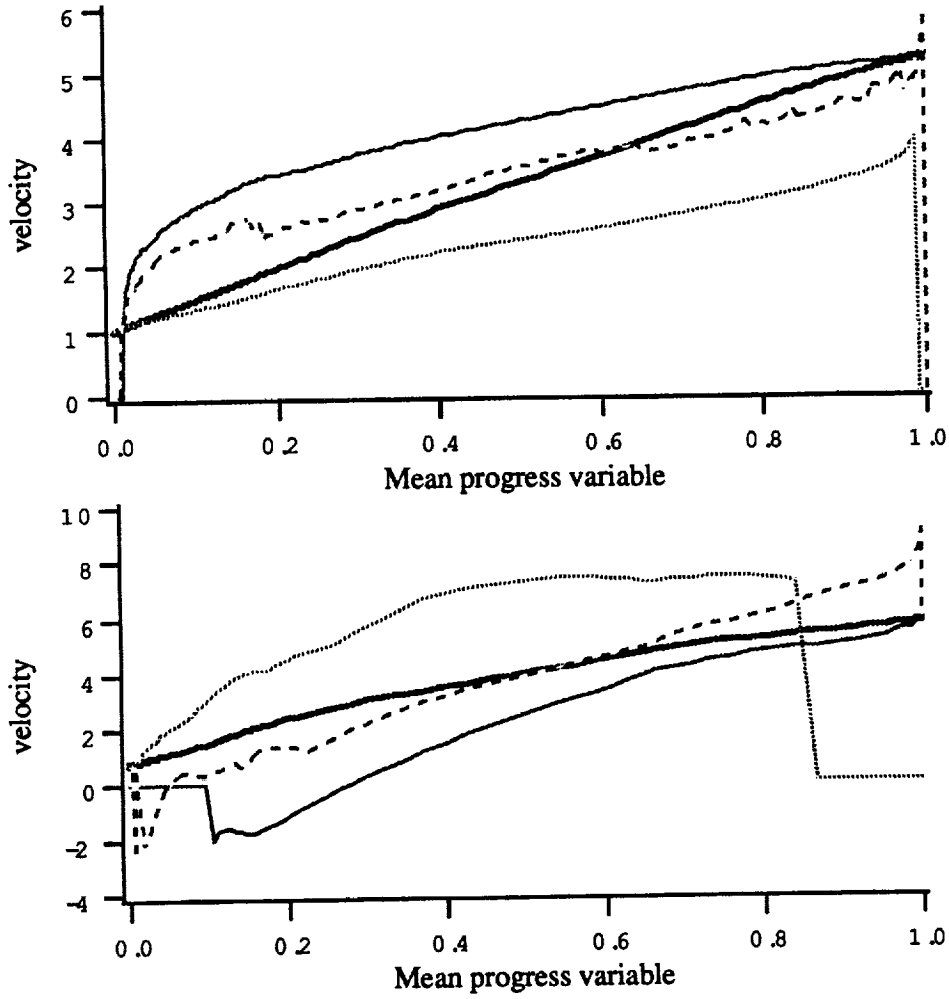

FIGURE 5. Mean flow velocities across the turbulent flame. The Favre-averaged velocity, $\widetilde{U}$, the conditional mean velocities, $\overline{U}_u$ and $\overline{U}_b$, and the surface-averaged velocity, $\langle u \rangle_S$, are plotted in $\widetilde{c}$-space. Velocities are made non-dimensional by the laminar burning velocity, s_L. Top: Rutland database. Bottom: CTR database. ——— : Favre average; ——— : products; ····· : reactants; ---- : $< u >_S$.

the progress variable $c = 1$, and $\overline{U}_b$ is determined from a small number of samples. The discrepancy between Figs. 5a and 5b is one of the keys to understanding when gradient or counter-gradient diffusion occurs and will be examined in further sections.

Different Lewis numbers Le (ratio of thermal to mass molecular diffusivities) have been investigated in the CTR database. Fig. 6 shows the spatial variations of the turbulent flux, $\widetilde{u''c''}$, across the turbulent flame brush at various times in the simulation, for two different Lewis numbers $Le = 0.8$ and $Le = 1.0$. In this figure, $\widetilde{u''c''}$ is made non-dimensional using the instantaneous rms turbulent velocity taken in the fresh gases. This non-dimensionalization allows separation of the decrease of the turbulent flux due to the decay of the turbulence from the variations due to other phenomena. Two different behaviors are observed. For $Le = 1.0$, the $\widetilde{u''c''}$-profile is changing rapidly during an initial phase and remains approximately constant after three eddy turnover times. In contrast, for $Le = 0.8$ the $\widetilde{u''c''}$-profile keeps changing in time and exhibits a continuous variation from negative towards positive values. These results are also shown in Fig. 7 where $\overline{\rho}\widetilde{u''c''}$ is first integrated across the turbulent flame brush and then plotted versus time. In Fig. 7, the $Le = 1$ flame reaches an asymptotic value, indicating thereby that no transition towards counter-gradient diffusion is to be expected and that a non-dimensional time of 4 is sufficient for data processing of the turbulent flame brush. Gradient turbulent transport observed in this case does not seem to be related to effects of initial conditions. For $Le = 0.8$, there is a clear trend towards transition to counter-gradient turbulent transport that might be related to thermal diffusive instabilities.

We now examine the idea that the differences in turbulent transport properties between the two databases are due to basic differences in the flame-flow dynamics (as opposed to numerical artifacts). These differences are further characterized using a local analysis of the flow field near the flame (section 3). Section 4 presents a comparison between the turbulent fluxes of $\widetilde{c}$ and Σ. A classical analysis of gradient versus counter-gradient turbulent diffusion based on the conservation equation for $\widetilde{u''c''}$ is presented in section 5. Finally, a theoretical analysis using a thin flame model is developed in section 6.

3. Local flow structure near the flame surface

As discussed in §2, the $Le = 1$ case from the CTR database and the Rutland simulation correspond to turbulent flames characterized by the same laminar flame thickness, δ_L, the same laminar burning velocity, s_L, the same molecular transport coefficients, but embedded in different turbulent flow fields. These simulated flames feature different global (spatially-averaged) properties, as illustrated in Figs. 1 and 2. A different perspective is adopted in this section where the flow velocity and the c-field are spatially resolved and analyzed in the vicinity of the reactive layers in a frame of reference attached to the flame. This frame of reference is used to determine, in particular, whether local flow variations occur in directions that are normal or tangential to the flame surface, *i.e.* whether local flow velocity gradients are aligned with local concentration gradients of reactive species.

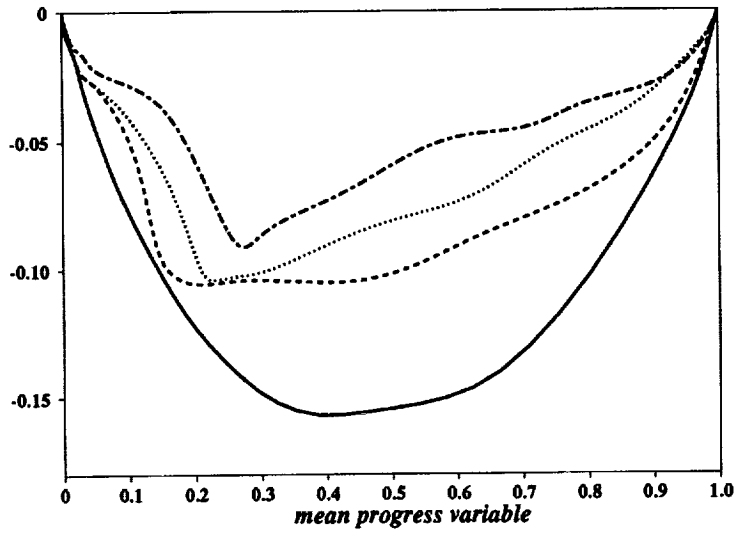

a)

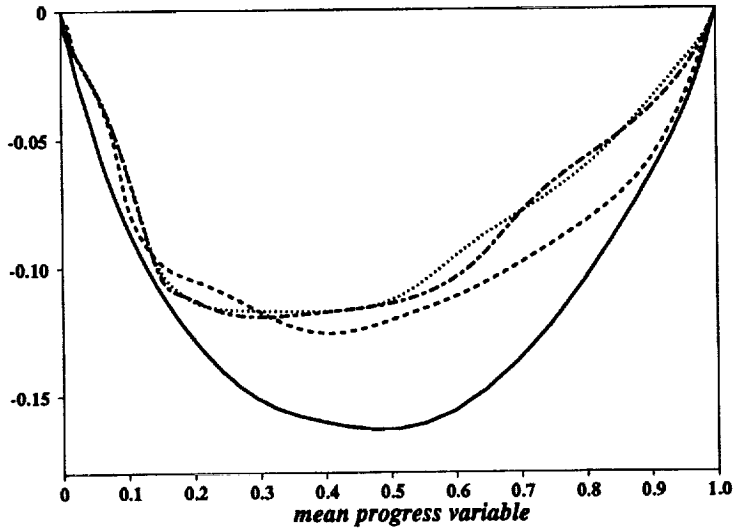

b)

FIGURE 6. Evolution of $\widetilde{u''c''}$ across the turbulent flame brush at different times in the simulations *a)* Le = 0.8; *b)* Le = 1.0. Time is made non-dimensional by the initial turbulent eddy turnover time. ——— : $t = 1.4$; ---- : $t = 2.7$; ····· : $t = 3.6$; —·— : $t = 4.5$.

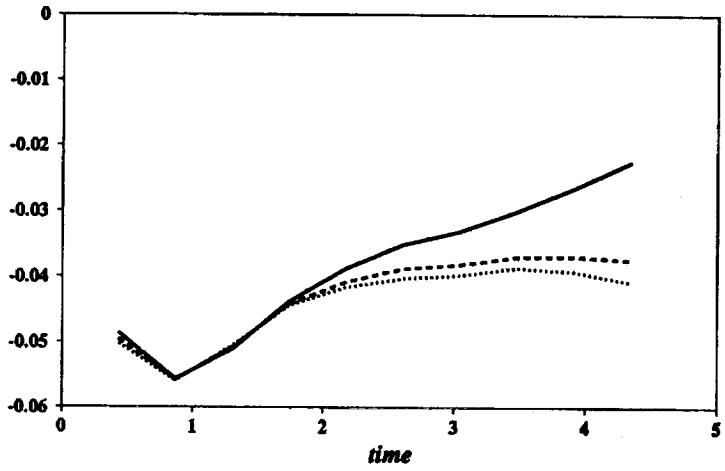

FIGURE 7. Evolution of the x-integral of $\overline{\rho u'' c''}$, integrated across the turbulent flame brush, versus time for different Lewis numbers ——— : $Le = 0.8$; ---- : $Le = 1.0$; ····· : $Le = 1.2$.

The flame-based analysis reveals that the local reaction rate profiles across the flame remain approximately uniform along the flame surface and are similar in the CTR and Rutland simulations. In other words, the local chemical structure of the flame remains laminar-like, a result that is consistent with a flamelet analysis and shows that the chemistry of such flames with unity Lewis number is relatively insensitive to flow perturbations. The local flow velocity profiles, however, exhibit striking differences, as discussed below.

Figs. 8a and 8b show the local flow dilatation across the flame at various locations along the flame surface, respectively for the Rutland and the CTR simulations. The dilatation of the flow is produced by both heat transfer in the flame preheat zone and heat release in the reaction zone. These local dilatation profiles remain approximately uniform along the flame surface and laminar-like in the Rutland simulation, whereas they exhibit more variations and significant deviations from the laminar case in the CTR simulation.

In the Rutland simulation, the flow field is found to be essentially one-dimensional and quasi-steady close to the flame. Most of the flame acceleration occurs along the flame normal direction:

$$\nabla.\mathbf{u} \approx \nabla(\mathbf{u}.\mathbf{n}).\mathbf{n}. \tag{8}$$

In that situation, the flow field within the flamelets is well described using the classical expressions that describe plane stretch-free laminar flames, where the flow velocity varies linearly with c in the flame normal direction:

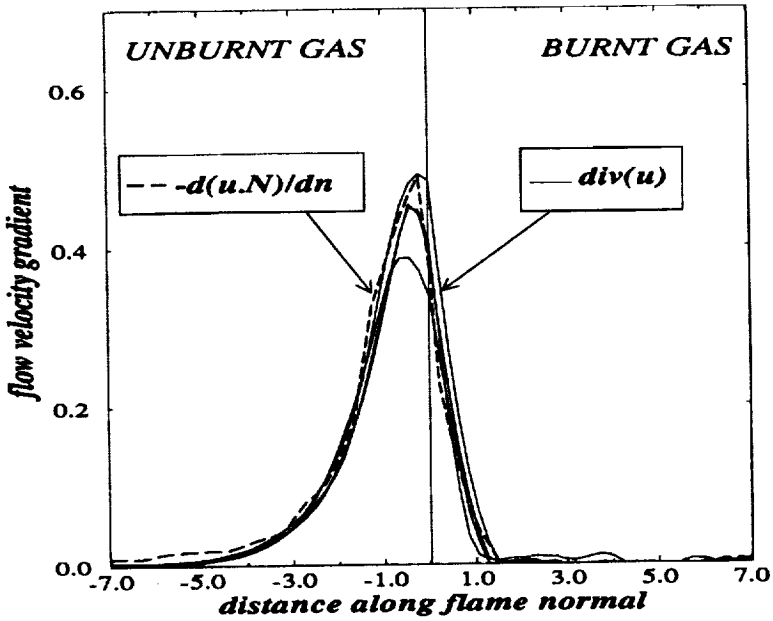

a)

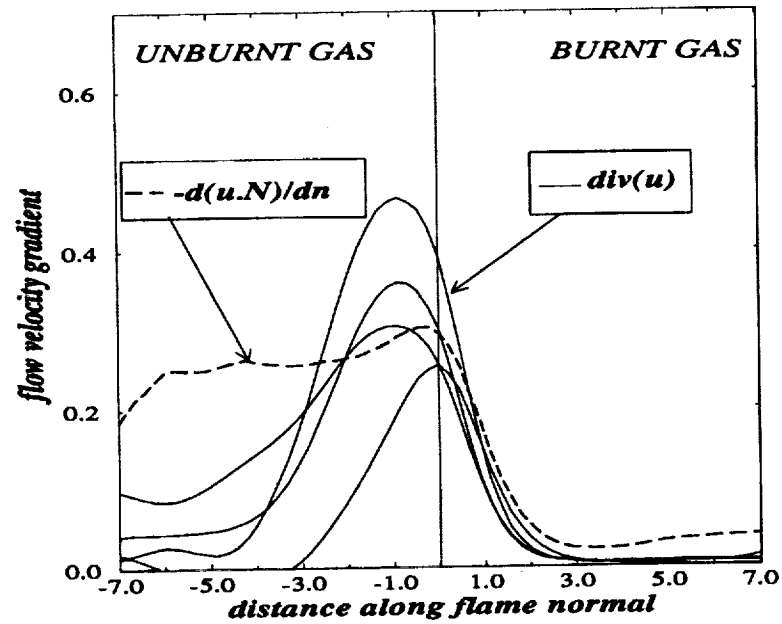

b)

FIGURE 8. A selection of local flow dilatation profiles normal to the turbulent flame for a) the Rutland database; b) the CTR database. In both figures, a local profile of the normal component of the flow velocity is also shown for comparison (a test of Eq. (8)). Quantities are made non-dimensional by the laminar burning velocity, s_L, and the laminar flame thickness, δ_L.

$$\mathbf{u}.\mathbf{n}(c) \approx \mathbf{u}.\mathbf{n}(c') + \tau(c' - c)s_L, \tag{9}$$

$$\mathbf{u}.\mathbf{t}(c) \approx \mathbf{u}.\mathbf{t}(c'), \tag{10}$$

where τ is the heat release factor, $\tau = T_b - T_u/T_u$, T_u, and T_b being respectively the temperature within fresh and burnt gases; $\mathbf{t}$ is a unit vector in the flame tangent plane. The relations (9) and (10) may be re-written as:

$$(\mathbf{u}.\mathbf{n}(c = 0.8) - \mathbf{u}.\mathbf{n}(c))/\tau s_L + 0.8 \approx c, \tag{11}$$

$$(\mathbf{u}.\mathbf{t}(c) - \mathbf{u}.\mathbf{t}(c = 0.8))/\tau s_L \approx 0. \tag{12}$$

Expressions (11) and (12) are found to provide good descriptions of the flow variations within the flamelets, as seen in Fig. 9a.

In the CTR simulation, however, the flow field is not one-dimensional and cannot be deduced directly from the dilatational field. Fig. 8b shows that (8) does not hold and Fig. 9b shows that the normal component of the flow velocity within the flamelets does not vary linearly with c; its gradient is not aligned with the gradient of c and exhibits large variations from one flame location to another. While in the Rutland simulation the flow field is determined by the dilatation occurring within the flame, the flow field in the CTR simulation appears dominated by the turbulent motions. These results will be used in section 6.

4. The relation between the turbulent fluxes of $\widetilde{c}$ and Σ

As shown in Fig. 4, the sign of the turbulent flux of $\widetilde{c}$ is different in the Rutland and CTR simulations. We now examine the turbulent flux of Σ, $\langle u'' \rangle_S \Sigma$. Fig. 10 shows that the CTR database features gradient diffusion transport for the flame surface density, whereas the Rutland database corresponds to counter-gradient diffusion. Note that since the turbulence intensities are higher in the CTR simulations, the magnitude of the turbulent fluxes are also found to be higher.

Following Bidaux and Bray (1994), an estimate of $\langle u \rangle_S$ is given by:

$$\langle u \rangle_S = \overline{U}_u + c^* \left(\overline{U}_b - \overline{U}_u \right), \tag{13}$$

where c^* is the progress variable level used to trace the flame front. This expression assumes a linear evolution of the mean velocity in the flame zone and is supported by Figs. 5a and 5b. Using the classical Bray-Moss-Libby (BML) relation $\widetilde{U} = (1 - \widetilde{c})\overline{U}_u + \widetilde{c}\overline{U}_b$, we can also write:

$$\langle u'' \rangle_S = \langle u \rangle_S - \widetilde{U} = (c^* - \widetilde{c}) \left(\overline{U}_b - \overline{U}_u \right). \tag{14}$$

Combining (6) and (14), we obtain:

$$\langle u'' \rangle_S \Sigma = \frac{(c^* - \widetilde{c})}{\widetilde{c}(1 - \widetilde{c})} \widetilde{u''c''} \Sigma, \tag{15}$$

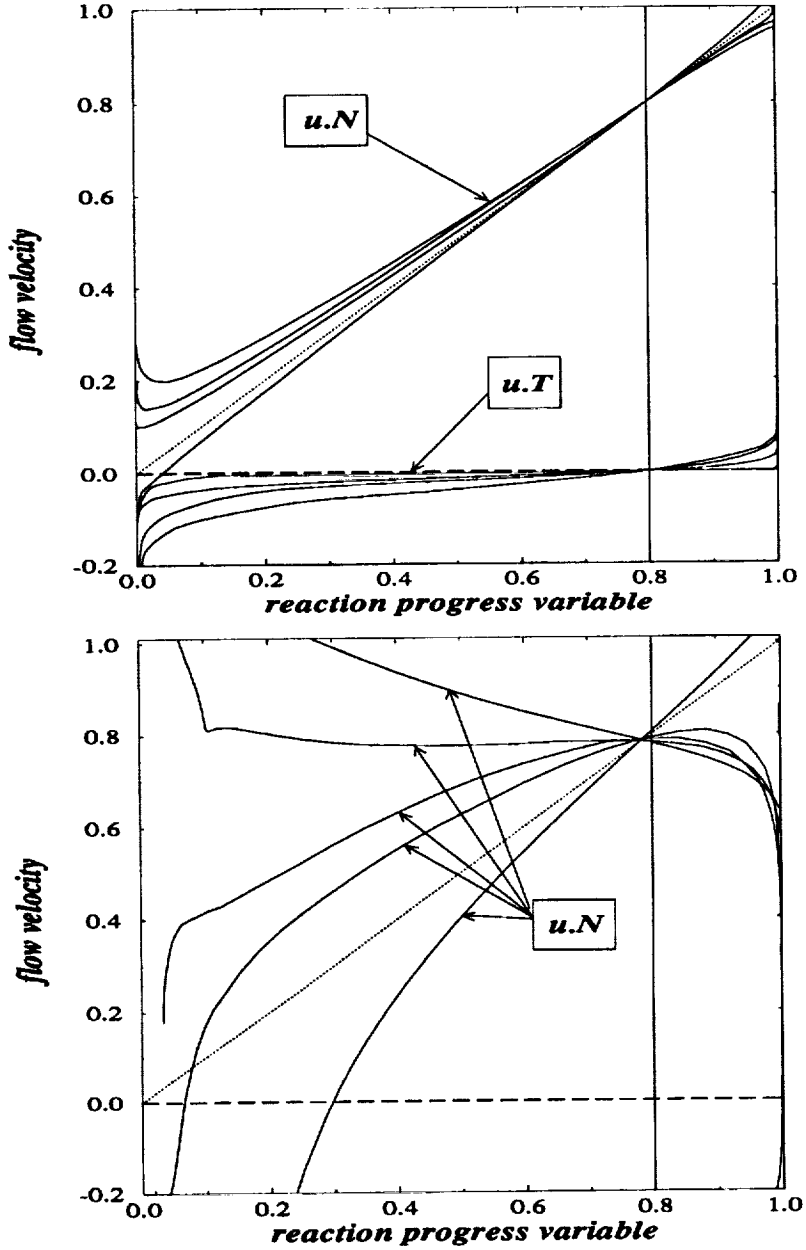

FIGURE 9. A selection of local profiles of the normal component of the flow velocity normal to the turbulent flame for a) the Rutland database; b) the CTR database (a test of Eq. (11)). The dotted line is the curve obtained for a plane, stretch-free laminar flame. In Fig. 9a, a selection of local profiles of the tangential component of the flow velocity is also shown for comparison (a test of Eq. (12)). Quantities are made non-dimensional by the laminar burning velocity, s_L, and the laminar flame thickness, δ_L.

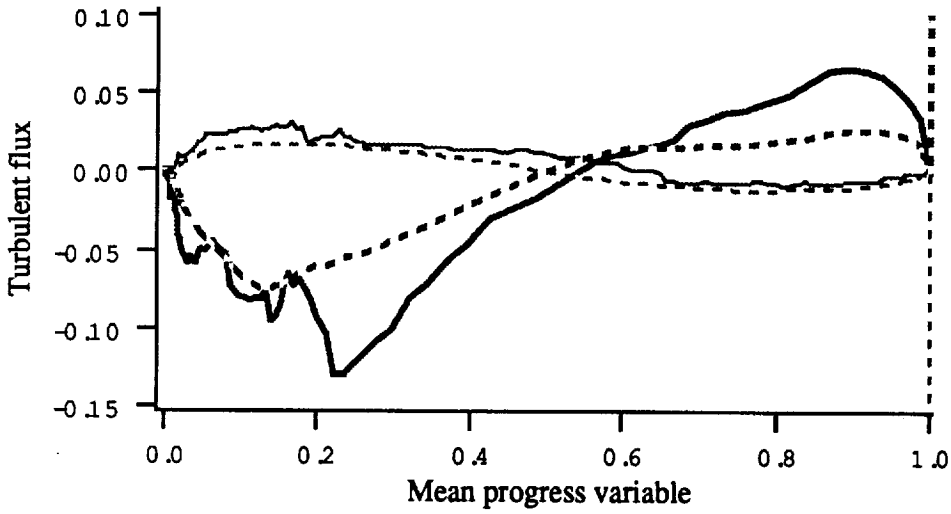

FIGURE 10. Comparison of the CTR and the Rutland DNS. The turbulent Σ-flux, $\langle u'' \rangle_S \Sigma$, is plotted as a function of the mean reaction progress variable, $\widetilde{c}$. Dashed lines corresponds to the estimate from Eq. (15) assuming $c^* = 0.5$. Velocities are made non-dimensional by the laminar burning velocity, s_L. ——— : CTR database; ——— : Rutland database.

which provides a simple relation between the turbulent fluxes for Σ and $\widetilde{c}$. This relation shows that $\langle u'' \rangle_S \Sigma$ and $\widetilde{u''c''}$ have the same sign at the leading edge of the turbulent flame, near $\widetilde{c} = 0$, and opposite signs on the burnt gas side, near $\widetilde{c} = 1$. Gradient (respectively counter-gradient) turbulent diffusion of the mean progress variable, $\widetilde{c}$, implies gradient (counter-gradient) turbulent diffusion of the flame surface density, Σ. The estimates obtained from Eq. (15) are also displayed in Fig. 10 and are seen to provide a very good estimate of $\langle u'' \rangle_S \Sigma$. In any case, the main result is that the turbulent diffusion term in the evolution equation for Σ is strongly correlated to the turbulent diffusion term in the equation for $\widetilde{c}$. In the following, we focus attention on the turbulent $\widetilde{c}$-flux.

5. Study of the transport equation for $\widetilde{u_i'' c''}$

5.1 Preliminaries

To identify the physical phenomena responsible for turbulent diffusion of $\widetilde{c}$, a classical analysis consists of examining in detail the terms of the transport equation for the second order moment $\widetilde{u_i'' c''}$. This balance equation can be obtained in a classical way from the continuity, the Navier-Stokes and the progress variable transport equations. After some algebra, the complete equation for $\widetilde{u_i'' c''}$ may be expressed (Favre *et al.* 1976; Launder 1976):

$$\underbrace{\frac{\partial}{\partial t}\overline{\rho}\widetilde{u_i''c''}}_{\text{(I)}} + \underbrace{\frac{\partial}{\partial x_j}(\overline{\rho}\widetilde{U}_j\widetilde{u_i''c''})}_{\text{(II)}} = \underbrace{-\frac{\partial}{\partial x_j}\left(\overline{\rho}\widetilde{u_j''u_i''c''}\right)}_{\text{(III)}} \underbrace{-\overline{\rho}\widetilde{u_i''u_j''}\frac{\partial\widetilde{c}}{\partial x_j}}_{\text{(IV)}} \underbrace{-\overline{\rho}\widetilde{u_j''c''}\frac{\partial\widetilde{U}_i}{\partial x_j}}_{\text{(V)}}$$
$$\underbrace{-\overline{c''}\frac{\partial\overline{p}}{\partial x_i}}_{\text{(VI)}} \underbrace{-\overline{c''\frac{\partial p'}{\partial x_i}}}_{\text{(VII)}} \underbrace{-\overline{u_i''\frac{\partial\mathcal{J}_k}{\partial x_k}}}_{\text{(VIII)}} \underbrace{+\overline{c''\frac{\partial\tau_{ik}}{\partial x_k}}}_{\text{(IX)}} \underbrace{+\overline{\rho}\widetilde{u_i''\dot{\omega}}}_{\text{(X)}} \tag{16}$$

where $\mathcal{J}_k$ represents the molecular diffusion flux of c and τ_{ik} is the viscous stress tensor.

All the terms in (16) can be extracted from the simulations (including the unsteady term). For instance, Fig. 11 shows typical spatial variations of the different terms of (16), written for the x-component of the turbulent flux $\widetilde{u''c''}$, as obtained from the CTR database.

Fig. 11 shows that some of the terms in (16) are dominant and will determine the sign of $\widetilde{u''c''}$. The dominant contributions are due to the terms I, IV, VI, and VII. In the following section, our attention will be focused on the role played by these terms and their temporal evolution. Moreover, we have to notice that the imbalance term due to the inherent numerical approximations is one order of magnitude smaller than all the terms appearing in Eq. (16). This result is satisfactory and shows that the quality of the CTR database and that of the post-processing are sufficient to analyze the variations of second order moments.

5.2 Effect of the turbulence intensity and of the mean pressure gradient

In order to better understand the time evolution of $\widetilde{u''c''}$ (see Figs. 6 and 7), some terms in (16) are studied in more detail for two different Lewis numbers, $Le = 0.8$ and $Le = 1.0$. These terms are:

- the unsteady term I
- the production due to the interaction of the mean progress variable gradient and the turbulent flow field (term IV in (16)). Since this term is by definition always positive, it is responsible for gradient type diffusion.
- the production due to the mean pressure gradient (term VI in (16)) is supposed to be responsible for counter-gradient diffusion as pointed out by Libby & Bray (1981). These authors argue that the pressure gradient across the flame front preferentially accelerates the low density gases, creating a relative motion between fully burnt and fresh gases.
- the correlation between the fluctuations of the progress variable and the fluctuations of the pressure gradient (term VII). Little is known about this term which is usually considered as a dissipation term in non-reacting flows (Launder 1976).

Fig. 12 displays the time evolution of the terms I, IV, VI, and VII integrated across the turbulent flame brush ($\int_0^1 \frac{\partial}{\partial t}\overline{\rho}\widetilde{u_i''c''}d\widetilde{c}$, $\int_0^1 \overline{\rho}\widetilde{u''^2}\frac{\partial\widetilde{c}}{\partial x}d\widetilde{c}$, $\int_0^1 \overline{c''}\frac{\partial\overline{p}}{\partial x}d\widetilde{c}$ and $\int_0^1 \overline{c''\frac{\partial p'}{\partial x_i}}d\widetilde{c}$).

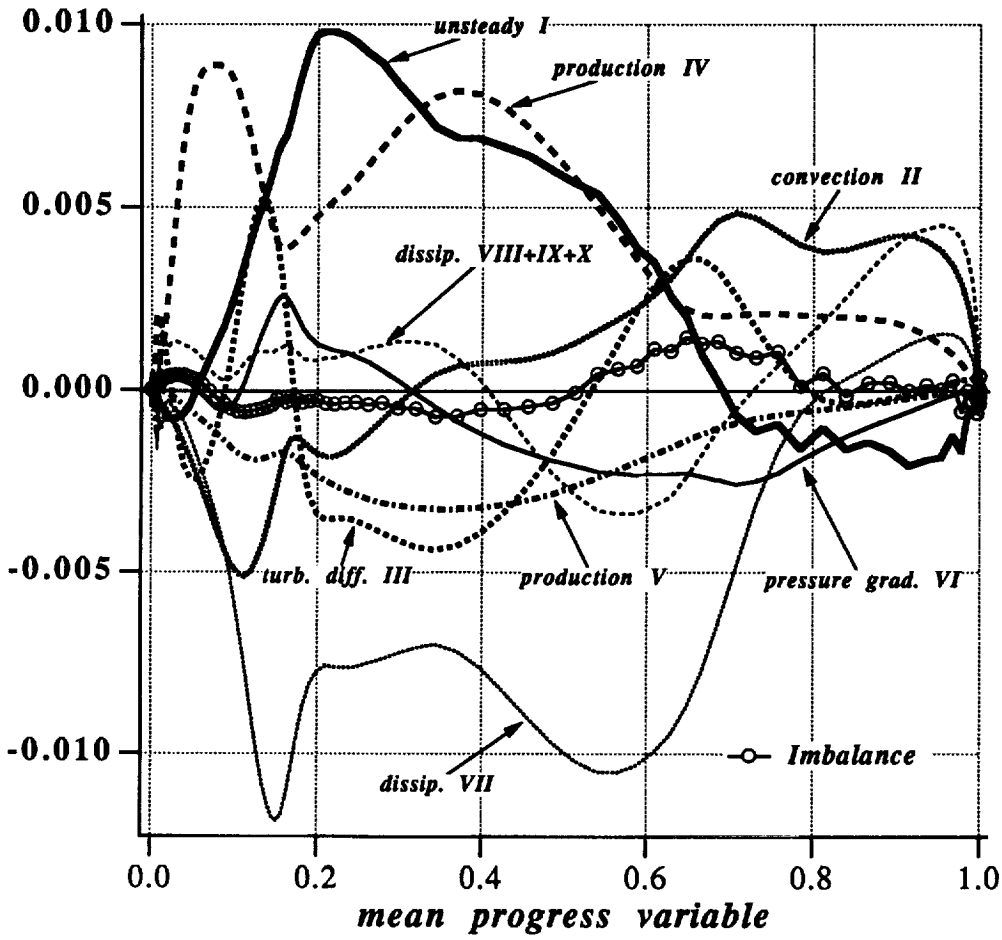

FIGURE 11. Spatial variations of the different terms in Eq. (16) versus $\widetilde{c}$, for the CTR case $Le = 1.0$ and $t/\tau_0 = 4.5$. The terms in (16) are made non-dimensional by $\rho_u \widetilde{u_u''^2}/l_{t_u}$. The curve with open circles correspond to the numerical errors that were found when closing the budget (16) and provides an estimate of the magnitude of the error for each term.

For both $Le = 0.8$ and $Le = 1.0$, the unsteady term I and the dissipation term VII behave in the same way. At early times, the unsteady term is negative producing counter-gradient diffusion and becomes positive later in the simulation playing the opposite role. The term VII is always negative in the simulations and acts to promote counter-gradient diffusion.

We now analyze the terms IV and VI which are supposed to be the key terms responsible for the turbulent gradient transport observed in the simulations. At initial times, both of these terms are positive and tend to produce gradient diffusion. Due to the high turbulence level (at $t/\tau_0 = 1.4$, $u'/s_L = 9.1$) and the relatively small thickness of the flame brush, the term IV appears to be the most dominant

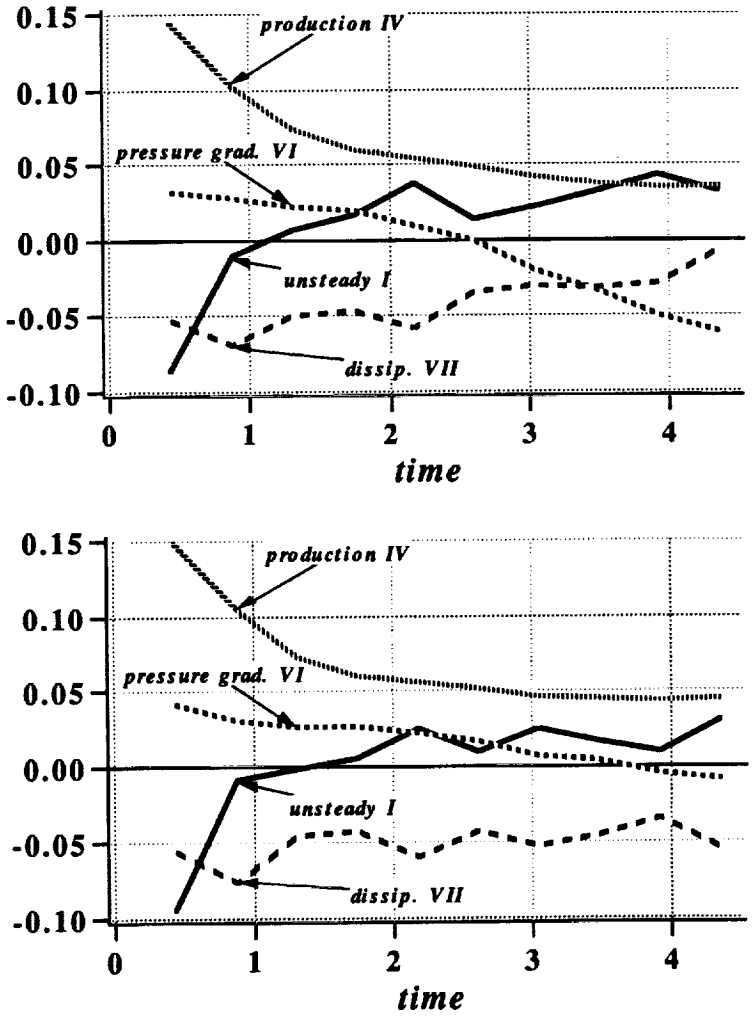

FIGURE 12. Time evolution of the terms I, IV, VI, and VII of Eq. (16) integrated across the turbulent flame brush, for (a) $Le = 0.8$ and (b) $Le = 1.0$. Terms I, IV, VI, and VII are made non-dimensional by the instantaneous value of $\rho_u \widetilde{u_u''^2}/l_{t_u}$. Time is made non-dimensional by the initial turbulent eddy turnover time.

term in (16). This result is consistent with the numerical study of Masuya (1986) who observes the flux becoming gradient diffusion type as the turbulence intensity increases.

As time proceeds, these two terms decrease continuously. While the term IV reaches an asymptotic value, the term VI changes sign and acts to promote counter-gradient diffusion. This feature is especially noticeable for the case $Le = 0.8$ where the term VI becomes the largest term in (16) after 4 turbulent eddy turnover time. This can be explained by the fact that for $Le = 0.8$ the turbulent flame speed is

much higher than in the case $Le = 1$ (Trouvé & Poinsot 1994) and consequently provokes a higher pressure jump across the turbulent flame which is approximately given by $\Delta p \sim \tau \rho_u S_T^2$.

5.3 Conclusions

At this point, we can tentatively conclude that the different behaviors for $\widetilde{u''c''}$ observed in the CTR database for $Le = 0.8$ and $Le = 1.0$ are essentially due to a higher mean pressure gradient in the case $Le = 0.8$, which is mainly due to a higher turbulent flame speed.

In a more general sense, it is well known experimentally that the turbulent flame speed, S_T, increases almost linearly with the turbulence intensity. Thus, the terms IV and VI are of the same order of magnitude and may even compensate themselves if the heat release parameter is sufficiently low (we can roughly estimate the ratio of the terms IV and VI to be of order τ^{-1}). This simplistic argument is in agreement with the work of Masuya (1986), who shows a stronger effect of τ compared to the effect of the ratio u'/s_L on the sign of $\widetilde{u''c''}$.

6. An analysis based on a thin flame model

6.1 An expression for turbulent diffusion transport

An analysis of the turbulent diffusion of the mean reaction progress variable may be conducted under the assumption of an infinitely thin flame front. Following Cant *et al.* (1990) or Trouvé and Poinsot (1994), the flame is viewed as a thin surface propagating towards the fresh gases with a velocity $\dot{\mathbf{X}}$ given by the sum of the fluid velocity and the flame propagation speed in the normal direction: $\dot{\mathbf{X}} = \mathbf{u} + w\mathbf{n}$. It may be shown that:

$$\frac{\partial \overline{c}}{\partial t} = \langle \dot{\mathbf{X}}.\mathbf{n} \rangle_S \Sigma = \langle \mathbf{u}.\mathbf{n} \rangle_S \Sigma + \langle w \rangle_S \Sigma, \tag{17}$$

where $\overline{c}$ is the Reynolds-averaged progress variable. This equation may be re-written as:

$$\frac{\partial \overline{c}}{\partial t} + \widetilde{\mathbf{U}}.\nabla \overline{c} = \langle \mathbf{u}.\mathbf{n} \rangle_S \Sigma + \langle w \rangle_S \Sigma + \widetilde{\mathbf{U}}.\nabla \overline{c}. \tag{18}$$

Using the geometrical relation $\nabla \overline{c} = -\langle \mathbf{n} \rangle_S \Sigma$, (17) becomes:

$$\frac{\partial \overline{c}}{\partial t} + \widetilde{\mathbf{U}}.\nabla \overline{c} = \langle \mathbf{u}''.\mathbf{n} \rangle_S \Sigma + \langle w \rangle_S \Sigma. \tag{19}$$

In the Bray-Moss-Libby theory, Reynolds and Favre averages of the progress variable c are related through the following expression: $\overline{c} = \overline{\rho c}/\rho_b$, where ρ_b is the mass density in the burnt gas. (18) and (19) can then be recast as transport equations for $\widetilde{c}$:

$$\frac{\partial \overline{\rho}\widetilde{c}}{\partial t} + \widetilde{\mathbf{U}}.\nabla \overline{\rho}\widetilde{c} = \rho_b \langle \mathbf{u}.\mathbf{n} \rangle_S \Sigma + \rho_b \langle w \rangle_S \Sigma + \widetilde{\mathbf{U}}.\nabla \overline{\rho}\widetilde{c}, \tag{20}$$

or

$$\frac{\partial \overline{\rho c}}{\partial t} + \tilde{\mathbf{U}}.\nabla \overline{\rho c} = \rho_b \langle \mathbf{u}''.\mathbf{n} \rangle_S \Sigma + \rho_b \langle w \rangle_S \Sigma. \tag{21}$$

An exact equation for the Favre-averaged progress variable is:

$$\frac{\partial \overline{\rho} \tilde{c}}{\partial t} + \nabla.\overline{\rho} \tilde{\mathbf{U}} \tilde{c} = -\nabla.\overline{\rho \mathbf{u}'' c''} + \langle \rho w \rangle_S \Sigma, \tag{22}$$

where molecular species diffusion and chemical reaction are included in $\langle \rho w \rangle_S$.

Combining (22) with (20) or (21), two expressions for the turbulent transport of $\tilde{c}$ as a function of flame surface-averaged quantities are obtained:

$$-\nabla.\overline{\rho \mathbf{u}'' c''} = \rho_b \langle \mathbf{u}.\mathbf{n} \rangle_S \Sigma + (\rho_b \langle w \rangle_S - \langle \rho w \rangle_S) \Sigma + \nabla.\overline{\rho} \tilde{\mathbf{U}} \tilde{c}, \tag{23}$$

$$-\nabla.\overline{\rho \mathbf{u}'' c''} = \rho_b \langle \mathbf{u}''.\mathbf{n} \rangle_S \Sigma + (\rho_b \langle w \rangle_S - \langle \rho w \rangle_S) \Sigma + \overline{\rho c} \nabla.\tilde{\mathbf{U}}. \tag{24}$$

These two expressions exhibit three contributions to the turbulent diffusion of $\tilde{c}$. The first term on the right-hand side represents the correlation between the flame front movement and the velocity field. The second term involves the reaction rate, and the third term is clearly related to the thermal expansion. One may also note that with a model for the reaction rate, the only remaining unclosed term is $\langle \mathbf{u}''.\mathbf{n} \rangle_S$.

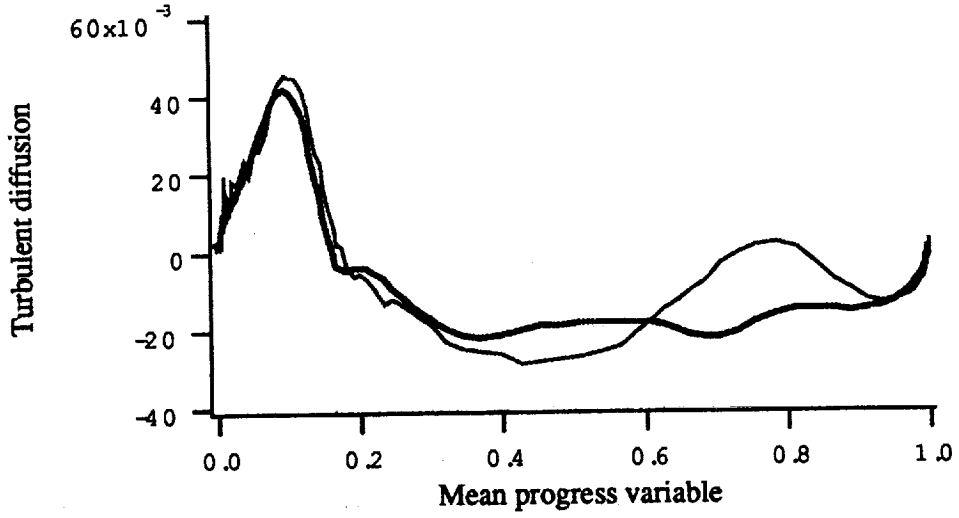

FIGURE 13. Comparison of the exact turbulent diffusion term $-\nabla.\overline{\rho \mathbf{u}'' c''}$ with its estimate from Eq. (23) in the CTR database. ——— : CTR database; ——— : estimation from (23).

Fig. 13 presents a comparison of the right-hand side and left-hand side of (23) in the CTR database ($Le = 1$). The agreement is quite good even though the probability density function of c is not fully bimodal in the database as assumed to derive expression (23). Fig. 14 shows the correlation $\langle \mathbf{u}.\mathbf{n} \rangle_S$ as a function of $\widetilde{c}$ for the two databases. This term is quite different in the two data sets. In the CTR database featuring a gradient turbulent transport, $\langle \mathbf{u}.\mathbf{n} \rangle_S$ decreases almost linearly with $\widetilde{c}$ from positive values near $\widetilde{c} = 0$ to negative ones near $\widetilde{c} = 1$. The positive values of $\langle \mathbf{u}.\mathbf{n} \rangle_S$ near $\widetilde{c} = 0$ correspond to local flow velocity vectors pointing into the reactants. At the leading edge, the flame front is convected towards fresh gases by the turbulent motions. This phenomenon accounts for the negative value of $\overline{U}_t$ seen in Fig. 5b. The product $\langle \mathbf{u}.\mathbf{n} \rangle_S \Sigma$ in (23) corresponds to a strong gradient trend (positive at the leading edge and negative at the trailing edge). On the other hand, in the Rutland database featuring a counter-gradient turbulent transport, $\langle \mathbf{u}.\mathbf{n} \rangle_S$ is negative with an almost constant value. In (23), the product $\langle \mathbf{u}.\mathbf{n} \rangle_S \Sigma$ is counter-gradient at the leading edge and becomes gradient at the trailing edge. Its effect is opposite to the one due to thermal expansion, $\nabla \overline{\rho} \widetilde{U} \widetilde{c}$.

Fig. 14 also shows the uncorrelated ($\langle \mathbf{u} \rangle_S . \langle \mathbf{n} \rangle_S$) and the correlated ($\langle \mathbf{u}.\mathbf{n} \rangle_S - \langle \mathbf{u} \rangle_S . \langle \mathbf{n} \rangle_S$) parts of the term $\langle \mathbf{u}.\mathbf{n} \rangle_S$. It is seen that $\mathbf{u}$ and $\mathbf{n}$ are mainly uncorrelated in the CTR database, whereas the correlation is not negligible in the Rutland case. This result is also in agreement with the local analysis developed in section 3.

6.2 Analysis of $\langle \mathbf{u}.\mathbf{n} \rangle_S$ *and* $\langle \mathbf{u}''.\mathbf{n} \rangle_S$ *terms*

From the previous analysis, the terms $\langle \mathbf{u}.\mathbf{n} \rangle_S$ and $\langle \mathbf{u}''.\mathbf{n} \rangle_S$ are found to be important ingredients of the turbulent transport of $\widetilde{c}$. Their trends are quite different in the two databases and provide a way to delineate between gradient and counter-gradient diffusion transport. As previously shown, the main differences between the two databases are the turbulence levels and the flame front wrinkling.

6.2.1 Low turbulence level

In the case of a low turbulence level and a low flame front wrinkling, $\langle \mathbf{u}.\mathbf{n} \rangle_S$ may be assumed almost constant and equal to its value at $\widetilde{c} = 0$ where the normal component is equal to -1 in the mean propagation direction x:

$$\langle \mathbf{u}.\mathbf{n} \rangle_S = -U_F, \tag{25}$$

where U_F is the flow velocity at the flame front and may be estimated with the same argument as previously used by Bidaux & Bray (1994) to derive an expression for the turbulent flux of flame surface density (Eq. (13)):

$$U_F = U_0 (1 + \tau c^*), \tag{26}$$

where U_0 is the fresh gases velocity and c^* the flame reference level. Assuming a stationary flame brush and using mass conservation, an estimate of $\langle \mathbf{u}.\mathbf{n} \rangle_S$ is:

$$\langle \mathbf{u}.\mathbf{n} \rangle_S = -\frac{\widetilde{U}}{(1 + \tau \widetilde{c})} (1 + \tau c^*), \tag{27}$$

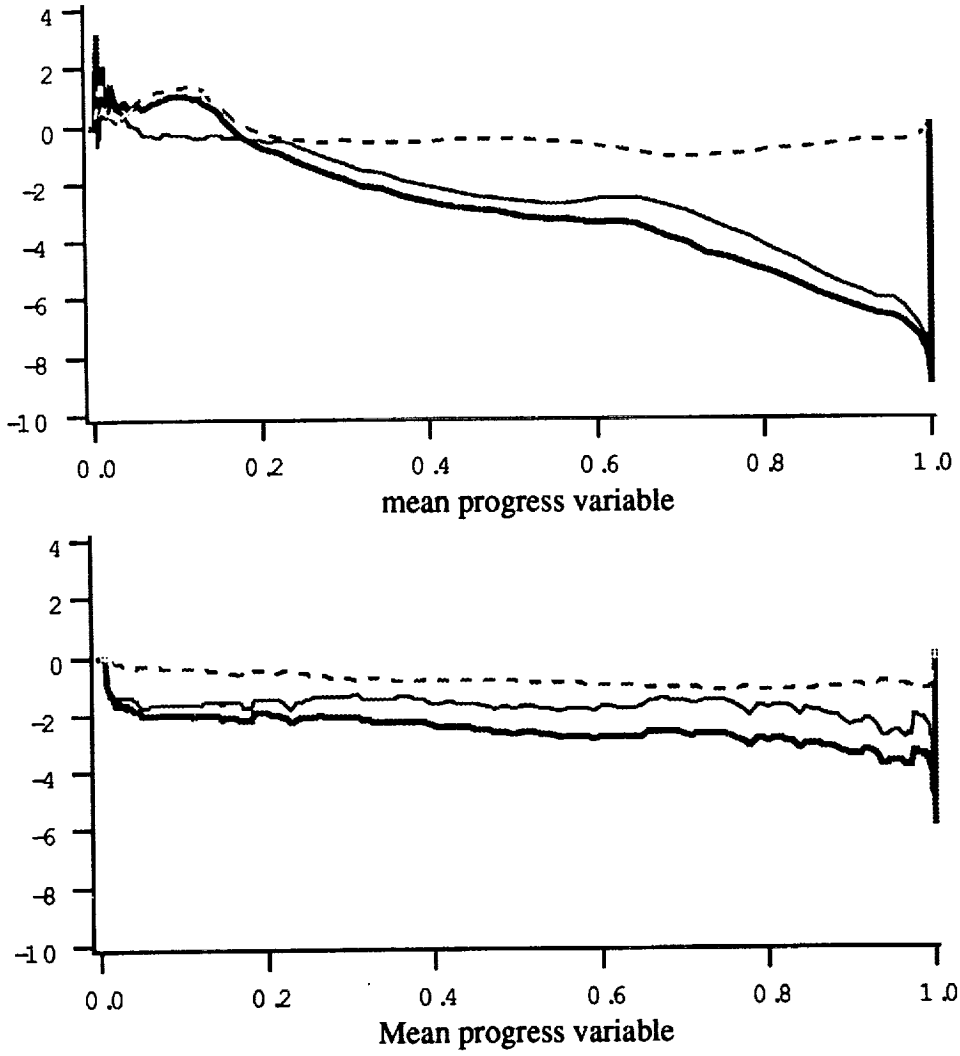

FIGURE 14. $\langle \mathbf{u}.\mathbf{n} \rangle_S$ (——), uncorrelated part $\langle \mathbf{u} \rangle_S . \langle \mathbf{n} \rangle_S$ (——), and correlated part $\langle \mathbf{u}.\mathbf{n} \rangle_S - \langle \mathbf{u} \rangle_S . \langle \mathbf{n} \rangle_S$ (----) plotted as a function of the mean progress variable, $\widetilde{c}$, for the two available databases (top: CTR, bottom: Rutland).

which is very well verified in the Rutland database. In this case, the flame front dynamics and the turbulent transport are mainly dominated by the mean flow

velocity and the thermal expansion.

6.2.2 High turbulence level

In the CTR database, the fluctuations at the flame front of the flow velocity and the flame normal vector may be assumed uncorrelated:

$$\langle \mathbf{u}''.\mathbf{n} \rangle_S \Sigma = \langle \mathbf{u}'' \rangle_S . \langle \mathbf{n} \rangle_S \Sigma. \tag{28}$$

Combining (28) and (15), it may be easily shown that:

$$\rho_b \langle \mathbf{u}''.\mathbf{n} \rangle_S \Sigma = -\frac{(c^* - \widetilde{c})}{\widetilde{c}(1-\widetilde{c})} \widetilde{u''c''} \frac{\partial \widetilde{\rho c}}{\partial x}. \tag{29}$$

which suggests that $\langle \mathbf{u}''.\mathbf{n} \rangle_S$ might provide a way to analyze the turbulent diffusion transport of $\widetilde{c}$.

The only unclosed term in Eq. (24) is $\langle \mathbf{u}'' \rangle_S$. In the CTR DNS, the flame front movements are mainly dominated by the turbulent motions in the fresh gases (due to the higher viscosity, turbulent motions have a lower strength in the burnt gases). At the leading edge of the flame brush, the flame front is convected towards the fresh gases with a turbulent speed of the order of $-u'$ where u' is the turbulent rms velocity in the fresh gases. At the trailing edge, the flame front is convected towards the burnt gases by the most energetic turbulent eddies inside the fresh gases with a turbulent speed of the order of u'. Then, a simple model for $\langle \mathbf{u}'' \rangle_S$ is:

$$\langle \mathbf{u}'' \rangle_S = u' (2\widetilde{c} - 1), \tag{30}$$

which is in agreement with the CTR database as shown in Fig. 15.
From (28) and (30), one obtains:

$$\rho_b \langle \mathbf{u}''.\mathbf{n} \rangle_S \Sigma = -u' (2\widetilde{c} - 1) \nabla \widetilde{\rho c}. \tag{31}$$

Using (29), assuming that $c^* = 0.5$, the turbulent flux of $\widetilde{c}$ becomes:

$$\widetilde{u''c''} = -2u'\widetilde{c}(1-\widetilde{c}), \tag{32}$$

which clearly corresponds to gradient turbulent transport.

6.2.3 Mechanisms for turbulent transport diffusion

From the previous analysis, the turbulent diffusion of $\widetilde{c}$ comes from two different mechanisms. The first one is the dynamics of the flame front itself, mainly due to thermal expansion. This phenomenon (clearly apparent in the term $\overline{\rho c} \nabla . \widetilde{\mathbf{U}}$ of Eq. (24)) induces counter-gradient diffusions (CGD) as shown by the classical Bray-Moss-Libby expression (6). Due to thermal expansion and without any other effect, $\overline{U}_b$ is greater than $\overline{U}_u$ leading to CGD of $\widetilde{c}$.

In contrast, with a sufficiently high turbulence level, the flame front movement is dominated by the turbulent motions in the fresh gases as already seen in the CTR database. At the leading edge, the flame front is convected towards fresh gases, inducing negative velocities near the front, positive values of $\langle \mathbf{u}.\mathbf{n} \rangle_S$, and $\overline{U}_b$ lower

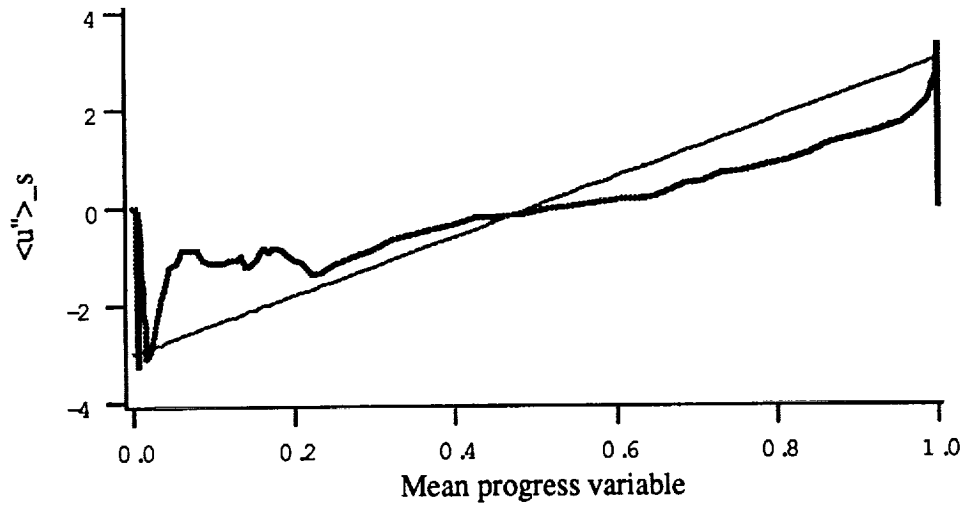

FIGURE 15. Comparison of $\langle \mathbf{u}'' \rangle_S$ and the modeled expression (30) in the CTR database. ——— : CTR database; ——— : estimation from (30).

than $\overline{U}_u$. At the trailing edge, intense turbulent motions in the fresh gases convect the flame front towards burnt gases and $\overline{U}_u$ is greater than $\overline{U}_b$ (see Fig. 16). In that case, the turbulent diffusion of $\widetilde{c}$ becomes gradient.

To summarize, with a high turbulence level, the flame front dynamics is dominated by the turbulent motions and the mean progress variable is similar to any passive scalar, leading to a classical gradient diffusion turbulent transport. With a low turbulence level, the intrinsic dynamics of the flame is important, and the mean progress variable cannot be reduced to a passive scalar. A counter-gradient diffusion turbulent transport is then encountered. It is well known that counter-gradient diffusion is promoted by a high heat release (i.e. a high value of τ). On the other hand, high turbulence levels induce gradient turbulent transport. The next step is to quantify the limits between gradient (GD) and counter-gradient (CGD) turbulent diffusion.

6.3 A criterion for gradient/counter-gradient turbulent diffusion

The objective is to derive a criterion for turbulent diffusion transport of the Favre-averaged mean progress variable, $\widetilde{c}$. Our analysis is based on Eq. (24). For GD, $-\nabla.\overline{\rho}\widetilde{\mathbf{u}''c''}$ has to be positive at the leading edge of the flame and negative at the trailing edge. As previously shown, this term may be expressed as the sum of three contributions. At the trailing edge, the first term, $\rho_b\langle \mathbf{u}''.\mathbf{n}\rangle_S\Sigma$, is negative, the second one, $(\rho_b\langle w\rangle_S - \langle \rho w\rangle_S J)\,\Sigma$ vanishes and has a higher order, and the third one, $\overline{\rho}\widetilde{c}\nabla.\widetilde{\mathbf{U}}$ is positive. Then, a necessary condition for GD is:

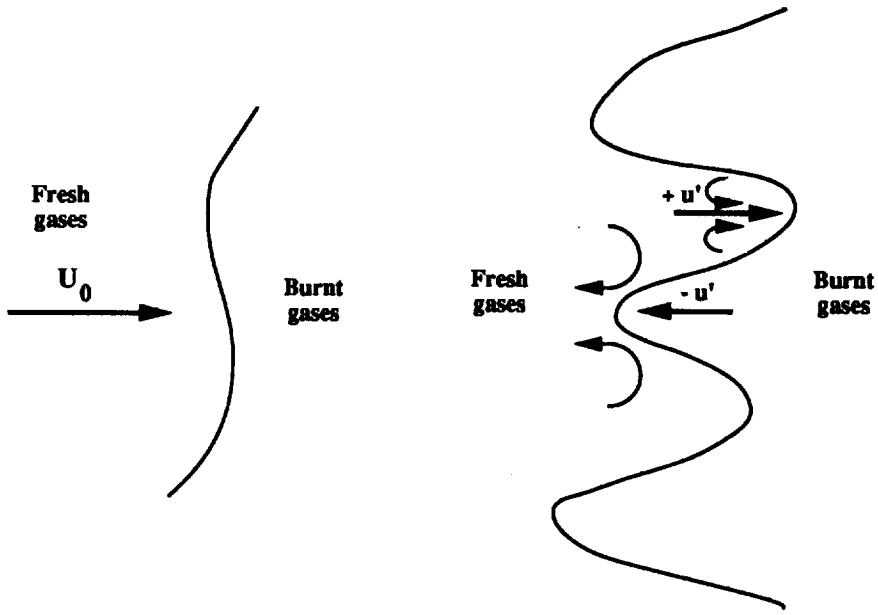

FIGURE 16. Mechanisms of counter-gradient (left) and gradient (right) turbulent diffusion transport for $\widetilde{c}$ and Σ.

$$\rho_b \left|\langle \mathbf{u}''.\mathbf{n}\rangle_S\right| \Sigma > \overline{\rho c}\nabla\widetilde{\mathbf{U}}. \tag{33}$$

Some assumptions are now introduced to evaluate the terms appearing in (33). The mean velocity may be estimated by:

$$\widetilde{U} = U_0 + \tau S_T \widetilde{c}. \tag{34}$$

$\overline{\rho}$ is estimated from the Bray-Moss-Libby (BML) formulation:

$$\overline{\rho} = \frac{\rho_b(1+\tau)}{1+\tau\widetilde{c}}. \tag{35}$$

The BML algebraic closure for the flame surface density, Σ, is also used:

$$\Sigma = \frac{g}{\sigma_y L_y}\overline{c}(1-\overline{c}) = \frac{g}{\sigma_y L_y}\frac{1+\tau}{(1+\tau\widetilde{c})^2}\widetilde{c}(1-\widetilde{c}), \tag{36}$$

where L_y is the wrinkling scale of the flame front, g a model constant, and σ_y an orientation factor assumed to be a constant. The gradient of the mean progress variable is estimated from the flame brush thickness, δ_B, as:

$$\nabla\widetilde{c} = \frac{\widetilde{c}(1-\widetilde{c})}{\delta_B}. \tag{37}$$

After some calculations, the condition (33) becomes:

$$N_B = \frac{\sigma_y L_y}{g\delta_B} S_T \frac{\tau(1+\tau)}{|\langle \mathbf{u}''.\mathbf{n}\rangle_S|} < 1, \tag{38}$$

evaluated for $\widetilde{c} = 1$. This expression may be simplified by evaluating the turbulent flame speed, S_T, from the integral of the reaction rate over the flame brush. Assuming that $\langle \rho w\rangle_S = \rho_u \langle w\rangle_S$, one obtains:

$$S_T = \frac{g\delta_B}{\sigma_y L_y} \rho_u \langle w\rangle_S. \tag{39}$$

Then the proposed criterion becomes:

$$N_B = \langle w\rangle_S \frac{\tau(1+\tau)}{|\langle \mathbf{u}''.\mathbf{n}\rangle_S|} < 1. \tag{40}$$

A similar analysis, conducted with Eq. (23), leads to a similar criterion:

$$N'_B = \langle w\rangle_S \frac{1+\tau(2+\tau)}{|\langle \mathbf{u}.\mathbf{n}\rangle_S|} < 1. \tag{41}$$

Table 1. Numerical estimates of the proposed criterions from the two available databases

Database	u'	s_L	τ	S_T	$\lvert\langle \mathbf{u}.\mathbf{n}\rangle_S\rvert$ $(\widetilde{c}=1.)$	$\lvert\langle \mathbf{u}''.\mathbf{n}\rangle_S\rvert$ $(\widetilde{c}=1.)$	N_B	N'_B
CTR	3.	1.	3.	1.7	8.	3.	4.	2.
Rutland	1.	1.	2.3	1.8	3.	1.	7.6	3.6

Table 1 provides the values of the numbers N_B and N'_B, for the two available databases, using the assumption $\langle w\rangle_S = s_L$. Both N_B and N'_B are lower in the CTR database (exhibiting GD) than in the Rutland database (with CGD), a result that is consistent with our expectations. Nevertheless, the limiting value is not found to be equal to 1. This is mainly due to some assumptions made in the derivation. In particular, expressions (36) for the flame surface density Σ and (37) for the gradient of the mean progress variable $\widetilde{c}$ are not well verified at the trailing edge of the flame front and only provide an order of magnitude. The criterion is also somewhat approximate because it corresponds only to a necessary condition to have a gradient diffusion transport. Two quantities are not exactly known in this criterion: the surface average of the flame front displacement speed, $\langle w\rangle_S$, which differs in general from the laminar flame speed s_L (see Trouvé & Poinsot 1994); and $\langle \mathbf{u}''.\mathbf{n}\rangle_S$ which probably involves wrinkling scales of the flame front. Nevertheless,

a rough estimate may be made assuming $\langle w \rangle_S = s_L$ and $|\langle \mathbf{u}''.\mathbf{n} \rangle_S| = u'$. Then, the proposed criterion becomes:

$$N_B = \frac{\tau(1+\tau)}{\frac{u'}{S_L}} < 1, \tag{42}$$

which corresponds to a horizontal line in the classical Borghi/Barrère diagram (figure 3). Below this line, corresponding to low turbulence levels, turbulent transport occurs opposite to the direction of mean gradients. Above that line, turbulent transport occurs in the direction of mean gradients. This first simple criterion is also in agreement with the classical analysis of turbulent transport where counter-gradient diffusion is promoted by the increase of the heat release parameter τ (Masuya 1986).

The present analysis should be understood as a first attempt to differentiate between gradient and counter-gradient turbulent diffusion phenomena in premixed flames. The criterion (42) is probably too simple, and the transition between counter-gradient and gradient transport as turbulence levels are increased will not be abrupt and will involve a transition zone. It remains, however, that such a transition will probably occur as supported by our comparison of the two available DNS databases. Future work will be aimed at validating the present analysis and providing a more precise description of the transition between the two situations.

7. Conclusions

We use in this study direct numerical simulations to describe the coupling between the transport equations for mean reaction progress variable, $\widetilde{c}$, and flame surface density, Σ. We are particularly interested in the turbulent transport terms appearing in the equations for $\widetilde{c}$ and Σ since the modeling of those terms remains somewhat controversial: standard gradient transport approximations as proposed in the Coherent Flame Model, or additional transport equations for the turbulent fluxes as proposed in the Bray-Moss-Libby theory. Two different direct numerical simulation databases, the CTR database and the Rutland database, have been used. Both databases correspond to statistically one-dimensional premixed flames in isotopic turbulent flow. The run parameters are significantly different and the two databases correspond to different turbulent combustion regimes (see Fig. 3).

A systematic comparison between the different simulated flames reveals striking differences in their turbulent transport properties. The Rutland case exhibits counter-gradient diffusion of $\widetilde{c}$, a result that is consistent with the Bray-Moss-Libby theory. In contrast, the CTR database features turbulent $\widetilde{c}$-fluxes that are consistent with a gradient transport approximation. In addition, the turbulent diffusion of Σ is found to be strongly correlated to the turbulent diffusion of $\widetilde{c}$. In the Rutland database, counter-gradient diffusion of $\widetilde{c}$ is occurring with counter-gradient diffusion of Σ, whereas in the CTR database, gradient diffusion of $\widetilde{c}$ and Σ is observed. A simple expression proposed by Bray to relate the turbulent flux of Σ to the turbulent flux of $\widetilde{c}$ is found to be valid (Eq. (15)). One important implication of this result is that the modeling of the turbulent flux of $\widetilde{c}$ cannot be made independently of that for the turbulent flux of Σ.

A detailed analysis of all the terms appearing in the conservation equation for the turbulent $\widetilde{c}$-flux, $\overline{\rho}\widetilde{u''c''}$, is also performed. This analysis shows that while pressure effects act to promote counter-gradient diffusion, a result that is consistent with the Bray-Moss-Libby theory, they fail to prevail in the CTR case. Finally, a simple theoretical analysis based on a thin flame model is developed to explain the different turbulent transport properties observed in the CTR and the Rutland simulations. This simple theory distinguishes between situations where the flow field near the flame surface is dominated by the turbulent motions and situations where it is mainly determined by the dilatation occurring within the reaction zone. The CTR simulations belong to the first category, the Rutland simulation to the second. The first category of flames is expected to feature gradient turbulent transport, whereas counter-gradient phenomena will dominate in the second. The analysis also provides a criterion to determine the domain of occurrence of gradient/counter-gradient turbulent transport of $\widetilde{c}$ and Σ (Eq. (42)). This criterion suggests that counter-gradient diffusion is promoted by increasing values of the heat release factor, τ, a result that is consistent with the Bray-Moss-Libby theory as well as by low turbulence levels, whereas gradient diffusion might prevail as turbulence intensities are increased. Future work will be aimed at validating and refining this criterion.

Acknowledgements

The authors wish to thank Prof. C. J. Rutland for providing access to his direct numerical simulation database. The authors acknowledge the fruitful interaction with other members of the combustion group during the summer program. In particular, we thank Prof. C. J. Rutland and Prof. R. S. Cant for many discussions in the course of this study.

REFERENCES

ARMSTRONG, N. W. H. & BRAY, K. N. C. 1992 Premixed turbulent combustion flowfield measurements using PIV and LST and their application to flamelet modeling of engine combustion. *S.A.E. Meeting*, Paper 922322.

BIDAUX, E. & BRAY, K. N. C. 1994 Unpublished work.

BORGHI, R. 1985 On the structure and morphology of turbulent premixed flames. *in Recent Advances in Aerospace Science.* (ed. C. Bruno & C. Casci). Pergamon.

BRAY, K. N. C. 1980 Turbulent flows with premixed reactants. *in Topics in Applied Physics* **44**. Springer-Verlag.

BRAY, K. N. C. 1990 Studies of the turbulent burning velocity. *Proc. R. Soc. Lond. A.* **431,** 315-335.

BRAY, K. N. C., LIBBY, P. A., MASUYA, G. & MOSS, J. B. 1981 Turbulence production in premixed turbulent flames. *Combust. Sci. Tech.* **25,** 127-140.

BRAY, K. N. C., CHAMPION, M. & LIBBY, P. A. 1989 The interaction between turbulence and chemistry in premixed turbulent flames. In *Turbulent Reactive Flows, Lecture Notes in Eng.* **40,** Springer-Verlag.

CANDEL, S. M. & POINSOT, T. 1990 Flame stretch and the balance equation for the flame surface area. *Combust. Sci. Tech.* **70,** 1-15.

CANDEL, S. M., VEYNANTE, D., LACAS, F., MAISTRET, E., DARABIHA, N. & POINSOT, T. 1990 Coherent flame model: applications and recent extensions. *in Series on Advances in Mathematics for Applied Sciences.* World Scientific.

CANT, R. S., POPE, S. B. & BRAY, K. N. C. 1990 Modeling of flamelet surface to volume ratio in turbulent premixed combustion. *Twenty-Third Symp. (International) on Combust. 809-815. The Combustion Institute.*

CHENG, R. K. & SHEPHERD I. G. 1991 The influence of burner geometry on premixed turbulent flame propagation. *Combust. Flame.* **85,** 7-26.

DARABIHA, N., GIOVANGIGLI, V., TROUVÉ, A., CANDEL, S. M. & ESPOSITO, E. 1987 Coherent flame description of turbulent premixed ducted flames. *in Proc. of the France-USA Joint Workshop on Turbulent Combustion.* Springer Verlag.

DUCLOS, J. M., VEYNANTE, D. & POINSOT, T. 1993 A comparison of flamelet models for premixed turbulent combustion. *Combust. Flame.* **95,** 101-117.

FAVRE A., KOVASNAY, L. S. G., DUMAS, R., GAVIGLIO, J. & COANTIC, M. 1976 *La turbulence en mécanique des fluides.* Gauthier Villars.

HAWORTH, D. C. & POINSOT, T. 1992 Numerical simulations of Lewis number effects in turbulent premixed flames. *J. Fluid Mech.* **244,** 405-436.

LAUNDER, B. E. 1976 Heat and mass transport by turbulence. *in Topics in Applied Physics* **12.** Springer-Verlag.

LIBBY, P. A. & BRAY, K. N. C. 1981 Countergradient diffusion in premixed turbulent flames. *AIAA J.* **19,** 205-213.

MAISTRET, E., DARABIHA, N., POINSOT, T., VEYNANTE, D., LACAS, F., CANDEL, S. M. & ESPOSITO, E. 1989 Recent developments in the coherent flamelet description of turbulent combustion. In *Proc. 3rd Int. SIAM Conf. on Numerical Combustion.*

MARBLE, F. E. & BROADWELL, J. E. 1977 The coherent flame model for turbulent chemical reactions. *Project Squid Technical Report.* TRW-9-PU.

MASUYA G. 1986 Influence of Laminar Flame Speed on Turbulent Premixed Combustion. *Combustion and Flame.* **64,** 353-367

MOSS J. B. 1980 Simultaneous Measurements of Concentration and Velocity in an Open Premixed Turbulent Flame. *Combust. Sci. Tech.* **22,** 119-129.

PETERS, N. 1986 Laminar flamelet concepts in turbulent combustion. *Twenty-First Symp. (International) on Combust.* 1231-1250. The Combustion Institute.

PETERS, N. 1992 A spectral closure for premixed turbulent combustion in the flamelet regime. *J. Fluid Mech.* (Submitted for publication).

POINSOT, T., VEYNANTE, D. & CANDEL, S. M. 1991 Quenching processes and premixed turbulent combustion diagrams. *J. Fluid Mech.* **228,** 561-605.

POPE, S. B. 1988 Evolution of surfaces in turbulence. *International J. Engng. Sci.* **26,** 445-469.

RUTLAND, C. J. & TROUVÉ, A. 1993 Direct simulations of premixed turbulent flames with non-unity Lewis numbers. *Combust. Flame.* **94,** 41-57.

RUTLAND, C. J. & CANT, R. S. 1994 Turbulent transport in premixed flames. *Proc. of the Summer Program,* Center for Turbulence Research, NASA Ames/ Stanford Univ.

SHEPHERD, I. G., MOSS, J. B. & BRAY, K. N. C. 1982 Turbulent transport in a confined premixed flame. *Nineteenth Symp. (International) on Combust.* 423-431. The Combustion Institute.

TROUVÉ, A. & POINSOT, T. 1994 The evolution equation for the flame surface density in turbulent premixed combustion. *J. Fluid Mech.* **278,** 1-31.

WILLIAMS, F. A. 1985 *Combustion theory.* 2nd ed., Benjamin Cummings.

37-25
39737
N95-21042 125

Center for Turbulence Research
Proceedings of the Summer Program 1994

Pdf modeling for premixed turbulent combustion based on the properties of iso-concentration surfaces

By L. Vervisch[1], W. Kollmann[2], K. N. C. Bray[3], AND T. Mantel[4]

In premixed turbulent flames the presence of intense mixing zones located in front of and behind the flame surface leads to a requirement to study the behavior of iso-concentration surfaces defined for all values of the progress variable (equal to unity in burnt gases and to zero in fresh mixtures). To support this study, some theoretical and mathematical tools devoted to level surfaces are first developed. Then a database of direct numerical simulations of turbulent premixed flames is generated and used to investigate the internal structure of the flame brush, and a new pdf model based on the properties of iso-surfaces is proposed.

1. Introduction

In order to improve existing models of premixed turbulent combustion (Borghi 1988), it is necessary to build a bridge from zones where intense reactive activity occurs in laminar flamelets to the more distributed reaction zones found in front of and behind these propagating flame surfaces. This is especially true if one wishes to predict not only the global structure of the flame, but also the concentration level of pollutants using any probabilistic approach. Indeed, the turbulent mixing acting in the preheat zone can strongly influence the structure of the entire flame; therefore, a description of this mixing, together with descriptions of chemical sources or of topological properties of the flame surface, must be used to account for their mutual interactions.

The objective of this work is the development of a formalism, adapted to premixed turbulent combustion modeling, which brings the possibility to treat simultaneously flamelet behavior and out-of-flamelet mixing. This is a crucial point because they both interact to control the properties of the propagation velocity of the flame front (Bray 1990, Pocheau 1992).

To account for the possible presence of flamelets, the flame surface density approach (Marble and Broadwell 1977) is extended to the concept of a surface density function and coupled with probability density function (pdf) method (Pope 1985).

1 LMFN-INSA, URA - CNRS 230 - CORIA, France
2 MAE, University of California at Davis
3 Cambridge University, Engineering Department, U.K.
4 Center for Turbulence Research

First some theoretical considerations and mathematical tools concerning iso-surfaces in fluid mechanical problems are developed. In Section 2.1 a useful mathematical relation between surface and volume integrals is introduced which has several applications of theoretical and practical importance. It is used first (Section 2.2) to establish the transport equation for global variables such as the total surface area of iso-concentration surfaces, and from this the classical expression for premixed flame stretch is recovered. The solution of the area equation for a material surface is proposed (Section 2.3). In particular, it is shown that the combination of the introduced mathematical relation with Lagrangian variables leads to an expression for the area of a temporally evolving level surface, which only requires the integration over the surface at a fixed time. In Section 2.4 the same formalism is used in conjunction with an integral transform for the computation of the area of iso-surfaces without computing the location of the surfaces. This leads to a novel method for the efficient computation of the surface area of iso-surfaces, which is superior to triangulation methods that keep track of the connectedness of the surface. Finally, the concept of a surface density function (sdf) emerges (Section 2.5) along with its transport equation, and a unified treatment of pdf and sdf equations is discussed (Section 2.6).

A direct numerical simulation (DNS) database of premixed turbulent combustion is developed and used in Section 3 to study the internal structure of the turbulent flame, and various key quantities identified in Section 2 are analyzed. In particular, the behavior of quantities integrated over iso-concentration surfaces is carefully examined within the inner structure of the premixed flame, for surfaces located between fresh and burnt gases.

The pdf formulation reduces the modeling difficulties emerging when the mean burning rate needs to be estimated to the finding of a closed expression for the small scales mixing which depends on the distribution of the gradient of the reactive species along their iso-surfaces. The surface density function contains information about these gradients, especially within the flamelet zone. Based on this remark, an attempt to couple the pdf with the sdf is proposed in Section 4, and the resulting modeled expressions are tested against their exact values extracted from the DNS.

2. Transport equations for surfaces

2.1 Introduction

In multi-composition fluid mechanical problems, the starting point for studying the quantities characterizing the physical properties of the flow field are usually budget equations for volume integrals over a volume of fluid $\mathcal{D}$. To derive equations for the corresponding properties of iso-surfaces, it is necessary to link volume integrals and integrals over these surfaces. The following theorem of geometric measure theory (Maz'ja 1985, ch.1.2.4, p.37, Constantin 1992) provides the bridge between volume integrals and integrals over iso-surfaces.

Theorem: Let $F(\underline{x})$ be a Borel-measurable nonnegative function on $\mathcal{D} \subseteq R^3$ open. Let $\Phi(\underline{x}) \in C^\infty(\mathcal{D})$. Then

$$\int_{\mathcal{D}} d\underline{x} F(\underline{x}) |\nabla \Phi(\underline{x})| = \int_0^\infty d\varphi \int_{S_\Phi(\varphi)} dA(\underline{x}) F(\underline{x}) \quad , \tag{1}$$

where $S_\Phi(\varphi) = \{\underline{x} \in \mathcal{D} : \Phi(\underline{x}) = \varphi\}$ is the level surface or iso-surface of the field $\Phi(\underline{x})$ on which $\Phi(\underline{x})$ takes the value φ. This condition specifies that the level surfaces are contained in the domain $\mathcal{D}$ (no intersection of the surfaces with the domain boundary). It is possible to remove this restriction, but this case will not be pursued here.

The co-area formula follows at once if the function $F(\underline{x})$ is specified as:

$$F(\underline{x}) = f(\underline{x}) \delta(\Phi(\underline{x}) - \varphi) \quad ,$$

where $\delta(\Phi(\underline{x}) - \varphi)$ is the diract delta function, leading to the desired result

$$\int_{\mathcal{D}} d\underline{x} f(\underline{x}) |\nabla \Phi(\underline{x})| \delta(\Phi(\underline{x}) - \varphi) = \int_{S_\Phi(\varphi)} dA(\underline{x}) f(\underline{x}) \quad . \tag{2}$$

2.2 Transport equation for global variables

The total area of level surfaces is an example of a global variable. In general, a global variable is defined by

$$\mathcal{F}_\Phi(\varphi, t) \equiv \int_{S_\Phi(\varphi)} dA(\underline{x}) f(\underline{x}, t) \quad , \tag{3}$$

where the unspecified function $f(\underline{x}, t)$ must satisfy the conditions of the above theorem. In most cases it will be a smooth function of location and time to allow differentiation. Application of Eq. 2 to Eq. 3 and differentiation with respect to time leads to the transport equation for $\mathcal{F}_\Phi$ in terms of volume integrals

$$\frac{\partial \mathcal{F}_\Phi}{\partial t}(\varphi, t) + \frac{\partial}{\partial \varphi} \mathcal{L}_\Phi = S_f + S_\Phi \quad . \tag{4}$$

Three contributions determine the time rate of change of the global variable $\mathcal{F}_\Phi(\varphi, t)$: a convective transport term in scalar space and two source terms. The flux in scalar space is defined by

$$\mathcal{L}_\Phi \equiv \int_{\mathcal{D}} d\underline{x} \delta(\Phi - \varphi) |\nabla \Phi| f(\underline{x}, t) \frac{\partial \Phi}{\partial t} \quad , \tag{5}$$

the source due to the evolution of $f(\underline{x}, t)$ is

$$S_f(\varphi, t) \equiv \int_{\mathcal{D}} d\underline{x} \delta(\Phi - \varphi) |\nabla \Phi| \frac{\partial f}{\partial t} \quad , \tag{6}$$

and finally the source due to the evolution of the scalar field defining the level surfaces is

$$S_\Phi(\varphi,t) \equiv \int_{\mathcal{D}} d\underline{x}\,\delta(\Phi-\varphi) f(\underline{x},t) \frac{\partial|\nabla\Phi|}{\partial t} \quad . \tag{7}$$

The co-area formula Eq. 2 can be applied once more to obtain an equivalent version in terms of surface integrals

$$\frac{\partial \mathcal{F}_\Phi}{\partial t}(\varphi,t) = \int_{S_\Phi(\varphi)} dA \left(\frac{D^s f}{Dt} + f \frac{D^s}{Dt} \log(|\nabla\Phi|) + f \frac{\partial v_\alpha^s}{\partial x_\alpha} \right) \quad , \tag{8}$$

where $\frac{D^s}{Dt}$ is the time rate of change following points on the level surface. The time rate of change of the global variable $\mathcal{F}_\Phi$ is seen to be caused by the change of the function $f(\underline{x},t)$ on the level surface, the time rate of change of $\log(|\nabla\Phi|)$ on the level surface, and the surface divergence of flow velocity.

The dynamic equations for global variables can be established once the transport equations for the scalar $\Phi(\underline{x},t)$ defining the level surfaces and the scalar $f(\underline{x},t)$ are known. In the case of flames, the transport equation for a reactive scalar field may be written:

$$\frac{D\Phi}{Dt} = \Omega_\Phi \quad , \tag{9}$$

where $D/Dt = \partial/\partial t + \underline{v}.\nabla$ is the substantial derivative and

$$\Omega_\Phi = \frac{1}{\rho}\frac{\partial}{\partial x_\alpha}\left(\rho\Gamma\frac{\partial\Phi}{\partial x_\alpha}\right) + \dot{W}_\Phi(\Phi) \quad , \tag{10}$$

denotes the imbalance of diffusion and source terms. The transport equation for f is assumed to be in the generic form

$$\rho\left(\frac{\partial f}{\partial t} + v_\alpha \frac{\partial f}{\partial x_\alpha}\right) = \frac{\partial}{\partial x_\alpha}\left(\rho\lambda\frac{\partial f}{\partial x_\alpha}\right) + \rho\dot{W}_f(f) \quad . \tag{11}$$

The iso-surfaces are defined implicitly as solution of

$$S_\Phi(\varphi,t) \equiv \Phi(\underline{x},t) - \varphi = 0 \quad , \tag{12}$$

and the unit normal vector of the iso-surface is defined by

$$n_\alpha \equiv -\frac{1}{|\nabla\Phi|}\frac{\partial\Phi}{\partial x_\alpha} \quad . \tag{13}$$

The surfaces move in their normal direction, with the velocity

$$v_\alpha^s = v_\alpha + V n_\alpha \quad . \tag{14}$$

The relative progression velocity V of the level surfaces is determined by the imbalance Eq. 10 of diffusion and source term in Eq. 9:

$$V = \frac{1}{\rho|\nabla\Phi|}\frac{\partial}{\partial x_\alpha}(\rho\Gamma\frac{\partial\Phi}{\partial x_\alpha}) + \frac{1}{|\nabla\Phi|}\dot{W}_\Phi = \frac{1}{|\nabla\Phi|}\Omega_\Phi \quad . \tag{15}$$

The dynamic equation for the global variable $\mathcal{F}_\Phi$ then follows in terms of volume integrals as

$$\begin{aligned}\frac{\partial\mathcal{F}_\Phi}{\partial t} = &\int_{\mathcal{D}} d\underline{x}\,\delta(\Phi-\varphi)|\nabla\Phi|\left[\frac{1}{\rho}\frac{\partial}{\partial x_\alpha}\left(\rho\lambda\frac{\partial f}{\partial x_\alpha}\right) + \dot{W}_f + f\left(\frac{\partial v_\alpha}{\partial x_\alpha} - n_\alpha n_\beta\frac{\partial v_\beta}{\partial x_\alpha}\right)\right] \\ &+ \int_{\mathcal{D}} d\underline{x}\,\delta(\Phi-\varphi)|\nabla\Phi|\left[\left(\frac{1}{\rho}\frac{\partial}{\partial x_\alpha}\left(\rho\Gamma\frac{\partial\Phi}{\partial x_\alpha}\right) + \dot{W}_\Phi\right)\frac{\partial n_\alpha f}{\partial x_\alpha}\right] \quad .\end{aligned} \tag{16}$$

This is one of several equivalent versions of the dynamic equation for the global variable $\mathcal{F}_\Phi(\varphi,t)$ in variable density turbulence. The equation for the surface area $A_\Phi(\varphi,t)$ is obtained by choosing $f=1$ (see Eq. 3)

$$\frac{\partial\mathcal{A}_\Phi}{\partial t} = \int_{\mathcal{D}} d\underline{x}\,\delta(\Phi-\varphi)\left[|\nabla\Phi|\left(\frac{\partial v_\alpha}{\partial x_\alpha} - n_\alpha n_\beta\frac{\partial v_\beta}{\partial x_\alpha}\right) + \left(\frac{1}{\rho}\frac{\partial}{\partial x_\alpha}\left(\rho\Gamma\frac{\partial\Phi}{\partial x_\alpha}\right) + \dot{W}_\Phi\right)\frac{\partial n_\alpha}{\partial x_\alpha}\right] \tag{17}$$

The corresponding equation in terms of surface integrals can easily be obtained from Eq. 17 by using Eq. 2. In particular, the surface stretch

$$\mathcal{H}(t) = \frac{1}{\mathcal{A}_\Phi}\frac{d\mathcal{A}_\Phi}{dt} \quad , \tag{18}$$

may be cast in the form:

$$\mathcal{H}(t) = \frac{1}{\mathcal{A}_\Phi}\left(\mathcal{I}_1 + \mathcal{I}_2\right) \quad , \tag{19}$$

where

$$\begin{aligned}\mathcal{I}_1 &= \int_{S_\Phi(\varphi)} dA(\underline{x})\phi_s(\underline{x},t) \quad , \\ \mathcal{I}_2 &= \int_{S_\Phi(\varphi)} dA(\underline{x})V(\underline{x},t)\frac{\partial n_\alpha}{\partial x_\alpha} \quad .\end{aligned} \tag{20}$$

In Eq. 20 ϕ_s is a notation for the in-plane strain rate:

$$\phi_s = \frac{\partial v_\alpha}{\partial x_\alpha} - n_\alpha n_\beta\frac{\partial v_\beta}{\partial x_\alpha} \quad , \tag{21}$$

and the imbalance between reactive and diffusive effects Ω_Φ has been written in terms of the relative progression velocity V by using Eq. 10. When the scalar $\Phi(\underline{x},t)$ denotes the progress variable used in premixed combustion ($\Phi = 0$ in fresh gases and $\Phi = 1$ in burnt gases), then by choosing as iso-surface the surface corresponding to the value of the progress variable used to locate the flame front, the well-known result is found that flame stretch is directly related to both contributions of strain rate acting along the flame front ($\mathcal{I}_1$) and curvature linked with propagation of the premixed flame ($\mathcal{I}_2$) (Candel and Poinsot 1990).

Inspection of Eq. 17 shows that the surface area changes due to the strain rate in the tangential plane of the surface caused by the motion of the fluid and the dynamic change of the scalar field defining the level surface. Both phenomena may increase or decrease the surface area. The dynamics of the scalar variable defining the level surface appear in Eq. 17 as molecular diffusion and the source term. It is clear that both may be positive or negative, hence may increase or decrease the surface area as time evolves. The molecular diffusion term can be analyzed in more detail for incompressible flows with constant diffusivity Γ, since it is then proportional to

$$\frac{1}{|\nabla\Phi|}\triangle\Phi\frac{\partial n_\alpha}{\partial x_\alpha} = \frac{\partial n_\alpha}{\partial x_\alpha}\frac{\partial n_\beta}{\partial x_\beta} + \frac{\partial n_\gamma}{\partial x_\gamma}\frac{n_\alpha n_\beta}{|\nabla\Phi|}\frac{\partial^2\Phi}{\partial x_\alpha \partial x_\beta} \quad .$$

The first term on the right side is purely geometrical since it only depends on the mean curvature H

$$H = -\frac{1}{2}\frac{\partial n_\alpha}{\partial x_\alpha} \quad ,$$

whereas the second term depends on the variation of the defining scalar normal to the level surface

$$\frac{\partial\Phi}{\partial n} = \underline{n}\cdot\nabla\Phi \quad ,$$

and it follows that

$$\frac{1}{|\nabla\Phi|}\triangle\Phi\frac{\partial n_\alpha}{\partial x_\alpha} = 4H^2 - 2\frac{H}{|\nabla\Phi|}\frac{\partial^2\Phi}{\partial n^2}$$

holds, which proves that the effect of molecular diffusion on the surface area is not definite: The first term on the right side always increases the surface area, if the mean curvature is nonzero, but the second term may decrease or increase it depending on the signs of the normal derivative and the mean curvature.

2.3 Solution of the area equation for material surfaces

For material surfaces Eq. 17 for the area of level surfaces is reduced to

$$\frac{\partial\mathcal{A}_\Phi}{\partial t}(\varphi,t) = \int\limits_{S_\Phi(\varphi,t)} dA\left(\frac{\partial v_\alpha}{\partial x_\alpha} - n_\alpha n_\beta\frac{\partial v_\beta}{\partial x_\alpha}\right) \quad , \tag{22}$$

with the initial condition

$$\mathcal{A}_\Phi(\varphi,0) = \int\limits_{S_\Phi(\varphi,0)} dA \ , \tag{23}$$

as the area of the surface $\Phi(\underline{x},0) = \varphi$. Material surfaces enjoy the property that they are the one-to-one image of the initial surfaces. It is clear that Lagrangian variables are the proper choice for the formulation of their evolution. Denoting by τ and $\underline{a}$ the Lagrangian variables defined as time and initial position of material points, the position $\underline{X}(\tau,\underline{a})$ at a later time is then the solution of

$$\frac{dX_\alpha}{d\tau} = v_\alpha(\tau,\underline{X}), \quad X_\alpha(0,\underline{a}) = a_\alpha \ , \tag{24}$$

where $v_\alpha(t,\underline{x})$ is the Eulerian velocity and t, $\underline{x}$ are the usual Eulerian variables. The inverse transformation (from Eulerian field to Lagrangian field) $a_\alpha = X_\alpha^{-1}(t,\underline{x})$ is unique and smooth as long as the Eulerian velocity field is smooth. The solution to Eq. 23-24 can be constructed if the co-area formula is applied

$$\mathcal{A}_\Phi(\varphi,t) = \int\limits_{\mathcal{D}} d\underline{x}|\nabla\Phi|\delta(\Phi(\underline{x},t)-\varphi) \ ,$$

and the fact that the level surface is embedded in a part of the flow field is used. Taking for $\mathcal{D}(\tau)$ a subset of the flow field that contains the level surface at time τ and using the fact that the mapping $\underline{X}(\tau,\underline{a})$ is defined not only of the level surface but on the set $\mathcal{D}(\tau)$, we transform the volume integral to the Lagrangian frame as integral over $\mathcal{D}(0)$

$$\mathcal{A}_\Phi(\varphi,\tau) = \int\limits_{\mathcal{D}(0)} d\underline{a}J(\underline{a},\tau)|\nabla\Phi|(\underline{a},\tau)\delta(\Phi(\underline{X},\tau)-\varphi) \ , \tag{25}$$

where J denotes the Jacobian of the transformation given by

$$J(\underline{a},\tau) = \frac{1}{6}\epsilon_{\alpha\beta\gamma}\epsilon_{\delta\eta\omega}\frac{\partial X_\alpha}{\partial a_\delta}\frac{\partial X_\beta}{\partial a_\eta}\frac{\partial X_\gamma}{\partial a_\omega} \ . \tag{26}$$

This Jacobian is the determinant of the Lagrangian deformation tensor $J_{\alpha\beta}$

$$J_{\alpha\beta} = \frac{\partial X_\alpha}{\partial a_\beta} \ ,$$

which is nonsingular for smooth flows with $J > 0$. The points on the level surface are materially invariant so

$$\delta(\Phi(\underline{X},\tau)-\varphi) = \delta(\Phi(\underline{a},0)-\varphi) \ ,$$

and it follows that the area at time τ is given by

$$\mathcal{A}_\Phi(\varphi,\tau) = \int\limits_{\mathcal{D}(0)} d\underline{a}|\nabla\Phi|(\underline{a},0)\delta(\Phi(\underline{a},0)-\varphi)J(\underline{a},\tau)\frac{|\nabla\Phi|(\underline{a},\tau)}{|\nabla\Phi|(\underline{a},0)}$$

where $d\underline{a}$ is the volume differential at time zero. Application of the co-area formula leads to a surface integral over the initial surface

$$\mathcal{A}_\Phi(\varphi,\tau) = \int\limits_{S_\Phi(\varphi,0)} dA(0)J(\underline{a},\tau)\frac{|\nabla\Phi|(\underline{a},\tau)}{|\nabla\Phi|(\underline{a},0)} \quad , \tag{27}$$

where $dA(0)$ denotes the surface differential at time zero. This is the desired solution of Eq. 23 and Eq. 24, as can be verified easily by differentiation. The solution Eq. 27 can be recast in terms of the Lagrangian deformation tensor if the kinematic relation (Ottino 1989, section 2.7)

$$dA(\tau) = dA(0)J(\underline{a},\tau)\left(n_\alpha n_\beta J^{-1}_{\gamma\alpha}J^{-1}_{\gamma\beta}\right)^{\frac{1}{2}} \tag{28}$$

is applied. It follows at once that the solution Eq. 28 is thus given by

$$\mathcal{A}_\Phi(\varphi,\tau) = \int\limits_{S_\Phi(\varphi,0)} dA(0)J(\underline{a},\tau)\left(n_\alpha n_\beta J^{-1}_{\gamma\alpha}J^{-1}_{\gamma\beta}\right)^{\frac{1}{2}} \quad , \tag{29}$$

valid for material surfaces. The version Eq. 29 of the solution shows the special property of material surfaces possessing nonsingular Jacobians. This is not the case for surfaces moving relative to the fluid, and Eq. 27 and Eq. 29 are then not necessarily well defined.

It is worth noting that for incompressible flows $J = 1$ holds and, assuming constant molecular diffusivity Γ, the result

$$\mathcal{A}_\Phi(\varphi,\tau) = \int\limits_{S_\Phi(\varphi,0)} dA(0)\left(\frac{\epsilon_\Phi(\underline{a},\tau)}{\epsilon_\Phi(\underline{a},0)}\right)^{\frac{1}{2}} \tag{30}$$

follows from Eq. 27. It shows that the evolution of the area of material surfaces for incompressible flows is determined by the initial surface and the values of the scalar dissipation $\epsilon_\Phi \equiv \Gamma\nabla\Phi\cdot\nabla\Phi$ on the surface. The integral can be computed if the Lagrangian scalar dissipation $\epsilon_\Phi(\underline{a},\tau)$ is known, which is often the hard part of the problem. The expression for the area Eq. 27 does not contain any statistical information as only surface integrals are involved. It is equal to the expected area for homogeneous turbulence but is different from expected values for non-homogeneous flows.

2.4 Computation of the area of level surfaces

Consider a scalar field $\Phi(\underline{x},t) \geq 0$, such as enstrophy, temperature, density etc., that is a realization of a turbulent field. The equation of the iso-surfaces of Φ is

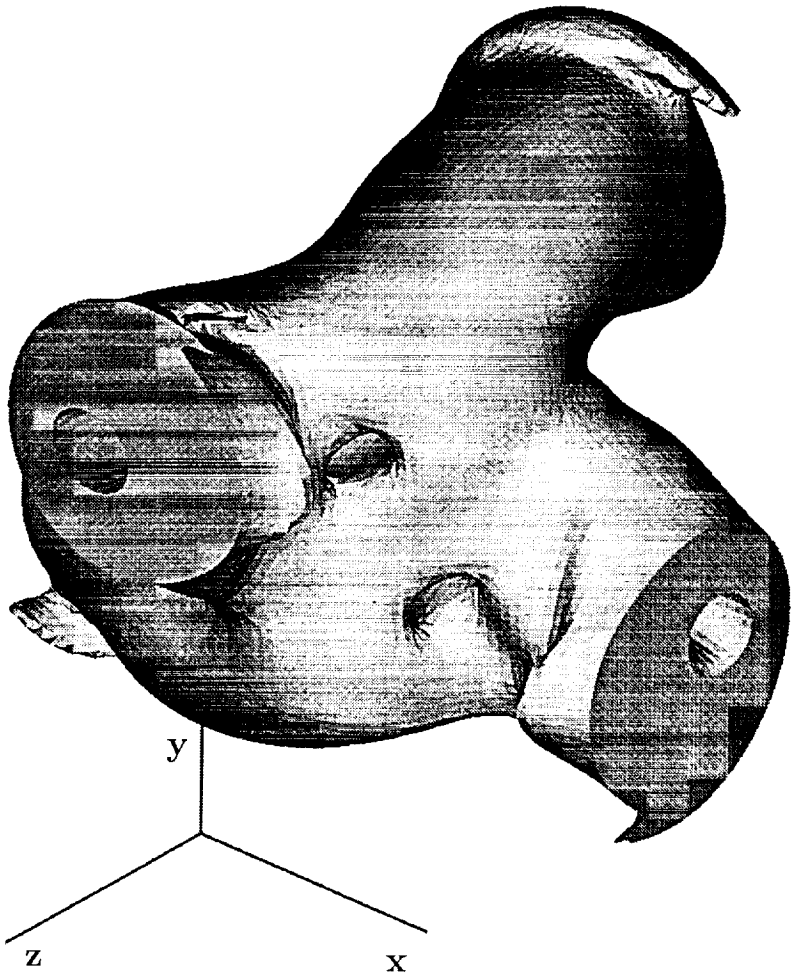

FIGURE 1. Level surface of kinetic energy for a periodic viscous flow generated by the interaction of two vortex tubes, which are initially off-set and orthogonal. The flow is used as example for the computation of the surface area.

then given implicitly by $S_\Phi(\varphi) = \{\underline{x} \in \mathcal{D} : \Phi(\underline{x}) = \varphi\}$. It follows from Eq. 2 that surface integrals can be represented as volume integrals over a fixed domain $\mathcal{D}$ (note that $S_\Phi(\varphi)$ is not the boundary of the domain $\mathcal{D}$; hence, the Gauss theorem is not applicable). The surface area is

$$\mathcal{A}_\Phi(\varphi, t) = \int_{\mathcal{D}} d\underline{x} |\nabla\Phi| \delta(\Phi(\underline{x}, t) - \varphi) \tag{31}$$

in which the Dirac-pseudofunction selects the points in space where the level surface is located. This property indicates that an integral transform with respect to the range of the scalar Φ would remove the delta function. Since the scalar Φ is

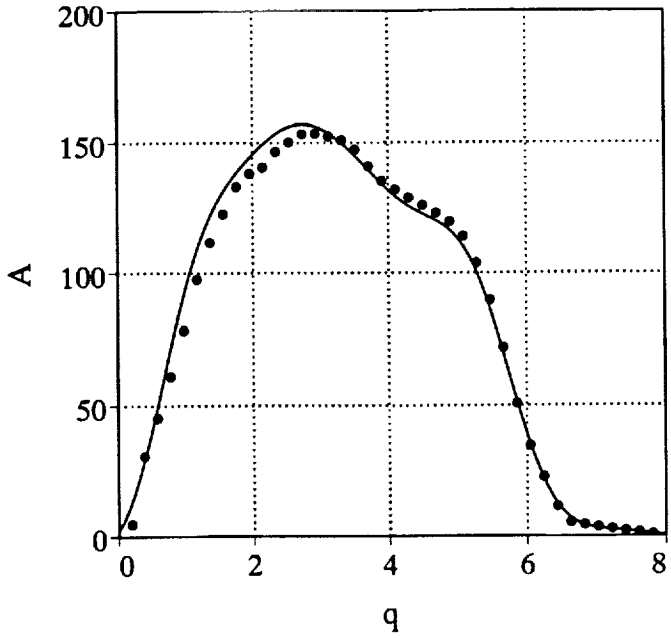

FIGURE 2. Surface area of level surfaces for the flow illustrated in Fig. 1. The symbols correspond to the triangulation method and the line to the Laplace transform method Eq. 33 and Eq. 34.

nonnegative, it follows that the Laplace transform is the appropriate tool. Hence, the transformed surface area is then defined by

$$\hat{\mathcal{A}}_\Phi(s) \equiv \int_0^\infty d\varphi \mathcal{A}_\Phi(\varphi) \exp(-s\varphi) \ , \tag{32}$$

where $s = u + iw$ is a complex variable. Using Eq. 31 we obtain

$$\hat{\mathcal{A}}_\Phi(s) = \int_0^\infty d\varphi \exp(-s\varphi) \int_{\mathcal{D}} d\underline{x} \delta(\Phi(\underline{x}) - \varphi) |\nabla\Phi| \ ,$$

which leads to

$$\hat{\mathcal{A}}_\Phi(s) = \int_{\mathcal{D}} d\underline{x} |\nabla\Phi| \exp(-s\Phi(\underline{x})) \ . \tag{33}$$

This is a powerful result with both practical and theoretical implications: the Laplace transform of the surface area of level surfaces for all level values can be computed without computing the location of a single level surface. Furthermore, this computation is much more efficient than methods based on triangulation of level surfaces that keep track of the connectedness of the triangles. It is also useful for theoretical considerations since the integrand in Eq. 33 is a well defined function

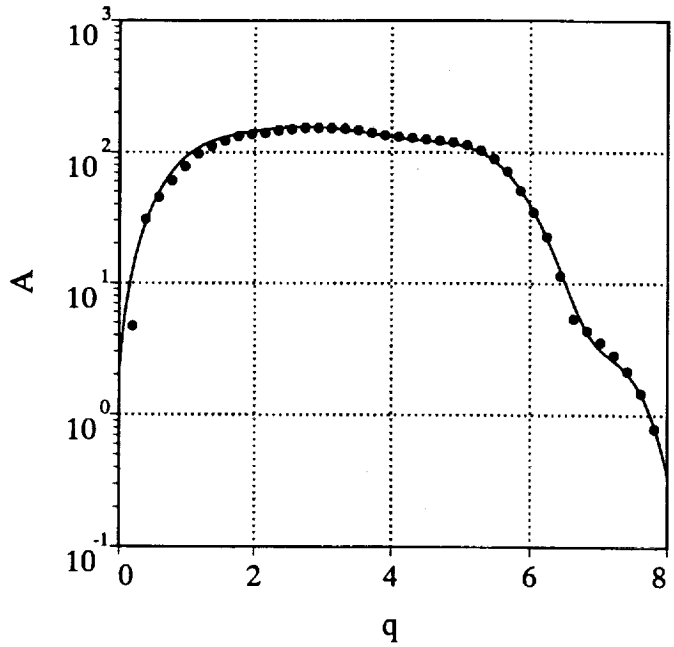

FIGURE 3. Same as Fig. 2 with logarithmic scale for the vertical axis.

for finite s and not a distribution, and is accessible to the methods of classical analysis. Once the Laplace transform has been determined, the inverse transform produces the desired surface area according to

$$\mathcal{A}_\Phi(\varphi) = \frac{1}{2\pi i} \int_{u-i\infty}^{u+i\infty} ds \hat{\mathcal{A}}_\Phi(s) \exp(s\varphi) \quad . \tag{34}$$

The numerical computation of the integrals in Eq. 33 and Eq. 34 requires some care. It is easy to see that the range of w in the independent variable $s = u + iw$ in Eq. 33 and Eq. 34 is limited by the highest wave-number that can be resolved on the lattice of discrete values of φ

$$w_{max} \| \triangle \Phi(\underline{x}, t) \| \leq \pi \quad ,$$

where $\| \cdot \|$ is an appropriate norm and $\triangle\Phi$ denotes the difference of Φ between two neighboring lattice points. Choosing w_{max} significantly larger than this limit leads to integrals over rapidly oscillating functions which diverge. For the present case the maximum norm was initially chosen, which turned out to be too restrictive, and the limit was relaxed to twice the value given above. This aspect of the transform method requires further analysis.

As an example, the scalar kinetic energy $\Phi(\underline{x}, t) \equiv q(\underline{x}, t) = v_\alpha v_\alpha$ generated as a numerical solution of the Navier-Stokes equations for the interaction of two initially orthogonally offset vortex tubes ($Re = 1500$) at time $t = 1.375$ is used to illustrate the transform method outlined above. One of the level surfaces is shown in Fig. 1 for

the level value which is 48.78% of the maximum. It has the Euler number (Kollmann and Chen 1994) $\chi = -10$, which corresponds to the genus $g = 1 - \frac{1}{2}\chi = 6$ or a sphere with six handles, and the fragmentation $N = 1$, which means that there is only one surface component. The intersections of the level surface (the flow field is periodic in all three directions) with the cubic flow domain are artificially closed with lids. The area of the lids is not included in the results for the surface area. Two methods for the computation of the surface area are applied: Triangulation of the level surfaces, which determines the connectedness information for all triangles and thus allows also the computation of the topological properties χ and N, and the Laplace transform method given by Eq. 33 and Eq. 34. The results in Fig. 2 (linear scale, the full line is the transform method and the symbols the triangulation) and Fig. 3 (semi-logarithmic plot) show that good agreement between the two methods is achieved. The advantage of the Laplace transform method becomes apparent if the CPU times are compared: The Laplace transform method (using 100 points on the φ-axis) is about 1000 times faster than the triangulation method (using 40 points).

2.5 Surface density function

In modeling purposes one wishes to seek out closed equations for point quantities that can be easily discretized and introduced in fluid mechanics codes. The density of iso-surface is introduced in this section as a quantity that characterizes, in mean, the behavior of iso-concentration surfaces for a reactive scalar field $\Phi(\underline{x})$ that follows Eq. 9.

The basic relation (Eq. 2) set out in Section 2.1 suggests that for $f = 1$ a local and instantaneous measure of the density per unit volume of iso-surface is provided by

$$\Sigma(\varphi;\underline{x},t) = |\nabla\Phi(\underline{x})|\delta(\Phi(\underline{x}) - \varphi) \quad .$$

Indeed from Eq. 2

$$\int_{\mathcal{D}} d\underline{x}\Sigma(\varphi;\underline{x},t) = \int_{S_\Phi(\varphi)} dA(\underline{x}) = \mathcal{A}_\Phi \quad , \tag{35}$$

and $\Sigma(\varphi;\underline{x},t)$ corresponds to the ratio $\frac{\delta A_\Phi}{\delta V}$ in the limit $\delta V \to 0$. This expression indicates that, within a turbulent environment, the mean surface density function (sdf) $\overline{\Sigma}(\varphi;\underline{x},t)$ is the product of the expected value for the magnitude of the gradient of $\Phi(\underline{x},t)$, conditioned on being on one iso-surface $\Phi(\underline{x},t) = \varphi$, times the probability of being on that surface. Indeed introducing the pdf of $\Phi(\underline{x},t) = \varphi$, namely $\overline{P}(\varphi;\underline{x},t) = \overline{\delta(\varphi - \Phi(\underline{x},t))}$, one may write:

$$\overline{\Sigma}(\varphi;\underline{x},t) = \overline{|\nabla\Phi(\underline{x},t)|\,\delta(\varphi - \Phi(\underline{x},t))} = \left(\overline{|\nabla\Phi(\underline{x},t)|\,\Big|\Phi(\underline{x},t) = \varphi}\right)\overline{P}(\varphi;\underline{x},t) \quad , \tag{36}$$

where $\left(\overline{\mid \nabla\Phi(\underline{x},t) \mid \left| \Phi(\underline{x},t)=\varphi \right.}\right)$ denotes a conditional average. (This definition of surface density has been previously used by Trouvé and Poinsot (1994) to evaluate flame surface density from DNS.)

All information contained in the sdf is also available through the joint pdf of Φ and its gradient; models have been proposed for this joint pdf in the case of reacting and non-reacting flows (Meyers and O'Brien 1981, Dopazo 1994, Fox 1994). The iso-surface is one of the standard concepts used to investigate complex phenomena in premixed turbulent flames (Veynante *et al.* 1994); therefore, despite the detailed statistical description involved in this joint pdf, it is interesting to restrict the present study to the specific equation for $\overline{\Sigma}(\varphi;\underline{x},t)$.

An exact transport equation for the surface density function $\overline{\Sigma}(\varphi;\underline{x},t)$ may be written (Vervisch *et al.* 1994):

$$\begin{aligned}\overline{\frac{D\Sigma(\varphi;\underline{x},t)}{Dt}} &= \left(\overline{(-\underline{n}\,\underline{n}{:}\nabla\underline{v}) \mid \nabla\Phi(\underline{x},t) \mid \left| \Phi(\underline{x},t)=\varphi \right.}\right)\overline{P}(\varphi;\underline{x},t) \\ &- \left(\overline{\underline{n}.\nabla\Omega_\Phi(\underline{x},t)\left|\Phi(\underline{x},t)=\varphi\right.}\right)\overline{P}(\varphi;\underline{x},t) \\ &- \frac{\partial}{\partial\varphi}\left[\left(\overline{\Omega_\Phi(\underline{x},t)\left|\Phi(\underline{x},t)=\varphi\right.}\right)\overline{P}(\varphi;\underline{x},t)\right] \quad .\end{aligned} \tag{37}$$

It is important to note that in Eq. 37 φ is an independent variable (sample space variable), and Eq. 37 is valid for all the iso-concentration surfaces defined from the progress variable field. When the various terms contributing to the sdf evolution are transposed to a surface formalism, they are equivalent to those of Eq. 4 or Eq. 17.

2.6 Unified treatment of pdf and sdf equations

Pdf modeling has been shown to be an efficient tool for the computation of turbulent non-premixed flames (Kollmann 1990, Borghi *et al.* 1991). The pdf approach has a great potential because it allows for including the description of the chemistry in a closed form, the modeling issue related to the evaluation of the mean burning rate being reduced to the estimation of the small-scale mixing. However, in the case of turbulent premixed flames, classical mixing models may fail because of the particular properties of the reactive and diffusive zones. Indeed, mixing is a prerequisite for reactions in non-premixed systems as is preheating in premixed flows; therefore, the resulting predictions depend crucially on the properties of the mixing model, no matter how accurately the chemical reactions can be represented.

The pdf equation may be written (Kollmann 1990):

$$\overline{\frac{DP(\varphi;\underline{x},t)}{Dt}} = -\frac{\partial}{\partial\varphi}\left[\left(\overline{\Omega_\Phi(\underline{x},t)\left|\Phi(\underline{x},t)=\varphi\right.}\right)\overline{P}(\varphi;\underline{x},t)\right] \quad , \tag{38}$$

where the bar over the substantial derivative indicates that turbulent transport effects are included. By introducing the dissipation of the scalar field $\epsilon_\Phi = \Gamma \mid \nabla\Phi \mid^2$,

the modification of the pdf in composition space may be written in an alternative form

$$\overline{\frac{DP(\varphi;\underline{x},t)}{Dt}} = -\frac{\partial}{\partial\varphi}\left[\left(\overline{\dot{W}_\Phi\middle|\Phi(\underline{x},t)=\varphi}\right)\overline{P}(\varphi;\underline{x},t)\right] - \frac{\partial^2}{\partial\varphi^2}\left[\left(\overline{\epsilon_\Phi\middle|\Phi(\underline{x},t)=\varphi}\right)\overline{P}(\varphi;\underline{x},t)\right] \tag{39}$$

In Eq. 39 the chemical source is closed, but the mixing term involving second order derivative in composition space is unknown when a one-point description is adopted for the turbulent flow. This term is actually representative of the distribution of the magnitude of gradient of the scalar field along the iso-concentration surfaces. It is therefore natural to look for a closure of this term that takes advantage of the information included in $\overline{\Sigma}(\varphi;\underline{x},t)$ concerning the dynamics of these iso-surfaces. This approach leads to the development of a PDF-SDF model in which a system of equations consisting of the transport equations for the pdf and the sdf is solved.

The sdf equation can be recast in a form that emphasizes the similarity to the pdf equation if a relation between conditional and surface means is established. Surface means may be defined by

$$\left(\overline{\Omega_\Phi(\underline{x},t)\middle|\mathcal{A}_{\Phi=\varphi}}\right) = \frac{\int_{\mathcal{D}} d\underline{x}\Omega_\Phi(\underline{x},t)\Sigma(\varphi;\underline{x},t)}{\int_{\mathcal{D}} d\underline{x}\Sigma(\varphi;\underline{x},t)} = \frac{1}{\mathcal{A}_\Phi}\int_{S_\Phi(\varphi)} dA(\underline{x})\Omega_\Phi(\underline{x},t) \quad , \tag{40}$$

where Eq. 2 has been used when $\Sigma(\varphi;\underline{x},t) = \mid \nabla\Phi \mid \delta(\varphi - \Phi)$ is the instantaneous surface density function.

The conditional mean of $\Omega_\Phi(\underline{x},t)$ may be written:

$$\left(\overline{\Omega_\Phi(\underline{x},t)\middle|\Phi(\underline{x},t)=\varphi}\right) = \frac{\overline{\Omega_\Phi(\underline{x},t)\delta(\Phi(\underline{x},t)-\varphi))}}{\overline{\delta(\Phi(\underline{x},t)-\varphi)}} \quad . \tag{41}$$

A relation to the surface mean can be established for homogeneous flows if the co-area formula Eq. 2 is applied to Eq. 41. It follows for homogeneous flows that the conditional mean is the ratio of volume integrals which become surface integrals using Eq. 2

$$\left(\overline{\Omega_\Phi(\underline{x},t)\middle|\Phi(\underline{x},t)=\varphi}\right) = \frac{\int_{S_\Phi(\varphi)} dA(\underline{x})\frac{\Omega_\Phi(\underline{x},t)}{\mid\nabla\Phi\mid}}{\int_{S_\Phi(\varphi)} dA(\underline{x})\frac{1}{\mid\nabla\Phi\mid}} \quad ,$$

which is recognized as the desired relation between conditional and surface means

$$\left(\overline{\Omega_\Phi(\underline{x},t)\Big|\Phi(\underline{x},t)=\varphi}\right)=\frac{\left(\overline{\frac{\Omega_\Phi(\underline{x},t)}{|\nabla\Phi|}\Big|\mathcal{A}_{\Phi=\varphi}}\right)}{\left(\overline{\frac{1}{|\nabla\Phi|}\Big|\mathcal{A}_{\Phi=\varphi}}\right)} \quad .$$

Both sides are defined for non-homogeneous flows but are not equal since the right side is the ratio of geometrical means Eq. 40 and not statistical expectations. Conversly, the surface mean can be expressed in terms of conditional means

$$\left(\overline{\Omega_\Phi(\underline{x},t)\Big|\mathcal{A}_{\Phi=\varphi}}\right)=\frac{\left(\overline{\Omega_\Phi(\underline{x},t)\mid\nabla\Phi\mid\Big|\Phi(\underline{x},t)=\varphi}\right)}{\left(\overline{\mid\nabla\Phi\mid\Big|\Phi(\underline{x},t)=\varphi}\right)} \quad , \tag{42}$$

valid for homogeneous flows.

The application of the previous results to homogeneous flows converts the sdf equation (Eq. 37) in the form

$$\frac{\partial\overline{\Sigma}(\varphi;\underline{x},t)}{\partial t}=-\frac{\partial}{\partial\varphi}\left[\left(\overline{\Omega_\Phi\Big|\mathcal{A}_{\Phi=\varphi}}\right)\overline{\Sigma}(\varphi;\underline{x},t)\right]+\left(\overline{\theta_s\Big|\mathcal{A}_{\Phi=\varphi}}\right)\overline{\Sigma}(\varphi;\underline{x},t) \quad , \tag{43}$$

where θ_s denotes the total rate of generation of surface area per unit volume

$$\theta_s=-\underline{n}\,\underline{n}:\nabla\underline{v}-\frac{1}{\mid\nabla\Phi\mid}\underline{n}.\nabla\Omega_\Phi \quad .$$

Comparison of the pdf Eq. 38 with the Eq. 43 for the mean sdf shows that the sdf is transported in scalar space by the same mechanism as the pdf, but is also created or destroyed by the tangential strain rate and by the flux of the imbalance between diffusion and reactions normal to the level surfaces.

The equations for the pdf and the sdf in homogeneous flows pose two closure problems: the fluxes in scalar space and the surface mean of the total generation rate of the sdf. The particular structure of premixed flames and the previous analysis suggests dealing with mixing and chemical reactions in a unified way by developing a closure model for their combined effects. Pdf and sdf are moved in scalar space by the conditional mean and the surface mean of the same quantity, namely the imbalance between diffusion and reactions.

3. The internal structure of premixed turbulent flames (DNS)

A database of turbulent premixed flames has been generated by using a fully compressible direct numerical simulation code (Guichard, Vervisch and Domingo 1994). These simulations are three dimensional, and fields are computed by using a 129x129x129 grid. The numerical approach chosen has been proposed by Lele (1990), Poinsot and Lele (1992).

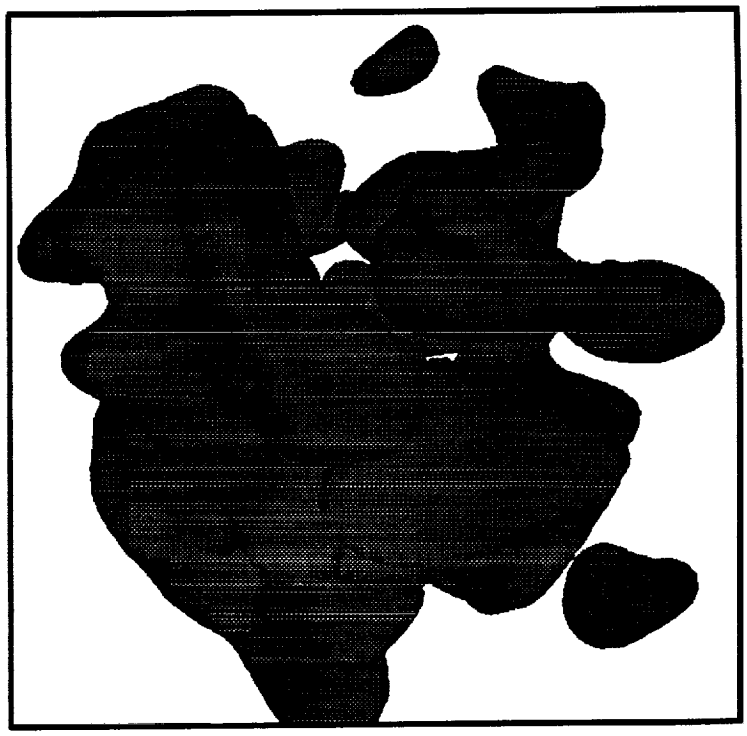

FIGURE 4. Snapshots of the flame surface contour ($\varphi = 0.8$).

In previous studies of premixed and non-premixed turbulent flames at CTR (Trouvé and Poinsot 1994, Vervisch 1992), initial conditions were generated by using a laminar and planar flame on which a homogeneous turbulent field was superimposed. As a consequence, prior to being distorted by the turbulence, the structure of the reactive zone corresponded to the one of a laminar flame. Globally, the computational domain was divided into fresh and burnt gases separated by a propagating turbulent flame. These simulations have been proven to be an efficient tool for studying, through the flame brush, the topology of one iso-surface identified as the flame-surface and corresponding to the location of intense reactive activity.

In order to increase the number of possibilities of sampling for all the values of the progress variable field, in the present simulations the initial scalar field is prescribed according to a pdf and to a turbulent spectrum. It is then possible to generate as initial condition a homogeneous progress variable field with pockets of burnt gases and fresh gases. A turbulence velocity field is added to this scalar field, and turbulence is allowed to decay. These pockets are convected by the turbulence, and reactive layers are created. To avoid spurious effects that can emerge from this initial condition, the procedure used to initialize the scalar field insures that the transition between fresh and burnt gases is achieved according to a smooth distribution. Non-reflecting boundary conditions are used on each side of the computational domain, and pressure waves can leave this domain.

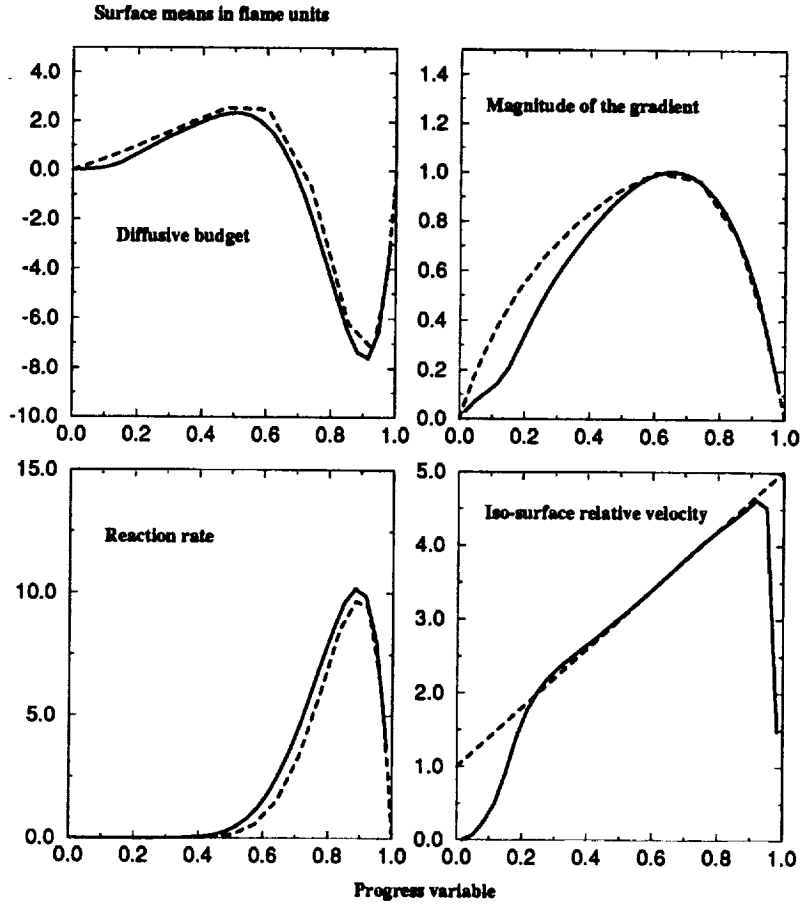

FIGURE 5. Distribution in progress variable space of surface means. ——— : turbulent flame; ---- ; laminar flame.

From the initial condition, the progress variable field is convected by the turbulence, and propagation of premixed flames is observed. A single-step chemistry with a reaction rate cast in the form of an Arrhenius law represents the chemical activity. The ratio of temperature between burnt and fresh gases is five, the Zeldovich number has a value of eight. The initial ratio between the rms turbulent velocity and laminar flame speed is the order of three, and the value of the Damköhler number based on the Kolmogorov time scale and the laminar flame time is about unity. The initial turbulent Reynolds number based on the integral length scale is about seventeen, while the Reynolds number based on the initial Taylor microscale is about fifteen. The formalism which has been developed above is used to analyze data from this calculation.

After one flame time, the flame surface exhibits a very complex and convoluted shape that can be observed in Fig. 4.

Fig. 5 presents the distribution in progress variable space of surface means as

defined in Eq. 40 for various quantities; their corresponding distribution across a one-dimensional steady unstrained laminar flame is also plotted. The distribution of surface means for the diffusive budget of the progress variable $\frac{1}{\rho}(\nabla.(\rho\Gamma\nabla\Phi(\underline{x},t)))$, of the chemical source $\dot{W}_\Phi$, and of the magnitude of the gradient $\mid \nabla\Phi(\underline{x},t) \mid$ follow the laminar response except in the preheat zone ($\Phi < 0.5$), where, because of the turbulence activity, the flame is not able to sustain the flamelet structure. The turbulence clearly affects the progress variable gradient in the preheating region. As a consequence, the surface mean of the iso-surface relative progression velocity

$$V = \frac{1}{\rho|\nabla\Phi|}\frac{\partial}{\partial x_\alpha}(\rho\Gamma\frac{\partial\Phi}{\partial x_\alpha}) + \frac{1}{|\nabla\Phi|}\dot{W}_\Phi = \frac{1}{\mid\nabla\Phi\mid}\Omega_\Phi \quad ,$$

drops in the preheat zone and in the burnt gases. One may observe with the help of these plots how the imbalance between chemical source and diffusion leads to the propagation of the various iso-surfaces. However, even though the surface mean value of this velocity is close to the laminar flamelet value, the scatter plot (Fig. 6) of this quantity shows that locally the effect of the turbulence can be very large in this DNS. This result suggests that there is not a unique deterministic relationship between progress variable and propagation speed. The same observation has been made in connection with the imbalance between reaction and diffusion as well as for the magnitude of the gradient.

Fig. 6 also displays the pdf of the progress variable at time $t = 0$ and the pdf after one flame time; a bimodal shape is observed in accordance with the existence of the flamelets seen in Fig. 5. The effects of the turbulence on the preheating zone is emphasized in Fig. 6 where the area of the iso-surface is increased for small value of the progress variable.

All of these observations suggest the existence of a flamelet zone within the turbulent flame brush, where mean conditional surface values follow the laminar flame structure. However, the existence of a preheating region is also observed, and the properties of the mixing in this zone may control the behavior of the entire flame structure.

The total flame stretch, defined for the iso-surface corresponding to the progress variable that gives the peak value of the reactive activity, is at a time in the simulation corresponding to Fig. 5 and Fig. 6 positive when the mean value for the progress variable evaluated over all the computational domain is $\overline{\Phi} = 0.55$. Flame stretch is known from DNS or experimental observation (Trouvé and Poinsot (1994) Veynante *et al.* 1994) to evolve from positive to negative values as a function of the mean progress variable. In accordance with these observations, later in time, flame stretch becomes negative when the mean value of the progress variable within the domain becomes larger.

4. PDF-SDF modeling

DNS observation suggests that the premixed turbulent flame may be organized in progress variable space in three zones: a preheat zone and a burnt gas zone where mixing needs to be treated separately from the slow chemical reaction, and

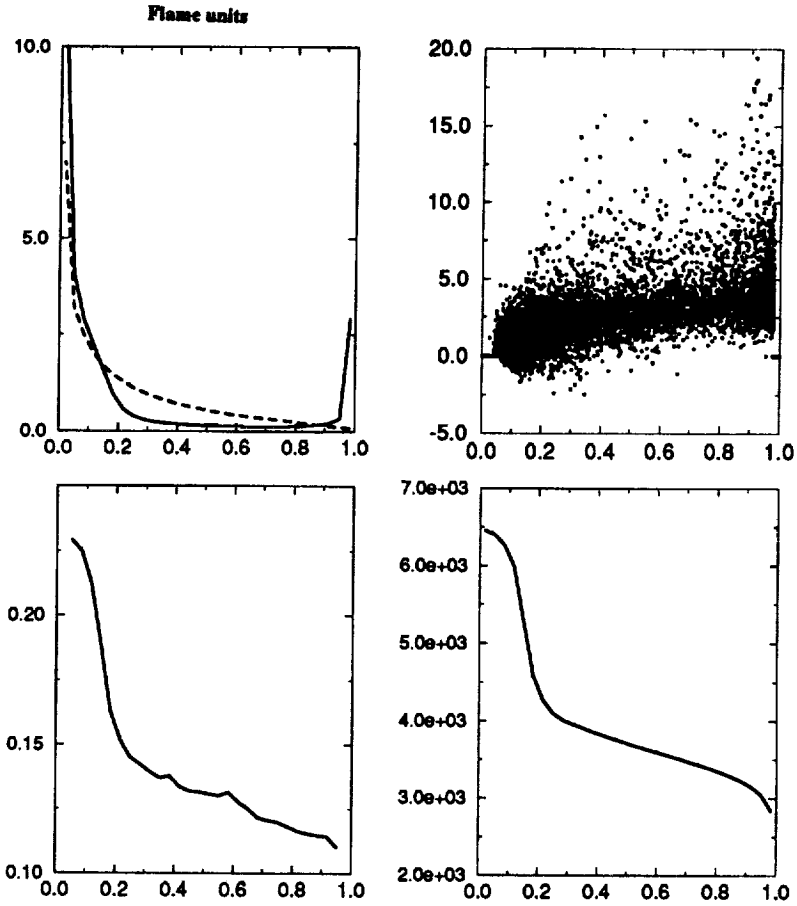

FIGURE 6. Clockwise from upper left: Pdf of the progress variable (——— , pdf; ---- , initial pdf), scatter plot of iso-surface relative progression velocity, area of iso-surfaces, and iso-surface density function.

a flamelet zone where the mean conditional surface value of the velocity of the iso-surface meets the one of a laminar flame and where laminar flamelet behavior may be invoked. Because of the necessity of introducing the chemical rate within both the preheat and burnt gases zones, Eq. 39 is appropriated for the pdf, while Eq. 38 is well suited for the flamelet zone where the convection in composition space will be deduced from flamelet behavior and $\overline{\Sigma}(\varphi; \underline{x}, t)$ represents the laminar flamelet isosurface density. It is zero when no laminar flamelet burning zone exists.

A direct approach to close the pdf equation can be developed by prescribing for the imbalance Ω_Φ the value corresponding to the planar unstrained laminar flame $\Omega_{\Phi_{fl}}$. When combining $\Omega_{\Phi_{fl}}$ with a classical mixing model, a closed pdf mixing term emerges (Anand and Pope 1987). Here, our objective is to take advantage of both pdf and sdf transport equations at the same time. The value of Ω_Φ corresponding to the laminar flamelet structure will be used, but in conjunction with strain-rate curvature and related mixing effects in both pdf and sdf equations.

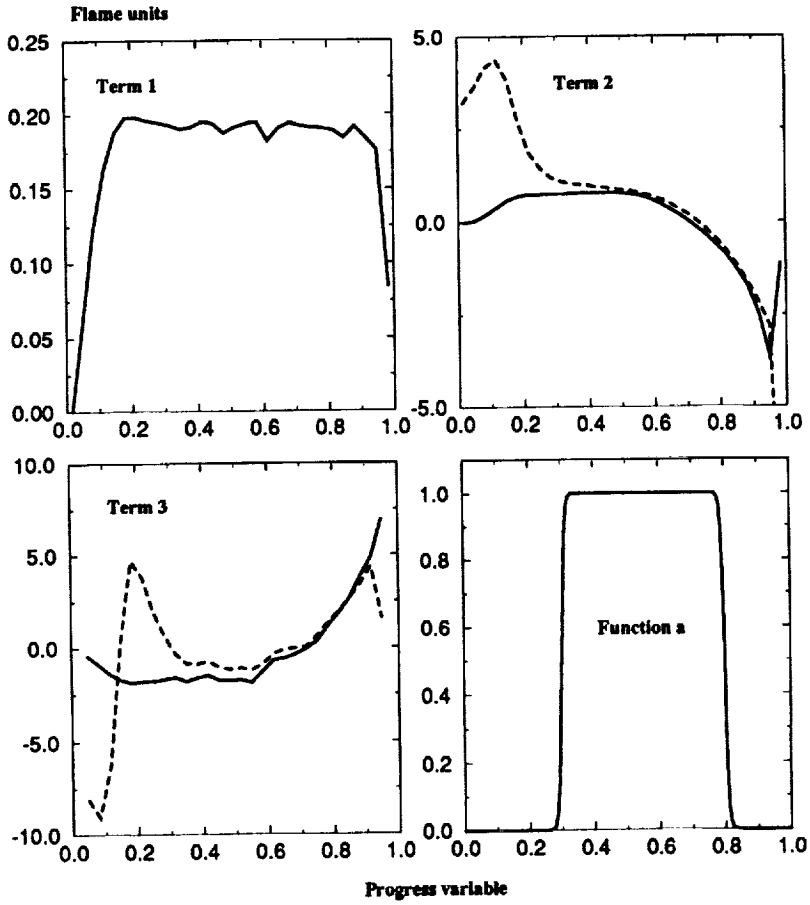

FIGURE 7. Comparison between modeled sdf terms (valid within the flamelet range) and DNS. ——— : DNS; ---- : proposed model.

4.1 Modeling for the sdf equation

In this work, the turbulent convection will not be considered and its investigation may be found in this book elsewhere (Trouvé *et al.* 1994).

From the above analysis, the equation for the flamelet sdf

$$\overline{\Sigma}(\varphi;\underline{x},t) = \left(\overline{|\nabla\Phi| \,\middle|\, \Phi(\underline{x},t)=\varphi}\right)\overline{P}(\varphi;\underline{x},t) \quad , \tag{44}$$

may be written:

$$\frac{\partial\overline{\Sigma}(\varphi;\underline{x},t)}{\partial t} + \overline{\nabla.(\Sigma(\varphi;\underline{x},t)\mathbf{v})} = \underbrace{\left(\overline{\phi_s \,\middle|\, \mathcal{A}_{\Phi=\varphi}}\right)}_{\text{Term 1}}\overline{\Sigma}(\varphi;\underline{x},t)$$

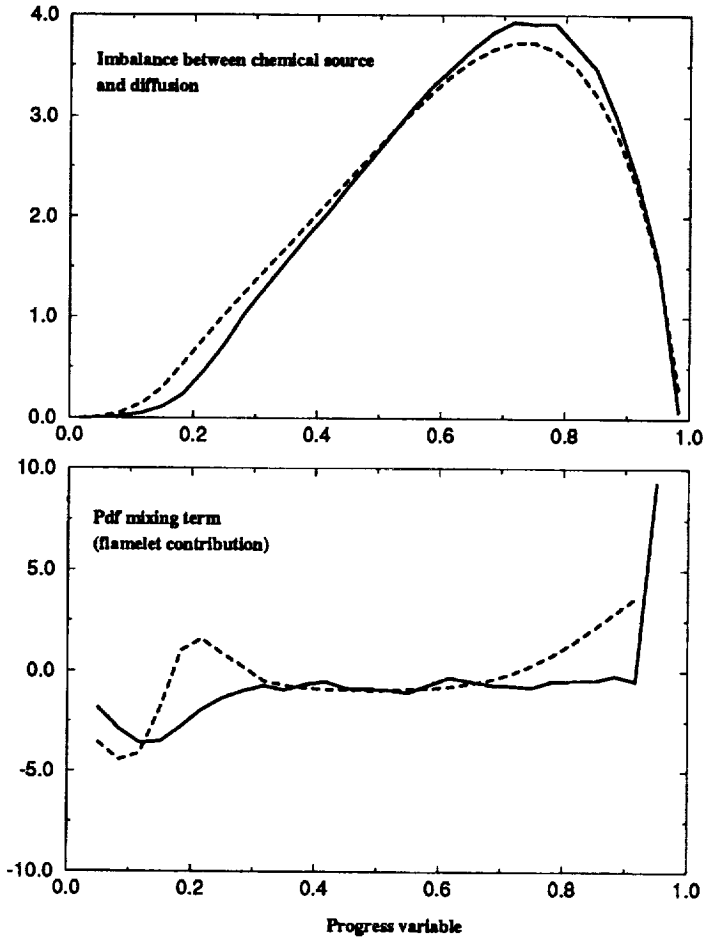

FIGURE 8. Comparison between modeled pdf terms (valid within the flamelet range), top, and DNS (flame units), bottom. Top: ——— , conditional mean value; ---- , conditional surface mean value. Bottom: ——— , DNS; ---- , proposed model.

$$\underbrace{-\left(\overline{\underline{n}.\nabla\Omega_\Phi(\underline{x},t)\Big|\Phi(\underline{x},t)=\varphi}\right)\overline{P}(\varphi;\underline{x},t)}_{\text{Term 2}} \qquad (45)$$

$$\underbrace{-\frac{\partial}{\partial\varphi}\left[\left(\overline{\Omega_\Phi(\underline{x},t)\mid\nabla\Phi(\underline{x},t)\mid\Big|\Phi(\underline{x},t)=\varphi}\right)\overline{P}(\varphi;\underline{x},t)\right]}_{\text{Term 3}} \quad .$$

The strain rate term $\left(\overline{\phi_s\Big|\mathcal{A}_{\Phi=\varphi}}\right)$ is representative of a physical process that affects in a similar way all the iso-surfaces of the scalar field. As presented in Fig. 7 (Term 1) this contribution does not strongly depend on the progress variable. Therefore, it is possible to speculate that model closures developed for the in-plane

strain rate in the framework of the flame-surface density approach can be extended to the sdf equation (Meneveau and Poinsot 1991). Attention will be especially focused on Term 2 and Term 3.

For Term 2 one may prove that the expression

$$-\left(\overline{\underline{n}.\nabla\Omega_\Phi(\underline{x},t)\Big|\Phi(\underline{x},t)=\varphi}\right) \quad ,$$

does not explicitly contain curvature effects (Vervisch *et al.* 1994). The contribution of curvature of the field is actually present through the pdf $\overline{P}(\varphi;\underline{x},t)$ that multiplies this term in the sdf budget. Hence it is possible to build a closure by using the flamelet structure. If $S_{fl}(\varphi)$ denotes the known laminar flame speed, evaluated in the premixed laminar unstrained flame as

$$S_{fl}(\varphi)=\frac{\Omega_\varphi}{\mid\nabla\varphi\mid}=\frac{\Omega_\varphi}{G(\varphi)} \quad ,$$

where $G(\varphi)$ is the known magnitude of the gradient of the progress variable within the laminar flame, then one may write:

$$-\left(\overline{\underline{n}.\nabla\Omega_\Phi(\underline{x},t)\Big|\Phi(\underline{x},t)=\varphi}\right)\overline{P}(\varphi;\underline{x},t)\simeq\overline{P}(\varphi;\underline{x},t)G(\varphi)\frac{\partial}{\partial\varphi}\Big(S_{fl}(\varphi)G(\varphi)\Big) \quad .$$

Evaluated from DNS the exact expression (left side) and the proposed model (right side) are displayed in Fig. 7 (Term 2). Good agreement is found according to a possible definition of the flamelet range $[\varphi_0,\varphi_1]=[0.4,0.8]$.

The same approach is followed for Term 3, and this leads to

$$-\frac{\partial}{\partial\varphi}\left[\left(\overline{\Omega_\Phi\mid\nabla\Phi\mid\Big|\Phi)=\varphi}\right)\overline{P}(\varphi;\underline{x},t)\right]\simeq-\frac{\partial}{\partial\varphi}\left[S_{fl}(\varphi)G^2(\varphi)\overline{P}(\varphi;\underline{x},t)\right] \quad .$$

The validity of this modeled expression within the flamelet range is evaluated in Fig. 7 (Term 3). One may note from Fig. 5 that according to the distribution of the progress variable gradient, flamelet range could be $[\varphi_0,\varphi_1]=[0.6,1]$ while the iso-surface relative progression velocity follows flamelet behavior for the range $[0.4,0.8]$. The same trend is observed in Fig. 7 where the modeled term related to the propagation (Term 2) follows its exact DNS expression in the range $[0.4,0.8]$, while good agreement is obtained for the closure related to mixing in the range $[0.6,0.8]$.

The closed transport equation for the sdf is only valid within the flamelet zone; however, information coming from the preheat and burnt gases zones is present through the pdf $\overline{P}(\varphi;\underline{x},t)$. The partially closed equation contains one source term and one term representing transport in composition space and reads:

$$\frac{\partial\overline{\Sigma}(\varphi;\underline{x},t)}{\partial t}+\overline{\nabla.(\Sigma(\varphi;\underline{x},t)\mathbf{v})}=\left(\overline{\phi_s\Big|\mathcal{A}_{\Phi=\varphi}}\right)\overline{\Sigma}(\varphi;\underline{x},t)$$
$$-\mathcal{W}(\varphi_0,\varphi_1)\left(\frac{1}{2}\overline{P}(\varphi;\underline{x},t)S_{fl}(\varphi)\frac{\partial}{\partial\varphi}G^2(\varphi)+S_{fl}(\varphi)G^2(\varphi)\frac{\partial}{\partial\varphi}\overline{P}(\varphi;\underline{x},t)\right), \tag{46}$$

where the turbulent transport effects are included in the second term on the left hand-side. The function $\mathcal{W}(\varphi_0,\varphi_1)$ insures that when flamelets are not present the RHS of Eq. 46 goes to zero ($\mathcal{W}(\varphi_0,\varphi_1)$ is equal to zero when the flamelet range $[\varphi_0,\varphi_1]$ is not defined and unity when flamelets are present).

4.2 Modeling for the pdf equation

To treat both flamelet part and mixing zones, from Eq. 38 and Eq. 39 the exact transport equation for the pdf may be cast in the form

$$\overline{\frac{DP(\varphi;\underline{x},t)}{Dt}}=-a(\varphi;\underline{x},t)\frac{\partial}{\partial\varphi}\left[\left(\overline{\Omega_\Phi(\underline{x},t)\Big|\Phi(\underline{x},t)=\varphi}\right)\overline{P}(\varphi;\underline{x},t)\right]$$
$$-(1.-a(\varphi;\underline{x},t))\frac{\partial}{\partial\varphi}\left[\left(\overline{\dot{W}_\Phi\Big|\Phi(\underline{x},t)=\varphi}\right)\overline{P}(\varphi;\underline{x},t)\right] \tag{47}$$
$$-(1.-a(\varphi;\underline{x},t))\frac{\partial^2}{\partial\varphi^2}\left[\left(\overline{\epsilon_\Phi\Big|\Phi(\underline{x},t)=\varphi}\right)\overline{P}(\varphi;\underline{x},t)\right],$$

where $a(\varphi;\underline{x},t)$ is a smooth function equal to unity in the flamelet zone of φ space and to zero in the outer flamelet regions. A possible shape for the function a is proposed in Fig. 7. The way in which the flamelet range $[\varphi_0(\underline{x},t),\varphi_1(\underline{x},t)]$ is to be determined will be considered later.

Within the out-of-flamelet zone, a classical mixing modeling (Kollmann 1990) can be used with complex chemistry to evaluate the contribution of the reactive activity.

In the flamelet zone, from Fig. 8 it is observed that the surface mean of the imbalance Ω_Φ is almost equal to its conditional mean; from this we deduce the following modeled expression for the flamelet part of the pdf equation

$$\left(\overline{\Omega_\Phi\Big|\Phi(\underline{x},t)=\varphi}\right)\simeq\left(\overline{\Omega_\Phi\Big|\mathcal{A}_{\Phi=\varphi}}\right)=\frac{\overline{\Omega_\Phi\Sigma(\varphi;\underline{x},t)}}{\overline{\Sigma}(\varphi;\underline{x},t)}\simeq S_{fl}(\varphi)G^2(\varphi)\frac{\overline{P}(\varphi;\underline{x},t)}{\overline{\Sigma}(\varphi;\underline{x},t)},$$

and hence

$$-\frac{\partial}{\partial\varphi}\left[\left(\overline{\Omega_\Phi\Big|\Phi=\varphi}\right)\overline{P}(\varphi;\underline{x},t)\right]\simeq-\left(\frac{1}{\overline{\Phi}\,(1-\overline{\Phi})}\right)\frac{\partial}{\partial\varphi}\left[S_{fl}(\varphi)G^2(\varphi)\frac{\overline{P}^2(\varphi;\underline{x},t)}{\overline{\Sigma}(\varphi;\underline{x},t)}\right], \tag{48}$$

is introduced as a closure in Eq. 47. The validity of this expression is evaluated against the DNS results in Fig. 8.

The determination of this flamelet range is still unproven at this stage. However, we speculate that a criterion based on the imbalance between the reactive-mixing terms and the flamelet term (Eq. 48), both present in the pdf equation, may emerge to determine dynamically the values $\varphi_0(\underline{x},t)$ and $\varphi_1(\underline{x},t)$.

The partially closed system may be written:

$$\left\{\begin{array}{l} \dfrac{\partial\overline{\Sigma}(\varphi;\underline{x},t)}{\partial t}+\overline{\nabla.(\Sigma(\varphi;\underline{x},t)\mathbf{v})}=\left(\overline{\phi_s\left|\mathcal{A}_{\Phi=\varphi}\right.}\right)\overline{\Sigma}(\varphi;\underline{x},t) \\ \qquad -\mathcal{W}(\varphi_0,\varphi_1)\left(\dfrac{1}{2}\overline{P}(\varphi;\underline{x},t)S_{fl}(\varphi)\dfrac{\partial}{\partial\varphi}G^2(\varphi)+S_{fl}(\varphi)G^2(\varphi)\dfrac{\partial}{\partial\varphi}\overline{P}(\varphi;\underline{x},t)\right) \\ \dfrac{\overline{DP(\varphi;\underline{x},t)}}{Dt}=-a(\varphi;\underline{x},t)\left(\dfrac{1}{\overline{\Phi}\,(1-\overline{\Phi})}\right)\dfrac{\partial}{\partial\varphi}\left[S_{fl}(\varphi)G^2(\varphi)\dfrac{\overline{P}^2(\varphi;\underline{x},t)}{\overline{\Sigma}(\varphi;\underline{x},t)}\right] \\ \qquad -(1.-a(\varphi;\underline{x},t))\dfrac{\partial}{\partial\varphi}\left[\left(\overline{\dot{W}_\Phi\left|\Phi(\underline{x},t)=\varphi\right.}\right)\overline{P}(\varphi;\underline{x},t)\right] \\ \qquad -(1.-a(\varphi;\underline{x},t))\dfrac{\partial}{\partial\varphi}\left[\left(\dfrac{\overline{\Phi}-\varphi}{\tau_t}\right)\overline{P}(\varphi;\underline{x},t)\right] \quad , \end{array}\right.$$

in which closed expressions for the strain rate and for turbulent transport remain to be included. The LMSE (or IEM) mixing model (Dopazo 1994) has been chosen for the outer flamelet zone and τ_t is a characteristic mixing time scale. Monte, Carlo simulation is appropriated for the pdf equation (Pope 1985), while a continuous solution can be considered for a determinate numbers of bins for which the sdf equation is solved.

5. Conclusion

Because the motion of iso-surfaces is strongly connected with the transport phenomena at all scales of the turbulent flow, the behavior of scalar iso-surfaces in multi-component reacting mixture is a topic of fundamental interest. It is possible to develop some mathematical tools that describe the properties of these surfaces. In particular, a transport equation for global variable has been established and a solution for material surfaces evolution has been proposed. When introducing a surface density function, a possible link between the well-known pdf approach for turbulent combustion modeling and surface modeling emerges. From this point an attempt is made to develop a unified treatment of pdf and sdf for premixed turbulent flames. Direct numerical simulations results are used to analyze the internal structure of turbulent premixed flames and to estimate the validity of the proposed modeling.

Acknowledgements

The authors would like to thank their CTR hosts G. Ruetsch and J.-M. Samaniego for helpful assistance. J. Réveillon and L. Guichard are thanked for their help in the

development of the DNS database. Authors have benefited from many discussions with the participants of the "combustion group" during the CTR summer program.

REFERENCES

ANAND, M. S., POPE, S. B. 1987 Calculations of premixed turbulent flames by pdf methods. *Comb. and Flame.* **67,** 127-142.

BORGHI, R. 1988 Turbulent combustion modeling. *Progr. Energy Comb. Sci..* **14.**

BORGHI, R., VERVISCH, L., GARRÉTON D. 1991 The calculation of local fluctuations in non-premixed turbulent flames. *(Eds. Carvalho M. G., Lockwood, F., Taine, J.), Springer Verlag, 83-113.*

BRAY, K. N. C. 1990 Studies of the turbulent burning velocity. *Proc. R. Soc, Lond.* A, 431, 315-335.

CANDEL, S. M., POINSOT, T. J., 1990 Flame stretch and the balance equation for the flame area. *Combust. Sci. and Tech.* **70,** 1-15.

CONSTANTIN, P. 1992 Remarks on the Navier-Stokes equations. To appear.

DOPAZO, C. 1994 Recent developments in pdf methods. In *Turbulent Reacting Flows* (Eds P. A. Libby and F. A. Williams), Academic Press London, 375-474.

FOX, R. O. 1994 Improved Fokker-Planck model for the joint scalar, scalar gradient pdf. *Phys. of Fluid.* **6** (1), 334-348.

GUICHARD, L., VERVISCH, L., DOMINGO, P. 1994 Numerical study of the interaction between a mixing zone and a pressure discontinuity. *AIAA 95-0877,* to be published.

KOLLMANN, W. 1990 The pdf approach to turbulent flow. *Theoret. Comput. Fluid Dynamics.* **1,** 249-285.

KOLLMANN, W., CHEN, J. H. 1994 Dynamics of the flame surface area in turbulent non-premixed combustion. *Twenty-Fifth International Symp. on Comb.*

LELE, S. K. 1990 Compact finite difference schemes with spectral like resolution. Center for Turbulence Research, Stanford Univ./NASA Ames, Manuscript 107.

MENEVEAU, C., POINSOT, T. 1991 Stretching and quenching of flamelets in premixed turbulent combustion. *Comb. and Flame.* **86,** 3311-332.

MEYERS R. E., O'BRIEN, E. E. 1981 The joint Pdf of scalar and its gradient at a point in a turbulent fluid. *Comb. Sci and Tech.* **26,** 123-134.

MARBLE, F. E., BROADWELL, J. E. 1977 The coherent flame model for turbulent chemical reactions. *Project Squid Report,* TRW-9-PU, TRW, EI Secundo.

MAZ'JA, V. G. 1985 Sobolev spaces. *Springer V. Berlin.*

OTTINO, J. M. 1989 The kinematics of mixing: Stretching, chaos and transport. *Cambridge Texts in Applied Mathematics,* Cambridge University Press 1989.

POCHEAU, A. 1992 Front propagation in a turbulent medium. *Europhys. Lett.* **20** (5),, 401-406.

POINSOT, T., LELE, S. K. 1992 Boundary conditions for direct simulations of compressible viscous flows. *J. Comput. Phys.* **101**(1), July 92.

POPE, S. B. 1985 Pdf method for turbulent reacting flows. *Comb. Sci. and Tech.* **11**, 119-195.

TROUVÉ, A., POINSOT, T. 1994 The evolution for the flame surface density in turbulent premixed combustion. *J. Fluid Mech.* To be published.

TROUVÉ, A., VEYNANTE, D., BRAY, K. N. C., MANTEL, T. 1994 The coupling between flame surface dynamics and species mass conservation in premixed turbulent combustion. In *Proceedings of the 1994 CTR Summer Program,* Center for Turbulence Research, NASA Ames/Stanford Univ.

VEYNANTE, D., DUCLOS, J. M., PIANA, J. 1994 Experimental analysis of flamelet models for premixed combustion. *Twenty-Fifth International Symp. on Comb.*

VERVISCH, L, BIDAUX, E., BRAY, K. N. C., &, KOLLMANN, W. 1994 The transport equation for an iso-surface density function. Submitted to *Phys. of Fluids.*

VERVISCH, L. 1993 Study and modeling of finite-rate chemistry effects in turbulent non-premixed flames. *Annual Research Briefs 1992.* CTR, Stanford U./NASA Ames.

39738

N95-21043

Passive turbulent flamelet propagation

By Wm. T. Ashurst,[1] G. R. Ruetsch[2] AND T. S. Lund[2]

We analyze results of a premixed constant density flame propagating in three-dimensional turbulence, where a flame model developed by Kerstein *et al.* (1988) has been used. Simulations with constant and evolving velocity fields are used, where peculiar results were obtain from the constant velocity field runs. Data from the evolving flow runs with various flame speeds are used to determine two-point correlations of the fluctuating scalar field and implications for flamelet modeling are discussed.

1. Introduction

For some applications, it is useful to consider the premixed flame structure as unchanged by turbulence and to cast the problem as a flamelet moving through the flow with a known density jump (Liñán & Williams, 1993). A further assumption is to ignore the density change and consider passive flamelet propagation. We find that these constant-density flames do reveal possible mechanisms of turbulent flame propagation (Ashurst, 1994). Therefore, the flamelet assumption has been exploited in order to decouple the complexity of chemistry from that of turbulence. To investigate flame stability, Markstein wrote a flame evolution equation in 1964, but lacking a computer, he was restricted to a stability analysis. Markstein's notation was f for a flame with volume expansion; while a passive formulation has acquired the letter G; we distinguish between these flamelet models by using f when volume expansion is considered and G when it is not. The special initial condition formulated by Kerstein *et al.* (1988) is $G = x$ for the evolution equation

$$\frac{\partial G}{\partial t} + \mathbf{u} \cdot \nabla G = S_L |\nabla G| \tag{1}$$

where the right side describes Huygens' propagation with S_L as the burning velocity. This nonlinear term makes the initial condition very special: it provides a connection between flame area and the gradient of G. The scalar gradient corresponds to the flame surface density, that is, flame area per unit volume. In this passive formulation any level surface represents a flame and spatial derivatives of G define the geometry of that particular surface, thus the actual magnitude of G is not important. This formulation allows a numerical simulation which follows Damköhler's idea: creation of flame area by turbulent motion causes an increased consumption rate. Now, with the passage of fifty years, the computer can easily determine passive flame area within a turbulence simulation and, when the motion is forced, a statistically steady propagation is achieved.

1 Combustion Research Facility, Sandia National Laboratories, Livermore, CA
2 Center for Turbulence Research

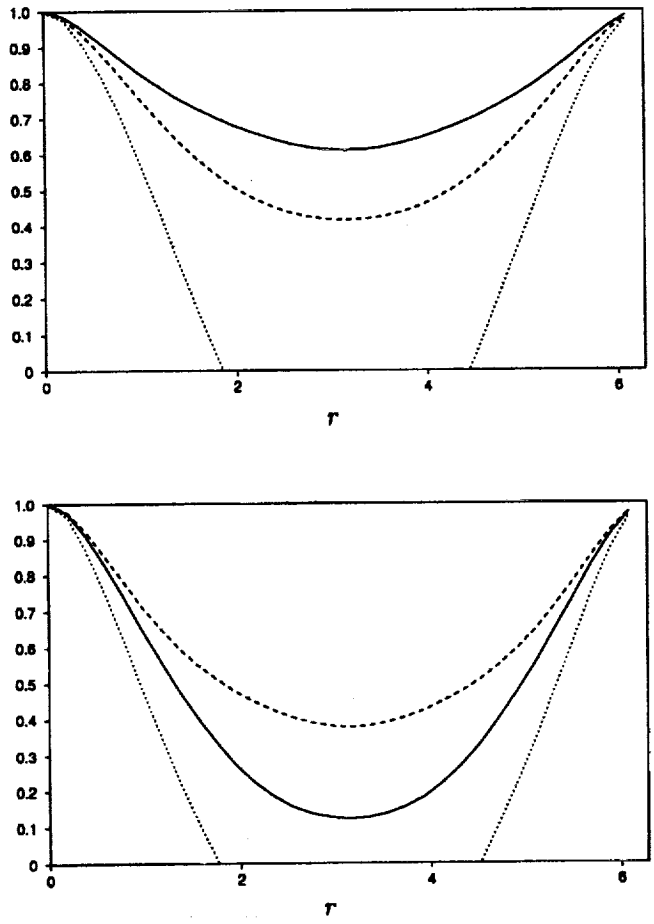

FIGURE 1. Autocorrelations ${}_iR_{11}$ (top) and ${}_iR_{22}$ (bottom) for $u' = S_L/2$. —— $:i = 1$, ---- $:i = 2$, and ····· $:i = 3$.

2. Summer objective

The initial suggestion for the Summer Program was motivated by the previous work of Lund & Rogers (1994) which examined the eigenvalues of the strain-rate tensor in forced, homogeneous, isotropic turbulence. Their velocity fields, on meshes up to 256^3, could be used as a frozen flow in which the propagation of the scalar G would be done, and thereby, obtain the G statistics at a smaller cost. This suggestion did not work. The frozen flow created very large distortions in the G level surfaces, so large that a single surface was connected across the periodic system length. This occurred because the amplitude of flame distortion in a frozen flow is proportional to the rms velocity of the velocity mode (Ashurst *et al.*, 1988) and the lowest modes have the largest energy content in these forced simulations. Since any level surface represents a flame in this passive model, the large distortions

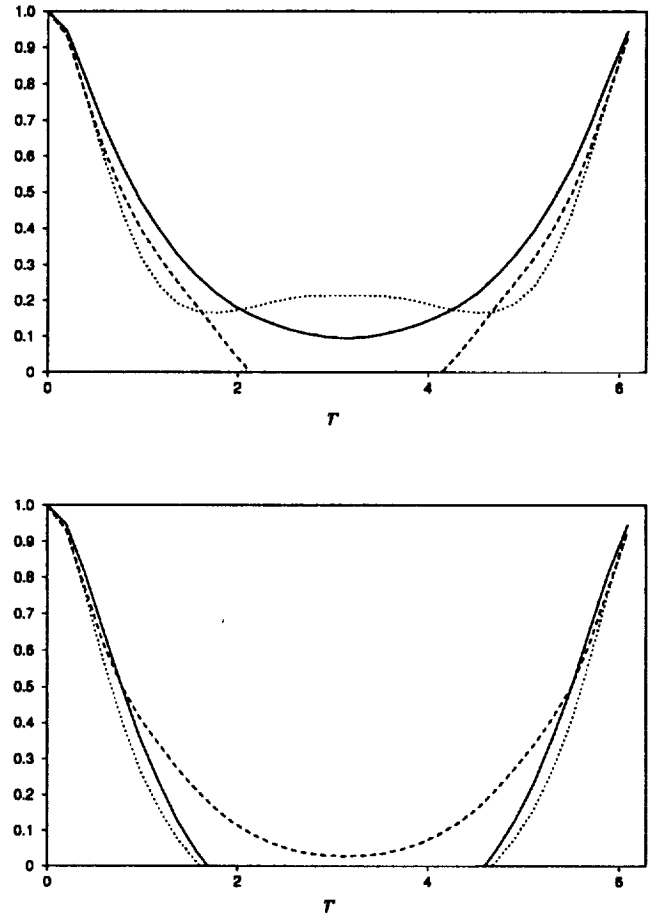

FIGURE 2. Autocorrelations ${}_iR_{11}$ (top) and ${}_iR_{22}$ (bottom) for $u' = 2S_L$. The line types follow the convention in Fig. 1.

correspond to flames interacting with their own periodic image and this is not desirable. The distortion amplitude is reduced when the flow has a time variation, and so evolution of both the velocity field and the scalar G field has been done with 32^3 systems.

Previous G field simulations have been done with finite-difference techniques where the truncation error combined with grid-resolution suppresses large gradients in the G field. These large gradients correspond to a cusp in a G surface, and the cusps are formed by the Huygens' propagation mechanism. Cusp formation and the pseudo-spectral solution technique are not compatible, and so a hyperdiffusivity term was added to the dynamical equation of the form $D\nabla^4 G$ with $D = 4\nu$.

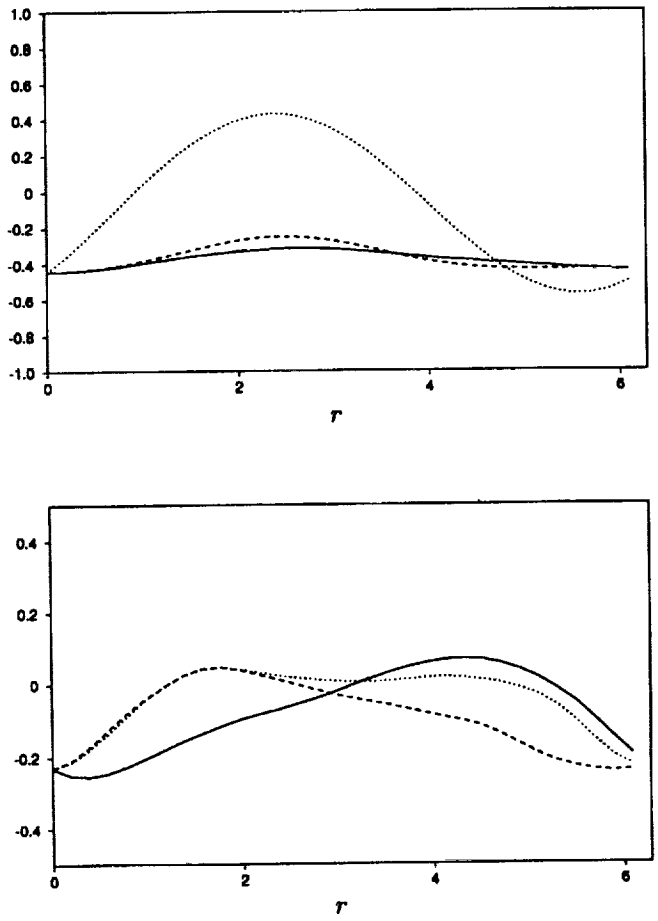

FIGURE 3. Cross-correlations ${}_iR_{12}$ for $u' = S_L/2$ (top) and $u' = 2S_L$ (bottom). The line types follow the convention in Fig. 1.

3. Isotropic propagation

Are the scalar fluctuations of G isotropic? Peters (1992) considers an ensemble of flamelets travelling from all directions into a spatial domain, and so within this domain the fluctuations are assumed to be isotropic. Thus, the well-developed analysis of isotropic, homogeneous turbulence may be applied to the geometry of these flamelets. The geometry is related to the scalar fluctuations as a consequence of the initial condition that $G = x$. The fluctuations correspond to the negative of the flame displacement from the transverse plane associated with that particular flame: use $g' = G - x$, and by adding a constant so that $G = 0$, we obtain g' as the negative displacement from the mean flame location where $G = 0$. The additive constant can be done for any plane normal to the mean propagation direction, and thereby we relate g' values to flame displacement from a transverse plane.

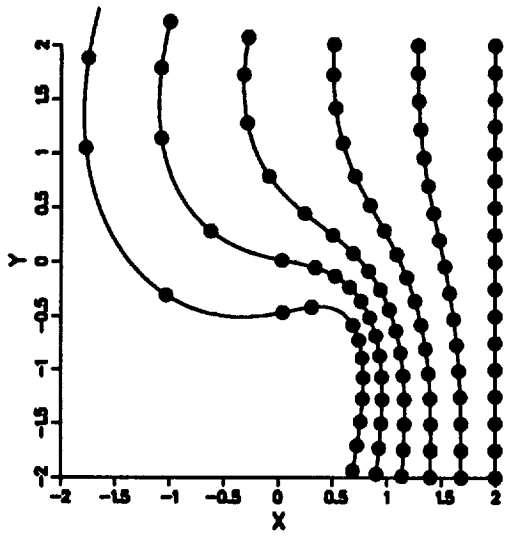

FIGURE 4. Passive front propagation through the swirling flow created by a Gaussian distribution of vorticity, the maximum swirl velocity is $0.8S_L$ and the spatial unit is 4η with a time interval between flame images of $2\eta/S_L$. The filled circles are points which are moved in the local flame normal direction, and the change in their spacing with time indicates the stretching of the flame surface.

To examine this issue with the numerical simulations, two scalar fields were computed within the domain: G_1 with mean gradient in the x direction and G_2 with a gradient in the y direction. For analysis of the scalar fluctuations, the mean gradient is removed ($g_1 = G_1 - x + x_o$ and $g_2 = G_2 - y + y_o$) and the values of x_o and y_o are determined so that g_1 and g_2 have a zero mean volume average. Division by their rms values provides autocorrelations with value of unity for zero separation. We can define a general two-point correlation as:

$$_iR_{jk}(r) = \overline{g_j(\mathbf{x})g_k(\mathbf{x} + r\mathbf{e}_i)}$$

where autocorrelations refer to instances where $j = k$ and cross-correlations otherwise. Autocorrelations for simulations with $u' = S_L/2$ and $u' = 2S_L$ are shown in Figs. 1 and 2. This data in these figures are taken from a single realization of the scalar field. Due to the limited sampling the correlations are not fully converged, but do exhibit dominant trends which we now discuss.

When $u' = S_L/2$, the autocorrelation is larger in the direction of the imposed mean gradient (for either g_1 or g_2). Therefore, the Huygens' propagation dominates over the distortions created by the velocity fluctuations and the passive scalar

fluctuations do have a directional bias. However, when $u' = 2S_L$, then the autocorrelations no longer show as strong a directional dependence.

The cross correlations indicate a negative value for zero separation and an asymmetric nature with respect to direction of the separation, see Fig. 3. We now speculate on why this is so. In Fig. 4, we present flame shapes created by passive propagation through the swirling flow created by a Gaussian distribution of vorticity. The propagation is from right to left, corresponding to a scalar G field with mean gradient increasing towards positive x. To the right, before the flame interacts with the vortex, the straight flame implies that $g' \sim 0$ along that flame surface. On the left side, after the interaction, the flame is distorted so that above the vortex center $g' > 0$ and below the center $g' < 0$. Hence, the swirling flow combined with Huygens' propagation creates asymmetric flame shapes. Taking Fig. 4 and rotating it a quarter of a turn counter-clockwise gives the solution for the scalar field G_2 which has its mean gradient towards $+y$. Now the cross-correlation between G_1 and G_2, using g_1' and g_2', has a significant contribution in only one quadrant, the lower-left quadrant in Fig. 4, where $g_1' < 0$ and $g_2' > 0$ producing a negative cross-correlation for zero separation.

4. Future work

Visualization of the intense vorticity and its relationship to flame area will be one aspect of future work. In previous work, Ruetsch & Maxey (1992) found that intense passive scalar gradients occur between vortical regions; will the same structure occur in a propagating, passive scalar field?

REFERENCES

ASHURST, WM. T., SIVASHINSKY, G. I. & YAKHOT, V. 1988 Flame front propagation in nonsteady hydrodynamic fields. *Combust. Sci. & Tech.* **62,** 273-284.

ASHURST, WM. T. 1994 Modeling turbulent flame propagation. *Twenty-Fifth Symposium (International) on Combustion/The Combustion Institute.* **25,** in press.

KERSTEIN, A. R., ASHURST, WM. T. & WILLIAMS, F. A. 1988 Field equation for interface propagation in an unsteady homogeneous flow field. *Phys. Rev. A.* **37,** 2728.

LIÑÁN, A. & WILLIAMS, F. A. 1993 *Fundamental Aspects of Combustion.* Oxford Univ. Press.

LUND, T. S. & ROGERS, M. M. 1994 An improved measure of strain rate probability in turbulent flows. *Phys. Fluids.* **6,** 1838-1847.

PETERS, N. 1992 A spectral closure for premixed turbulent combustion in the flamelet regime. *J. Fluid Mech.* **242,** 611-629.

RUETSCH, G. R. & MAXEY, M. R. 1992 The evolution of small-scale structures in homogeneous isotropic turbulence. *Phys. Fluids A.* **4,** 2747.

39739
N95-21044

Simulation of a turbulent flame in a channel

By G. Bruneaux[1], K. Akselvoll[2], T. Poinsot[3] AND J. H. Ferziger[2]

The interaction between turbulent premixed flames and channel walls is studied. Combustion is represented by a simple irreversible reaction with a large activation temperature. Feedback to the flowfield is suppressed by invoking a constant density assumption. The effect of wall distance on local and global flame structure is investigated. Quenching distances and maximum wall heat fluxes computed in laminar cases are compared to DNS results. It is found that quenching distances decrease and maximum heat fluxes increase relative to laminar flame values. It is shown that these effects are due to large coherent structures which push flame elements towards the wall. The effect of wall strain is studied in flame-wall interaction in a stagnation line flow; this is used to explain the DNS results. It is also shown that 'remarkable' flame events are produced by interaction with a horseshoe vortex: burnt gases are pushed towards the wall at high speed and induce quenching and high wall heat fluxes while fresh gases are expelled from the wall region and form finger-like structures. Effects of the wall on flame surface density are investigated, and a simple model for flame-wall interaction is proposed; its predictions compare well with the DNS results.

1. Introduction

The interaction of a turbulent premixed flame with a wall is quite complex. First the flame is strongly influenced by the presence of the wall; which limits flame wrinkling and may cause the flame front to quench. Moreover, the flame has a significant effect on the flow in the vicinity of the wall: viscosity is greatly increased in the burnt gases, inhibiting turbulence. At the same time, flame elements approaching the wall increase the heat flux to as much as 1 MW/m^2 in practical situations. For these reasons, modeling flame–wall interactions in turbulent flows is an important issue (Amsden *et al.* 1985, Clendening *et al.* 1981, Lu *et al.* 1990). Models which try to predict these phenomena are available (Jennings 1992, Poinsot *et al.* 1993). However, little fundamental information is available so model building is a difficult exercise. An additional problem is that experiments are difficult to perform because the interesting phenomena occur very close to walls (typically less than 1 mm).

Our objective is to explore the flame-wall interaction mechanisms using three-dimensional direct numerical simulation (DNS). Two-dimensional variable-density simulations were performed in 1992 (Poinsot and Haworth, 1992) and led to a model

1 Institut Francais du Petrole, France and CTR, Stanford University

2 Stanford University

3 Institut de Mecanique des Fluides de Toulouse and CERFACS, France

used in piston engines (Poinsot *et al.* 1993). One of the main difficulties was the lack of a statistically stationary turbulent flow field. In the present study, a constant density turbulent channel flow was used. This has advantages and drawbacks: (1) the turbulence characteristics in the channel flow are well known and stationary which allows easy computation and (2), a constant density approximation has to be used, prohibiting feedback of the flame effects to the flow. However, this is a cost-effective approach.

2. Numerical method and configuration

In this study we extended the three dimensional DNS channel flow code written by Akselvoll & Moin (1993) to take reaction into account. Temperature and fuel mass fraction are treated as passive scalars and do not affect the flow. The flow solver has not been modified and is independent of the solver for the chemical species.

2.1 Basic equations

The flow solver solves the Navier-Stokes equations for an incompressible, constant viscosity flow:

$$\frac{\partial \widetilde{\rho u_i}}{\partial \tilde{t}} = -\frac{\partial \tilde{p}}{\partial \tilde{x}_i} - \frac{\partial \tilde{\rho}\ \widetilde{u_j u_i}}{\partial \tilde{x}_j} + \mu \frac{\partial^2 \tilde{u}_i}{\partial \tilde{x}_j^2} \tag{1}$$

$$\frac{\partial \tilde{u}_i}{\partial \tilde{x}_i} = 0 \tag{2}$$

The reaction solver solves the energy and species conservation equations, which allow convection, diffusion, and reaction effects:

$$\frac{\partial \tilde{\rho} c_p \tilde{T}}{\partial \tilde{t}} + \frac{\partial \tilde{\rho} c_p \widetilde{u_i T}}{\partial \tilde{x}_i} = \frac{\partial}{\partial \tilde{x}_i}\left(\lambda \frac{\partial \tilde{T}}{\partial \tilde{x}_i}\right) + c_p(\tilde{T}_2 - \tilde{T}_1)\widetilde{\dot{w}_R} \tag{3}$$

$$\frac{\partial \tilde{\rho} \tilde{Y}_F}{\partial \tilde{t}} + \frac{\partial \widetilde{\rho u_i Y_F}}{\partial \tilde{x}_i} = \frac{\partial}{\partial \tilde{x}_i}\left(\tilde{\rho} D \frac{\partial \tilde{Y}_F}{\partial \tilde{x}_i}\right) - \widetilde{\dot{w}_R} \tag{4}$$

The superscript ($\tilde{}$) refers to physical variables; absence of a superscript indicates a dimensionless variable.

We assume that $\tilde{\rho} D = \tilde{\rho} D_1 D^*$ where $D^* = (\tilde{T}/\tilde{T}_1)^b$ and $\lambda = \lambda_1 \lambda^*$ where $\lambda^* = D^*$. The subscript 1 refers to the fresh gases, and the subscript 2 refers to the burnt gases.

The reaction is represented by a simple one-step mechanism, corresponding, for example, to lean combustion in which fuel is the limiting factor in determining the reaction rate (Williams, 1985). The reaction rate is expressed as:

$$\widetilde{\dot{w}_R} = \tilde{\rho}\, \tilde{Y}_F B\ exp\left(-\frac{\tilde{T}_a}{\tilde{T}}\right) \tag{5}$$

where B is the pre-exponential factor and $\tilde{T}_a$ is the activation temperature.

The equations are nondimensionalized using the following dimensional quantities: $\widetilde{u}_\tau$, the friction velocity at the wall, $\widetilde{h}$, the channel half width, $\widetilde{T}_1$, the temperature in the fresh gases, $\widetilde{T}_2$, the temperature in the hot gases, $\widetilde{Y}_1$, the fuel mass fraction in the fresh gases.

Physical and dimensionless variables are related in the following way:
$\widetilde{u} = \widetilde{u}_\tau u$, $\widetilde{t} = \widetilde{h}t/\widetilde{u}_\tau$, $\widetilde{p} = \widetilde{\rho}\widetilde{u}_\tau^2 p$, $\widetilde{x} = \widetilde{h}x$, $T = \left(\widetilde{T} - \widetilde{T}_1\right)/\left(\widetilde{T}_2 - \widetilde{T}_1\right)$, $\widetilde{Y}_F = \widetilde{Y}_1 Y_F$ giving the set of dimensionless equations:

$$\frac{\partial u_i}{\partial t} = -\frac{\partial p}{\partial x_i} - \frac{\partial u_j u_i}{\partial x_j} + \frac{1}{Re}\frac{\partial^2 u_i}{\partial x_j^2} \tag{6}$$

$$\frac{\partial u_i}{\partial x_i} = 0 \tag{7}$$

$$\frac{\partial T}{\partial t} + \frac{\partial u_i T}{\partial x_i} = \frac{1}{RePr}\frac{\partial}{\partial x_i}\left(\lambda^* \frac{\partial T}{\partial x_i}\right) + \dot{w}_R \tag{8}$$

$$\frac{\partial Y_F}{\partial t} + \frac{\partial u_i Y_F}{\partial x_i} = \frac{1}{RePrLe}\frac{\partial}{\partial x_i}\left(D^* \frac{\partial Y_F}{\partial x_i}\right) - \dot{w}_R \tag{9}$$

where the Reynolds number is $Re = \frac{\widetilde{\rho}\widetilde{u}_\tau\widetilde{h}}{\mu}$, the Prandtl number is $Pr = \frac{\mu c_p}{\lambda_1}$, and the Lewis number is $Le = \frac{\lambda_1}{\rho c_p D_1}$. The reaction rate expression can be reduced to (Williams, 1985):

$$\dot{w}_R = DaY_F exp\left(-\frac{\beta(1-T)}{1-\alpha(1-T)}\right) \tag{10}$$

where α is the temperature factor $\alpha = (\widetilde{T}_2 - \widetilde{T}_1)/\widetilde{T}_2$, β is the reduced activation energy $\beta = \alpha\widetilde{T}_a/\widetilde{T}_2$, and Da is the reduced pre-exponential factor $Da = \frac{B\widetilde{h}}{\widetilde{u}_\tau} exp\left(-\frac{\beta}{\alpha}\right)$.

2.2 Numerical implementation

These equations are solved in a Cartesian coordinate system using a second-order finite difference scheme. All terms are treated explicitly except the diffusive terms in the wall-normal direction in the momentum equation, which are treated implicitly. The time discretization is second-order Adams-Bashforth for the explicit terms and second order Crank-Nicolson for the implicit terms. The pressure is used to correct the velocity field so that it satisfies the continuity equation; this requires a Poisson solver.

The flow and flame structure are computed on different meshes. The mesh spacing for the flow needs to be small enough near the wall to resolve the viscous sublayer, typically $\Delta y^+ = 0.1$, but in the center of the channel, $\Delta y^+ = 8$ is sufficient (Kim *et al.* 1987); here the superscript $(^+)$ denotes wall units. Because the structure of the turbulence is elongated in the streamwise direction, $\Delta x^+ = 35$ and $\Delta z^+ = 5$. The mesh distribution along the y axis is given by $y_j = \left(1 - \frac{\tanh\left(a\frac{Y_L}{2}(1-(j-1)/(NY-1))\right)}{\tanh\left(a\frac{Y_L}{2}\right)}\right)\frac{Y_L}{2}$ where a is a stretching parameter. Large

values of a distribute more points near the wall. NY is the number of points and Y_L is the size of the box in the y direction.

The flame computation is best done on a uniform mesh in all directions in order to resolve the flame equally well everywhere in the computational domain.

For this reason, different meshes are used in the computation, one for the velocity and pressure, and another for the temperature and fuel mass fraction. The velocities are interpolated from the flow mesh to the reaction mesh. Three-dimensional linear interpolation based on data at the eight corners of the smallest box (of the flow mesh) surrounding the reaction grid point is used. This interpolation procedure was tested by running laminar flame-wall interaction cases in two dimensions and does not introduce additional error because the velocity grid near the wall is much denser than the temperature grid.

2.3 Initial and boundary conditions

The walls are no-slip and isothermal. The flow, temperature and mass fraction fields are periodic in the x and z directions.

The initial conditions for the flow are obtained by running the flow solver until stabilized (in the statistical sense) values of the velocities and pressure are obtained. The temperature and mass fraction are introduced at $t = 0$ as two back-to-back one-dimensional laminar flames propagating towards the walls.

3. Code validation and computation of reference flows

3.1 Computation of non-reacting turbulent channel flow

A first calculation was made without a flame to validate the flow solver. The flow field is initialized from a random field, and is run until the values of velocities and pressure stabilize. Mean quantities are calculated by averaging in the x and z directions and time.

The configuration is the minimal channel flow with $Re = 180$, and uses a stretching factor $a = 2.9$. The dimensions of the domain are $X_L = 3.14159$, $Y_L = 2.$, and $Z_L = 0.908$, with $NX = 18$, $NY = 130$ and $NZ = 34$. The results are consistent with well-known results of channel calculations (Kim *et al.* 1987). Fig. 1 shows the mean velocity profile along with the log law, and Fig. 2 shows the profiles of turbulent velocity components compared to the results of Kim *et al.* 1987. The discrepancies are due to the fact that we have performed a minimal channel simulation while Kim *et al.* did a full channel simulation.

3.2 Quenching of laminar flames on walls in stagnant flow

One-dimensional calculations were performed to validate the reaction solver. The temperature profile of a constant viscosity flame is calculated using an analytical-numerical approach (Rutland 1989). Then this profile is used as an initial condition to compute a flame having variable transport properties with the reaction code, in which the flame is stabilized by prescribing a uniform inlet velocity equal to the flame speed. The temperature profile obtained is then used to initialize the flame-wall interaction calculation (laminar or turbulent).

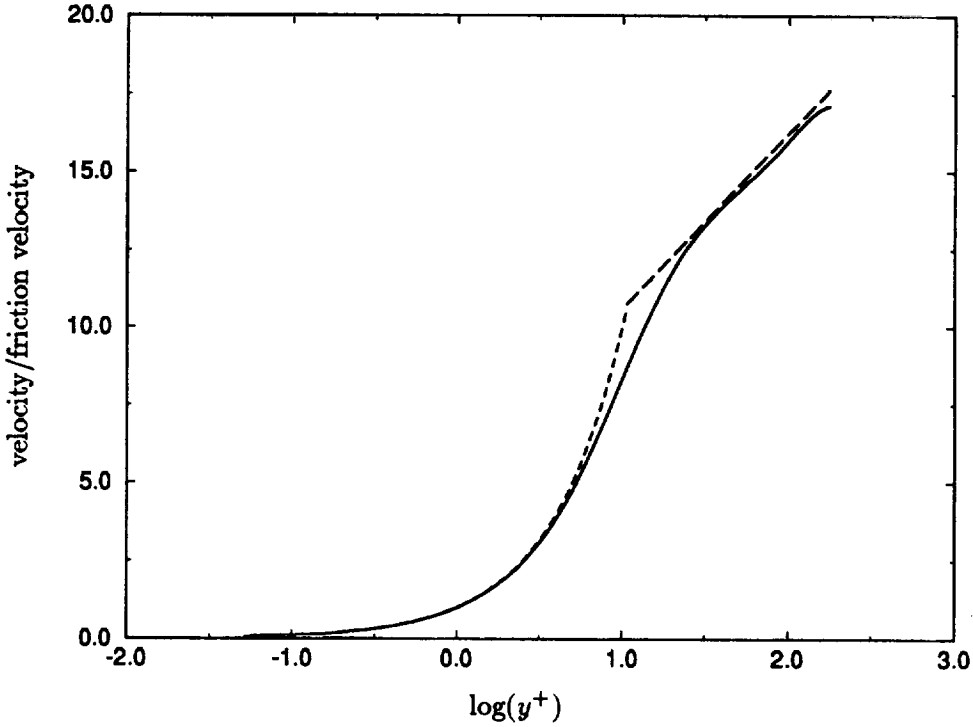

FIGURE 1. Profiles of mean velocity compared to the laminar and log laws. ---- linear law, ——— log law, ——— mean velocity.

We first performed a one-dimensional calculation corresponding to head-on quenching in stagnant fluid. The flame propagates normal to the wall, fresh gases are trapped between the flame and the wall, and the fluid velocity is zero everywhere. The flame consumes reactant as it moves towards the wall. When the flame-wall distance δ reaches its minimum, the wall heat flux Φ is maximum; the consumption rate s_c decreases to zero exponentially thereafter, as shown in Fig. 3. The phenomena occurring in this interaction have been discussed previously (Adamczyk and Lavoie 1978, Carrier *et al.* 1979, Wichman and Bruneaux 1994). The flame-wall distance is non-dimensionalized by a typical flame thickness $d = \lambda/(\widetilde{\rho} c_p s_l^0)$ to form a Peclet number $Pe = \delta/d$ and the wall heat flux is non-dimensionalized by the flame power $P = \widetilde{\rho} c_p s_l^0 (\widetilde{T}_2 - \widetilde{T}_1)$ to produce a reduced heat flux $\phi = \Phi/P$. At quenching the minimum Peclet number is $Pe = 3.68$ and the maximum reduced wall heat flux is $\phi = 0.56$. These values are different from the previous results of Poinsot *et al.* (1993) because the assumptions are different; in particular, they allowed variable density and had a different Prandtl number ($Pr = 0.75$).

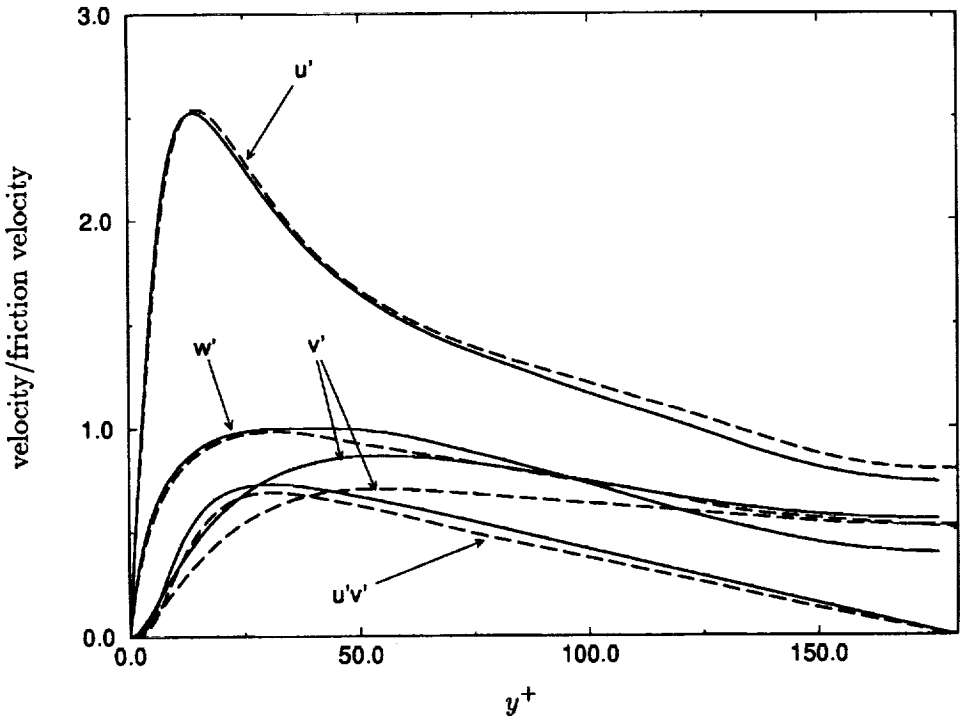

FIGURE 2. Profiles of fluctuating velocities. —— DNS minimum channel, ——— Kim *et al* 1987.

Table I. Fixed parameters for DNS of turbulent channel.

Re	Le	Pr	b	α	β	Da	s_l^0/u_τ	δ_l^0/h	δ_l^0/d
180.	1.	0.5	1.	0.75	6.	80.4	0.36	0.15	5.0

We investigated the influence of grid resolution on the laminar flame speed (mass consumption rate) for a stabilized flame and on the maximum wall heat flux during flame-wall interaction. The results are shown in Fig. 4. For the maximum wall heat flux we also compared first and second order treatment of the wall boundary condition $\left(\frac{\partial Y_F}{\partial y}\right)_{wall} = 0$. The results show that 65 points in the half-channel and a second order scheme at the wall suffice.

3.3 Quenching of laminar flames on walls in stagnation line flow

We also performed one-dimensional calculation of flame interacting with a wall in a stagnation line flow. A flow field corresponding to a stagnation line flow with $\frac{\partial v}{\partial y} = -\Gamma$; Γ, the strain rate is non-dimensionalized by the inverse characteristic

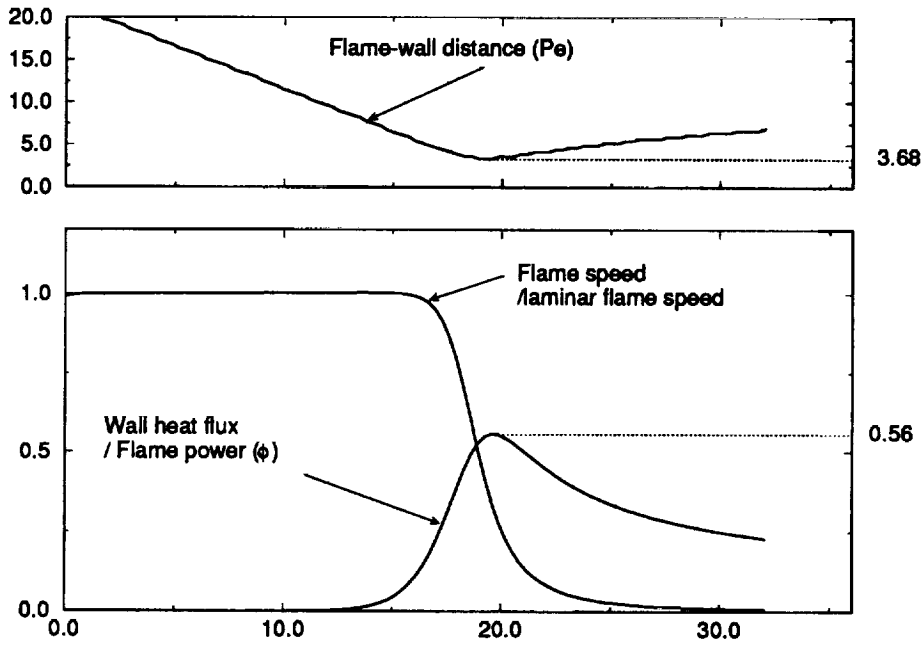

FIGURE 3. Time evolution of wall heat flux, flame speed (consumption rate), and flame-wall distance for a laminar flame-wall interaction in a stagnant flow.

flame time scale s_l^0/δ_l^0 to produce a reduced strain rate $\gamma = \Gamma/(s_l^0/\delta_l^0)$. A typical result for strained flame-wall interaction is presented in Fig. 5, for $\gamma = 5$. At first, the flame adjusts to the flow and the flame speed decreases to a stable value. Then the flame begins to interact with the wall. Because the flame is convected towards the wall, the interaction is faster than in the stagnant flow and produces a higher maximum wall heat flux and a smaller minimum flame wall-distance. In the stagnant case, the interaction lasts about 6 flame times, while for a strained flame with $\gamma = 1$, it lasts 3.5 flame times, and for $\gamma = 5$, 3 flame times. Fig. 6 shows the effect of the strain rate γ on the maximum wall heat flux ϕ and on the minimum flame-wall distance Pe.

4. Results for turbulent flame wall interaction

4.1 Evolution of global quantities during interaction

Fig. 7 presents the evolution of the mean fuel mass fraction, the turbulent flame speed, and the total turbulent flame surface for a typical periodic run together with the laminar values. The parameters are those of the non-reacting flow and the laminar flame.

Early in the simulation, the flames are not yet wrinkled and are located near

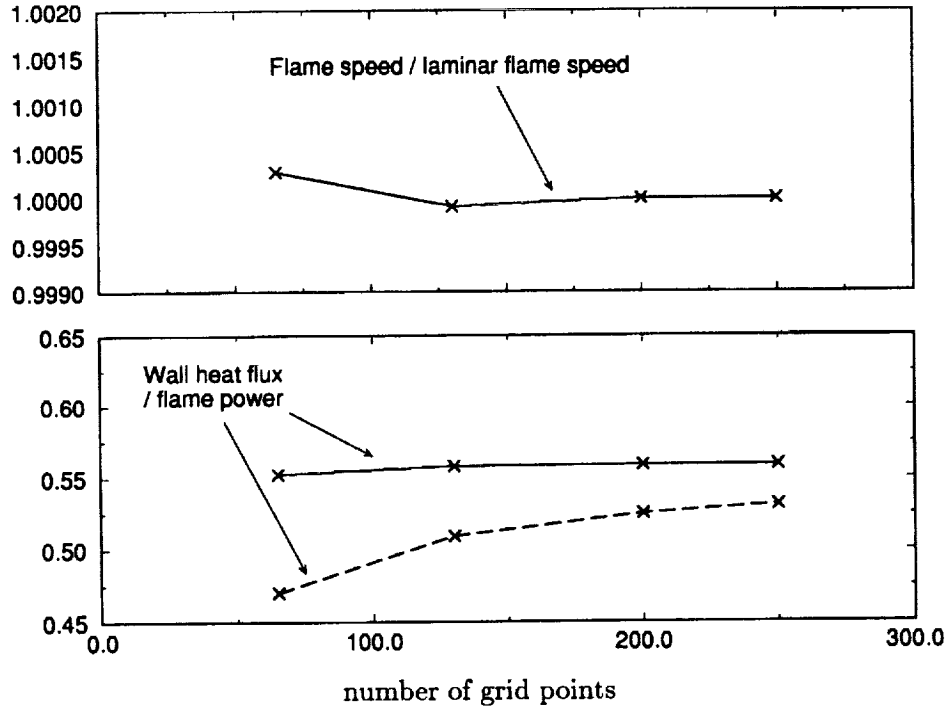

FIGURE 4. Influence of grid resolution and order of accuracy on laminar flame speed and maximum wall heat flux. × ——— × first order, × ——— × second order.

the center of the channel where the turbulence is weak. After $t/t_f > 3$ where $t_f = d/s_l = \lambda_1/\rho c_p (s_l^0)^2$, d is a typical flame thickness and s_l^0, the laminar flame speed, wrinkling increases as does the consumption rate of reactants, producing a maximum turbulent flame speed 1.5 times the laminar flame speed. Then, at $t/t_f = 10$, the flames begin to interact with the walls and the consumption rate is reduced due to lack of reactants. The turbulent flame speed is never constant.

Fig. 8 presents the surface with $T = .85$ and the reaction rate in the turbulent flame at $t/t_f = 9$. Quenching is observed, and a finger-like structure is also present. The mechanism of formation of this structure will be explained below.

4.2 A correlation between local wall strain rate and flame quenching

For practical applications the most important quantity is the maximum wall heat flux. Fig. 9 displays the variations of the minimum flame wall distance and the maximum wall heat flux (normalized by laminar quantities) with time. Fig. 9 also displays the effect of grid resolution on these quantities: a second calculation was performed with twice the number of points in the y direction. No effect of grid resolution is seen. Clearly, the turbulent flame comes closer to the wall and produces higher heat fluxes than the unstrained laminar flame. This differs from results obtained previously and appears to be due to the structure of the turbulence.

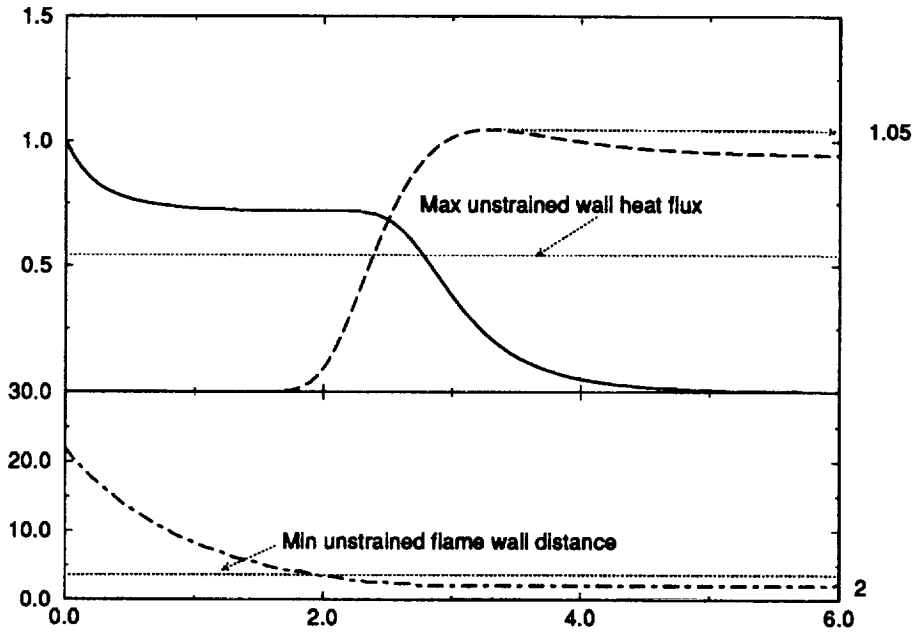

FIGURE 5. Time evolution of wall heat flux, flame speed and flame-wall distance in a laminar flame-wall interaction in a stagnation line flow with $\gamma = 5$. —— flame speed/laminar flame speed, — — — wall heat flux/flame power (ϕ), — · — flame-wall distance (Pe).

In the simulations of Poinsot *et al.* (1993), the turbulence was two-dimensional so there was no small scale structure near the walls. In the present case, the typical quenching distance δ_Q is larger than the viscous sublayer thickness (typically $\delta_Q^+ \simeq 28$) and turbulent structures modify the structure of the flame near the wall.

Another way of presenting this phenomenon is to look at trajectories in a (Peclet number–heat flux) diagram. Fig. 10 presents such trajectories for the laminar flame, for the turbulent flame at $t/t_f = 7.3$, and for two strained laminar flames. The envelop of the turbulent results lie close to the trajectory of the laminar strained flame with $\gamma = 5$, indicating that the effect is primarily due to the strain. This was further checked by computing the strain rate statistics shown in Fig. 11. Because the strain rate is not constant in the turbulent case, we plotted the normal component of the velocity at the flame location divided by the flame-wall distance. We will see in the next section how these large strain rates are created.

4.3 The importance of flow structures

Near-wall coherent structures have a strong effect on the flame. In the case presented here, we find the interaction of a horseshoe vortex with the flame is quite

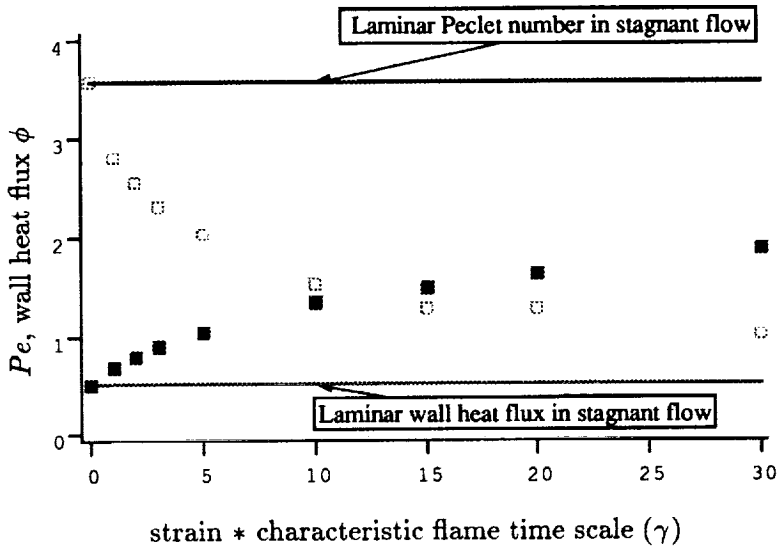

FIGURE 6. Effects of wall normal strain γ on flame-wall quenching of laminar flames. ■ wall heat flux/flame power (ϕ), □ flame wall distance (Pe).

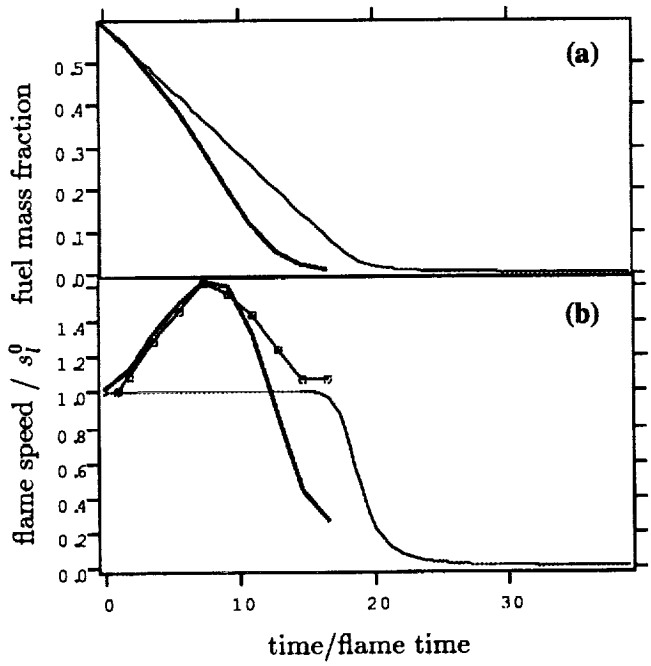

FIGURE 7. Evolution of global quantities during turbulent flame wall interaction. (a) —— laminar, ——— turbulent, (b) —— laminar flame speed, ——— turbulent flame speed, -□- total flame surface/initial flame surface.

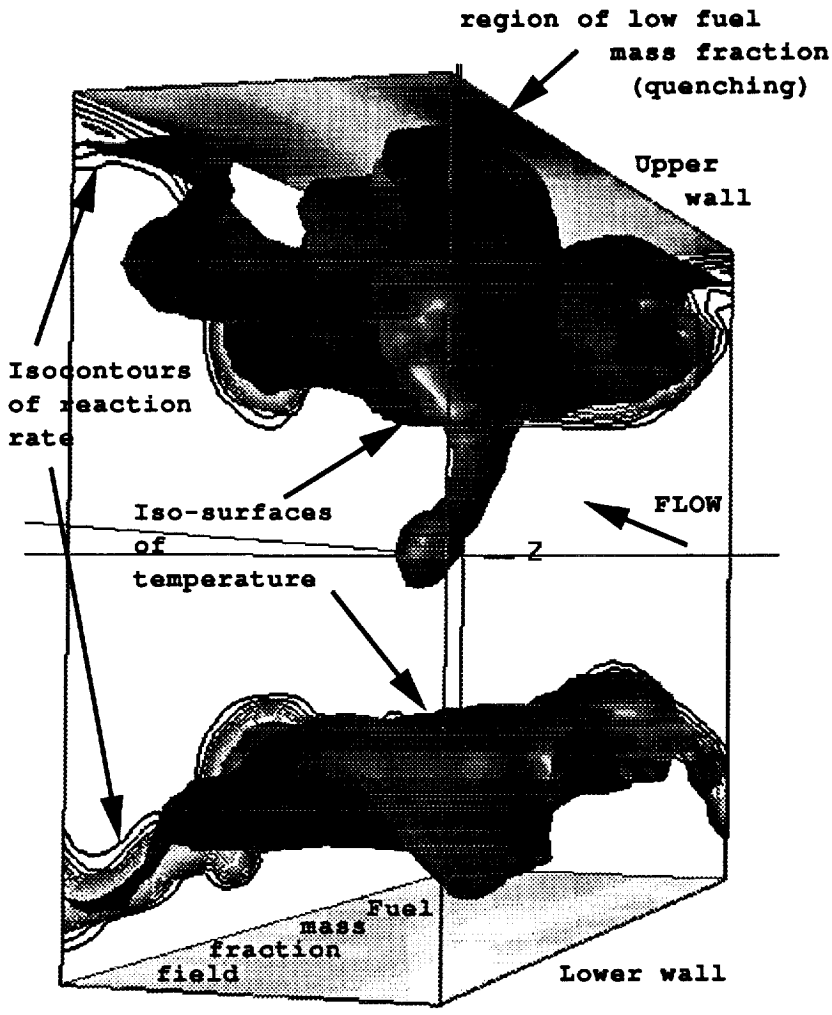

FIGURE 8. Snapshot of isosurface of temperature $T = 0.85$, along with reaction rate isolines and fuel mass fraction field, $t/t_f = 9$.

important. It produces the following events:

(1) The horseshoe vortex pushes burnt gases towards the wall and leads to flame quenching with small Peclet number and large heat flux.

(2) At the same time, the other side of the horseshoe vortex pushes fresh gas away from the wall, leading to the formation of an unburnt gas tongue; tongues similar to this one have been seen in experiments.

Fig. 12 shows an instantaneous picture of a one-legged horseshoe vortex wrapping a flame and leading to quenching at the wall and ejection of fresh gas.

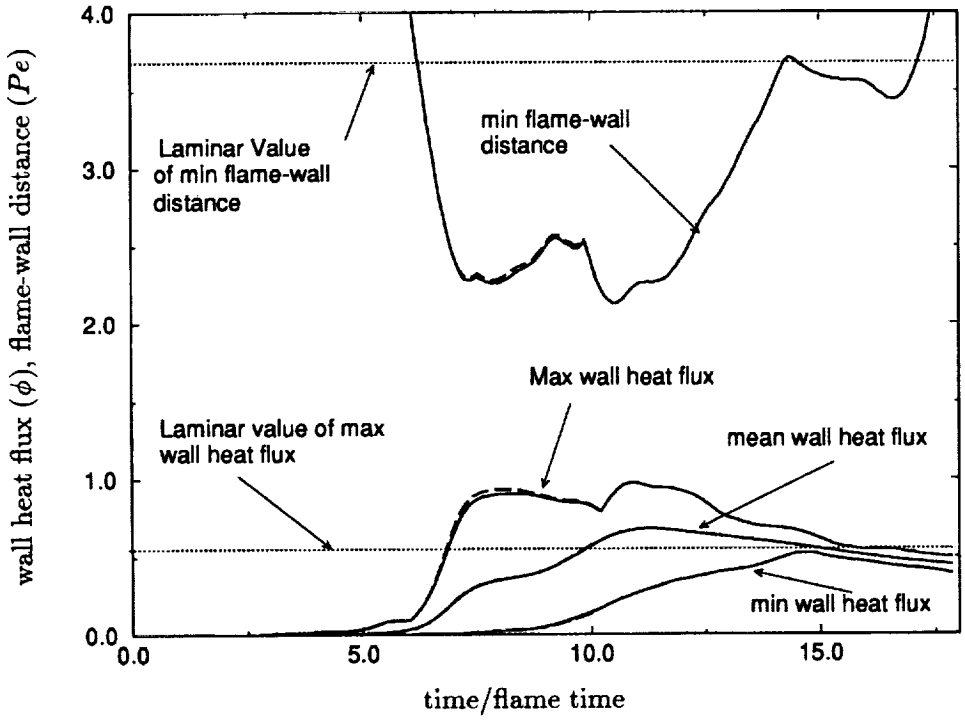

FIGURE 9. Time evolution of minimum flame-wall distance, minimum, mean, and maximum wall heat flux in the turbulent calculation. Comparison with a higher resolution calculation is also shown. —— $NY = 130$, −−− $NY = 260$.

5. A model for the quenched interface density

5.1 Mean quantities

Since periodic boundary conditions were used, averaging may be performed in the two directions parallel to the wall (x and z) at each instant. Quantities computed using conventional averaging include the mean fuel mass fraction $\overline{Y}_F$, the mean temperature T, and the mean reaction rate $\overline{\omega}$. It is convenient to replace the mean reaction rate $\overline{\omega}$ by an equivalent reactive flame surface density $\overline{\Sigma}_R$ defined by $\overline{\Sigma}_R = \overline{\omega}/s_l^0$. Profiles of these quantities are plotted in Fig. 13.

We also estimated the density $\overline{\Sigma} = \langle \Sigma' \rangle$ of interface between fresh and burnt gases. Σ' is the local surface to volume ratio, calculated where the surface (defined as the isosurface with reduced temperature 0.85) is approximated using the angle between the local temperature gradient and a coordinate direction (Rutland 1989). In the absence of quenching or strain, $\overline{\Sigma}$ is related to $\overline{\omega}$ by $\overline{\omega} = \overline{\Sigma} s_l^0$ or $\overline{\Sigma}_R = \overline{\Sigma}$ (we used Lewis number unity for this flame. Near the wall, part of this interface is quenched so $\overline{\omega} < \overline{\Sigma} s_l^0$. We will characterize quenching by the quenched fraction defined by $Q = \frac{\overline{\Sigma} - \overline{\Sigma}_R}{\overline{\Sigma}}$.

Early in the simulation ($t/t_f = 1.8$, Fig. 13), the flame is far from the wall, no

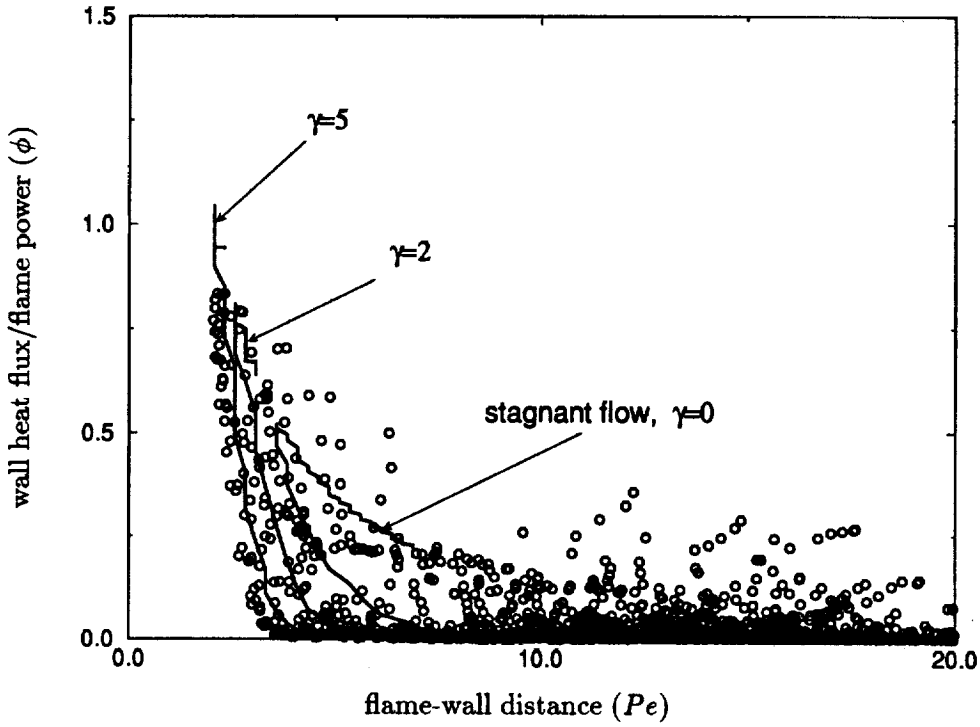

FIGURE 10. Trajectory in the Pe-wall heat flux plane of the turbulent flame at $t/t_f = 7.3$, along with trajectories for laminar flame-wall interaction in stagnant flow and stagnation line flow. o turbulent $t/t_f = 7.3$, —— laminar.

quenching takes place, and the profile of the interface density $\overline{\Sigma}$ matches the profile of the normalized reaction rate $\overline{\Sigma}_R$. The noise in Fig. 13 is due to the fact that $\overline{\Sigma}$ is computed by estimating surface area while the mean reaction rate $\overline{\omega}$ and the reactive interface density $\overline{\Sigma}_R$ are computed using conventional averages. The mean fuel mass fraction at the wall is still the initial value and the burnt gases occupy only a small fraction of the channel. The quenched fraction Q is zero everywhere; the wall heat flux is also essentially zero.

Later ($t/t_f = 12.8$, Fig. 13), the flame brush starts to interact with the wall and quenching takes place. This increases the interface density relative to the reactive interface density and thus the quenched fraction near the wall. The mean temperature gradient is not zero at the wall, indicating that the mean wall heat flux is no longer zero (see Fig. 9). In addition, the mean fuel mass fraction at the wall starts to decrease.

Finally ($t/t_f = 14.7$, Fig. 13), most of the fresh gases in the channel have been consumed and the interface density is much larger than the reactive surface density. Most of the interface is quenched. Very little fuel is available and the wall heat flux is large.

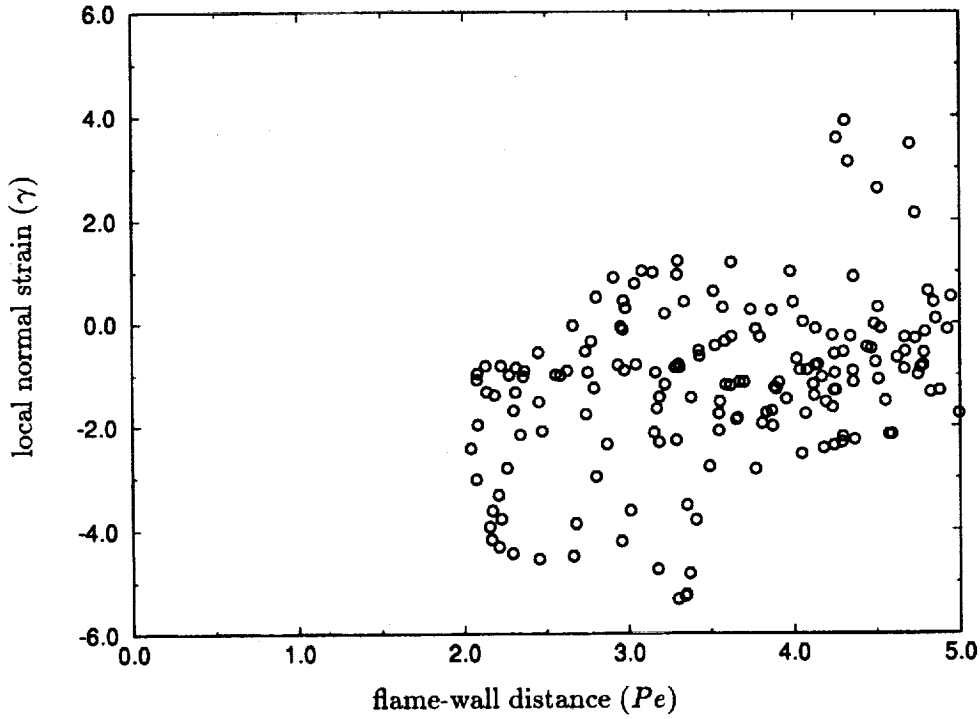

FIGURE 11. Trajectories in Pe-(equivalent) normal wall strain rate diagram at $t/t_f = 7.3$.

5.2 A model for the quenched interface fraction

It is well known that interaction between flames and walls or, more generally, the behavior of non-adiabatic flames may be characterized in terms of enthalpy loss L_H (Williams 1985, Wichman and Bruneaux 1994) defined by

$$L_H = 1 - (Y_F + T) \tag{11}$$

In an adiabatic premixed flame with unity Lewis number, L_H is zero everywhere. When the flame is non-adiabatic (as near walls), L_H increases, which indicates that quenching is possible. This is true for turbulent flames if we assume that heat and species diffuse at the same rate (turbulent Lewis number equal to unity).

A simple model for the quenched interface fraction Q may be derived by assuming that Q is proportional to the enthalpy loss L_H times the interface density:

$$Q_{model} = L_H * \overline{\Sigma} * L_Q \tag{12}$$

where L_Q is a multiple of the laminar flame thickness δ_l^0. For the present, we assume $L_Q = 10\delta_l^0$.

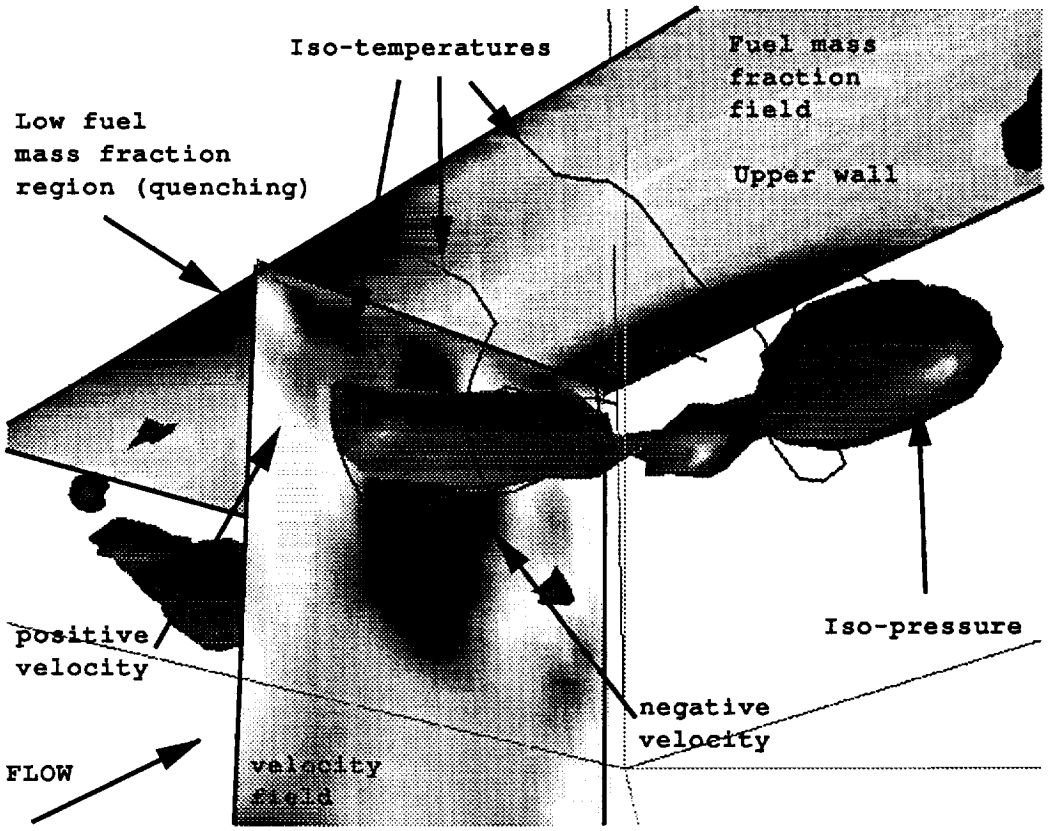

FIGURE 12. Snapshot of isosurface of low pressure (which marks a horseshoe vortex) together with the velocity and fuel mass fraction fields at $t/t_f = 7.3$.

Despite its simplicity, this model retains much of the physics of flame quenching: quenching occurs only where flame surface is present and the flame has lost significant enthalpy.

This model was tested against DNS results and the results are given in Fig. 14. The agreement between the modeled value Q_{model} and the DNS value Q is good. The model predicts both the spatial extent of the quenching as well as its magnitude. Only late in the simulation ($t/t_f = 14.7$, Fig. 14) does the model underpredict the extent of quenching and then only in the region far from the wall.

Conclusions

Direct numerical simulations of flame-wall interactions have been performed using a three-dimensional channel flow code and a constant density reaction solver. Non-reacting turbulent flow and laminar reaction in stagnant and stagnation line flow were used to validate the code. In turbulent flows the wall heat fluxes are much higher than in the laminar stagnant flame-wall interaction. This is due to the turbulence which convects flame elements towards the wall, inducing high heat fluxes

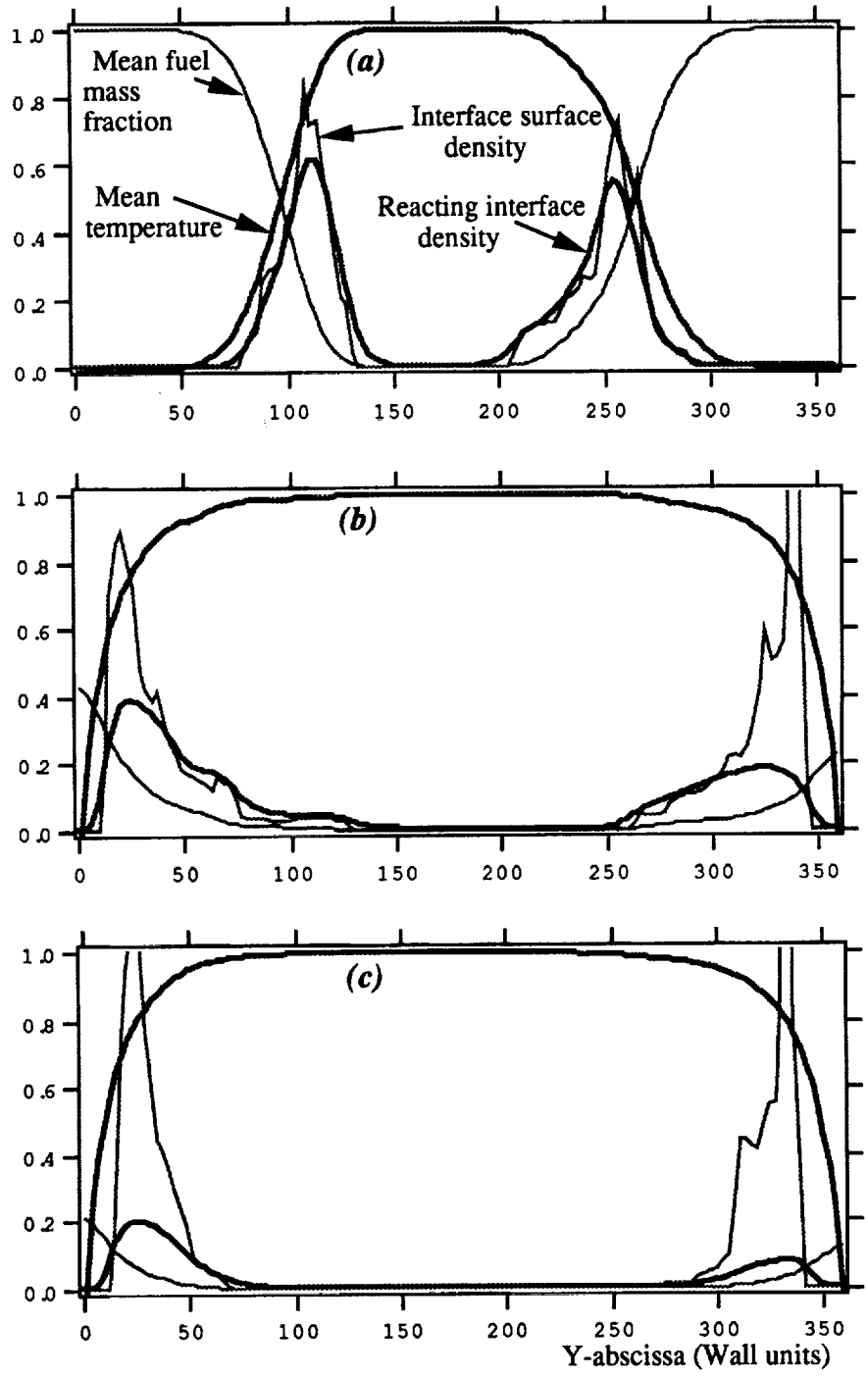

FIGURE 13. Mean values of temperature, mean fuel mass fraction, reactive surface, and interface density. a): $t/tf = 1.8$; b): $t/tf = 12.8$; c): $t/tf = 14.7$.

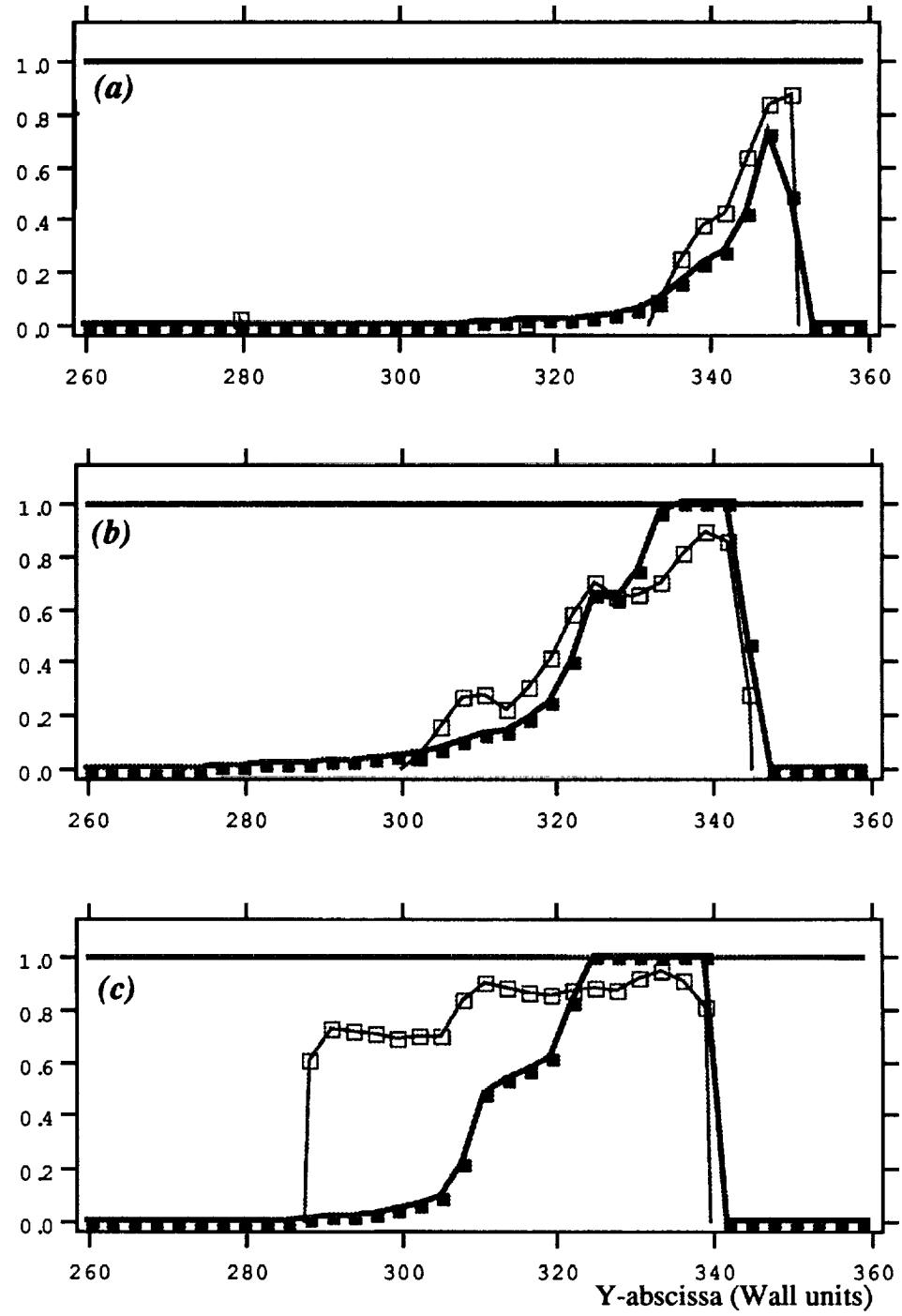

FIGURE 14. Comparison between modeled and DNS-measured quenched fractions. -□- DNS mesured quenched fraction, -■- Model for quenched fraction. a): $t/tf = 9$; b): $t/tf = 12.8$; c) $t/tf = 14.7$.

to the wall. The turbulent flame was compared to a flame in a stagnation line flow, leading to the conclusion that high wall heat fluxes are due to high normal strain. In the turbulent case, the high normal strain is generated by horseshoe vortices which push flame elements towards the wall while fresh gases are convected away from the wall, forming finger-like structures. A model for the quenched fraction of interface was proposed and compares well to the DNS results, despite its simplicity.

REFERENCES

ADAMCZYK, A. A. & LAVOIE, G. A. 1978 Laminar head-on flame quenching: a theoretical study. *SAE Transactions 87, SAE Paper 780969.*

AKSELVOLL, K. & MOIN, P. 1993 Large eddy simulation of a backward facing step flow. *Engineering Turbulence Modeling and Experiments 2.* W. Rodi and F. Martelli eds., Elsevier, 303-313.

AMSDEN, A., RAMSHAW, J., O'ROURKE, P. & DUCKOWICZ, J. 1985 SAE Paper 850554.

CARRIER, G. F., FENDELL, F. E., BUSH, W. B., & FELDMAN, P. S. 1979 Nonisenthalpic interaction of a planar premixed laminar flame with a parallel end wall. *SAE Paper 790245.*

CLENDENING, J. C. W., SHACKLEFORD, W. & HILYARD, R. 1981 Raman scattering measurement in a side wall quench layer. *18th Symp. (Intl.) on Combust.* The Combustion Institute, Pittsburgh, 1583-1589.

JENNINGS, M. 1992 SAE Paper 920589.

KIM, J., MOIN, P., & MOSER, R. 1987 Turbulence statistics in fully developed channel flow at low Reynolds number. *J. Fluid Mech.* **177,** 133-166.

LU, J. H., EZENKOYE, O., GREIF, R. & SAWYER, R. F. 1990 Unsteady heat transfer during side wall quenching of a laminar flame. *23rd Symp. (Intl.) on Combust.* The Combustion Institute, Pittsburgh, 441-446.

POINSOT, T. J., & HAWORTH, D. C. 1992 Proceedings of the 1992 Summer Program. CTR, NASA Ames/Stanford University, Stanford.

POINSOT, T. J., HAWORTH, D. C., & BRUNEAUX, G. 1993 Direct simulation and modeling of flame-wall interaction for premixed turbulent combustion. *Combust. & Flame.* **95,** 118-132.

RUTLAND, C. 1989 Effects of strain, vorticity, and turbulence on premixed flame. Ph.D. Thesis, Stanford University, Stanford.

WICHMAN, I. S. & BRUNEAUX, G. 1994 Head-on quenching of a premixed flame by a cold wall. *submitted to Combust. & Flame.*

WILLIAMS, F. A. 1985 *Combustion theory.* B. Cummings, Menlo Park, CA, 73-76.

Fundamentals group

The participants in the fundamentals section used numerical simulation results to answer fundamental questions regarding the nature of turbulence. Of the six papers in this section, three are concerned with homogeneous turbulence. Gotoh & Rogallo and Pullin & Rogallo investigated the statistics of the pressure in isotropic turbulence while Chasnov studied the the existence of asymptotic similarity states in decaying axisymmetric turbulence. The other three papers are on a wide range of topics. Verzicco & Shariff report on studies of sound generation by three-dimensional instabilities of vortex rings. Three-dimensional instabilities of stream-wise vortices in channel and Couette flow were investigated by Coughlin, Jiménez & Moser. Finally, simulations of supersonic turbulent boundary layers were studied by Guo & Adams. A brief discussion of these reports follows.

In Pullin & Rogallo, the pressure as well as dissipation and enstrophy spectra obtained from DNS and LES simulations of isotropic turbulence were studied. There was weak evidence of a $k^{-7/3}$ spectrum, as expected from Kolmogorov-like analysis. There was also evidence of an inertial range in the dissipation and enstrophy power spectra. Of key interest here, though, was the Kolmogorov constants for the pressure spectra, which were compared to predictions based on two models of the turbulence statistics, one being based on a joint normal hypothesis, and the other based on the spiral vortex model of Lundgren (1982). The value obtained from the simulations is more than a factor of two higher than the model predictions. However, there are uncertainties in the simulation results for the pressure related to the finite domain size and modest Reynolds number, so these results are not conclusive.

Gotoh & Rogallo also looked at the pressure statistics in isotropic turbulence, but in their case the main interest was in the PDF's and other statistics of pressure and its gradients. Several interesting observations were made. For example, they note that the pressure PDF is highly asymmetric, with an exponential tail for the negative fluctuations. This is consistent with the occurrence of low pressure in the core of intense vortices. Also, the Lagrangian two-time correlations of the pressure gradient has a much smaller time scale than the velocity.

Using large-eddy simulation, Chasnov found that decaying axisymmetric homogeneous turbulence evolves to similarity states, with different states depending on the nature of the initial spectrum. In the similarity state, the spectrum decays self-similarly as a power-law in time. As in isotropic turbulence, the power law exponent depends on the form of the initial spectrum at low wavenumber (i.e. $E(k) \propto k^s$ for $s = 2$ or $s > 2$) Interestingly, Chasnov also found that only for $s > 2$ does the flow relax toward isotropy. When $s = 2$, the low wavenumbers are frozen into the k^2 form and are also frozen into anisotropy.

Instabilities in vortex rings were studied by Verzicco & Shariff, and in particular, they were interested in the sound generated by the evolution of three-dimensional modes on a vortex ring. They successfully simulated a vortex ring undergoing three-dimensional break-down and obtained results consistent with previous observations.

However, the computation of the resulting sound proved more difficult. To compute the sound via the theory of Möhring, moments of the vorticity are computed, and these cause difficulties due to the artificially imposed radial and stream-wise (periodic) boundary conditions. The authors were not able to obtain a result that was independent of the size of the integration domain for computing the moments.

The work by Coughlin *et al.* was based on the speculation that the evolution of three-dimensional instabilities in the near-wall region of a turbulent flow may be similar to the instabilities of the vortices in Taylor-Couette flow. This is studied by applying an analysis similar to that of Coughlin & Marcus to the minimal channel and the minimal Couette flow. The stream-wise vortices in these flows are considered to be quasi-steady since they decay very slowly, and instabilities growing with these vortices as a base-flow are investigated. It is found that these vortices are indeed unstable to three-dimensional disturbances on a time scale much shorter than the decay of the vortices, suggesting that this instability is responsible for the growth of turbulence in the minimal flows. It would be interesting if these results could be applied to a full-scale turbulent wall-bounded flow.

In Guo & Adams, direct numerical simulations of compressible boundary layers with Mach number up to 6 were attempted. A parallel flow approximation similar to that used by Spalart for incompressible boundary layers was used. In this work the numerical simulations were actually done elsewhere (at DLR in Germany) and the data was brought for analysis during the summer program. During the course of the analysis, it became clear that the high Mach number flows suffered from too small a computational domain. This was caused by the hot wall (adiabatic in the mean) boundary conditions which cause the viscosity to increase markedly near the wall. This resulted in streaks with stream-wise and span-wise sizes that were too large for the computational domain. In these cases the turbulence length scales are much larger near the wall than away from the wall, which is the opposite problem from incompressible flows.

Robert D. Moser

39740

N95-21045

Pressure and higher-order spectra for homogeneous isotropic turbulence

By D. I. Pullin[1] AND R. S. Rogallo[2]

The spectra of the pressure, and other higher-order quantities including the dissipation, the enstrophy, and the square of the longitudinal velocity derivative are computed using data obtained from direct numerical simulation of homogeneous isotropic turbulence at Taylor-Reynolds numbers R_λ in the range $38 - 170$. For the pressure spectra we find reasonable collapse in the dissipation range (of the velocity spectrum) when scaled in Kolmogorov variables and some evidence, which is not conclusive, for the existence of a $k^{-7/3}$ inertial range, where $k = |\mathbf{k}|$ is the modulus of the wavenumber. The power spectra of the dissipation, the enstrophy, and the square of the longitudinal velocity derivative separate in the dissipation range, but appear to converge together in the short inertial range of the simulations. A least-squares curve-fit in the dissipation range for one value of $R_\lambda = 96$ gives a form for the spectrum of the dissipation as $k^0 \exp(-Ck\eta)$, for $k\eta > 0.2$, where η is the Kolmogorov length and $C \approx 2.5$.

1. Introduction

The collapse of data for the various forms of the velocity power spectrum when scaled in Kolmogorov variables of the form

$$E(k) = (\nu^5\langle\varepsilon\rangle)^{1/4} f_1(k\eta), \tag{1}$$

is well established as either an exact, or at least a very good approximation at large Reynolds numbers, by both experiment and numerical simulation; see for example Saddoughi & Veeravalli (1994) for an update of a graphical compilation originally due to Chapman (1979). In (1) E is either the shell-summed spectrum or a form of the related one-dimensional spectra, $\eta = (\nu^3/\langle\varepsilon\rangle)^{1/4}$ is the Kolmogorov length, and $\langle\varepsilon\rangle$ is the volume-averaged dissipation. The aim of the present work is to use numerical data bases obtained from direct numerical simulation (DNS) of homogeneous isotropic turbulence to study the power spectra of several quantities that are quadratic in the velocity or its spatial derivative. It is hoped that the results may be useful for testing the predictive capability of theories or models of turbulent fine scales as well as adding to our basic understanding of turbulence in the inertial and dissipation ranges.

1 Graduate Aeronautical Laboratory, California Institute of Technology, Pasadena CA 91125
2 NASA Ames Research Center

PAGE 176 INTENTIONALLY BLANK

We shall consider two-point correlations and associated power spectra of quantities that are scalar functions of position in homogeneous isotropic turbulence. Let $q(\mathbf{x},t)$ be an arbitrary function of position $\mathbf{x} \equiv (x_1, x_2, x_3)$ and time t, and denote its Fourier transform by

$$\hat{q}(\mathbf{k}) = \frac{1}{8\pi^3} \int\int\int q(\mathbf{x}) \mathrm{e}^{-i\mathbf{k}\cdot\mathbf{x}} \, d\mathbf{x}. \tag{2}$$

In (2) and subsequently we have suppressed the explicit dependence on t. Define the two-point one-time correlation of $q(\mathbf{x})$ at points $\mathbf{x}$, $\mathbf{x}+\mathbf{r}$ by

$$Q(\mathbf{r}) = \langle q(\mathbf{x}) q(\mathbf{x}+\mathbf{r}) \rangle, \tag{3}$$

where $\langle ... \rangle$ is a volume average over $\mathbf{x}$. The Fourier transform of $Q(\mathbf{r})$ is

$$\Pi(\mathbf{k}) = \frac{1}{8\pi^3} \int\int\int Q(\mathbf{r}) \mathrm{e}^{-i\mathbf{k}\cdot\mathbf{r}} \, d\mathbf{r}, \tag{4}$$

and it is easy to show that

$$\Pi(\mathbf{k}) = \hat{q}(\mathbf{k}) \hat{q}^*(\mathbf{k}), \tag{5}$$

where $*$ denotes the complex conjugate. On integrating (5) over the surface of a sphere $S(\mathbf{k})$ of radius k in $\mathbf{k}$-space, we obtain

$$E_q(k) = \int\int_{S(\mathbf{k})} \Pi(\mathbf{k}) \, dS(\mathbf{k}). \tag{6}$$

We shall refer to $\hat{q}(\mathbf{k}) \hat{q}^*(\mathbf{k})$ as the power spectrum of $q(\mathbf{x})$ and to $E_q(k)$ defined by (6) as its shell-summed power spectrum. When the turbulence is isotropic and $q(\mathbf{x})$ is an invariant scalar in the sense that its value at any point is axis independent, then $Q(\mathbf{r}) = Q(r)$, $r = |\mathbf{r}|$, and $\Pi(\mathbf{k}) = \Pi(k)$, $k = |\mathbf{k}|$. The right-hand side of (6) is then equal to $4\pi k^2 \Pi(k)$.

We consider power spectra of four quantities for which $q(\mathbf{x})$ is identified in turn with the following: the pressure-density ratio $p(\mathbf{x})$, the dissipation $\varepsilon = 2\nu(\partial u_i/\partial x_j + \partial u_j/\partial x_i)^2$, the enstrophy density $\Omega = \boldsymbol{\omega}^2$, and a quantity proportional to the square of the longitudinal velocity derivative $\Upsilon = 15(\partial u)^2$, where $\partial u \equiv \partial u_1/\partial x_1$ and $\mathbf{u} = (u_1, u_2, u_3)$ is the velocity vector. We denote the shell-summed power spectra of these quantities, in Kolmogorov scaling variables, respectively by

$$E_p(k) = \langle \varepsilon \rangle^{3/4} \nu^{7/4} f_2(k\eta), \tag{7}$$

$$E_\varepsilon(k) = \langle \varepsilon \rangle^{7/4} \nu^{3/4} f_3(k\eta), \tag{8}$$

$$E_\Omega(k) = \langle \varepsilon \rangle^{7/4} \nu^{-5/4} f_4(k\eta), \tag{9}$$

$$E_\Upsilon(k) = \langle \varepsilon \rangle^{7/4} \nu^{-5/4} f_5(k\eta). \tag{10}$$

For homogeneous isotropic turbulence, $\langle\varepsilon\rangle$, $\langle\Omega\rangle$, and $\langle\Upsilon\rangle$ are nonzero and satisfy the relations

$$\langle\varepsilon\rangle = \nu\langle\Omega\rangle = \nu\langle\Upsilon\rangle. \tag{11}$$

In (8-10) these mean values are subtracted, and the integrals of the right-hand sides over $k = (0, \infty)$ are equal to the fluctuations, respectively, $\left\langle \epsilon'^2 \right\rangle \equiv \langle(\varepsilon - \langle\varepsilon\rangle)^2\rangle$, $\left\langle \Omega'^2 \right\rangle \equiv \langle(\Omega - \langle\Omega\rangle)^2\rangle$, and $\left\langle \Upsilon'^2 \right\rangle \equiv \langle(\Upsilon - \langle\Upsilon\rangle)^2\rangle$.

We remark that $(\partial u_1/\partial x_1)^2$ is not a proper scalar, but is one component of the fourth-order tensor

$$\left(\frac{\partial u_i}{\partial x_j}\right)\left(\frac{\partial u_l}{\partial x_m}\right)$$

whose two-point correlation is an eighth-order tensor. As a consequence the power spectrum of Υ is not uniform over spherical surfaces in **k**-space. We nevertheless treat Υ as if it were a scalar for the reason that it has been used as a surrogate for ε in experiment, being the gradient-variance that can most easily be measured with a hot-wire probe. It is therefore of interest to compare its fluctuations with those of ε and Ω. Note that (3-5) remain valid and (6) may still be applied.

2. Data bases

For the most part we have used data from the forced DNS runs of Jiménez *et al.* (1993), henceforth referred to as *JWSR*. See their §2 for a detailed description of the numerical experiments and their Table 1 for a summary of the flow parameters. Our data base differs from *JWSR* Table 1 as follows: first, *JWSR* take both volume and time averages, the latter being over several large-eddy turnover times, whereas our results are based on Fourier coefficients of the velocity from a single time frame, being the last for the run. Comparisons made with one-time results at earlier times separated by a substantial fraction of a large-eddy turnover time indicated that statistical equilibrium had been obtained. Because we are using a single time frame our values $R_\lambda = 38\,(64^3)$, $65\,(128^3)$, $96\,(256^3)$, and $170\,(256^3)$ (the bracketed number gives the numerical grid resolution N^3) differ slightly from those of *JWSR*. Secondly and more importantly, our largest R_λ run was at a resolution of 256^3 compared to the 512^3 run of *JWSR* which was unavailable to us. Since the 256^3 data at $R_\lambda = 170$ has $k_{max}\eta \approx 1.0$ compared with $k_{max}\eta \approx 2.0$ for all the *JWSR* runs, it may be somewhat under-resolved. All shell-summed spectra were calculated directly from coefficients in **k**-space with de-aliased quadratic products evaluated in physical space. Those for the pressure were obtained from a solution of the relevant Poisson equation.

For the pressure spectra, in addition to the DNS runs, we also consider results from two kinds of LES (large-eddy simulation) runs. The first of these utilizes a method in which, at every time step, the magnitudes of the Fourier components of the velocity are adjusted, with no change to either the relative magnitudes in the (x_1, x_2, x_3) directions or the complex phases, such that the velocity spectrum was locked to a $k^{-5/3}$ form. We will refer to this as *Locked-E* LES (She & Jackson,

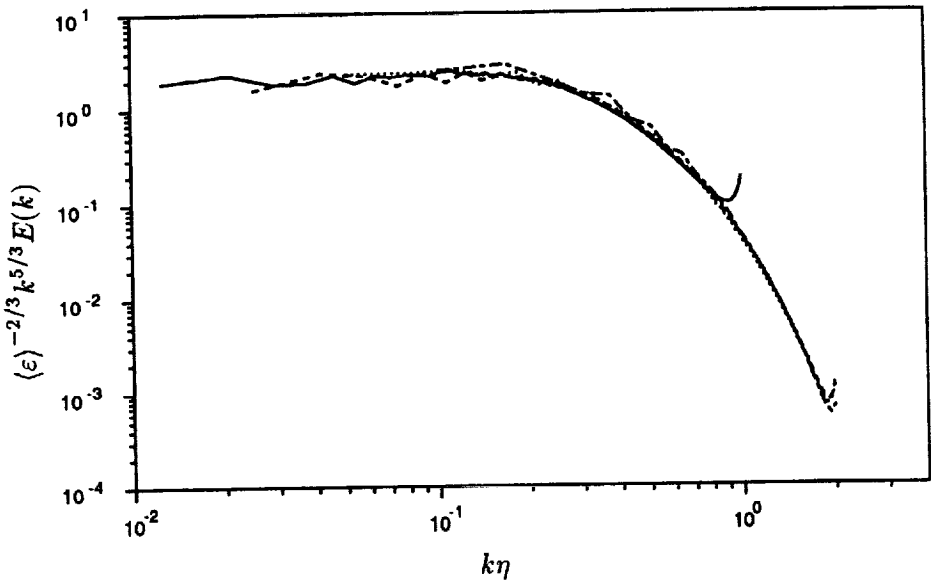

FIGURE 1. Compensated velocity power spectra in Kolmogorov units. —— $R_\lambda = 170$, ---- $R_\lambda = 96$, ····· $R_\lambda = 65$, —·— $R_\lambda = 38$.

1993). In addition some pressure spectra calculated from a Smagorinsky subgrid approach using the so called *dynamic localization model* (*DLM*, Ghosal *et al.* 1994) are also presented.

3. Spectrum of the pressure

Fig. 1 shows the velocity (energy) spectrum plotted in the compensated inertial-range form $\langle\varepsilon\rangle^{-2/3}k^{5/3}E(k) = (k\eta)^{5/3}f_1(k\eta)$. The data, including the $R_\lambda = 170$ case, collapses reasonably across the whole range of $k\eta$. A Kolmogorov constant of $\mathcal{K}_0 \approx 2.2$ appears to be indicated, but as pointed out by Jiménez (private communication), the plateau at $k\eta < 0.2$ may in fact be part of a bump in the spectrum near the beginning of the dissipation range (see Saddoughi & Veeravalli, 1994, for related experimental evidence), which is not properly resolved owing to the small inertial range of the DNS. The above quoted $\mathcal{K}_0$ may then be an overestimate.

It is well known that Kolmogorov-type dimensional arguments suggest a form for E_p in the inertial range

$$E_p(k) = \mathcal{K}_p \langle\varepsilon\rangle^{4/3} k^{-7/3}, \tag{12}$$

where $\mathcal{K}_p$ is a dimensionless number which may or may not be a universal constant. In Fig. 2 $E_p(k)$ is plotted in the compensated form suggested by (12), $\langle\varepsilon\rangle^{-4/3}k^{7/3}E_p(k) = (k\eta)^{7/3}f_2(k\eta)$. The collapse in the dissipation range (by which we mean $k\eta$ greater than about 0.125) is only fair if one discards the $R_\lambda = 170$ case as under-resolved, and poor if it is included. If this case is discarded Fig. 2 is consistent with a possible plateau corresponding to $\mathcal{K}_p \approx 8.5$, which is somewhat higher than the value $\mathcal{K}_p \approx 7$ suggested by Pumir (1994). Again, owing to the small

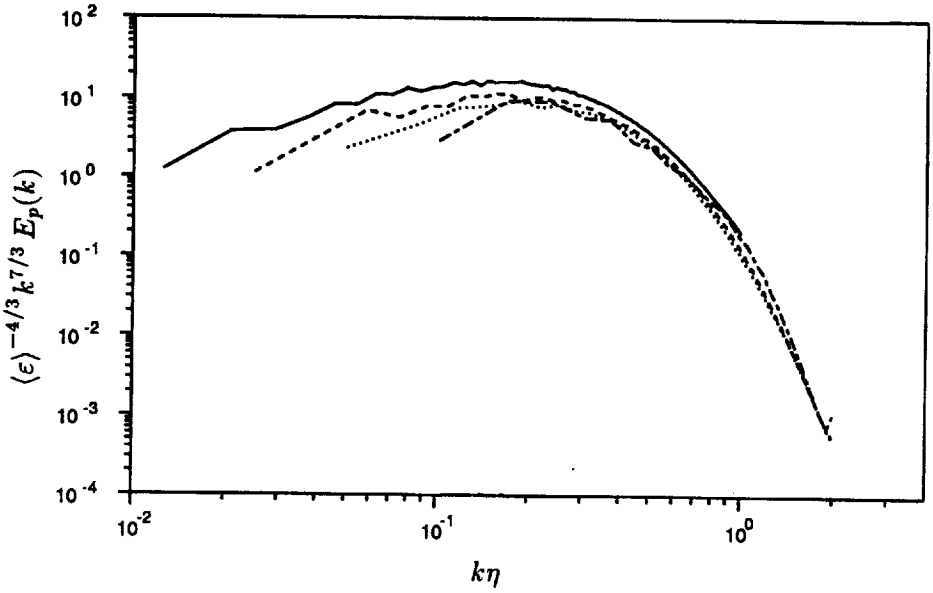

FIGURE 2. Compensated pressure spectra in Kolmogorov units. —— $R_\lambda = 170$, ---- $R_\lambda = 96$, ····· $R_\lambda = 65$, —·— $R_\lambda = 38$.

inertial range, definitive conclusions cannot be drawn and we cannot rule out the possibility of a bump analogous to that found found for $E(k)$ with or without a plateau at lower $k\eta$.

An argument due to Obukov (1949) and Batchelor (1951) based on a joint-normal hypothesis for the two-point probability distribution of the velocity field suggests that $\mathcal{K}_0$ and $\mathcal{K}_p$ (if they exist) are related as

$$\mathcal{K}_p = \frac{4536\,\left(\Gamma\left[\frac{4}{3}\right]\right)^2}{3025\,\Gamma\left[\frac{5}{3}\right]}\mathcal{K}_0^2 = 1.3245105..\mathcal{K}_0^2. \tag{13}$$

Taking $\mathcal{K}_0 = 1.5$ gives, from (13), $\mathcal{K}_p = 2.98$ which is much lower than the peak shown in Fig. 2 but which agrees approximately with the range of values $2.4 - 3.4$ estimated by Pullin (1994) from the Lundgren (1982) stretched spiral vortex model.

The ratio $E_p(k)/(k\,E(k)^2)$ is shown in Figs. 3-4. If both $E(k)$ and $E_p(k)$ follow their respective K-41 power laws in the inertial range, this ratio should plateau at $\mathcal{K}_p/\mathcal{K}_0^2$. As a test of our means of calculating E_p, the phases of the Fourier coefficients of the velocity field for the *Locked-E* LES run were randomized without change to their magnitudes. This should produce a Gaussian joint-normal velocity probability distribution while maintaining a $k^{-5/3}$ inertial range. The plateau shown in Fig. 3 for this case is in good agreement with (13) as indeed it should be (see the article by Gotoh & Rogallo in these proceedings for a discussion of various spectra for Gaussian velocity pdf's). The roll-off at both large and small k is attributed to the finite range of k in the calculation of the pressure via the (elliptic) Poisson equation, which evidently "feels" the bounded dimensions of the box. The

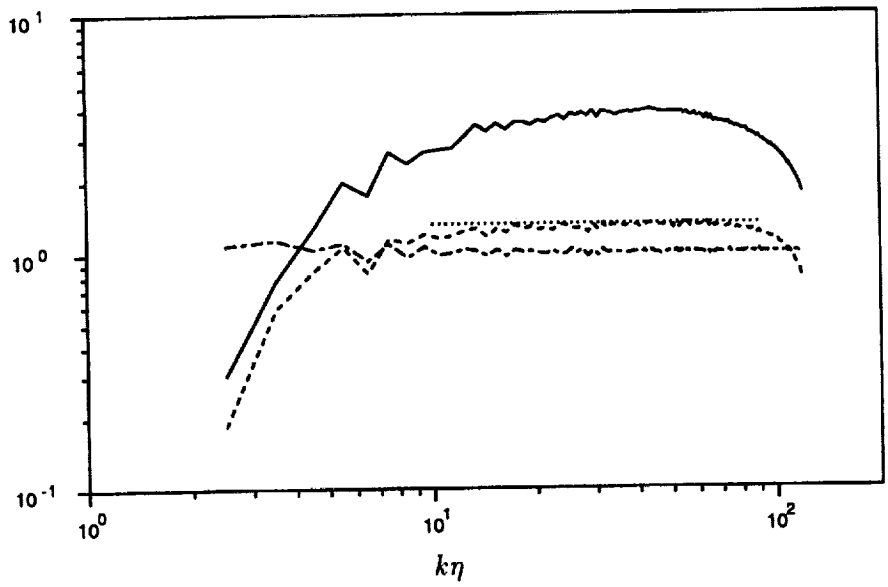

FIGURE 3. Deviation of the pressure spectrum in an inertial range from the joint-normal theory. ——— , $k^{5/3}E(k)$; —— $E_p(k)/(k\,E(k)^2)$ from 256^3 *Locked-E* LES. ---- $E_p(k)/(k\,E(k)^2)$ from 256^3 joint-normal velocity field. ····· equation 13.

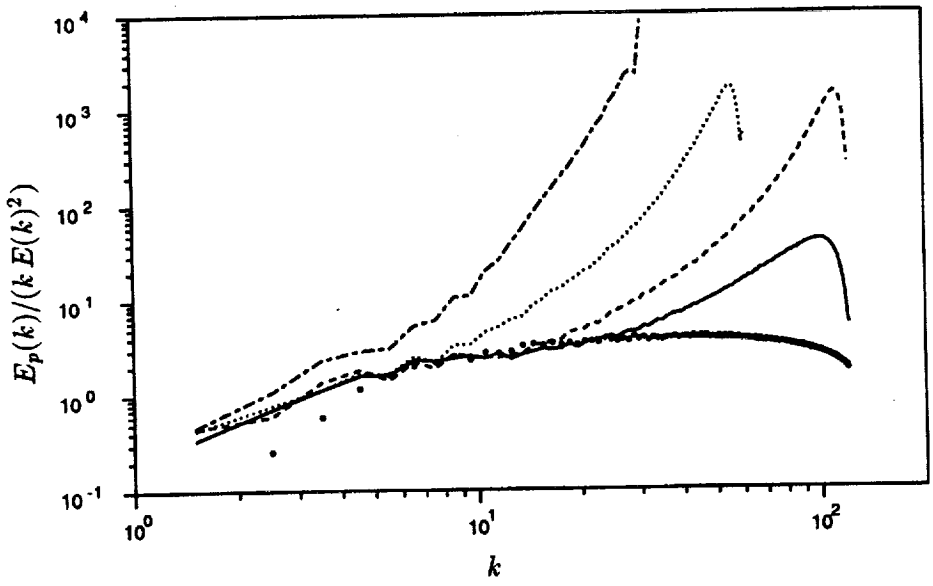

FIGURE 4. Variation of $E_p(k)/(k\,E(k)^2)$ with Reynolds number. —— $R_\lambda = 170$, ---- $R_\lambda = 96$, ····· $R_\lambda = 65$, ——— $R_\lambda = 38$. • 256^3 *Locked-E* LES.

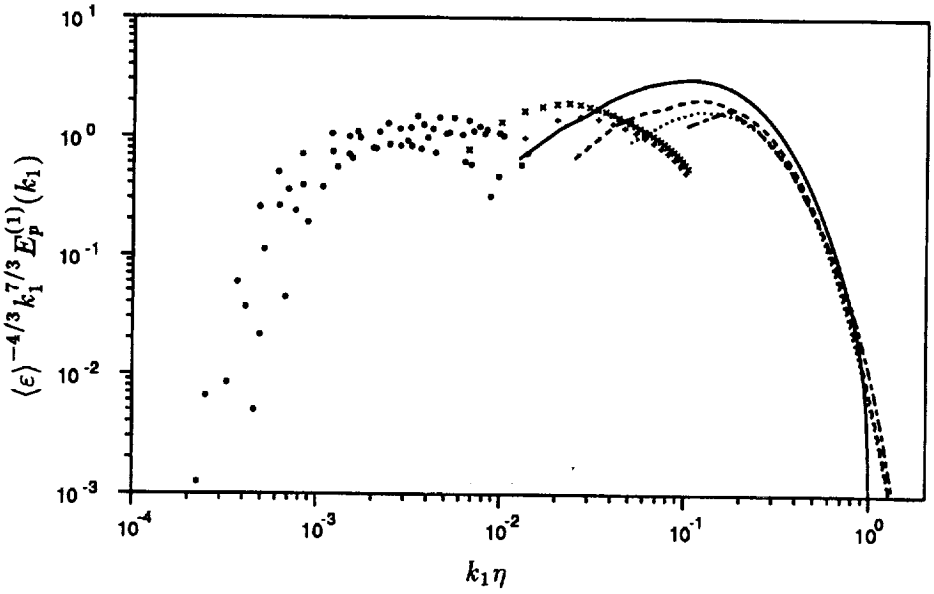

FIGURE 5. Compensated one-dimensional pressure spectra in Kolmogorov units. —— $R_\lambda = 170$, ---- $R_\lambda = 96$, ····· $R_\lambda = 65$, —·— $R_\lambda = 38$. × *DLM* LES (64^3), $R_\lambda = 269$. + *DLM* LES (32^3), $R_\lambda = 176$. • experiment of George *et al.* (1984).

true *Locked-E* LES also shows a plateau in Figs. 3-4, but at a value close to 3.8. In Fig. 4 the DNS and *Locked-E* LES show agreement in a small range of k at the larger R_λ.

An attempt to bring experiment, DNS, and LES results together is made in Fig. 5 which plots the one-dimensional form of the pressure spectrum

$$E_p^{(1)}(k_1) = \frac{1}{2}\int_{k_1}^{\infty} \frac{1}{\kappa'} E_p(\kappa')\, d\kappa'. \tag{14}$$

The measurements of George *et al.* (1984) shown in Fig. 5 were made in the mixing layer of a turbulent jet at $1.5 - 3$ diameters downstream of the jet exit. Reynolds numbers based on the exit velocity and jet diameter were 4.0×10^5 and 6.2×10^5. Taylor Reynolds numbers were in the range $R_\lambda \approx 350 - 600$. George *et al.* nondimensionalized their data with large-scale parameters which may be more appropriate at the fairly low wavenumbers of the experiment. We have rescaled their results using estimates of the dissipation and of the Kolmogorov microscale given in §17 of their paper. They state that velocity contamination caused by flow-probe interactions may have had some effect on the accuracy of the data. Fig. 5 well illustrates the difficulties of studying pressure correlations. Neither DNS, which is currently limited to low R_λ, nor experiment, which is limited by accuracy problems at large wavenumbers, can span an appreciable spectral band. The combined experiment, *DLM* LES, and DNS results may indicate a plateau in

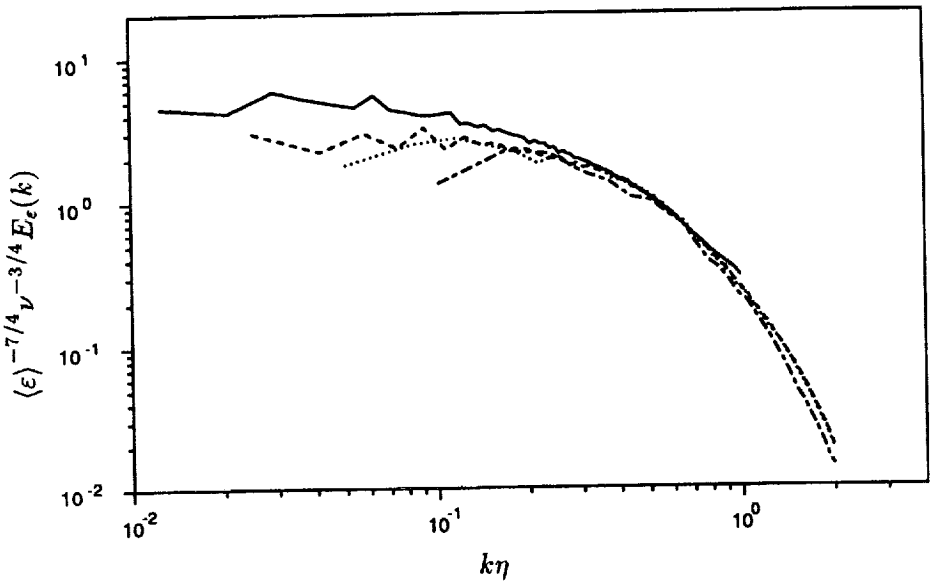

FIGURE 6. Power spectra of the dissipation in Kolmogorov units. —— $R_\lambda = 170$, ---- $R_\lambda = 96$, ····· $R_\lambda = 65$, —·— $R_\lambda = 38$.

the $k_1^{7/3}$-compensated spectra, but the scatter is very large. If (12) is true then from (14) the one-dimensional inertial-range coefficient is $\mathcal{K}_p^{(1)} = \frac{3}{14}\mathcal{K}_p$.

4. Spectra of ϵ, Ω, and Υ

Calculated dissipation spectra E_ε and enstrophy spectra E_Ω are shown in Figs. 6 and 7 respectively. Fig. 8 shows a comparison of these together with the spectrum of $\Upsilon = 15(\partial u_1/\partial x_1)^2$ at $R_\lambda = 96$. This indicates that the fluctuations of Ω are rather larger than those of ε/ν with fluctuations of $15(\partial u_1/\partial x_1)^2$ larger still. If Kolmogorov scaling is exact then the quantities $\langle\varepsilon^2\rangle/\langle\varepsilon\rangle^2$, $\langle\Omega^2\rangle/\langle\Omega\rangle^2$, and $\langle(\partial u)^4\rangle/\langle(\partial u)\rangle^2$ should each be constant independent of Reynolds number. There is evidence from DNS, *e.g.* Kerr (1985), *JWSR*, that this is not the case for $\langle(\partial u)^4\rangle/\langle(\partial u)\rangle^2$, which exhibits a weak dependence on the Taylor Reynolds number $R_\lambda = u\lambda/\nu$, where u is the root-mean square of one component of the velocity and λ is the Taylor microscale. This is confirmed by Gotoh & Rogallo in these proceedings who also tabulate $\langle\varepsilon^2\rangle/\langle\varepsilon\rangle^2$, $\langle\Omega^2\rangle/\langle\Omega\rangle^2$ for the present data set.

It is notable that Fig. 8 shows no sign of power-law behavior at low k, and indeed an asymptote to a constant appears to be indicated for all three quantities. This is in qualitative agreement with measurements, made using a multi-wire probe, of Tsinober *et al.* (1992) (see their Fig. 9(a)). In Fig. 9 we have plotted the spectra of Fig. 8 in the form $d[\log(f_n(k\eta))]/d[\log(k\eta)]$, $n = 3,4,5$ where f_n are defined by Equations (8-10). If curves are of the form $(k\eta)^\beta \exp(-Ck\eta)$, then this plot should be a straight line of slope $-C$ that intercepts the vertical axis at β. The fit of a

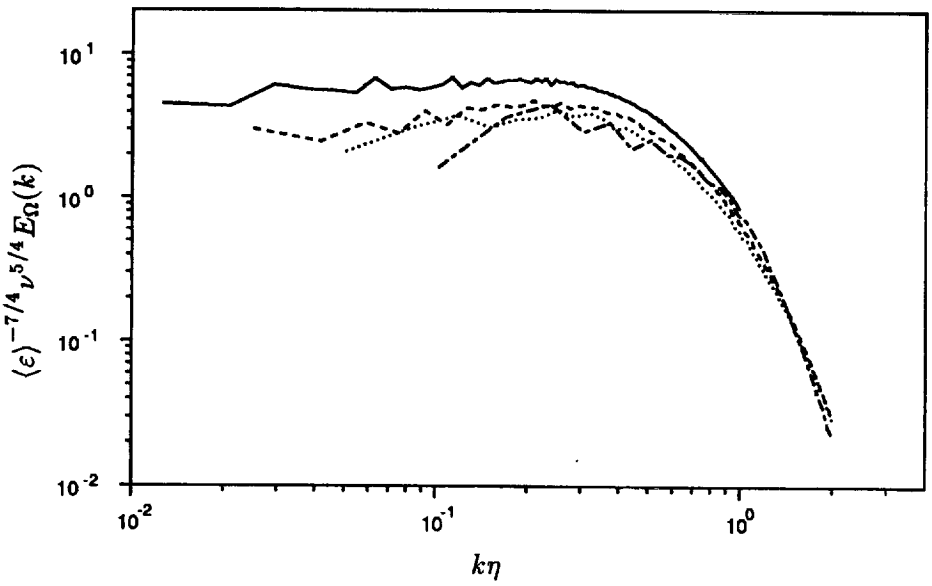

FIGURE 7. Power spectra of the enstrophy in Kolmogorov units. —— $R_\lambda = 170$, ---- $R_\lambda = 96$, ····· $R_\lambda = 65$, —·— $R_\lambda = 38$.

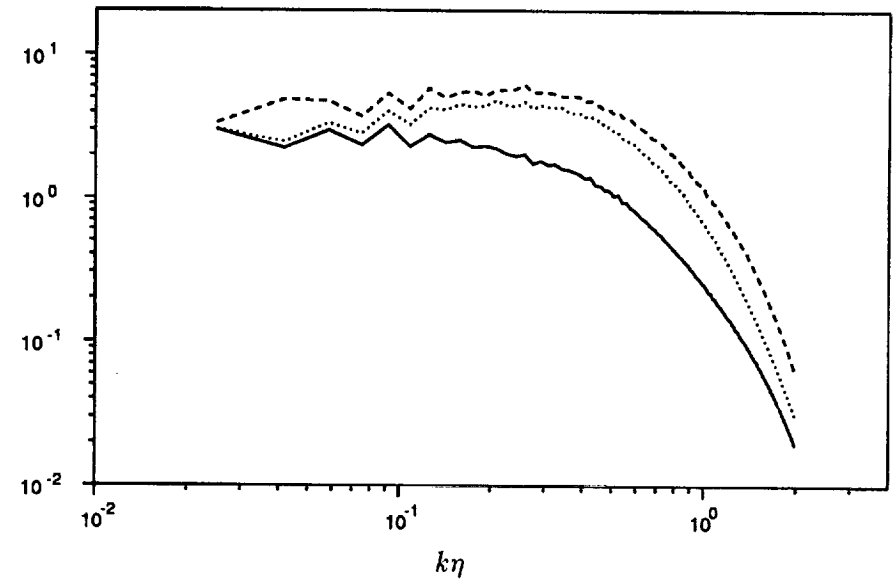

FIGURE 8. Comparison of quadratic velocity-derivative spectra at $R_\lambda = 96$. —— ϵ, ····· Ω, ---- $\Upsilon = 15(\partial u_1/\partial x_1)^2$.

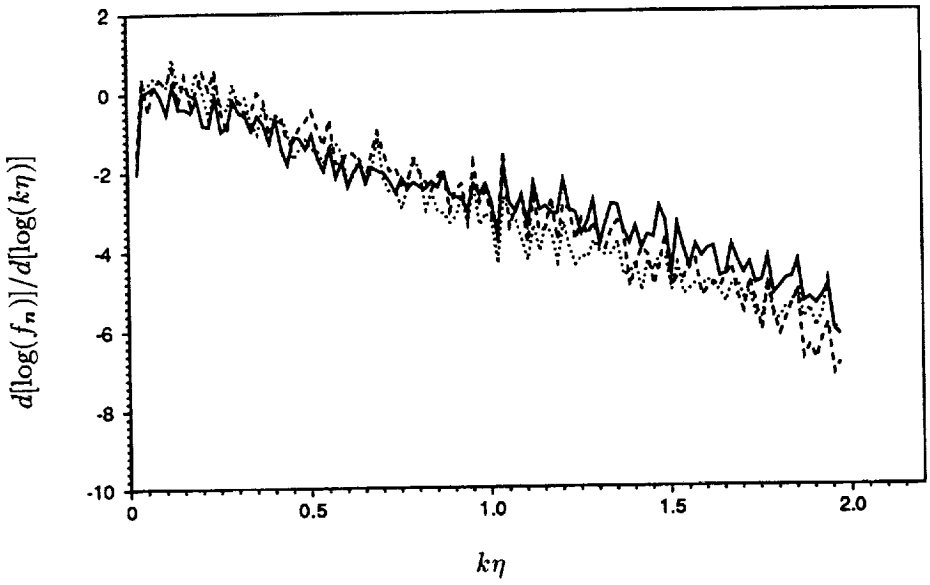

FIGURE 9. Spectra of Fig. 8 plotted in the form $d[\log(f_n(k\eta))]/d[\log(k\eta)]$, $n = 3,4,5$ where f_n are defined by Equations (8-10). —— ϵ, ····· Ω, ---- $\Upsilon = 15(\partial u_1/\partial x_1)^2$.

straight line to the data sets in Fig. 9 is very approximate. Nevertheless a least-squares best fit was made in each case in the window $0.2 < k < 1.8$. The method was tested using the velocity spectrum (not shown) for which we found $\beta = -1.6$ and $C = 4.9$ in fair agreement with Kerr (1990) and others. We find that for E_ϵ; $\beta \approx 0.$, $C \approx 2.5$, E_Ω; $\beta \approx 0.5$, $C \approx 3.5$. There was some sensitivity to the chosen range, so the errors are substantial, of order ± 0.1 for β and ± 0.2 for C. Clearly a larger resolved dissipation range is needed to improve accuracy.

5. Concluding remarks

We have examined the power spectra of several quantities using numerical data bases from DNS and LES box turbulence, focusing mainly on flow variables that are quadratic in the velocity components and which have proven difficult to measure experimentally. When taken in conjunction with the one-dimensional spectra of Figure 5, the DNS shell-summed spectra provide tentative evidence for the presence of a $k^{-7/3}$ range with $\mathcal{K}_p \approx 8.5$ and a corresponding $\mathcal{K}_p^{(1)} \approx 1.8$, but with large error. These are higher than those predicted by either the joint-Gaussian model ($\mathcal{K}_p \approx 2.98$ corresponding to $\mathcal{K}_0 = 1.5$) or the stretched-spiral vortex model ($\mathcal{K}_p = 2.4 - 3.4$ depending on R_λ). Since it is unlikely that the spectral range of DNS will increase sufficiently in the near future to resolve this issue, there is clearly a need for a definitive experiment of the Saddoughi & Veeravalli (1994) type. The spectra of $\langle\varepsilon\rangle$ and $\langle\Omega\rangle$ show significant differences in the dissipation range but appear to behave similarly in the short inertial range, where a k^0 form is indicated, in agreement with the prediction of the stretched spiral-vortex model (Pullin *et al.* 1994).

Acknowledgments

The authors wish to thank T. Gotoh for helpful discussions. DIP was partially supported under NSF Grant CTS-9311811. Hospitality provided by CTR during the 1994 Summer Research Program is gratefully acknowledged.

REFERENCES

BATCHELOR, G. K. 1951 Pressure fluctuations in isotropic turbulence. *Proc. Camb. Phil. Soc.* **47**, 359-374.

CHAPMAN, D. 1979 Computational aerodynamics development and outlook. *AIAA J.* **17** 1293.

GEORGE, W. K., BEUTHER, P. D. & ARNDT, R. E. A. 1984 Pressure spectra in turbulent free shear flows. *J. Fluid Mech.* **148**, 155-191.

GHOSAL, S., LUND, T. S., MOIN. P. & AKSELVOLL, K. 1994 A localization model for large-eddy simulation of turbulent flows. Submitted to *J. Fluid Mech.*

JIMÉNEZ, J., WRAY, A., SAFFMAN, P. G. & ROGALLO, R. S. 1993 The structure of intense vorticity in homogeneous isotropic turbulence. *J.Fluid Mech.* **255** 65-90.

KERR, R. M. 1985 Higher-order derivative correlations and the alignment of small-scale structures in isotropic numerical turbulence. *J. Fluid Mech.* **153**, 31-58.

KERR, R. M., 1990 Velocity, scalar and transfer spectra in numerical turbulence. *J. Fluid Mech.* **211**, 309-322.

LUNDGREN, T. S. 1982 Strained spiral vortex model for turbulent fine structure. *Phys Fluids* **25**, 2193-2203.

OBUKHOV, A. M. 1949 Pressure fluctuations in a turbulent flow *Dokl. Akad, Nauk SSSR, Ser. Geofiz.* **3**, 49-68.

PULLIN, D. I. 1994 Pressure spectra for vortex models of fine-scale homogeneous turbulence. *Phys Fluids* (in press).

PULLIN, D. I., BUNTINE, J. D. & SAFFMAN P. G. 1994 On the spectrum of a stretched spiral vortex. *Phys Fluids* **6**, 3010.

PUMIR, A. 1994 A numerical study of pressure fluctuations in three-dimensional, incompressible, homogeneous, isotropic turbulence. *Phys Fluids* **6** 2071.

SHE, Z.-S. & JACKSON, E. 1993 A constrained Euler system for Navier-Stokes turbulence. *Phys. Rev. Lett.* **70** 1255.

TSINOBER, A., KITT, E. & DRACOS, T. 1992 Experimental investigation of the field of velocity gradients in turbulent flows. *J. Fluid Mech.* **242** 169.

SADDOUGHI, S. G. & VEERAVALLI, S. V. 1994 Local isotropy in turbulent boundary layers at high Reynolds number. *J. Fluid Mech.* **268**, 333.

311-34
39741

N95-21046

17

Statistics of pressure and pressure gradient in homogeneous isotropic turbulence

By T. Gotoh[1] AND R. S. Rogallo[2]

The statistics of pressure and pressure gradient in stationary isotropic turbulence are measured within direct numerical simulations at low to moderate Reynolds numbers. It is found that the one-point pdf of the pressure is highly skewed and that the pdf of the pressure gradient is of stretched exponential form. The power spectrum of the pressure $P(k)$ is found to be larger than the corresponding spectrum $P_G(k)$ computed from a Gaussian velocity field having the same energy spectrum as that of the DNS field. The ratio $P(k)/P_G(k)$, a measure of the pressure-field intermittence, grows with wavenumber and Reynolds number as $-R_\lambda^{1/2}\log(k/k_d)$ for $k < k_d/2$ where k_d is the Kolmogorov wavenumber. The Lagrangian correlations of pressure gradient and velocity are compared and the Lagrangian time scale of the pressure gradient is observed to be much shorter than that of the velocity.

1. Introduction

The pressure field plays an important role in the turbulent motion of an incompressible fluid. The pressure, or more precisely its gradient, accelerates and deforms fluid blobs in a manner that prevents them from being compressed. The pressure is given by the solution of a Poisson equation, implying that it is a quantity dominated by the large scales of the velocity field, but the source term is quadratic in the velocity gradient and leads to non-Gaussian statistics of the pressure field. Recent studies have shown that the pdf of the pressure field is highly skewed and has a long tail for negative fluctuations. These fluctuations correspond to intense vortices with radii of the order of the Kolmogorov length (Holtzer & Siggia 1993, Pumir 1994).

The internal dynamics of a turbulent fluid motion can be extracted in a frame moving with the fluid (the Lagrangian point of view). At moderate to high Reynolds number, the pressure gradient rather than the viscous stress is responsible for the deformation and acceleration of fluid regions larger than the dissipation scale. For example the time scale of small scales of turbulent motion can be inferred from the curvature of the Lagrangian velocity auto-correlation obtained from the expansion

$$R_L(t,s) = \langle \mathbf{v}(t)\cdot\mathbf{v}(s)\rangle = C_0 - \frac{1}{2}C_2(t-s)^2 + \cdots, \qquad t \geq s, \tag{1.1}$$

1 Nagoya Institute of Technology, Japan
2 NASA Ames Research Center

PRECEDING PAGE BLANK NOT FILMED

PAGE 188 INTENTIONALLY

$$C_0 = 2\int_0^\infty E(k,s)dk, \tag{1.2}$$

$$C_2 = -\langle(\nabla p(\mathbf{x},s))^2\rangle = -\int_0^\infty k^2 P(k,s)dk = -\int \frac{\langle D(\mathbf{k},s)D(-\mathbf{k},s)\rangle}{k^2}d\mathbf{k}, \tag{1.3}$$

$$D(\mathbf{k}) = k_i k_l \iint_{\mathbf{p}+\mathbf{q}=\mathbf{k}} d\mathbf{p}d\mathbf{q}\; u_i(\mathbf{p},s)u_l(\mathbf{q},s), \tag{1.4}$$

for small $t-s$. Here for simplicity we have neglected the viscous term and have taken $\rho = 1$. The power spectrum of the pressure $P(k,t)$ gives the pressure variance as

$$\langle p^2(\mathbf{x},t)\rangle = \int_0^\infty P(k,t)\; dk.$$

Eqs. (1.3) and (1.4) imply that the spectrum of the pressure gradient depends on a fourth-order moment of the velocity field, and roughly speaking the largest contribution to the pressure-gradient variance comes from wavenumbers lower than the peak wavenumber of $k^2E(k)$ when Reynolds number is large. This can be compared with the variance of the pressure itself, which is dominated by wavenumbers near the peak of the energy spectrum $E(k)$, and with the variance of the dissipation ϵ, which is dominated by wavenumbers near the peak of $k^2E(k)$.

It is well known that the small scales of turbulent motion are intermittent (we shall use this term herein to mean simply a departure from Gaussian statistics) and fourth-order moments have contributions from the cumulant part. An example is seen in Gotoh *et al* (1993) where the initial curvature $|C_2^{DNS}|$ is larger than $|C_2^G|$ computed from a Gaussian velocity field

$$\begin{aligned} C_2^G &= -\langle(\nabla p(\mathbf{x},s))^2\rangle_G = -\int_0^\infty k^2 P_G(k,s)dk \\ &= -\int_0^\infty dk \int_0^\infty dq\; kq\; J\left(\frac{q}{k}\right) E(k,s)E(q,s), \end{aligned} \tag{1.5}$$

$$J(x) = \{(a^2-1)^2 \log\frac{1+a}{|1-a|} - 2a + \frac{10}{3}a^3\}/(2a^4), \qquad a = \frac{2x}{1+x^2}. \tag{1.6}$$

This suggests that turbulence has a faster decay of $R_L(\tau)$ and a smaller turbulent diffusivity (as given by the time integral of $R_L(\tau)$) than predicted by the Gaussian theory. In other words, it suggests that the dynamics of the Navier-Stokes equation causes a fluid blob to forget its past history more effectively than would convection by a Gaussian velocity field. Therefore intermittence effects appear in the dynamics of a fluid particle through the pressure gradient and are expected to be different from those of the viscous stress, but we do not know how fast intermittence in the pressure increases with wavenumber, how it differs from the intermittence of the dissipation, what its time scale depends on, and so on.

There have been many studies of the fluctuations of pressure and its gradient in turbulence (Monin & Yaglom 1975, and Nelkin 1994) but few fundamental studies

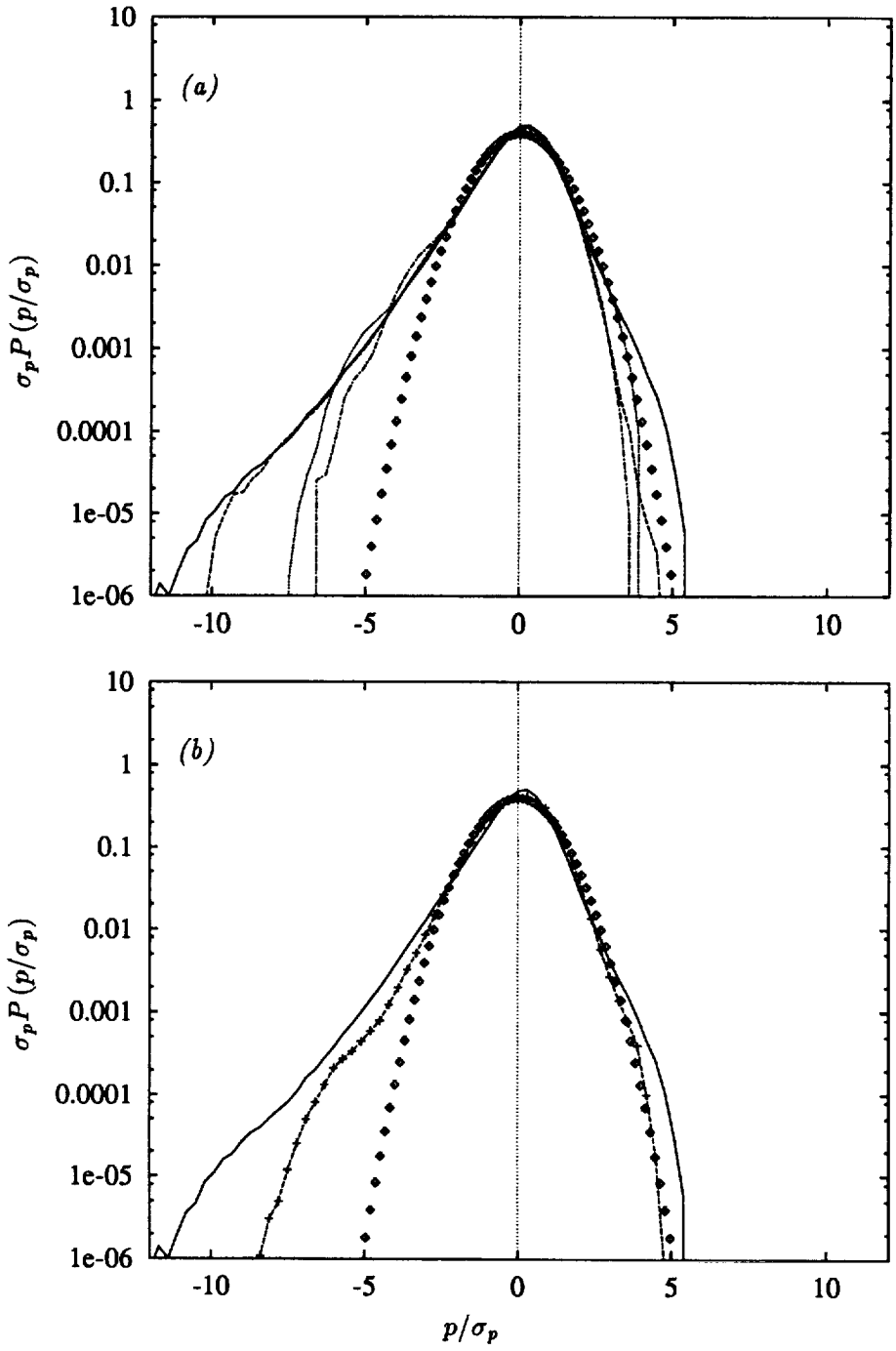

FIGURE 1. The pdf of pressure. (a) turbulent velocity field. ——— : $R_\lambda = 172$, - - - - : $R_\lambda = 96$, ····· : $R_\lambda = 63$, —·— : $R_\lambda = 38$, ◇: Gaussian, (b) Gaussian velocity field with the same energy spectrum for $R_\lambda = 172$. ——— : turbulent velocity field, +- - - - : Gaussian velocity field, ◇: Gaussian.

of pressure intermittence and its effects on the flow dynamics. This is partly because experimental measurement of the pressure spectrum is difficult (Uberoi 1953 and George *et al* 1984). Now that extensive numerical data are available, we can examine the statistics of the pressure field systematically, albeit at rather low Reynolds numbers. Here we present some measurements taken from the DNS data base available during the summer program and examine the statistics of the pressure field.

2. Numerical simulation

The turbulent flow fields used here (Jiménez *et al* 1993) are all homogeneous and isotropic and are held stationary by forcing at low wavenumber. They are arranged into four groups according to the Reynolds number R_λ, with statistical quantities computed as averages over two fields at well separated times for $R_\lambda = 172$ and over three fields for $R_\lambda = 96, 63, 38$. The numerical grid sizes were $N = 256^3$ for $R_\lambda = 172, 96$, $N = 128^3$ for $R_\lambda = 63$, and $N = 64^3$ for $R_\lambda = 38$. The Lagrangian autocorrelations of velocity and pressure gradient were computed by the passive-vector method (Kaneda & Gotoh 1991, Gotoh *et al* 1993). The pressure field $p(\mathbf{k}, t)$ was computed using de-aliased spectral methods.

3. Results

3.1. One-point one-time statistics

The one-point pdf of the pressure in Fig. 1a is skewed as reported by Pumir (1994). For negative pressure fluctuations the asymptotic form of the pdf tends to be nearly exponential $P(p) \propto \exp\left(-a|p/\sigma_p|^\alpha\right)$, where a is a non-dimensional constant and the exponent α is slightly less than one, which is consistent with low pressure in the core regions of intense vortex filaments. The tail of the pdf extends towards negative values with large amplitude as R_λ increases but α is independent of R_λ. For positive fluctuations the pdf is close to Gaussian and is insensitive to R_λ (Pumir 1994). Furthermore the pdf $P_G(p)$ of the pressure field computed from a Gaussian velocity field having the same energy spectrum has the same behavior (Fig. 1b) for the negative fluctuations as predicted by Holtzer & Siggia (1993).

The pdf of one component of the pressure gradient is shown in Fig. 2a for different Reynolds numbers. The pdf is symmetric and its tails become wider as R_λ increases. Fig. 2b shows that the pdf of the pressure gradient is isotropic and that it differs markedly from that computed from a Gaussian velocity field, unlike the case of the pressure itself. The asymptotic form of the tails of these pdf's appears to be a stretched exponential $P(p_{,i}) \propto \exp\left(-b\left|p_{,i}/\sigma_{p_{,i}}\right|^\beta\right)$ with $0 < \beta < 1$, where b is a non-dimensional constant, while that of its Gaussian counterpart is exponential as expected. This means that the pressure-gradient field is very intermittent and is quite different from the pressure gradient in a Gaussian velocity field. Holtzer & Siggia (1993) studied the pdf of the pressure gradient and suggested $\beta \sim 1/2$. The pdfs plotted against $\sqrt{p_{,y}/\sigma_{p_{,y}}}$ (figure not shown) indicate that β is close to $1/2$ for large amplitudes and becomes smaller as R_λ increases.

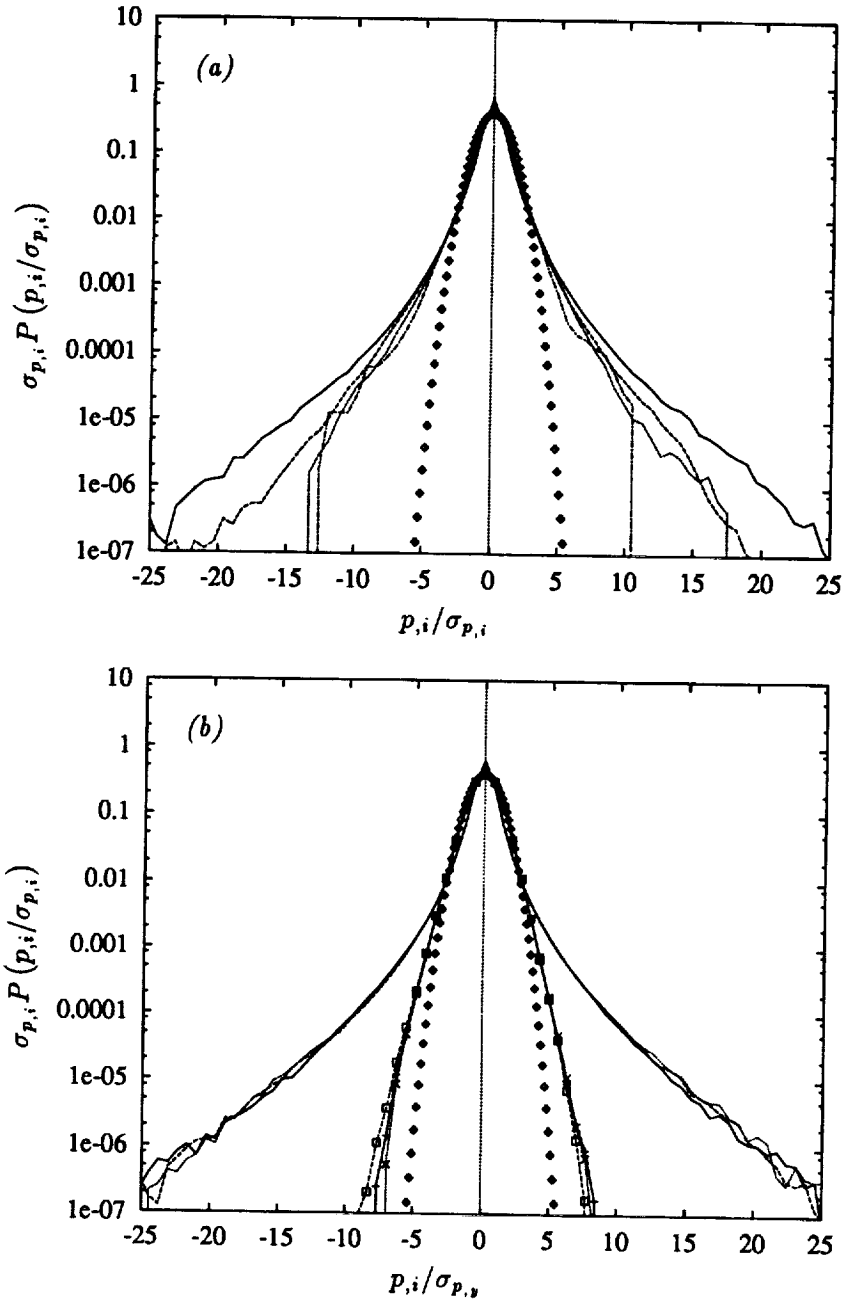

FIGURE 2. The pdf of pressure gradient. (a) variation with Reynolds number for a single component. ——— : $R_\lambda = 172$, ---- : $R_\lambda = 96$, ····· : $R_\lambda = 63$, —·— : $R_\lambda = 38$, ◇: Gaussian, (b) Comparison of turbulent and Gaussian values for all components at $R_\lambda = 172$. ——— : $\partial p/\partial x$, ---- : $\partial p/\partial y$, ····· : $\partial p/\partial z$ for turbulent velocity field; +——— : $\partial p/\partial x$, □---- : $\partial p/\partial y$, ×····· : $\partial p/\partial z$ Gaussian velocity field; ◇: Gaussian.

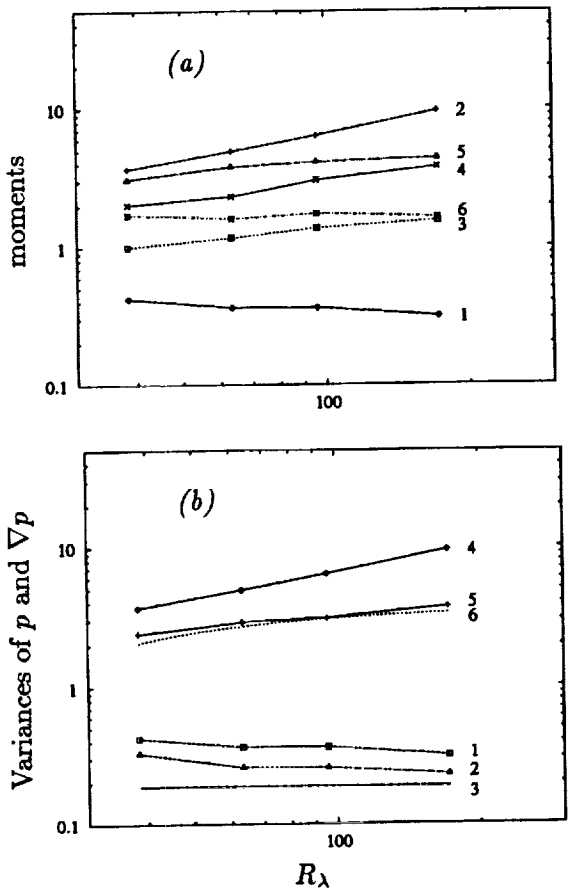

FIGURE 3. Variation with Reynolds number of velocity moments. (a) Various moments of turbulent velocity field. 1: F_p, 2: $F_{\nabla p}$, 3: F_ϵ, 4: F_ω, 5: $F_{\partial_1 u_1}$, 6: F_{u_1}. (b) Comparison with values from the corresponding Gaussian velocity fields. 1: F_p (DNS), 2: F_p (Gaussian), 3: F_p (George *et al* 1984), 4: $F_{\nabla p}(DNS)$, 5: $F_{\nabla p}$ (Gaussian), 6: $F_{\nabla p}$ (George *et al* 1984).

The variation with R_λ of normalized moments of the pressure and pressure gradient are shown in Fig. 3a. Included there for comparison are other normalized fourth-order moments of velocity:

$$F_p = \frac{\langle p^2 \rangle}{(\frac{1}{2}\langle \mathbf{u}^2 \rangle)^2}, \qquad F_{\nabla p} = \frac{\langle (\nabla p)^2 \rangle}{\bar{\epsilon}^{3/2}\nu^{-1/2}}, \tag{3.1}$$

$$F_\epsilon = \frac{\langle \epsilon^2 \rangle}{\langle \epsilon \rangle^2}, \quad F_\omega = \frac{\langle \omega^4 \rangle}{\langle \omega^2 \rangle^2}, \quad F_{\partial_1 u_1} = \frac{\langle (\partial u_1/\partial x_1)^4 \rangle}{\langle (\partial u_1/\partial x_1)^2 \rangle^2}, \quad F_{u_1} = \frac{\langle (u_1)^4 \rangle}{\langle (u_1)^2 \rangle^2}, \tag{3.2}$$

where $\bar{\epsilon} = \langle \epsilon \rangle$. The normalized variance of the pressure F_p is insensitive to R_λ (Batchelor 1951 and Pumir 1994). On the other hand the normalized variance of

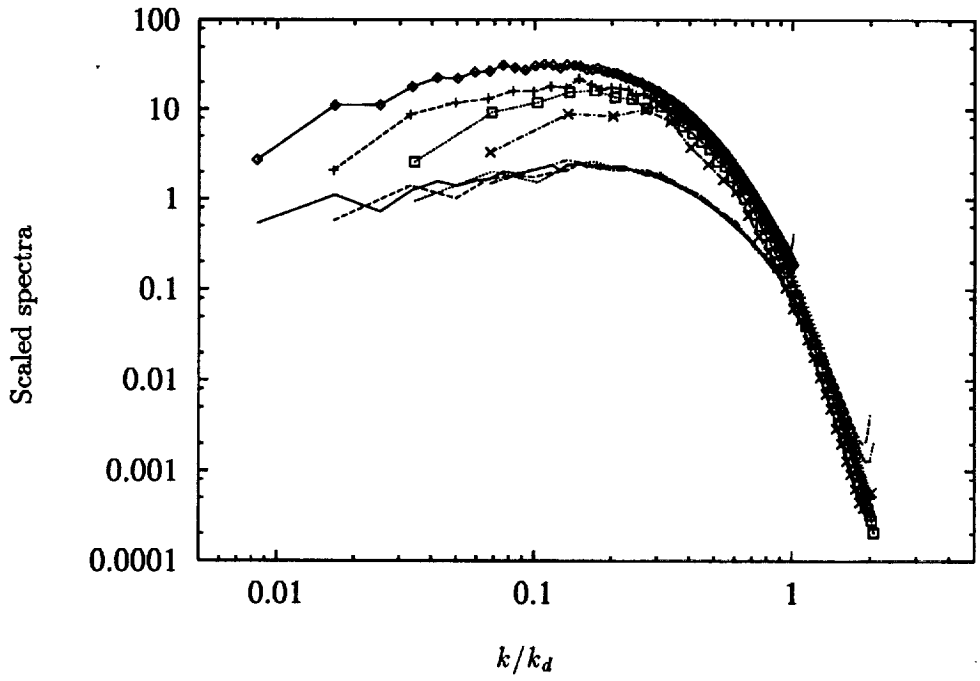

FIGURE 4. Velocity-gradient and pressure-gradient power spectra in Kolmogorov units. ——— : $R_\lambda = 172$, ---- : $R_\lambda = 96$, ····· : $R_\lambda = 63$, —·— : $R_\lambda = 38$. Curves without symbols: $\bar{\epsilon}^{-3/4}\nu^{1/4}k^2E(k)$. Curves with symbols: $\bar{\epsilon}^{-5/4}\nu^{-1/4}k^2P(k)$.

the pressure gradient $F_{\nabla p}$ increases rapidly with R_λ and is roughly proportional to $R_\lambda^{1/2}$ for the range of Reynolds numbers studied here. This tendency is in agreement with Yeung & Pope (1989), where R_λ was below 93. On the other hand F_ϵ and F_ω increase slowly with R_λ in agreement with the data of Kerr (1985). This difference is surprising because functions of the velocity gradient such as vorticity or $\partial u_1/\partial x_1$ are quantities representing small scales of turbulent motion (characterized by wavenumbers near the maximum of $k^2E(k)$) and are believed to be more intermittent than the pressure-gradient field whose characteristic wavenumber is lower than that of $k^2E(k)$ when the Reynolds number is high (see Fig. 4).

When the universal equilibrium form of the energy spectrum (Kolmogorov 1941) is used with the Gaussian-velocity approximation (1.5) we obtain

$$\begin{aligned} E(k) &= \bar{\epsilon}^{1/4}\nu^{5/4}f(k/k_d), \\ \langle(\nabla p(\mathbf{x}))^2\rangle &= \bar{\epsilon}^{3/2}\nu^{-1/2}F_{\nabla p}, \\ F_{\nabla p} &= 2\int_0^\infty dx \int_0^x dy\; xy\; J\left(\frac{y}{x}\right) f(x)f(y), \end{aligned} \tag{3.3}$$

Kaneda (1993) analyzed (3.3) and found that the largest contribution to the integral comes from the region $y \le k_c/k_d \le x$, where k_c is the wavenumber above which

$E(x) \propto \exp(-cx)$ and c is a non-dimensional constant, which means that the integral $F_{\nabla p}$ is governed by the energy spectrum up to the dissipation range. Batchelor (1951) estimated $F_{\nabla p} \sim 3.9$ independent of R_λ. George *et al* (1984) used (3.3) with an empirical energy spectrum for $E(k)$ and found

$$F_{\nabla p} = \left(\beta_p - \frac{\gamma_p}{R_\lambda}\right), \tag{3.4}$$

with $\beta_p = 3.7$ and $\gamma_p = 62.7$. The constant β_p is universal while γ_p depends on the macro-scale of the turbulence.

Fig. 3b compares the variances of the pressure and its gradient with those computed from Gaussian velocity fields. The values computed from the Gaussian fields are close to those found from (3.4) using the values of George *et al* (1984) but are significantly lower than the DNS values. The R_λ dependence of the turbulent pressure gradient is stronger than that of its Gaussian counterpart, and it seems likely that any theoretical explanation must take into account the non-Gaussian statistics.

3.2. Two-point one-time statistics

Eqs. (1.3) and (1.4) show that the power spectrum of the pressure gradient is a function of a fourth-order moment of the velocity field. The Gaussian approximation for the velocity field leads to (1.5), which implies that the peak of $k^2P(k)$ occurs at a lower wavenumber than that of $k^2E(k)$. Comparison of these spectra, plotted in Kolmogorov units in Fig. 4, confirms that at low R_λ both spectra peak at nearly the same wavenumber, but as R_λ increases the peak of $k^2P(k)$ moves to lower wavenumber. Collapse of the enstrophy spectra is excellent but that of the pressure gradient is not. This implies that the Kolmogorov scaling is not appropriate for the pressure field (Moin & Yaglom 1975). The cumulative contributions of these spectra to the total enstrophy and pressure-gradient variance

$$Q_1(k) \equiv \frac{\int_0^k q^2 E(q)dq}{\int_0^{K_{max}} q^2 E(q)dq}, \quad Q_2(k) \equiv \frac{\int_0^k q^2 P(q)dq}{\int_0^{K_{max}} q^2 P(q)dq}, \tag{3.5a,b}$$

for the four R_λ's reach 80% at $k_p/k_d \approx 0.35$ for the pressure gradient and at $k_\omega/k_d \approx 0.5$ for total enstrophy, but their scale separation k_p/k_ω is small (Batchelor 1951).

One way to measure the variation of pressure intermittence across the spectrum is to compare the pressure power spectrum $P(k)$ of the turbulence with that $P_G(k)$ computed from a Gaussian velocity field (Hudong *et al* 1987). Fig. 5a presents such a comparison for $R_\lambda = 172$. The pressure spectrum $P(k)$ is larger than $P_G(k)$ for all wavenumbers beyond the forced range, meaning that the cumulant contribution $P_C(k)$,

$$P(k) = P_G(k) + P_C(k), \tag{3.6}$$

is positive. This suggests that the inertial-range constant K_p for the pressure spectrum $P(k) = K_p\bar{\epsilon}^{4/3}k^{-7/3}$ is larger than that predicted from the Gaussian velocity

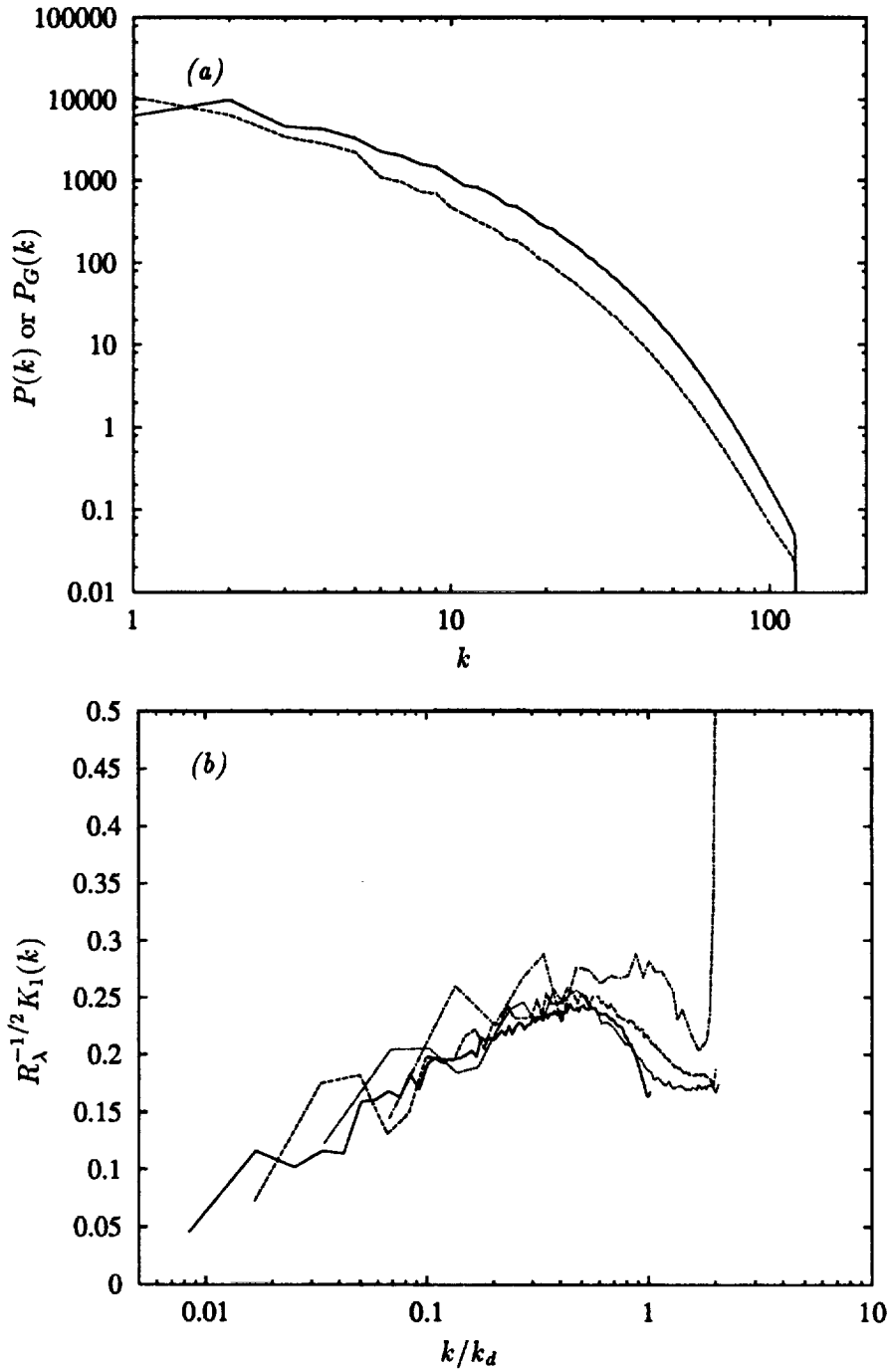

FIGURE 5. Comparison of pressure power spectra in turbulence with those computed from Gaussian velocity fields. (a) at $R_\lambda = 172$. ——— : $P(k)$, ---- : $P_G(k)$. (b) variation of their (scaled) ratio $R_\lambda^{-1/2}K_1(k)$ with Reynolds number. ——— : $R_\lambda = 172$, ---- : $R_\lambda = 96$, ····· : $R_\lambda = 63$, —·— : $R_\lambda = 38$.

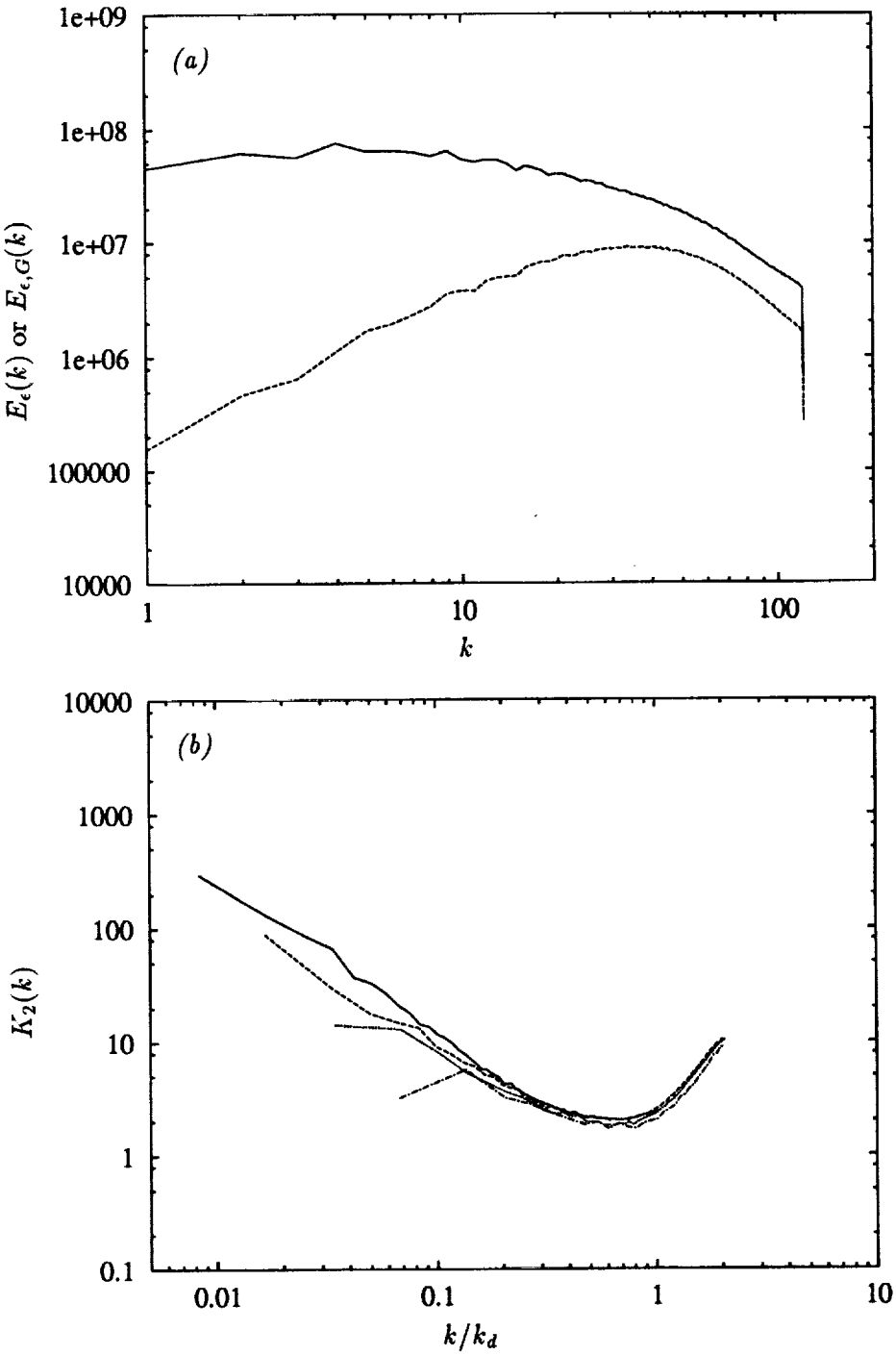

FIGURE 6. Comparison of dissipation power spectra in turbulence with those computed from Gaussian velocity fields. (a) at $R_\lambda = 172$. ——— : $E_\epsilon(k)$, ---- : $E_{\epsilon,G}(k)$. (b) variation of their ratio $K_2(k)$ with Reynolds number. ——— : $R_\lambda = 172$, ---- : $R_\lambda = 96$, ····· : $R_\lambda = 63$, —·— : $R_\lambda = 38$.

field (Nelkin & Tabor 1990, Fung *et al* 1992, and the article by Pullin & Rogallo in this proceedings). We consider the spectrum ratio

$$K_1(k) = \frac{P(k)}{P_G(k)} \tag{3.7}$$

as a measure of the variation of pressure (and pressure gradient) intermittence across the spectrum. A $R_\lambda^{1/2}$ dependence of $K_1(k)$ is suggested by the good collapse of $R_\lambda^{-1/2} K_1(k)$ shown in Fig. 5b. This implies that

$$K_1(k) = 1 + \frac{P_C(k)}{P_G(k)} \propto -R_\lambda^{1/2} \log\left(\frac{k}{k_d}\right), \qquad k/k_d \leq 1/2. \tag{3.8}$$

The growth with wavenumber of the intermittence of second-order moments of the pressure field is very slow (it appears to be logarithmic, but the scale range is not sufficient to preclude a weak algebraic dependence) but the growth with Reynolds number as $R_\lambda^{1/2}$ is faster than that of other small-scale quantities. At $R_\lambda = 172$

$$\frac{\langle (\nabla p)^2 \rangle}{\langle (\nabla p)^2 \rangle_G} = 2.58 \tag{3.9}$$

and the initial curvature of the Lagrangian velocity autocorrelation is larger than that of the Gaussian field (Gotoh *et al* 1993). Navier-Stokes dynamics decorrelates the velocity of fluid particles faster than convection by a Gaussian velocity field would.

The variation of the dissipation intermittence across the spectrum is measured in a similar way. Fig. 6 compares the dissipation power spectra of turbulent-velocity fields with those of the corresponding Gaussian-velocity fields. Here we define the power spectrum of the dissipation and its intermittence (ratio of turbulent to Gaussian spectra) as

$$\langle \epsilon^2(\mathbf{x}, t) \rangle = \int_0^\infty E_\epsilon(k, t)\, dk, \tag{3.10}$$

$$K_2(k) = \frac{E_\epsilon(k)}{E_{\epsilon,G}(k)}. \tag{3.11}$$

The intermittence within the dissipation range is independent of Reynolds number. It is interesting to note that the maxima of $K_1(k)$ and minima of $K_2(k)$ both occur at $k/k_d \approx 1/2$ and that the diameter of intense vortex tubes is also of order $1/k_d$ (Jiménez *et al* 1993). The strong variation of the dissipation intermittence across the spectrum is opposite to that of the pressure field due to the modulation of the energy spectrum by the small-scale structures (Hudong *et al* 1987). For example when strong singularities of the velocity field with support size $1/k_d$ are placed periodically at a fixed separation $l \gg 1/k_d$, the power spectrum of the dissipation field has an excitation at $k \sim 1/l \ll k_d$ as well as at $k \sim k_d$, while a Gaussian velocity field with a compact spectrum centered on k_d simply generates a compact dissipation spectrum centered on k_d.

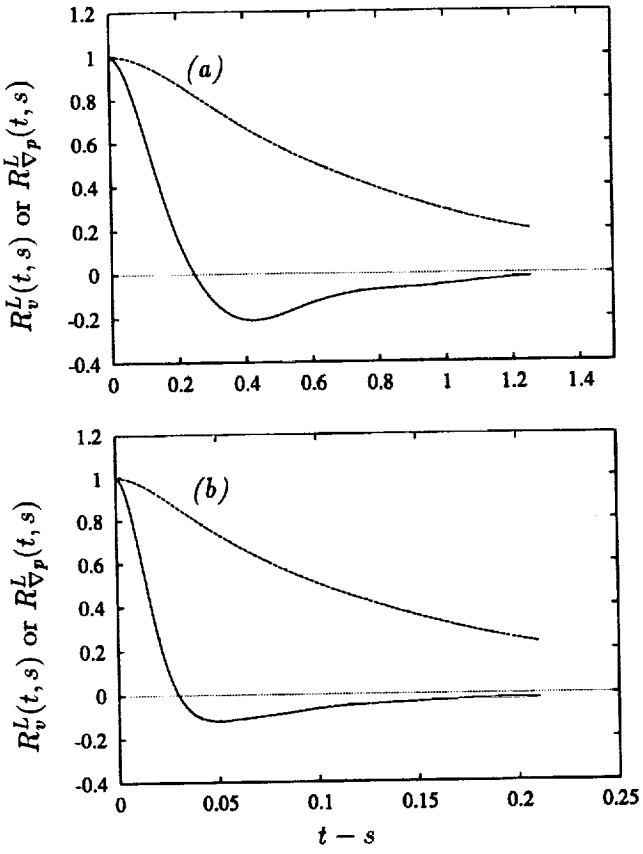

FIGURE 7. Lagrangian correlations of velocity and pressure gradient. (a) $R_\lambda = 63$. (b) $R_\lambda = 96$. ——— : $R_{\nabla p}^L(t,s)$, ---- : $R_v^L(t,s)$.

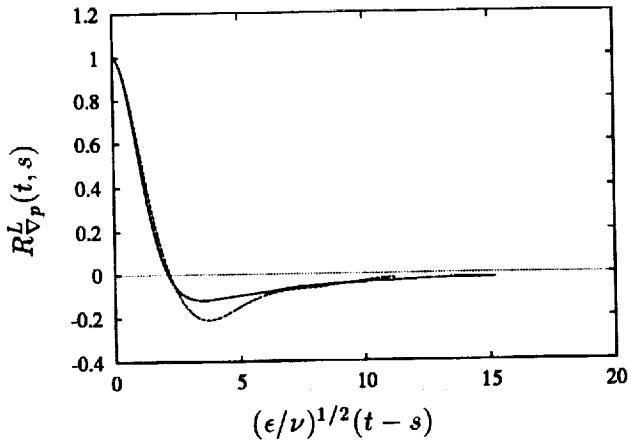

FIGURE 8. Kolmogorov time-scaling of the Lagrangian pressure-gradient correlation. ——— : $R_\lambda = 96$, ---- : $R_\lambda = 63$.

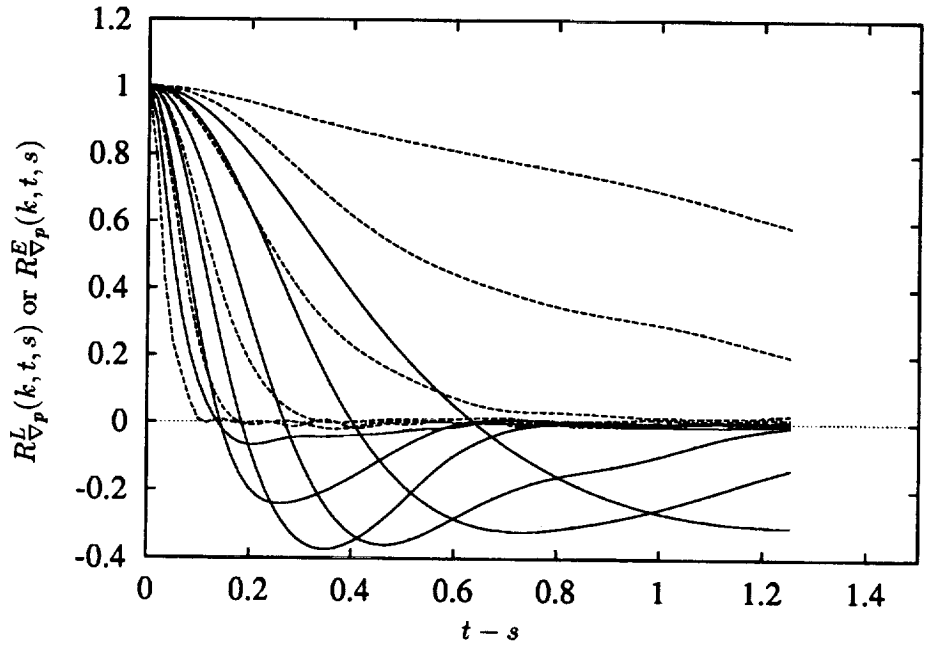

FIGURE 9. The decay of Lagrangian and Eulerian pressure-gradient correlations within octave bands at $R_\lambda = 63$. ——— : Lagrangian, ---- : Eulerian. The uppermost curves correspond to the lowest octaves and the correlations decrease monotonically for higher octaves.

3.3. Two-time statistics

The normalized Lagrangian auto-correlations of velocity and pressure gradient are defined in a stationary flow as

$$R^L_v(t,s) = \frac{\langle \mathbf{v}(\mathbf{x},t|t)\cdot\mathbf{v}(\mathbf{x},t|s)\rangle}{\langle|\mathbf{v}(\mathbf{x},s|s)|^2\rangle}, \qquad \text{for } t \geq s, \tag{3.12a}$$

$$R^L_{\nabla p}(t,s) = \frac{\langle \mathbf{F}(\mathbf{x},t|t)\cdot\mathbf{F}(\mathbf{x},t|s)\rangle}{\langle|\mathbf{F}(\mathbf{x},s|s)|^2\rangle}, \qquad \text{for } t \geq s, \tag{3.12b}$$

where $\mathbf{v}(\mathbf{x},t|s)$ is the velocity at time s of the fluid particle whose space-time trajectory passes through $(\mathbf{x},t)$, and $\mathbf{F}(\mathbf{x},t|s)$ is the pressure gradient acting on that particle at time s. Note that $\mathbf{v}(\mathbf{x},t|t) = \mathbf{u}(\mathbf{x},t)$ and $\mathbf{F}(\mathbf{x},t|t) = \nabla p(\mathbf{x},t)$.

Fig. 7 compares the Lagrangian auto-correlations $R^L_v(t,s)$ and $R^L_{\nabla p}(t,s)$ at $R_\lambda = 63$ and 96. The correlations of the pressure gradient decay much faster than those of the velocity and have negative correlation at later times. In Fig. 8 $R^L_{\nabla p}(t,s)$ is replotted with time scaled in Kolmogorov units. Collapse of the curves is excellent up to the time at which they change sign.

We define octave-band Lagrangian correlation spectra for the pressure gradient

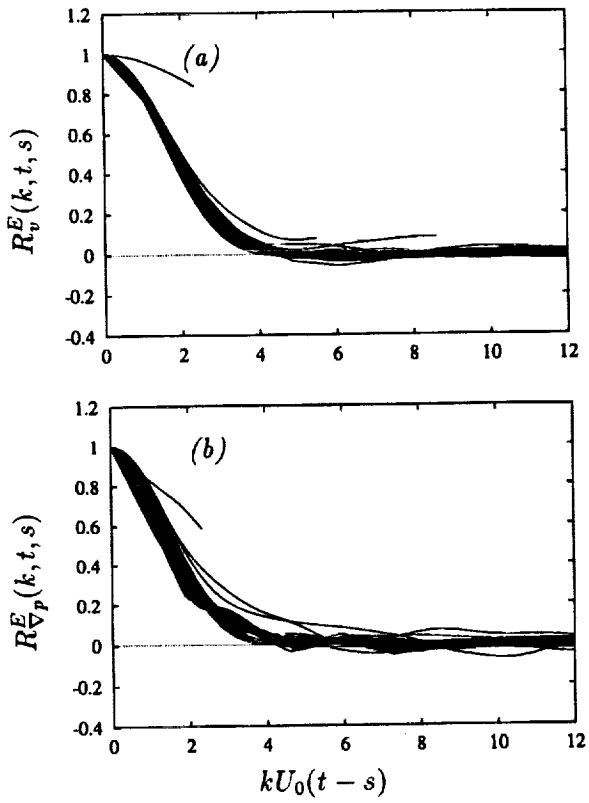

FIGURE 10. Time-scaled narrow-band Eulerian correlations of velocity and pressure gradient for wavenumber-bands $k = 2 + 2n, n = 0, \cdots 29$ at $R_\lambda = 63$. (a) $R_v^E(k,t,s)$. (b) $R_{\nabla p}^E(k,t,s)$.

as

$$\widehat{R}_{\nabla p}^L(k,t,s) = \frac{\sum\limits_{oct} \langle \mathbf{F}(\mathbf{k},t|t) \cdot \mathbf{F}(-\mathbf{k},t|s) \rangle}{\left[\sum\limits_{oct} |\mathbf{F}(\mathbf{k},t|t)|^2 \sum\limits_{oct} |\mathbf{F}(\mathbf{k},t|s)|^2 \right]^{1/2}}, \tag{3.13}$$

where $\sum\limits_{oct} \equiv \sum_{k=2^l}^{k=2^{l+1}}$ and $\mathbf{F}(\mathbf{k},t|s)$ is the Fourier transform of $\mathbf{F}(\mathbf{x},t|s)$ with respect to the *Lagrangian coordinates* at *labeling time* t (Kraichnan 1966 and Gotoh *et al* 1993). The octave-band Eulerian correlations are defined in a similar way.

The comparison of these spectra in Fig. 9 indicates that at high wavenumbers the Lagrangian correlation decays slower than the Eulerian, but that at low wavenumbers the decay rates are roughly equal. The Eulerian decorrelation of the small scales is caused primarily by their sweeping by larger scales while their Lagrangian decorrelation is due to deformation by larger scales. The sweeping effect on the Eulerian correlation is clearly demonstrated in Fig. 10 where narrow-band Eulerian correlation spectra, defined similarly to (3.13) with $\sum_{oct}$ replaced by $\sum_{shell}$, are

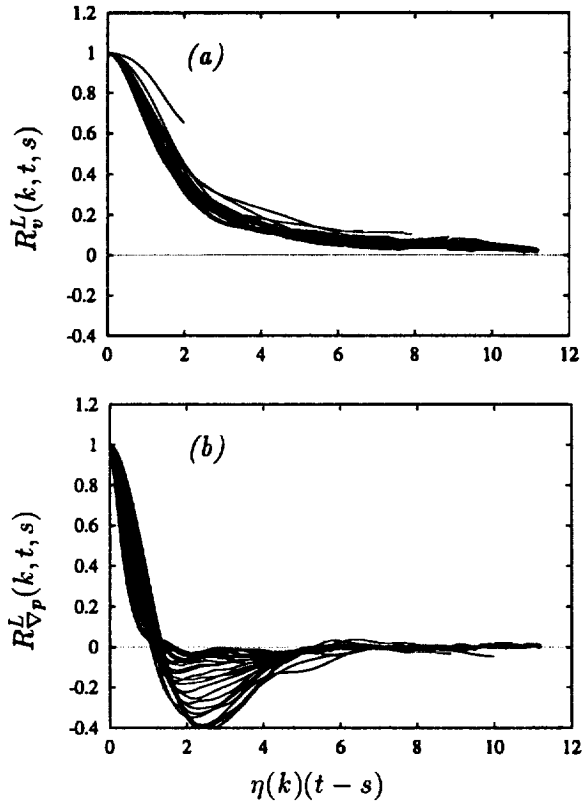

FIGURE 11. Time-scaled narrow-band Lagrangian correlations of velocity and pressure gradient for wavenumber-bands $k = 2 + 2n, n = 0, \cdots 29$ at $R_\lambda = 63$. (a) $R_v^L(k,t,s)$. (b) $R_{\nabla p}^L(k,t,s)$. The low-wavenumber bands display pronounced negative values.

plotted against the normalized time $kU_0(t-s)$. On the other hand, in Fig. 11, the narrow-band Lagrangian correlation spectra collapse when plotted against the normalized time $\eta(k)(t-s)$, where

$$\eta(k) = \left(\int_0^k q^2 E(q)\, dq \right)^{1/2} \tag{3.14}$$

is the rms strain rate of eddies larger than $1/k$ (the inverse of the turnover time for an eddy of that size), which is obtained from (1.5) by using the expansion of $J(x) \sim \frac{16\pi}{15} x$ for small x (Gotoh *et al* 1993). The success of these scalings is confirmed by a comparison of Figs. 10b and 11b with the unscaled data in Fig. 9.

4. Conclusions

Pressure statistics have been examined within a DNS of stationary isotropic turbulence. The one-point pdf of the pressure has an exponential tail for negative

fluctuations while that of the pressure gradient is symmetric and of stretched exponential form. The normalized variance of the pressure is insensitive to R_λ but the normalized variance of the pressure gradient increases as $R_\lambda^{1/2}$. The variances of both pressure and its gradient in the DNS are higher than those computed from a Gaussian field having the same energy spectrum.

The growth of intermittence across the pressure spectrum, characterized by the ratio of power spectra $P(k)/P_G(k)$, was found to be proportional to $-R_\lambda^{1/2}\log(k/k_d)$ for $k/k_d < 1/2$. The Lagrangian pressure-gradient correlation has a time scale much shorter than that of the velocity and its narrow-band spectra change sign at the normalized time $\eta(k)(t-s) \approx 1$. This is consistent with the notion of a fluid particle being accelerated toward the center of a vortex of size $1/k$ by the pressure gradient acting on that particle.

Previous theoretical analyses of these observations are rather scarce (Pullin 1994 and Nelkin 1994) due to the difficulty of dealing with the nonlocality in physical space of the Poisson equation for the pressure field. Most studies so far are based on the Gaussian velocity approximation, but intermittence effects in the pressure field are clearly evident in its one-point statistics as well as its spectrum. The construction of a theory that is able to explain these observations is a real challenge.

Acknowlegements

The authors have benefited from fruitful discussions with Profs. D. Pullin, Y. Kaneda, and Dr. R. H. Kraichnan. TG also expresses his thanks for partial support from the Tatematsu and the Daiko foundations.

REFERENCES

BATCHELOR, G. K. 1951 Pressure fluctuations in isotropic turbulence. *Proc. Camb. Phil. Soc.* **47,** 359-374.

FUNG, J. C. H., HUNT, J. C. R., MALIK, N. A., & PERKINS, R. J. 1992 Kinematic simulation of homogeneous turbulence by unsteady random Fourier modes. *J. Fluid Mech.* **236,** 281-318.

GOTOH, T., ROGALLO, R. S., HERRING, J. R., & KRAICHNAN, R. H. 1993 Lagrangian velocity correlations in homogeneous isotropic turbulence. *Phys. Fluids A.* **5,** 2846-2864.

GEORGE, W., BEUTHER, P. D., & ARNDT, R. E. 1984 Pressure spectra in turbulent free shear flows. *J. Fluid Mech.* **148,** 155-191.

HOLTZER, M. & SIGGIA, E. 1993 Skewed, exponential pressure distributions from Gaussian velocities. *Phys. Fluids A.* **5,** 2525-2532.

HUDONG, C., HERRING, J. R., KERR, R. M., & KRAICHNAN, R. H. 1987 Non-Gaussian statistics in isotropic turbulence. *Phys. Fluids A.* **1,** 1844-1854.

JIMÉNEZ, J., WRAY, A. A., SAFFMAN, P. G., & ROGALLO, R. S. 1993 The structure of intense vorticity in isotropic turbulence. *J. Fluid Mech.* **255,** 65-90.

KANEDA, Y. 1993 Lagrangian and Eulerian time correlations in turbulence. *Phys. Fluids A.* **5,** 2835-2845.

KANEDA, Y. & GOTOH, T. 1991 Lagrangian velocity autocorrelation in isotropic turbulence. *Phys. Fluids A.* **3,** 1924-1933.

KERR, R. M. 1985 High-order derivative correlations and the alignment of small-scale structures in isotropic numerical turbulence. *J. Fluid Mech.* **153,** 31-58.

KRAICHNAN, R. H. 1966 Isotropic turbulence and inertial-range structure. *Phys. Fluids.* **9,** 1728-1752.

MONIN, A. S. & YAGLOM, A. M. 1975 *Statistical Fluid Mechanics, Mechanics of Turbulence, Vol. 2.* MIT press.

NELKIN, M. 1994 Universality and scaling in fully developed turbulence. *Advances in Physics* (preprint).

NELKIN, M. & TABOR, M. 1990 Time correlations and random sweeping in isotropic turbulence. *Phys. Fluids A.* **2,** 81-83.

PULLIN, D. I. 1994 Pressure spectra for vortex models of fine-scale homogenous turbulence (preprint).

PUMIR, A. 1994 A numerical study of pressure fluctuations in three-dimensional, incompressible, homogeneous, isotropic turbulence. *Phys. Fluids.* **6,** 2071-2083.

UBEROI, M. S. 1953 Quadruple velocity correlations and pressure fluctuations in isotropic turbulence. *J. Aero. Sci.* **20,** 197-204.

YEUNG, P. K. & POPE, S. B. 1989 Lagrangian statistics from direct numerical simulations of isotropic turbulence. *J. Fluid Mech.* **207,** 531-586.

512-34
39542
N95-21047
207
P. 13

Center for Turbulence Research
Proceedings of the Summer Program 1994

The decay of axisymmetric homogeneous turbulence

By J. R. Chasnov[1]

The decay of a homogeneous turbulence generated by an axisymmetric distribution of random impulsive forces acting at the initial instant is considered. The impulsive forces may be either parallel or perpendicular to the symmetry axis. For impulsive forces which result in a k^4 low wavenumber energy spectrum of the turbulence, it is determined that the flow approaches isotropy on all scales of motion at long-times provided the Reynolds number is large. However, for the type of impulsive forces originally proposed by Saffman [*J. Fluid Mech* **27**, 581 (1967); *Phys. Fluids* **10**, 1349 (1967)] in which a k^2 low wavenumber energy spectrum is produced, the turbulence approaches isotropy only at the smallest scales and remains significantly anisotropic at the largest and energy-containing scales. Nevertheless, a similarity state of the flow field establishes itself asymptotically, in which the kinetic energy per unit mass of the turbulence decays as $t^{-6/5}$.

1. Introduction

An asymptotic similarity state of decaying isotropic turbulence was predicted by Kolmogorov (1941) based on a supposed dynamical invariant of the flow field (Loitsianski, 1939). It was later shown by theoretical arguments (Batchelor and Proudman, 1956) that the Loitsianski integral is in fact not invariant, and under certain conditions of turbulence generation may even diverge (Saffman, 1967a). For this Saffman-type flow, a new invariant was discovered and a similarity state of decaying homogeneous turbulence at high Reynolds numbers was postulated based on this invariant (Saffman, 1967b). Recent large-eddy simulations of isotropic turbulence (Chasnov, 1994) have confirmed the existence of this exact similarity state to within a few percent. Here, we extend these recent large-eddy simulations of isotropic turbulence to a decaying statistically axisymmetric flow field. Our main objective here is to determine if a long-time, high Reynolds number similarity state of decaying axisymmetric turbulence occurs. Of course, if the axisymmetric turbulence approaches isotropy asymptotically, then the earlier found similarity state would necessarily be recovered.

However, a complete return-to-isotropy of the turbulence is impossible for the Saffman-type of flow since the large-scale structure of the turbulence is preserved for all times. For instance, if the initial flow field was anisotropic due to some anisotropy in the method of turbulence generation, then this initial anisotropy would remain in the large-scales of the flow for all times. Of course, the small scales of the flow

1 The Hong Kong University of Science and Technology

PRECEDING PAGE BLANK NOT FILMED PAGE 206 INTENTIONALLY BLANK

may become isotropic, but the main scales of interest to us here with regards to an asymptotic similarity state are those which contain most of the energy of the turbulence; these scales may be more directly affected by the presence of large-scale anisotropy.

Previous closure calculations and numerical simulations have studied the decay of an initially axisymmetric turbulence (Herring, 1974; Schumann and Herring, 1976; Schumann and Patterson, 1978) in the context of the return-to-isotropy problem. The direct numerical simulations performed in the latter two works were necessarily limited to low Reynolds numbers, and the computer resources available at those times allowed only a resolution of 32^3. Nevertheless, an approach of the anisotropic initial state towards isotropy was indicated.

This earlier work postulated arbitrary initial states of the axisymmetric turbulence without considering whether or not the large-scale structure of the flow was invariant. Here, following closely the work of Saffman (1967a), we assume that our initial flow fields are generated by random axisymmetric impulsive forces at the initial instant such as may be generated by laminar flow passing through a vigorously shaken grid. We consider impulsive forces which are either parallel or perpendicular to the symmetry axis. Both the Saffman-type flow and the original Batchelor-Proudman flow will also be considered. In the latter type of flow, the large-scale structure of the turbulence is not permanent due to nonlinear transfer from small-to-large scales, so that a return-to-isotropy of all scales of motion is possible.

2. Generation by random axisymmetric impulsive forces

We consider an infinite incompressible fluid initially at rest to which is applied random impulsive forces at the initial instant. The continuity and Navier-Stokes equations which govern the fluid motion are

$$\nabla \cdot \mathbf{u} = 0, \tag{1}$$

$$\frac{\partial \mathbf{u}}{\partial t} + \mathbf{u} \cdot \nabla \mathbf{u} = -\frac{\nabla p}{\rho_0} + \nu \nabla^2 \mathbf{u} + \mathbf{f}\delta(t), \tag{2}$$

where $\mathbf{f}$ is the impulsive force field per unit mass distributed throughout the fluid; we assume that this vector force field is a stationary random function of the coordinate $\mathbf{x}$. Its multiplier $\delta(t)$ is the usual Dirac-delta function, which confines the impulse to the initial instant. Eq. (2) may be integrated to $t = 0^+$ at which time the impulse ceases. Denoting the Fourier transform of $u_i(\mathbf{x}, t)$ by $\hat{u}_i(\mathbf{k}, t)$ and the Fourier transform of $f_i(\mathbf{x})$ by $\hat{f}_i(\mathbf{k})$, the Fourier components of the resulting impulse-generated velocity field at $t = 0^+$ is given by

$$\hat{u}_i(\mathbf{k}, 0^+) = P_{ij}(\mathbf{k})\hat{f}_j(\mathbf{k}), \tag{3}$$

where $P_{ij}(\mathbf{k}) = \delta_{ij} - k_i k_j; /k^2$, and δ_{ij} is the usual Kronecker-delta. The projection operator $P_{ij}(\mathbf{k})$ appearing on the right hand side of (3) occurs because the pressure forces respond to the initial impulse so as to maintain the incompressibility of the

fluid. The spectral tensor $\Phi_{ij}(\mathbf{k},t)$ of the velocity correlation after the fluid is acted on by the impulsive forces is thus given by

$$\Phi_{ij}(\mathbf{k},0^+) = P_{im}(\mathbf{k})P_{jn}(\mathbf{k})\mathcal{M}_{mn}(\mathbf{k}), \tag{4}$$

where $\mathcal{M}_{mn}(\mathbf{k})$ is the spectral tensor of the force correlation, which is assumed to exist. The result (4) was previously obtained by Saffman (1967a). We now specialize to two particular impulsive force distributions which exhibit statistical axisymmetry and could conceivably be generated in a laboratory experiment.

2.1 Impulse parallel to the symmetry axis

The physical situation we envision is that of grid-generated turbulence in which the grid is randomly shaken along the direction of the mean fluid velocity. The impulsive force of the grid on the fluid should ideally be a stationary random function of time and of the coordinates in the plane perpendicular to the mean velocity. Taylor's hypothesis can then be invoked to relate the grid turbulence experiment to the decaying homogeneous turbulence considered here.

We shall, without loss of generality, assume symmetry about the x_3 axis. The spectral tensor of the force correlation corresponding to the above physical experiment can be written as

$$\mathcal{M}_{ij}(\mathbf{k}) = \delta_{i3}\delta_{j3}M(\mathbf{k}), \tag{5}$$

and the corresponding spectral tensor of the velocity correlation generated at the initial instant thus becomes

$$\Phi_{ij}(\mathbf{k},0^+) = P_{i3}(\mathbf{k})P_{j3}(\mathbf{k})M(\mathbf{k}). \tag{6}$$

It will be convenient to write the spectral tensor in terms of two unit vectors which are perpendicular to $\mathbf{k}$ and thus explicitly satisfy the continuity equation (Herring, 1974). These unit vectors are defined as

$$\mathbf{e}^{(1)}(\mathbf{k}) = \frac{\mathbf{k}\times\mathbf{n}}{|\mathbf{k}\times\mathbf{n}|}, \qquad \mathbf{e}^{(2)}(\mathbf{k}) = \frac{\mathbf{k}\times\mathbf{e}^{(1)}(\mathbf{k})}{|\mathbf{k}\times\mathbf{e}^{(1)}(\mathbf{k})|}, \tag{7}$$

where $\mathbf{n} = (0,0,1)$ is the unit vector along the symmetry axis. Using the relation $P_{ij}(\mathbf{k}) = e_i^{(1)}(\mathbf{k})e_j^{(1)}(\mathbf{k}) + e_i^{(2)}(\mathbf{k})e_j^{(2)}(\mathbf{k})$, it is easy to show that (6) becomes

$$\Phi_{ij}(\mathbf{k},0^+) = \left(1 - \frac{k_3^2}{k^2}\right) e_i^{(2)}(\mathbf{k})e_j^{(2)}(\mathbf{k})M(\mathbf{k}). \tag{8}$$

2.2 Impulse perpendicular to the symmetry axis

Here, the grid-generated turbulence experiment we envision is the same as above except that now the grid is randomly shaken in the direction perpendicular to the mean fluid velocity. To maintain the statistical axisymmetry of the force distribution and the resulting flow field, we assume that the random impulsive forces acting on

the fluid have no preferred direction in the plane perpendicular to the symmetry axis. The spectral tensor of the force correlation may now be written as

$$\mathcal{M}_{ij}(\mathbf{k}) = \frac{1}{2}(\delta_{ij} - \delta_{i3}\delta_{j3})M(\mathbf{k}), \tag{9}$$

where the factor of 1/2 has been inserted for later convenience. The spectral tensor of the velocity correlation at the initial instant thus becomes

$$\Phi_{ij}(\mathbf{k}, 0^+) = \frac{1}{2}\left[P_{ij}(\mathbf{k}) - P_{i3}(\mathbf{k})P_{j3}(\mathbf{k})\right] M(\mathbf{k}), \tag{10}$$

which in terms of the e-basis can be written as

$$\Phi_{ij}(\mathbf{k}, 0^+) = \frac{1}{2}\left[e_i^{(1)}(\mathbf{k})e_j^{(1)}(\mathbf{k}) + \frac{k_3^2}{k^2}e_i^{(2)}(\mathbf{k})e_j^{(2)}(\mathbf{k})\right] M(\mathbf{k}). \tag{11}$$

2.3 Specification of the spectral tensor of the force correlation

The initial spectrum of the homogeneous turbulence flow field immediately after generation by the random impulsive forces is now completely specified provided the form of the spectrum $M(\mathbf{k})$ of the force correlation is known. For simplicity, we assume that M is a function only of the wavenumber magnitude k. The general form we choose for $M(k)$ is

$$M(k) = \frac{3}{8\pi}a_s u_0^2 k_p^{-3}\left(\frac{k}{k_p}\right)^{s-2}\exp\left[-\frac{1}{2}s\left(\frac{k}{k_p}\right)^2\right], \tag{12}$$

where u_0 is the root-mean-square velocity of the fluid immediately after generation by both types of impulsive force distributions, k_p is the wavenumber at which the initial spherically integrated energy spectrum of the turbulence is maximum, and $s = 2$ or 4, corresponding either to a Saffman-type flow (Saffman, 1967) or a Batchelor-Proudman-type flow (Batchelor & Proudman, 1956), further details of which will be presented in the next Section. The normalization constant a_s is given by

$$a_s = \sqrt{\frac{2}{\pi}}\frac{s^{\frac{1}{2}(s+1)}}{1\cdot 3\cdot\cdots\cdot(s-1)}. \tag{13}$$

3. Possible similarity states

We consider whether a similarity state of the decaying turbulence develops asymptotically in time provided the Reynolds number of the flow is large. Saffman (1967a) has shown that when $s = 2$ in (12), the form of the spectral tensor, (8) or (11), persists for all times near $k = 0$. It is customary to define the associated dynamical invariant of the flow field in terms of the leading-order spectral coefficient of the spherically-integrated energy spectrum $E(k)$. By spherically-integrating either (8) or (11), using (12), the energy spectrum at the initial instant can be shown to have the form

$$E(k,0^+) = \frac{1}{2}a_s u_0^2 k_p^{-1} \left(\frac{k}{k_p}\right)^s \exp\left[-\frac{1}{2}s\left(\frac{k}{k_p}\right)^2\right], \tag{14}$$

so that when $s = 2$, $E(k,t)$ behaves for all times near $k = 0$ as $E(k,t) \sim 2\pi k^2 B_0$, where

$$B_0 = \frac{a_2 u_0^2}{4\pi k_p^3} \tag{15}$$

is a dynamical invariant. Normalization constants in (12) have been chosen so that (14) agrees with our previous large-eddy simulations of decaying isotropic turbulence (Chasnov, 1994).

A similarity state of the turbulence which is now based on the invariant B_0 leads directly to the decay of the mean-square kinetic energy per unit mass as (Saffman, 1967b)

$$\langle \mathbf{u}^2 \rangle \propto B_0^{\frac{2}{5}} t^{-\frac{6}{5}}. \tag{16}$$

The power-law exponent $-6/5$ was verified to within a few percent in a decaying isotropic turbulence (Chasnov, 1994). Saffman (1967a) has further speculated that the decay law given by (16) may be valid for a decaying turbulence which does not exhibit isotropic symmetry, and one of the purposes of the present work is to test this hypothesis.

When the initial impulsive force distribution is such that $s = 4$ in (14), the spherically integrated three-dimensional energy spectrum of the turbulence follows $E(k) \sim 2\pi k^4 B_2$ near $k = 0$, where now $B_2 = B_2(t)$ is a function of time, as shown analytically by Batchelor and Proudman (1957). Lesieur and collaborators (Lesieur, 1990), following earlier work of Kolmogorov (1941) and Comte-Bellot and Corrsin (1966), have postulated a similarity state of the flow field based on $B_2(t)$, which was then confirmed within the framework of two-point closure calculations. A numerical calculation of $B_2(t)$ was also performed by computing an ensemble average of a large number (1024) of large-eddy simulations of decaying isotropic turbulence (Chasnov, 1993). From the two-point closure calculations and large-eddy simulations, the time-dependence of $B_2(t)$ has been shown to be weak relative to the overall turbulence decay (the large-eddy simulations of isotropic turbulence determined approximately $B_2(t) \sim t^{0.25}$). The decay of the mean-square kinetic energy per unit mass may thus be written as

$$\langle \mathbf{u}^2 \rangle \propto B_2^{\frac{2}{7}} t^{-\frac{10}{7}}, \tag{17}$$

where the power-law exponent $-10/7$ is only approximate (a more precise exponent of -1.36 results when the time-dependence of B_2 is taken into account).

Of special interest to the present work is the approach of the initially axisymmetric turbulence to isotropy. As a simple measure of the anisotropy of the energy containing scales, we define the parameter γ to be

$$\gamma(t) = \frac{2\langle u_3^2 \rangle}{\langle u_1^2 + u_2^2 \rangle}. \tag{18}$$

The value of γ is easily computed for the flow fields generated at the initial instant: we determine that $\gamma(0) = 8$ or $\gamma(0) = 2/9$ for impulsive forces which are parallel or perpendicular to the symmetry axis, respectively. Non-linear transfer processes may reasonably be expected to bring the turbulence closer to statistical isotropy ($\gamma = 1$) at later times.

We have already noted an interesting difference between flows with $s = 2$ or 4 in (12) which may affect the eventual return-to-isotropy of the flow fields. When $s = 2$ in (12), the permanence of the large-scale structure of the flow precludes the entire flow from ever becoming isotropic. However, the parameter γ is primarily a measure of the anisotropy of the energy-containing scales so it is yet unclear whether these scales will approach isotropy, or whether the anisotropy present in the largest scales will affect the asymptotic state of the energy-containing scales. When $s = 4$ in (12), the large-scale structure of the turbulence is no longer preserved for all times since the low wavenumber coefficients of the spectral tensor are no longer invariant. It is plausible, although perhaps not entirely obvious, that non-linear interactions can in this case produce an isotropic flow field asymptotically in time for sufficiently large Reynolds numbers.

Large-eddy simulations presented in the next Section will shed further light on the existence of an asymptotic similarity state in decaying axisymmetric turbulence, and the approach (or non-approach) to isotropy of the flow fields.

4. Large-eddy simulation

The large-eddy simulations presented here were performed using a pseudospectral code for turbulence in a periodic box of length 2π (Rogallo, 1981), and a spectral eddy-viscosity subgrid-scale model (Kraichnan, 1976; Chollet and Lesieur, 1981). More details about the large-eddy simulation technique can be found in Chasnov (1994). Four 128^3 resolution simulations were performed corresponding to an impulse parallel or perpendicular to the symmetry axis, and $s = 2$ or 4 in (12) and (14). We also choose $u_0 = 1$ and $k_p = 50$. The relatively large value of k_p allows a similarity state to develop before the integral scales of the flow grow to a size comparable to the periodicity length.

Particular realizations of the impulsive-force-generated velocity fields are constructed as follows. By virtue of the continuity equation, the Fourier components of the velocity field may be projected onto the two unit vectors perpendicular to $\mathbf{k}$ given by (7):

$$u_i(\mathbf{k}) = \phi_1(\mathbf{k}) e_i^{(1)}(\mathbf{k}) + \phi_2(\mathbf{k}) e_i^{(2)}(\mathbf{k}). \tag{19}$$

When the impulsive forces are parallel to the symmetry axis, the spectral tensor at $t = 0^+$ is given by (8) with $M(k)$ given by (12), and we construct random fields which satisfy (8) by setting

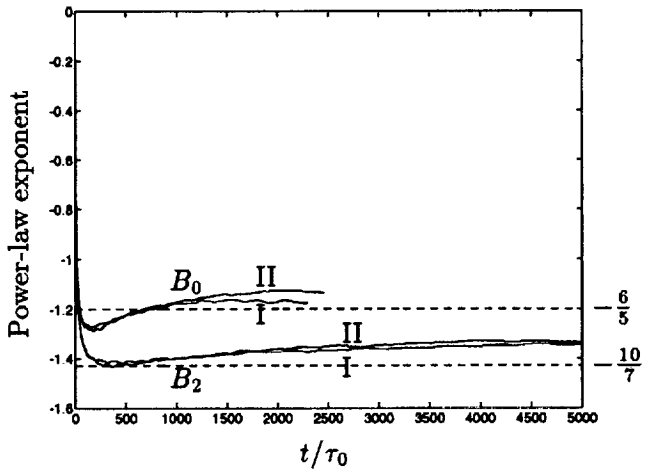

FIGURE 1. Time-evolution of the power-law exponent of $\langle \mathbf{u}^2 \rangle$. The solid lines correspond to the results of the four large-eddy simulations and the dashed lines correspond to the Saffman and Kolmogorov laws discussed in Section 3. The curves are labelled by B_0 and B_2 corresponding to $s = 2$ or 4 in (12), respectively; and by I and II corresponding to impulsive forces parallel or perpendicular to the symmetry axis, respectively.

$$\phi_1(\mathbf{k}) = 0, \qquad \phi_2(\mathbf{k}) = \left[\left(1 - \frac{k_3^2}{k^2}\right) M(k)\right]^{\frac{1}{2}} \exp i2\pi\theta, \tag{20}$$

where θ is a uniformly distributed random number between 0 and 1, chosen independently for each $\mathbf{k}$ subject to the complex conjugate symmetry of the Fourier components of the velocity field. Similarly, when the impulsive forces are perpendicular to the symmetry axis, the relevant equations are (11) and (12), and the random fields are chosen as

$$\phi_1(\mathbf{k}) = \left[\frac{M(k)}{2}\right]^{\frac{1}{2}} \exp i2\pi\theta_1, \qquad \phi_2(\mathbf{k}) = \frac{k_3}{k}\left[\frac{M(k)}{2}\right]^{\frac{1}{2}} \exp i2\pi\theta_2, \tag{21}$$

with θ_1 and θ_2 random numbers as above. The three components of the velocity field may then be determined directly from (20) and (21) using (19). The particular realization of the velocity field constructed above is a generalization of the method proposed by Rogallo (1981) for isotropic turbulence.

In Fig. 1, we present the time-evolution of the power-law exponent (logarithmic derivative) of $\langle \mathbf{u}^2 \rangle$. Time is normalized in terms of the initial large-eddy turnover time τ_0, where $\tau_0 = L_0/u_0$, and L_0 is the initial spherically-averaged integral scale of the flow, given by $L_0 = \sqrt{\pi}/k_p$ for $s = 2$ and $L_0 = 2\sqrt{2\pi}/3k_p$ for $s = 4$. The curves are labeled by B_0 or B_2, the leading-order spectral coefficients of the energy spectrum corresponding to $s = 2$ or 4 in (12), and the Roman number I or

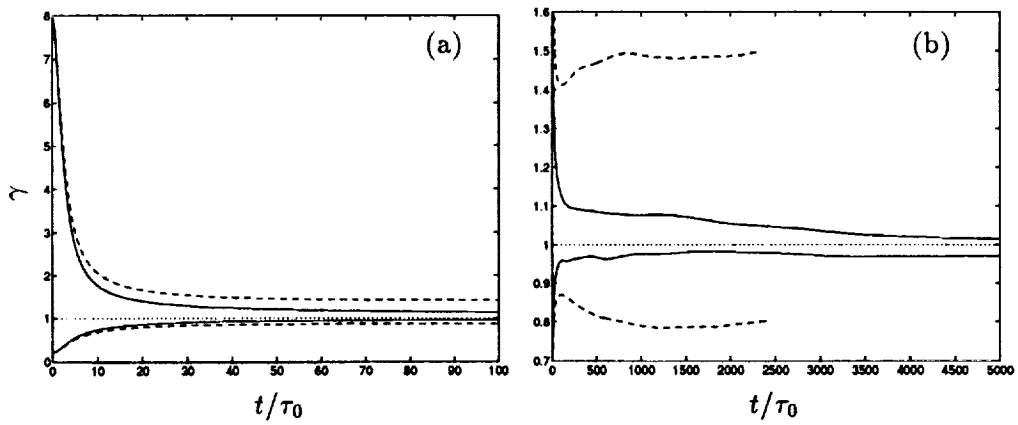

FIGURE 2. Time-evolution of the anisotropy factor γ, defined in (18). The dashed and solid lines correspond to $s = 2$ and $s = 4$ in (12), respectively; $\gamma = 1$ for an isotropic turbulence. Curves above or below $\gamma = 1$ correspond to impulsive forces parallel or perpendicular to the symmetry axis, respectively. (a) Short time evolution to $t/\tau_0 = 100$; (b) Long time evolution to $t/\tau_0 = 5000$.

II, corresponding to whether the impulsive forces are parallel or perpendicular to the symmetry axis, respectively. The dashed lines are the exact and approximate results discussed in Section 3. It is immediately apparent that similarity states in good agreement with either the Saffman and Kolmogorov laws develop in all of the simulations.

An evolution of the anisotropy parameter $\gamma(t)$ as defined in Eq. (18), for short- and long-time evolutions, is shown in Fig. 2. Over short-time evolutions, it is apparent that all four of the flow fields rapidly become more isotropic than the initial state. However, consideration of the long-time asymptotics of γ clearly demonstrates that only when $s = 4$ (solid-lines) does γ approach its isotropic value of unity, whereas when $s = 2$ (dashed- lines), γ deviates substantially from unity at the latest times. In fact, the asymptotic values of γ for these Saffman-type flows are approximately $\gamma \to 1.5$ or $\gamma \to 0.8$ for impulsive forces parallel or perpendicular to the symmetry axis, respectively.

The anisotropy of turbulent eddies should depend on their length scales. To observe this effect, we apply the projection of the velocity field defined in (19) to construct the following spherically-integrated spectral functions:

$$F_1(k,t) = 4\pi k^2 \langle \phi_1(\mathbf{k},t)\phi_1^*(\mathbf{k},t)\rangle, \qquad F_2(k,t) = 4\pi k^2 \langle \phi_2(\mathbf{k},t)\phi_2^*(\mathbf{k},t)\rangle, \tag{22}$$

where $*$ denotes the complex conjugate, and the angular brackets used here denote an average over a spherical shell (of unit thickness) in wave space. The usual energy spectrum is obtained from $E(k,t) = \frac{1}{2}(F_1(k,t) + F_2(k,t))$. In an isotropic turbulence $F_1(k,t) = F_2(k,t)$, and this will serve as an indication of isotropy for scales characterized by a wavenumber magnitude k. In Figs. 3(a) and 3(b) we

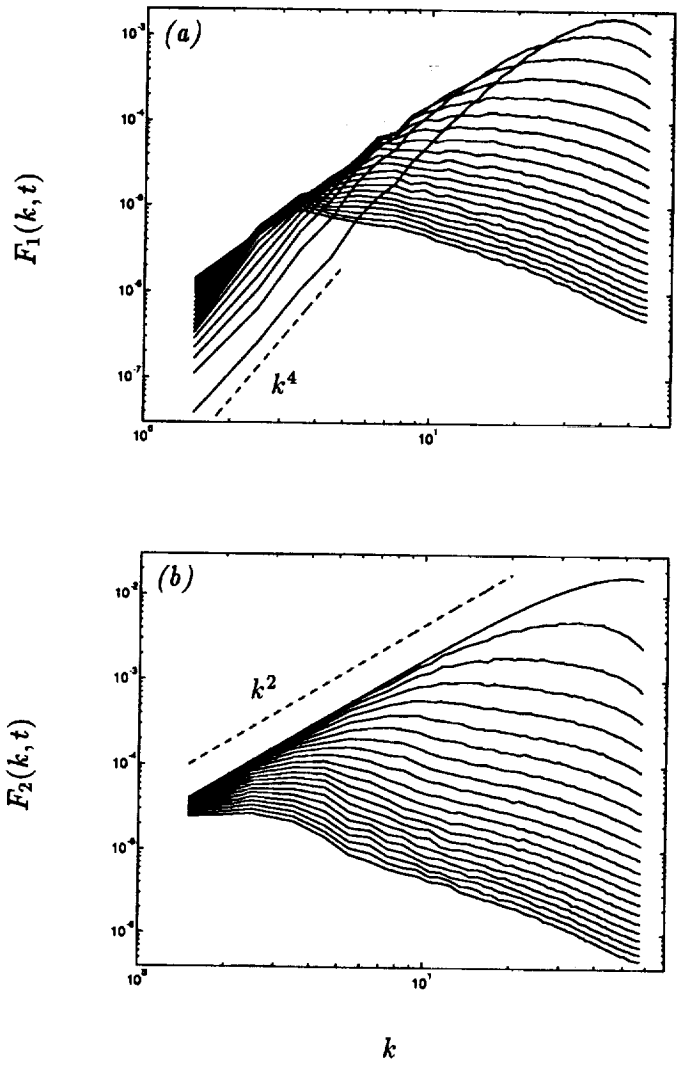

FIGURE 3. Time-evolution of the spectra defined in (22), for $s = 2$ in (12) and impulsive forces parallel to the symmetry axis. (a) $F_1(k,t)$; (b) $F_2(k,t)$.

plot the $F_1(k,t)$ and $F_2(k,t)$ spectra computed from the flow simulation when the impulsive forces are parallel to the symmetry axis and $s = 2$ in (12). At the initial instant, $F_1(k,0^+) = 0$, as seen from (20). The spectrum of $F_1(k,t)$ develops rapidly in time and a k^4 low wavenumber spectral form becomes apparent at small wavenumbers due to the nonlinear transfer of energy from small-to-large scales. The form of the $F_2(k,t)$ spectrum as $k \to 0$ is exactly $4\pi B_0 k^2$ for all times.

Using the invariant B_0, asymptotic similarity states can be constructed for the spectra $F_1(k,t)$ and $F_2(k,t)$:

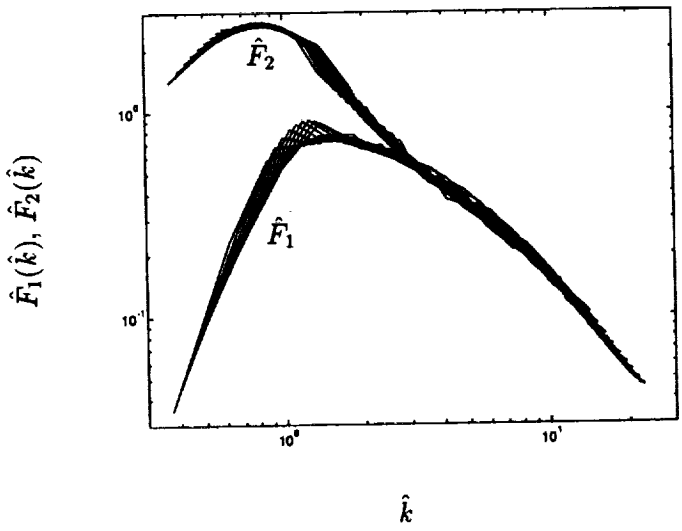

FIGURE 4. Time-evolution of the similarity spectra defined in (23), for $s = 2$ in (12) and impulsive forces parallel to the symmetry axis.

$$F_1(k,t) = B_0^{\frac{3}{5}} t^{-\frac{4}{5}} \hat{F}_1(\hat{k}), \qquad F_2(k,t) = B_0^{\frac{3}{5}} t^{-\frac{4}{5}} \hat{F}_2(\hat{k}), \qquad \hat{k} = B_0^{\frac{1}{5}} t^{\frac{2}{5}} k. \tag{23}$$

The last nine spectra of Figs. 3a and 3b are replotted on the same graph in Fig. 4 using the scalings given by (23). An excellent collapse of the $\hat{F}_1(\hat{k})$ and $\hat{F}_2(\hat{k})$ spectra at different times is observed. Furthermore, the collapse of $\hat{F}_1(\hat{k})$ and $\hat{F}_2(\hat{k})$ together at large values of $\hat{k}$ indicates an approach of the small-scale turbulence to isotropy. Clearly, however, the flow remains anisotropic at the largest and energy-containing scales, as already indicated by the deviation of γ from unity at large times. Apparently, the local value of $\gamma = 8$ for the largest scales of the flow, and $\gamma = 1$ for the smallest scales results in a balance in the energy containing scales of $\gamma \approx 1.5$.

An interesting result can be obtained from the similarity state given in (23) and confirmed by the results of Fig. 4. The form of the $F_1(k,t)$ spectrum near $k = 0$ can be written as

$$F_1(k,t) \sim C(t)k^4, \tag{24}$$

where, as we have already noted, the k^4 spectrum arises from the nonlinear transfer from small-to-large scales. Substitution of this low wavenumber form of the $F_1(k,t)$ spectrum into (23), and using the independence of $\hat{F}_1(\hat{k})$ on t and B_0, yields the exact result

$$C(t) \propto B_0^{\frac{7}{5}} t^{\frac{4}{5}}. \tag{25}$$

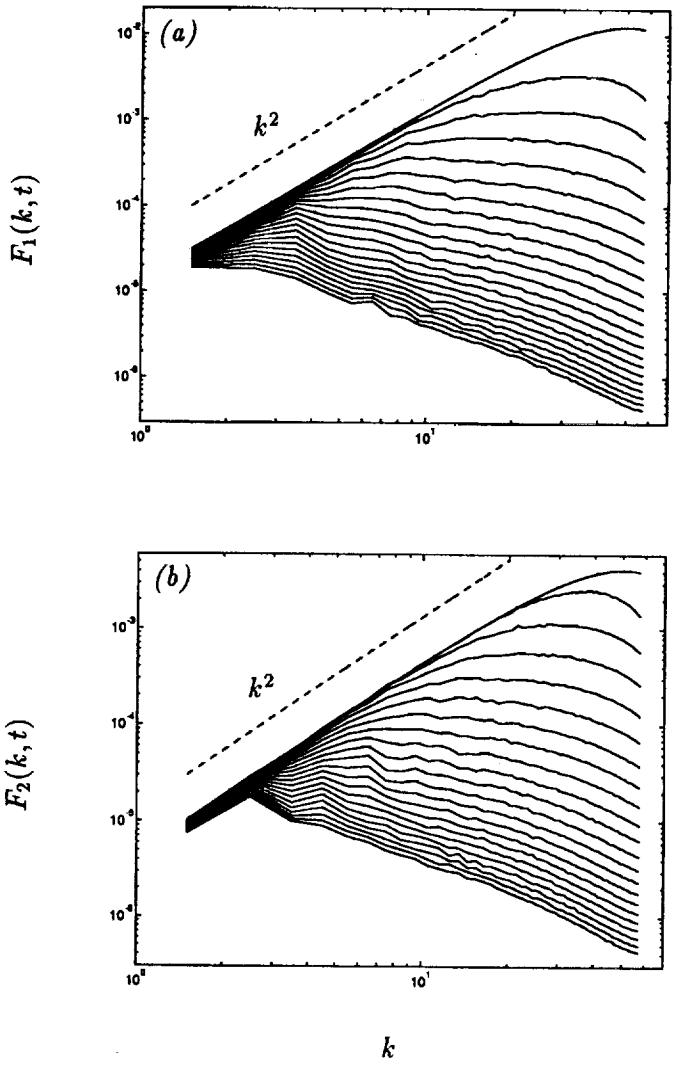

FIGURE 5. Time-evolution of the spectra defined in (22), for $s = 2$ in (12) and impulsive forces perpendicular to the symmetry axis. (a) $F_1(k,t)$; (b) $F_2(k,t)$.

Hence, we have determined the large-scale structure of the turbulence characterized by the spectrum $F_1(k,t)$, even though this structure is a consequence of complicated non-linear interactions.

Similar ideas apply when the impulsive forces are perpendicular to the symmetry axis. In Figs. 5, the time-evolution of the $F_1(k,t)$ and $F_2(k,t)$ spectra are plotted. The forms of the $F_1(k,t)$ and $F_2(k,t)$ spectra near $k = 0$ are $F_1(k,t) \sim 3\pi B_0 k^2$ and $F_2(k,t) \sim \pi B_0 k^2$ for all times. The rescaled spectra are plotted in Fig. 6 and again we find that the largest scales and the energy-containing scales of the flow remain anisotropic at the latest times, and the smallest scales approach isotropy.

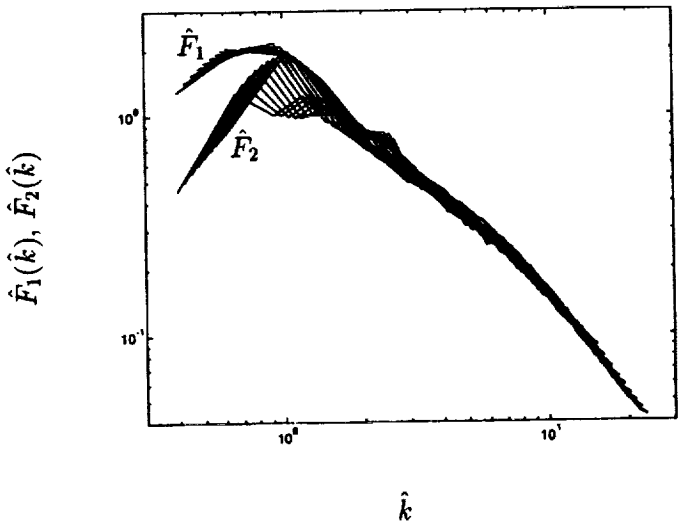

FIGURE 6. Time-evolution of the similarity spectra defined in (23), for $s = 2$ in (12) and impulsive forces perpendicular to the symmetry axis.

When $s = 4$ in (12) (and (14)), corresponding to a Batchelor-Proudman-type flow, the turbulence becomes isotropic asymptotically and the present results reduce to the decay of an isotropic turbulence, whose asymptotic similarity state has already been discussed in sufficient detail by Chasnov (1994).

5. Conclusions

We have thus demonstrated the existence of asymptotic similarity states of a decaying axisymmetric turbulence at high Reynolds numbers. A complete return-to-isotropy of the turbulence occurs in Batchelor-Proudman type flows but does not occur in Saffman-type flows due to the permanence of the anisotropic structure of the large scales. Simulations were performed based on initial flow fields which were generated by axisymmetric random impulsive forces acting at the initial instant. Such a turbulence generation mechanism has an analogy in active grid turbulence experiments, and it would be of interest to see if the results obtained here may be reproducible in the laboratory.

Acknowledgments

I wish to thank R. Rogallo and A. Wray for allowing me use of their homogeneous turbulence code for the Intel iPSC/860 hypercube machine at NAS. I would also like to thank C. Cambon, P. Durbin, N. Mansour, and K. Squires for useful discussions during the Summer Program.

REFERENCES

BATCHELOR, G. K. AND PROUDMAN, I. 1956 The large-scale structure of homogeneous turbulence. *Philos. Trans. R. Soc. London.* **248,** 369.

CHASNOV, J. R. 1993 Computation of the Loitsianski integral in decaying isotropic turbulence. *Phys. Fluids A.* **5,** 2579.

CHASNOV, J. R. 1994 Similarity states of passive scalar transport in isotropic turbulence. *Phys. Fluids.* **6,** 1036.

CHOLLET, J. P., AND LESIEUR, M. 1981 Parameterization of small scales of three dimensional isotropic turbulence utilizing spectral closures. *J. Atmos. Sci.* **38,** 2747.

COMTE-BELLOT, G. AND CORRSIN, S. 1966 The use of a contraction to improve the isotropy of grid-generated turbulence. *J. Fluid Mech.* **25,** 657.

HERRING, J. R. 1974 Approach of axisymmetric turbulence to isotropy. *Phys. Fluids.* **17,** 859.

KOLMOGOROV, A. N. 1941 On degeneration of isotropic turbulence in an incompressible viscous liquid. *Dokl. Akad. Nauk. SSSR.* **31,** 538.

KRAICHNAN, R. H. 1976 Eddy viscosity in two and three dimensions. *J. Atmos. Sci.* **33,** 1521.

LESIEUR, M. 1990 *Turbulence in Fluids.* Kluwer Academic Publishers.

LOITSIANSKI, L. G. 1939 Some basic laws for isotropic turbulent flow. *Trudy Tsentr. Aero.-Giedrodin. Inst.* **440,** 31.

ROGALLO, R. S. 1981 Numerical experiments in homogeneous turbulence. NASA TM 81315.

SAFFMAN, P. G. 1967a The large-scale structure of homogeneous turbulence. *J. Fluid Mech.* **27,** 581.

SAFFMAN, P. G. 1967b Note on decay of homogeneous turbulence. *Phys. Fluids.* **10,** 1349.

SCHUMANN, U. AND HERRING, J. R. 1976 Axisymmetric homogeneous turbulence: a comparison of direct spectral simulations with the direct-interaction approximation. *J. Fluid Mech.* **76,** 755.

SCHUMANN, U. AND PATTERSON, G. S. 1978 Numerical study of the return of axisymmetric turbulence to isotropy. *J. Fluid Mech.* **88,** 711.

53-34
9743
P. 8

Center for Turbulence Research
Proceedings of the Summer Program 1994

N95-21048
221

Vortex ring instability and its sound

By R. Verzicco[1] AND K. Shariff[2]

This work carries earlier finite-difference calculations of the Widnall instability of vortex rings into the late non-linear stage. Plots of energy in azimuthal Fourier modes indicate that low-order modes dominate at large times; their structure and dynamics remain unexplored, however. An attempt was made to calculate the acoustic signal using the theory of Möhring (1978), valid for unbounded flow. This theory shows that only low-order azimuthal modes contribute to the sound. As a check on the effects of axial periodicity and a slip wall at large radius imposed by the numerical scheme, the acoustic integrals were also computed in a truncated region. Half of the terms contributing to the sound have large differences between the two regions, and the results are therefore unreliable. The error is less severe for a contribution involving only the $m = 2$ mode, and its low frequency is consistent with a free elliptic bending wave on a thin ring.

1. Introduction

Many shear flows of practical interest contain large-scale coherent motions, and some aspects of their dynamics must be responsible for the generation of sound (smaller scale motions affect the dynamics of the large scales but themselves radiate as higher order poles). What these aspects might be is difficult to identify from experiments since the most energetic or most visually apparent motions may not be the most radiative and a detailed knowledge of time-dependence is required. It is a usual procedure in fluid dynamics to extract from a flow the most representative structure with the hope that its evolution alone still retains the important features of the whole flow. In the present case the evolution of azimuthal instabilities on an isolated vortex ring is numerically simulated into the late non-linear stage. We are motivated by the following: (i) Observations using phased arrays of microphones which indicate that the acoustic source location in jets is near the end of the potential core where vortex ring structures break down (Bridges & Hussain 1987, p. 309). Implicit in the consideration of a single ring is the premise that the actual breakdown process does not involve interactions between rings. Factors which may be important in reality are enhanced growth-rate and mode selection due to mutual straining and tearing or pairing. (ii) A good fit (Shariff & Leonard 1992, p. 275) of the acoustic frequency of a turbulent vortex ring measured by Zaitsev *et al.* (1990) to the axisymmetric elliptic core ring but a poor fit to the elliptic bending mode. Further studies along these lines were carried out in Zaitsev & Ko'pev (1993)

1 Università di Roma, "La Sapienza", Dipartimento di Meccanica e Aeronautica
2 NASA Ames Research Center

PRECEDING PAGE BLANK NOT FILMED
PAGE 220 INTENTIONALLY

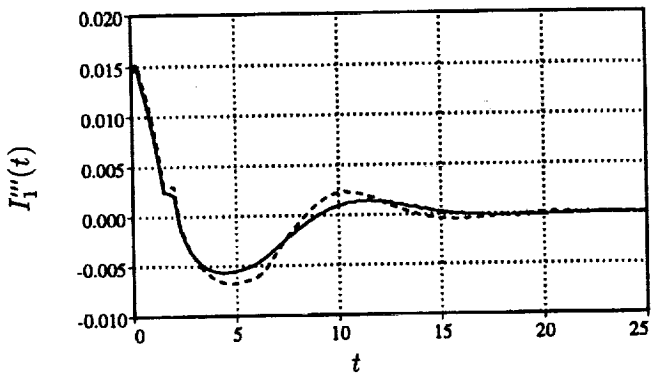

FIGURE 1. Acoustic signal due to axisymmetric elliptically distorted vortex ring. ——— , $\Gamma/\nu = 1200$; ---- , $\Gamma/\nu = 3000$.

and Kop'ev & Chernyshev (1993). (iii) The observations of Maxworthy (1977) of the development of swirling flow and a solitary bulge wave following the Widnall instability.

2. Methods

Calculations were performed using a second order finite difference code in cylindrical coordinates (x, r, ϕ) assuming axial periodicity (with length L_x) and a slip wall at $r = R_o$ as described in Verzicco & Orlandi (1993). The spurious straining due to the infinite row of rings and due to the wall is estimated to be less than 2% of the strain (due to ring curvature) which drives the instability. Units are chosen so that the circulation, Γ, and ring radius, R, are unity. To avoid effects of axisymmetric unsteadiness, a ring with an initially Gaussian core (of radius $\sigma = .4131$) and $\Gamma/\nu = 3000$ was axisymmetrically relaxed to a quasi steady state in which ω_ϕ/r becomes some function of the streamfunction. The number of grid intervals in each direction is 128 with a smaller radial spacing, obtained by a non uniform mesh, near the vortex core. The domain size is $R_o = L_x = 6$. A random divergence-free perturbation is applied to the basic-state velocity.

The acoustic pressure, p_a, is obtained from the theory of Möhring (1978):

$$p_a = \frac{\rho_o}{c_o^2}\frac{x_i x_j}{\Delta^3} Q_{ij}'''(t - \Delta/c_o), \quad Q_{ij} \equiv \frac{1}{12\pi}\int x_i(\mathbf{x}\times\boldsymbol{\omega})_j \, d^3x, \tag{1}$$

where $\Delta \equiv x_i x_i$. The triple prime denotes the third time derivative and is numerically evaluated using cubic splines. Due to the factor $x_i x_j$ only the symmetrized Q_{ij} are required, and in cylindrical coordinates one obtains:

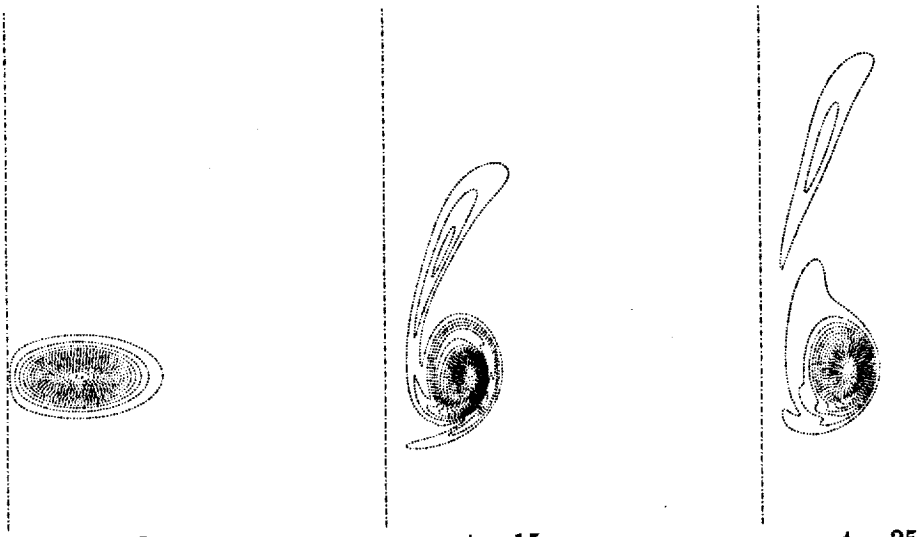

FIGURE 2. Contour-plots of azimuthal vorticity fon an elliptically distorted Gaussian core vortex ring at $\Gamma/\nu = 3000$. Contour increments are $\Delta = 0.1$, —·— , axis of symmetry. The ring motion is downward.

$$
\begin{aligned}
Q_{11} &= 2\pi I_1 \text{ (0 mode only)} \\
Q_{22} &= \frac{\pi}{2}(K_1 - I_4 - 2I_1 - I_8) \text{ (0 and 2 modes)} \\
Q_{33} &= \frac{\pi}{2}(I_4 - 2I_1 + I_8 - K_1) \text{ (0 and 2 modes)} \\
Q_{12} + Q_{21} &= \pi(I_2 - J_1 - J_2 + K_3) \text{ (1 mode only)} \\
Q_{13} + Q_{31} &= \pi(J_4 - J_3 - I_3 + K_2) \text{ (1 mode only)} \\
Q_{23} + Q_{32} &= \pi(I_6 - I_7 - K_5) \text{ (2 mode only)}
\end{aligned}
\tag{2}
$$

The various integrals in Eq. (2) are

$$
\begin{aligned}
&I_1 = \int xr^2\widetilde{\omega}_\phi(0)\,dxdr, \quad I_2 = \int xr^2\widehat{\omega}_x(1)\,dxdr, \quad I_3 = \int xr^2\widetilde{\omega}_x(1)\,dxdr, \\
&I_4 = \int xr^2\widehat{\omega}_r(2)\,dxdr, \quad I_6 = \int xr^2\widetilde{\omega}_r(2)\,dxdr, \quad I_7 = \int xr^2\widehat{\omega}_\phi(2)\,dxdr, \\
&I_8 = \int xr^2\widetilde{\omega}_\phi(2)\,dxdr, \quad J_1 = \int x^2r\widehat{\omega}_r(1)\,dxdr, \quad J_2 = \int x^2r\widetilde{\omega}_\phi(1)\,dxdr, \\
&J_3 = \int x^2r\widehat{\omega}_\phi(1)\,dxdr, \quad J_4 = \int x^2r\widetilde{\omega}_r(1)\,dxdr, \quad K_1 = \int r^3\widehat{\omega}_x(2)\,dxdr, \\
&K_2 = \int r^3\widehat{\omega}_\phi(1)\,dxdr, \quad K_3 = \int r^3\widetilde{\omega}_\phi(1)\,dxdr, \quad K_5 = \int r^3\widetilde{\omega}_x(2)\,dxdr,
\end{aligned}
\tag{3}
$$

where, for instance, $\widehat{\omega}_x(m)$ and $\widetilde{\omega}_x(m)$ denote the mth sin and cos azimuthal modes, respectively, of the axial vorticity. Note that only the modes $m \leq 2$ are involved.

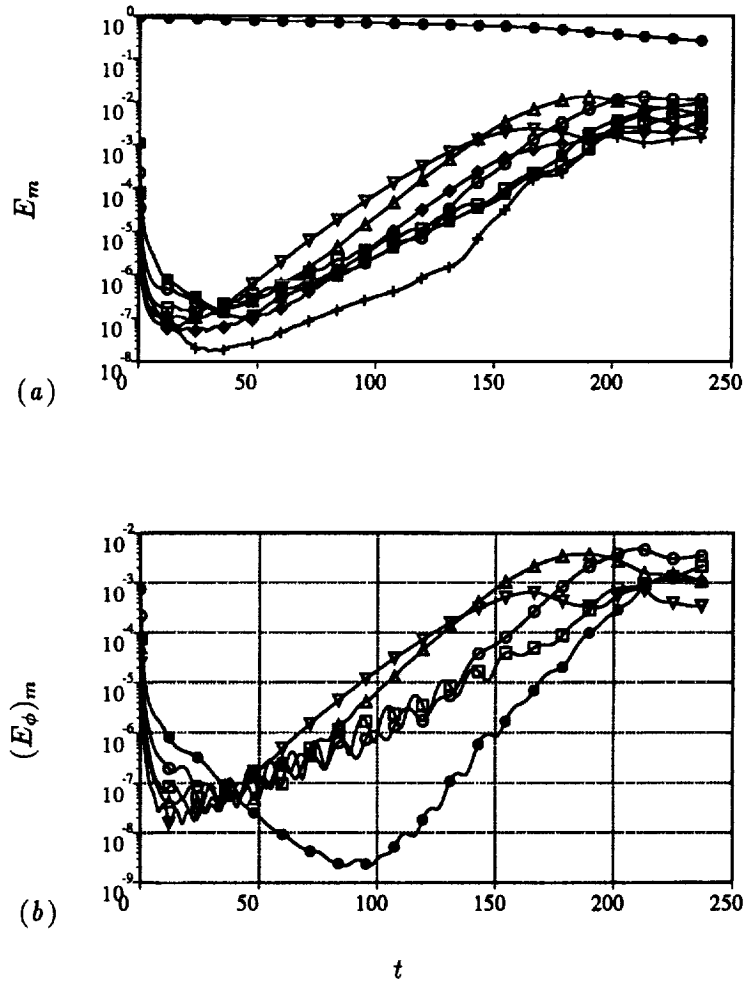

FIGURE 3. Evolution of energy in azimuthal modes. Mode index m: • , 0; ■ , 1; ○ , 2; □ , 3; △ , 4; ◇ , 5; ▽ , 6; + , 7. (a) Total energy. (b) Energy in azimuthal velocity component. Certain modes have been omitted for clarity.

The theory of Möhring is valid for an unbounded domain in which the vorticity decays exponentially at infinity. This holds provided the computational domain is large compared with the vortical region. As the ring leaves and re-enters the period, what its position would be in an unbounded domain is tracked in order to obtain an x value in the unbounded domain for every grid point. The field is phase shifted axially so that the vortical region is centered in the integration domain and mid-point rule quadrature is employed. To assess errors due to out-lying vorticity, integration is also performed in a smaller domain of radial and axial dimensions $R_T = 5R_o/6$ and $L_T = 5L_x/6$, respectively. As a test, the acoustic signal for an axisymmetric ring with an elliptically distorted Gaussian core was obtained (Fig. 1).

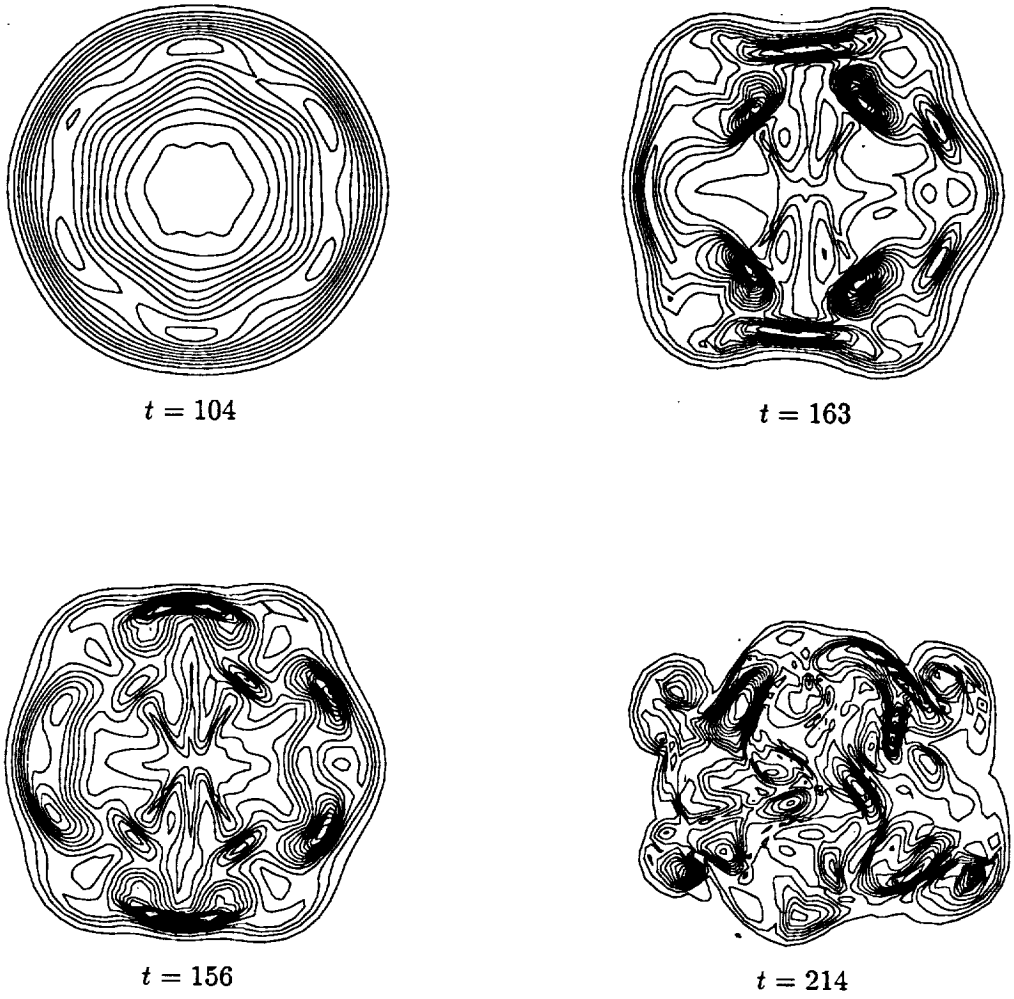

FIGURE 4. Contours of vorticity magnitude in the (r, θ) plane of maximum $|\,\omega\,|$. The spatial resolution of the simulation is twice the resolution of the figure.

It has the form of a damped cosine. The damping is due to the readjustment of the initial vorticity distribution towards an equilibrium distribution (Fig. 2). For an inviscid axisymmetric elliptic core ring with uniform vorticity, the acoustic signal is easily worked out (Shariff *et al.* 1989, p. 112) from the dynamics of Moore (1980). For the present case it is an undamped cosine with amplitude .022 which is close to the initial amplitude computed. Also, the period of the acoustic signal agrees with the theoretical prediction.

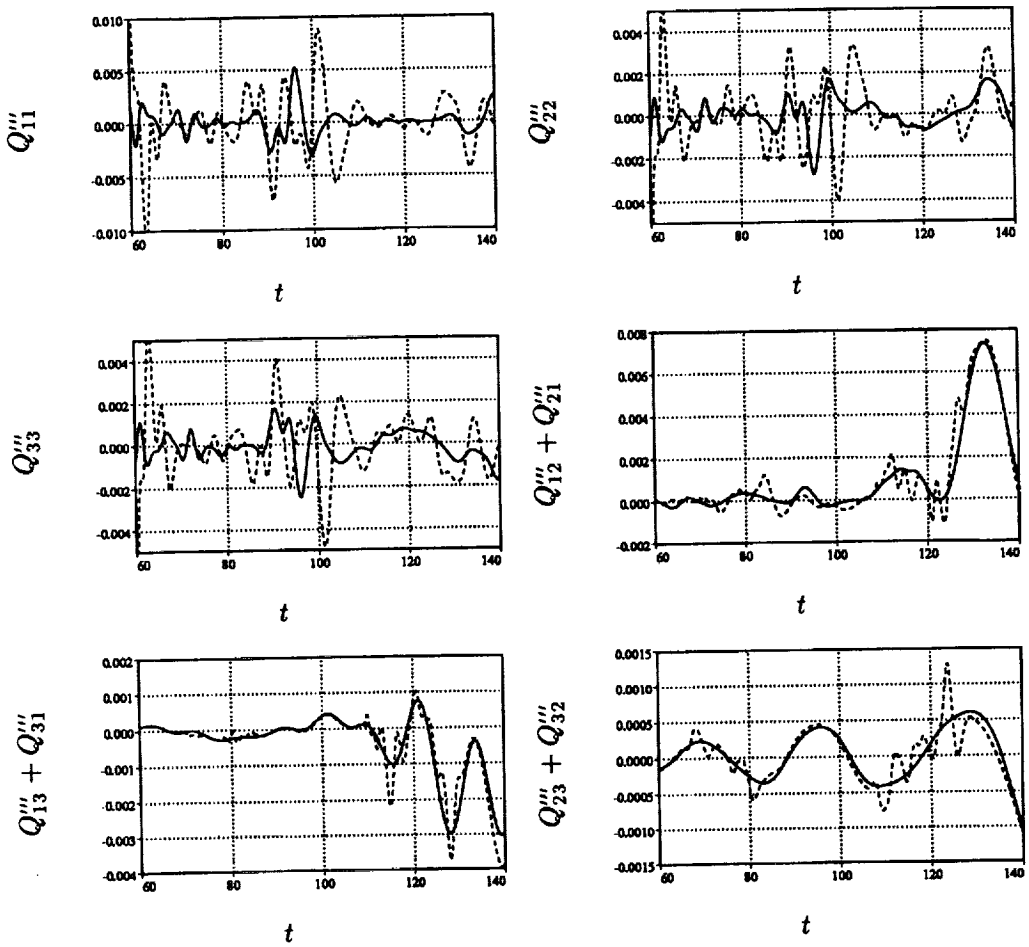

FIGURE 5. Acoustic components. ——— , Full-domain; ---- , Truncated domain.

3. Results

Applying the inviscid stability theory of Widnall *et al.* (1974), valid for thin cores, to the Gaussian profile, one finds that the so-called 'non-rotating second radial mode' corresponds to $m = 2.26R/\sigma = 5.47$ so that either $m = 5$ or 6 should be most unstable. The theory also predicts that there should be a band of growing modes around the most unstable one. Fig. 3*a* shows that the numerical result is consistent with this picture. Since the initial perturbation is not a combination of eigenmodes, there is an initial transient, after which the $m = 6$ mode is dominant showing a large range of linear growth. At $t = 150$ the $m = 6$ mode gives way to $m = 4$, likely due to viscous spreading of $\sigma(t)$; this switching of the dominant mode has also been previously observed by Hasselbrink (1992) and Shariff *et al.* (1994). At later times the non-linearly amplified $m = 1$ and 2 modes become dominant and all modes saturate. That the overall ring shape follows the dominant mode is shown in Fig. 4 where contour plots of $|\omega|$ in the (r, ϕ) plane of maximum $|\omega|$ are

displayed.

Maxworthy (1977) used dye visualization to infer that following breaking of the instability wave, a swirling flow developed in the azimuthal direction accompanied by a propagating solitary bulge wave. Fig. 3*b* plots modal energies in the azimuthal velocity component to illustrate the rapid development of a mean swirl (•). This fact together with the nonlinear growth of the $m = 1$ wave already shown in Fig. 3*a* may be related to Maxworthy's observation.

Fig. 5 shows contributions to the acoustic signal during the linear instability phase comparing the results for the full and truncated integration domains. For the diagonal terms the two domains have differences comparable to the amplitude. These terms involve the $m = 0$ and $m = 2$ modes. The off-diagonal terms have smaller differences mainly in the form of high frequency oscillations present in the truncated domain. The particle turn-around time is about 12 initially, and it corresponds to the period of acoustic oscillations due to an elliptically distorted core. On the other hand, the term $Q'''_{23} + Q'''_{32}$, which involves only the $m = 2$ mode, has a larger period. This is consistent with the frequency ratio of the two modes for thin uniform vorticity cores: using Eq. (35) in Widnall & Sullivan (1973) we obtain

$$\frac{f_{\text{elliptic ring}}}{f_{\text{elliptic core}}} = \sqrt{3}\frac{a^2}{R^2}\log(a/R),$$

which gives an estimate of 0.3 for the present case (a is the radius of the uniform vorticity core).

Further work using the same method should either focus on the sound for axially periodic flow (cylindrical wavefronts at infinity) using the appropriate acoustic analogy or employ a larger domain.

4. Conclusions

The time evolution of azimuthal instabilities on a thick isolated vortex ring into the late non-linear stage was studied by a numerical simulation of the Navier-Stokes equations. Initially the $m = 6$ mode is most amplified, consistent with the linear theory of Widnall *et al.* (1974). Subsequently, due to the viscous spreading of the ring, the $m = 6$ gave way to $m = 4$. In the late non-linear stage low order modes ($m = 2$ and $m = 1$) became dominant and a rapid growth of a mean swirl is present, which may be related to some dye observations of Maxworthy (1977).

The acoustic signal computed using the theory of Möhring (1978) was presented for the linear instability phase. Since this theory is valid for unbounded flow, each contribution (Q_{ij}) was computed in a full and in a truncated domain to estimate errors associated with outlying vorticity. The errors were quite large for the diagonal terms. Further work is needed to eliminate these errors.

REFERENCES

BRIDGES, J. E. & HUSSAIN, A. K. M. F. 1987 Roles of initial condition and vortex pairing in jet noise. *J. Sound. Vib.* **117**, 289–311.

HASSELBRINK, E. F. 1992 Breakdown and mixing in a viscous circular vortex ring. BS thesis, Dept. of Mech. Eng., Univ. Houston.

KOP'EV, V. F. & CHERNYCHEV, S. A. 1993 Sound radiation by high frequency oscillations of the vortex ring. AIAA Paper 93-4362. 15th Aeroacoustics Conf.

MAXWORTHY, T. 1977 Some experimental studies of vortex rings. *J. Fluid Mech.* **81,** 465–95.

MÖHRING, W. 1978 On vortex sound at low Mach number. *J. Fluid Mech.* **85,** 685–691.

MOORE, D. W. 1980 The velocity of a vortex ring with a thin core of elliptical cross-section. *Proc. Roy. Soc. Lond. A.* **370,** 407–415.

SHARIFF, K. & LEONARD, A. 1992 Vortex rings. *Ann. Rev. Fluid Mech.* **24,** 235–279.

SHARIFF, K., LEONARD, A. & FERZIGER, J. H. 1989 Dynamics of a class of vortex rings. NASA TM 102257

SHARIFF, K., VERZICCO, R. & ORLANDI, P. 1994 A numerical study of three-dimensional vortex ring instabilities: viscous corrections and early non-linear stage. *J. Fluid Mech.* **279,** 351–375.

VERZICCO, R. & ORLANDI, P. 1993 A finite-difference scheme for three-dimensional incompressible flows in cylindrical coordinates. Submitted to *J. Comput. Phys.*

WIDNALL, S. E., BLISS, D. B. & TSAI, C.-Y. 1974 The instability of short waves on a vortex ring. *J. Fluid Mech.* **66,** 35–47.

WIDNALL, S. E. & SULLIVAN, J. P. 1973 On the stability of vortex rings. *Proc. Roy. Soc. Lond. A.* **332,** 335–353.

ZAITSEV, M. Y., KOP'EV, V. F., MUNIN, A. G. & POTOKIN, A. A. 1990 Sound radiation by a turbulent vortex ring. *Sov. Phys. Dokl.* **35,** 488-489.

ZAITSEV, M. Y. & KOP'EV, V. F. 1993 Mechanism of sound generation by a turbulent vortex ring. *Acoust. Phys.* **39,** 562–565.

S14-34
N95-21049 229
P.16

Center for Turbulence Research
Proceedings of the Summer Program 1994

Instability of streamwise vortices in plane channel flows

By K. Coughlin[1], J. Jiménez[2] AND R. D. Moser[3]

We present analysis and numerical experiments on the instability of streamwise vortices in 'minimal channel' flows and argue that this instability is a key feature in the observed intermittent cycle of formation, break-up, and re-formation of these structures. The base flow is a three-component, two-dimensional pair of counter-rotating rolls with axes aligned along the direction of the mean shear. While it is not a steady solution to the Navier-Stokes equations, we show numerically that this flow is unstable on a fast time scale to a secondary, three-dimensional Floquet mode. The growth of the secondary instability does not saturate in a new equilibrium, but continues until highly unstable local shear layers form and the entire flow breaks down into turbulence. Our analysis is motivated in part by the strong similarities between the intermittent turbulent cycle in minimal channel flows and one studied, both experimentally and in computations, in Couette-Taylor flow.

1. Introduction

The existence of coherent structures in boundary layers has a significant effect on the dynamics of wall-bounded turbulence, and a great deal of work has been done to try to characterize and explain their dynamics. The structures have been identified as streamwise 'streaks' of relatively low speed fluid and are associated with the existence of pairs of counter-rotating, streamwise vortices. Dynamically, the streaks are created as part of a repeating cycle of formation, break-down, and regeneration. While the specific mechanisms of streak formation vary from case to case, certain characteristics of the break-down process appear to be quite general. In particular, the streaks are typically observed to become wavy with the waviness increasing until the coherence of the flow breaks down into turbulence.

A number of investigators have looked in more detail at the process of streak break-down in different situations. Swearingen & Blackwelder (1987), using Görtler vortices as an experimental model of the coherent structures in planar geometries, found that the resulting streaks were unstable to downstream traveling waves, and subsequently to a rapid breakdown into turbulence.

The instability was attributed to the spanwise velocity gradient created by the streamwise vortex/streak combination. Jiménez & Moin (1991), in numerical computations of plane Poiseuille flow in a doubly periodic channel, found that turbulence could be sustained provided that the the spanwise dimension was larger than

1 CERCA, University of Montreal, Canada
2 Center for Turbulence Research
3 NASA Ames Research Center

about 100 wall units. In these so-called 'minimal channels', the flow consists of a single low-velocity streak, which undergoes an intermittent cycle of onset and collapse of turbulence. The onset of turbulence is again associated with the appearance and growth of a sinusoidal perturbation of the streak. Hamilton *et al.* (1994), in minimal channel calculations of plane Couette flow, found the same type of intermittent, turbulent cycle and further evidence that breakdown of the streaks is associated with some kind of instability mechanism.

Recently, an intermittent turbulent cycle similar to those occurring in minimal channels was discovered experimentally in Couette-Taylor flow (Hammil *et al.*, 1994). In this system, fluid is confined between parallel, concentric cylinders which rotate independently. It can be thought of as a parallel shear layer with experimentally realizable, periodic boundary conditions in the streamwise direction. Using direct numerical simulations, Coughlin & Marcus (1994) have formulated a simple conceptual model which accounts for most of the observed features of the flow. The feature most relevant to this paper is that the onset of turbulence is directly attributable to a well-defined linear instability of coherent structures (Taylor vortices) in the flow. This supports the idea that there is some generic mechanism whereby streamwise vortical structures in a parallel shear become unstable, and their instability leads to the onset of turbulence.

The purpose of this paper is to investigate this idea further, making use of analogies with the Couette-Taylor system. In the latter, careful analysis of transient data and subsequent design of appropriate numerical experiments were used to verify that a linear mechanism was involved in the transition process. Briefly, coherent structures (spiral Taylor vortices) form in the Couette-Taylor system due to centrifugal instability, and then go unstable to secondary modes (modulated traveling waves). The spatial configuration of the secondary mode is such that, when it grows linearly to large enough amplitude, strong local shear layers are produced, and these trigger the sudden onset of the turbulence. The turbulence has a finite lifetime simply because energy is dissipated by turbulent fluctuations at a faster rate than the mean flow can draw energy through the torques at the walls. After the turbulence collapses, the coherent structures reform, and the cycle repeats (Coughlin & Marcus, 1994).

We hypothesize that essentially the same type of cycle is occurring in plane channel flows (we consider only the minimal channel, for which the cycle is roughly periodic in time). The analysis relies on treating the streamwise rolls/streaks as a quasi-equilibrium, and investigating their stability. We find that the rolls are indeed unstable to a secondary, three-dimensional mode, which can be characterized by its symmetry and time dependence. This mode grows linearly and, as in the Couette-Taylor system, its growth to large amplitude produces highly unstable local shear layers; hence, the transition to turbulence. The turbulence has a finite lifetime, the flow returns to its laminar configuration, and the cycle repeats. The intermittency in this cycle thus corresponds to quasi-regular excursions away from a flow configuration defined by the coherent structures plus the secondary mode.

In this paper, our focus is on the mathematical description of the instability for

several reasons. First, because it facilitates analysis of the physical mechanisms of instability. Second, because it is a necessary condition for modeling of the system: In our scenario, up to the onset of turbulence the flow is low-dimensional and, therefore, in principle can be modeled accurately using a small number of modes. From center manifold theory, we know that these modes must be the linear eigenmodes of the system and their nonlinear harmonics. The use of the right modes is essential to constructing models which can be useful in applications; if the modes chosen do not correspond to the real instabilities, there will be no reliable relation between the model parameters and the physical control parameters. Third, the state that the flow returns to during the laminar phase of each cycle, whether it is an equilibrium or not, is clearly an important starting point for trying to understand the more complex transition from order to turbulence. Flow visualizations verify that this state is the configuration characteristic of the coherent structures and their secondary instability mode.

The organization of the paper is as follows: In Section 2 we present a description of the conceptual model we propose for the intermittent turbulent cycle. We then give, in Section 3, a complete description of the symmetries in the problem, which have been used to verify some hypotheses of the model. Section 4 contains a presentation of the numerical results supporting the model, and Section 5 the conclusions and an outline of future work.

2. The conceptual model

2.1 Mathematical preliminaries

2.1.1 Definition of the channel

The base flow is assumed to be either plane Poiseuille (driven by a mean pressure gradient) or plane Couette (driven by motion of the walls). The channel half-width is h, and the velocity maximum (the centerline velocity for Poiseuille flow and the wall velocity for Couette flow) is U. The Reynolds number is Uh/ν, and we use U as the unit of velocity, h as the unit of length, and h/U as the unit of time. The velocities u, v, and w are the dimensionless streamwise (x), cross-stream (y), and spanwise (z) components respectively. In dimensionless units $x \in [0, l_x]$, $y \in [-1, 1]$, $z \in [0, l_z]$. The streamwise and spanwise wavenumbers are $\alpha = 2\pi/l_x$ and $\beta = 2\pi/l_z$. For plane Couette flow, the two-dimensional, steady, streamwise flow is $U(y) = y$ and the corresponding spanwise vorticity is $\Omega = -dU/dy = -1$. For Poiseuille flow, $U(y) = 1 - y^2$ and $\Omega = 2y$. Note that these flows differ in several important ways: First, the symmetry of the base flow under reflection in y is different, leading to different allowed symmetries for the two- and three-dimensional flows; second, in Poiseuille flow the non-uniformity of Ω across the channel distinguishes the wall and outer regions, whereas no such distinction exists for plane Couette flow; third, in Poiseuille flow there is always a positive net mass flux in the down-stream direction.

2.1.2 Numerical method

The Navier-Stokes equations are solved in a doubly periodic channel geometry using a spectral initial value code. The numerical computations were begun using

the code developed at CTR (Kim *et al.*, 1987), and continued using a similar code developed independently (Coughlin, 1994). The velocity field is represented as a Fourier-Tchebyshev sum:

$$\mathbf{u} = \sum_{m=-M/2+1}^{M/2} \sum_{k=-K/2+1}^{K/2} \mathbf{u}_{km}(y,t) e^{ik\alpha x} e^{im\beta z}, \tag{1}$$

with $\mathbf{u}_{km}(y,t) = \sum_{n=0}^{N} \mathbf{a}_{nkm}(t) T_n(y)$. We write $\mathbf{u}$ for the velocity component in physical space, and $\mathbf{u}_{km}$ for the same component in Fourier space. Since $\mathbf{u}$ is real, $\mathbf{u}_{km} = \bar{\mathbf{u}}_{-k-m}$, where the overbar denotes complex conjugation. No-slip boundary conditions are imposed at the walls, and the pressure boundary condition is chosen to enforce constant mass flux in the streamwise direction.

2.2 Formation of streamwise rolls

Curvature in the Couette-Taylor system is responsible for the initial appearance of the Taylor vortices, and this constitutes the biggest difference from planar channels. In the latter, there is as yet no well-accepted linear mechanism for the formation of streamwise rolls and the associated streaks, nor for the selection of the observed average spanwise wavelength of 100 wall units. It is not the purpose of this paper to address these questions. Instead, we will take the streamwise rolls and streaks as given.

It is well known that such a flow cannot be a steady equilibrium solution to the Navier-Stokes equations since without streamwise variation there is no way for the structures to extract energy from the mean flow. However, the numerical work of Hamilton *et al.* (1994) shows that streamwise vortices are persistent underlying features of the flow, and that they decay on a time scale which is slow compared to the time scale of the intermittent cycle. They used a converged turbulent flow to initialize a computation with spanwise domain size too small to sustain the intermittent cycle. In this case, after one or two more cycles the flow decays away. Specifically, after the last burst of turbulence the flow relaminarizes, the three-dimensional laminar flow then decays to the x-independent streamwise rolls and streaks, and these then decay viscously to two-dimensional plane Couette flow. This decay is illustrated in Fig. 1, where the streamwise vorticity ω_x is plotted in the (y,z) plane at $x = 0$. The horizontal direction is z and the vertical is y. In these figures, the grey scale is a translation of a full color scale and is, therefore, somewhat arbitrary. The bright contours correspond to regions of negative vorticity, and the dark contours to positive vorticity. The lower left corner of the plot is the point $x = 0$, $y = -1$, $z = 0$. The flow is shown at nine equally spaced times with time increasing from the upper left to the lower right. The time scale for the entire intermittent cycle is of order 50-100. The x-dependent part of the flow decays by a factor of ten in a time of order 1-10, while the streamwise rolls decay (when $\partial/\partial x = 0$) by a factor of ten in a time of order 100.

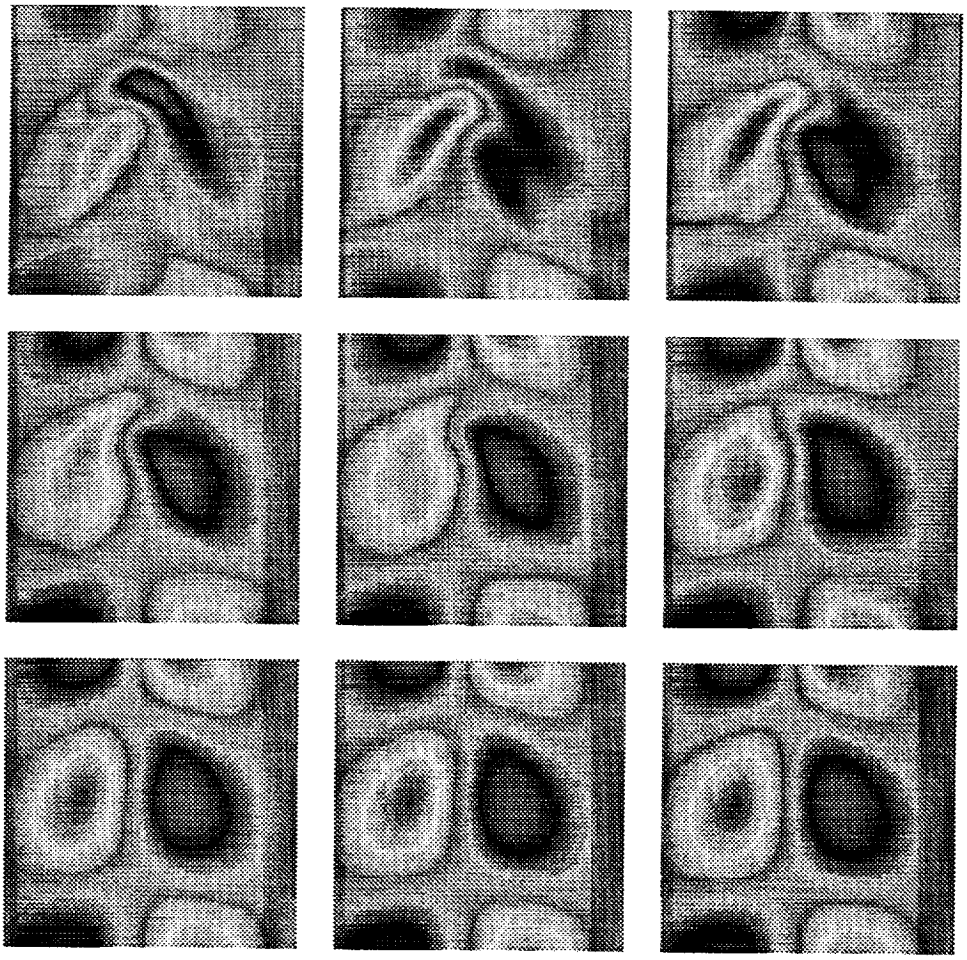

FIGURE 1. Grey-scale plots of the streamwise vorticity ω_x in the (y, z) plane at $x = 0$ at nine consecutive equally-spaced times. Time increase from left to right and top to bottom. The horizontal axis is z, and the vertical is y.

2.3 Linear stability of streamwise rolls

The separation of time scales noted above and the fact that the streamwise rolls are always the last thing to decay suggest that they are a robust quasi-equilibrium, which may be unstable to three-dimensional perturbations on a time scale fast compared to 100. A similar idea was explored by Orszag & Patera (1983) for slowly decaying Tollmein-Schlichting waves, which they found to be strongly unstable to three-dimensional modes. If there is a three-dimensional instability of the rolls, we would expect it to be the second slowest component of the flow to disappear as the turbulence dies away. The data of Hamilton *et al.* show that the configuration of the three-dimensional, decaying laminar flow is always more or less the same, as illustrated in Fig. 1. If our hypothesis is correct, then a growing linear perturbation to the rolls should, irrespective of its initial spatial configuration, end up looking

like Fig. 1 run backwards in time. This is precisely what we find in our numerical experiments.

2.4 Formal statement of the problem

Investigating the stability of a flow that is not an equilibrium is well defined if the time scale for change of the base flow is slow compared to the growth rate of the instability. Formally, we write $\mathbf{u}_{\text{rolls}} = \mathbf{u}_{\text{rolls}}(x, y, \tau)$ where $\tau \equiv \epsilon t$ defines the slow time scale for viscous decay of the vortices. From numerical experiments, we have verified that $\epsilon \sim R^{-1}$. Letting $\mathbf{u}_{\text{lin}}$ be an eigenmode of the Navier-Stokes equations linearized around $\mathbf{u}_{\text{rolls}}$, we can write (neglecting the space dependence) $\mathbf{u}_{\text{lin}} = e^{\lambda t}\mathbf{u}_{\text{lin}}(\tau)$ and consider t and τ to be independent variables. Schematically, the equation for $\mathbf{u}_{\text{lin}}$ becomes

$$(\lambda + \epsilon\partial/\partial\tau)\mathbf{u}_{\text{lin}} = \mathcal{L}\mathbf{u}_{\text{lin}} \tag{2}$$

where $\mathcal{L}$ is a linear operator depending on $\mathbf{u}_{\text{rolls}}$. By construction $\partial/\partial\tau \sim \mathcal{O}(1)$; therefore,if real$(\lambda) >> \epsilon$, we are justified in neglecting the τ dependence in Eq. (2). The simplest hypothetical instability mechanism for $\mathbf{u}_{\text{rolls}}$ is a Kelvin-Helmholtz type instability of the streak, which would have an advective time scale and therefore predict real$(\lambda) = \mathcal{O}(1)$ in our dimensionless units (Drazin & Reid, 1981). Thus, our condition for neglecting $\partial/\partial\tau$ reduces to $\epsilon \sim R^{-1} << 1$, which is well-satisfied in the cases of interest. Thus, in the discussion below we will neglect the presence of the slow time scale τ in the dynamics.

The solution $\mathbf{u}_{\text{rolls}}$ can in fact be turned into a true, steady equilibrium by adding a small forcing to the flow. Experimentally, we find that the most effective way to do this is to force the fundamental spanwise Fourier mode of v (v_{01} in Eq. (1)) to have a constant amplitude (Coughlin, 1994). Forcing v automatically forces w through the divergence equation, and v and w together produce the streak. To fix v at a value typical of the flow during the quiescent part of the cycle requires a forcing that increases the kinetic energy of the flow by less than $\sim 0.1\%$. This leads to a maximum value of v_{01} of about 0.006, and produces a streak which changes the mean profile by about 10%; hence, a very small forcing of the rolls produces a streak of fairly large amplitude. Linear instabilities of these forced rolls have the same characteristic features as those of the decaying, unforced $\mathbf{u}_{\text{rolls}}$. The forcing provides a new control parameter which can be used to look at linear stability of the rolls in a more systematic way, which will be done in future work.

3. Symmetries

The primary advantage of working with solutions having a well-defined symmetry is that the symmetry is *invariant* under nonlinear development of the flow. This can be extremely useful in understanding the origin of complicated changes in the flow pattern. These can be attributed to new bifurcations only if the symmetry changes; otherwise, no matter how much a particular visual signature of the flow may change with time, the change should (generically) be due to the generation of higher harmonics of the original linear modes. Conversely, a change in the predicted

relationships among the Fourier modes signals a qualitative change in the nature of the solution.

We have established from the numerical simulations of Couette flow that the laminar flow, started with arbitrary initial conditions, has almost exactly the symmetries described below in (Eqs. (8) and (9), and that when the flow is initialized and maintained with perfect symmetry, the dynamics is essentially unaffected. Moreover, up until the onset of turbulence, the symmetry of the initial condition doesn't change. The implication is that, beyond the onset of linear instability of $\mathbf{u}_{\text{rolls}}$, there are no other bifurcations; hence, it is the growth of the linear mode which leads to the breakdown of the laminar streak. For completeness, we present a full derivation of the relevant symmetries in this section.

9.1 Linear modes

The simplest way to deduce the allowed symmetries of the flow is to begin with the linear problem: Let $\mathbf{h}(y)e^{i(\lambda t+\alpha x+\beta z)}+\text{c.c.}$ be an eigenmode of the Navier-Stokes equations linearized around the two-dimensional laminar solution U. It is then a solution to

$$\lambda h_x = (-i\alpha U + \nu\Delta)h_x - i\alpha p + \Omega h_y$$

$$\lambda h_y = (-i\alpha U + \nu\Delta)h_y - Dp$$

$$\lambda h_z = (-i\alpha U + \nu\Delta)h_z - i\beta p$$

$$0 = -i\alpha h_x + Dh_y - i\beta h_z$$

with boundary conditions $h_i(y = \pm 1) = 0$ (i labels the x, y, and z components). Here $D \equiv d/dy$ and $\Delta \equiv D^2 - \alpha^2 - \beta^2$. We define $\lambda = \sigma + i\omega$, where the growth rate σ and the phase speed ω are real.

For Couette flow, it is straightforward to show that if $(h_x, h_y, h_z)(y)$ is an eigenvector with eigenvalue λ for the parameter values (α, β), then for the same λ the following degenerate eigenvectors exist: $(-h_x, -h_y, h_z)(-y)$ for $(-\alpha, \beta)$, $(-h_x, -h_y, h_z)(y)$ for $(\alpha, -\beta)$, and $(h_x, h_y, h_z)(-y)$ for $(-\alpha, -\beta)$. When $\alpha = 0$, the eigenvectors correspond to streamwise rolls, the eigenvalue λ is real ($\omega = 0$), and the eigenfunctions satisfy $(h_x, h_y, h_z)(-y) = \pm(h_x, h_y, -h_z)(y)$. When $\alpha \neq 0$, eigenvectors with $\text{sign}(\omega/\alpha) > 0$ correspond to left-traveling waves, and their eigenfunctions h_i are not symmetric under $y \to -y$, having significant amplitude only for $y < 0$. Symmetry implies that for every left-traveling wave there is a right-traveling wave which is non-zero in $y > 0$. Since the eigenfunctions define structures, this means that these structures tend to travel with the local mean flow.

The degeneracies of linear modes for Poiseuille flow are different. In this case, for $\alpha \neq 0$ all eigenmodes have $\text{sign}(\omega/\alpha) < 0$, which again corresponds to the restriction that traveling waves go with the direction of local mean flow. For all values of α and β, the eigenfunctions satisfy $(h_x, h_y, h_z)(-y) = \pm(h_x, -h_y, h_z)(y)$. As in Couette flow, if $\alpha = 0$ the eigenvalues are real and the eigenfunctions correspond to streamwise roll solutions.

3.2 Stream-wise roll solutions

We define nonlinear streamwise rolls to be solutions resulting from the time development of the Navier-Stokes equations initialized with a linear mode with $\alpha = 0$. Note that the linear system has a higher degree of symmetry than the nonlinear, so that some of the relations found above are modified.

In the case of Couette flow, the eigenmode with maximum growth rate corresponds to a single pair of rolls in the vertical domain. In numerical experiments, this is also the nonlinear flow which emerges from arbitrary initial conditions. It has the following symmetries:

$$(u, v, w)(y, z) = (u, v, -w)(y, -z), \tag{3}$$

(reflection in z), and

$$(u, v, w)(-y, z) = (-u, -v, w)(-y, z + \pi/\beta). \tag{4}$$

The latter is the nonlinear analogue of inversion in y, which we will refer to as 'shift-and-invert' symmetry. It ensures that the streaks created by the up/down flow between the vortices at opposite walls are of equal and opposite strength. Eq. (3) implies that the rolls in a pair have opposite circulation under reflection in z.

For Poiseuille flow, the eigenmode with maximum growth rate also corresponds to a single pair of rolls in the vertical domain and leads to a nonlinear solution which satisfies (3) and

$$(u, v, w)(y, z) = (u, -v, w)(-y, z + \pi/\beta) \tag{5}$$

instead of (4). One can also obtain solutions with two roll pairs in the vertical domain; one pair of vortices is in $y \in [-1, 0]$, the other is in $y \in [0, 1]$, and there are stagnation points of the transverse flow at $(y, z) = (0, 0)$ and $(0, \pi/\beta)$. This corresponds to the eigenmode with the second largest growth rate. These solutions satisfy Eq. (3), while inversion symmetry in this case becomes

$$(u, v, w)(y, z) = (u, -v, w)(-y, z).$$

In numerical experiments, we find that the flow with two roll pairs has a higher kinetic energy than the flow with a single roll pair, and thus the former is finite-amplitude unstable to the latter (Coughlin, 1994).

3.3 Linear modes of streamwise rolls

We write down the solution for streamwise rolls as

$$\mathbf{u}_{\mathbf{rolls}} = \sum_{m=-M/2+1}^{M/2} \mathbf{u}_m(y) e^{im\beta z} \tag{6}$$

where the origin in z is chosen such that u_m and v_m are real, and w_m is pure imaginary so that (3) is satisfied.

From Floquet theory, linear eigenmodes of the base state $\mathbf{u}_{\text{rolls}}$ will have the form

$$\mathbf{u}_{\text{lin}} = e^{i\alpha x} e^{\lambda t} \mathbf{u}'(y,z) + \text{c.c.}, \tag{7}$$

where $\mathbf{u}' = \sum_m \mathbf{u}'_m(y) e^{im\beta z}$ has the same symmetry as $\mathbf{u}_{\text{rolls}}$. Given an eigenvector $\mathbf{u}' = (u', v', w')$ with eigenvalue λ, applying symmetry operations produces new eigenfunctions with the same λ. For both Couette and Poiseuille flow, reflection in z leads to $(u', v', -w')(y, -z)$. For Couette flow, shift-and-invert symmetry produces the new vector $(-u', -v', w')(-y, z + \pi/\beta)$. If $\alpha \neq 0$ and $\text{imag}(\lambda) \neq 0$, then (as in the two-dimensional case) these linear modes correspond to left- and right-traveling waves. The left-going modes have non-zero amplitude in the region $y < 0$, while the right-going modes are of significant amplitude only in $y > 0$. For Poiseuille flow, the shift-and-invert symmetric mode is $(u', -v', w')(-y, z+\pi/\beta)$, and eigenfunctions are always even or odd in y.

3.4 Nonlinear three-dimensional flow

If the initial condition is symmetric, the time-development of the Navier-Stokes equations will, in the absence of numerical noise, preserve the symmetry. If a flow is initialized with equal amplitudes of $(u', v', w')(y, z)$ and $(u', v', -w')(y, -z)$, the nonlinear solutions will display 'shift-and-reflect' symmetry (Marcus, 1985):

$$(u, v, w)(x, y, z, t) = (u, v, -w)(x + \pi/\alpha, y, -z, t). \tag{8}$$

Note that this symmetry does not distinguish between 'sinuous' (in-phase motion of the two streaks accompanying a vortex pair) and 'varicose' (out-of-phase) modes. If the initial condition consists of equal amplitudes of $(u', v', w')(y, z)$ and $(-u', -v', w')(-y, z + \pi/\beta)$, then the three-dimensional version of shift-and-invert symmetry results. For Couette flow this is

$$(u, v, w)(x, y, z, t) = (-u, -v, w)(-x, -y, z + \pi/\beta, t). \tag{9}$$

Note that solutions with this symmetry cannot be traveling waves since there will be no translating frame in which the flow appears steady. For Poiseuille flow we have

$$(u, v, w)(x, y, z, t) = (u, -v, w)(x, -y, z + \pi/\beta, t), \tag{10}$$

instead of (9), a form which does allow traveling wave solutions.

From the Couette flow data of Hamilton *et al.* (1994) we have verified that both Eqs. (8) and (9) are satisfied approximately without being imposed on the flow. Since the code is spectral, it is convenient to express these relations in Fourier space. Using Eq. (1), shift-and-reflect symmetry becomes

$$u_{i,km}(y, t) = \gamma_i (-1)^k u_{i,k-m}(y, t).$$

Here $\gamma_i \equiv (1,1,-1)$, $u_i \equiv (u,v,w)$, and there is no sum on i. For Couette flow shift-and-invert symmetry leads to

$$u_{i,km}(-y,t) = -\gamma_i(-1)^m u_{i,-km}(y,t).$$

For a flow which is symmetric under both (8) and (9) we have

$$u_{i,km}(-y,t) = (-1)^{k+m+1}\bar{u}_{i,km}(y,t).$$

If $\mathrm{imag}(\lambda) \neq 0$, then given the form of the linear mode and the fact that the nonlinear term in the Navier-Stokes equations is quadratic, one can also predict the time dependence of individual Fourier modes (Coughlin, 1994).

4. Numerical Results

4.1 Procedures

The stability of Couette flow has been looked at in detail, and this program will be carried out for Poiseuille flow in later work. To look at the stability properties of the flow, the two procedures described below were followed:

(i) Quasi-linear initial value calculations (the same procedure was used in Hamilton *et al.*, 1994): We begin with the full solution as in Eq. (1) at some time t and from it define

$$\mathbf{u}_{\mathrm{rolls}} = \sum_{m=-M/2+1}^{M/2} \mathbf{u}_{0m}(y,t)e^{im\beta z},$$

and the perturbation

$$\mathbf{u}_{\mathrm{lin}} = e^{i\alpha x} \sum_{m=-M/2+1}^{M/2} \mathbf{u}_{1m}(y,t)e^{im\beta z} + \mathrm{c.c.}$$

The streamwise flow $\mathbf{u}_{\mathrm{rolls}}$ is frozen to its initial value, and $\mathbf{u}_{\mathrm{lin}}$ (times a constant) is added and allowed to develop in time. As long as the amplitude of $\mathbf{u}_{\mathrm{lin}}$ remains small compared to $\mathbf{u}_{\mathrm{rolls}}$, the effect of freezing the base flow is equivalent to doing a linear computation; at later times, the solution becomes unphysical.

(ii) Nonlinear initial value calculations: We define $\mathbf{u}_{\mathrm{rolls}}$ and $\mathbf{u}_{\mathrm{lin}}$ as in case (i). The flow is initialized using the combination $c_0\mathbf{u}_{\mathrm{rolls}} + c_1\mathbf{u}_{\mathrm{lin}}$, with $c_1/c_0 << 1$. The constant c_0 is used to control the strength of the rolls. While this initial condition is not a solution to the Navier-Stokes equations, after a short transient the flow settles into slowly decaying $\mathbf{u}_{\mathrm{rolls}}$ plus a linearly growing mode. The growth rate of the linear mode depends on c_0. As soon as the computation is turned on, $\mathbf{u}_{\mathrm{rolls}}$ starts to decay, and the growth rate of the instability depends very strongly on the roll amplitude, so setting $c_0 > 1$ allows the instability to develop over a longer time so that we can determine its characteristic features.

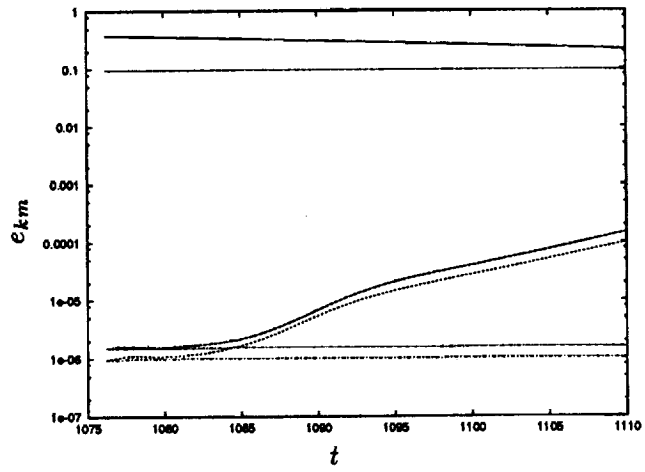

FIGURE 2. Time series of modal energies e_{km} (see text). Method (i); e_{01} ····· , e_{10} — — — , e_{11} —·— . Method (ii); e_{01} ——— , e_{10} — — — , e_{11} - - - - .

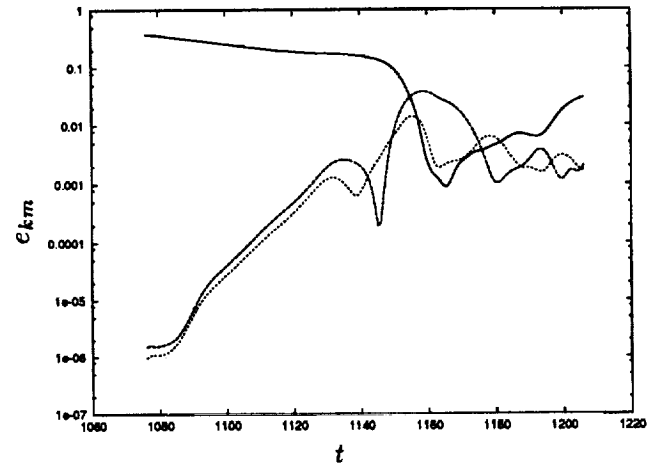

FIGURE 3. Time series of modal energies e_{km} (see text). Method (ii); e_{01} ——— , e_{10} — — — , e_{11} - - - - .

Both procedures were repeated using a different initial $\mathbf{u}_{\text{lin}} = \mathbf{u}_{11}(y,t)e^{i\alpha x}e^{i\beta z}$, where $\mathbf{u}_{11}$ is divergence-free and zero on the boundaries but otherwise arbitrary, and also with exact symmetry imposed on the initial conditions (this symmetry is maintained to order round-off error by the code). In all cases the linear mode acquires, after an initial transient, the same spatial structure and functional form in agreement with the derivation of Section 3.

4.2 Results

Method (i) was used to verify the hypothesis made above that the decaying flow configuration illustrated in Fig. 1 corresponds to a linear mode of the streamwise

rolls. The computation is initialized with the flow of Fig. 1, the decay of the rolls is halted, and the three-dimensional piece of the flow consequently stops decaying and begins to grow. It retains essentially the same spatial configuration. Recall that this configuration is also that of the fully nonlinear flow during the quiescent part of the intermittent cycle. Method (ii) was used to investigate the dependence of the growth rate σ of the three-dimensional Floquet mode on the strength of the rolls (equivalently the velocity difference across the streak), which is proportional to c_0. We find (for $R = 450$, $l_x = 1.75\pi$, and $l_z = 1.2\pi$) that $\sigma \sim c_0 - c_0^c$, with a constant of proportionality of about 0.2. Here c_0^c is the value where σ becomes negative, and depends on the initial condition. For the flow described here $c_0^c = 0.98$, so that the linear mode initially grows but starts to decay as the rolls decay. These results are consistent with the assumption that the streaks are unstable on an advective time scale. This scaling translates into a strong sensitivity of the growth rate to the strength of the rolls in the relevant regime ($c_0 \sim 1$). For example, when $c_0 \sim 1.05$, $\sigma \sim 0.01$ while for $c_0 \sim 1.6$, $\sigma \sim 0.1$. We emphasize that since the flow is in a subcritical regime, c_0 has no absolute significance, but the scaling implies that that if the energy in the streamwise flow is increased by a moderate amount, the instability growth rate can increase dramatically. We also note that apart from influencing the value of σ, the value of c_0 does not affect the linear mode; we find the same characteristic spatial pattern for all test cases.

These experiments are illustrated in Figs. 2 and 3, where we show times series of the modal energies $e_{km} = \int_{-1}^{1} |\mathbf{u}_{km}|^2 dy$ for $(k,m) = (0,1)$ (essentially the roll amplitude), (1,0) and (1,1) (the linear modes). Note that the theoretical model predicts that modes (1,0) and (1,1) will have the same linear growth rate. In Fig. 2, these modes are plotted for two experiments using procedures (i) and (ii) with the same initial condition. In Fig. 3, the experiment using method (ii) is shown for a much longer time. We see that the (1,0) and (1,1) modes grow roughly three orders of magnitude with a nearly constant growth rate. The growth rate is not exactly constant because we do not begin the computation with the true linear eigenmode. When the $k = 1$ modes reach large enough amplitude, the flow goes over into the intermittent turbulent cycle and the time series become disordered.

4.3 Spatial structure of the linear mode

In this section we describe briefly the spatial structure of the instability of the streamwise rolls/streak. As both methods described above produce essentially the same flow, we will describe the results only for method (ii). We show in Figs. 4 and 5 visualizations of the linear instability of the rolls as it grows to finite amplitude. As in Fig. 1, we plot the streamwise vorticity ω_x using a grey scale, with dark values corresponding to positive ω_x and bright values to negative ω_x. Each frame is scaled individually so that the actual numerical value of ω_x corresponding to a particular grey level is not constant from frame to frame. Note that the change in the flow seen in these figures is due entirely to the growth of the secondary instability as it preserves the symmetry and time dependence of the flow.

Fig. 4 shows the vorticity ω_x in the (x,y) plane at nine equally spaced times with t increasing from left to right and top to bottom. The horizontal direction is

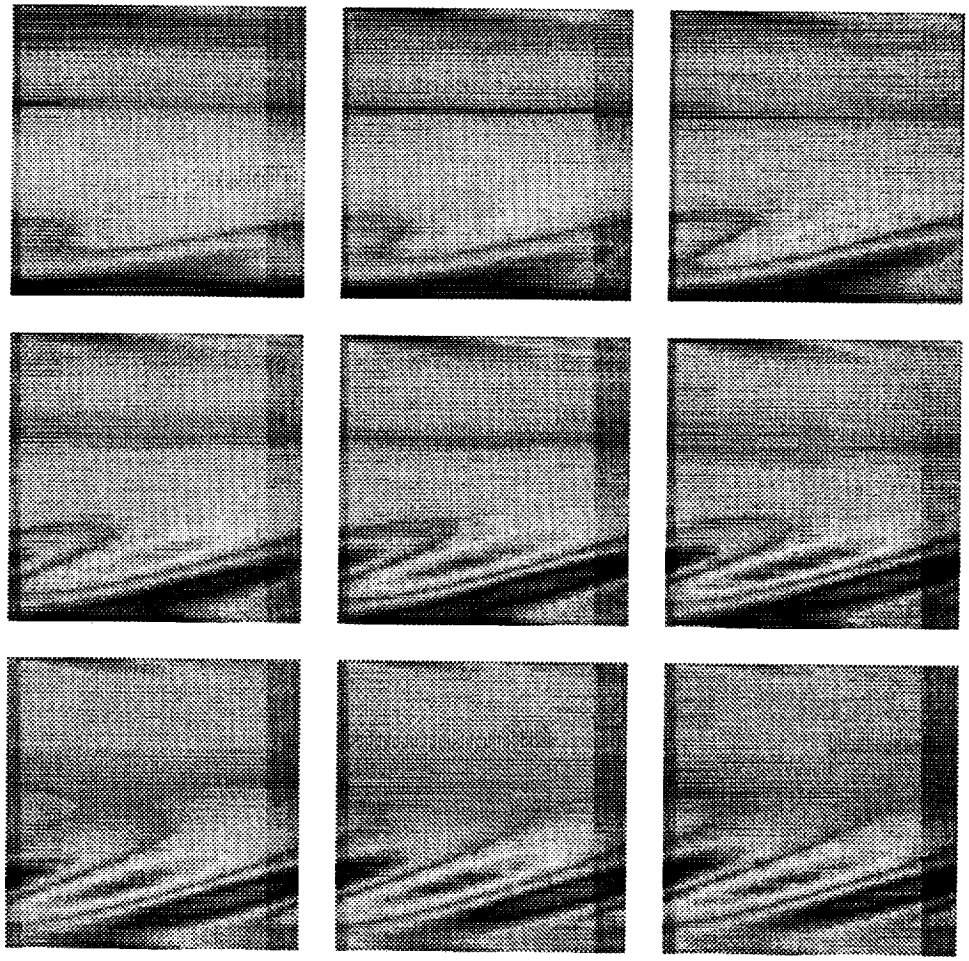

FIGURE 4. Stream-wise vorticity ω_x plotted in the (x, y) plane at $z = \pi/2\beta$, at nine consecutive equally-spaced times, for the growing three-dimensional instability. Time increase from left to right and top to bottom. The horizontal axis is x, and the vertical is y.

x and the vertical is y. This view shows a slice through the negative streamwise vortex at $z = \pi/2\beta$; the mean flow is from left to right in the lower part of the frame and from right to left in the upper part. The instability first appears as a sinusoidal deformation of the the vortex which is strongest at the cross-stream location where the vorticity ω_x changes sign. As it grows there is an interaction between the negative vorticity in the roll with the induced positive vorticity at the wall. This leads to the characteristic configuration of tilted layers of vorticity of alternating sign near the lower wall. The same pattern, inverted according to (8) and (9), appears at the upper wall at $z = 3\pi/2\beta$.

In Fig. 5 we plot ω_x in the (x, z) plane, with x the horizontal and z the vertical coordinate, for the same flow at the same times as in Fig. 4. The horizontal section

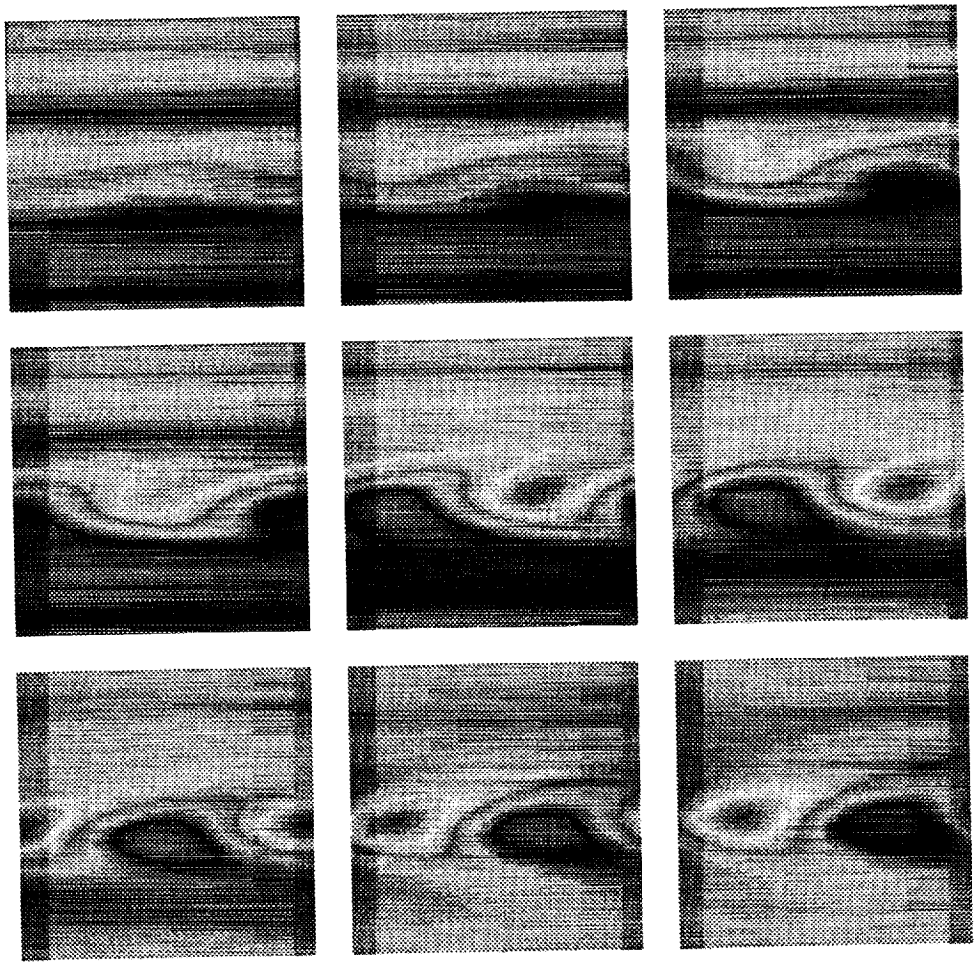

FIGURE 5. Stream-wise vorticity ω_x plotted in the (x, z) plane at $y = 0.5$ for the same flow as in Fig. 4. The horizontal axis is x, and the vertical is z.

is taken at $y = 1/2$ and passes through the upper half of the streamwise vortex pair. The streak is visualized in these plots as the grey region between the bright, negative vortex and the darker positive vortex. From these plots, it is clear that the instability begins as a waviness of the streak, which as it develops leads to a concentration of the streamwise vorticity into disc-like regions of alternating sign. These discs are tilted and layered one over the other in the (x, y) plane, as was shown in Fig. 4. The vorticity configuration seen in this plot is due primarily to the gradient $\partial w/\partial y$. It is important to note that these plots show vorticity, not vortices. Vector plots of the velocity field in the (y, z) plane, as shown for example in Hamilton *et al.* (1994), show that at all times the streamwise rolls are present; the concentration of the vorticity into the configurations seen in Figs. 1, 4, and 5 is due to a local intensification of the fluxes and gradients of the transverse velocity field. Thus, in the last row of Fig. 5, the rolls remain more or less in the same place,

but the vorticity has been concentrated into the region near the streak.

As the flow becomes more strongly nonlinear, these structures start to advect with the local mean flow, which is from left to right in Fig. 4, and in Fig. 5 from right to left. This behavior is consistent with $\mathrm{imag}(\lambda) \neq 0$ in Eq. (2), but should be verified by more detailed linear calculations. Streak break-down in this visualization corresponds to a sudden loss of the spatial regularity of the pattern and the appearance of fluctuations in the vorticity field over short time scales. Beyond this point, it is difficult to get useful information from flow visualization.

5. Conclusions

We have argued that the intermittent cycle in minimal channels consists of excursions away from a laminar base flow and that the base flow arises from linear instability of a two-dimensional flow consisting of streamwise vortices and streaks. We have shown for plane Couette flow that there is a robust, three-dimensional instability of the two-dimensional flow and that the instability can grow to large amplitude on a time scale fast relative to the decay rate of the vortices. We have given a complete description of the mathematical form of the instability and have calculated the linear mode using several (approximate) numerical techniques. We have discussed the similarities between the intermittent cycles in minimal channel flows and those occurring in the experimentally realizable Couette-Taylor system (Coughlin & Marcus, 1994). Note that these similarities suggest that the minimal channel, although it is an idealized model of the real system, does contain the relevant physics.

This study is preliminary and has raised a number of questions which we will investigate in future work. We plan to complete the analysis given above for Poiseuille flow; it would be particularly interesting to see whether the hypothesized secondary instability resembles in any way hairpin vortices. We are also interested in whether any of the mechanisms which have been proposed for the formation of streamwise vortices (for example, Butler & Farrell, 1992) are consistent with the spatial structure and stability properties of the decaying (or forced, steady) streamwise rolls found in the computations. More work also remains to be done to understand the physical nature of the instability and to what extent it can be attributed to a two-dimensional, Kelvin-Helmholz type of mechanism. Its features should also be compared in more detail to the observations of Swearingen & Blackwelder (1987) and other available experimental data.

Last but not least, there is the problem of understanding in mathematical terms the transition to turbulence. The minimal channel and Couette-Taylor simulations show that while the turbulent cycle does return intermittently to a low-dimensional dynamical state, the intervening state is almost certainly high-dimensional. The transition between them is characterized by the abrupt loss of spatial coherence of the flow, which has as yet found no adequate mathematical expression. Low dimensional models, for example as derived by Aubry *et al.* (1988) for turbulent bursts in the boundary layer of pipe flow, are inherently incapable of addressing this problem as they *a priori* eliminate most spatial degrees of freedom. The flows

discussed here isolate these fundamental issues in an elegant but not over-simplified way, and are thus deserving of further study.

REFERENCES

AUBRY, N., HOLMES, P., LUMLEY, J. L. & STONE, E. 1988 The dynamics of coherent structures in the wall region of a turbulent boundary layer. *J. Fluid Mech.* **192,** 115-173.

BUTLER, K. M. & FARRELL, B. F. 1992 Three-dimensional optimal perturbations in viscous shear flow. *Phys. Fluids A.* **4,** 1637-1650.

COUGHLIN, K. 1994 In preparation.

COUGHLIN, K. & MARCUS, P. 1994 Turbulent bursts in Couette-Taylor flow. Pre-print.

DRAZIN, P. G. & REID, W. H. 1981 *Hydrodynamic stability.*Cambridge University Press.

HAMILTON, J., KIM, J., & WALEFFE, F. 1994 Dynamics of near-wall turbulence structures. Pre-print.

HAMMIL, F., PREDTECHENSKY, A. A., SHA, E., & SWINNEY, H. L. 1994 To be published.

JIMÉNEZ, J. & MOIN, P. 1991 The minimal flow unit in near-wall turbulence. *J. Fluid Mech.* **225,** 213-240.

KIM, J., MOIN, P. & MOSER, R. 1987 Turbulence statistics in fully developed channel flow at low Reynolds number. *J. Fluid Mech.* **177,** 133-156.

ORSZAG, S. A. & PETERA, A. T. 1983 Secondary instability of wall-bounded shear flows. *J. Fluid Mech.* **128,** 347-385.

SWEARINGEN, J. D. & BLACKWELDER, R. F. 1987 The growth and breakdown of streamwise vortices in the presence of a wall. *J. Fluid Mech.* **182,** 255-290.

39745
N95-21050
245
23

Center for Turbulence Research
Proceedings of the Summer Program 1994

Numerical investigation of supersonic turbulent boundary layers with high wall temperature

By Y. Guo[1] AND N. A. Adams[2]

A direct numerical approach has been developed to simulate supersonic turbulent boundary layers. The mean flow quantities are obtained by solving the parabolized Reynolds-averaged Navier-Stokes equations (globally). Fluctuating quantities are computed locally with a temporal direct numerical simulation approach, in which nonparallel effects of boundary layers are partially modeled. Preliminary numerical results obtained at the free-stream Mach numbers 3, 4.5, and 6 with hot-wall conditions are presented. Approximately 5 million grid points are used in all three cases. The numerical results indicate that compressibility effects on turbulent kinetic energy, in terms of dilatational dissipation and pressure-dilatation correlation, are small. Due to the hot-wall conditions the results show significant low Reynolds number effects and large streamwise streaks. Further simulations with a bigger computational box or a cold-wall condition are desirable.

1. Introduction

Studies of compressible turbulent boundary layer flows are of fundamental interest. Understanding of such flows, particularly the effects of compressibility on turbulence, may help to improve turbulence models used in many industrial applications. Over the years, many experimental efforts have been made (cf. Spina *et al.*, 1994), and a great deal of knowledge has been obtained about these flows. But due to the difficulties encountered in high speed flow experiments, many aspects of these flows still remain unclear (cf. Lele, 1994 and Spina *et al.*, 1994). Recently with the rapid increase of computing power, direct numerical simulation (DNS) has become one alternative tool to investigate these flows. In this study, we present our first effort in this direction. Preliminary results from three case studies at Mach numbers 3, 4.5, and 6 are reported.

The problem in this study is the compressible turbulent boundary layer flow over a flat plate. We consider a region after the leading edge, where the flow is free of the shock caused by the leading edge and the boundary layer forms over the wall and grows in the streamwise direction. Generally, there are two ways to do DNS of boundary layer flows: spatial DNS and temporal DNS (cf. Kleiser & Zang, 1991 for a review). A spatial DNS approach (SDNS) is the closest numerical realization of a turbulent boundary layer experiment, but it demands an enormous amount

1 DLR, Institute for Fluid Mechanics, Germany. Current address: Institute of Fluid Dynamics, ETH Zürich, Switzerland.

2 Center for Turbulence Research

of computing resources and therefore is prohibitively expensive, especially in the case of compressible boundary layer flows. So far its application has been limited to producing a few benchmark data (Spalart & Watmuff, 1993). A temporal DNS approach (TDNS), where the flow is assumed to be locally parallel and develops in time, is highly efficient and requires no inflow and outflow boundary conditions (cf. Kleiser & Zang, 1991). It has been applied successfully to the direct simulations of turbulent channel flows (cf. Kim *et al.*, 1987, Coleman *et al.*1993) and has provided considerable details and insights about the turbulence in these flows. But due to the use of the parallel flow assumption in its formulation, its applications to turbulent boundary layers have suffered certain drawbacks. Firstly, the mean flow quantities do not satisfy the Navier-Stokes equations and always exhibit undesirable temporal growth. Secondly, the nonparallel effects of a turbulent boundary layer cannot be considered. To overcome these problems, Spalart & Leonard (1985) and Spalart (1986) assumed self-similarity both for the mean velocity and for the Reynolds stresses in their studies of equilibrium turbulent boundary layers and sink flows. This assumption is reasonable, but is strictly justified only in the case of sink flows. In Spalart (1988), a more general approach was developed using a multiple-scale analysis to approximate the local effects of the streamwise growth of the flow. Satisfactory results have been obtained for boundary layer flows on a flat plate.

However, a direct application of Spalart's multiple-scale analysis (1988) to compressible flow is rather tedious and difficult, due to many nonlinear terms in the compressible Navier-Stokes equations. In order to avoid this problem, a different approach has been used in this study. In the following section, we present the details of this approach, together with discussions concerning its application to more general cases. Brief comments on the numerical implementation and validation of this approach are given in §3. In §4, we present preliminary numerical results of turbulent boundary layers at $M_\infty = 3$, 4.5, and 6. Concluding remarks are given in §5.

2. Numerical method

It is known that there exist two different scales in a turbulent boundary layer: mean flow quantities exhibit large scales and slow variations in the streamwise direction, while turbulence quantities are generally of small scale and fast variation (cf. Spalart, 1988). In some sense, mean flow quantities can be viewed as global quantities, carrying upstream information downstream. For example, the downstream profiles of mean flow quantities depend on the upstream profiles of these quantities. Therefore these quantities cannot be solved by any local procedure without resorting to any similarity assumption (note that a TDNS approach is a local procedure). Turbulence quantities, on the other hand, are generally "local", being generated and dissipated within short time and small space. Intuitively, one would expect that it would be more efficient to compute these two different scales with different numerical approaches.

Motivated by the above observation, we developed an approach which computes the turbulence quantities locally with a TDNS approach, and computes the mean

flow quantities globally by solving the Reynolds-averaged Navier-Stokes equations. This approach is formulated in such a way that it allows the solutions of the Reynolds-averaged Navier-Stokes equations be marched downstream spatially using the Reynolds stresses, which are computed locally at each spatial step by a TDNS approach. Special care has been taken to include the nonparallel effects of the turbulent boundary layer flows into the TDNS approach, which is a natural extension of our earlier work on TDNS of growing transitional boundary layers (Guo *et al.*, 1994).

2.1 Solving Reynolds-averaged equations for mean flow quantities within TDNS

For simplicity, we first demonstrate our numerical approach using an incompressible boundary layer flow as an example. Application of this approach to compressible flow is presented in §2.3. In this report, we designate x as the streamwise direction, y as the spanwise direction, and z as the wall-normal direction. Vector notations are preferred due to irregular terms introduced by parabolization procedures.

For any turbulent boundary layer flow, the flow field can be decomposed as

$$\mathbf{u} = \mathbf{u}^0 + \mathbf{u}' \,, \tag{1}$$

where $\mathbf{u}^0$ represents the stationary part, which usually includes the mean flow, $\mathbf{u}_0^0$ (i.e. $(0,0)$ mode), and all stationary streamwise vortices, $\mathbf{u}_1^0$ (i.e. $(0,k_y)$ modes, $k_y \neq 0$). The term $\mathbf{u}'$ represents the remaining part which fluctuates with time. The governing equations for $\mathbf{u}^0$ are the Reynolds averaged Navier-Stokes equations (in dimensionless form):

$$\nabla \cdot (\mathbf{u}^0 \mathbf{u}^0) = -\nabla p^0 + \frac{1}{Re} \nabla^2 \mathbf{u}^0 - \nabla \cdot (\overline{\mathbf{u}'\mathbf{u}'}) \,, \tag{2}$$

$$\nabla \cdot \mathbf{u}^0 = \mathbf{0} \,, \tag{3}$$

where $\mathbf{u}'\mathbf{u}'$ are the well-known Reynolds stresses, and an overline represents a time-averaged quantity. In boundary layers, $\mathbf{u}^0$ usually has slow variation in the streamwise direction, thus the governing Eqs. (2) and (3) can be parabolized (cf. Fletcher, 1988 and Guo & Finlay, 1994): the term ∇^2 is replaced by ∇_P^2,

$$\nabla_P^2 = \frac{\partial^2}{\partial y^2} + \frac{\partial^2}{\partial z^2} \,, \tag{4}$$

and the pressure p^0 in the $x-$momentum equation is replaced by the mean pressure averaged across the $y-z$ plane, p_0^0. The solutions of the resulting equations then can be marched downstream efficiently using a spatial marching scheme. Parabolization procedures for more general cases can be found in Fletcher (1988).

One important issue in solving the parabolized version of (2) and (3) is the numerical treatment of the Reynolds stress terms. In a turbulent boundary layer, these are the dominant terms, and it is desirable to treat these terms implicitly in spatial marching schemes in order to avoid any severe restriction on spatial marching step sizes. Since the Reynolds stress terms are computed by a TDNS approach in this

study, they cannot be expressed explicitly in terms of $\mathbf{u}^0$. Thus an efficient way has to be found to deal with these terms implicitly.

It can be shown that in a conventional TDNS approach, the actual equations solved for $\mathbf{u}^0$ are:

$$\frac{\partial \mathbf{u}^0}{\partial t} + \nabla_P \cdot (\mathbf{u}^0 \mathbf{u}^0) = -\nabla_P p^0 + \frac{1}{Re} \nabla_P^2 \mathbf{u}^0 - \nabla_P \cdot (\overline{\mathbf{u}'\mathbf{u}'}) \,, \tag{5}$$

$$\frac{\partial \mathbf{u}^0}{\partial t} + \nabla_P \cdot \mathbf{u}^0 = \mathbf{0} \,. \tag{6}$$

Note that in (5-6), $\mathbf{u}^0$ is a function of time and an overline represents a *spatial-averaged* quantity. Compared to the parabolized (2-3), the following term is missing from the right hand sides of (5-6):

$$\mathbf{Z_0} = (z_{01}, z_{02}, z_{03}, z_{04})^T \,, \tag{7}$$

where

$$\begin{aligned}
z_{01} &= -\frac{\partial u^0 u^0}{\partial x} - \frac{\partial p_0^0}{\partial x} - \frac{\partial \overline{u'u'}}{\partial x} \,, \\
z_{02} &= -\frac{\partial u^0 v^0}{\partial x} - \frac{\partial \overline{u'v'}}{\partial x} \,, \\
z_{03} &= -\frac{\partial u^0 w^0}{\partial x} - \frac{\partial \overline{u'w'}}{\partial x} \,, \\
z_{04} &= -\frac{\partial u^0}{\partial x} \,.
\end{aligned}$$

Assuming spatial-averaged quantities are good approximations to time-averaged quantities, Eqs. (5-6), with the missing term (7) added, constitute a transient problem of the parabolized (2-3). The solutions of these equations converge to those of the parabolized (2-3) when $\partial \mathbf{u}^0 / \partial t \to \mathbf{0}$. Note that the term $\mathbf{Z_0}$ only acts on the governing equations for $\mathbf{u}^0$. The streamwise variation of the Reynolds stress terms are also included in (7).

To further demonstrate how Eqs. (5-6) are solved in a TDNS together with the term $\mathbf{Z_0}$, we discretize the $x-$momentum equation in the x direction with an Euler implicit scheme:

$$\begin{aligned}
\frac{\partial {u^0}_{n+1}}{\partial t} = &-\frac{\partial (u^0 v^0)_{n+1}}{\partial y} - \frac{\partial (u^0 w^0)_{n+1}}{\partial z} + \frac{1}{Re}\left(\frac{\partial^2 {u^0}_{n+1}}{\partial y^2} + \frac{\partial^2 {u^0}_{n+1}}{\partial z^2}\right) \\
&- \left(\frac{\partial (\overline{u'v'})_{n+1}}{\partial y} + \frac{\partial (\overline{u'w'})_{n+1}}{\partial z}\right) - \frac{(u^0 u^0)_{n+1} - (u^0 u^0)_n}{\Delta x_{n+1}} \\
&- \frac{p^0_{0\,n+1} - p^0_{0n}}{\Delta x_{n+1}} - \frac{(\overline{u'u'})_{n+1} - (\overline{u'u'})_n}{\Delta x_{n+1}} \,,
\end{aligned} \tag{8}$$

where a subscript "$n+1$" denotes the solution evaluated at the downstream location $x = x_{n+1}$, and $\Delta x_{n+1} = x_{n+1} - x_n$. At each station $x = x_{n+1}$, the solution of (8)

is iterated in time until a steady-state solution is reached. Then the solution of (8) is marched spatially to the next station $x = x_{n+2}$. In practice, we find high order backward-differentiation-formulas (BDF) with variable step sizes (cf. Hairer *et al.*, 1987) are rather satisfactory: these schemes with accuracy up to sixth order are unconditionally stable, and the implementation only involves the term $\mathbf{Z}_0$ in an existing TDNS code. In our code, a second order BDF is used:

$$\frac{\partial(\ )}{\partial x} = \frac{1}{x_{n+1} - x_n}\left[\frac{1+2\omega_n}{1+\omega_n}(\ )_{n+1} - (1+\omega_n)(\ )_n + \frac{\omega_n^2}{1+\omega_n}(\ )_{n-1}\right], \tag{9}$$

where $\omega_n = (x_{n+1} - x_n)/(x_n - x_{n-1})$.

2.2 Computing turbulence quantities with TDNS: nonparallel effects

Turbulence quantities in boundary layers are not homogeneous locally in the x direction. When a TDNS approach is used to compute these quantities, the issue of nonparallel effects arises. In Guo *et al.* (1994), we have discussed extensively this issue in the case of transitional flows. Here we adopt a similar methodology. The basic idea of this approach is as follows: we assume that the nonparallel flow $\mathbf{u}$ can be decomposed as the perturbation expansion:

$$\mathbf{u} = \mathbf{u}_0 + \mathbf{u}_1\epsilon + \mathbf{u}_2\epsilon^2 + \cdots, \tag{10}$$

where $\mathbf{u}_i$ $(i = 0, 1, 2, \cdots)$ are periodic functions in both x and y, and ϵ is some perturbation parameter. Substituting Eq. (10) into the Navier-Stokes equations, we can derive one set of equations for each power i of the parameter ϵ. These equation sets all have the periodic functions $\mathbf{u}_i$ as unknowns. In a sense, the original nonperiodic system has been decomposed into periodic subsystems, where then Fourier schemes can be used. If Eq. (10) is truncated at $i = n-1$, the approximation error is given by

$$\delta = \mathbf{u}_n\epsilon^n + \mathbf{u}_{n+1}\epsilon^{n+1} + \cdots . \tag{11}$$

If δ is bounded and decays with n, then Fourier schemes can be used to obtain the solution of a nonparallel system. In Guo *et al.* (1994), we have shown that the decomposition (10) can be obtained for transitional boundary layer flows, and Eq. (11) is bounded and decays with n.

For a turbulent boundary layer, we can perform the following analysis. Following Spalart (1988), $\mathbf{u}$ can be decomposed as

$$\mathbf{u} = \mathbf{u}^0 + \mathbf{u}' = \mathbf{u}^0 + \mathbf{A}(x, z)\mathbf{B}(x, y, z, t) , \tag{12}$$

where $\mathbf{u}^0$ represents mean flow quantities, and $\mathbf{A}(x, z)$ is the "amplitude function", which is proportional to the r.m.s. of $\mathbf{u}$. Both $\mathbf{u}^0$ and $\mathbf{A}(x, z)$ have slow variations in the x directions. The term $\mathbf{B}(x, y, z, t)$ represents the fast fluctuating part. Taylor-expanding $\mathbf{u}^0$ and $\mathbf{A}(x, z)$ in the neighborhood of x_0, we have

$$\mathbf{u}^0(x, z) = \mathbf{u}^0(x_0, z) + \frac{\partial \mathbf{u}^0}{\partial x}(x - x_0) + \frac{1}{2!}\frac{\partial^2 \mathbf{u}^0}{\partial x^2}(x - x_0)^2 + \cdots , \tag{13}$$

$$\mathbf{A}(x,z) = \mathbf{A}(x_0,z) + \frac{\partial \mathbf{A}}{\partial x}(x-x_0) + \frac{1}{2!}\frac{\partial^2 \mathbf{A}}{\partial x^2}(x-x_0)^2 + \cdots . \tag{14}$$

We denote the length scale of the fluctuating part $\mathbf{B}(x,y,z,t)$ as l, and the length scale of the mean flow quantities as L. Assuming that $\partial/\partial x$ can be scaled with L and $x - x_0$ with l, we have the expansions (13-14) decay asymptotically at a rate $O(l/L)^n/n!$.

In Spalart (1988), $\mathbf{B}(x,y,z,t)$ was assumed to be periodic in the x direction. More generally, we can assume that

$$\mathbf{B}(x,y,z,t) = \mathbf{B}_0 + \mathbf{B}_1(x-x_0) + \mathbf{B}_2(x-x_0)^2 + ..., \tag{15}$$

where $\mathbf{B}_j$ $(j = 0, 1, \cdots)$ are periodic in both x and y. Generally, we can assume that $\mathbf{B}_{i-1}$ is one order smaller than $\mathbf{B}_i$. Note that this assumption cannot be proved theoretically, but it is less restrictive than assuming $\mathbf{B}$ to be periodic. Substituting (13-15) into (12), one can show that $\mathbf{u}'$ can be written in the form of

$$\mathbf{u}' = \mathbf{u}'_0 + \mathbf{u}'_1(x-x_0) + \mathbf{u}'_2(x-x_0)^2 + \cdots , \tag{16}$$

where $\mathbf{u}'_j$ $(j = 0, 1, \cdots)$ are periodic in x and y, and $\mathbf{u}'_i$ is generally one order larger than $\mathbf{u}'_{i-1}$. Then the error defined by (11) is bounded and decays with n.

Due to the complexity, only the first set of equations $(i = 0)$ are considered in this study. The derivative of $\mathbf{u}$ is approximated by

$$\frac{\partial \mathbf{u}}{\partial x} \approx \frac{\partial \mathbf{u}^0}{\partial x} + \frac{\partial \mathbf{u}'_0}{\partial x} + \mathbf{u}'_1 \tag{17}$$

For a turbulent boundary layer, the nonparallel effect contributed by $\mathbf{u}'_1$ cannot be modeled due to the lack of information about $\mathbf{u}'_1$. In a transitional flow, this term can be partially modeled, and has been shown to be small in Guo *et al.* (1994). In a standard TDNS approach, the term $\partial \mathbf{u}^0/\partial x$ is zero, and thus the nonparallel effect contributed by this term is not considered. In this study, the nonparallel contribution of this term is considered by adding the following term to the right-hand side of the governing equations solved by a TDNS approach,

$$\mathbf{Z}_1 = (z_{11}, z_{12}, z_{13}, z_{14})^T , \tag{18}$$

where

$$\begin{aligned}
z_{11} &= -2(u-u^0)\frac{\partial u^0}{\partial x} , \\
z_{12} &= -(u-u^0)\frac{\partial v^0}{\partial x} - (v-v^0)\frac{\partial u^0}{\partial x} , \\
z_{13} &= -(u-u^0)\frac{\partial w^0}{\partial x} - (w-w^0)\frac{\partial u^0}{\partial x} , \\
z_{14} &= 0 .
\end{aligned}$$

The term $\mathbf{Z}_1$ is equivalent to the forcing term $\mathbf{Z}_1$ in Guo *et al.* (1994), and it only acts on the governing equations for $\mathbf{u}'$.

2.3 Application to compressible boundary flow

In the case of compressible boundary layer flows, the governing equations we have solved can be written in the dimensionless conservative form as:

$$\frac{\partial \mathbf{U}}{\partial t} = \frac{\partial \mathbf{F}}{\partial x} + \frac{\partial \mathbf{G}}{\partial y} + \frac{\partial \mathbf{H}}{\partial z} + \mathbf{Z}_0 + \mathbf{Z}_1 \ . \tag{19}$$

The vector $\mathbf{U}$ is the solution vector defined by $\mathbf{U} = (\rho, \rho u, \rho v, \rho w, E)^T$, where ρ is the density normalized with the free-stream density ρ^*_∞, and u, v, and w are the velocity components normalized with the free-stream velocity u^*_∞. Here, a subscript "∞" denotes the quantity evaluated at the freestream and an asterisk denotes a dimensional quantity. The total energy E is defined by

$$E = \frac{1}{\kappa - 1} p + \frac{\rho}{2}(u^2 + v^2 + w^2)$$

where κ is the ratio of specific heats and p is the pressure normalized with $\rho^*_\infty {u^*_\infty}^2$. The pressure p is related to the temperature T by a perfect-gas law

$$p \kappa M^2_\infty = \rho T \ .$$

Sutherland's law is used for the viscosity calculation. The vectors $\mathbf{F}$, $\mathbf{G}$ and $\mathbf{H}$ are the standard flux vectors in the x, y, and z directions respectively.

The term $\mathbf{Z}_0$ is derived in the same way as described early in §2.1. It has the following form:

$$\mathbf{Z}_0 = \frac{\partial}{\partial x} \begin{bmatrix} -\overline{\rho u} \\ -\overline{\rho u^2} - p_0^0 + (\overline{\tau_{xx}})_T \\ -\overline{\rho u v} + (\overline{\tau_{xy}})_T \\ -\overline{\rho u w} + (\overline{\tau_{xz}})_T \\ -\overline{u(E+p)} - (\overline{q_x})_T + (\overline{u \tau_{xx}})_T + (\overline{v \tau_{xy}})_T + (\overline{w \tau_{xz}})_T \end{bmatrix} + \mathbf{Z}_m \ , \tag{20}$$

where τ_{xx}, τ_{xy}, and τ_{xz} are the components of the shear stress tensor and q_x is the heat flux component in the x direction. Here an overline denotes a spatial-averaged quantity. A subscript "T" denotes the quantity been evaluated in a TDNS scheme. The term $\mathbf{Z}_m$ contains the terms missing in the terms $(\ )_T$, due to the use of Fourier schemes. It has a form of

$$\mathbf{Z}_m = (z_{1m}, z_{2m}, z_{3m}, z_{4m}, z_{5m})^T \ , \tag{21}$$

where

$$z_{1m} = 0 \ ,$$

$$z_{2m} = \frac{4}{3}\frac{\partial}{\partial x}\left(\frac{\bar{\mu}}{Re}\right)\frac{\partial \bar{u}}{\partial x} + \frac{\partial}{\partial y}\left(\frac{\bar{\mu}}{Re}\frac{\partial \bar{v}}{\partial x}\right) + \frac{\partial}{\partial z}\left(\frac{\bar{\mu}}{Re}\frac{\partial \bar{w}}{\partial x}\right) \ ,$$

$$z_{3m} = \frac{\partial}{\partial x}\left(\frac{\bar{\mu}}{Re}\right)\frac{\partial \bar{w}}{\partial x} - \frac{2}{3}\frac{\partial}{\partial y}\left(\frac{\bar{\mu}}{Re}\frac{\partial \bar{u}}{\partial x}\right) - \frac{2}{3}\frac{\partial}{\partial z}\left(\frac{\bar{\mu}}{Re}\frac{\partial \bar{u}}{\partial x}\right),$$

$$z_{4m} = \frac{\partial}{\partial x}\left(\frac{\bar{\mu}}{Re}\right)\frac{\partial \bar{v}}{\partial x},$$

$$\begin{aligned} z_{5m} = {} & \frac{1}{(\kappa-1)M_\infty^2 Pr}\frac{\partial}{\partial x}\left(\frac{\bar{\mu}}{Re}\right)\frac{\partial \bar{T}}{\partial x} + \frac{4}{3}\frac{\bar{\mu}}{Re}\left(\frac{\partial \bar{u}}{\partial x}\right)^2 + \frac{4}{3}\bar{u}\frac{\partial}{\partial x}\left(\frac{\bar{\mu}}{Re}\right)\frac{\partial \bar{u}}{\partial x} \\ & + \frac{\bar{\mu}}{Re}\left(\frac{\partial \bar{v}}{\partial x}\right)^2 + \bar{v}\frac{\partial}{\partial x}\left(\frac{\bar{\mu}}{Re}\right)\frac{\partial \bar{v}}{\partial x} + \frac{\bar{\mu}}{Re}\left(\frac{\partial \bar{w}}{\partial x}\right)^2 + \bar{w}\frac{\partial}{\partial x}\left(\bar{u}\frac{\bar{\mu}}{Re}\right)\frac{\partial \bar{v}}{\partial x} \\ & + \frac{\partial}{\partial y}\left(\frac{\bar{\mu}}{Re}\frac{\partial \bar{w}}{\partial x}\right) - \frac{2}{3}\frac{\partial}{\partial y}\left(\bar{v}\frac{\bar{\mu}}{Re}\frac{\partial \bar{u}}{\partial x}\right) + \frac{\partial}{\partial z}\left(\bar{u}\frac{\bar{\mu}}{Re}\frac{\partial \bar{w}}{\partial x}\right) - \frac{2}{3}\frac{\partial}{\partial z}\left(\bar{w}\frac{\bar{\mu}}{Re}\frac{\partial \bar{u}}{\partial x}\right). \end{aligned}$$

It can be shown that $\mathbf{Z}_m$ is very small, and can be neglected. For completeness, we retain this term in our scheme.

Note that in Eq. (20), a parabolization procedure similar to the one described in Fletcher (1988) has been used: the pressure p in the $x-$momentum equation is first replaced by the mean pressure p_0^0; secondly, the mean pressure p_0^0 in the subsonic section of the boundary layer is extrapolated from the adjacent supersonic layer. For a boundary layer over a flat plate, we set $\partial p_0^0/\partial x$ to be zero.

The term $\mathbf{Z}_1$ in Eq. (19) is given by

$$\mathbf{Z}_1 = (z_{11}, z_{12}, z_{13}, z_{14}, z_{15})^T, \tag{22}$$

where

$$z_{11} = -\rho\frac{\partial u^0}{\partial x} - u\frac{\partial \rho^0}{\partial x} + \frac{\partial(\rho^2 u^0)}{\partial x},$$

$$z_{12} = -(u-u^0)\frac{\partial \overline{\rho u}}{\partial x} - (\rho u - \overline{\rho u})\frac{\partial u^0}{\partial x},$$

$$z_{13} = -(u-u^0)\frac{\partial \overline{\rho v}}{\partial x} - (\rho v - \overline{\rho v})\frac{\partial u^0}{\partial x},$$

$$z_{14} = -(u-u^0)\frac{\partial \overline{\rho w}}{\partial x} - (\rho w - \overline{\rho w})\frac{\partial u^0}{\partial x},$$

$$z_{15} = -(u-u^0)\frac{\partial}{\partial x}(E^0+p^0) - (E+p-E^0-p^0)\frac{\partial u^0}{\partial x}.$$

2.4 Some comments

It can be shown that the governing equations obtained from our approach for an incompressible boundary layer over a flat plate are identical to those of Spalart (1988) when the coordinate transformation in Spalart (1988) is not used. In a sense, our approach is similar to Spalart's (1988) in that in both two scales are utilized. In our approach, the long-scale analysis is explicitly applied to the *governing equations* for mean flow quantities (i.e. $(0, k_y)$ modes), and the short-scale analysis to the *governing equations* for turbulence quantities. When there are large streamwise streaks, e.g. in a three-dimensional boundary layer, our approach may be more

general since the related governing equations for mean flow quantities are explicitly parabolized, making the use of spatial marching schemes more justifiable.

In Spalart (1988), coordinate tilting has been introduced to model the nonparallel effects of boundary layers. In Guo *et al.* (1994), our experience with transitional compressible boundary layer flows shows that the coordinate transformation technique does not guarantee an improved result, partly due to the difficulty in selecting a proper tilting angle. In this study, this technique is not used.

Compared to the parabolized stability equations (PSE) approach developed for transitional flows (Bertolotti, Herbert & Spalart, 1991), we have the following comments. The PSE has been proven to be a very powerful tool in studying the transition process in spatially growing boundary layers up to the early stage of breakdown. The possibility of developing a PSE type approach for turbulent boundary layers has been appealing (Zang, 1991). To our understanding, the PSE relies on the spatial marching of shape functions (eigenfunctions) of all modes in the streamwise direction. This requires the spatial evolutions of all shape functions to be slow in this direction. In turbulent boundary layers, only the mean flow $\mathbf{u}_1^0$ and the stationary spanwise modes $\mathbf{u}_2^0$ have slowly evolving shape functions in the streamwise direction. The shape functions of other modes do not have slow variations in the streamwise direction, and thus cannot be marched downstream by a spatial marching scheme. The method we described in this study has explored the possibility of marching downstream the shape functions of $\mathbf{u}_1^0$ and $\mathbf{u}_2^0$, and computes the other modes locally. Thus it can be viewed as a version of PSE for turbulent boundary layer flows.

3. Implementation and code validation

The numerical method discussed in §2 has been implemented in a TDNS code developed by Adams (1993). Fourier collocation methods are employed for the spatial derivative calculations in the spanwise and streamwise directions, and a compact central finite-difference (Padé) scheme is employed in the non-periodic wall-normal direction. The solution is advanced in time fully explicitly by a third-order low-storage Runge-Kutta scheme. More details of this TDNS code can be found in Adams (1993).

In order to maintain flexibility, both streamwise and spanwise spatial-averaging can be performed on the quantities at x_{n+1}. For the quantities at x_n and x_{n-1}, time-averaging is also implemented as an option, since the spanwise modes $\mathbf{u}_2^0$ in some cases evolve with time t and a time-averaging is needed to obtain stationary solutions. In this study, spanwise spatial-averaging is not used.

In order to validate the code, we first simulate a laminar boundary layer flow at $M_\infty = 4.5$, with all non-zero streamwise modes set to be zero (i.e. the Reynolds stress terms are set to be zero). Similarity solutions for the boundary layer were used as the initial profiles to start the downstream spatial marching. At each spatial step, the solution is advanced in time until a steady-state solution is reached. Once the steady-state solution is achieved, the solution is marched downstream again one step. At all spatial steps, our code can duplicate the similarity solutions accurately.

Simulations of turbulent boundary layer flows cannot be validated directly due to the lack of comprehensive database for these flows. In the following section, we present preliminary results for the turbulent boundary layers at three different Mach numbers.

4. Preliminary results

4.1 Simulation parameters and procedures

In order to study the compressibility effects at different free-stream Mach number, we have done three case studies at $M_\infty = 3$, 4.5, and 6. The simulation parameters for these three cases are listed in Table 1. The sizes of the computational boxes, L_x in the x direction, L_y in the y direction, and L_z in the wall-normal direction, are given in the terms of both boundary layer thickness, δ_0, and wall unit. The numbers of grids in the x, y, and z directions are given by N_x, N_y, and N_z respectively. Sampling time t_s is non-dimensionalized by the free-stream variables. In all cases, the laminar adiabatic wall temperatures were used as the constant wall temperatures in the simulations, with $T_\infty = 61.15K$.

TABLE 1. Simulation parameters.

M_∞	Re_θ	T_w/T_∞	L_x	L_y	L_z	$N_x \times N_y \times N_z$	t_s
3	3015	2.5	$1.67\delta_0$	$0.96\delta_0$	$3.59\delta_0$	192×144×180	34
			527^+	300^+	1133^+		
4.5	2618	4.38	$1.59\delta_0$	$0.95\delta_0$	$3.18\delta_0$	180×144×190	32
			260^+	155^+	520^+		
6	2652	6.98	$2.16\delta_0$	$1.3\delta_0$	$3.68\delta_0$	180×128×200	19
			229^+	137^+	390^+		

The computation at $M_\infty = 4.5$ was first performed. The TDNS of a subharmonic transition process at $M_\infty = 4.5$ (Adams, 1993) was continued until the flow has gone through the breakdown stage and become turbulence. Then the TDNS transition data were used as the initial solution to start the spatial marching with the approach described in §2. Since the TDNS transition data are not the solutions of the Reynolds-average Navier-Stokes equations, spatial transients are expected in the first few steps. Usually, the transients diminish after a few steps. The spatial extent affected by the transient solutions depends on both the character of the Reynolds-averaged Navier-Stokes equations and the initial conditions. This issue is beyond the scope of this report.

All computations are performed on a NEC-SX3 computer with one processor, with the code running typically at 1.8 GFLOPS. To cut down computation cost, a smaller box was used at the first step, and the solution is advanced in time until a statistically steady-state is reached. Then the solution was marched downstream one step spatially with a bigger computation box. In the cases of $M_\infty = 3$ and 6, the solutions from the $M_\infty = 4.5$ case were first rescaled and used as the initial data to start the spatial marching. Similar to the case of $M_\infty = 4.5$, smaller boxes were used in the first two steps, and then a bigger box was used at the third step.

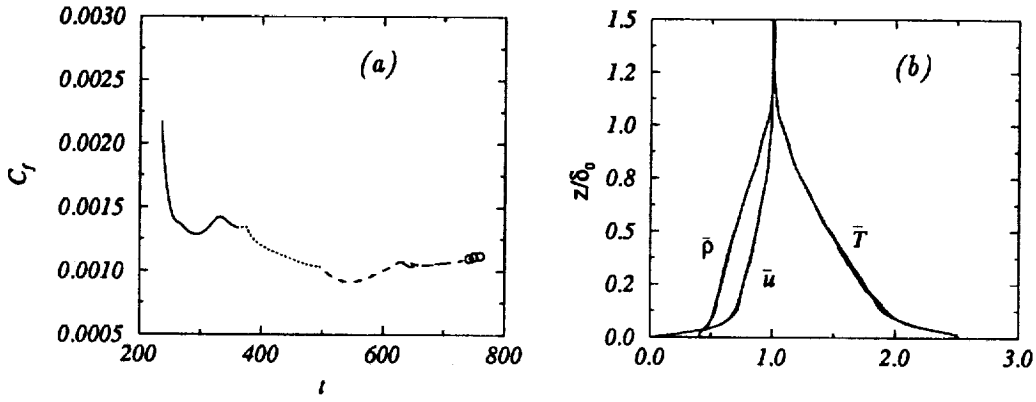

FIGURE 1. (*a*) Time history of skin friction coefficient, C_f. Legend: ——— step 1; ····· step 2; ---- step 3; -·- step 3 with a big box; o sampling period. (*b*) Mean profiles of $\overline{u}$, $\overline{T}$ and $\overline{\rho}$ at $M_\infty = 3$ over $t = 438 - 472$. The profiles at $t = 472$ are indicated by ——— .

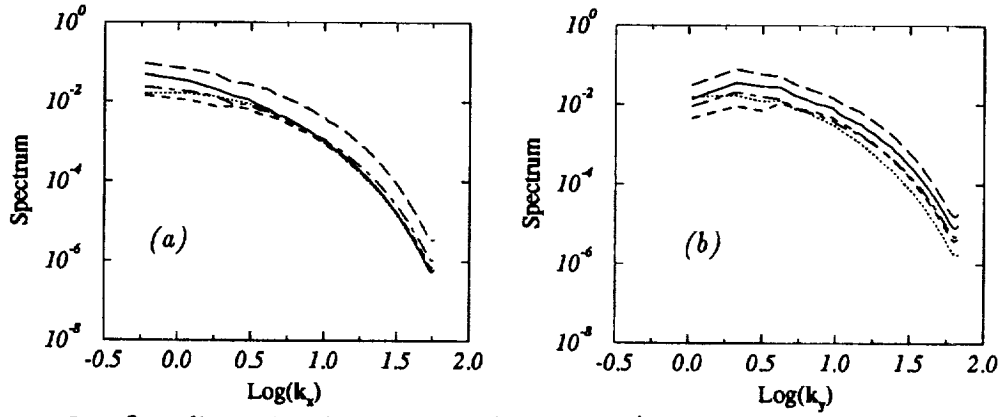

FIGURE 2. One-dimensional spectra of $\mathbf{u}'$ at $z = 30^+$ and $M_\infty = 3$: (*a*) in the x direction; (*b*) in the y direction. Legend: ——— u; ····· v; ---- w; —— T; -·- ρ.

Fig. 1(*a*) shows the time history of skin coefficient, C_f, during the first three steps at $M_\infty = 6$. Here t is non-dimensionalized by the free-stream quantities. It can be seen that at each station, C_f is able to reach a statistically steady state. The data presented in this report is taken from the third step. At the first step, a large variation of C_f is observed. We believe this is due to the large transient caused by the initial conditions. Note that the initial data is rescaled from that of $M_\infty = 4.5$ case. A similar pattern has also been observed at $M_\infty = 3$.

Fig. 1(*b*) shows the variations of the mean profiles, $\overline{u}$, $\overline{T}$ and $\overline{\rho}$ over the time period $438 - 472$ at $M_\infty = 3$. It can be seen that though the boundary layer does not grow with t, it does vary with t. We expect that the fluctuations of the mean flow quantities with time will become smaller when a bigger computational box is used.

In all cases, one-dimensional spectrum is monitored to ensure that the computations are well resolved. Fig. 2 shows the one-dimensional spectra near the wall at $M_\infty = 3$. Here the wavenumbers, k_x and k_y, are normalized by the boundary layer thickness. It can be seen that in both plots, the difference between maximum and minimum spectral components is maintained to be at least $10^{3.5}$ to 10^4. Similar situations are found in the cases of $M_\infty = 4.5$ and 6.

Figs. 3-5 show the two-point correlations for all three cases. Compared to incompressible channel or boundary layer simulations (Kim *et al.*, 1987 and Spalart, 1988), the values of these functions are too high near the centers of the boxes. A similar situation was also reported in the compressible channel simulations of Coleman *et al.* (1993). In Coleman *et al.* (1993), acoustic effects are found to be responsible for high correlations observed in the compressible channel flows. Here this issue has not been investigated thoroughly so far. In all our cases, rather large streaks have been observed (cf. §4.2). We speculate that the existence of these large streaks near the wall might be the primary reason for the high two-point correlations.

Note that the downstream developments of the solutions have not been investigated in this study, since such investigations require the solutions to be marched downstream a few steps. So far we have only marched the solution downstream three steps at most. The solutions at these steps might still be affected by the spatial transients.

4.2 Large streamwise streaks

In all cases, large streamwise streaks have been observed. Fig. 6 shows the contour surface of $\overline{u} = 0.4$ at $M_\infty = 3$. In the figure, the spanwise dimensions of the streaks are about 100^+, which are close to those found in an incompressible boundary layer flow. The streamwise dimension of these streaks cannot be obtained from the figure since the computational box is not large enough. Fig. 7 gives an impression of the extent of these streaks in the wall-normal direction. Compared to the boundary layer thickness ($\delta_0 = 314^+$), they are rather large, affecting almost one third of the boundary layer.

Figs. 8 and 9 show a similar situation at $M_\infty = 4.5$, except that here the streaks are even bigger compared to the boundary layer thickness ($\delta_0 = 163^+$). So far we have not been able to study the spanwise and streamwise extents of these streaks systematically, primarily due to the their large size together with the present limitation to small computational boxes (in terms of wall units). Since these streaks are rather large compared to the computational boxes, their evolution affect both mean flow quantities $\mathbf{u}^0$ and turbulence quantities $\mathbf{u}'$ (note that $\mathbf{u}'$ is solved from (19) correctly only if $\mathbf{u}^0$ is steady). Thus the quality of our DNS data needs still to be assessed, and readers should be aware of that in comparing our DNS results with other sources.

The mechanism for the formation of these large streaks are not clear to us. In compressible channel flows, DNS results have shown that compressibility effects may be responsible for rather large structures in the streamwise directions (Coleman *et al.*, 1993, Coleman, 1993 and Moser, private communication, 1994). In our cases, we speculate that both compressibility effects and low Reynolds number effects due to

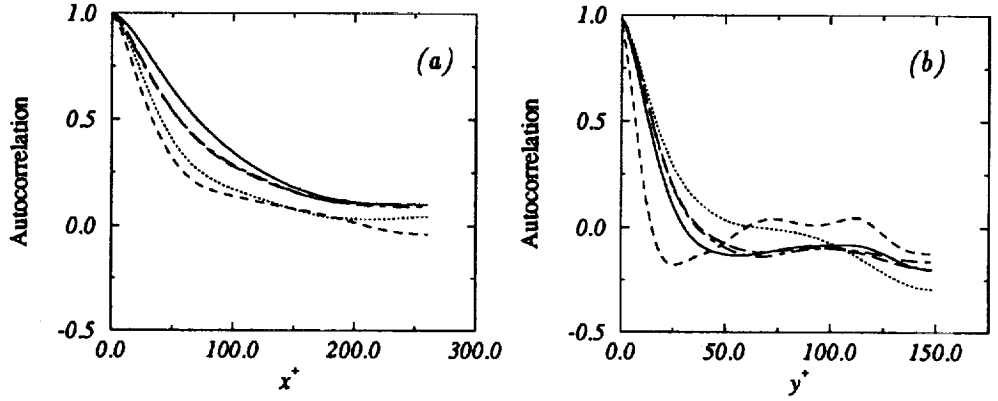

FIGURE 3. Two-point correlations at $z = 18.8^+$ and $M_\infty = 3$: (a) in the x direction; (b) in the y direction. Legend: —— u; ····· v; - - - - w; —— T; - · - ρ.

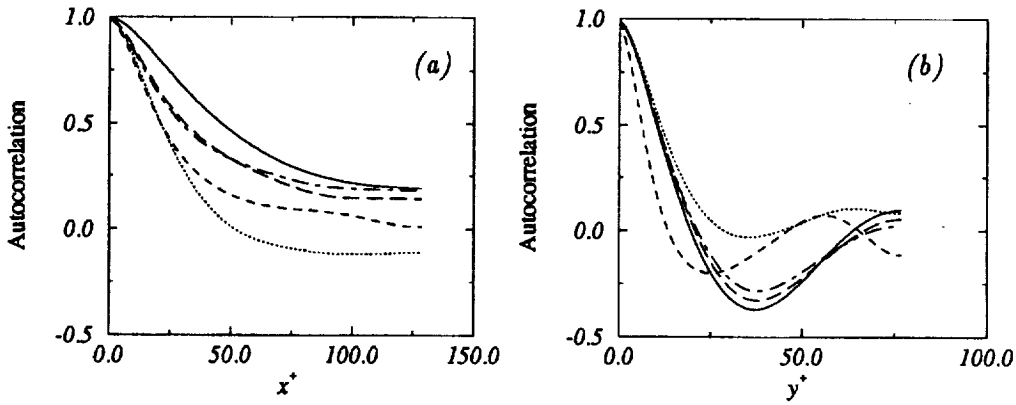

FIGURE 4. Two-point correlations at $z = 17.3^+$ and $M_\infty = 4.5$: (a) in the x direction; (b) in the y direction. Legend is the same as Fig. 3.

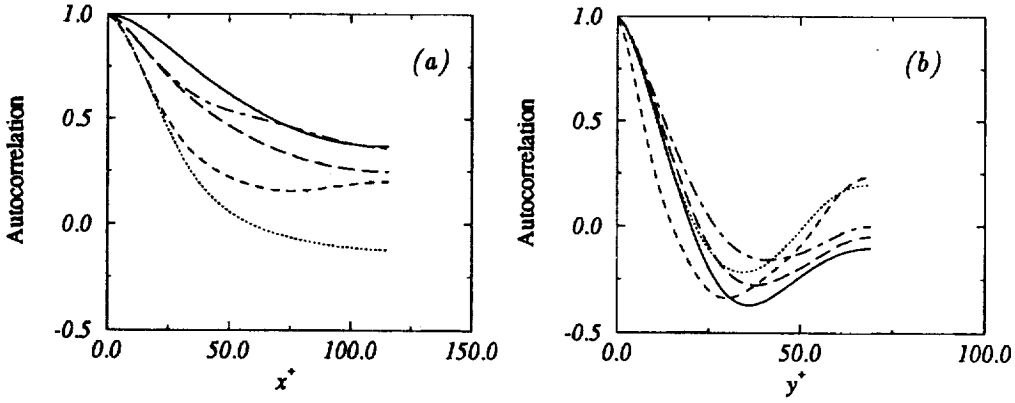

FIGURE 5. Two-point correlations at $z = 15.6^+$ and $M_\infty = 6$: (a) in the x direction; (b) in the y direction. Legend is the same as Fig. 3.

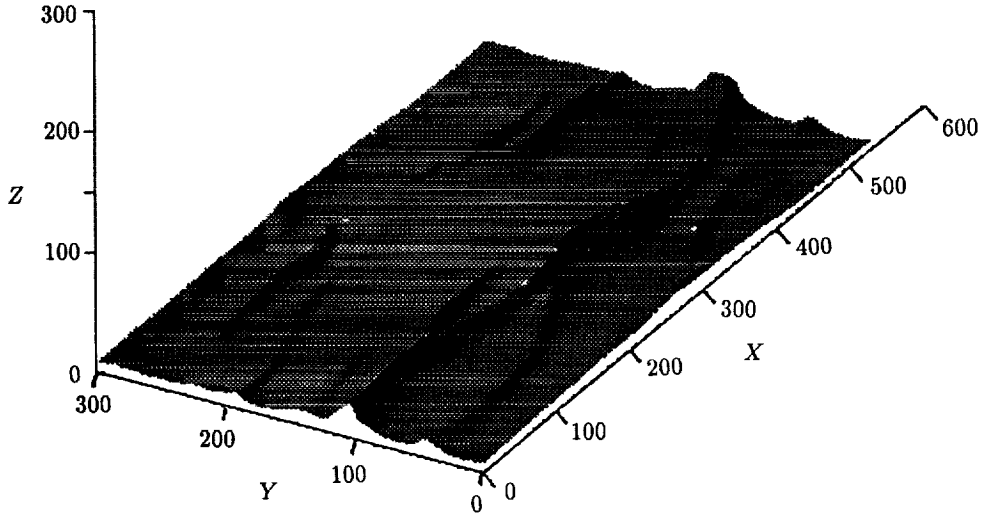

FIGURE 6. Contour surface of $\overline{u} = 0.4$ at $M_\infty = 3$.

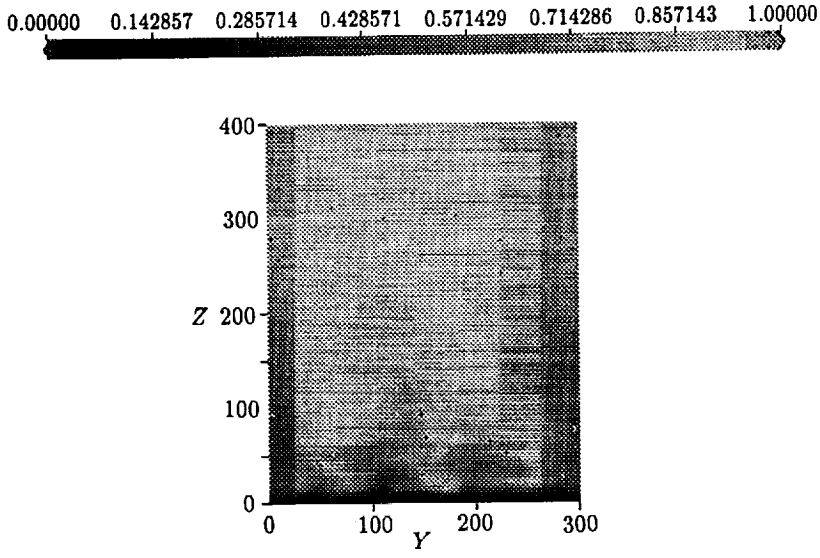

FIGURE 7. Contour plot of $\overline{u}$ on the $y - z$ plane at $x = 0$ and $M_\infty = 3$.

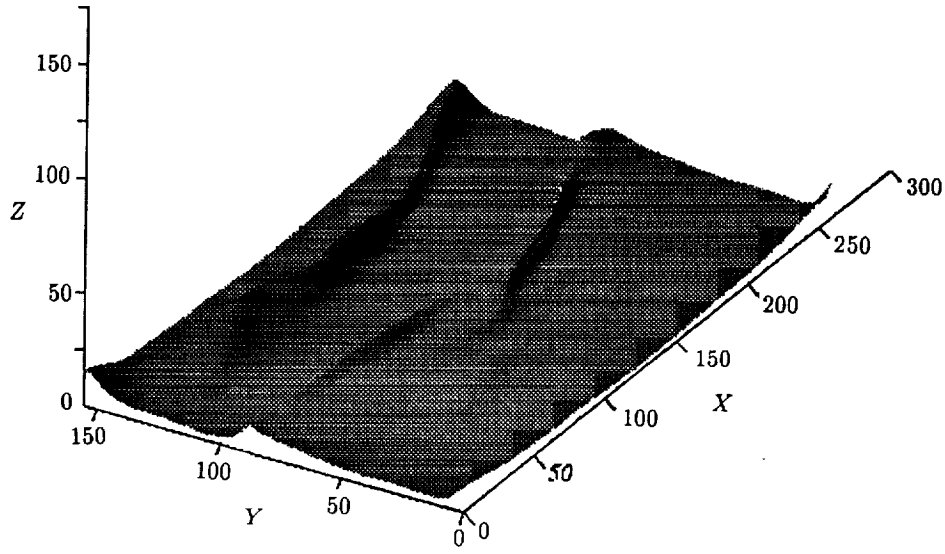

FIGURE 8. Contour surface of $\overline{u} = 0.3$ at $M_\infty = 4.5$.

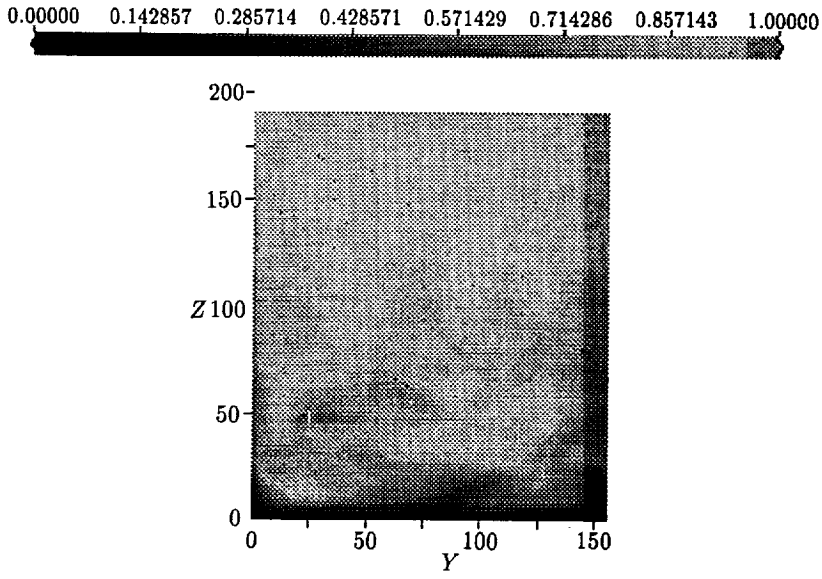

FIGURE 9. Contour plot of $\overline{u}$ on the $y - z$ plane at $x = 0$ and $M_\infty = 4.5$.

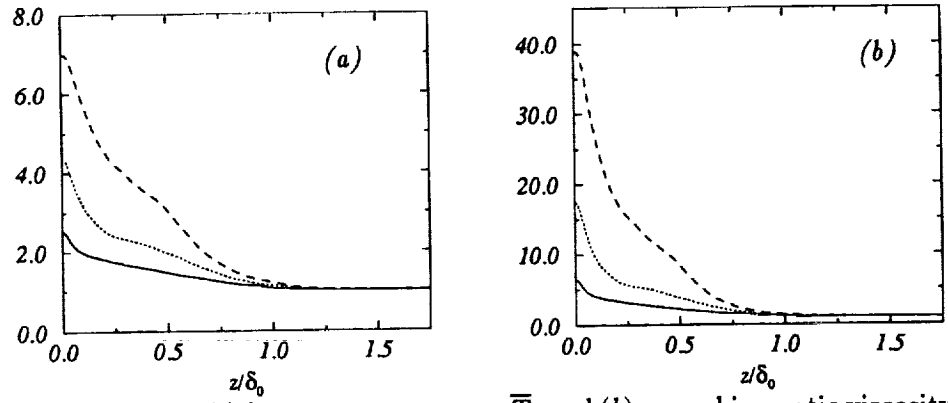

FIGURE 10. Profiles of (a) mean temperature, $\overline{T}$, and (b) mean kinematic viscosity, $\overline{\nu}$. Legend: —— $M_\infty = 3$, ····· $M_\infty = 4.5$, ---- $M_\infty = 6$.

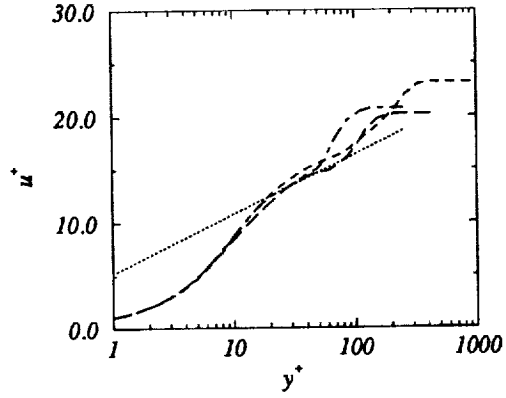

FIGURE 11. Mean streamwise velocity, $\overline{u}$, after Van Driest transformation. Legend: ---- $M_\infty = 3$, —— $M_\infty = 4.5$, -·- $M_\infty = 6$, ····· $2.44\ln(y^+) + 5.5$.

hot-wall conditions may play important roles. With an increase in wall temperature, the density of air decreases and its viscosity increases. This effectively reduces the Reynolds number in the near wall region. Fig. 10(a) shows the averaged temperature profiles across the boundary layers at different Mach numbers. The corresponding profiles for the kinematic viscosity, $\overline{\nu}$, are shown in Fig. 10(b). It can be seen that the increase of $\overline{\nu}$ is roughly proportional to $\overline{T}^2$. Therefore, the reductions of effective Reynolds numbers in the near wall regions due to the hot-wall conditions are significant.

4.3 Mean flow quantities

Fig. 11 shows the streamwise velocity profiles after the Van Driest transforms. Here the Van Driest transformation is defined by

$$\overline{u}^+_{VD} = \int_0^{\overline{u}^+} \left(\frac{\overline{\rho}}{\rho_w}\right)^{\frac{1}{2}} d\overline{u}^+ .$$

It can be seen that in all three cases, there are no apparent log-law regions. Note that at similar Reynolds numbers, some log-law regions can be observed in incompressible boundary layer flows (cf. Spalart, 1988). Thus we may conclude that the low Reynolds number effects due to the hot-wall conditions in our cases are significant.

Table 2 shows the skin friction coefficients, in comparison with the results of Van Driest transformation II, computed by Zeman (1993) at $Re_\theta = 10000$. Note that the Van Driest transformation II is usually formulated in terms of Re_x. Due to the difficulty in converting Re_x to Re_θ for a compressible turbulent boundary layer, we did not compute C_f at the relevant Re_θ so far.

TABLE 2. Computed skin friction coefficients compared to the calculations of Zeman (1993) using Van Driest transform II at $Re_\theta = 10000$.

M_∞	$C_f \times 10^{-3}$	C_f/C_{fi}	Van Driest II
3	1.854	0.522	0.58
4.5	1.729	0.470	0.40
6	1.110	0.303	0.30

Due to significant low Reynolds number effects in our DNS data, the effectiveness of Van Driest transformation cannot be demonstrated in this report. Readers are referred to Huang & Coleman (1994) for a further discussion on this issue.

4.4 Compressibility effects

Fig. 12 shows the profiles of turbulent Mach numbers. Note that M_t does not increase to the value that one would expect at $M_\infty = 6$. We believe that this is primarily due to the higher wall temperature at $M_\infty = 6$. We have seen in Fig. 10(b) that the kinematic viscosity, $\overline{\nu}$, is roughly proportional to $\overline{T}^2$. A lower than expected M_t at $M_\infty = 6$ is presumably caused by the high $\overline{\nu}$, which damps out the fluctuations in the near wall region.

In homogeneous flows, compressibility effects in the turbulent kinetic energy (TKE) equation can be measured by the dilatational dissipation, $\overline{\rho}\epsilon_d = \frac{4}{3}\overline{\mu u''^2_{i,i}}$, and the pressure-dilatation correlation, $p_d = \overline{pu''_{i,i}}$ (cf. Friedrich, 1993, Sarkar,1993, Spina *et al.*, 1994 and Lele, 1994 for a review). Recent work by Huang *et al.* (1994) also indicates that this is true for the near-wall turbulence. The inhomogeneous terms resulted from the compressibility of fluid are small and confined to the region very close to the wall. In Fig. 13, we have plotted these two terms, in comparison to the incompressible part of the dissipation, solenoidal dissipation $\overline{\rho}\epsilon_s = \overline{\mu\omega''_i\omega''_i}$, where ω_i is the component of vorticity. It can be seen that in all three cases, these two terms are small compared to solenoidal dissipation, $\overline{\rho}\epsilon_s$. This indicates that the influence of fluid compressibility on TKE is rather small in the flat plate boundary layer flows investigated here. Similar observations are also made by Huang *et al.* (1994) for near-wall turbulence in compressible channel flows at Mach number 3, and by Dinavahi & Pruett (1993) and Adams (1993) for late stage transitional boundary layer flows at $M_\infty = 4.5$.

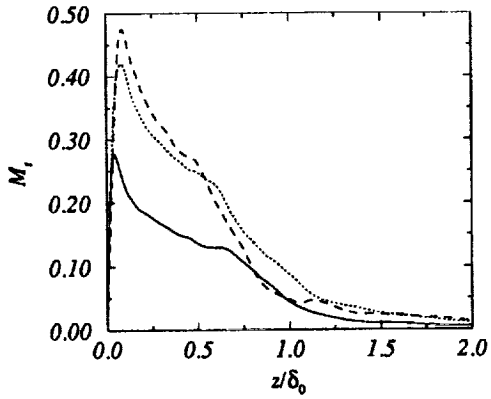

FIGURE 12. Turbulent number Mach number, $M_t = M_\infty \sqrt{\widetilde{u_i'' u_i''}}/\sqrt{\widetilde{T}}$. Legend: —— $M_\infty = 3$, ····· $M_\infty = 4.5$, ---- $M_\infty = 6$.

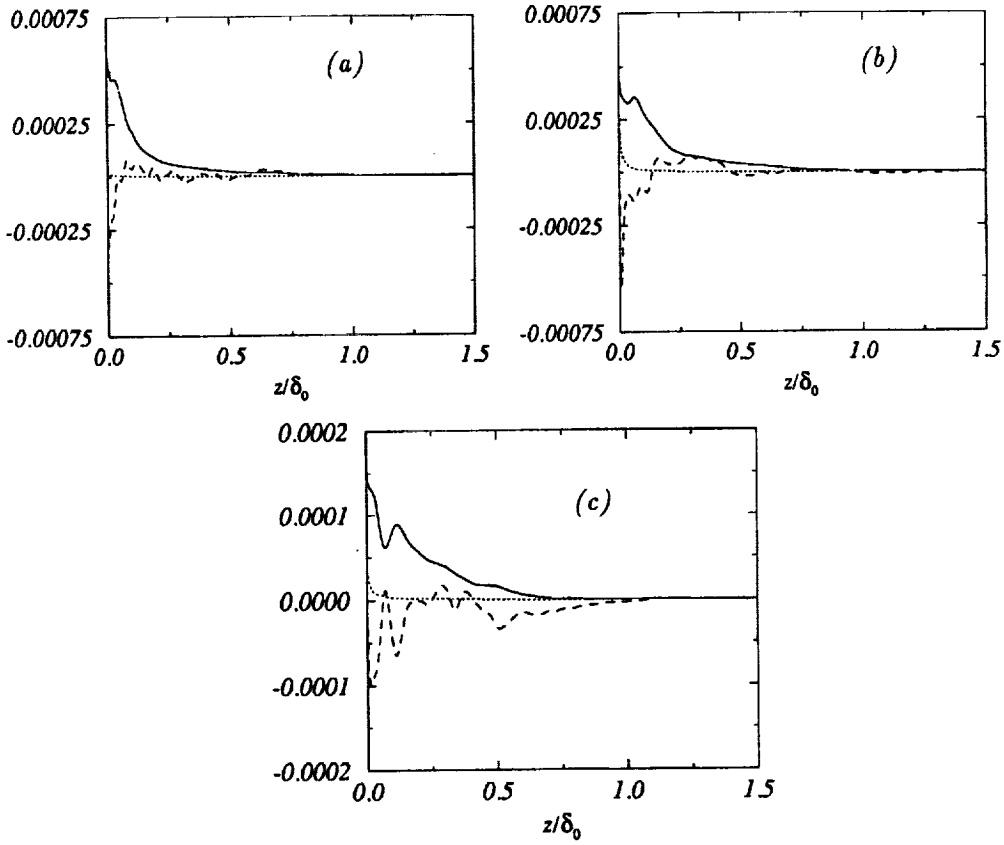

FIGURE 13. Compressibility effects: —— solenoidal dissipation, $\overline{\rho}\epsilon_s$, ····· dilatational dissipation, $\overline{\rho}\epsilon_d$, ---- pressure-dilatation correlation, p_d. (*a*) $M_\infty = 3$. $\overline{\rho}\epsilon_d$ and p_d have been enlarged 100 times. (*b*) $M_\infty = 4.5$. $\overline{\rho}\epsilon_d$ and p_d have been enlarged 10 times. (*c*) $M_\infty = 6$. $\overline{\rho}\epsilon_d$ and p_d have been enlarged 10 times.

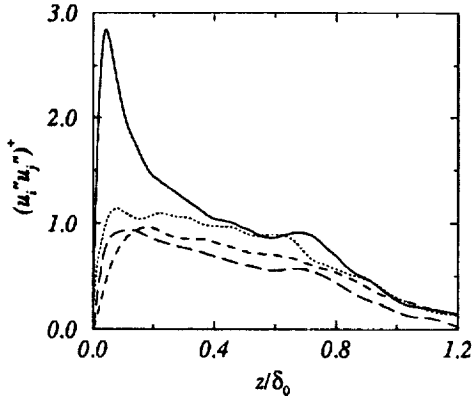

FIGURE 14. Favre-averaged Reynolds stress terms normalized by wall unit: —— $u''u''$; ····· $v''v''$; ---- $w''w''$; and —— $u''w''$.

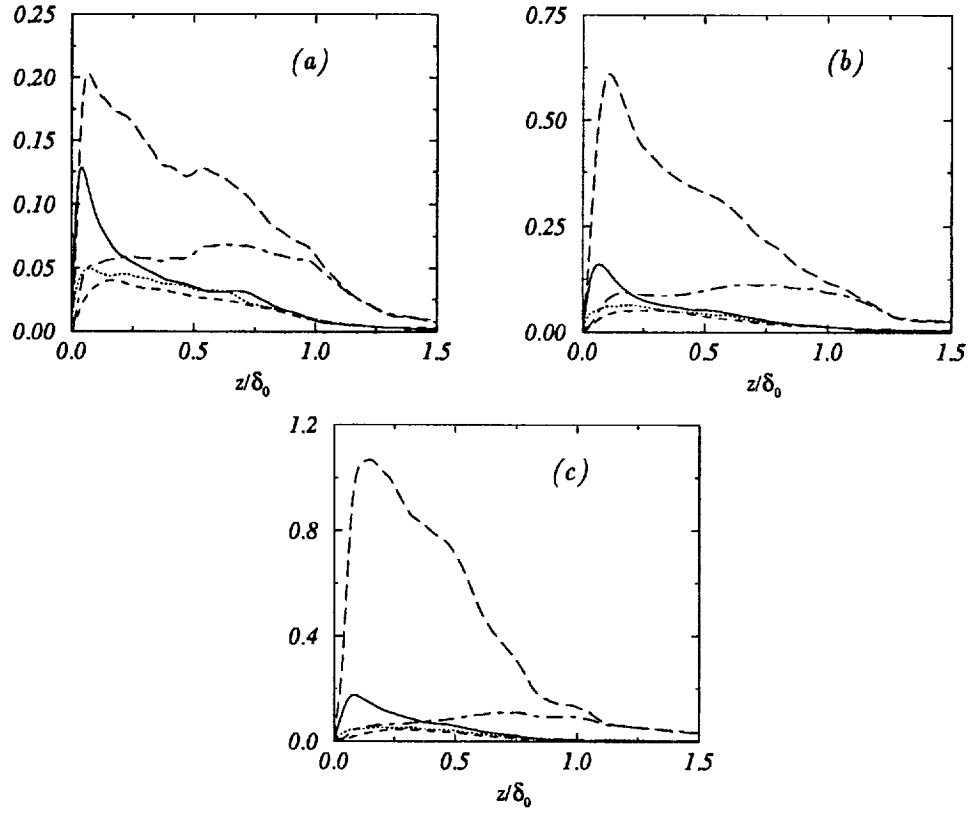

FIGURE 15. The *r.m.s.* of turbulence quantities: —— u', ····· v', ---- w', —— T', -·- ρ'. (*a*) $M_\infty = 3$; (*b*) $M_\infty = 4.5$; (*c*) $M_\infty = 6$.

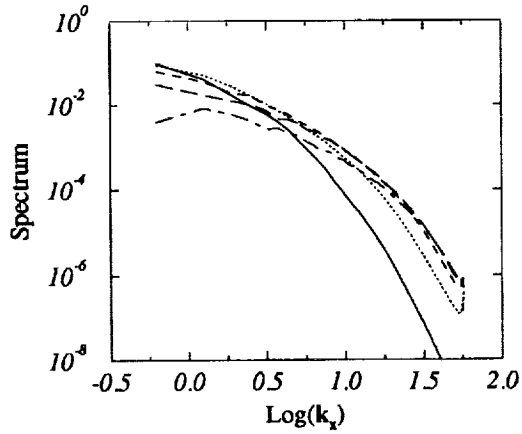

FIGURE 16. Spectra of u in the x direction taken from $z/\delta_0 = 0.04$ ——— , 0.1 ····· , 0.16 ---- , 0.42 —— , and 0.85 -·- at $M_\infty = 4.5$.

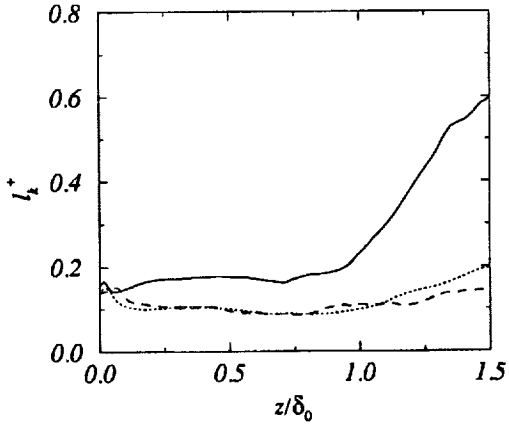

FIGURE 17. Kolmogorov scales, l_k^+, normalized by wall unit. Legend: ——— $M_\infty = 3$, ····· $M_\infty = 4.5$, ---- $M_\infty = 6$.

4.5 Other quantities

Since our DNS data are severely affected by low Reynolds number effects, large streaks, and small computational boxes, we do not expect to get good statistics in all three cases. In this subsection, we shall only present a few basic quantities to give readers a qualitative impression.

The Favre-averaged Reynolds stress terms normalized by the wall units at $M_\infty = 3$ are shown in Fig. 14. Fig. 15 shows the turbulence fluctuation $\mathbf{u}'$ for the three cases. It can be seen that the density fluctuations, ρ', have larger amplitudes near the edges of the boundary layers in all three cases.

5. Discussions

In all our computations, the computational boxes are rather small in terms of wall units, but not small at all in terms of boundary layer thickness. That is due to the fact that the hot-wall conditions increase the wall units in terms of boundary layer thickness. Apparently for the cases studied in this report, larger boxes are needed in order to give improved turbulence statistics. This, however, is expected to be computationally very expensive if the resolution used in this study is to be kept. One may argue that coarser grids might be sufficient since the hot-wall conditions reduce the effective Reynolds number in the near wall region and turbulence scales are large away from the walls. This argument is not supported by our numerical experience so far. Fig. 16 shows the one-dimensional spectra taken at different distances from the wall at $M_\infty = 4.5$. It can be seen that the spectra have almost the same value at high wavenumber from $z/\delta_0 = 0.21$ to 0.85. This indicates that the resolution requirement is not reduced at all away from the wall. In order to find the explanation, we plot in figure 17 the Kolmogorov scale, l_k^+, as functions of z. In the figure, we can see that l_k^+ has roughly the same value in most part of the boundary layer. Similar situations can be seen in $M_\infty = 3$ and 6 cases. Since one needs rather dense grids in the near wall region to resolve mean flow profiles, the resolution requirement may be more or less the same throughout the whole boundary layer. This observation is basically supported by the one-dimensional spectra in Fig. 16. Apparently, this situation is rather different from that in incompressible boundary layer flows, where dense grids are needed only in the near wall region. From the above discussion, we can conclude that turbulent boundary layers with hot-wall conditions require a larger computational effort than in the cold-wall case.

In Fig. 17, one can also see that l_k^+ is much smaller than that in an incompressible fluid case, where $l_k^+ \approx 2^+$ (Moser, private communication, 1994). This suggests that the grid spacing rules derived from DNS of incompressible boundary layer flows cannot be applied to a compressible flow case.

6. Concluding remarks

In this report, we have presented a numerical approach for DNS of compressible turbulent boundary layer flows, which solves the parabolized Reynolds-average Navier-Stokes equations for mean flow quantities and computes turbulence quantities locally with a temporal DNS approach. Preliminary results from three cases at $M_\infty = 3$, 4.5, and 6 are presented. All our results indicate that compressibility effects on turbulent kinetic energy equations, i.e. dilatational dissipation and pressure-dilatation correlation, are small. Due to the hot-wall conditions used in all cases, these preliminary results are severely affected by low Reynolds number effects, large streaks, and small computational boxes. Hot-wall conditions seem to be more difficult to deal with than cold-wall conditions. Grid spacing rules derived from the DNS of incompressible boundary flows are not valid in a compressible case.

Acknowledgments

We gratefully acknowledge the invaluable discussions with Dr. Kleiser during the

course of this work. Thanks are due Drs. G. A. Blaisdell, P. Bradshaw, G. N. Coleman, P. G. Huang, R. Moser, M. Rai, and O. Zeman for their many helpful comments and suggestions during the 1994 summer program at CTR.

REFERENCES

ADAMS, N. A. 1993 Numerische Simulation von Transitionsmechanismen in kompressiblen Grenzschichten . *Doctoral Dissertation,* Technical University of Munich, Germany. Also DLR-FB 93-29, DLR, Germany (in German).

BERTOLOTTI, F. P., HERBERT, TH. & SPALART, P. R. 1992 Linear and nonlinear stability of the Blasius boundary layer. *J. Fluid Mech.* **242,** 441-471.

COLEMAN, G. N., BUELL, J. G., KIM, J. & MOSER, R. D. 1993 Direct simulation of compressible wall-bounded turbulence. *Proc. 9th Symp. on Turbulent Shear flow.* Kyoto, Japan.

COLEMAN, G. N. 1993 Direct simulation of isothermal-wall supersonic channel flow. *CTR Annual Research Briefs 1993.*Center for Turbulence Research, Stanford Univ./NASA Ames Research Center, 313-328.

FLETCHER, C. A. J. 1988 *Computational Techniques for Fluid Dynamics, Volume II.* Springer-Verlag, Berlin.

FRIEDRICH, R. 1993 Compressible turbulence. *Space Course 1993.* Technical University of München, Germany.

GUO, Y., ADAMS, N. A. & KLEISER, L. 1994 Modeling of nonparallel effects in temporal DNS of compressible boundary layer transition . *Theoret. Comput. Fluid Dynamics.* in press.

GUO, Y. & FINLAY, W. H. 1994 Wavenumber selection and irregularity of spatially developing Dean and Görtler vortices . *J. Fluid Mech.* **264,** 1-40.

HAIRER, E., NØRSETT, S. P. & WANNER, G. 1987 *Solving Ordinary Differential Equations I.* Springer-Verlag, Berlin.

HUANG, P. G. & COLEMAN, G. N. 1994 Van Driest transformation and compressible wall-bounded flows. *AIAA J.* in press.

HUANG, P. G., COLEMAN, G. N. & BRADSHAW, P. 1994 Compressible turbulent channel flows - a closer look using DNS data. Submitted for publication.

KIM, J., MOIN, P. & MOSER, R. 1987 Turbulence statistics in fully developed channel flow at low Reynolds number. *J. Fluid Mech.* **177,** 133-166.

KLEISER, L. & ZANG, T. A. 1991 Numerical simulation of transition in wall-bounded shear flows. *Ann. Rev. Fluid Mech.* **23,** 495-537.

LELE, S. L. 1994 Notes on the effects of compressibility on turbulence. *Ann. Rev. Fluid Mech.* **26,** 211-254.

SARKAR, S. 199 Turbulence modeling and simulation of high-speed flows. *Space Course 1993.* Technical University of München, Germany.

SPALART, P. R. & LEONARD, A. 1985 Direct numerical simulation of equilibrium turbulent boundary layers. *Proc. 5th Symp. on Turbulent Shear Flows.* Ithaca, NY.

SPALART, P. R. 1986 Numerical study of sink-flow boundary layers. *J. Fluid Mech.* **172,** 307-328.

SPALART, P. R. 1988 Direct simulation of a turbulent boundary layer up to $Re_\theta = 1410$. *J. Fluid Mech.* **187,** 61-98.

SPALART, P. R. & WATMUFF, U. H. 1993 Experimental and numerical study of turbulent boundary layer with pressure gradients. *J. Fluid Mech.* **249,** 337-371.

SPINA, E. F., SMITS, A. J. & ROBINSON, S. K. 1994 The physics of supersonic turbulent boundary layers. *Ann. Rev. Fluid Mech.* **26,** 287-319.

ZANG, T. A. 1991 Numerical simulation of the dynamics of turbulent boundary layers: perspective of transition simulator. *Phil. Trans. R. Soc. Lond. A.* **337,** 95-102.

ZEMAN, O. 1993 A new model for super/hypersonic turbulent boundary layers. *AIAA Paper* 93-0897.

Modeling and LES group

There are five papers in the modeling and large-eddy simulation (LES) group. Three of the studies had the common objective of introducing spatially non-local information into single-point closures. The papers by Laurence & Durbin and Demuren, Lele & Durbin use the elliptic relaxation idea. Durbin (JFM, 1993) introduced non-local effects in his models of pressure-strain rate correlation by an elliptic differential operator. This approach has been very successful in predicting wall-bounded flows without ad-hoc damping functions and explicit use of the distance to the wall. In his full Reynolds stress closures, Durbin had used a rather simple linear isotropization (IP) model for the pressure-strain correlation as input to the elliptic relaxation operator. The non-linear model of Craft & Launder has been shown to be superior to the IP models in a variety of flows. Laurence's project was to combine the elliptic relaxation idea with the Craft & Launder model. He also conducted a detailed analysis of the Reynolds stress budgets, which revealed the importance of the elliptic relaxation part. That is, near the wall, the homogeneous solution of the elliptic relaxation operator was dominant and led to significantly improved agreement with the direct numerical simulation data irrespective of the basic pressure-strain model.

Demuren used the elliptic relaxation idea to develop a non-local pressure-diffusion model for use with the $k - \epsilon$ equations. In practice the pressure-diffusion term is usually combined with the turbulent diffusion, and their combination is modeled by gradient-diffusion. This practice appears to be reasonable except near a turbulent/non-turbulent interface such as those at the edges of boundary layers and jets and wakes. The symptom of its failure is a very rapid and unphysical drop of turbulent kinetic energy and eddy viscosity near the free-stream edge, which, at the very least, casts doubt on the prediction of the free-stream turbulence effects on shear layers and boundary layers. The elliptic relaxation leads to a more gradual transition near the free-stream edge by transporting more turbulent kinetic energy from the turbulence core to the free-stream.

Non-local information can also be introduced in the framework of one-point closures by including variables that involve the derivatives and integrals of flow quantities in the formulation. One such variable is the vector stream function; the Reynolds stresses can be extracted from the derivatives of its two-point correlation function, evaluated at zero separation. Oberlack, Rogers & Reynolds developed a new model for the two-point correlation of the vector stream function and compared it with the DNS data of homogeneous shear flow. The model coefficient was chosen to minimize the $L2$ norm of the difference between the model and the DNS data. The model predicts the two-point correlation function accurately. Since the derivatives of the two-point correlation function were not calculated, it is difficult to judge the ability of the model to predict the Reynolds stresses. The rapid part of the pressure strain predicted by this model is evidently deficient. It consists of

PRECEDING PAGE BLANK NOT FILMED

the familiar linear model, with its well-known deficiency in reproducing the effects of rotation.

In recent years several models have been introduced to account for the effects of compressibility on turbulence. The dilatation dissipation model introduced by Zeman and Sarkar is known to be effective in the prediction of free-shear flows, but its impact in boundary layers has been insignificant. The pressure-dilatation term in the turbulent kinetic energy equation is expected to be important in the shock/turbulence interaction problem. Brankovic & Zeman incorporated Zeman's pressure dilatation model into a Pratt & Whitney code for computation of complex flows and used it to compute a compression corner flow. Although they found some improvement in the prediction of the mean velocity profiles, the experimentally reported unsteadiness in the separation bubble was not predicted even when the code was run in a "time accurate" mode. This failure may be attributed to the turbulence models used, but the effects of numerical dissipation in the code can not be dismissed.

The only LES project in this Summer Program was initiated by Meneveau. His objective was to test an alternative formulation of the dynamic subgrid-scale model. His alteration addresses a well-known numerical difficulty which appeared in its early formulations: The dynamic model produces negative eddy viscosity in some regions of space. In the past this problem has been addressed either by spatial averaging of the eddy viscosity or by the variational formulations of Ghosal, Lund & Moin (CTR Annual Res. Briefs, 1992). Meneveau Lund & Cabot point out that if averaging is to be performed, it is more physically appropriate to perform it in a Lagrangian frame following the turbulence structures. Moreover, in complex three-dimensional flows, where there are no directions of flow homogeneity, it is virtually impossible to carry out spatial averaging. They formulated a dynamic model with Lagrangian averaging and successfully tested it in isotropic turbulence and turbulent channel flow. Surprisingly, the model is computationally efficient and does a good job of predicting the flows considered. However, this formulation does introduce new model parameters, which is contrary to the key advantage of the dynamic model where all parameters are computed dynamically. It remains to be seen whether this model is more accurate and robust than some of the recently developed dynamic localization models.

Parviz Moin

Center for Turbulence Research
Proceedings of the Summer Program 1994

N95-21051

A Lagrangian dynamic subgrid-scale model of turbulence

By C. Meneveau[1], T. S. Lund[2] AND W. Cabot[2]

A new formulation of the dynamic subgrid-scale model is tested in which the error associated with the Germano identity is minimized over flow pathlines rather than over directions of statistical homogeneity. This procedure allows the application of the dynamic model *with averaging* to flows in complex geometries that do not possess homogeneous directions. The characteristic Lagrangian time scale over which the averaging is performed is chosen such that the model is purely dissipative, guaranteeing numerical stability when coupled with the Smagorinsky model. The formulation is tested successfully in forced and decaying isotropic turbulence and in fully developed and transitional channel flow. In homogeneous flows, the results are similar to those of the volume-averaged dynamic model, while in channel flow, the predictions are superior to those of the plane-averaged dynamic model. The relationship between the averaged terms in the model and vortical structures (worms) that appear in the LES is investigated. Computational overhead is kept small (about 10 % above the CPU requirements of the volume or plane-averaged dynamic model) by using an approximate scheme to advance the Lagrangian tracking through first-order Euler time integration and linear interpolation in space.

1. Introduction

The dynamic model (Germano *et al.*, 1991) for the parametrization of subgrid stresses in a Large-Eddy-Simulation (LES) is a means of utilizing information from the resolved turbulent velocity field $\tilde{u}_i(\mathbf{x},t)$ to dynamically compute model coefficients. It is based on the algebraic identity,

$$L_{ij} = T_{ij} - \overline{\tau}_{ij}, \tag{1}$$

where

$$L_{ij} = \widetilde{\tilde{u}_i\tilde{u}_j} - \tilde{\overline{u}}_i\tilde{\overline{u}}_i, \qquad T_{ij} = \widetilde{\widetilde{u_iu_j}} - \tilde{\overline{u}}_i\tilde{\overline{u}}_j, \quad \text{and} \quad \tau_{ij} = \widetilde{u_iu_j} - \tilde{u}_i\tilde{u}_j. \tag{2}$$

Above, a *tilde* represents low-pass filtering with a filter-width of size Δ (comparable to the grid-size of the LES), while an *overbar* represents filtering at a scale 2Δ. When the identity is written with the stresses T_{ij} and τ_{ij} replaced by the Smagorinsky model, and Eq. (1) is enforced in a least-square error sense over all five independent

1 The Johns Hopkins University
2 Center for Turbulence Research

tensor elements (Lilly, 92), one obtains the following expression for the (dynamic) Smagorinsky coefficient:

$$c_s^2(\mathbf{x},t) = \frac{L_{pq}M_{pq}}{M_{pq}M_{pq}}, \tag{3}$$

where

$$M_{ij} = -2\Delta^2 \left[4\overline{|\tilde{S}|\tilde{S}_{ij}} - \overline{|\tilde{S}|\tilde{S}_{ij}}\right], \tag{4}$$

and $\tilde{S}_{ij}$ is the resolved rate-of-strain tensor. This version of the dynamic model in which the coefficient can vary from point to point is often referred to as the 'local dynamic model'.

There are two problems associated with the local dynamic model (Eq. (3)). First, as pointed out by Ghosal *et al.* (1994), it is mathematically inconsistent to remove the coefficient from the filter operation (in $\overline{\tau_{ij}}$) as if it were a constant. Second, as observed during LES, during *a-priori* analysis of DNS data (Lund *et al.*, 1993) and when analyzing experimental data at high Reynolds numbers (Liu *et al.*, 1994; O'Neil & Meneveau, 1994), the coefficient field predicted by the local model varies strongly in space and contains a significant fraction of negative values. Negative values of c_s^2 are of particular concern because they lead to negative values of eddy viscosity in the Smagorinsky parameterization. This is destabilizing in a numerical simulation, and non-physical growth in the resolved velocity fluctuations is often observed (Lund *et al.*, 1993).

Historically, the first problem was given very little attention while the second problem was dealt with by averaging terms in the equations for c_s^2 over space and/or time. When averaged, the numerator in Eq. (3) was generally found to be positive, thus recovering the statistical notion of energy transfer to the subgrid scales. Averaging over homogeneous directions has been a popular choice, and excellent results were obtained in a variety of flows. As examples, Germano *et al.* (1991) and Piomelli (1993) average the equations over planes parallel to the walls in channel flow simulations whereas Akselvoll and Moin (1993) average over the spanwise direction in a backward-facing step flow. While these averaging schemes proved to be effective at controlling possible instabilities and led to accurate results, rigorous justification for them was lacking. Additionally, homogeneity in either space or time was required.

These problems as well as the lingering issue of extracting c_s^2 from the filtering operation were addressed by Ghosal *et al.* (1994) where a variational approach was used to account properly for the spatial variation of the coefficient within the filter operation. Using this approach, various prior models employing averaging were rigorously derived by imposing appropriate constraints in the solution to the variational problem. Finally, two stable local models were derived that did not make use of homogeneous directions. The first simply imposes the constraint that c_s^2 be non-negative. The second allows negative c_s^2 but enforces a budget for the reversed energy transfer through inclusion of a subgrid-scale kinetic energy equation. These latter two models have been tested in a variety of flows and are applicable to complex geometry flows under unsteady conditions.

While the work of Ghosal *et al.* (1994) has provided rigorously-derived methods applicable to inhomogeneous flows, there is still room for improvement. The constraint $c_s^2 \geq 0$ is hard to justify on other than heuristic grounds, and the numerical solution of the integral equation can be expensive. The kinetic energy formulation removes the conceptual problem associated with the constraint $c_s^2 \geq 0$, but only at the additional expense of two more integral equations and one transport equation. Also, new constraints for model coefficients in the kinetic energy equation have to be introduced. Therefore, schemes that make use of averaging continue to have appeal due to their demonstrated accuracy and relative ease of implementation. At the same time, current averaging schemes require at least one homogeneous direction (in space or time) and are therefore not applicable in fully inhomogeneous unsteady flows. If this restriction could be removed, an equally general and perhaps simpler alternative to the integral equation of Ghosal *et al.* (1994) would be available for inhomogeneous flow simulations.

The objective of this work is to develop a simple, but generally applicable, averaging scheme. As originally suggested by O'Neil & Meneveau (1993), we propose to average over particle trajectories rather than directions of statistical homogeneity. Particle trajectories are always well defined objects that in no way rely on special boundary conditions or assumptions of statistical homogeneity. Since particle trajectories are the natural directions associated with fluid flow, averaging the equations for c_s^2 over these directions has some physical appeal. It is reasonable to expect that turbulent eddies evolve along particle paths and that the turbulence energy cascade should be most apparent when viewed in a Lagrangian coordinate system. As reported by Meneveau & Lund (1994), there is evidence to suggest that this is indeed the case. If the energy cascade does in fact proceed mainly along fluid trajectories, then it would seem logical to postulate that the subgrid-scale model coefficient at a given point $\mathbf{x}$ should depend in some way on the history of the flow along the trajectory leading to $\mathbf{x}$. This picture should be contrasted with that of conventional schemes where spatial averaging removes the local details of the flow structure and the turbulence development history is completely ignored. Eulerian time averaging suffers from similar deficiencies since the advection of structures is ignored.

The Lagrangian model is derived by requiring that the error in Germano's identity be minimized along fluid trajectories. This procedure leads to a pair of relaxation transport equations that carry the statistics forward in Lagrangian time. We show that these equations can be solved in an approximate fashion in a numerically efficient way. The model is applied to a variety of test cases including forced and decaying isotropic turbulence, fully developed channel flow, and transitional channel flow. In each case, the model is shown to produce results equal or superior to those of spatially-averaged versions of the dynamic model. At the same time, the numerical solutions to the transport equations increase the computational workload by only about 10% as compared with the spatially-averaged approach.

2. The Lagrangian dynamic model

2.1 Formulation

We propose to determine the model coefficient $c_s^2(\mathbf{x},t)$ by minimizing the error in Germano's identity along particle trajectories. Consider a particle located at position $\mathbf{x}$ at time t. The trajectory of this particle for earlier times $t' < t$ is

$$\mathbf{z}(t) = \mathbf{x} - \int_{t'}^{t} \tilde{\mathbf{u}}[z(t''),t'']dt'' \tag{5}$$

The error associated with Germano's identity at any point along the trajectory is

$$e_{ij}(\mathbf{z},t') = c_s^2(\mathbf{z},t')M_{ij}(\mathbf{z},t') - L_{ij}(\mathbf{z},t'). \tag{6}$$

Here we have assumed that c_s^2 varies negligibly in space over the scale of the test filter and have therefore removed it from the filter operation.

The total error is defined as the pathline accumulation of the local error squared,

$$E = \int_{-\infty}^{t} e_{ij}(\mathbf{z}(t'),t')\, e_{ij}(\mathbf{z}(t'),t')\, W(t-t')\, dt' \tag{7}$$

The weighting function $W(t-t')$ is introduced here in order to control the relative importance of events near time t with those of earlier times. As described below, we shall weight the error at time t most strongly and assign a decreasing weight to earlier times. It is now assumed that c_s^2 varies negligibly in time over the scale of the weighting function $W(t-t')$. In this case, $c_s^2(\mathbf{z},t')$ may be replaced by $c_s^2(\mathbf{x},t)$, and the total error is then minimized with respect to c_s^2 by enforcing

$$\frac{\partial E}{\partial c_s^2} = \int_{-\infty}^{t} 2e_{ij}\frac{\partial e_{ij}}{\partial c_s^2}\, W(t-t')\, dt' = 0. \tag{8}$$

Making use of Eq. (6) (with $c_s^2(\mathbf{z},t')$ replaced by $c_s^2(\mathbf{x},t)$) and solving for c_s^2, one then obtains

$$c_s^2(\mathbf{x},t) = \frac{\mathcal{I}_{LM}}{\mathcal{I}_{MM}}, \tag{9}$$

where

$$\mathcal{I}_{LM}(\mathbf{x},t) = \int_{-\infty}^{t} L_{ij}M_{ij}(\mathbf{z}(t'),t')\, W(t-t')\, dt', \tag{10}$$

$$\mathcal{I}_{MM}(\mathbf{x},t) = \int_{-\infty}^{t} M_{ij}M_{ij}(\mathbf{z}(t'),t')\, W(t-t')\, dt', \tag{11}$$

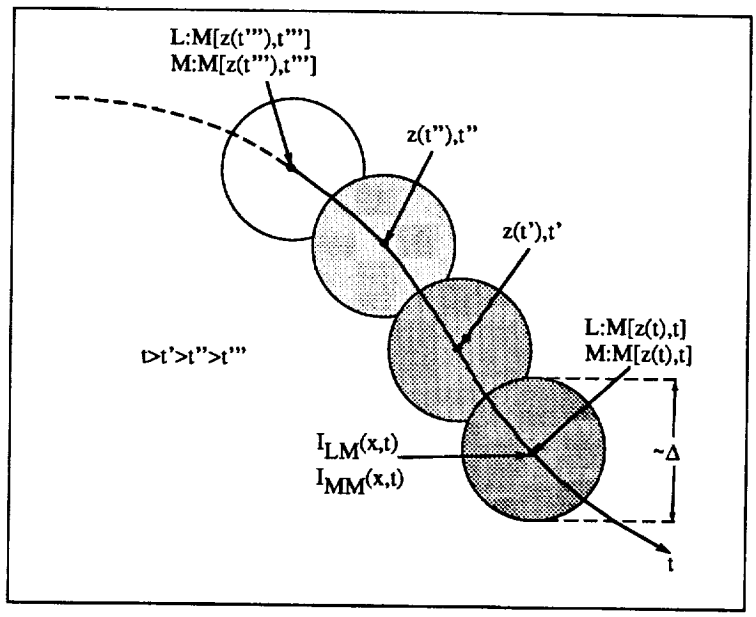

FIGURE 1. Sketch of fluid trajectory of the resolved LES velocity field. The error associated with the Germano identity is weighted with an exponentially decreasing function (indicated as different gray levels), backwards in time, to yield a current value for the model coefficient at point $\mathbf{x}$ and time t.

The function $W(t-t')$ is a free parameter in the current formulation, essentially defining the extent backward along the pathline over which we choose to minimize the error. Although several appropriate weighting functions are possible, an exponential weighting of the form $W(t-t') = T^{-1}e^{-(t-t')/T}$ has the distinct practical advantage that the integrals $\mathcal{I}_{LM}$ and $\mathcal{I}_{MM}$ are solutions to the following relaxation equations

$$\frac{D\mathcal{I}_{LM}}{Dt} \equiv \frac{\partial \mathcal{I}_{LM}}{\partial t} + \tilde{\mathbf{u}}\cdot\nabla\mathcal{I}_{LM} = \frac{1}{T}(L_{ij}M_{ij} - \mathcal{I}_{LM}), \tag{12}$$

$$\frac{D\mathcal{I}_{MM}}{Dt} \equiv \frac{\partial \mathcal{I}_{MM}}{\partial t} + \tilde{\mathbf{u}}\cdot\nabla\mathcal{I}_{MM} = \frac{1}{T}(M_{ij}M_{ij} - \mathcal{I}_{MM}). \tag{13}$$

In the context of LES, solving such transport equations is much more natural than having to perform integrals backwards in time according to Eqs. (10) and (11). Fig. 1 illustrates the basic idea of averaging over pathlines with an exponentially decreasing memory.

2.2 Relaxation time scale

The time-scale T controls the memory length of the Lagrangian averaging, and several choices can be made. The model coefficient should be responsive to changes that occur on the time-scales associated with the smallest resolved turbulent motions. Thus, one could choose T based on variables at the grid-scale. Some possible

choices are the following: (a) $T \sim |\tilde{S}|^{-1}$, (b) $T \sim |\overline{\tilde{S}}|^{-1}$, (c) $T \sim \Delta(M_{ij}M_{ij})^{-1/4}$, (d) $T \sim \Delta(L_{ij}M_{ij})^{-1/4}$, (e) $T \sim \Delta \mathcal{I}_{MM}^{-1/4}$, and (f) $T \sim \Delta \mathcal{I}_{LM}^{-1/4}$. In fully developed turbulence, all of these time-scales are of the same order of magnitude on average. The first four choices are based on local values, which would mean that T is a strongly fluctuating variable while (e) and (f) are based on the smoother, Lagrangian averages themselves.

Option (f) has several attractive features. Physically, it can be interpreted as a time scale for energy flux since it is formed by contracting a stress L with the strain-rate like tensor M. Thus, it may be indicative of the speed at which energy is being cascaded towards the grid-scale. Furthermore, if $L_{ij}M_{ij} \leq 0$ for a persistent time along the pathline, then $\mathcal{I}_{LM}$ approaches zero. T evaluated according to (f) then tends to ∞, i.e. the memory time increases. In other words, the current values are weighted less and less strongly relative to the past ones, if they are of the backscattering type. This is useful in the implementation with the Smagorinsky model where we wish to restrict the Smagorinsky expression for the modeling of energy dissipation only. The Germano identity is thus weighted much less heavily when $L_{ij}M_{ij} \leq 0$ in a persistent fashion, i.e. we opt for 'learning' as little as possible about the coefficient from the resolved field when it would predict backscatter.

Equation (12) can now be written as

$$\frac{D\mathcal{I}_{LM}}{Dt} = \frac{\theta}{\Delta} \mathcal{I}_{LM}^{\frac{1}{4}} (L_{ij}M_{ij} - \mathcal{I}_{LM}), \tag{14}$$

where θ is a dimensionless coefficient of order unity. If $\mathcal{I}_{LM}$ reaches zero, its rate of change is zero as well. Therefore, $\mathcal{I}_{LM}$ cannot become negative, and the resulting dynamic model will not suffer from numerical instability due to negative-eddy viscosities. We point out, however, that if $L_{ij}M_{ij} \leq 0$, the approach of $\mathcal{I}_{LM}$ to zero is not exponential, but of the power-law type (as $(t_0 - t)^{4/3}$). This means that after the (finite) time t_0 at which $\mathcal{I}_{LM} = 0$, the solution becomes complex. Thus, in practice, the solution must still be 'clipped' to zero during such times. This type of clipping is much less drastic than previous approaches since the coefficient field approaches zero smoothly with zero slope.

A judicious choice for the dimensionless coefficient θ must now be made. Intuitively, we must average over a few 'events' of the variable $L_{ij}M_{ij}$ along the pathline. The average duration of such events is expected to be of the order of $\Delta < L_{ij}M_{ij} >^{-\frac{1}{4}}$, but in order to quantify this assertion, we analyze results from DNS of forced isotropic turbulence. The goal is to compute the Lagrangian autocorrelation function of the scalar variable $L_{ij}M_{ij}$. The method employed to follow fluid trajectories and to compute the autocorrelation is the same as described in Meneveau & Lund (1994). For comparison, we also compute the Lagrangian autocorrelation function of the scalar $|\mathbf{M}|^2$ as well as their Eulerian fixed-point two-time autocorrelation functions. The Lagrangian tracking was done in a sequence of DNS velocity fields computed on a 128^3 mesh. The ensemble has a microscale Reynolds number of $R_\lambda = 95.8$. Each field was filtered with a Fourier cutoff filter at a scale corresponding to 4 mesh spacings. Lagrangian and Eulerian autocorrelations were then computed for quantities derived from the filtered velocity fields.

C-4

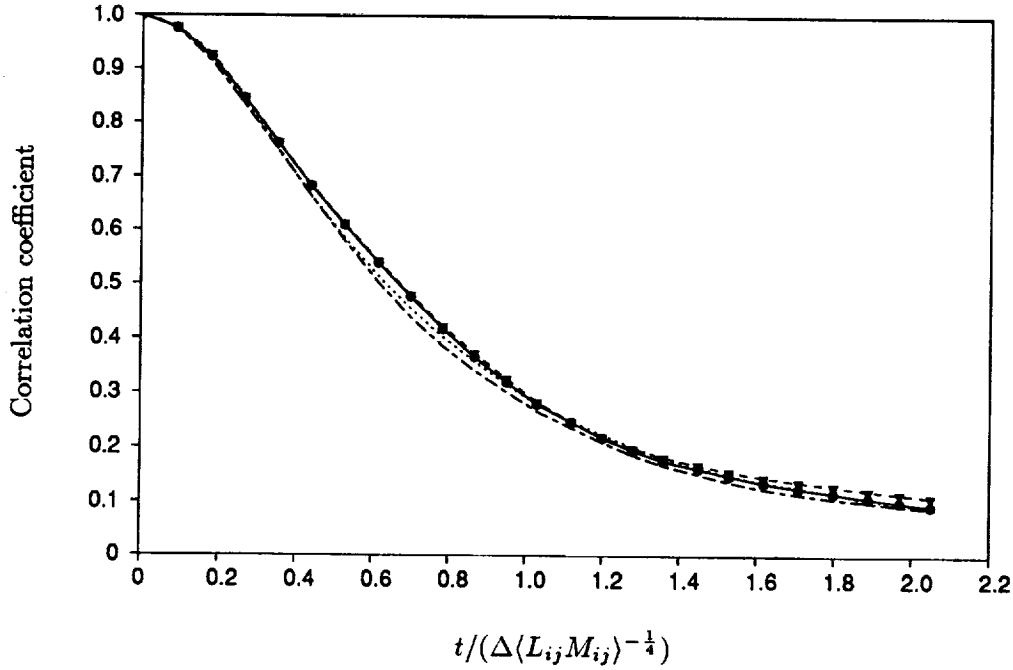

FIGURE 2. Lagrangian and Eulerian autocorrelation functions calculated from a filtered DNS of forced isotropic turbulence. • : Lagrangian autocorrelations of $L_{ij}M_{ij}$; ▲ : Lagrangian autocorrelations of $M_{ij}M_{ij}$; —·— : Eulerian temporal autocorrelations of $L_{ij}M_{ij}$; ····· : Eulerian temporal autocorrelations of $M_{ij}M_{ij}$.

Fig. 2 shows the computed autocorrelations. Time is non-dimensionalized based on the space-averaged value of $L_{ij}M_{ij}$. As expected, the Lagrangian autocorrelations decay at a slower rate than the Eulerian ones, but the difference is small due to the fact that the mean velocity of this flow is zero. Also, the decay of the LM and MM terms is quite similar. The main observation is that after a time $\sim 2\Delta < L_{ij}M_{ij} >^{-\frac{1}{4}}$, the autocorrelation almost vanishes. This suggests that averaging over Lagrangian time spans equal to this interval is sufficient to smooth instantaneous fluctuations. In summary, during the present work we choose

$$T = 2\ \Delta\ \mathcal{I}_{LM}^{-\frac{1}{4}} \tag{15}$$

as the time-scale characterizing the exponential memory with which the Germano identity is enforced.

2.3 Numerical method

In principle, the implementation of the Lagrangian dynamic model requires the solution of two additional transport equations (Eqs. (12) and (13)) during the LES. This undoubtedly increases the computational cost associated with the subgrid modeling. However, the considerable flexibility of choice of the averaging domain

suggests that high numerical accuracy in solving Eqs. (12) and (13) may be unnecessary. Therefore, we use a particularly simple formulation based on discretizing Eq. (12) in time as follows:

$$\frac{\mathcal{I}_{LM}^{n+1}(\mathbf{x}) - \mathcal{I}_{LM}^{n}(\mathbf{x} - \tilde{\mathbf{u}}^n \Delta t)}{\Delta t} = \frac{1}{T^n} \left([L_{ij} M_{ij}]^{n+1}(\mathbf{x}) - \mathcal{I}_{LM}^{n+1}(\mathbf{x}) \right). \quad (16)$$

Eq. (13) is dealt with in a similar manner. Positions $\mathbf{x}$ are coincident with grid points of the simulation. The value of $\mathcal{I}_{LM}^{n}$ at the previous time-step and at the upstream location $\mathbf{x} - \tilde{\mathbf{u}}^n \Delta t$ can be obtained by multilinear interpolation. Finally, the new values at the grid points are solved for. The result is a weighted sum of the interpolated prior value and the current source term at the grid point:

$$\mathcal{I}_{LM}^{n+1}(\mathbf{x}) = H \left\{ \epsilon \, [L_{ij} M_{ij}]^{n+1}(\mathbf{x}) + (1 - \epsilon) \mathcal{I}_{LM}^{n}(\mathbf{x} - \tilde{\mathbf{u}}^n \Delta t) \right\} \quad (17)$$

and

$$\mathcal{I}_{MM}^{n+1}(\mathbf{x}) = \epsilon \, [M_{ij} M_{ij}]^{n+1}(\mathbf{x}) + (1 - \epsilon) \mathcal{I}_{MM}^{n}(\mathbf{x} - \tilde{\mathbf{u}}^n \Delta t),$$

where

$$\epsilon \equiv \frac{\Delta t / T^n}{1 + \Delta t / T^n}, \quad \text{and} \quad T^n = 2 \, \Delta \, (\mathcal{I}_{LM}^{n})^{-\frac{1}{4}}, \quad (18)$$

where $H\{x\}$ is the ramp function ($H\{x\} = x$ if $x \geq 0$, and zero otherwise). The ramp function is introduced to clip the solution away from complex values.

Finally, we point out that the process of spatial interpolation between grid points introduces some numerical diffusion to the fields $\mathcal{I}_{LM}$ and $\mathcal{I}_{MM}$. Physically, such diffusion effectively 'thickens' the pathline over which the averaging is being performed, but this would not seem to be a worrisome aspect for this model.

2.4 Statistical features of the model

As a next step, the model is implemented in a LES for the simulation of forced isotropic turbulence on a 32^3 grid. The code is a variant of the pseudo-spectral method developed by Rogallo (1981). Forcing is achieved by holding the Fourier amplitudes fixed within the sphere $k < 2$. Test filtering is achieved through a Fourier cutoff at twice the grid scale.

The velocity field is initialized in the usual manner by superposing Fourier modes with a prescribed spectrum but random phases, and projection onto the divergence-free space. Additionally, initial condition for the fields $\mathcal{I}_{LM}$ and $\mathcal{I}_{MM}$ must be prescribed. For initializations corresponding to turbulent flows, we propose to set

$$\mathcal{I}_{MM}(\mathbf{x}, 0) = M_{ij} M_{ij}(\mathbf{x}, 0), \quad \mathcal{I}_{LM}(\mathbf{x}, 0) = c_s^2(0) \, M_{ij} M_{ij}(\mathbf{x}, 0), \quad (19)$$

where $c_s(0) = 0.16$ is the traditional value of the Smagorinsky constant. Thus at the initial time, the model involves a position-independent, prescribed coefficient.

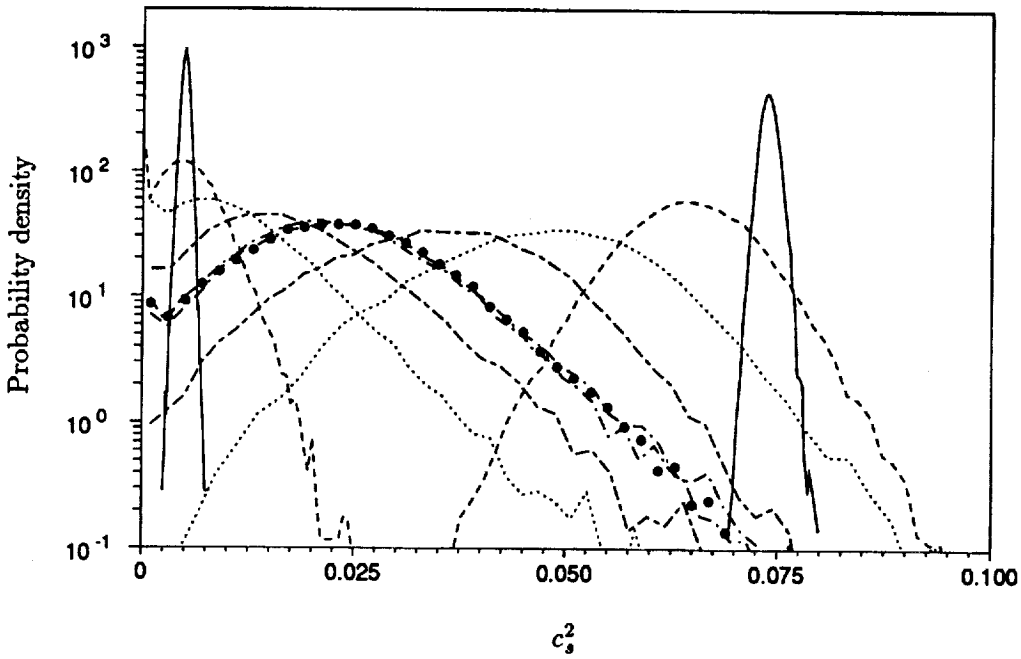

FIGURE 3. Probability density functions of the coefficient c_s^2, computed from the Lagrangian dynamic model in a pseudo-spectral LES of forced isotropic turbulence at $Re = \infty$, on a 32^3 mesh. The circles represent the asymptotic pdf long after initial transients have died out (obtained here at $t = 6 < T >$, where $< T >= 2\Delta < L_{ij}M_{ij} >^{-1/4}$). Evolving pdfs on both sides illustrate delta function pdfs with the wrong initial conditions quickly reach the asymptotic statistics. Curves that peak to the left of the asymptotic curve correspond to $c_s^2(0) = 0.005$; those peaking to the right evolve starting from $c_s^2 = 0.075$. ——— : (1 time-step); ---- : $(t = 0.1 < T >)$; ····· : $(t = 0.45 < T >)$; —·— : $(t = 0.95 < T >)$; —·— : $(t = 1.9 < T >)$. For reference, in this simulation the time scale associated with the resolved strain-rates was $< \tilde{S}_{ij}\tilde{S}_{ij} >^{-1/2} = 0.26 < T >$.

For initializations corresponding to laminar flows, we propose to set $c_s = 0$ in the above expressions.

When the LES of forced isotropic turbulence is started, fluctuations of the Lagrangian dynamic coefficient c_s quickly build as different values of $L_{ij}M_{ij}$ begin to affect the averages. Once a statistical steady-state has been reached, these fluctuations are characterized by the probability density function of the coefficient shown by solid circles in Fig. 3. Notice the small spike at $c_s = 0$, arising from the regions in which c_s is clipped at zero, away from complex values (on about 5% of the points in this case). Initial transients leading to such a steady-state distribution are relatively short. This can be appreciated by observing the time development of the pdfs when the 'wrong' initial condition is employed for $c_s(0)$. In one case, we start with

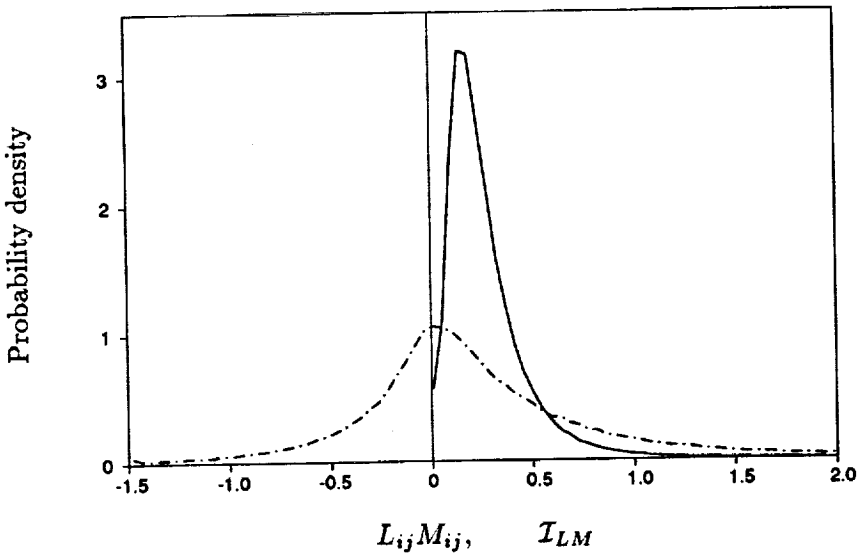

FIGURE 4. Probability density functions of numerators. —·— : evaluated locally ($L_{ij}M_{ij}$); ——— : after Lagrangian averaging ($\mathcal{I}_{LM}$). These distributions are calculated from a 32^3-node, pseudo-spectral LES of forced isotropic turbulence that uses the Lagrangian dynamic Smagorinsky model. To increase the sample, pdfs are accumulated over several independent fields.

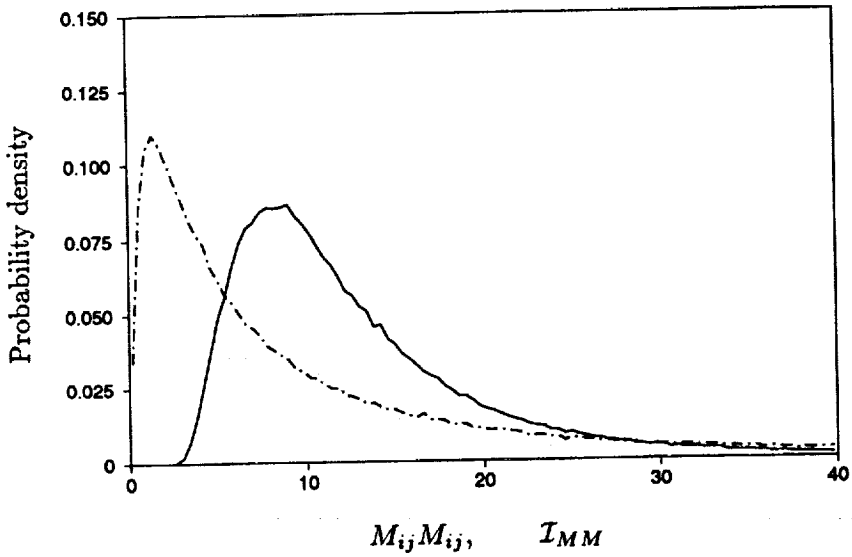

FIGURE 5. Probability density functions of denominators. —·— : evaluated locally ($M_{ij}M_{ij}$); ——— : after Lagrangian averaging ($\mathcal{I}_{MM}$). Details as in Fig. 4.

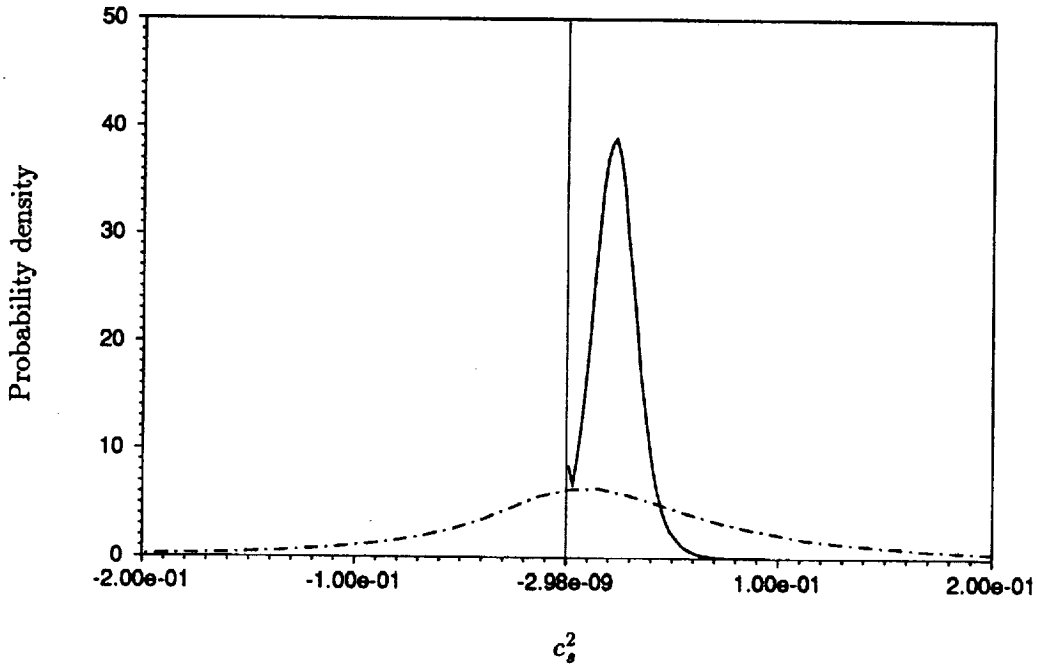

FIGURE 6. Probability density functions of model coefficients taken from a 32^3 Lagrangian dynamic model LES of forced isotropic turbulence. —·— : coefficient evaluated locally; ——— : coefficient from the Lagrangian model.

$c_s^2(0) = 0.005$, and in another case with $c_s^2(0) = 0.075$. In both cases the asymptotic distribution is reached after times of the order of $2 < T >$ where T is the time scale defined by Eq. (15). We conclude that the proposed method of initialization is acceptable since the simulation 'forgets' the initial state after only few grid-scale turnover times. This is comparable to the time it takes the simulation to build up realistic phases in the resolved velocity field, starting from the random-phase initial condition. To further document the effect of the Lagrangian averaging, we compute the probability density functions of $\mathcal{I}_{LM}$ and $\mathcal{I}_{MM}$ and compare them with those of the local values $L_{ij}M_{ij}$ and $M_{ij}M_{ij}$. Figs. 4 and 5 show these results. As expected, the distributions become narrower after the Lagrangian averaging. By construction, there are no negative values of $\mathcal{I}_{LM}$ (Fig. 4). In terms of denominators, the averaging is seen to virtually eliminate values near zero. The pdf of $\mathcal{I}_{MM}$ approaches the origin with negligible slope while the probability of the local value of $M_{ij}M_{ij}$ being close to zero is considerable. In Fig. 6, we show the measured pdf of the coefficient c_s^2 itself. As can be seen, the variance of the coefficient in the local formulation is greatly reduced by the Lagrangian averaging. Also, no negative values exist although a finite number of points ($\sim 5\%$) exhibit $c_s^2 = 0$ as indicated by the spike at the origin.

2.5 Relationship to vortical flow-structures

The goal of this section is to make qualitative observations pertaining to possible relations between the terms $\mathcal{I}_{LM}$, $\mathcal{I}_{MM}$, and discernible flow structures that may appear in the resolved velocity field during LES.

First, we report the existence of tubular structures that characterize regions in which the resolved vorticity vector has high magnitude, in our 32^3 LES. Fig. 7a shows iso-surfaces of vorticity magnitude (at a threshold of $|\omega|_{th} = 2.4 < \omega^2 >^{1/2}$). Clearly, 'fat worms' exist in the solution. The existence of tubular vortical structures in LES has also been observed recently by Briscolini and Santangelo (1994), using a different subgrid model. One interesting question to be answered is whether the prediction of such 'fat worms' by LES is realistic. We recall that DNS predicts worms with very small diameters of about four Kolmogorov scales (Jimenez *et al.*, 1993)). Surely they cannot be captured by a LES at $Re = \infty$. The relevant question is whether a field generated by DNS and then low-pass filtered at inertial-range scales comparable to the LES grid-size exhibits 'fat worms' that are comparable to those predicted by LES. We have performed such an operation based on the 128^3 forced DNS described earlier and have visualized regions of high vorticity-magnitude. We indeed observed 'fat worms' that were of similar appearance than those of the LES (see also Fig. 17 of Vincent & Meneguzzi, 1991). It must be recognized that the 'high-vorticity' regions in the filtered DNS correspond to much lower vorticity-magnitudes than those of the unfiltered fields. This is the reason why these 'fat worms' are not visible when analyzing the unfiltered DNS fields. In summary, we observe elongated vortical regions in LES and believe that their existence is a realistic prediction by the simulation since they also exist in low-pass filtered DNS fields.

The next issue to be addressed is whether the Lagrange-averaged quantities that enter our dynamic model bear any relationship to such local structures. Fig. 7(a) shows contour plots of $\mathcal{I}_{LM}$ on two planes of the computational cube, selected to cut some of the most visible vortical structures. The field is chosen at some time *long* after the simulation has reached statistical steady-state (15,000 time-steps). Fig. 7(b) shows a similar graph for $\mathcal{I}_{MM}$. Generally, it is apparent the contours of both $\mathcal{I}_{LM}$ and $\mathcal{I}_{MM}$ are somewhat 'correlated' with the presence of worms. The contours peak in the neighborhood of the worms while not much activity is seen in regions that are far removed from the structures. Upon closer examination, we observe that the peaks in $\mathcal{I}_{LM}$ and $\mathcal{I}_{MM}$ are most often located near the cores of the worms but not inside of them. Many times the maximum values occur between two closely spaced worms. These are expected to be regions of large straining and turbulence generation. Also, considerable correlation is seen between both fields $\mathcal{I}_{LM}$ and $\mathcal{I}_{MM}$ (it is $\rho(\mathcal{I}_{LM}, \mathcal{I}_{MM}) \sim 0.8$ while the correlation between the local values is much lower, $\rho(L_{ij}M_{ij}, M_{ij}M_{ij}) \sim 0.4$). This increased correlation between numerator and denominator is instrumental in decreasing the variance of the predicted model coefficient.

Clearly, a detailed understanding of the relationship between the coefficient c_s^2 and local flow structures, and of their dynamical interplay and relevance, is still

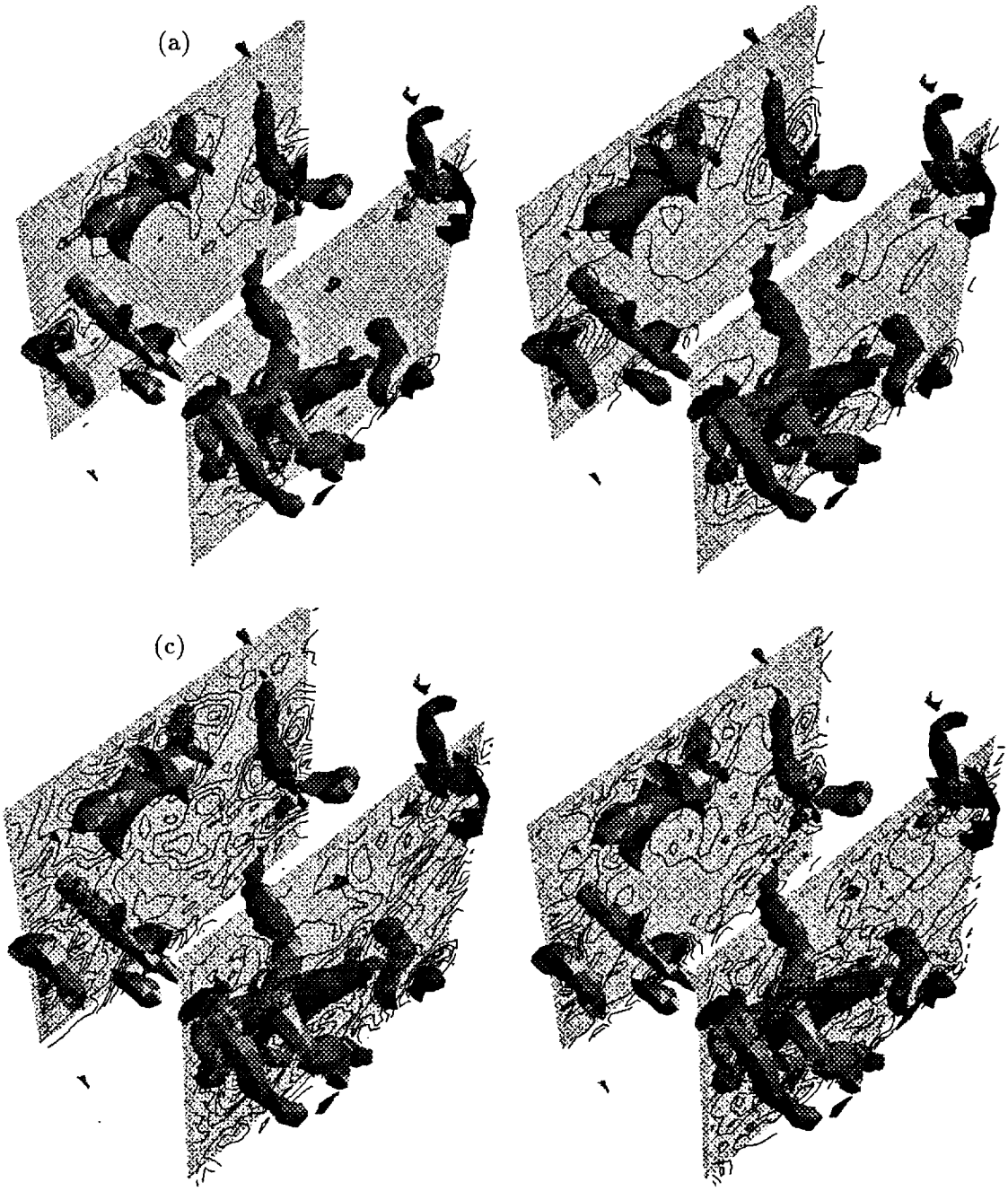

FIGURE 7. Visualization of high-magnitude vorticity regions in LES of isotropic forced turbulence at $Re = \infty$. Surfaces correspond to points at which $|\tilde{\omega}| = 2.4 < \tilde{\omega}^2 >^{1/2}$. On planes, contours of different variables shown. (a) $\mathcal{I}_{LM}$, (b) $\mathcal{I}_{MM}$, (c) $|\tilde{S}|$ (proportional to eddy viscosity with volume-averaged coefficient) and (d) $(\mathcal{I}_{LM}/\mathcal{I}_{MM})\ |\tilde{S}|$ (proportional to eddy viscosity computed from Lagrangian dynamic model).

elusive. Nevertheless, we have shown that the Lagrangian averaging preserves some spatial locality in the model. Spatially localized events in the numerators and denominators used to compute the model coefficient bear some relationship to local flow structures. The volume-averaged dynamic model would have generated a position-independent coefficient that is oblivious to local flow structures. To observe the effect on the predicted eddy viscosity, Figs. 7(c) and 7(d) show contour plots of the strain-rate magnitude $|\tilde{S}|$ and of the expression $(\mathcal{I}_{LM}/\mathcal{I}_{MM})|\tilde{S}|$. The former is proportional to the eddy viscosity predicted with a volume averaged coefficient while the latter is proportional to the eddy viscosity predicted by the Lagrangian dynamic model. Both show peaks surrounding the worms, but the precise location of these peaks differs. Also, the Lagrangian dynamic eddy viscosity appears to be more intermittent in the sense that more eddy viscosity is concentrated near the structures while being lower and fluctuating less in the regions far away from the structures.

3. Applications

In this section, we report applications of the Lagrangian dynamic model to several test-cases. We consider forced and decaying isotropic turbulence and channel flow. These flows could have also been treated with the traditional dynamic model with averaging over statistically homogeneous directions (and they have in the past). Our purpose in choosing these simple flows is to test the model in well-understood cases and show that good results can be obtained. This is a necessary first step before applications to unsteady and complex-geometry flows should be attempted where many other effects such as numerics, etc. may influence the results and obscure the role of the subgrid model.

3.1 Forced isotropic turbulence

LES of forced isotropic turbulence is performed on both 32^3 and 128^3 grids, using the code already described in section 2.4. The simulation is run for 15,000 and 6,600 time-steps on the 32^3 and 128^3 grids, respectively.

Figs. 8(a) and 8(b) show the resulting radial energy spectra. The wavenumbers and energy density are made dimensionless with the grid wavenumber and the averaged subgrid-scale energy dissipation $(- < \tilde{S}_{ij}\tau_{ij} >)$. Figure 8(b) is premultiplied by $k^{5/3}$. In these 'mesh-Kolmogorov units', one expects simulations with different meshes to collapse at high wavenumbers, and the spectra to follow the universal power-law in the inertial range. The dotted line in Fig. 8(a) shows a power-law $(k/k_\Delta)^{-5/3}$. A slight decay below the power law for $k/k_\Delta > 0.3$ and a 'pile-up' very close to the cut-off wavenumber k_Δ are visible. These are known effects of physical space eddy viscosity closures, which do not have a 'cusp' near k_Δ. These defects appear not to be remedied by the dynamic model in its Lagrangian implementation. We have confirmed that the same is true for the traditional dynamic model by running the same program with the volume-averaged dynamic coefficient.

With regard to computational cost, we find that the CPU time for the simulation with the Lagrangian averaging was higher by about 9% when compared to that of the volume-averaged dynamic model. Most of the additional time was spent in the

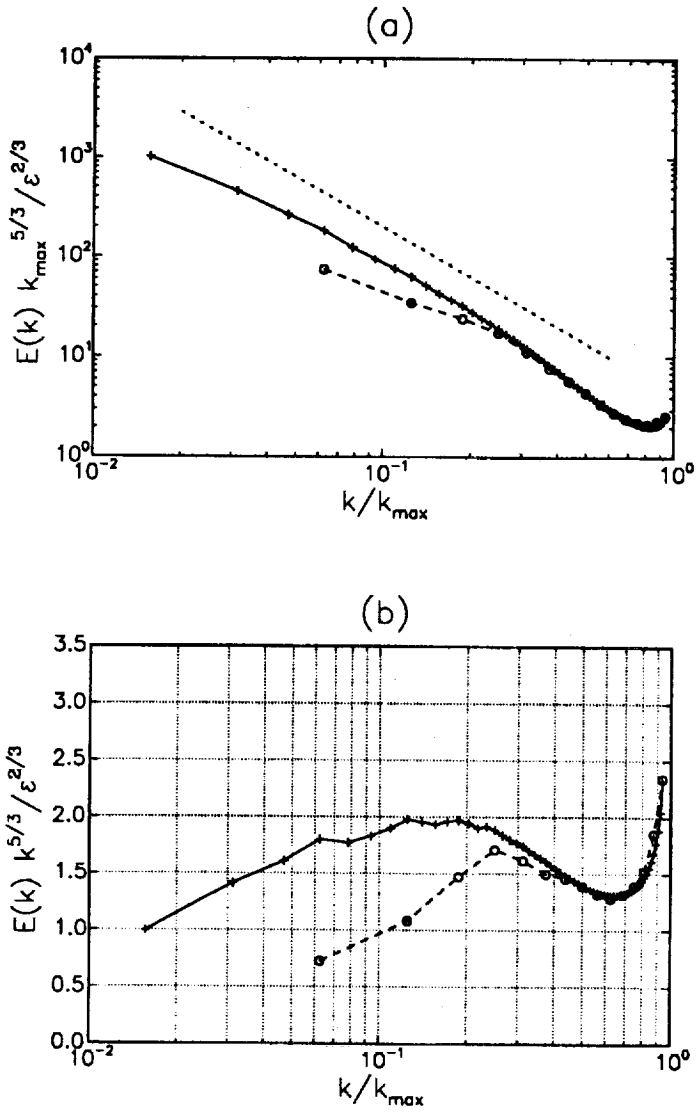

FIGURE 8. Radial energy spectra of LES using Lagrangian dynamic Smagorinsky model at $Re = \infty$. Wavenumbers are non-dimensionalized with grid-wavenumber while non-dimensionalization of energy density also involves mean subgrid-scale energy dissipation rate, $\epsilon = - < \tau_{ij} \tilde{S}_{ij} >$, computed from simulation. (a) conventional spectra, (b) premultiplied spectra. ——— : 128^3 simulation; - - - - : 32^3 run; ····· : slope $-5/3$. 32^3 spectrum averaged over 374 independent samples taken from 15,000 time-steps (approximately 13 integral large-scale turnover times L/u', with $L = 2\pi$). The 128^3 spectrum is based on 290 samples taken from 6,600 time-steps (approximately 4 large-scale turnover times).

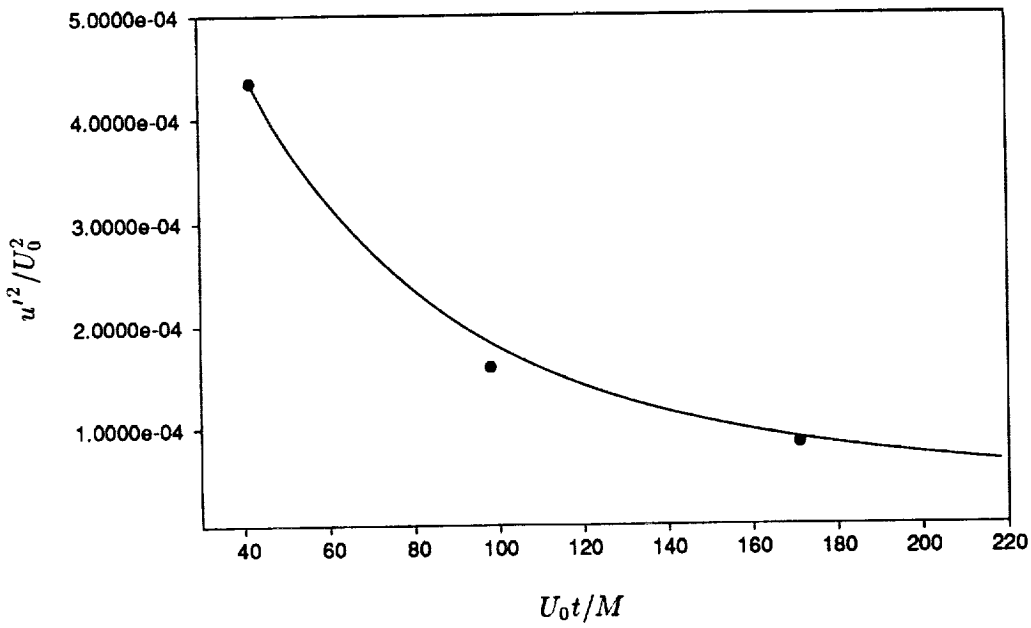

FIGURE 9. Temporal decay of turbulent kinetic energy in isotropic turbulence. ——— : 32^3 LES using the Lagrangian dynamic model; • : filtered experimental results (Comte-Bellot & Corrsin, 1971) in grid turbulence which decays downstream of a grid. U_0 and M are the mean fluid speed and the spacing of the turbulence-generating grid in the experiment.

linear interpolations. Two additional scalar arrays had to be defined, for $\mathcal{I}_{LM}$ and $\mathcal{I}_{MM}$. Compared to overall memory requirements, this addition was not significant.

3.2 Decaying isotropic turbulence

In order to test the model in an unsteady case, we perform LES of decaying isotropic turbulence. Meaningful comparisons can then be made with the experimental results of Comte-Bellot & Corrsin (1971). The initial 3-D energy spectrum is made to match the experimental measurements at their earliest time. The phase of the Fourier coefficients is chosen to be random so that the initial velocity field had Gaussian statistics. The dimension of the computational box is chosen to be roughly 4 integral scales.

Fig. 9 shows the decay of the kinetic energy compared with the experimental results of Comte-Bellot & Corrsin (1971). The predicted initial decay appears to be a little slower than the experimental rate, but the overall agreement is good. Of course the agreement could have been improved by using a slightly larger value of $c_s^2(0)$ as initial condition - an after-the-fact adjustment that we opted to avoid. A comparison of the spectra at the three different times at which experimental results are available is shown in Fig. 10. The decrease in overall kinetic energy and the decrease of k at which the spectra peak (increasing integral scale) is clearly

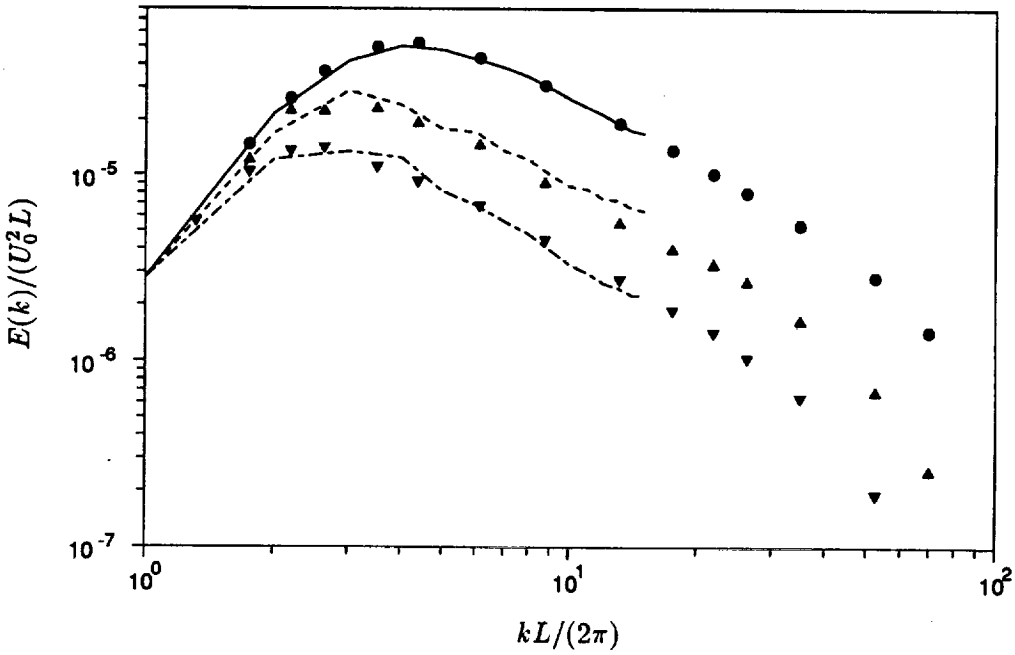

FIGURE 10. Radial energy spectra for decaying isotropic turbulence at different times. ——— : 32^3 LES with Lagrangian dynamic model; • : experimental results of Comte-Bellot & Corrsin (1971). Scaling parameters are defined in Fig. 9. $L = 10.8M$ is the computational box size.

reproduced well.

We conclude that the model is able to reproduce important features of this time-dependent flow.

3.3 Fully developed channel flow

In this section we describe the application of the Lagrangian dynamic model to a pseudo-spectral simulation of plane channel flow. For comparison, another LES is performed with the traditional implementation of the dynamic model in which the terms are averaged over planes parallel to the wall. The flow Reynolds number is selected to match the experimental data by Hussain & Reynolds (1970) to permit detailed comparison.

The channel flow simulations are performed with in a pseudo-spectral code (Kim *et al.*, 1987) in a numerical domain with streamwise, wall-normal, and spanwise dimensions of $3\pi \times 2 \times 3\pi/4$ (in units of channel half-width d) on a $48 \times 65 \times 64$ mesh. Chebyshev polynomials are used in the wall-normal direction on a collocated grid; Fourier transforms are used in the homogeneous streamwise and spanwise directions on a uniform grid. Real space (tophat) filtering is used for the dynamic test filtering procedure and is performed explicitly only in horizontal planes. The equivalent filter width Δ_{eq} is taken to be the geometric mean of unidirectional grid

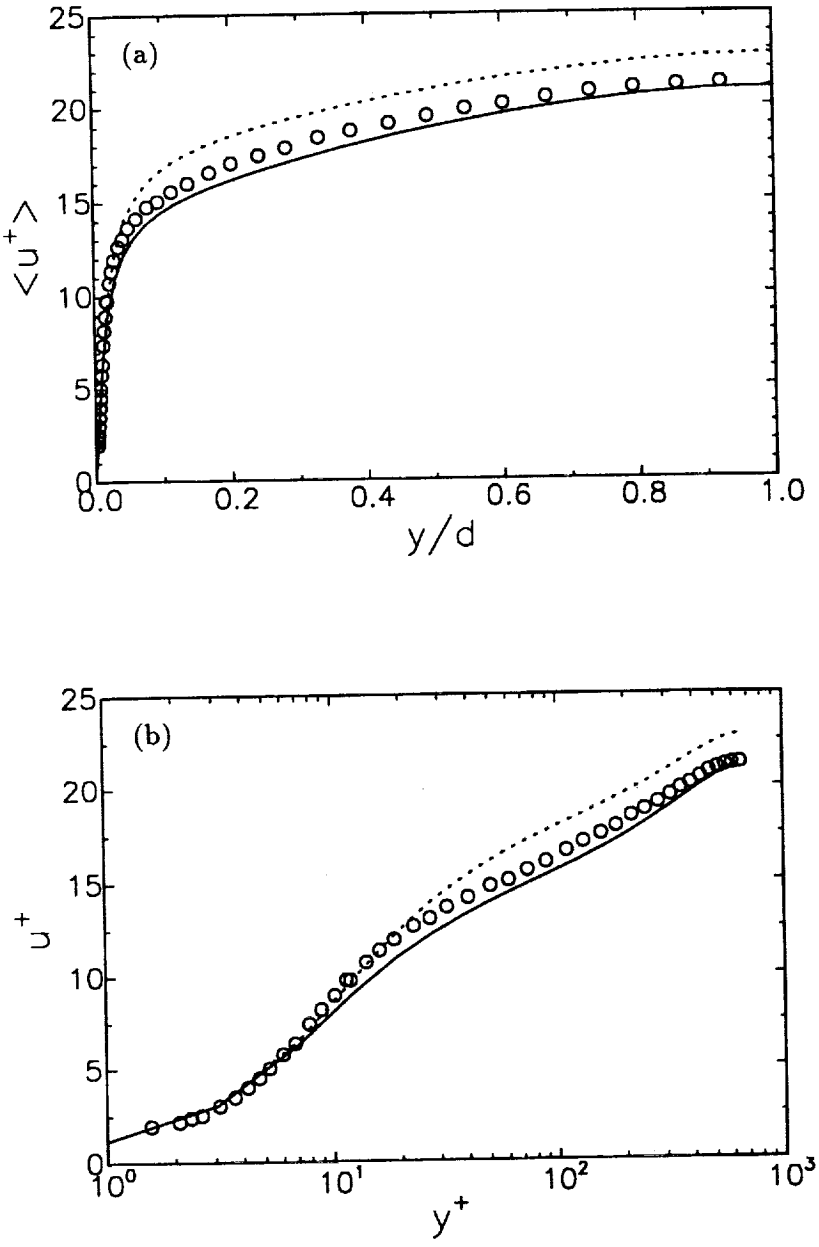

FIGURE 11. Mean velocity profiles in fully developed channel flow. ····· : LES with plane-averaged dynamic model; ——— : LES with Lagrangian dynamic model; • : Experimental measurements of Hussain & Reynolds (1970). (a) Wall distance in units of the half-channel width d, (b) in wall units.

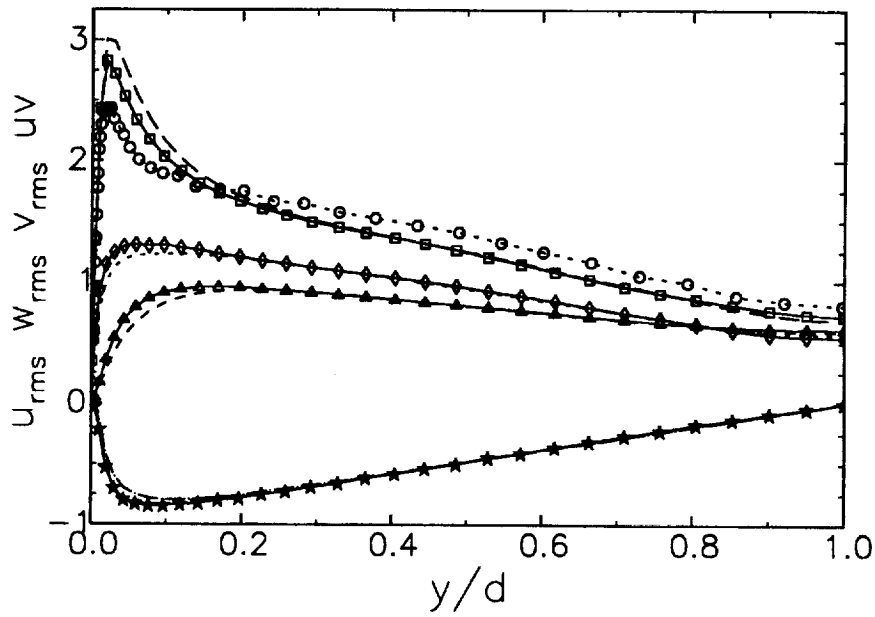

FIGURE 12. Profiles of second-order moments of the resolved velocity field. ---- : u'_{rms} from the plane-averaged LES; □ : u'_{rms} from Lagrangian model; ○ : u'_{rms} from the experimental measurements of Hussain & Reynolds (1970). ◇ : Spanwise w'_{rms} from Lagrangian LES; ····· : from plane-averaged model. △ : Wall-normal v'_{rms} from Lagrangian LES; ---- : from plane-averaged model. ⋆ : Resolved shear stress $< u'v' >$ from Lagrangian LES; —·— : from plane-averaged model.

widths (this procedure is justified for moderate grid anisotropies as shown in Scotti *et al.*, 1993). For the plane-averaged LES, averaging of the dynamic coefficient is performed in horizontal planes.

The approximate Lagrangian interpolation for the horizontal directions is implemented in this code as described in §2.3. The wall-normal direction requires different treatment due to the stretched mesh used in that direction. The transformation $\theta = \cos^{-1}(y/d)$ is used to map the stretched mesh into a uniform one. The wall-normal advection term, $v\partial/\partial y$, is recast as $v_\theta \partial/\partial\theta$ and the interpolation is performed in θ identically to the horizontal directions, but using $v_\theta = -v/\sin\theta$. The wall planes are treated specially with $\mathcal{I}_{LM} \equiv 0$ and $\mathcal{I}_{MM}$ approximated by values at the nearest off-wall plane. There was also the possibility that the interpolation might attempt to place approximated points at the previous time step beyond the walls; however, the CFL condition gives sufficiently small time steps that this situation is never encountered.

A target friction Reynolds number Re_τ ($\equiv u_\tau d/\nu$, where the friction speed u_τ

is the square root of the mean total wall stress, and ν is the molecular viscosity) of 650 was chosen, corresponding to one set of experimental data by Hussain & Reynolds (1970). The channel flow is started from a flow field at lower Reynolds number and is allowed to evolve to near statistical equilibrium, with $Re_\tau \approx 641$ in the last runs. The initial conditions for $\mathcal{I}_{LM}$ and $\mathcal{I}_{MM}$ are chosen as in the homogeneous case but with $c_s^2(0)$ as function of y matching the values of a previous plane-averaged dynamic simulation. Using the Lagrangian formulation proved to be more expensive than the standard plane-averaged method by 10% in CPU due, in part, for the need to perform a division at each point to compute the dynamic coefficient rather than at each plane. The Lagrangian method also requires extra mass storage of $\mathcal{I}_{LM}$ and $\mathcal{I}_{MM}$ between runs.

The averaged statistics will be shown first, followed by a more detailed analysis of additional variables.

Fig. 11 shows the mean velocity profile in the half-channel, in outer units (a) and wall units (b). As can be seen, at the resolution of the present LES, the plane-averaged model predicts an excessive center-line velocity (smaller losses) for the prescribed pressure gradient. The Lagrangian model yields a centerline velocity slightly below the measured values although the magnitude of the error is considerably smaller than that of the plane-averaged case (6.8% error in centerline velocity for the plane-averaged model and -1.8% for the Lagrangian model). Fig. 12 shows the profiles of *rms* velocities and Reynolds shear stress of the resolved fields, and a comparison of the *rms* streamwise velocity with the measurements of Hussain & Reynolds (1970). In the core region (for $y/d > 0.2$), the LES with both models fall below the measured values to a large extent because the former do not include the subgrid portion of the energy. Closer to the wall, both LES erroneously over-predict u'_{rms}, but the Lagrangian model does a better job than the plane-averaged one. Interestingly, the magnitude of the resolved shear stress for the Lagrangian model is larger than that of the plane-averaged case. This is possibly the cause for the increased (more realistic) losses in the Lagrangian simulation. The mean eddy viscosity predicted by both LES is shown in Fig. 13. It is computed according to

$$< \nu_t > (y) = < c_s^2(x,y,z,t)^2 \ \Delta_{eq} |\tilde{S}| >_{x,z}, \tag{20}$$

where the averaging is performed along x, z planes and over several times. The coefficient c_s^2 is either computed according to the plane-averaged or the Lagrangian dynamic model. It can be seen that over much of the log-layer, the Lagrangian model generates a lower eddy viscosity compared to the plane-averaged dynamic model. We have checked that this reduction is due primarily to a decrease in the dynamic coefficient c_s^2 as opposed to reduced strain-rate magnitudes. The reduced eddy viscosity is likely to generate less SGS dissipation of resolved turbulence, which in turn is probably the cause for the increased resolved shear-stress observed before.

As an aside, an important feature of the dynamic model is that it exhibits the proper near-wall scaling for the SGS eddy viscosity when the sublayer is numerically resolved (Germano *et al.*, 1991), namely $\nu_t \sim (y^+)^3$. As can be seen in Fig. 13, this scaling is followed quite well by the plane-averaged case (as observed before by

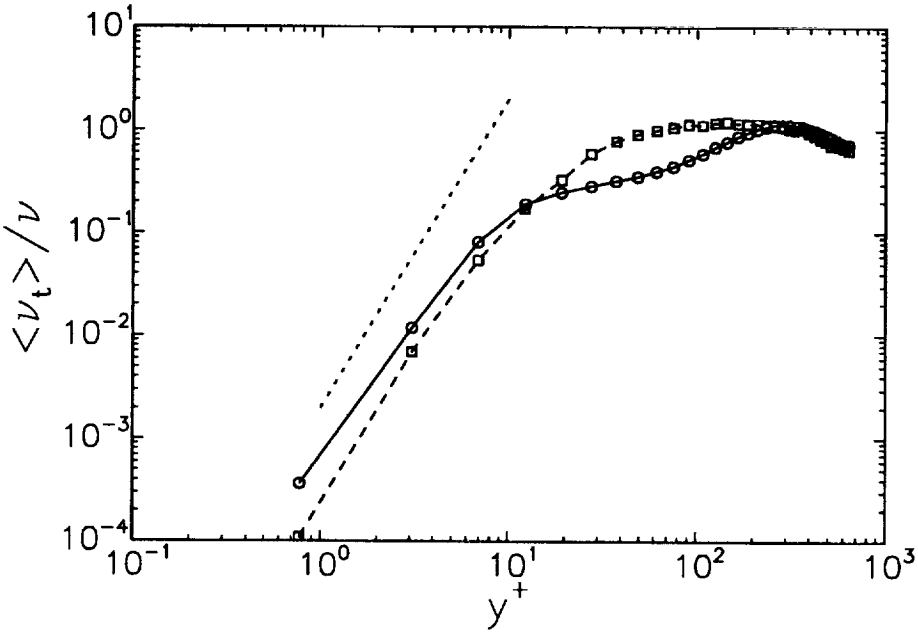

FIGURE 13. Ratio of mean eddy viscosity to molecular viscosity taken from the channel flow simulation. o : Lagrangian dynamic model; □ : plane-averaged dynamic model; ····· : $\nu_t \sim (y^+)^3$ power-law.

Germano *et al.* 1991; Piomelli, 1993). The mean eddy viscosity from the Lagrangian model also decays very quickly but at a somewhat slower rate (approximately as $\nu_t \sim (y^+)^{2.5}$ in our case). We shall return to this issue at a later stage. But we stress that near the wall such minute differences are unlikely to have any practical effect since there the molecular viscosity strongly dominates. With the purpose of documenting the statistics of the model coefficient c_s^2 and its evolution away from the initial condition, we show in Figs. 14(a)-(c) probability-density-functions of c_s^2 at different times and different elevations from the wall. The pdf at $t = 0$ is a *delta*-function at the plane-averaged value of the dynamic coefficient, which is used as an initial condition. As can be seen for $y^+ = 641$ and $y^+ = 12$ (core and near-wall region), the convergence of the pdf to the asymptotic value (circles) is nearly complete after 80-160 time-steps. This duration corresponds to about $\nu/u_\tau^2 \sim 25 - 50$ viscous times or $d/u_\tau \sim 0.04 - 0.08$ outer times. At $y^+ = 108$, the convergence is slower because in the log-layer the initial guess for c_s^2 is worst. Still, after between 300 and 600 time-steps, the asymptotic state is reached for the fluctuations in c_s^2. Figs. 14(b) and (c) clearly show the considerable decrease of typical c_s^2 values in the Lagrangian model as compared to the plane-averaged model.

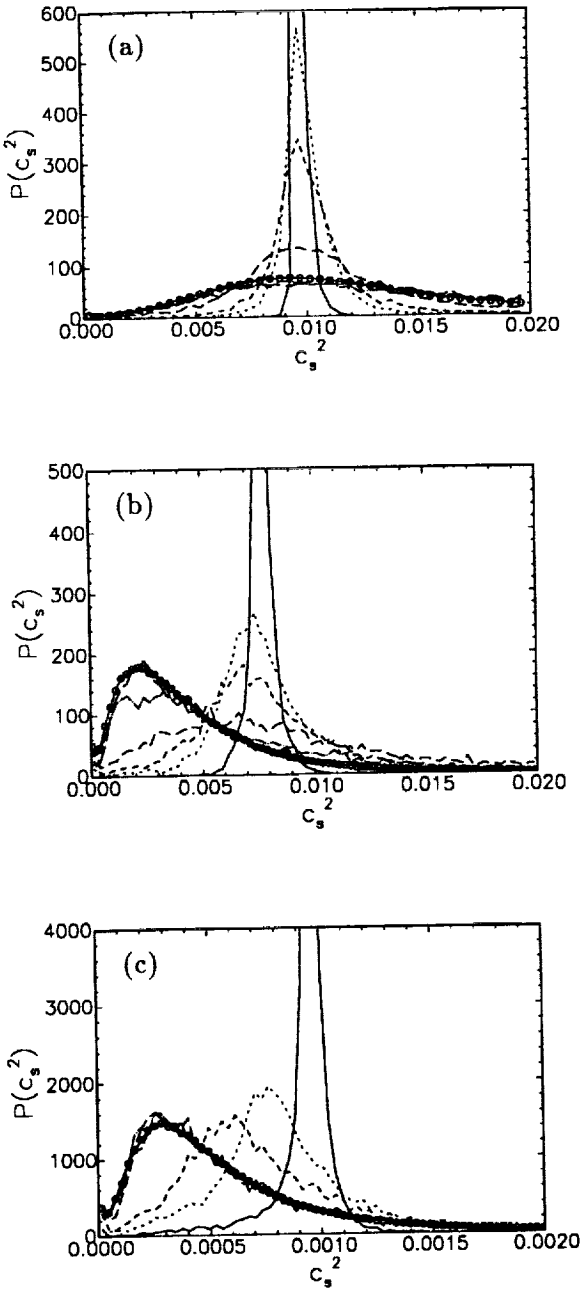

FIGURE 14. Probability-density functions of dynamic model coefficient c_s^2 for different time steps, n. ——— : n=2; ····· : n=10; ---- : n=20; — — — : n=80; — — — : n=320; —·— : n=640; o : $n \sim 38,000$. Different graphs are at different heights above the wall: (a) is at $y^+ = 641$, (b) at $y^+ = 108$ and (c) at $y^+ = 12$.

LES – plane-averaged			
y^+	12	108	640
$< L_{ij}M_{ij} >$	$2.912\ 10^4$	$5.362\ 10^2$	$1.099\ 10^1$
$< M_{ij}M_{ij} >$	$3.054\ 10^7$	$4.932\ 10^4$	$6.998\ 10^2$
LES – local Lagrangian			
y^+	12	108	641
$< \mathcal{I}_{LM} >$	$2.690\ 10^4$	$7.076\ 10^2$	$1.056\ 10^1$
$< \mathcal{I}_{MM} >$	$2.814\ 10^7$	$2.537\ 10^5$	$7.777\ 10^2$

TABLE 1. Numerators and denominators in the expressions for the dynamic coefficients averaged over sample planes.

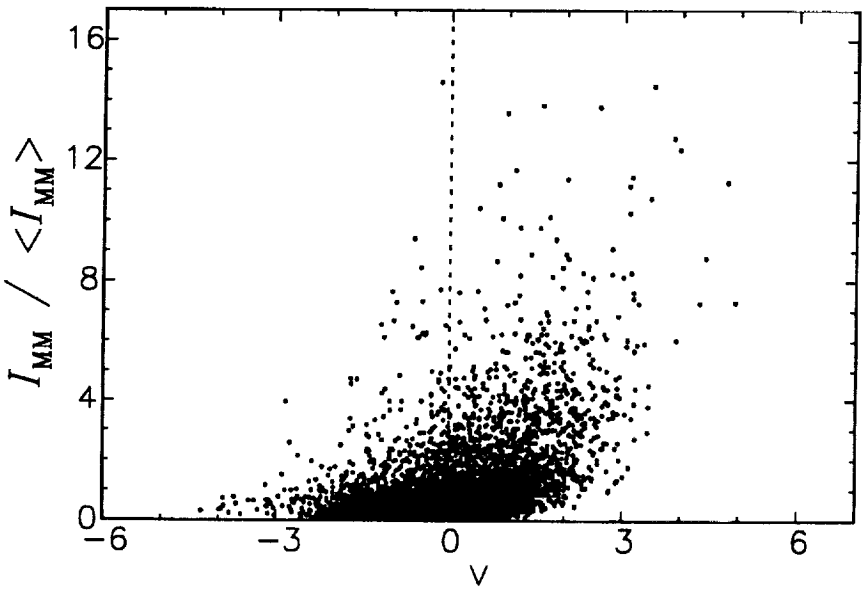

FIGURE 15. Scatter plot of $\mathcal{I}_{MM}$ versus vertical velocity v' in LES of channel flow, using the Lagrangian dynamic model.

The main issue left to answer is why the Lagrangian model generates such decreased coefficients in the log-layer. For this purpose, the average values of numerators and denominators are evaluated separately for both models on some sample planes as given in Table 1.

The largest discrepancy can be seen by comparing the denominators $< M_{ij}M_{ij} >$ and $< \mathcal{I}_{MM} >$ at $y^+ = 108$. A possible reason for this discrepancy can be deduced

by comparing $< M_{ij}M_{ij} >$ at $y^+ = 12$ and at $y^+ = 108$. $< M_{ij}M_{ij} >$ and $< \mathcal{I}_{MM} >$ are several orders of magnitude higher in the near-wall region, as is to be expected for a variable based on the strain-rate (to the fourth power). During ejection events, fluid particles that were close to the wall reach deep into the log-layer, thus convecting elevated values of $\mathcal{I}_{MM}$ upwards. This feature can be deduced from Fig. 15, which shows a scatter plot of the Lagrangian denominator $\mathcal{I}_{MM}$ as function of the local vertical velocity. Clearly, large values of $\mathcal{I}_{MM}$ are associated with positive values of v', which are indicative of ejection events or bursts.

The net effect is that the Lagrangian model is less dissipative as far as bursts are concerned. They can survive longer and feed more turbulence into the channel flow, producing more realistic (higher) levels of Reynolds-averaged (resolved) eddy viscosity and losses.

It is likely that a similar phenomenon causes the near-wall scaling of Lagrangian eddy viscosity to be less steep than that of the plane-averaged model. Occasionally, 'sweeps' bring log-layer material into the sublayer and effectively increase the model coefficient and eddy viscosity above that of the plane-averaged model. Numerical diffusion is also likely to play a role in reducing spatial differences in $\mathcal{I}_{LM}$ and $\mathcal{I}_{MM}$.

3.4 Transitional channel flow

A known drawback of the traditional eddy viscosity closure for LES of transitional flows is that it is overly dissipative, possibly eliminating instabilities altogether (Piomelli & Zang, 1990). The dynamic model, on the other hand, yields essentially zero eddy viscosity if the resolved part of the flow is not turbulent. Instabilities are thus allowed to grow initially in a realistic fashion, as shown in simulations of transitional channel flow using the dynamic model, with planar averaging (Germano *et al.*, 1991). Once the non-linear breakdown phase is reached, the SGS model must become active in order to prevent excessive growth of turbulent kinetic energy, wall shear-stresses, etc. In the Lagrangian model, the variable $\mathcal{I}_{\mathcal{LM}}$ must be initialized to zero everywhere in the laminar region. As turbulence is generated, this variable (and therefore the eddy viscosity) will rise from zero. The rate at which $\mathcal{I}_{\mathcal{LM}}$ rises from zero is controlled in part by the memory time scale. If the memory time scale, T, is too long, the rise in eddy viscosity may occur too late in the transition process. In order to investigate this potential problem, we have performed an LES of transitional channel flow. In this section we attempt to ascertain if the Lagrangian model as proposed here (with the time scale given by Eq. 15) is able to (i) allow for initial instabilities to grow in a realistic fashion, and then to (ii) sufficiently damp the turbulence at the appropriate time.

The transition channel case is identical to that of Zang *et al.* (1990), Piomelli & Zang (1991) and Germano *et al.* (1991). The initial (laminar) centerline Reynolds number is 8,000. The initial condition consists of a parabolic mean flow plus a 2-D Tollmien-Schlichting wave of 2% amplitude and a pair of 3-D Tollmien-Schlichting waves of 0.02% amplitude. The streamwise wavenumber for both the 2-D and 3-D modes is 1.0, whereas the spanwise wavenumber for the 3-D modes is ± 1.5. See Zang *et al.* (1990) for more details on the initial conditions. The dimensions of the computational domain (streamwise, wall-normal, and spanwise) are $2\pi \times 2 \times 4\pi/3$

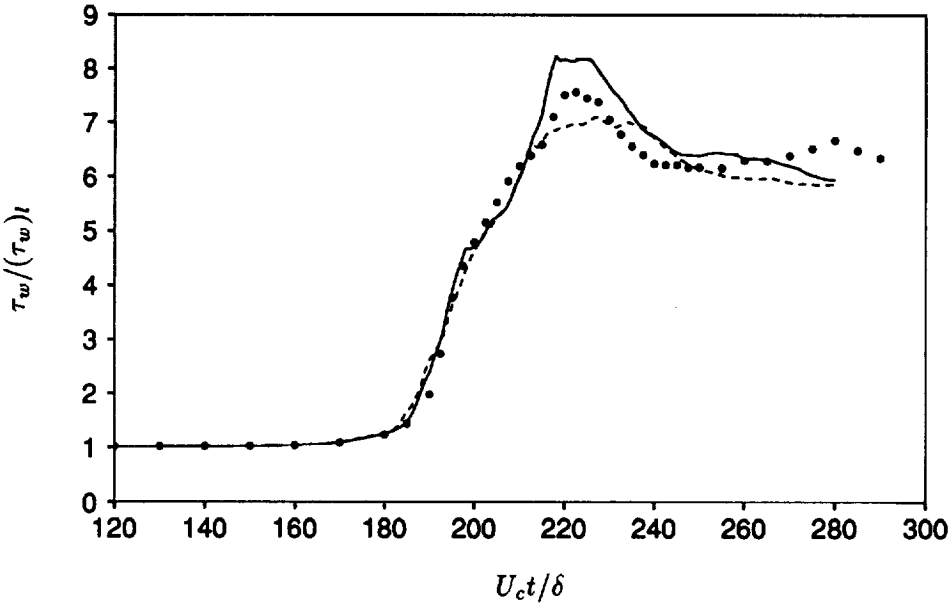

FIGURE 16. Time history of wall-shear stress from the transitional channel simulation. ——— : Lagrangian model LES; ---- : plane-averaged dynamic model LES; • : DNS of Zang *et al.* (1990).

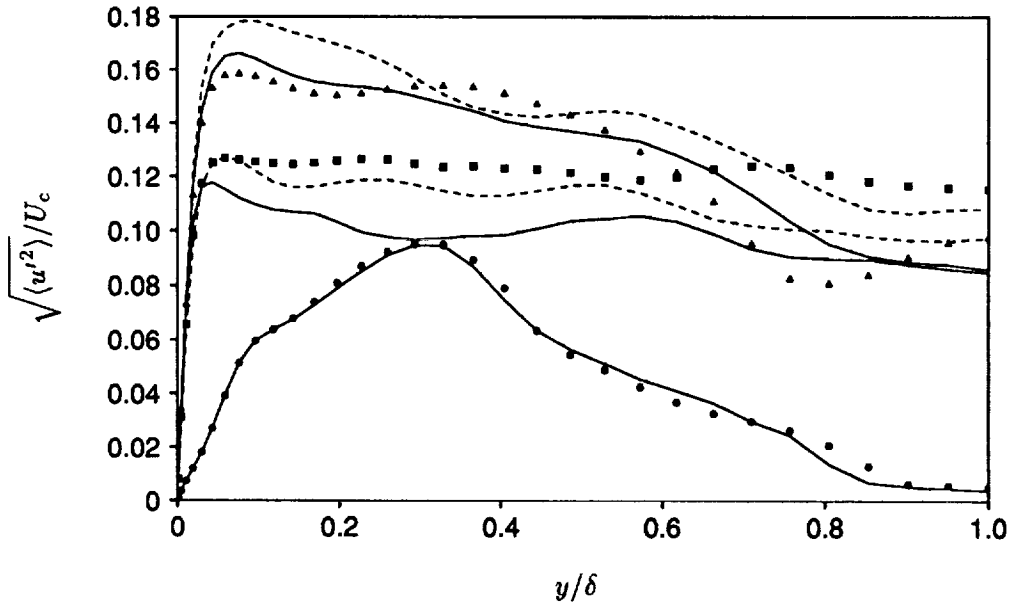

FIGURE 17. Streamwise velocity fluctuation profiles from the transitional channel flow simulation. Symbols: DNS of Zang *et al.* (1990). • : $t = 176$; ▲ : $t = 200$; ■ : $t = 220$; ——— : Lagrangian model LES; ---- : plane-averaged dynamic model LES.

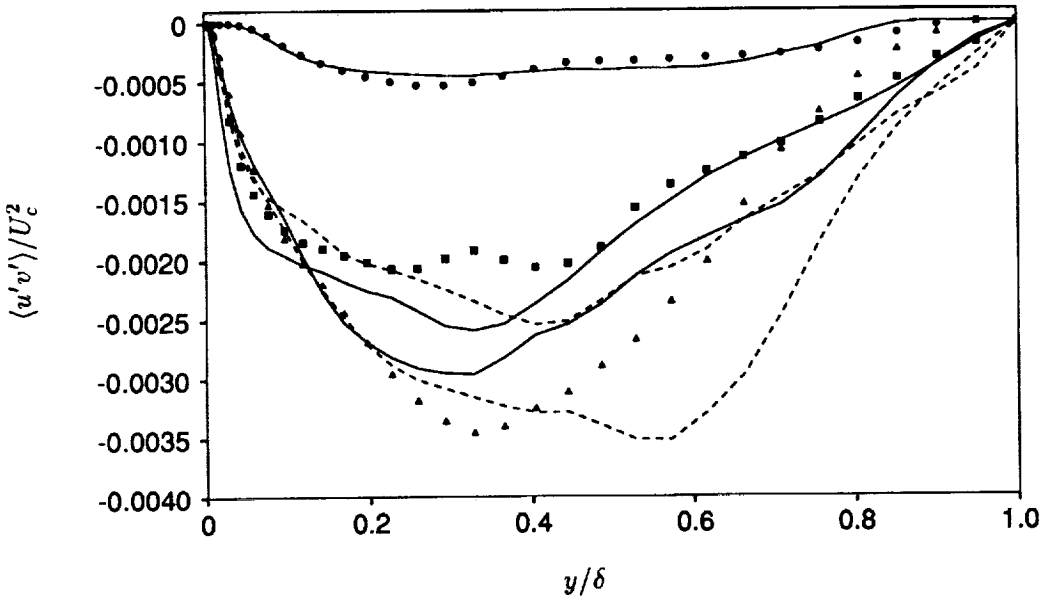

FIGURE 18. Reynolds shear stress profiles from the transitional channel flow simulation. Symbols: DNS of Zang *et al.* (1990). • : $t = 176$; ▲ : $t = 200$; ■ : $t = 220$; ——— : Lagrangian model LES; ---- : plane-averaged dynamic model LES.

(in units of δ). The term $\mathcal{I}_{LM}$ is initialized to 10^{-14} (instead of to zero) in order to allow the first-order Euler scheme (explicit in T^n) to move $\mathcal{I}_{LM}$ away from zero once the source term $\mathbf{L} : \mathbf{M}$ becomes non-zero.

The calculation is started on a $16 \times 65 \times 16$ mesh. As the transition process proceeds, the solution is interpolated onto increasingly finer meshes. The timings of the remeshings are determined by monitoring the energy content in the highest resolved frequencies in the streamwise and spanwise directions. The remeshing procedure was found to introduce a complication in the Lagrangian SGS model. Refining the mesh while holding the test-to-grid filter ratio fixed results in different values of $\mathbf{L} : \mathbf{M}$ and $\mathbf{M} : \mathbf{M}$. Because of its memory, the Lagrangian model requires a finite amount of time to adjust to the sudden changes in $\mathbf{L} : \mathbf{M}$ and $\mathbf{M} : \mathbf{M}$ (about $\Delta t = 5$, or 100 timesteps). In order to minimize this recovery time, the remeshing is performed with values of $\mathcal{I}_{LM}$ and $\mathcal{I}_{MM}$ rescaled so that their plane-averaged values are equal to those of the instantaneous $\mathbf{L} : \mathbf{M}$ and $\mathbf{M} : \mathbf{M}$, respectively. Early in the transition process the SGS dissipation is minuscule and errors associated with remeshing probably have a negligible effect. However, the flow may be more sensitive to remeshing at later times when the SGS dissipation is not negligible.

The $16 \times 65 \times 16$ mesh is used until $t = 145$ (in units of initial centerline velocity U_c and δ), when the grid is remeshed to $24 \times 65 \times 24$. The run is then continued to $t = 176$ on both $24 \times 65 \times 24$ and $32 \times 65 \times 32$ meshes (with little notable difference).

The field is then remeshed to $32 \times 65 \times 48$. Another remeshing to $48 \times 65 \times 64$ is performed at $t = 200$, and the simulation is then run without further remeshing to $t = 280$.

Figure 16 shows the time-history of the wall-shear stress compared with the DNS of Zang *et al.* (1990). Results from the plane-averaged dynamic model are included in this figure. The Lagrangian model is in good agreement with the DNS results up to $t = 210$. Then, the wall-shear stress slightly overshoots the peak after which it settles to a plateau, near the DNS value. The plane-averaged dynamic model results are similar, with the exception that the peak shear stress is underpredicted. Streamwise velocity fluctuations from the Lagrangian and plane-averaged models at times $t = 176$, 200, and 220 are compared with the (filtered) DNS data in Fig. 17. Overall the agreement is quite good, and at $t = 176$ it is excellent. At this time the Lagrangian and plane-averaged results are indistinguishable. Reynolds shear stresses are shown in Fig. 18. Very good agreement is obtained at $t = 176$, whereas some differences exist at $t = 200$ and $t = 220$.

Overall these results show that the Lagrangian model is capable of simulating transition. The eddy viscosity does rise from zero with a delay which is small enough so that turbulence is sufficiently damped after the rapid growth of kinetic energy during transition.

4. Summary and conclusions

A new version of the dynamic model has been tested in conjunction with the Smagorinsky closure. The model involves averaging the Germano identity for some time along fluid pathlines rather than over directions of statistical homogeneity, as was the practice in previous applications of the dynamic model. The present model is not restricted to flows with such special directions and should be readily applicable to complex-geometry, unsteady flows. We have shown that if an exponential memory is employed, the required averages can be obtained by solving a pair of relaxation-transport equations. In order to allow for the implementation of this model with minimal computational complications, we proposed to discretize the total derivatives that enter in these equations using a first-order expression in time, coupled with linear spatial interpolation to find the values required at the 'upstream' locations. The resulting formulation (embodied in Eqs. (17) and (18)) is very simple to implement.

Basic properties of the model were studied in DNS and LES of forced isotropic turbulence. The effect of the Lagrangian averaging on the pdfs of various quantities involved in the modeling were identified. It was also shown that the model preserves enough spatial locality to be influenced by vortical structures ('fat worms') that were identified in the LES.

Applications of LES to isotropic turbulence and fully developed and transitional channel flow has shown that the model performs well and should be readily applicable to more complex flows.

On a final note, we recognize that the Lagrangian dynamic model contains some arbitrary elements. In particular, an adjustable memory time scale T is involved.

This fact is unfortunate since it appears to conflict with the dynamic model philosophy of dispensing with adjustable parameters in favor of determining the subgrid-scale stress solely from information contained in the resolved velocity field. However, for any implementation which uses averaging, there is a similar ambiguity in choosing the domain over which Germano's identity is to be enforced. Schemes that make use of spatial averaging often average over all homogeneous directions although a smaller subspace may be sufficient to insure the stability of the model. Choosing a particular value of the averaging time scale in the Lagrangian model is analogous to choosing a particular region in space over which to average. When viewed in this way, the Lagrangian model actually has an advantage over spatially-averaged variants in that it is designed to average over the minimum time necessary to insure stability. This feature allows the model to retain the maximum amount of spatial and temporal variability while remaining stable.

Acknowledgements

The authors have benefited from fruitful discussions with Profs. P. Moin, J. Jimenez, and Dr. S. Ghosal. Most of this work was performed at CTR during the 1994 Summer Program. C.M. thankfully acknowledges this support from CTR, and partial support from ONR (grant N-00014-92-J-1109). T.S.L. acknowledges partial support from the ONR (grant N-00014-91-J-4072) and from the AFOSR (grant F49620-92-J0003).

REFERENCES

AKSELVOLL, K. & MOIN, P. 1993 Application of the dynamic localization model to large-eddy simulation of turbulent flow over a backward-facing step. In *Engineering applications to large-eddy simulation*, Edited by U. Piomelli and S. Ragab, ASME, New York, NY. 1–6.

BRISCOLINI, M. & SANTANGELO, P. 1994 The non-Gaussian statistics of the velocity field in low-resolution large-eddy simulation of homogeneous turbulence. *J. Fluid Mech.* **270,** 199–217.

COMTE-BELLOT, G. & CORRSIN, S. 1971 Simple Eulerian time correlation in full and narrow band velocity signals in grid generated, isotropic turbulence. *J. Fluid Mech.* **48,** 273–337.

GERMANO, M., PIOMELLI, U., MOIN, P., & CABOT, W. H. 1991 A dynamic subgrid-scale eddy viscosity model. *Phys. Fluids A.* **3,** 1760–1765.

GHOSAL, S., LUND, T. S., MOIN, P., & AKSELVOLL, K. 1994 A dynamic localization model for large-eddy simulation of turbulent flow. To appear in *J. Fluid Mech.*

JIMENEZ, J., WRAY, A. A., SAFFMAN, P.G. & ROGALLO, R. S. 1993 The structure of intense vorticity in isotropic turbulence. *J. Fluid Mech.* **255,** 65–90.

HUSSAIN, A. K. M. F., & REYNOLDS, W. C. 1970 The mechanics of a perturbation wave in turbulent shear flow. Stanford Univ. Dept. of Mech. Eng. Rep. FM-6.

KIM, J., MOIN, P., & MOSER, R. 1987 Turbulence statistics in fully developed channel flow at low Reynolds number. *J. Fluid Mech.* **177,** 133–166.

LILLY, D. K. 1992 A proposed modification of the Germano subgrid-scale closure method. *Phys. Fluids A.* **4,** 633–635.

LIU, S., MENEVEAU, C. & KATZ, J. 1994 Experimental study of similarity SGS models of turbulence in the far-field of a jet. in: *Direct and Large-Eddy Simulation of Turbulence* (eds: Voke, P., Kleiser, L., & Chollet, J. P.) , Kluwer Acad. Amsterdam. 37–49.

LUND, T. S., GHOSAL, S & MOIN, P. 1993 Numerical Experiments with highly-variable eddy viscosity models. In *Engineering applications to large-eddy simulation,* Edited by U. Piomelli and S. Ragab, ASME, New York, NY, 7–11.

MENEVEAU, C. & LUND, T. S. 1994 On the Lagrangian nature of the turbulence energy cascade. *Phys. Fluids.* **6,** 2820–2825.

O'NEIL, J. & MENEVEAU, C. 1993 On probability densities of turbulence subgrid-scale stresses and on local dynamic models (submitted to Phys. Fluids).

PIOMELLI, U. 1993 High Reynolds number calculations using the dynamic subgrid-scale stress model. *Phys. Fluids A.* **5,** 1484–1490.

PIOMELLI, U., & ZANG, T. A. 1991 Large-eddy simulation of transitional channel flow. *Comp. Phys. Comm.* **65,** 224

ROGALLO, R. 1981 Numerical experiments in homogeneous turbulence. *NASA TM 81315.*

SCOTTI, A., MENEVEAU, C. & LILLY, D. K. 1993 Generalized Smagorinsky model for anisotropic grids. *Phys. Fluids A.* **5,** 2306–2308.

VINCENT, A. & MENEGUZZI, M. 1991 The spatial structure and statistical properties of homogeneous turbulence. *J. Fluid Mech.* **225,** 1–20.

ZANG, T. A., GILBERT, N., & KLEISER, L. 1990 Direct numerical simulation of the transitional zone. In *Instability and Transition,* M. Y. Hussaini and R. G. Voigt eds., Springer-Verlag, New York, 283–299.

317-34

Center for Turbulence Research
Proceedings of the Summer Program 1994

N95-21052

P-11

Effects of turbulence compressibility and unsteadiness in compression corner flow

By A. Brankovic[1] AND O. Zeman[2]

The structure of the separated flow region over a 20° compression corner at a free-stream Mach number of 2.84 is investigated computationally using a Reynolds averaged Navier Stokes (R.A.N.S.) solver and $k-\epsilon$ model. At this Mach number and ramp angle, a steady-state recirculation region of order δ_o is observed, with onset of a "plateau" in the wall pressure distribution near the corner. At lower ramp angles, separation is negligible, while at an angle of 24°, separation regions of length $2\delta_o$ are expected. Of interest here is the response of the mathematical model to inclusion of the pressure dilatation term for turbulent kinetic energy. Compared with the experimental data of Smits and Muck (1987), steady-state computations show improvement when the pressure dilatation term is included. Unsteady computations, using both unforced and then forced inlet conditions, did not predict the oscillatory motion of the separation bubble as observed in laboratory experiments (see e.g. Dolling and Or 1983). An analysis of the separation bubble oscillation and the turbulent boundary layer (T.B.L.) frequencies for this flow suggests that the bubble oscillations are of nearly the same order as the turbulence frequencies, and therefore difficult for the model to separate and resolve.

1. Introduction

The accurate prediction of turbulent, compressible flow at low supersonic speeds ($M_\infty \leq 3$) is one of the most challenging and important problems facing aircraft engine component designers. For rotating components, flows typically feature unsteadiness (periodic and non-periodic) and mild compressibility effects, which when coupled prove difficult to isolate and understand from a fundamental point of view. Analysis of experimental data (Dolling and Or 1983) reveals that even wind tunnel generated flows feature significant flow field unsteadiness, which is difficult to isolate and control. Analysis of the unsteady pressure fluctuations at the foot of the separation shock indicates non-periodic, unsteady movement of the shock foot, with a highly non-Gaussian distribution of the wall pressure fluctuation. Near the bubble "steady-state" separation point where the wall pressure is highly intermittant and where the pressure fluctuations are most intense, the pressure distribution was found to be bi-modal. It was found that the characteristic frequency f_D of the

1 Pratt & Whitney, West Palm Beach, FL
2 Center for Turbulence Research

PRECEDING PAGE BLANK NOT FILMED

PAGE 300 INTENTIONALLY

separation bubble oscillations scales on the incoming boundary layer thickness δ_o and free-stream velocity U_o so that

$$f_D \delta_o / U_o = 0.13.$$

At this resonant frequency, the bubble leading edge moved forward by up to $1.5\delta_o$, doubling its length relative to the steady state value.

Compressibility corrections due to the pressure dilatation for two-equation turbulence models have previously been proposed by Zeman and Coleman (1991) and Horstman (1987). The Zeman-Coleman model was based on the results of a direct numerical simulation (DNS) of turbulence in which the mean flow is subjected to one-dimensional compression; Durbin and Zeman (1992) have formulated a rapid distortion theory which allows calculation of the pressure-dilatation term analytically for cases of rapid compression in one, two, or three directions. Vandromme and Zeman (1992) found that including this term in the $k-\epsilon$ model, using wall integration boundary conditions, significantly improved predictions for $M_\infty = 2.84$ flow over a 24^o ramp.

In addition to models for the pressure dilatation term, proposals for the dilatation dissipation and turbulence/pressure-gradient interaction terms, turbulent length-scale limiters, and low-Reynolds number corrections for turbulent viscosity have been made for specific features of highly compressible flows (Marvin 1991). Not all of these terms have been tested in mildly compressible flows. The present effort focuses on the evaluation of the pressure dilatation contribution in steady-state predictions of the compression corner flow.

It is noted that model predictions using the standard $k-\epsilon$ model tend to underestimate flow reattachment lengths even in incompressible flows such as backsteps and 180^o bend ducts. It is ambitious to expect a single turbulence compressibility term to compensate for underlying problems with the model. Nevertheless, it is of great interest to examine whether these terms are important in predicting complex compressible flows, and whether the terms should be generally included in production R.A.N.S. flow solvers.

2. Computational model and solution method

2.1 Governing equations

Computations were performed using the time-dependent form of the compressible R.A.N.S. equations. The continuity, momentum, and energy conservation equations used are shown below:

$$\frac{\partial \rho}{\partial t} + \frac{\partial}{\partial x_j}(\rho U_j) = 0.0 \tag{1}$$

$$\frac{\partial \rho U_i}{\partial t} + \frac{\partial}{\partial x_j}(\rho U_j U_i + \delta_{ij} P - \tau_{ij}) = 0.0 \tag{2}$$

$$\frac{\partial \rho e_t}{\partial t} + \frac{\partial}{\partial x_j}(\rho U_j e_t + P U_j - \tau_{ij} U_i - \frac{\kappa}{C_p}\frac{\partial h}{\partial x_j}) = 0.0 \tag{3}$$

where $P = \rho RT$, $e_t = h - \frac{P}{\rho} + \frac{1}{2}U_j^2$, and $\tau_{ij} = \mu(\frac{\partial U_i}{\partial x_j} + \frac{\partial U_j}{\partial x_i} - \frac{2}{3}\delta_{ij}\frac{\partial U_i}{\partial x_j})$.

The equation set is closed using the Boussinesq approximation for the Reynolds stress tensor:

$$-\rho\overline{u_i u_j} = \mu_t(\frac{\partial U_i}{\partial x_j} + \frac{\partial U_j}{\partial x_i} - \frac{2}{3}\delta_{ij}\nabla \cdot U) - \frac{2}{3}\rho k\delta_{ij} \tag{4}$$

where the turbulent viscosity is modeled as:

$$\mu_t = C_\mu \rho f_\mu \frac{k^2}{\epsilon} \tag{5}$$

The turbulent kinetic energy, k and its dissipation rate, ϵ are computed using modeled transport equations:

$$\frac{\partial \rho k}{\partial t} + \frac{\partial \rho U_j k}{\partial x_j} - \frac{\partial}{\partial x_j}(\mu + \frac{\mu_t}{\sigma_k})\frac{\partial k}{\partial x_j} = P - \rho\epsilon + (\overline{p\theta})_R \tag{6}$$

$$\frac{\partial \rho \epsilon}{\partial t} + \frac{\partial \rho U_j \epsilon}{\partial x_j} - \frac{\partial}{\partial x_j}(\mu + \frac{\mu_t}{\sigma_\epsilon})\frac{\partial \epsilon}{\partial x_j} = C_1 f_1 \frac{\epsilon}{k} P - C_2 f_2 \rho \frac{\epsilon^2}{k} \tag{7}$$

where $P = -\rho(\overline{u_i u_j})\frac{1}{2}(U_{i,j} + U_{j,i})$, is the production term, and the pressure dilatation term, $\overline{pu_{j,j}} \equiv \overline{p\theta}$, has been added to the R.H.S. of the k equation. Modeling of this term is the subject of the next section. The constants in the turbulence model are the standard values recommended by Jones and Launder (1972), and are $C_\mu = 0.09$, $C_1 = 1.44$, $C_2 = 1.92$, $\sigma_k = 1.0$, $\sigma_\epsilon = 1.30$, $f_\mu = 1.0$, $f_1 = 1.0$ and $f_2 = 1.0$.

2.2 The pressure dilatation model

As the boundary layer turbulence passes through the oblique shock generated by the compression corner, it undergoes a highly rapid compression. This effect is represented by the rapid pressure-dilatation model developed by Zeman (1991) and Zeman and Coleman (1991). The model is based on the physics and theories of rapid distortion and was verified against the DNS of rapidly compressed homogeneous turbulence.

The pressure dilatation term $\overline{p\theta}$ appears on the R.H.S. of the turbulent kinetic energy equation with positive sign. The rapid contribution to $\overline{p\theta}$ proposed by Zeman and co-workers to be tested is

$$(\overline{p\theta})_R = -C_{d1}\bar{\rho}k\tau(S_{ij}^*)^2 \tag{8}$$

where $S_{ij}^* = \frac{1}{2}(U_{j,i} + U_{i,j} - \frac{2}{3}\delta_{ij}\nabla \cdot U)$ is the trace-free mean strain rate, $\tau = k/\epsilon$ is the turbulent time scale, and $C_{d1} = -0.004$ is the model constant whose value was determined from the DNS computations. For one of the steady-state test runs, a value of C_{d1} = -0.006 was used to test the sensitivity of the separation bubble size to this coefficient. It is pointed out that the modeled pressure dilatation term acts as a sink term in the k transport equation and decreases the level of k values wherever it is numerically significant; this is the case in the vicinity of shocks, where mean velocity gradients are steep.

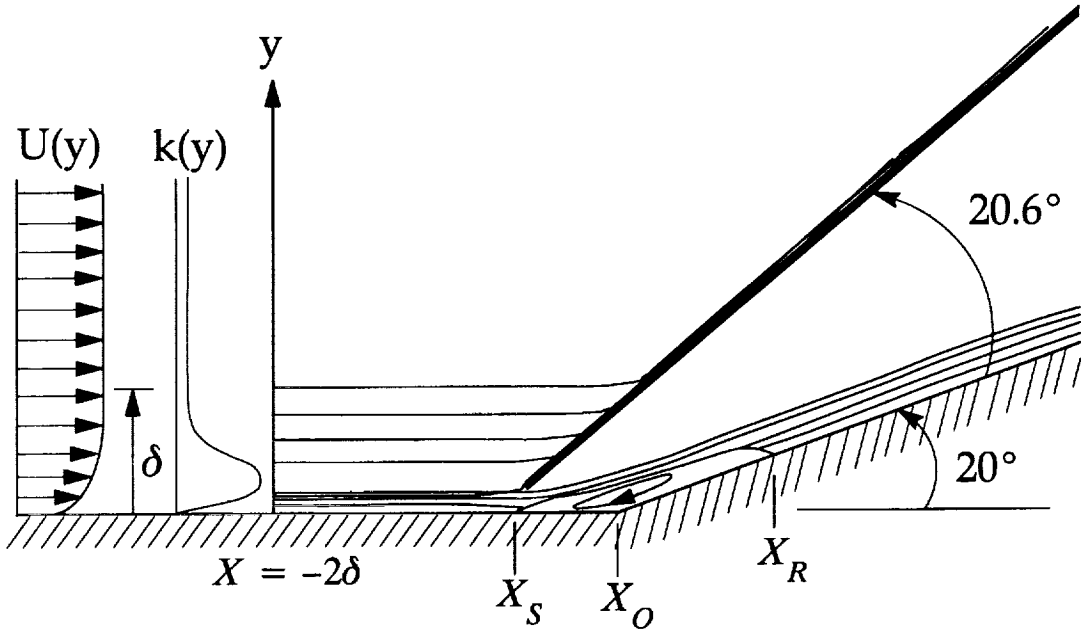

FIGURE 1. Schematic diagram of flow geometry and inlet conditions.

2.3 Numerical method

Computations were done with a code developed at Pratt & Whitney. The equations are transformed to a curvilinear coordinate system and integrated over arbitrary control volumes using a cell-centered grid. A pressure correction procedure is adapted to generalized coordinates. Second and third-order spatial discretization schemes are used interchangeably. A second-order backward temporal scheme is used for the time-dependent calculations.

Inflow conditions consisted of interpolated axial velocity and turbulent kinetic energy profiles obtained from measurements in Smits and Muck (1987). The inlet turbulence dissipation rate and the turbulent viscosity distribution were obtained from the boundary layer distributions given in Hinze (1975). The computational grid was 241 (axial) x 101 (vertical). Although formal grid independence is not claimed, the authors' previous experience with such grids for compression corner flows strongly suggests that the results are close to grid independent. Wall functions for the momentum and turbulence equations have been used to avoid the time consuming computations within the viscous sublayer. This required that the first grid node off the wall lies in the range of $30 \leq y^+ \leq 300$.

3. Steady state results

3.1 Flow structure

A schematic of the inflow conditions and overall flow structure is shown in Fig. 1. The diagram indicates an oblique shock angle of 20.6°, corresponding to the predicted and measured values for this Mach number. Computed contours of the

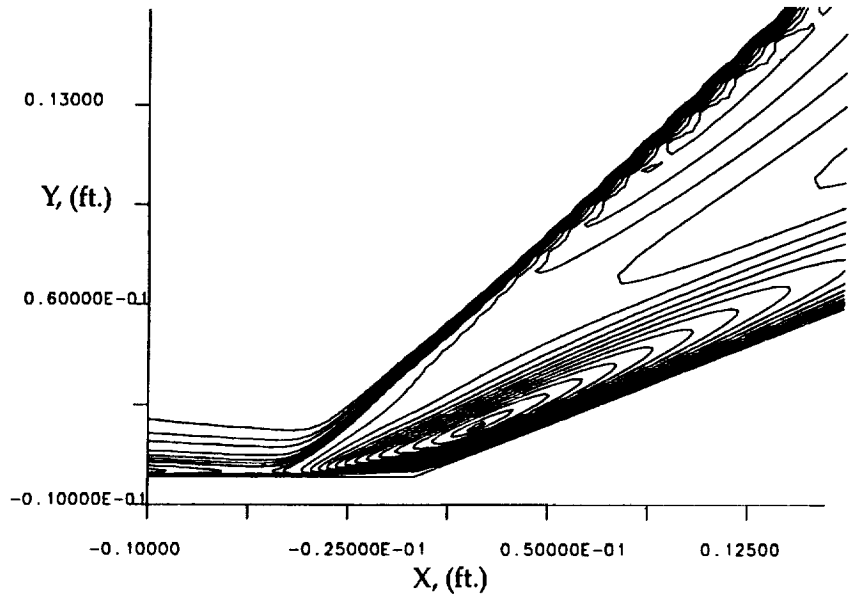

FIGURE 2. Turbulent kinetic energy contours for baseline $k - \epsilon$ model.

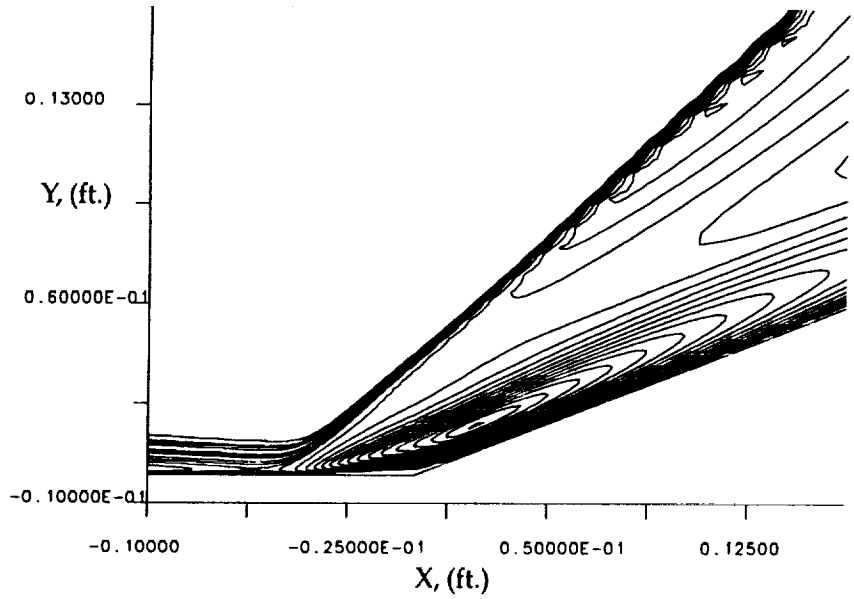

FIGURE 3. Turbulent kinetic energy contours for $k - \epsilon$ with modeled pressure dilatation term.

steady-state turbulent kinetic energy are shown in Figs. 2 and 3. For the baseline $k - \epsilon$ model, Fig. 2, the contour indicates shock formation upstream of the corner, with a strong, intensely turbulent vortex centered just downstream of the corner. The boundary layer redevelops downstream of the shock, with the flow relatively quiescent between the shock and the ramp wall.

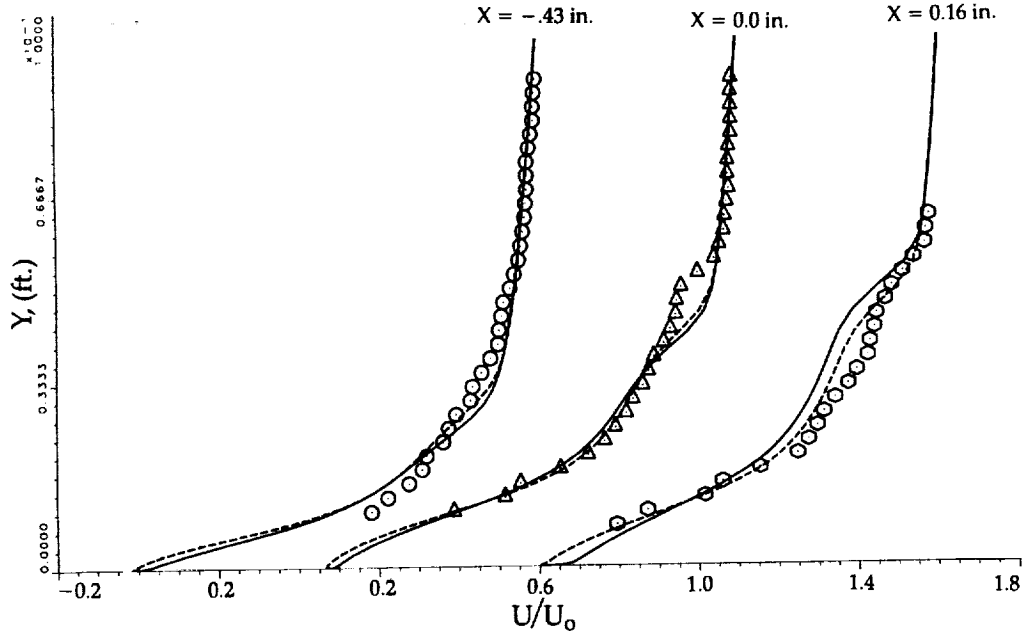

FIGURE 4. Streamwise velocity profiles in the vicinity of the separation bubble. o , data; ——— , baseline $k-\epsilon$; ---- , $k-\epsilon$ with pressure dilatation.

The contour showing the compressible flow model results, Fig. 3, indicates a similar flow structure to that of the baseline model. Flow separation begins slightly further upstream in this case, although this is only discernable through detailed post-processing of the results.

3.2 Mean velocity results

Mean streamwise velocity profiles at three key downstream locations are shown in Fig. 4. The locations selected for comparison are near the bubble separation point, the corner, and near the bubble reattachment point. Measurements do not extend all the way to the wall, hence it is difficult to determine exactly where separation begins and what is the magnitude of the reverse flow. In each profile, the model predictions using the pressure dilatation model show minor improvement in the prediction of axial velocity when compared to the baseline $k-\epsilon$ result. The compressible model shows a more rapid adjustment to the inflection of the velocity profile at the shock passage location, while the baseline $k-\epsilon$ model is noticeably more sluggish in its response here.

3.3 Wall static pressure

A comparison of wall static pressures is shown in Fig. 5. Experimental data, the baseline $k-\epsilon$ prediction, and compressible $k-\epsilon$ results using values of -0.004 and -0.006 for the C_{d1} coefficient are shown. The baseline model result (solid line) severely underpredicts the size of the separation region, recovers to the downstream pressure value too rapidly, and misses prediction of the pressure plateau indicative

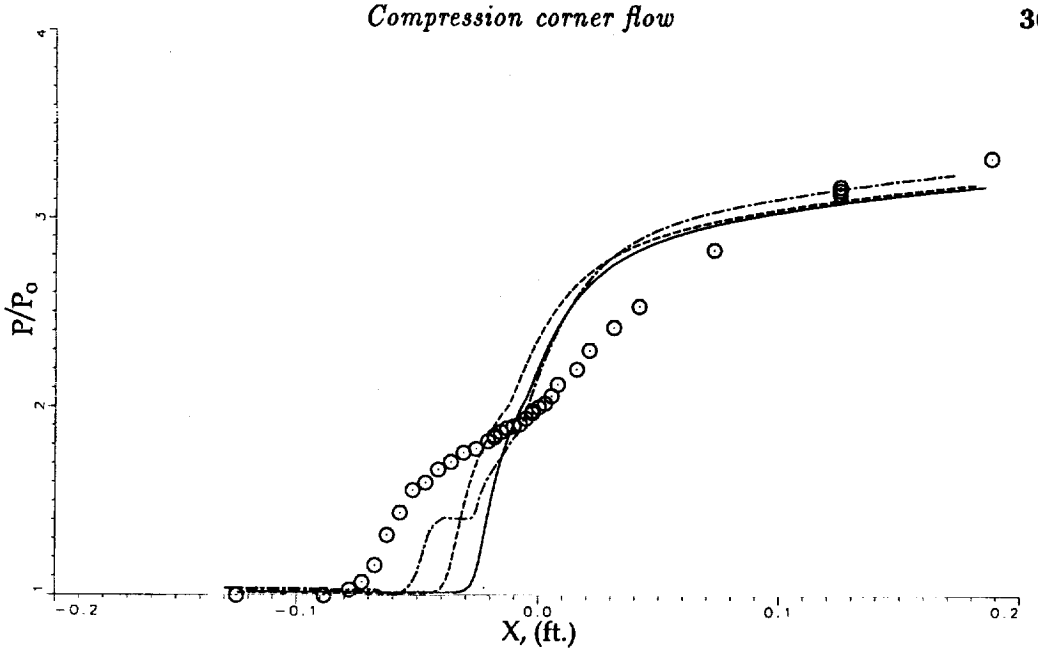

FIGURE 5. Wall static pressure profile. o , data; ——— , baseline $k-\epsilon$; ---- , $k-\epsilon$ with pressure dilatation and C_{d1} = -0.004; $k-\epsilon$ with pressure dilatation and C_{d1} = -0.006,

of the viscous region in flow separation. The compressible $k-\epsilon$ prediction using -0.004 shows an improvement in the upstream region, with pressure lift-off somewhat closer to experimental data, although even this pressure profile is characteristic of weak shock-boundary layer interaction (Delery and Marvin, 1986). As with the baseline case, the pressure plateau is absent, and recovery appears to be too rapid. When a value of -0.006 is used, the pressure plateau indicative of strong interaction has appeared, with the upstream separation point closer to the experimental value.

3.4 Turbulent kinetic energy profiles

The turbulent kinetic energy profiles are shown at a number of downstream locations along the wall and ramp in Fig. 6. As expected from the form of the pressure dilatation model, overall k values are damped at each downstream location for the compressible $k-\epsilon$ model relative to the baseline model. Starting with the profile at the corner, the presence of the shock is noted as a secondary peak in the profile. The shock amplifies the free-stream turbulence significantly; however, it does not quite reach the level of turbulence intensity generated by the wall, even in the strong interaction region immediately downstream of the corner (see Figs. 2 and 3).

4. Unsteady state results

4.1 Unforced boundary layer results

In order to investigate whether the bubble oscillations could be realized simply by running the code in a time-accurate manner, several cases were run in which the global time step was varied from 0.1 second to 10^{-5} seconds. This sampling

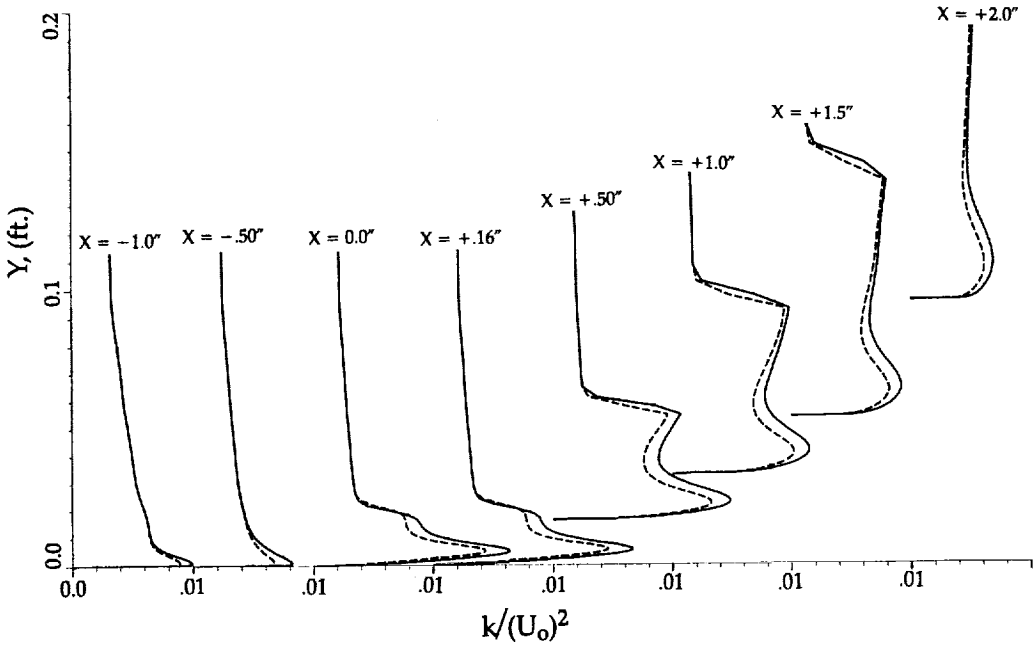

FIGURE 6. Turbulent kinetic energy profiles at various downstream locations. ——— , baseline $k-\epsilon$; ---- , $k-\epsilon$ with pressure dilatation, C_{d1} = -0.004.

range was selected as it was estimated that the characteristic bubble frequency for these inflow conditions is approximately 1300 Hz. Monitoring points were installed at multiple locations within the separation bubble to monitor axial and vertical velocity. Over the entire sampling range, negligible bubble oscillations were recorded in the simulations, with no particular resonance at the expected resonant frequency of 1300 Hz. The reasons for the failure to detect the bubble unsteadiness include numerical damping, use of wall functions in the momentum and turbulence equations, or simply the nature of the R.A.N.S. model. As the bubble self-excitation could not be detected, an attempt was made to excite bubble oscillations through perturbation of the inlet boundary layer.

4.2 Forced boundary layer results

In order to excite the bubble into a resonant frequency, an upstream boundary layer perturbation of the form:

$$U(X_o, y, t) = U(X_o, y, 0) + 0.05U(X_o, y)sin(\omega t)exp(-5y/\delta)$$

was applied. This provided a single wavelength oscillation whose amplitude decayed effectively to zero at the boundary layer edge. The perturbation amplitude of 5.0 % was approximately equal to the maximum streamwise turbulence intensity in the measured dataset of Smits and Muck (1987). To bracket the expected resonant

frequency at 1300 Hz, forcing frequencies ranging from 200 Hz to 10,000 Hz were run. Each cycle was sampled 50 times. For a free-stream velocity of 1800 ft/sec, the maximum perturbation velocity was +/-90 ft/sec. The average response at several sensing locations in and around the separation bubble is given in the table below:

Forcing Frequency	Peak-to-Peak Amplitude
200 Hz	+/- 0.252 ft/sec
1000 Hz	+/- 0.307 ft/sec
1500 Hz	+/- 0.235 ft/sec
2000 Hz	+/- 0.596 ft/sec
2500 Hz	+/- 0.795 ft/sec
4000 Hz	+/- 0.795 ft/sec
5000 Hz	+/- 0.686 ft/sec
6000 Hz	+/- 0.680 ft/sec
10000 Hz	Divergent

The results indicate that only a very mild separation bubble resonance was computed, in the range of 2500 to 4000 Hz, with lower amplitude of oscillation at lower and higher frequencies. Thus, even with a strong upstream boundary layer perturbation, bubble resonance proved exceptionally difficult to predict.

4.3 Time-scale considerations

The result of the unsteady, forced inflow investigation raises some important issues regarding the resolution of solvers based on R.A.N.S. equations and the k-ϵ model used for prediction of unsteady flow. Some insight into this problem can be gained from a comparison of the governing time scales which characterize the unsteadiness. Here the comparison is drawn between turbulent boundary layer (T.B.L.) oscillations in the supersonic compression corner and bluff-body flow oscillations due to vortex shedding which was successfully modeled by Durbin (1994). In boundary layers, the typical size of the large eddies is order δ, the T.B.L. thickness. Hence, a probe in this region would measure large-eddy frequencies on the order of $f_t \sim U/\delta$, where U is the average speed in the turbulent boundary layer and $U \sim U_\infty$ is the free-stream velocity. From the measurements of Dolling and Or (1993), it is known that the separation bubble oscillation frequency is $f_o \simeq 0.13U/\delta$, or only 1/7.7 that of the large-eddy frequency. It is noted that these oscillations could not accurately be computed using the R.A.N.S. solver, as described above.

In bluff body dynamics, such as the flow over circular, square, or triangular cylinders, the shedding or Strouhal frequency in the wake region is measured as $f_o \approx 0.2U_\infty/L$, where U_∞ = free-stream velocity and L is the cross-sectional dimension, the diameter in the case of a circular cylinder. This is true for flows where $Re_D = U_\infty D/\nu \geq 100$. When such cases are run in an unsteady mode using a computational domain with adequate upstream and downstream length (and unsteady boundary conditions, if necessary), vortex shedding of the correct frequency is obtained. We know from the T.B.L. case that the large-eddy frequency at separation

is $f_t \sim U_\infty/\delta$, where δ can be estimated from the relation for flow over circular cylinders as $\delta_o/D \sim 0.16/Re_D^{1/7}$. Thus, for $Re_D \simeq 10^6$, we get $\delta_o/D \sim 0.16/(10^6)^{1/7} \sim 0.0222$. We therefore compute a time-scale ratio of f_t / $f_o \simeq (10^6)^{1/7}/0.2/0.16 \simeq 224$. Hence, the ratio of turbulence-to-shedding frequencies is 224 / 7.7 $\sim$ 29.2.

The *ratio of characteristic frequencies* is thus a key parameter in determining whether R.A.N.S.-type solvers using the standard k-ϵ turbulence model will *resolve* the unsteadiness observed in the experimental data. In the compression corner case, the ratio of f_t / f_o was found to be only 7.7, while for bluff body flow, the same ratio was found to be 224 at $Re_D = 10^6$, nearly 30 times greater than that for the compression corner. Based on the limited data, it appears that for f_t/f_o of order 1, turbulence-driven oscillations will be submerged in the turbulence model and prove difficult to resolve. Unsteady turbulence models which adjust properly to both temporal and spatially local flow conditions may be necessary to resolve this level of unsteadiness. Large-scale or momentum-driven oscillations of order $f_t/f_o \sim 100$ or greater should be relatively easy to compute using unsteady R.A.N.S. solvers, with the selection of turbulence model not nearly as important in these cases. For the large body of cases which fall in between these two extremes or for cases which exhibit multiple levels of unsteadiness such as the rotational, supersonic flow in gas turbine compressors, a more critical analysis of the importance of time scales involved and the underlying turbulence model is necessary.

5. Conclusions

The results indicate that the compressibility correction term represented by the pressure dilatation model of Zeman (1991) improves the velocity profiles predictions in the vicinity of the separation bubble to a small degree. Wall pressure predictions were also slightly improved. The term generally had the effect of damping turbulent kinetic energy as was seen in a series of k profiles at various downstream locations. Increasing the value of the modeled coefficient C_{d1} from -0.004 to -0.006 had the effect of increasing the separation bubble size, resulting in a form of the pressure plateau reported in the steady-state wall pressure results for ramp angles of 20° or greater at $M_\infty = 2.84$. Unsteady runs with and without upstream boundary layer perturbations did not predict the measured separation bubble oscillations. An analysis of the characteristic time scales for this problem revealed that the expected bubble oscillation frequency was less than the characteristic large-eddy frequency, which proved numerically difficult for the R.A.N.S. solver and k-ϵ model to resolve. It was postulated that the condition $f_t/f_o >> 1$ must be met for the code to easily compute unsteadiness in the flow. An example from bluff body dynamics was used to illustrate this point.

REFERENCES

DELERY, J. & MARVIN, J. G. 1986 Shock-wave boundary layer interactions. *AGARD Report 280.*

DOLLING, D. S. & OR, C. T. 1983 Unsteadiness of the shock wave structure in attached and separated compression ramp flowfields. *AIAA Paper 83-3720.*

DURBIN, P. A. 1994 Separated flow computations with the $k - \epsilon - v^2$ turbulence model. *CTR Manuscript 152.* Also, to appear in *AIAA Journal.*

DURBIN, P. A. & ZEMAN, O. 1992 Rapid distortion theory for homogeneous compressed turbulence with application to modeling. *J. Fluid Mech.* **242,** 349-370.

HINZE, J. O. 1975 *Turbulence.* McGraw-Hill, New York.

HORSTMAN, C.C. 1987 Prediction of hypersonic shock wave/turbulent boundary layer interaction flows. *AIAA Paper 87-1367.*

JONES, W. P. & LAUNDER, B. E. 1972 The prediction of laminarization with a two-equation model of turbulence. *Int. J. Heat Mass Transfer.* **15,** 301-314.

MARVIN, J. G. 1991 Baseline Models for Turbulence Compressibility Studies. *NASP/NASA Ames GWP #18 Workshop on Turbulence Compressibility.*

SMITS, A. J. & MUCK, K.-C. 1987 Experimental study of three shock wave/ turbulent boundary layer interactions. *J. Fluid Mech.* **182,** 291-314.

VANDROMME, D. & ZEMAN, O. 1992 Response of a supersonic boundary layer to a compression corner. *Proc. of the Summer Program.* Center for Turbulence Research, NASA Ames/Stanford University. 247-258.

ZEMAN, O. 1991 Dilatation dissipation: The concept and application in modeling compressible mixing layers. *1991 Annual Res. Briefs.* Center for Turbulence Research, NASA Ames/Stanford University, 1991, 105-117.

ZEMAN, O. & COLEMAN, G. N. 1991 Compressible turbulence subjected to shear and rapid compression. *Turbulent Shear Flows 8.* Springer Verlag.

N95-21053

Center for Turbulence Research
Proceedings of the Summer Program 1994

Role of pressure diffusion in non-homogeneous shear flows

By A. O. Demuren,[1] S. K. Lele[2] AND P. Durbin[3]

A non-local model is presented for approximating the pressure diffusion in calculations of turbulent free shear and boundary layer flows. It is based on the solution of an elliptic relaxation equation which enables local diffusion sources to be distributed over lengths of the order of the integral scale. The pressure diffusion model was implemented in a boundary layer code within the framework of turbulence models based on both the $k-\varepsilon-\overline{v^2}$ system of equations and the full Reynolds stress equations. Model computations were performed for mixing layers and boundary layer flows. In each case, the pressure diffusion model enabled the well-known free-stream edge singularity problem to be eliminated. There was little effect on near-wall properties. Computed results agreed very well with experimental and DNS data for the mean flow velocity, the turbulent kinetic energy, and the skin-friction coefficient.

1. Introduction

In higher-order turbulence models 'pressure diffusion' is usually neglected, or at best added to 'turbulent diffusion' (Launder 1984) and the two modeled in aggregate. Pressure diffusion refers to the term $\partial_i \overline{u_j p}$ in the Reynolds stress budget; turbulent diffusion refers to $\partial_k \overline{u_i u_j u_k}$. The latter represents the ensemble averaged effect of turbulence convection and can often be modeled as a diffusion process; the former, however, is harder to explain as diffusion. Turbulent diffusion is usually considered to be the dominant diffusion mechanism and pressure diffusion is considered to be negligible. However, Lumley (1975) showed that, for homogeneous turbulence, the application of symmetry constraints to the exact equation for the "slow" or non-linear part of the pressure diffusion led to the result that its magnitude is 20% of that of the triple velocity correlation. In the present study, DNS databases for several shear flows were examined, namely: the mixing layer simulation of Rogers and Moser (1994); the wake simulation of Rogers (private communication); the boundary layer simulation of Spalart (1988); and the backward facing step simulation of Le & Moin (1994). These confirm that, in the main shear regions, pressure diffusion is roughly 20-30% of turbulent diffusion. However, it appears to be mostly counter-gradient transport, so that it merely reduces the effect of turbulent diffusion, which is mostly gradient transport. Thus, the current practice of absorbing pressure diffusion and turbulent diffusion into a single model

1 Old Dominion University
2 Stanford University
3 Center for Turbulence Research

PRECEDING PAGE BLANK NOT FILMED PAGE 312 INTENTIONALLY BLANK

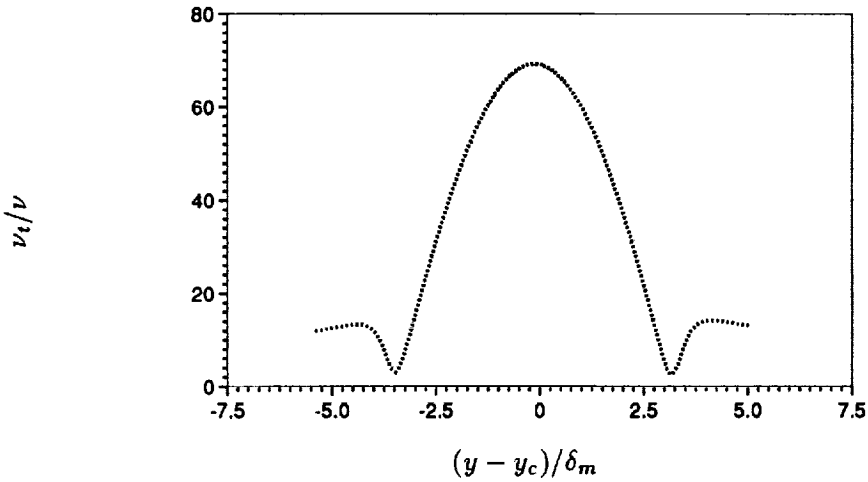

FIGURE 1. Computed eddy viscosity distribution in a two-stream mixing layer.

term appears reasonable, as far as the main shear regions are concerned. But the DNS data show that near the edges of the shear layers, turbulent diffusion decreases rapidly to zero, while pressure diffusion decreases only very gradually, so the latter then becomes dominant. Thus, the budgets show that near the free-stream edge the balance is between pressure transport and mean convection, or temporal drift, rather than between turbulent transport and the latter. When applied to one or two-equation models (Coles 1968, Cazalbou *et al.* 1994), an assumed balance between evolution and turbulent diffusion leads to an unsteady non-linear diffusion problem whose solution has a propagating front at the edge of which the eddy viscosity ν_t, the turbulent kinetic energy k, and its dissipation rate ε all go sharply to zero. Fig. 1 illustrates how the eddy viscosity drops abruptly at the edge of the shear layer, even though a non-zero value was imposed in the free stream. This singular solution is not in agreement with experimental data, which show that all these properties asymptote gradually to free-stream values. A consequence of the singularity is that computations with these turbulence models are unable to properly account for free-stream turbulence effects since the free stream and the main shear regions are decoupled, except where insufficient grid resolution produces smearing via numerical diffusion. This result would also apply to second moment closures which use gradient diffusion models for turbulent transport.

The free-stream edge singularity can be removed by introducing a model for the pressure diffusion which does not vanish abruptly at the edge of the main shear flow. Since pressure transport should be non-local, a new model for pressure diffusion is introduced based on the elliptic relaxation concept introduced by Durbin (1991, 1993) for modeling the pressure-strain correlation in non-homogeneous turbulent flows. Computations with the new model are compared to experimental data for the plane mixing layer and the boundary layer flows.

2. Mathematical model

In the present study only simply shear flows (mixing layers, wakes, boundary layers) are considered, so that boundary layer forms of the governing equations are applicable. For simplicity, we shall only present equations for the $k-\varepsilon-\overline{v^2}$ model (Durbin 1991, 1994). Though the $\overline{u_iu_j}-\overline{f_{ij}}$ model was also utilized, the results are virtually the same for the simple shear flows considered here.

The mean flow equations are:

$$D_tU = \partial_y[(\nu+\nu_t)\partial_yU] \tag{1}$$

$$\nabla\cdot U = 0 \tag{2}$$

for incompressible thin shear layers. (D_t represents the total derivative and ∂_y the cross-stream partial derivative.)

2.1 $k-\varepsilon-\overline{v^2}$ model

The usual $k-\varepsilon-\overline{v^2}$ model (Durbin 1994) is modified by the addition of a pressure diffusion term to the k-equation and the $\overline{v^2}$ equation. Thus, we have:

$$D_tk = P_k-\varepsilon+\partial_y[(\nu+\nu_t/\sigma_k)\partial_yk]-\partial_y(\overline{pv}) \tag{3}$$

$$D_t\varepsilon = \frac{C_{\epsilon_1}P_k-C_{\epsilon_2}\varepsilon}{T}+\partial_y[(\nu+\nu_t/\sigma_\epsilon)\partial_y\varepsilon] \tag{4}$$

$$D_t\overline{v^2} = kf_{22}-\overline{v^2}\frac{\varepsilon}{k}+\partial_y[(\nu+\nu_t/\sigma_k)\partial_y\overline{v^2}]-2\partial_y(\overline{pv}) \tag{5}$$

where the rate of turbulent energy production is

$$P_k = \nu_t(\partial_yU)^2 \tag{6}$$

and the eddy viscosity is given by

$$\nu_t = C_\mu\overline{v^2}T \tag{7}$$

The term $k\overline{f_{22}}$ is the source of $\overline{v^2}$ via redistribution from the streamise component $\overline{u^2}$. This is the pressure strain term in homogeneous turbulent flow. In non-homogeneous turbulent flows, non-local effect are introduced through the elliptic relaxation equation

$$L^2\partial_y^2f_{22}-f_{22} = (1-C_1)\frac{2/3-\overline{v^2}/k}{T}-C_2\frac{P_k}{k} \tag{8}$$

The length and time scales which appear in the equations are given by

$$L = C_L\max\left[\frac{k^{3/2}}{\varepsilon}, C_\eta\left(\frac{\nu^3}{\varepsilon}\right)^{1/4}\right] \tag{9}$$

$$T = \max\left[\frac{k}{\varepsilon}, C_T\left(\frac{\nu}{\varepsilon}\right)^{1/2}\right] \tag{10}$$

In free shear flows, equations (9) and (10) are modified by removing the Kolmogorov limits which are strictly only relevant to wall bounded flow. The boundary conditions follow Durbin (1994) and are not repeated. Their main effect is to produce the proper behavior of k, ε, and $\overline{v^2}$ near no-slip boundaries.

The empirical coefficients, are $C_L = 0.3$, $C_\mu = 0.19$, $C_{\epsilon_1} = 1.3$ and $C_{\epsilon_2} = 1.90, C_T = 6.0$, $C_\eta = 70.0$, $C_1 = 1.4$, $C_2 = 0.3$, $\sigma_k = 1.0$, $\sigma_\epsilon = 1.3$.

2.2 Pressure diffusion model

The pressure transport is modeled as:

$$-\partial_y \overline{pv} = \partial_y f \tag{11}$$

Non-local effects are introduced via the elliptic relaxation equation

$$L^2 \partial_y^2 f - f = -f^L \tag{12}$$

where f^L is a local gradient diffusion model

$$f^L = C_s \frac{\nu_t}{\sigma_k} \partial_y k \tag{13}$$

It is assumed that the same length scale which governs the non-locality in the pressure redistribution would also govern the non-locality in the pressure transport. C_s is a free parameter which is determined by optimization. The boundary conditions are

$$\begin{aligned} f &= 0 \quad ; \text{free stream} \\ \partial_y f &= 0 \quad ; \text{no-slip wall} \end{aligned} \tag{14}$$

3. Results and discussion

Model computations were performed for a two-stream mixing layer with the ratio of low to high free-stream velocities of 0.6 chosen to coincide with the experimental study of Bell and Mehta (1990). A parabolic forward marching code was utilized. Starting from hyperbolic tangent profiles, the solution was marched until self-similar results were obtained. Computations were performed with 3 values of C_s, namely 0.0, 0.5, and 1.0. $C_s = 0.0$ represents the case with no pressure diffusion. Computed results of ν_t/ν and k are compared in Figs. 2(a) and 2(b), respectively. It is clearly seen that, at the higher values of C_s, the edge singularity present with $C_s = 0$ has been removed. k profiles now go gradually to zero exhibiting long tails. Also ν_t profiles gradually approach the small values set in the free stream, though

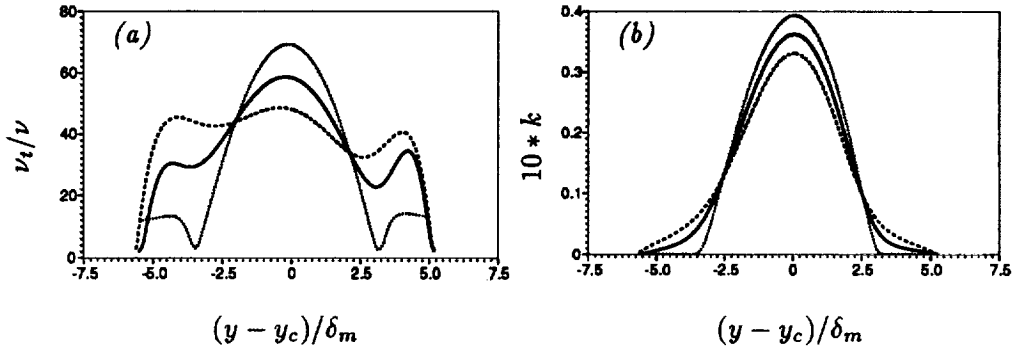

FIGURE 2. Effect of diffusion coefficient C_s on computations of the two-stream mixing layer:····· , $C_s = 0.0$;—— , $C_s = 0.5$;---- , $C_s = 1.0$. *(a)* eddy viscosity *(b)* turbulent kinetic energy.

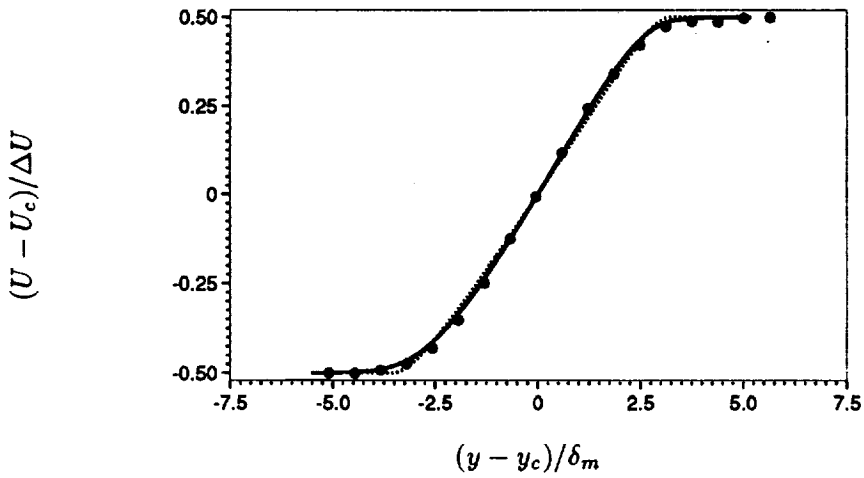

FIGURE 3. Comparison of velocity profiles in the two-stream mixing layer to • experimental data of Bell & Mehta (1990). (See figure 2 for legends.)

not monotonically. The ν_t profile obtained with $C_s = 0.5$ is quite similar to that given by the DNS data of Rogers and Moser (1994) with equation (7) as definition. The peak value computed with $C_s = 0.5$ was closest to that measured by Bell and Mehta (1990); hence $C_s = 0.5$ was chosen for all subsequent computations. Fig. 3 shows a comparison of computed velocity profiles with $C_s = 0.0$, 0.5 versus experimental data of Bell and Mehta (1990). Both model computations give the correct spread rate but the computation with the pressure diffusion model shows smoother profiles near the free-stream edges in agreement with experimental data. Similarly, k profiles are compared in Fig. 4. In this case, the differences between model computations with and without pressure diffusion are more dramatic. The non-local role of pressure diffusion in transporting turbulent kinetic energy from the center of the layer to the edges of the free stream is apparent.

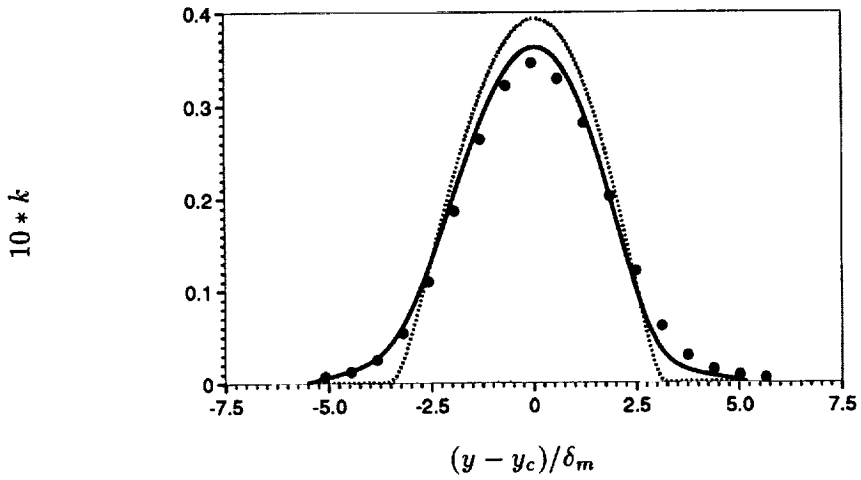

FIGURE 4. Comparison of k profiles in the two-stream mixing layer to • experimental data of Bell & Mehta (1990). (See figure 2 for legends.)

With the pressure diffusion model thus calibrated, the question is whether the improved agreement with data near free-stream edges would also be reproduced in a wall boundary layer flow without producing an adverse effect on near-wall agreement, where the role of pressure diffusion should be minimal. Computations were performed for a developing wall boundary layer using the DNS data of Spalart (1988) as inlet conditions. The solution was then marched until self-similar results were established. Profiles of ν_t/ν across the boundary layer are compared for C_s = 0.0, 0.5 and 1.0 in figure 5. The main effect of pressure diffusion is near the free-stream edge, with little or no effect on near wall values. Skin friction coefficients are compared to experimental data of Coles and Hirst (1968) in figure 6. This confirms that the pressure diffusion produces negligible effect on near-wall properties. Finally k profiles at R_θ = 7,500, normalized with the local friction velocity, are compared to experimental data of Klebanoff (1955) in figure 7. Again, pressure diffusion has negligible effect in the near-wall region, but produces more gradual decay near the free-stream edge.

Thus, the sharp free-stream edge problem can be cured by introducing a non-local model for the pressure diffusion. In the present study a gradient diffusion model was utilized for f^L. Although it enables the edge singularity problem to be overcome, it appears too simple to reproduce all features of the pressure transport through the layer and near the free stream. It can be argued that we are only modeling the deviation from the usual model treatment, i.e., the part which is not directly proportional to turbulent diffusion. Nevertheless, it is desirable to explore more general forms of f^L. Consideration is being given to such models. To aid in this study, we hope to obtain a splitting of the DNS mixing layer data of Rogers and Moser (1994) for the pressure diffusion into slow and rapid parts. We are also studying the form of the pressure diffusion term in the shearless mixing layer simulation of Briggs *et al.* (1994). Initial computations of the shearless flows studied

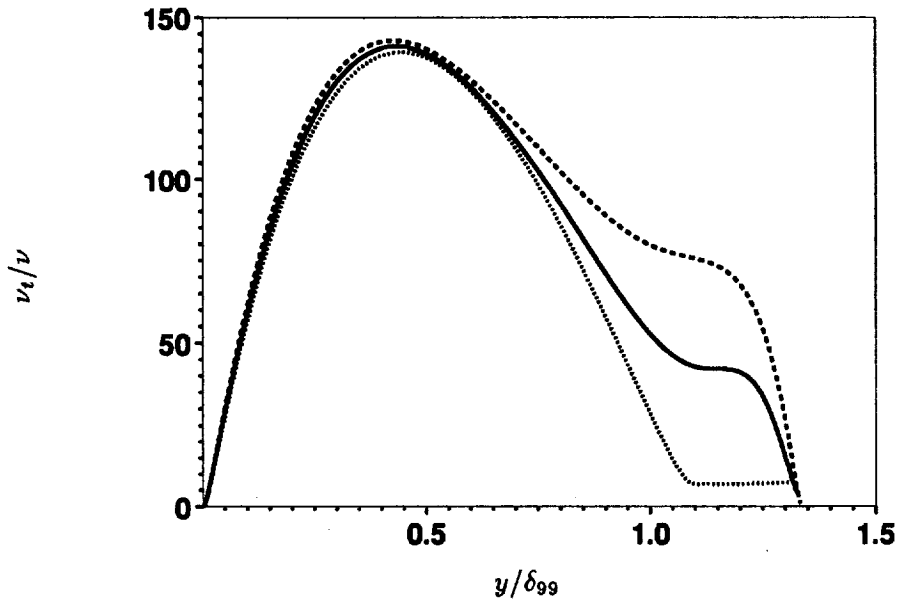

FIGURE 5. Effect of diffusion coefficient C_s on eddy viscosity distribution in boundary layer. (See figure 2 for legends.)

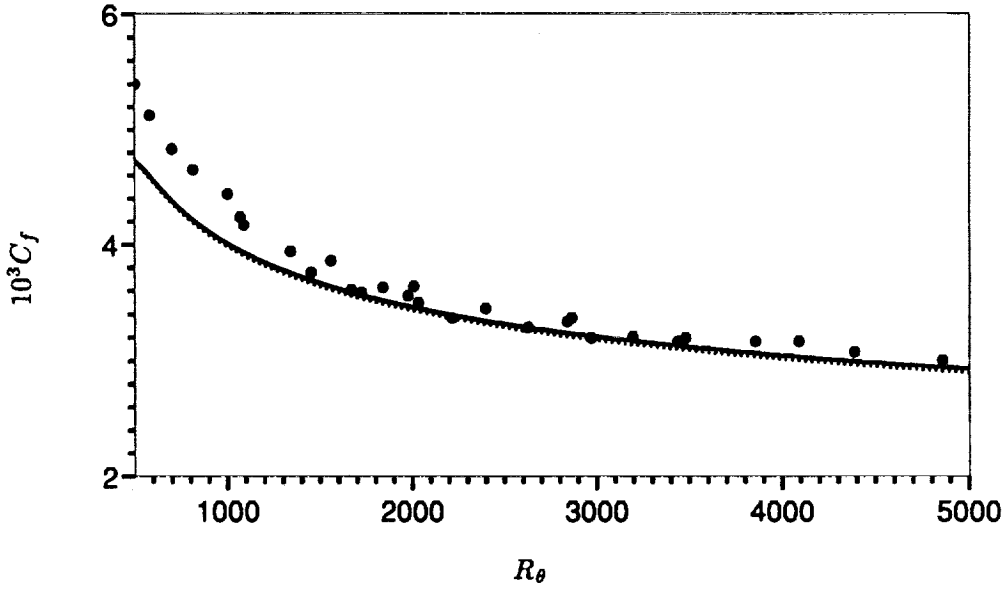

FIGURE 6. Comparison of skin friction coefficient in a boundary layer to • experimental data of Coles & Hirst (1968). (See figure 2 for legends.)

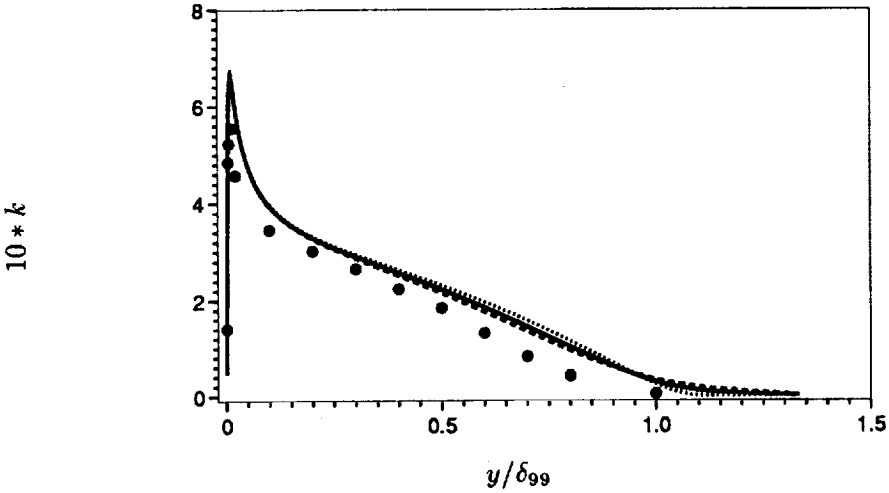

FIGURE 7. Comparison of k profiles in a boundary layer to • experimental data of Klebanoff (1955). (See figure 2 for legends.)

experimentally by Veeravalli and Warhaft (1989) show that most of the current turbulent diffusion models with or without the present diffusion model significantly underpredict the shear layer spread rate.

4. Conclusions

A non-local model for pressure diffusion has been developed based on the solution of an elliptic relaxation equation. This enabled the free-stream edge singularity problem, which most current turbulence models suffer from, to be eliminated. The pressure diffusion model did not produce any undesirable effects on near-wall properties. Current turbulent diffusion models with and without the new pressure diffusion model are unable to predict observed growth rates in shearless turbulence mixing layer.

REFERENCES

BELL, J. H., & MEHTA, R. D. 1990 Development of a two-stream mixing layer from tripped and untripped boundary layers. *AIAA J.* **28,** 2034-2041.

BRIGGS, D. A., FERZIGER, J. H., KOSEFF, J. R., & MONISMITH, S. G. 1994 Entrainment in a shear-free turbulent mixing layer. *Proc. AGARD 74th Fluid Dynamics Panel Meeting.*

CAZALBOU, J. B., SPALART, P. R., & BRADSHAW, P. 1994 On the behavior of two-equation models at the edge of a turbulent region. *Phys. Fluids.* **6,** 1797-1804.

COLES, D. E. 1968 In *Computations of Turbulent Boundary Layers,* AFOSR-IFP-Stanford Conference.

COLES, D. E., & HIRST, E. A. 1968 In *Computations of Turbulent Boundary Layers,* AFOSR-IFP-Stanford Conference.

DURBIN, P. 1991 Near-wall turbulence closure modeling without 'damping functions'. *Theoret. Comput. Fluid Dynamics.* **3,** 1-13.

DURBIN, P. 1993 A Reynolds stress model for near-wall turbulence. *J. Fluid Mech.* **249,** 465-498.

DURBIN, P. 1994 Separated flow computations with the $k - \varepsilon - \overline{v^2}$ model. *AIAA J.* to appear.

KLEBANOFF, S. 1955 Characteristics of turbulence in a boundary layer with zero pressure gradient. *NACA Rep. 1247*

LAUNDER, B. E. 1984 Second-moment closure: methodology and practice. *In Turbulence Models and Their Applications, (Editions Eyrolles, Paris).*

LE, H., & MOIN, P. 1994 Direct numerical simulation of turbulent flow over a backward-facing step. *Rep. TF-58,* Thermosciences Division, Department of Mechanical Engineering, Stanford University.

LUMLEY, J. L. 1975 Prediction methods for turbulent flows - Introduction. *Lecture Series 76, von Karman Inst., Rhodes St. Genese, Belgium*

ROGERS, M. M.,& MOSER, R. D. 1994 Direct simulation of a self-similar turbulent mixing layer. *Phys. Fluids.* **6,** 903-923.

SPALART, P. R. 1988 Direct simulation of a turbulent boundary layer up to $R_\theta =$ 1410. *J. Fluid Mech.* **187,** 61-98.

VEERAVALLI, S.,& WARHAFT, Z. 1989 The shearless turbulence mixing layer. *J. Fluid Mech.* **207,** 191-229.

Center for Turbulence Research
Proceedings of the Summer Program 1994

N95-21054

Modeling near wall effects in second moment closures by elliptic relaxation

By D. Laurence[1] and P. Durbin[2]

The elliptic relaxation model of Durbin (1993) for modeling near-wall turbulence using second moment closures (SMC) is compared to DNS data for a channel flow at $Re_t = 395$. The agreement for second order statistics and even the terms in their balance equation is quite satisfactory, confirming that very little viscous effects (via Kolmogoroff scales) need to be added to the high Reynolds versions of SMC for near-wall-turbulence. The essential near-wall feature is thus the kinematic blocking effect that a solid wall exerts on the turbulence through the fluctuating pressure, which is best modeled by an elliptic operator. Above the transition layer, the effect of the original elliptic operator decays rapidly, and it is suggested that the log-layer is better reproduced by adding a non-homogeneous reduction of the return to isotropy, the gradient of the turbulent length scale being used as a measure of the inhomogeneity of the log-layer. The elliptic operator was quite easily applied to the non-linear Craft & Launder pressure-strain model yielding an improved distinction between the spanwise and wall normal stresses, although at higher Reynolds number (Re) and away from the wall, the streamwise component is severely underpredicted, as well as the transition in the mean velocity from the log to the wake profiles. In this area a significant change of behavior was observed in the DNS pressure-strain term, entirely ignored in the models.

1. Introduction

Second moment closures have the ability to account exactly for turbulence "production" terms due to shear, rotation and stratification, and to provide a better description than eddy viscosity models of the Reynolds stresses—a corner stone for complex flows involving heat transfer, two-phase flows, or combustion. However they are mainly used by industry in their high Re form, since near-wall models are both unsatisfactory and rather difficult to solve numerically.

Since the publication of the budgets of the Reynolds stresses in a channel flow by Mansour, Kim & Moin (1988), a variety of near-wall second moment closures have been proposed (see review of 9 models by So *et al.*, 1990). Some of them were more or less successful, but they are very seldom used outside low Reynolds number channel flows. Most of them use damping functions to force homogeneous models to comply with near wall turbulence features. A sound general principle is to avoid explicit use of the distance to the wall; however, this tends to render the models

1 EDF/DER/LNH, 6 quai Watier, 78400 Chatou, France
2 Center for Turbulence Research

PRECEDING PAGE BLANK NOT FILMED

rather difficult to converge numerically since the damping functions then depend on parameters of the unknown solution (such as the turbulent Reynolds number $k^2/\varepsilon\nu$). Launder & Tselepidakis (1991), for instance, did a careful term by term fit to each component of the Reynolds stress balance obtained by DNS, but the overall model proved somewhat unstable especially when gravitational damping was added (Laurence, 1993).

A common feature of these models is that all the terms (except diffusion) are related algebraically to the local values of the solution. Such local representation is in contradiction to the very large structures (hundreds of wall units) interacting with the wall and inhomogeneity of the velocity profile.

In contrast to this previous approach, Durbin (1993) was able to reproduce quite satisfactorily the features of near-wall flows by combining the very simple 'IP' homogeneous second moment closure (Launder, Reece & Rodi, 1975) with a nonlocal (elliptic) approach representing the wall blocking effect on the large eddies. The present study was aimed at a closer comparison of the elliptic operator with DNS budgets and an analysis of what could be gained by combining it with a more sophisticated second moment closure (SMC).

The Craft-Launder (1991) cubic SMC, either in free flows or in combination with wall functions or a low Re two-equation model, was shown to give better predictions than the IP model in a variety of flows (round and plane jets, impinging jets, tube bundles, swirling jets). A characteristic of near wall flows (also present in shear flows) is the strong reduction of the normal stress compared to the spanwise and longitudinal stresses. The Launder-Craft cubic model reproduces this effect in free flows and to some extent in the log-layer of a channel flow (Launder and Tselepidakis, 1991). Lee, Kim & Moin (1990) showed that many features of wall flows are also present in high shear homogeneous flows, though not accounting totally for the very high anisotropies in a near wall flow. Thus, our project was motivated by the idea that by combining the cubic model with the elliptic operator, to correctly acknowledge what is due to the high shear and what is due to the wall blocking effect, an improved model would result.

2. Elliptic relaxation

Following the procedure developed by Durbin (1993) the Reynolds-stress transport equation is written as:

$$D_t\overline{u_iu_j} = P_{ij} + \wp_{ij} - \overline{u_iu_j}\frac{\varepsilon}{k} + T_{ij} + \nu\nabla^2\overline{u_iu_j} \tag{1}$$

$$\begin{aligned} P_{ij} &= -\overline{u_iu_k}\partial_k U_j - \overline{u_ju_k}\partial_k U_i \\ \wp_{ij} &= -\overline{u_i\partial_j p} - \overline{u_j\partial_i p} - \varepsilon_{ij} + \overline{u_iu_j}\frac{\varepsilon}{k} \\ T_{ij} &= -\partial_k\overline{u_ku_iu_j} \end{aligned} \tag{2}$$

The term $\wp_{ij}$ differs from the usual pressure-strain ϕ_{ij} since it includes the misalignment of the dissipation tensor and the Reynolds stress tensor:

$$\wp_{ij} = \phi_{ij} - \left(\varepsilon_{ij} - \overline{u_i u_j}\frac{\varepsilon}{k}\right). \tag{3}$$

This unclosed term, called hereafter 'relaxed pressure-strain', is obtained by solving an elliptic equation:

$$L^2\nabla^2\frac{\wp_{ij}}{k} = \frac{\wp_{ij} - \wp^h_{ij}}{k}. \tag{4}$$

For homogeneous turbulence $\wp_{ij}$ in Eq. 4 reduces to $\wp^h_{ij}$, for which any standard redistribution model ϕ^h_{ij} can be used:

$$\wp^h_{ij} = \phi^h_{ij} + \mathrm{dev}\,(\overline{u_i u_j})\frac{\varepsilon}{k}, \tag{5}$$

where 'dev' is the deviatoric operator:
$\mathrm{dev}\,(\overline{u_i u_j}) = \overline{u_i u_j} - \overline{u_k u_k}\,\delta_{ij}/3$
The simple 'IP' model uses the Rotta return to isotropy and the 'isotropization of production'; i.e., the slow and rapid parts are modeled as:

$$\begin{aligned}\phi^h_{ij} &= \phi_{ij,\,\mathrm{slow}} + \phi_{ij,\,\mathrm{rapid}} \\ &= -C_1\,\mathrm{dev}\,(\overline{u_i u_j})\frac{\varepsilon}{k} - C_2\,\mathrm{dev}\,(P_{ij})\end{aligned} \tag{6}$$

Durbin(1993) applied elliptic relaxation to the IP model with the following modifications which define what is called hereafter the 'R-linear model':

$$\wp^h_{ij} = -(C_1 - 1)\frac{\mathrm{dev}\,(\overline{u_i u_j})}{T} - C_2\,\mathrm{dev}\,(P_{ij}) \tag{7}$$

where the time scale is defined as:

$$T = \max\left[\frac{k}{\varepsilon}, 6\left(\frac{\nu}{\varepsilon}\right)^{1/2}\right]. \tag{8}$$

This time scale is also used in the dissipation equation in place of ε/k, preventing a singularity at the wall. The length scale L appearing in (4) is also prevented from going to zero at the wall using again a Kolmogoroff scale as a lower bound:

$$L = C_L \max\left[\frac{k^{3/2}}{\varepsilon}, C_\eta\left(\frac{\nu^3}{\varepsilon}\right)^{1/4}\right]. \tag{9}$$

Furthermore Eq. 4 is solved numerically by introducing an intermediate variable $f_{ij} = \wp_{ij}/k$, and boundary conditions at the wall are imposed on the coupled $\overline{u_i u_j} - f_{ij}$ equations.

Last, the Daly-Harlow expression for the turbulent diffusion was used to model T_{ij}:

$$T_{ij} = \partial_l\left(C_\mu\frac{\overline{u_l u_m}\,T}{\sigma_k}\partial_m\overline{u_i u_j}\right) \tag{10}$$

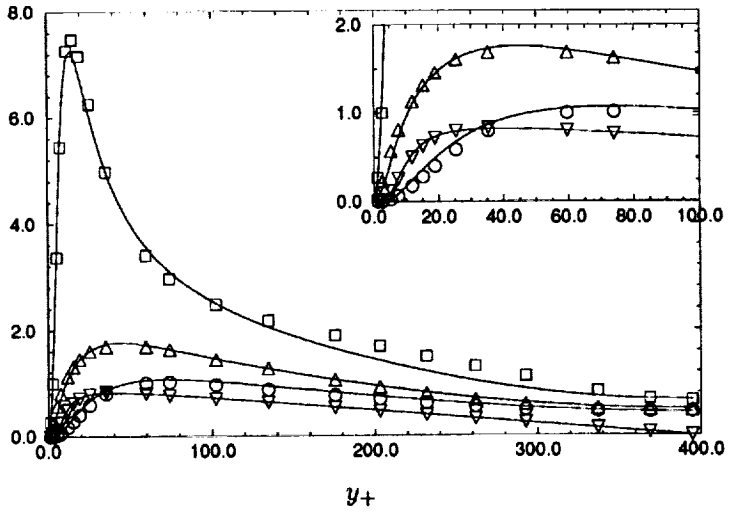

FIGURE 1. Reynolds Stresses, R-cubic model; □ , $\overline{u_1^2}$; ○ , $\overline{u_2^2}$; △ , $\overline{u_3^2}$; ∇, $\overline{u_1 u_2}$.

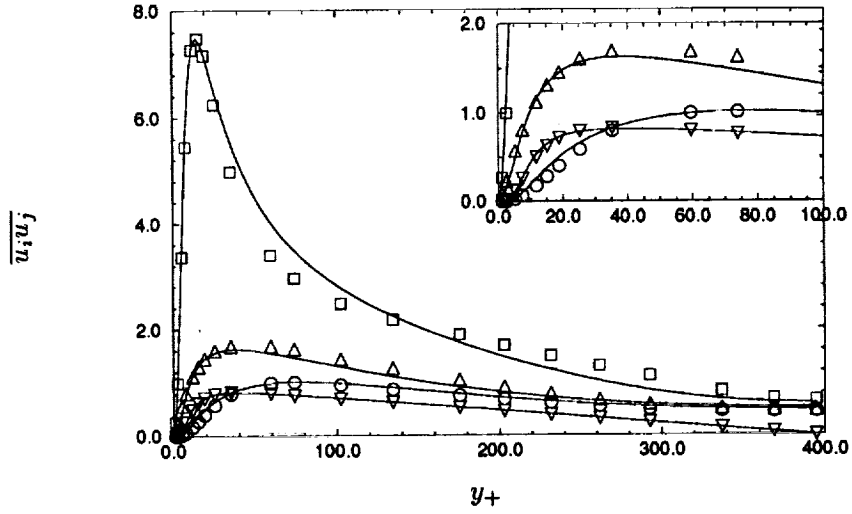

FIGURE 2. Reynolds Stresses, R-linear model. Symbols as in fig. 1.

3. Cubic order pressure-strain model

Defining the anisotropy tensor and its invariants as:

$$a_{ij} = \mathrm{dev}(\overline{u_i u_j})/k,\ A_2 = a_{ij}a_{ij},\ A_3 = a_{ij}a_{jk}a_{ki},\ A = 1 - 9/8(A_2 - A_3), \qquad (11)$$

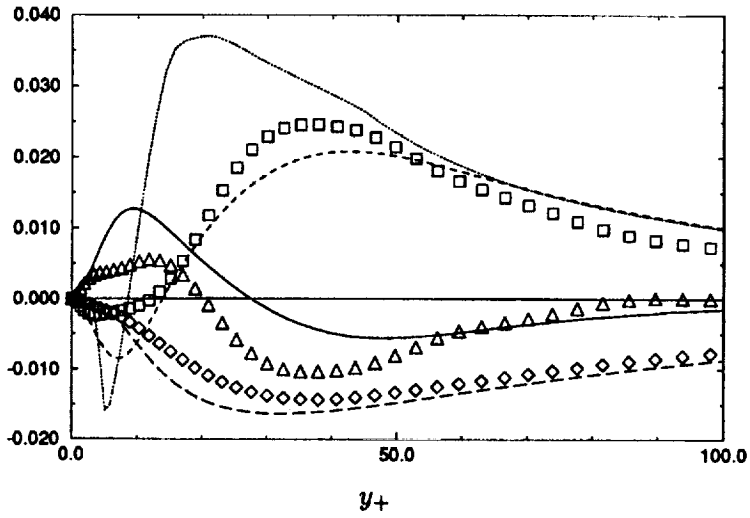

FIGURE 3. Balance terms of $\overline{u_2^2}$; lines, R-cubic model; symbols, DNS; ····· , $\wp_{22}^h$; ---- □ , $\wp_{22}$; —— △ , total diffusion; —·— ◇ , dissipation.

the cubic pressure-strain model of Craft & Launder (1991) is written as:

$$\begin{aligned}\phi_{ij}^{rapid} = &-0.6\mathrm{dev}\,(P_{ij}) + 0.3a_{ij}P_{kk} \\ &- 0.2(\frac{\overline{u_k u_j}\;\overline{u_l u_i}}{k}(\partial_l U_k + \partial_k U_l) - \frac{\overline{u_l u_k}}{k}(\overline{u_i u_k}\partial_l U_j + \overline{u_j u_k}\partial_l U_i)) \\ &- r(A_2(P_{ij} - D_{ij}) + 3a_{mi}a_{nj}(P_{mn} - D_{mn}))\end{aligned} \tag{12}$$

where: $D_{ij} = \overline{u_i u_k}\partial_j U_k - \overline{u_j u_k}\partial_i U_k$ and

$$\begin{aligned}\phi_{ij}^{slow} = &-(C_1 + 1)a_{ij}\varepsilon \\ &- C_1' C_1 \mathrm{dev}(a_{ik}a_{kj})\,\varepsilon\end{aligned} \tag{13}$$

Thus the R-cubic model is defined with the following expression for $\wp_{ij}^h$ on the RHS of (4):

$$\wp_{ij}^h = -C_1(a_{ij} + C_1'\mathrm{dev}(a_{ik}a_{kj}))\frac{k}{T} + \phi_{ij}^{rapid} \tag{14}$$

With the values:

$$C_1 = 3.1[A\min(A_2, 0.6)]^{1/2},\ C_1' = 1.2,\ r = 0.6$$

4. Low-Reynolds number channel flow

Figs. 1 & 2 show the Reynolds stresses compared to the DNS data at Re=395 (unpublished CTR simulation), as obtained by the relaxed cubic model and the relaxed IP model, respectively. The $\overline{u_3^2}$ component is slightly too close to the $\overline{u_2^2}$ component with the IP model. Both models predict a too steep decrease of $\overline{u_1^2}$ away from the wall.

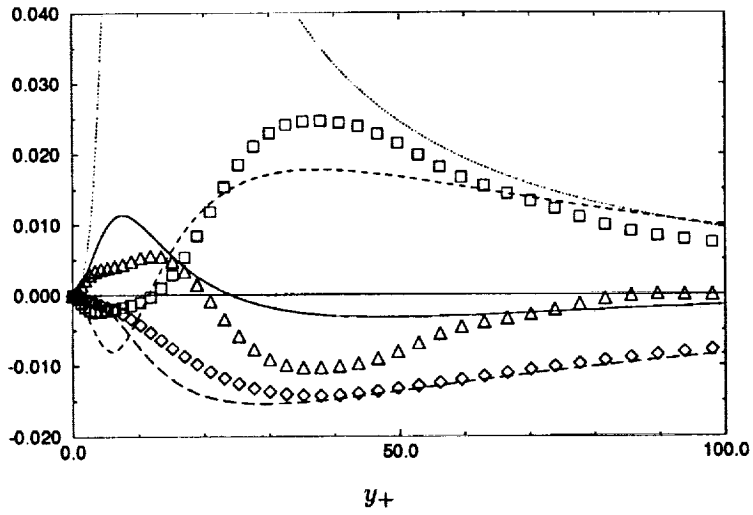

FIGURE 4. Balance terms of $\overline{u_2^2}$, R-linear model; captions as in Fig. 3.

The budgets of the normal stress $\overline{u_2^2}$ are given in Figs. 3 and 4 for the R-cubic and R-linear models respectively. The dotted lines are the source term φ_{ij}^h in Eq. 4; the dashed line is the solution to Eq. 4 and provides the relaxed pressure-strain that enters the solutions shown in Figs. 2 and 3. Note that by $y^+ \approx 80$, φ_{ij} has relaxed to φ_{ij}^h. Figs. 3 and 4 are plotted on the same scale to show that the relaxed pressure-strain terms are nearly identical even though the maximum of ϕ_{22} at $y^+ = 20$ in the homogeneous IP model is well out of range (0.11 in Fig. 4; i.e., 3 times that of the cubic model). This demonstrates that the solution to the relaxation equation has a large contribution coming through the boundary conditions. This blocking effect gives adequate near-wall behavior despite serious inaccuracies of the homogeneous model on the r.h.s of Eq. 4. The agreement with the balance terms obtained from DNS is satisfactory. For this comparison the DNS data were processed as in Eq. 1, in which T_{ij} and $\nu\nabla^2\overline{u_iu_j}$ are combined as total diffusion. Note that differences between the φ_{22} term and the corresponding DNS data are compensating for visible defects in the diffusion model, Eq. 10. Since the $\overline{u_2^2}$ profile was seen to be quite accurately predicted, the Daly Harlow model of turbulent diffusion needs to be revisited.

Previous experience with the standard Launder-Tselepidakis model exhibited difficulties in solving the $\overline{u_2^2}$ balance because the normal stress component goes to zero as y^4 at the wall, while its balance terms remain large. In the form of Eq. 1, pressure strain now balances most of the diffusion while the remaining dissipation is a small, numerically stabilizing term. As $y_+ \to 0$, the molecular diffusion balances the relaxed pressure-strain $\varphi_{22} \equiv kf_{22}$, both of them going to zero, which is precisely the boundary condition imposed on the coupled system $u_2^2 - f_{22}$.

A slightly less satisfactory agreement is obtained for the budget of $\overline{u_1u_2}$ shown in Fig. 5. The small overestimation of the normal stress seen in Fig. 1 results in

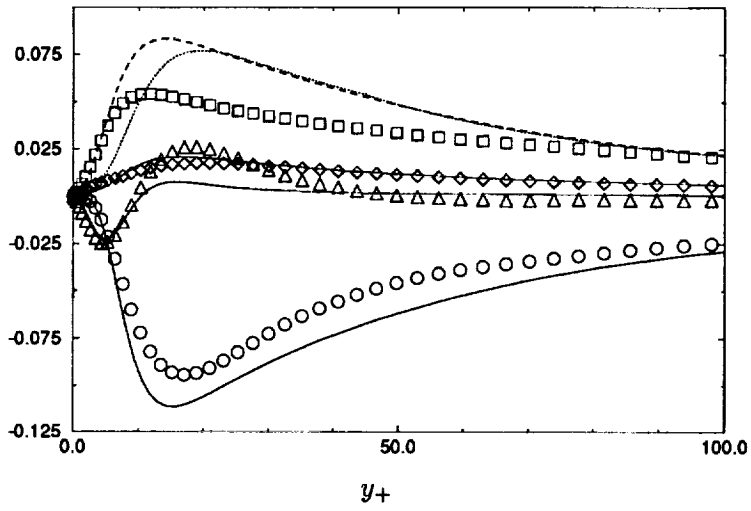

FIGURE 5. Balance terms of $\overline{u_1 u_2}$; lines, R-cubic model; symbols, DNS.; ——— o , production; ····· , $\wp_{12}^h$; ---- □ , $\wp_{12}$; ——— △ , total diffusion; ——— ◇ , dissipation.

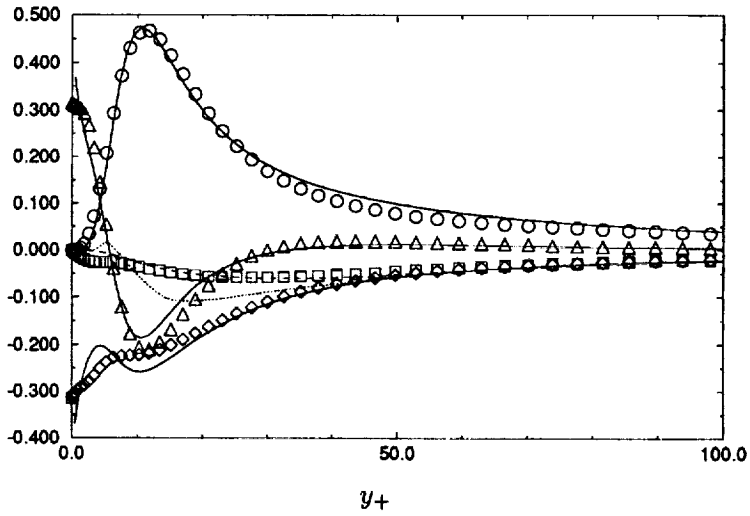

FIGURE 6. Balance terms of $\overline{u_1^2}$, R-cubic model; captions as Fig. 5.

a visible overprediction of the production in the near wall layer, compensated by a similar overprediction of the pressure-strain. Since the extent of agreement for the latter is quite different depending on which component is examined, further improvement could only be obtained by a tensorial correction whereas only global coefficient tuning was undertaken here.

Fig. 6 shows the balance of the streamwise stress $\overline{u_1^2}$. The production term becomes dominant and the pressure-strain is now a small part of the budget. The dissipation is quite well predicted. The ε model equation is only changed from its

standard high Re form by the use of T in place of k/ε (Durbin, 1993). The production of dissipation needs to be slightly increased very near the wall. Hanjalic & Launder (1976) introduced an extra production term, proportional to the second derivative of the mean velocity; but Rodi & Mansour (1990) showed that such a term was too strong below $y_+ = 10$. In the R-linear model production is enhanced by modifying the production constant $c_{\varepsilon 1}$ as:

$$c'_{\varepsilon_1} = c_{\varepsilon_1} + a_1 \frac{P}{\varepsilon} \tag{15}$$

with $a_1 \approx 0.1$. The dissipation equation is then:

$$D_t\varepsilon = \frac{c'_{\varepsilon_1} \frac{1}{2} P_{kk} - c_{\varepsilon 2}\varepsilon}{T} + \partial_k \left((\nu + \frac{C_\mu \overline{u_k u_l} T}{\sigma_\varepsilon}) \partial_l \varepsilon \right) \tag{16}$$

A dependence on A_2 was added in the present R-cubic model to make sure the modification would have no effect on free shear flows, since A_2 only attains values near unity in the buffer layer where the turbulence becomes highly anisotropic:

$$c'_{\varepsilon_1} = c_{\varepsilon_1}(1 + a_1 \min(A_2, 1)^2 \frac{P}{\varepsilon}) \tag{17}$$

The kink in ε_{11} near $y_+ = 10$ is exaggerated but again compensates for a defect in the diffusion model. Note that in (16) no damping function is needed before $c_{\varepsilon 2}$ since $\frac{\varepsilon^2}{k}$ has been replaced by $\frac{\varepsilon}{T}$ which is finite.

The distribution of the various structure parameters used throughout the paper are given in Fig. 7. The A_2 parameter becomes very large below $y_+ = 30$, characterizing nearly 2-D turbulence and providing a means of isolating the transition layer, whereas the ratio of production over dissipation reaches values of about 1.5, which can also be found in free shear flows. The Rotta constant C_1 from the Launder-Craft model goes to zero at the wall, indicating that one might need a smaller elliptic correction than the linear IP model. The difference $c_{\varepsilon 2} - c_{\varepsilon 1}$ which can be related to the von Karman constant is seen to be fairly constant in the log-layer.

We consider in Fig. 8 the split of ϕ_{22} into the slow part and the rapid part modeled by Eq. 12. The slow part (to which the quadratic component (s_2) makes a small contribution) is dominating the rapid part and is acting 'naturally' to reduce the isotropy. The rapid part is determined largely by the linear term (the first term on the r.h.s. of Eq. 12, which is referred to as r_1 in figure 8) since the second and third terms (r_2 and r_3) seem to cancel each other. However, the model does not reduce to the linear contributions to the slow and rapid part (s_1 and r_1) (which is just the IP model) because r_3 takes a positive ('natural') sign in the spanwise stress budget. Also, in the shear stress budget r_2 is now acting 'anti-naturally' and r_3 'naturally', as can be seen in Fig. 9.

Fig. 10 shows the velocity profile from the $Re_\tau = 395$ DNS and the Comte-Bellot (1965) experiment at $Re_\tau = 2420$ ($Re = 57,000$). The latter when matched with the standard log-law, $U^+ = 1/\kappa \log(y_+) + C$, gives an additive constant of C=7,

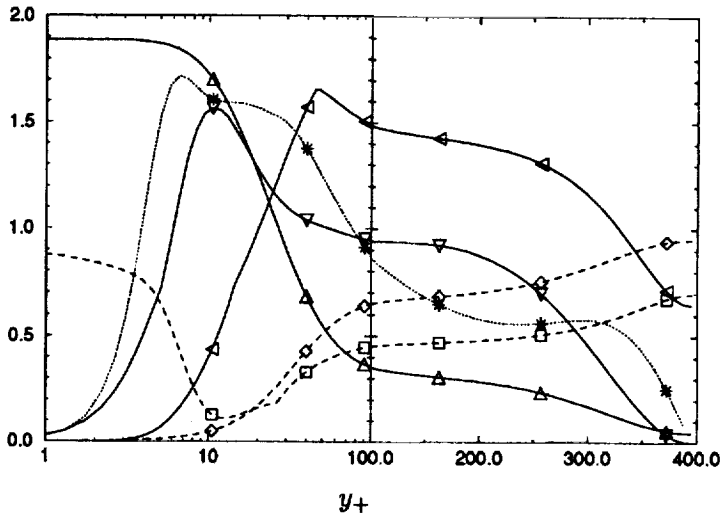

FIGURE 7. Structure parameters; see Eqs. 11 and 14. □ , $ce_2 - ce_1$; ◇, A; △ , A_2; ◁, C_1; ▽, P/ε; *, dl/dy.

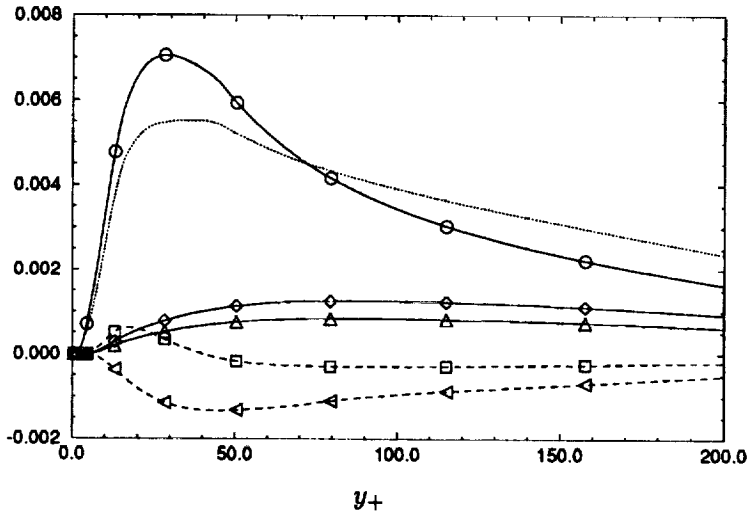

FIGURE 8. Split of ϕ_{22} in the cubic model. ○ , s_1; □ , s_2; ◇, r_1; △, r_2; ◁, r_3; ····· , total.

which is unusually high but will serve here to emphasize the effect of C_L in Eq. 9. Models are usually calibrated to yield C=5.5 and κ=.41 (dot-dashed line). The constant C is known to have a Reynolds dependence and is related to the Van Driest damping factor A^+; i.e., it depends on the rate at which the shear stress increases in the transition in the region $10 < y_+ < 30$, effectively accelerating the mean flow. This also introduces a pressure-gradient dependence.

With the R-cubic model described up to now, a best fit with the log-profile was

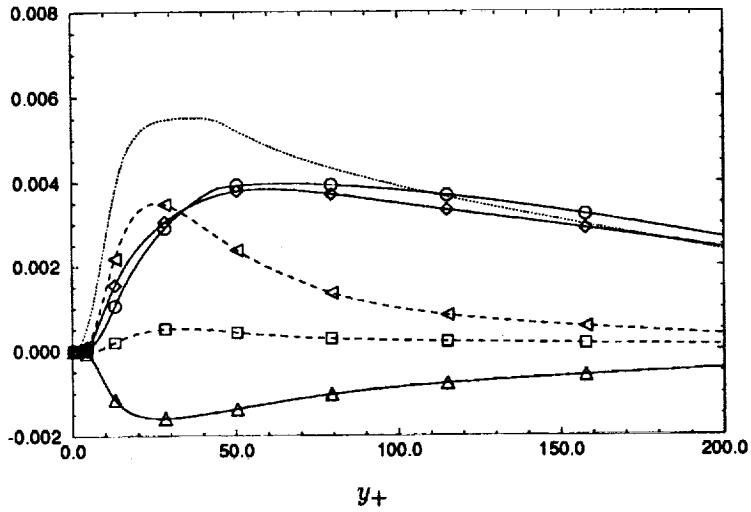

FIGURE 9. Split of ϕ_{12} in the cubic model. Symbols as in fig. 8.

obtained with $C_L = 0.25$. The homogeneous version of the cubic pressure-strain model yields an overestimation of the slope of the velocity profile. Thus Launder-Tselepidakis included a Gibson-Launder type of wall reflection (Eq. 24) to reduce the pressure-strain return to isotropy. Alternatively, they introduced an effective velocity gradient in the pressure strain model defined as:

$$\nabla U_i{}^{eff} = \nabla U_i + c^{eff} l(\nabla l \cdot \nabla)\nabla(U_i)\,, \quad l = \frac{k^{1/2}\overline{u_n u_n}}{\varepsilon} \tag{18}$$

In the present 1-D problem, this is equivalent to:

$$\frac{\partial U}{\partial y}^{eff} = \frac{\partial U}{\partial y} + c^{eff}\, l \frac{\partial l}{\partial y}\frac{\partial^2 U}{\partial y^2} \tag{19}$$

Or, since $\phi_{ij,r}$ is linear in the mean shear:

$$\phi^{eff}_{ij,r} = \phi_{ij,r} + c^{eff}\, l \frac{\partial l}{\partial y}\frac{\partial \phi^r_{ij}}{\partial y} \tag{20}$$

In the log-layer ϕ behaves as y^{-1} so the effect is to reduce ϕ_{ij} by a factor which can be estimated using standard log-law assumptions as about 40%.

Note that this non-local effect could be incorporated in the relaxation operator by replacing $kL^2\nabla^2\frac{\varphi_{ij}}{k}$ in (4) by:

$$\nabla\cdot(L^2\nabla\frac{\varphi_{ij}}{k}) = L^2\nabla^2\frac{\varphi_{ij}}{k} + 2L\nabla(L)\nabla\frac{\varphi_{ij}}{k} \tag{21}$$

In the log region, if we assume $\varphi_{ij} = \phi_{ij}$, and neglect the effect of variations of k, the first term on the RHS has the same sign as φ_{ij} thus increasing the return to

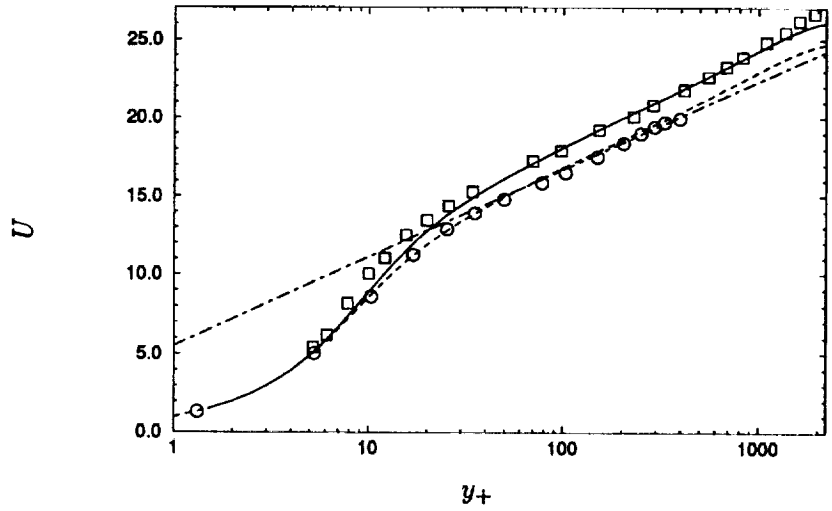

FIGURE 10. Velocity profiles, R-cubic model. ---- , $c_1^{eff} = 0.12$, $c_2^{eff} = 0.1$, cl = 0.15; ——— , c1eff = 0.12, c2eff =0.1, cl = 0.22; —·— , $U^+ = 1/\kappa \log(y_+) + C$; o , DNS; □ , Comte-Bellot

isotropy (observed if Fig. 4 is plotted for $y_+ > 100$) while the second term actually reduces the return to isotropy, which is the effect sought by using wall echo terms.

This interesting idea, which avoids any explicit reference to the distance to the wall, was for the time being retained in a simpler version as follows:

$$\phi_{ij,r}^{eff} = \left(1. - \min\left[c_2^{eff}\left(\frac{\partial l}{\partial y}\right)^2, .3\right]\right)\phi_{ij,r} \tag{22}$$

and

$$\phi_{ij,s}^{eff} = \left(1. - \min\left[c_1^{eff}\left(\frac{\partial l}{\partial y}\right)^2, .3\right]\right)\phi_{ij,s} \tag{23}$$

The following combination:

$$c_1^{eff} = .12,\ c_2^{eff} = .1,\ C_L = .15$$

yielded the more satisfactory agreement, increasing U in the transition layer and slightly decreasing the slope of U further away from the wall in better agreement with the log-law as shown by the dashed curve in Fig. 10. The solid line obtained with $c_1^{eff} = .12$, $c_2^{eff} = .1$, $C_L = .22$ shows that in the present form, the relaxation effect is limited to the transition layer, whereas in the R-linear model used without Eqs. 22, 23, it also strongly affects the log-layer (Fig. 11).

The final form of the model at this stage and for which the results were shown in Figs. 1-10 is thus the standard Craft-Launder model, with the elliptic relaxation and the modifications in Eq. 22 and the values:

c_{e_1}	c_{e_2}	c_μ	σ_ε	σ_k	C_L	C_η	a_1	c_1^{eff}	c_2^{eff}
1.	f(A,A_2)	.23	1.3	1.	.15	80.	.2	.12	.1

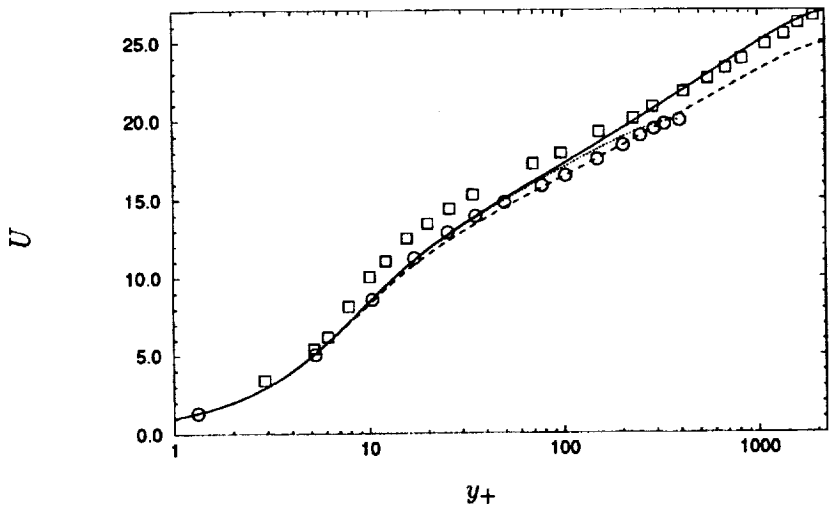

FIGURE 11. Mean velocity profiles, R-linear model. For captions see Fig. 10

while for the R-linear model used here the constants of Durbin (1993) were used:

c_{ε_1}	c_{ε_2}	C_μ	σ_ε	σ_k	C_L	C_η	a_1	C_1	C_2
1.44	1.9	.23	1.65	1.2	.2	80.	.1	1.22	0.6

Note that the pressure strain constant C_1 is lower than the standard value; this reduction could be avoided by using the gradient of the length scale as an inhomogeneity indicator. Also the following Gibson-Launder formulation,

$$\phi_{ij}^w = \phi_{kl} n_k n_l \delta_{ij} - 3/2 \phi_{ik} n_k n_j - 3/2 \phi_{jk} n_k n_i, \tag{24}$$

was not used with the Craft-Launder model since $\overline{u_2^2}$ is sufficiently suppressed by the rapid term of the cubic model.

At Re=395, Fig. 12 shows that the R-linear and R-cubic predictions are almost undistinguishable. The fact that all models known to the authors seem to underpredict the increase in velocity in the central part of the channel (the wake region) where they recover their homogeneous form is somewhat puzzling. The centerline velocity (and more importantly, the skin friction in boundary layers) seems to be recovered only at the expense of predicting a somewhat lower von Karman constant.

Considering the $\overline{u_1 u_2}$ balance equation, neglecting diffusion and dissipation,

$$0 = -\overline{u_2^2} \frac{\partial U}{\partial y} + \phi_{12}, \tag{25}$$

one sees that with $\overline{u_2^2}$ constant, the magnitude of the velocity gradient is allowed to increase (relative to y^{-1} in the log layer) only if the pressure strain decreases less than y^{-1}. This is indeed the behavior of exhibited by the DNS data (Fig. 13)

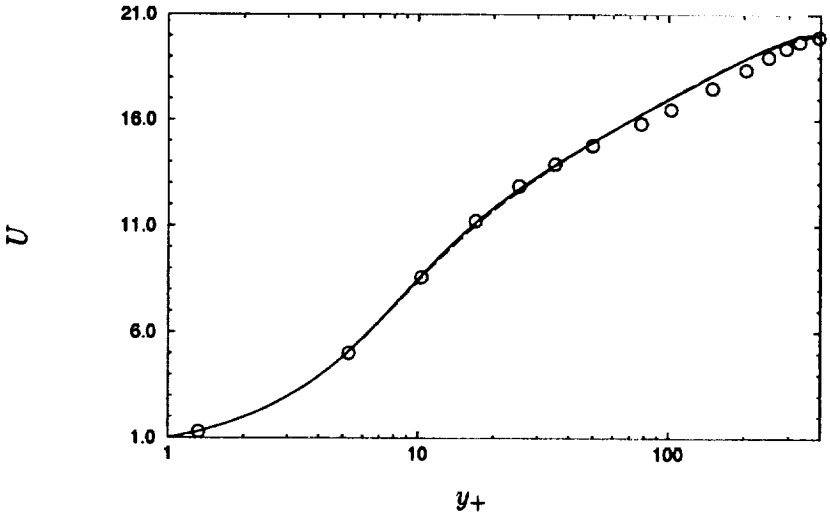

FIGURE 12. Velocity at Re=395: ——— , R-cubic; ---- , R-linear. For captions see Fig. 10.

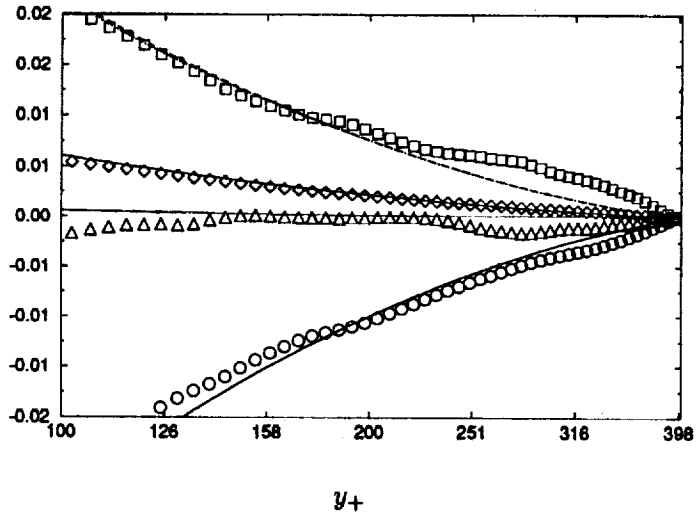

FIGURE 13. Budget of terms in the $\overline{u^2}$ equation near channel centerline, captions as Fig. 4.

and seems to be ignored by the models. In fact the relative increase of the pressure strain exceeds that of the production and is balanced by pressure diffusion. A similar behavior was found for all Reynolds-stress budgets.

With the present gradient transport assumption, a zero value is predicted for the total diffusion (pressure + turbulent) since $\overline{u_1 u_2}$ is linear, but non-zero pressure diffusion might be accounted for by the non-local formulation investigated by Demuren *et al.* in the present volume.

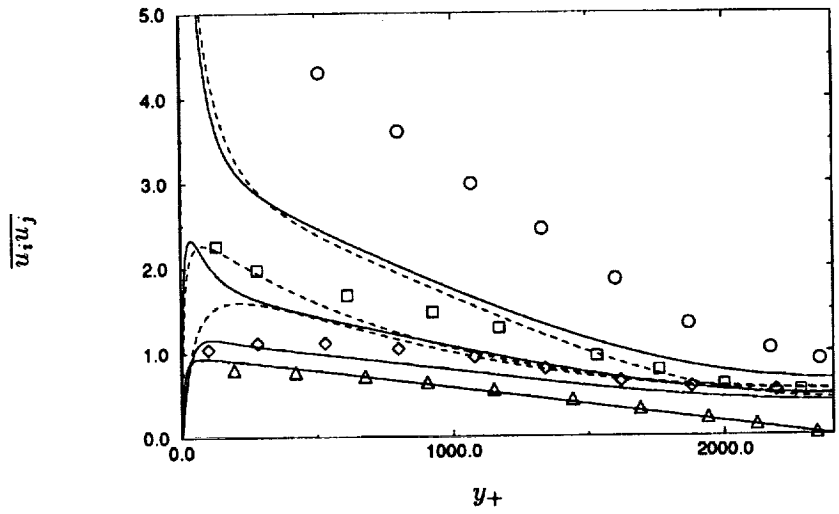

FIGURE 14. Reynolds stresses for the channel flow at Re=57,000. ○ , $\overline{u_1^2}$; ◇ , $\overline{u_2^2}$; □ , $\overline{u_3^2}$; △ , $\overline{u_1u_2}$. ——— , R-cubic; ---- , R-linear.

Fig. 14 compares the Reynolds-stress distributions throughout the channel at high Reynolds number (Comte-Bellot experiment $Re = 57,000$). One major drawback is that $\overline{u_1^2}$ is severely underestimated. Experiments show an extension with Re of the plateau region of the stress maxima (Antonia *et al.*, 1992), whereas the models follow this trend more moderately. This is a generic problem since the standard high Re Gibson-Launder model with wall functions yields similar underestimations away from the wall. One sees, however, that the R-cubic model reproduces a better separation between normal and spanwise components than the R-linear model for which this separation is limited to the log layer.

5. Other calculations

The skin friction was computed for a zero pressure gradient, boundary layer. The R-cubic model overpredicts C_f, which is related to the difficulty in predicting the wake region in the centerline of channel flow that was observed previously (Fig. 10).

The R-cubic model was also tested on the flow over a backward facing step but without Eqs. 22-23 and yielded similar, if not less satisfactory, predictions in comparison to the R-linear model used by Ko & Durbin (1993).

Conclusion

The present study used the DNS results of a channel flow at $Re_\tau = 395$ to confirm that homogeneous, second moment closures can be quite easily made to comply with near-wall turbulence characteristics by applying the elliptic relaxation procedure of Durbin (1993). Physically, it models the blocking effect that the wall imposes on the the fluctuating pressure, thus alleviating the need for Re dependent 'damping functions'.

It was found that the standard relaxation model produces a reduction of 'return to isotropy' in the near wall layer ($y_+ < 80$). This effect is essentially due to the boundary conditions. In this region, the elliptic relaxation is so strong that the switch from a linear to a cubic pressure strain model had a nearly unnoticeable effect on the budgets of the stresses. After imposing the elliptic relaxation these budgets compare very well with the DNS data. An urgently needed improvement concerns the Daly-Harlow turbulent diffusion term which was not studied here.

Further away from the wall, it seems that the strong inhomogeneity of the log-layer has also a significant blocking effect, underestimated by the original elliptic relaxation combined with the simple IP second moment closure. Using the Craft & Launder model, the wall normal stress was better reproduced, but still insufficiently to avoid further inhomogeneity corrections. This is the reason that the Gibson & Launder 'wall echo' model was still required at significant distances from the wall. In the latter, reference to the distance to the wall can be avoided by using the gradient of the turbulence length scale as suggested by Launder & Tselepidakis, and which could be included along with elliptic relaxation.

Outside the log-layer, the DNS data show a significant change in the behavior of the pressure strain terms, which explains the increase of the velocity gradient, but is not reproduced by the models. The latter seem to compensate for this omission by overpredicting the slope in the log-layer. Near wall models are usually compared to DNS data at low Re, but for practical applications more attention should be given to higher Re flows, with the challenging feature that the profiles of the stresses show a strong Re dependence (i.e., they do not collapse on plots scaled in wall units). In particular the streamwise stress is severely underpredicted at high Re.

REFERENCES

ANTONIA, R. A., TEITEL, M., KIM, J., & BROWNE, L. W. B. 1992 Low-Reynolds-number effects in a fully developed turbulent channel flow. *J. Fluid Mech.* **236,** 579-605.

COMTE-BELLOT, G. 1965 Ecoulement turbulent entre deux parois paralleles. *Pub. Scien. et Tech. du ministere de l'air.*

CRAFT, T. J., LAUNDER, B. E. 1991 Computation of impinging flows using second moment closures. *8th. Symp. on Turbulent Shear Flows, T. U. Munich.* 8-5.

DURBIN, P. 1991 Near wall second moment closures without 'damping functions'. *Theoret. Comp. Fluid Dyn.* **159,** 105.

DURBIN, P. 1993 A Reynolds-stress model for near-wall turbulence . *J. Fluid Mech.* **249,** 465-498.

GIBSON, M. M., & LAUNDER, B. E. 1978 Ground effects on pressure fluctuations in the atmospheric boundary layer. *J. Fluid Mech.* **86,** 491-511.

KO S., & DURBIN, P. 1993 Application of a near-wall turbulence model to adverse pressure gradient and separating boundary layers. *Proc. Int. Conf. on Near-Wall Turbulent Flows.* 145-154.

LAUNDER, B. E., REECE, G. J., & RODI, W. 1975 Progress in the development of a Reynolds-stress closure. *J. Fluid Mech.* **68,** 537-566.

LAUNDER, B. E., TSELEPDAKIS, D. P. 1991 Progress and Paradoxes in Modeling Near-Wall Turbulence. *8th. Symp. on Turbulent Shear Flows, T. U. Munich.* 29-15.

LAURENCE, D., MAUPU, V., GALLAND, J. C., & TEISSON, C. 1993 A sediment laden open channel flow simulation with recent Reynolds-stress-flux transport models. *Eng. Turb. Model. and Exp* Rodi, Martelli Eds., Elsevier. 73-82.

LEE, M. J., KIM, J., & MOIN, P. 1990 Structure of turbulence at high shear rate. *J. Fluid Mech.* **216,** 561-498.

MANSOUR, N. N., KIM, J., & MOIN, P. 1988 Reynolds-Stress and Dissipation-rate budgets in a turbulent channel flow. *J. Fluid Mech.* **194,** 15-44.

RODI, W., & MANSOUR, N. N. 1990 One equation near-wall turbulence modeling with the aid of direct simulation data. *Proc. 1990 Summer Program.* Center for Turbulence Research, NASA Ames/Stanford Univ. 107-124.

SO, R. M. C., LAI, Y. G., ZHANG H. S., & HWANG B. C. 1991 Second order near-wall turbulence closures: a review. *AIAA J.* **29-11,** 1819-1835

Center for Turbulence Research
Proceedings of the Summer Program 1994

N95-21055

Modeling the two-point correlation of the vector stream function

By M. Oberlack[1], M. M. Rogers[2] AND W. C. Reynolds[3]

A new model for the two-point vector stream function correlation has been developed using tensor invariant arguments and evaluated by the comparison of model predictions with DNS data for incompressible homogeneous turbulent shear flow. This two-point vector stream function model correlation can then be used to calculate the two-point velocity correlation function and other quantities useful in turbulence modeling. The model assumes that the two-point vector stream function correlation can be written in terms of the separation vector and a new tensor function that depends only on the magnitude of the separation vector. The model has a single free model coefficient, which has been chosen by comparison with the DNS data. The relative error of the model predictions of the two-point vector stream function correlation is only a few percent for a broad range of the model coefficient. Predictions of the derivatives of this correlation, which are of interest in turbulence modeling, may not be this accurate.

1. Introduction

In one-point modeling for second-moment closure, four different terms are unknown: the pressure-strain term Φ_{ij}, the dissipation term ε_{ij}, the pressure diffusion term ${}^{p}D_{ij}$, and the turbulent diffusion term ${}^{t}D_{ij}$. A large amount of information that is needed for closure is contained in the two-point correlation tensor R_{ij}. Given a model for R_{ij}, one can express the Reynolds stress tensor, the dissipation tensor, and the rapid part of the pressure-strain tensor as functions of R_{ij}:

$$\overline{u_i' u_j'} = R_{ij}(\vec{x}, \vec{r} = 0)\,, \tag{1}$$

$$\varepsilon_{ij} = \lim_{\vec{r}\to 0} \nu \left[\frac{\partial^2 R_{ij}}{\partial x_k \partial r_k} - \frac{\partial^2 R_{ij}}{\partial r_k \partial r_k} \right]\,, \tag{2}$$

$$\Phi_{ij}^{rapid} = \frac{1}{2\pi} \int_V \frac{\partial \bar{u}_k}{\partial x_l}(\vec{x} + \vec{r}) \left(\frac{\partial^2 R_{il}}{\partial x_j \partial r_k} - \frac{\partial^2 R_{il}}{\partial r_j \partial r_k} \right) \frac{d^3 r}{|\vec{r}|} + (i \leftrightarrow j)\,, \tag{3}$$

where $(i \leftrightarrow j)$ in Eq. (3) indicates the addition of the previous term with interchanged indices i and j. R_{ij} also provides turbulence length-scale information, including the integral length scale and the Taylor microscale.

1 Inst. für Technische Mechanik, RWTH-Aachen, Germany
2 NASA Ames Research Center
3 Center for Turbulence Research

For engineering applications it is impractical to solve the two-point correlation equation to get the required one-point information. The approach should be to extract information from the two-point correlation tensor and the two-point correlation equation in order to improve one-point models. A first step was provided by the two-point correlation equation for isotropic turbulence developed by von Kármán & Howarth (1939), which gave early insight into the decay of isotropic turbulence and the development of turbulence length scales. This isotropic tensor form was used by Crow (1969) to derive an exact expression for the rapid pressure-strain-rate correlation in isotropic turbulence. A crucial further step was taken by Naot *et al.* (1973), who extended the two-point correlation model for R_{ij}, which led to the linear rapid pressure-strain model utilized in the well known Launder, Reece and Rodi (1975) second-moment-closure model.

One-point turbulence models require some sort of length-scale equation. The first complete Reynolds stress model was developed by Rotta (1951a,b) in combination with a scalar integral length-scale equation. He developed the length-scale transport equation by introducing an integral operator to the trace of the two-point correlation equation. Wolfshtein (1970) has developed a similar equation. Neither Rotta or Wolfshtein introduced a model for the two-point correlation R_{ij}, but they did model all the sink, source, and diffusion terms on the right hand side of the length-scale equation empirically.

A completely different procedure was introduced by Donaldson and co-workers (Sandri (1977, 1978), Sandri & Cerasoli (1981), Donaldson & Sandri (1981)), who developed a new tensor length-scale equation. They approximated the correlation function R_{ij} as a delta peak at zero separation and applied an integral operator to the transport equation for R_{ij}. This crude assumption leads to the elimination of some important terms in the tensor length-scale equation. In addition, they introduced models for some terms where exact terms can be derived.

Recently Oberlack (1994a,b) developed a new tensor length-scale equation. In his approach he has introduced a new model for the two-point correlation equation on the basis of tensor invariant theory. With this new approach the linear part of the rapid pressure-strain model could also be rederived.

The objective of this paper is twofold. First, the model introduced by Oberlack (1994a) in terms of a tensor potential will be recast in terms of the two-point correlation of the vector stream function and generalized to facilitate comparison with the DNS results. Second, the basic model assumption made by Oberlack will be evaluated by comparing the model for the two-point vector stream function correlation with DNS data of a homogeneous shear flow calculated from Rogers *et al.* (1986).

Section 2 gives an introduction to the vector stream function and discusses the non-unique behavior resulting from its definition, and then gives the definition of the basic two-point variables in correlation space and the relationship between them. Section 3 focuses on the derivation of the two-point vector stream function correlation model. A procedure to compare the model with the DNS data is outlined, and the reduction to a one parameter family of model equations is explained. Section 4

presents the results. There we introduce a new scalar measure that quantifies the difference between the DNS data and the model predictions. This quantity is used in determining the single model parameter γ.

2. Definition of the vector stream function

The new model for the two-point velocity correlation function introduced by Oberlack (1994a,b) had to be redefined for comparison with the DNS data of Rogers *et al.* (1986). For this purpose it is helpful to start with the vector stream function formulation.

The turbulent fluctuation velocity u_i' can be expressed as the curl of the vector stream function fluctuation ψ_i' (Aris 1962),

$$u_i' = \epsilon_{ijk} \frac{\partial \psi_k'}{\partial x_j} , \tag{4}$$

where ϵ_{ijk} is the alternating tensor.

Obviously any given ψ_i' determines u_i' uniquely, but not vice versa because any curl-free vector field ψ_i^* can be added to ψ_i' without changing the velocity vector u_i'. Thus, Eq. (4) does not define a unique ψ_i', and an additional condition is required. Taking the curl of Eq. (4), we get the Poisson-like equation

$$\omega_i' = \frac{\partial^2 \psi_k'}{\partial x_i \partial x_k} - \frac{\partial^2 \psi_i'}{\partial x_k \partial x_k} , \tag{5}$$

where ω_i' is the turbulent vorticity fluctuation given by

$$\omega_i' = \epsilon_{ijk} \frac{\partial u_k'}{\partial x_j} . \tag{6}$$

Eq. (5) is fundamentally different from the standard Poisson equation, a fact that is easily seen in wavespace where the derivatives in (5) are replaced by multiplication by wavenumber components. In wavespace, the Poisson equation is a regular linear algebraic equation with a unique solution for ψ_i', whereas (5) is a singular linear algebraic system that requires the specification of an additional constraint to determine ψ_i'. To define a well-posed problem, it is necessary to introduce an additional restriction on ψ_i' as noted above.

A numerically very useful and often used condition on ψ_i' is that it be solenoidal

$$\frac{\partial \psi_i'}{\partial x_i} = 0 . \tag{7}$$

By using (7), Eq. (5) reduces to the usual Poisson equation

$$\omega_i' = -\frac{\partial^2 \psi_i'}{\partial x_k \partial x_k} . \tag{8}$$

Eq. (8) has been used to determine the vector stream function from the DNS data. However, this implicit use of (7) makes it necessary to reformulate the model of the tensor potential given by Oberlack (1994a).

All the two-point correlations functions below follow the definitions of Oberlack (1994a,b). We introduce the spatial vectors $\vec{x}$ and $\vec{x}^{(1)}$ and define the correlation-space vector as

$$\vec{r} = \vec{x}^{(1)} - \vec{x} \,. \tag{9}$$

In general, the two-point correlation functions depend on the physical and the correlation space coordinates $\vec{x}$ and $\vec{r}$ and on the time t.

The tensor potential V_{mn} introduced by Oberlack (1994a) can be expressed in terms of the two-point correlation of the vector stream function fluctuation

$$V_{mn}(\vec{x},\vec{r},t) = \overline{\psi'_m(\vec{x},t)\psi'_n(\vec{x}^{(1)},t)} \,. \tag{10}$$

V_{mn} contains important length-scale information of the turbulence and can be directly linked to the two-point velocity correlation function

$$R_{ij}(\vec{x},\vec{r},t) = \overline{u'_i(\vec{x},t)u'_j(\vec{x}^{(1)},t)} \,. \tag{11}$$

R_{ij} is the basic quantity in two-point modeling. The link between V_{mn} and R_{ij} can be found using Eq. (4) and the definition of the correlation space $\vec{r}$ given in Eq. (9),

$$R_{ij} = e_{ikm}\, e_{jln} \left[\frac{\partial}{\partial x_k} - \frac{\partial}{\partial r_k} \right] \frac{\partial V_{mn}}{\partial r_l} \,. \tag{12}$$

The tensor potential V_{mn} was originally introduced to form an R_{ij} that would automatically satisfy the two equations

$$\frac{\partial R_{ij}}{\partial x_i} - \frac{\partial R_{ij}}{\partial r_i} = 0 \quad \text{and} \quad \frac{\partial R_{ij}}{\partial r_j} = 0 \tag{13}$$

emerging from the continuity condition for the turbulent velocity fluctuation u'_i. The constraint for the vector stream function ψ'_i in Eq. (7) imposes two additional restrictions on the two-point vector stream function correlation

$$\frac{\partial V_{ij}}{\partial x_i} - \frac{\partial V_{ij}}{\partial r_i} = 0 \quad \text{and} \quad \frac{\partial V_{ij}}{\partial r_j} = 0 \,. \tag{14}$$

Oberlack (1994a,b) did not express V_{mn} in terms of ψ'_i, and hence the constraints (14) were not implemented. It can be shown that he used an implicit constraint on the two-point vector stream function, but this is not computationally useful.

An important consequence of introducing (7) is that it becomes necessary to reformulate the model for the two-point vector stream function correlation because the model of Oberlack is not able to satisfy (14). The derivation of the generalized model is described in the next section.

3. Derivation of the two-point vector stream function correlation model

The ideas used here to model the two-point vector stream function correlation are similar to those introduced by Oberlack (1994a), but additional terms have been introduced to generalize the formulation. Here only homogeneous flows in infinite domains are considered, hence statistical quantities are independent of spatial location and all the spatial derivatives $\frac{\partial}{\partial x_i}$ in Eqs. (12), (13), and (14) vanish.

We seek to model the two-point vector stream function correlation V_{mn} in terms of a new tensor function G_{mn} and the separation vector $\vec{r}$. The components of G_{mn} are all assumed to be functions only of the magnitude of the separation distance $r = |\vec{r}|$ and time t,

$$G_{mn} = G_{mn}(r,t)\,. \tag{15}$$

Because of the assumption (15), the tensor G_{mn} has no angular variation in correlation space; the value of each component is constant on spherical shells in $\vec{r}$-space. For simplicity, G_{mn} has also been assumed to be a symmetric tensor. Thus, for general homogeneous flows, G_{mn} is characterized by six independent functions of r and t. This is in contrast to isotropic turbulence, which is characterized by a single scalar function $f(r,t)$ (see Appendix).

The most general V_{mn} that is linear and non-differential in the tensor G_{mn} will involve the following terms:

$$G_{mn},\ \delta_{mn}G_{kk},\ \delta_{mn}\frac{r_k r_l}{r^2}G_{kl},\ \frac{r_m r_n}{r^2}G_{kk},\ \frac{r_m r_k}{r^2}G_{nk}+\frac{r_n r_k}{r^2}G_{mk},\ \frac{r_m r_n r_k r_l}{r^4}G_{kl}\,. \tag{16}$$

However, (14) can not be satisfied by an arbitrary linear combination of these forms. Therefore, we add an additional set where G_{mn} is replaced by

$$G_{mn} \to r\frac{\partial G_{mn}}{\partial r}\,. \tag{17}$$

The resulting generalized form of the model is then

$$\begin{aligned}
V_{mn} - V_{mn}^{(0)} = {} & \alpha_1 G_{mn} + \beta_1 r\frac{\partial G_{mn}}{\partial r} \\
& + \alpha_2 \delta_{mn}G_{kk} + \beta_2 \delta_{mn} r\frac{\partial G_{kk}}{\partial r} \\
& + \alpha_3 \delta_{mn}\frac{r_k r_l}{r^2}G_{kl} + \beta_3\delta_{mn}\frac{r_k r_l}{r^2}r\frac{\partial G_{kl}}{\partial r} \\
& + \alpha_4 \frac{r_m r_n}{r^2}G_{kk} + \beta_4\frac{r_m r_n}{r^2}r\frac{\partial G_{kk}}{\partial r} \\
& + \alpha_5\left[\frac{r_m r_k}{r^2}G_{nk} + \frac{r_n r_k}{r^2}G_{mk}\right] + \beta_5\left[\frac{r_m r_k}{r^2}r\frac{\partial G_{nk}}{\partial r} + \frac{r_n r_k}{r^2}r\frac{\partial G_{mk}}{\partial r}\right] \\
& + \alpha_6\frac{r_m r_n r_k r_l}{r^4}G_{kl} + \beta_6\frac{r_m r_n r_k r_l}{r^4}r\frac{\partial G_{kl}}{\partial r}\,.
\end{aligned} \tag{18}$$

The coefficients α_i and β_i are assumed to be constants for any given field. The tensor $V_{mn}^{(0)}$ contains the value of V_{mn} at $r = 0$ and has to be introduced to avoid a singularity at the origin. It does not contribute to R_{ij} or other quantities of interest derived from the model because $\frac{\partial}{\partial r_i} V_{mn}^{(0)} = 0$. Throughout the rest of this paper, we have absorbed $V_{mn}^{(0)}$ into V_{mn} so all elements of V_{mn} drop to zero at $r = 0$ (*i.e.*, we consider the quantities $V_{mn} - V_{mn}^{(0)}$).

From its definition, V_{mn} is Hermitian in homogeneous turbulence; that is $V_{mn}(\vec{r}) = V_{nm}(-\vec{r})$. The model Eq. (18) is more limited and predicts that V_{mn} is symmetric since G_{mn} has been assumed to be symmetric.

Because the tensors V_{mn} and G_{mn} are symmetric, only one condition in (14) has to be satisfied. Substituting the model (18) into (14) results in an equation containing nine independent vectors. The nine coefficients of these vectors are linear functions of α_i and β_i and are set to zero to satisfy (14). This ensures that the model two-point vector stream function correlation V_{mn} is consistent with the assumption of a solenoidal vector stream function.

We thus have 9 equations for the 12 coefficients α_i and β_i. Without any loss of generality, we have chosen α_5, β_4, and β_5 to be the independent coefficients and have solved the equations to express the remaining nine coefficients as linear functions of these three parameters. The solution yields

$$\alpha_1 = -\frac{1}{2}\alpha_5 - \beta_5 \ , \ \alpha_2 = \frac{1}{2}\alpha_5 - 2\beta_4 - \beta_5, \ \alpha_3 = -\frac{3}{2}\alpha_5, \ \alpha_4 = -\frac{1}{2}\alpha_5,$$
$$\alpha_6 = -\frac{1}{2}\alpha_5, \ \beta_1 = -\beta_5, \ \beta_2 = -\beta_4, \ \beta_3 = -\frac{1}{4}\alpha_5 - \beta_5, \quad \text{and} \quad \beta_6 = \frac{1}{4}\alpha_5 \ . \tag{19}$$

At this point, the DNS data of Rogers *et al.* (1986) can be used to optimize the choice of the model constants α_5, β_4, and β_5. From the DNS data, V_{mn} can be calculated directly, but we also need a procedure for evaluating the six independent functions G_{mn} in order to assess the quality of the model.

Eq. (18) consists of a coupled set of ordinary differential equations for G_{mn}. (Note that in previous formulations of the model that did not have the $r\frac{\partial G_{mn}}{\partial r}$ terms, G_{mn} could be obtained by solving a system of six linear algebraic equations.) The model does not specify the functional dependence of G_{mn} on r, and the DNS data must be used to evaluate these functions.

We have done this by equating the spherical-shell-averaged V_{mn}, computed from the DNS data, with the spherical-shell-averaged V_{mn} predicted by the model using (18). Applying the definition of spherical-shell averaging given by

$$\overline{V}_{mn} = \frac{1}{4\pi}\int_{\Omega} V_{mn} d\Omega' = \frac{1}{4\pi}\int_0^{2\pi}\int_0^{\pi} V_{mn}\sin(\theta) d\theta d\phi \tag{20}$$

to the model expression in Eq. (18) with the constants defined in (19) yields

$$\overline{V}_{mn} = \left(\frac{1}{30}\alpha_5 - \frac{1}{3}\beta_5\right)\left(3G_{mn} + r\frac{\partial G_{mn}}{\partial r}\right) + \left(-\frac{1}{15}\alpha_5 - \frac{2}{3}\beta_4 - \frac{1}{3}\beta_5\right)\delta_{mn}\left(3G_{kk} + r\frac{\partial G_{kk}}{\partial r}\right) . \tag{21}$$

This coupled system of ordinary differential equations can be solved by splitting G_{mn} into its trace G_{kk} and its anisotropic part $g_{mn} = G_{mn}/G_{kk} - \delta_{mn}/3$. This decomposition decouples the differential equations for G_{kk} and those for each element of g_{mn}. Solution of these uncoupled equations then results in the determination of $G_{mn}(r)$ in terms of the spherical-shell-averaged $\overline{V}_{mn}$

$$G_{mn} = \frac{A_1}{r^3}\int_0^r \overline{V}_{mn} r'^2 dr' + \frac{A_2}{r^3}\frac{\delta_{mn}}{3}\int_0^r \overline{V}_{kk} r'^2 dr' , \tag{22}$$

where

$$A_1 = \frac{30}{\alpha_5 - 10\beta_5} \quad \text{and} \quad A_2 = \frac{-6}{\alpha_5 + 12\beta_4 + 8\beta_5} - \frac{30}{\alpha_5 - 10\beta_5} . \tag{23}$$

All the integration constants have been set to zero to eliminate a singularity at $r = 0$.

For a given set of α_5, β_4, and β_5, the functions G_{mn} can be computed from the spherical-shell-averaged $\overline{V}_{mn}$ obtained from the DNS data. At this point it is clear that the functions G_{mn} computed in this manner do not depend on all of α_5, β_4, and β_5, but only on the reduced parameter set (A_1, A_2).

To distinguish clearly between V_{mn} predicted by the model (using the functions G_{mn} computed from the DNS data as described above) and V_{mn} calculated from the DNS data, superscripts are used. The vector stream function two-point correlation calculated from the DNS data will be labeled as V_{mn}^{DNS}, and that predicted by the model will be termed V_{mn}^{model}. Substituting G_{mn} as determined from (22) into the model (18) and (19) results in the following model expression:

$$\begin{aligned} V_{mn}^{model} = \frac{3}{10\gamma - 1}\Big[& 10\gamma\overline{V}_{mn} - 5(4\gamma - 1)\mathcal{R}_{mn} \\ & - (5\gamma + 1)\delta_{mn}\overline{V}_{kk} + (15\gamma - 4)\delta_{mn}\mathcal{R}_{kk} \\ & + \frac{5}{2}(4\gamma + 1)\delta_{mn}\frac{r_k r_l}{r^2}\overline{V}_{kl} - \frac{15}{2}(4\gamma - 1)\delta_{mn}\frac{r_k r_l}{r^2}\mathcal{R}_{kl} \\ & + (5\gamma - 1)\frac{r_m r_n}{r^2}\overline{V}_{kk} - (15\gamma - 2)\frac{r_m r_n}{r^2}\mathcal{R}_{kk} \\ & - 10\gamma\left(\frac{r_m r_k}{r^2}\overline{V}_{nk} + \frac{r_n r_k}{r^2}\overline{V}_{mk}\right) + 10(3\gamma - 1)\left(\frac{r_m r_k}{r^2}\mathcal{R}_{nk} + \frac{r_n r_k}{r^2}\mathcal{R}_{mk}\right) \\ & - \frac{5}{2}\frac{r_m r_n r_k r_l}{r^4}\overline{V}_{kl} + \frac{25}{2}\frac{r_m r_n r_k r_l}{r^4}\mathcal{R}_{kl}\Big] , \end{aligned} \tag{24}$$

where

$$\mathcal{R}_{mn} = \frac{1}{r^3}\int_0^r \overline{V}_{mn} r'^2 dr' \quad \text{and} \quad \gamma = \frac{\beta_5}{\alpha_5}\,. \tag{25}$$

Note that the model (24) does not now depend on α_4 and that α_5 and β_5 only appear in the ratio γ. Thus the model has only *one* free parameter that remains to be chosen by comparison with DNS data!

In the next section we compare the values of V_{mn} computed directly from the DNS with those predicted by the model given by (24). This comparison is made for many values of γ and permits the determination of an optimum value of γ that results in the best agreement between the model predictions and the DNS data.

4. Results

As noted above, direct numerical simulations of incompressible homogeneous turbulent shear flow generated by Rogers *et al.* (1986) have been used both to optimize the choice of the model constant γ and to test the validity of the model assumptions by comparing model predictions with DNS results. In these numerical simulations, the streamwise mean velocity $\overline{U}$ varies linearly in the cross-stream (y) direction, with the constant and uniform mean shear rate being given by $S = \partial\overline{U}/\partial y$. In this work the *C128U* simulation has been used. This case evolves until a non-dimensional time of $St = 16$, beyond which the computational domain becomes too small to capture an adequate sample of large-scale energetic turbulent eddies.

Although fields at various times St have been examined, results presented here are for $St = 10$. Results at other times are qualitatively similar, but after this time the stream function (primarily from eddies of larger scale than the energy-containing eddies) begins to be limited by the computational domain size. The flow cannot be regarded as a developed shear flow before about $St = 8$.

As noted earlier, the model has been constrained to predict symmetric vector stream function two-point correlations V_{mn}. Therefore the DNS results have been symmetrized prior to being used for model development and evaluation (this results in only minor adjustments to the off-diagonal tensor components of V_{mn}).

The degree to which V_{mn}^{DNS} and V_{mn}^{model} are different is a measure of the quality of the model. A simple measure to quantify this difference is given by

$$p = \frac{\int_{\mathcal{V}} \left(V_{mn}^{model} - V_{mn}^{DNS}\right)^2 d^3r}{\int_{\mathcal{V}} \left(V_{mn}^{DNS}\right)^2 d^3r}\,, \tag{26}$$

where the integration domain $\mathcal{V}$ is restricted to a sphere of radius r_{max}, the largest radius that will fit into the computational domain ($r_{max} = min(L_x/2, L_y/2, L_z/2)$, where L_i is the computational domain size (periodicity length) in the i^{th} direction). Integration over larger separation distances is not possible because the data would be contaminated by periodic images in the computation. Note that each point in correlation space is weighted equally in the above definition. Alternative measures

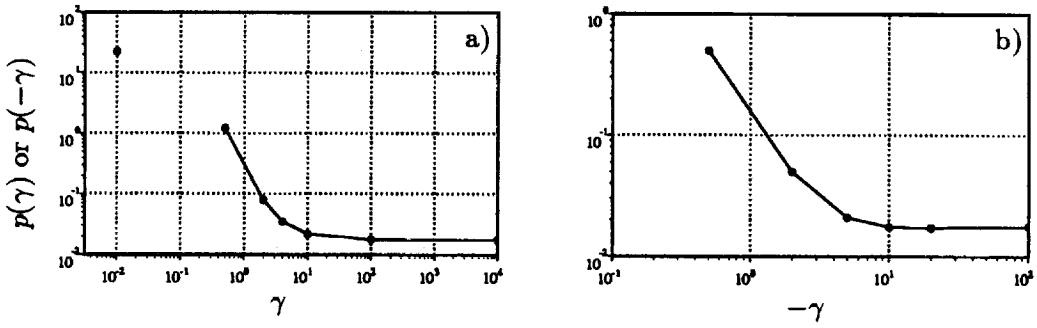

FIGURE 1. Dependence of the relative error p on the parameter γ for a) positive values of γ and b) negative values of γ. Note that there is a singularity at $\gamma = 0.1$.

that weight the data for smaller separation distances more heavily do not change the optimum value of the model constant γ significantly.

Fig. 1 illustrates the dependence of p on the model constant γ for both positive and negative values of γ. According to this measure, the model is equally good for both large positive and large negative values of γ, with a value of about 0.018. There is a singularity at $\gamma = 0.1$. Of the values of γ examined (indicated by solid circles in the figure), the lowest value of $p = 0.0172$ is achieved at $\gamma = -20$. However, there is a broad minimum with many other values of γ yielding values of p that are almost this low. Other considerations discussed below suggest an optimum value of $\gamma = -5$, with $p = 0.021$. Figs. 2 and 4 have been generated using this value of $\gamma = -5$.

The qualitative form of $p(\gamma)$ for the fields at $St = 8$ and $St = 12$ is similar to that shown in Fig. 1, although the value of p at the broad minimum is different. At $St = 8$, there is a minimum of $p = 0.0055$ at $\gamma = -20$; by $St = 12$, p increases to 0.060 at $\gamma = -20$. By $St = 12$ the computational domain is no longer sufficiently large to capture V_{33} and the increased value of p is therefore not surprising.

The functions G_{mn}, derived as outlined in §3, are shown in Fig. 2 for the *C128U* simulation at $St = 10$ using $\gamma = -5$ ($A_1 = 20/17$, $A_2 = -800/969$). Because $V_{mn}^{(0)}$ has been subtracted from the vector stream function two-point correlation to obtain $\overline{V}_{mn}$, $\overline{V}_{mn}$ starts at zero for $r = 0$ and approaches a constant value of $-V_{mn}^{(0)}$ for large separation distances where the correlation falls to zero. Using Eq. (22), it can be shown from this that G_{mn} is also zero for $r = 0$ and that the functions G_{mn} will also approach constant values as the separation distance r becomes large. From Fig. 2 it is clear that the tensor components G_{12} and G_{22} level off by $r = r_{max}$, whereas G_{11} and G_{33} do not. The off-diagonal components G_{13} and G_{23} are nearly zero compared to the other components (similar behavior is observed in the one-point correlations $\overline{u_1'u_3'}$ and $\overline{u_2'u_3'}$, which are also zero in homogeneous turbulent shear flow).

The measure p indicates what good choices for the model constant γ are, but it is also instructive to examine V_{mn}^{model} directly, and to compare it with V_{12}^{DNS}. Fig. 3 contains contour plots of the six independent V_{mn}^{DNS} components. All contour plots

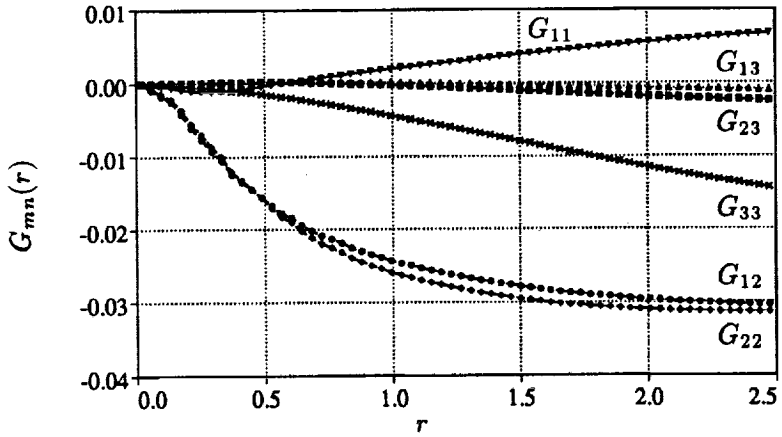

FIGURE 2. Functional dependence of G_{mn} on r for the *C128U* simulation at $St = 10$ and $\gamma = -5$ ($A_1 = 20/17$, $A_2 = -800/969$).

shown are in r_x-r_y-planes at $r_z = 0$. As a result of the mean shear, the contours are elongated in preferred directions. The "ridges" of the V_{11}^{DNS}, V_{12}^{DNS}, and V_{22}^{DNS} contours are inclined to the streamwise direction at an angle of somewhat less than 45°, as is often the case with many quantities in this flow. The V_{33}^{DNS} contours are qualitatively different, with the "ridge" running roughly orthogonal to that of the other components. Similar behavior is observed at other times St. The off-diagonal terms V_{13}^{DNS} and V_{23}^{DNS} are an order of magnitude smaller than the other terms and exhibit less organized structure; presumably they would be zero with an improved statistical sample of eddies. Examination of fields at earlier St lends credence to this suggestion. At earlier times the eddies are smaller, resulting in an increased sample and improved statistics. For these fields the V_{13}^{DNS} and V_{23}^{DNS} components are about two orders of magnitude smaller than the others and about the same magnitude as the level of the fluctuations for large r in the other components (unlike for the flow at $St = 10$, at earlier times the V_{mn}^{DNS} contours are confined to a much smaller region in the center of the computational domain).

Although the measure p is insensitive to the value of γ in the range $\gamma < -10$ and $\gamma > 10$, the orientation of the contour lines for V_{mn}^{model} varies significantly. The contours of V_{mn}^{model} for the *C128U* simulation at $St = 10$ for $\gamma = -5$ are illustrated in Fig. 4. The model predictions are limited to the interior of a sphere of radius r_{max}, because the functions G_{mn} cannot be determined from the DNS data for separations r greater than this as noted above. For this choice of γ, the contour ridge orientations of the various components are approximately the same as those of the V_{mn}^{DNS} shown in figure 3. The peak values and their decay in all directions are reasonably well represented within the radius considered. Beyond this radius, the DNS data show an increasing complexity of structures with additional secondary maxima that may be strongly influenced by the limited statistical sample of the computation and are not predicted by the model.

The orientation of the contour ridges for other values of γ is different. When γ is

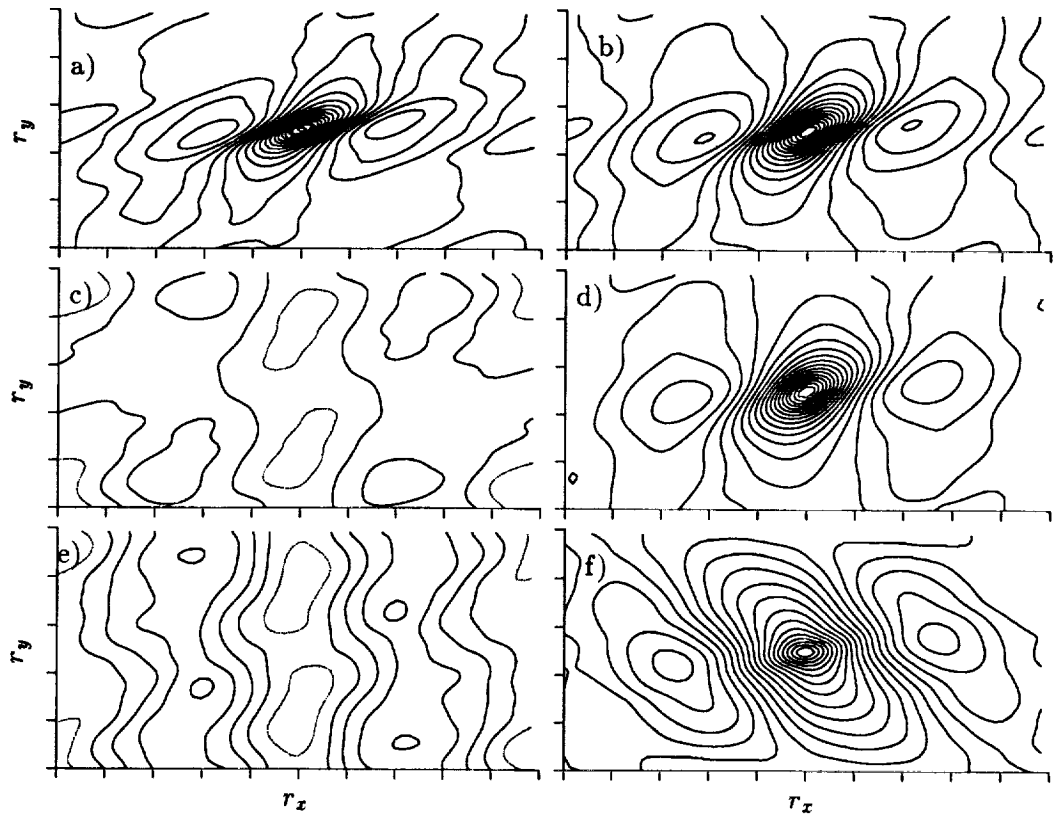

FIGURE 3. Iso-contours of a) V_{11}^{DNS}, b) V_{12}^{DNS}, c) V_{13}^{DNS}, d) V_{22}^{DNS}, e) V_{23}^{DNS}, and f) V_{33}^{DNS} for the *C128U* simulation at $St = 10$ in the r_x-r_y-plane at $r_z = 0$. Value at the center of the domain ($r_x = 0$ and $r_y = 0$) is zero, solid contours indicate negative contour levels, and dotted contours indicate positive contour levels. Contour increments are a) 0.004, b) 0.005, d) 0.010, f) 0.010, and contours levels in c) are -0.006, -0.002, and 0.002, and in e) are -0.014, -0.010, -0.006, -0.002, and 0.002.

decreased to larger negative values, the V_{11}^{model} and V_{22}^{model} contours become aligned with the coordinate directions, V_{11}^{model} being oriented in the streamwise direction and V_{22}^{model} being oriented vertically. The V_{12}^{model} and V_{33}^{model} contours do not change significantly.

The V_{mn}^{model} contours are the same for both large positive and large negative values of γ, but for smaller positive γ the orientation is different from that associated with negative γ. Again, the V_{12}^{model} and V_{33}^{model} components are relatively unaffected by changes in γ, but for $\gamma = 2$ the contour ridges of the V_{11}^{model} and V_{22}^{model} components are opposite those shown in Fig. 4, *i.e.* the V_{11}^{model} contours are inclined at a slightly negative angle to the streamwise direction rather than positive, and the V_{22}^{model} contours are inclined to the left of the vertical axis rather than to the right. For larger positive γ the coordinate axis-aligned contours associated with large γ are

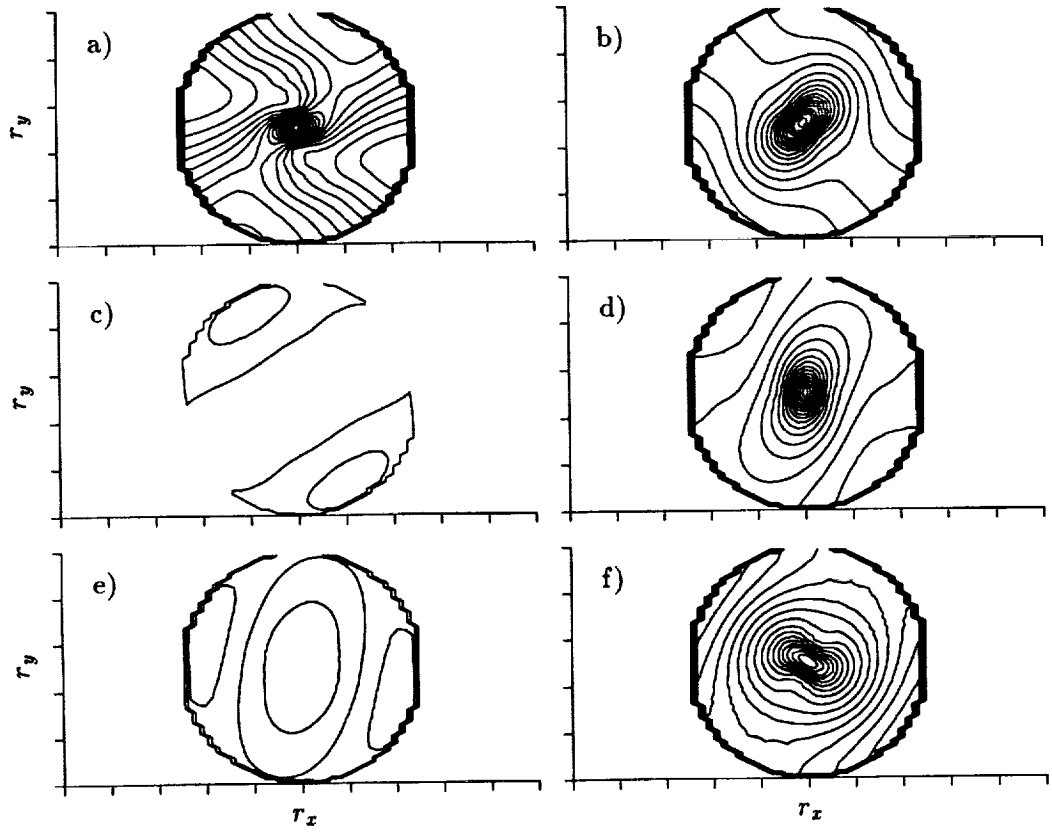

FIGURE 4. Iso-contours of a) V_{11}^{model}, b) V_{12}^{model}, c) V_{13}^{model}, d) V_{22}^{model}, e) V_{23}^{model}, and f) V_{33}^{model} for the *C128U* simulation at $St = 10$ in the r_x-r_y-plane at $r_z = 0$ for $\gamma = -5$. Value at the center of the domain ($r_x = 0$ and $r_y = 0$) is zero, solid contours indicate negative contour levels, and dotted contours indicate positive contour levels. Contour levels are the same as in Fig. 3.

rapidly approached.

It is thus apparent that negative values of γ should be chosen to best capture the contour orientation found in the DNS results. In this respect, this criterion leads to a similar conclusion as that based on the measure p (which reaches a minimum for negative γ). However, while the measure p suggests an optimum value of about $\gamma = -20$, matching the contour orientation would lead to a different choice of γ (smaller in magnitude). From Eq. (12) it is clear that to predict accurately the two-point velocity correlation function (and thus the Reynolds stresses) we need to be able to obtain accurate estimates of *derivatives* of V_{mn}. Simple agreement in the magnitude of V_{mn}, as measured by p, does not ensure good prediction of the Reynolds stresses. Since virtually all quantities of interest to be computed from the model require differentiation of V_{mn}^{model} to obtain, we felt that sacrificing a few tenths of a percent in p in order to get the contour orientation correctly would be

justified and have taken $\gamma = -5$ as the optimum model constant as noted above. Ideally one would like to optimize the choice of γ by comparing model predictions for the quantity of interest (*e.g.* Reynolds stress) directly with the DNS values of the same quantity. It is possible that in other flows the optimum value of γ would be different.

5. Conclusions

A new model for the two-point vector stream function correlation has been developed. The proposed model has been compared with DNS data for homogeneous turbulent shear flow. The model gives a relative error p of a few percent for a broad range of the single model parameter γ. A more limited range of γ also yields the correct orientation of the two-point vector stream function correlation contours. Any integral variables (like the integral length scale) calculated from the model are relatively insensitive to the parameter γ and should model the DNS data quite well. The model was developed for the purpose of modeling the two-point velocity correlation.

The results presented here suggest that the fundamental model assumption, namely that the two-point vector stream function correlation can be modeled in terms of the separation vector and a symmetric tensor G_{mn} whose components are only a function of the magnitude of the separation vector, is justified. However, if more directional information is needed and differentiation is applied to the model predictions, the resulting quantities may have some shortcomings. An example is the rapid part of the pressure-strain correlation, which can be calculated from the model but leads to the usual linear model with its known deficiencies.

Acknowledgements

Support was provided by the Institute für Technische Mechanik of Professor Peters at the RWTH Aachen. We would also like to thank Bob Rogallo, Claude Cambon, and Kyle Squires for helpful discussions.

Appendix

For homogeneous isotropic turbulence the tensor G_{mn} can be written in terms of a single function $G(r)$ as $G_{mn} = G(r)\delta_{mn}$. Substituting this into Eq. (18) and using (19) yields

$$V_{mn}^{model} - V_{mn}^{(0)} = \left(F(r) + \frac{r}{2}\frac{\partial F}{\partial r}\right)\delta_{mn} - \frac{r_m r_n}{r^2}\frac{r}{2}\frac{\partial F}{\partial r}\,, \qquad (A1)$$

where $F = -(\alpha_5/2+6\beta_4+4\beta_5)G$. Note that this is of the same form as the standard expression for the two-point velocity correlation tensor in isotropic turbulence

$$R_{ij} = \overline{u^2}\left[\left(f(r) + \frac{r}{2}f'(r)\right)\delta_{ij} - \frac{r}{2}f'(r)\frac{r_i r_j}{r^2}\right]\,. \qquad (A2)$$

Employing Eq. (12), we can relate the function $F(r)$ in equation (A1) to the function $f(r)$ in Eq. (A2)

$$F(r) = \frac{\overline{u^2}}{3}\left[\frac{1}{r^3}\int_0^r r'^4 f dr' - \int_0^r r' f dr'\right] . \qquad (A3)$$

REFERENCES

ARIS, R. 1962 Vectors, tensors, and the equations of fluid mechanics. Prentice Hall, Sect. 3.43.

CROW, S. C. 1968 Viscoelastic properties of fine-grained incompressible turbulence. *J. Fluid Mech.* **33,** 1-20.

DONALDSON, C. DUP.& SANDRI, G. 1981 On the inclusion of information on eddy structure in second-order-closure models of turbulent flows. *AGARD Rep.* **CP-308,** 25.1-25.14.

VON KÁRMÁN, T. & HOWARTH, L. 1938 On the statistical theory of isotropic turbulence. *Proc. Roy. Soc.* **A 164,** 192-215.

LAUNDER, B. E., REECE, G. C. & RODI, W. 1975 Progress in the development of a Reynolds-stress turbulence closure. *J. Fluid Mech.* **68,** 537-566.

NAOT, D., SHAVIT, A. & WOLFSHTEIN, M. 1973 Two-point correlation model and the redistribution of reynolds stress. *Phys. Fluids.* **16,** 738-743.

OBERLACK, M. 1994a Closure of the dissipation tensor and the pressure-strain tensor based on the two-point correlation equation. *Turbulent Shear Flows 9,* Springer-Verlag, eds. Durst, F., Kasagi, N., Launder, B. E., Schmidt, F. W., & Whitelaw, J. H.

OBERLACK, M. 1994b Herleitung und Lösung einer Längenmaß- und Dissipations-Tensorlängenmaßgleichung für turbulente Strömungen. *Ph.D. thesis RWTH-Aachen.*

ROGERS, M. M., MOIN, P. & REYNOLDS, W. C. 1986 The structure and modeling of the hydrodynamic and passive scalar fields in homogeneous turbulent shear flow. *Thermosci. Dev., Dep. Mech. Eng.* **TF-25,** Stanford University.

ROTTA, J. C. 1951 Statistische Theorie nichthomogener Turbulenz, 1. Mitteilung. *Z. Phys.* **129,** 547-572.

ROTTA, J. C. 1951 Statistische Theorie nichthomogener Turbulenz, 2. Mitteilung. *Z. Phys.* **131,** 51-77.

SANDRI, G. 1977 A new approach to the development of scale equations for turbulent flows. *ARAP Rep.* **302.**

SANDRI, G. 1978 Recent results obtained in the modeling of turbulent flows by second-order closure. *AFOSR.* **TR-78-0680.**

SANDRI, G. & CERASOLI, C. 1981 Fundamental research in turbulent modeling. *ARAP Rep.* **438.**

WOLFSHTEIN, M. 1970 On the length-scale-of-turbulence equation. *Isr. J. Technol.* **8,** 87-99.

Rotating turbulent flows and modeling

The motivation for the group effort in this section stems from the fact that it can be shown that all one point closure models currently used in RANS (Reynolds-averaged Navier-Stokes) codes fail to correctly model the effects of strong rotation on turbulence. Yet, turbulent flows that are subjected to system rotation are found in many situations, examples are turbomachines, the wing tip vortex, geophysical flows, and many others. A prime objective of the CTR is to foster a climate where new ideas on understanding and modeling of turbulent flows will generate innovations that become part of the foundation of the turbulence knowledge base. The five papers in this section form a good example where innovations in modeling and new insights into the effects of rotation on turbulence are achieved through the use of a combination of both theory and simulations (direct and large-eddy).

Blaisdell and Shariff performed direct numerical simulations of homogeneous turbulence in elliptic streamline flow. This is a new flow in a series of building block flows where particular issues about turbulence modeling and physics are addressed. In this flow, the effects of both rotation and strain combine to provide an instability mechanism that has been proposed as a universal mechanism for energy transfer from large scales to small scales. Four cases were simulated to investigate the effects of Rossby number and ellipticity. A fifth case at high resolution was carried out to test resolution and sampling issues. Statistics of interest to turbulence modeling are presented. The simulations lead to the discovery of a homogeneous flow where the non-linear cascade is periodically suppressed and re-established.

Mahalov derived and analyzed the evolution equations for long-time averaged rotating shallow-water equations. He then used the same approach to derive equations for homogeneous flows subjected to background rotation. In this case, he decomposed the flow field into two-dimensional modes that are unaffected by rotation and three-dimensional disturbances. He showed a connection between his physical space formalism and the helical wave space formalism. The derived equations may prove useful in explaining the effects of rotation on the turbulent transfer between the scales.

Squires, Chasnov and Mansour used large-eddy simulations to investigate the asymptotic similarity of rotating homogeneous turbulence. They build on their previous investigations where, in the limit of high Reynolds number and small Rossby number, power laws for the turbulent stresses and length scales were derived based on dimensional analysis and simulation results. In the present study, a search for similarity laws for the spectra was carried out. They defined four independent energy spectra and found scalings that would collapse three out of the four spectra. The spectrum which does not collapse corresponds to two component motions in the plane normal to the rotation axis. A strong reverse cascade of the energy from small-to-large scales is found. These results hint at the tendency of the flow to become two-dimensional.

Cambon, Mansour and Squires used the same large-eddy simulations as above to investigate the development of anisotropies and the tendency of the flow to become two-dimensional. This tendency is often used as a confirmation of the Taylor-Proudman theorem. However, it can be shown that a key assumption in the derivation of the theorem does not hold for homogeneous flows. Cambon has long argued that the observed two-dimensionalization in rotating flows is a non-linear phenomenon. In the present work, results from low-Reynolds number direct numerical simulations and from high-Reynolds number large-eddy simulation are unified by arguing for the existence of two transitions in rotating turbulence that can be identified by two key Rossby numbers. During the first transition, anisotropies develop when a macro Rossby number drops below unity. During the second transition, the nonlinear transfer is shut off when a micro Rossby number drops below unity. The large-eddy simulation fields were also analyzed for alignment between vorticity fluctuations and the rotation axis. The results confirm the dominance of corrotative vorticity in the long-time high-Reynolds number limit.

Hadid, Mansour and Zeman tested a new one-point closure model that incorporates the effects of rotation on the power-law decay exponent of the turbulent kinetic energy. This modification to the ϵ-equation was proposed by Zeman based on the large-eddy simulation results. During the summer program the model was successfully tested against experimental data of isotropic turbulence that was subjected to uniform rotation. A new definition of the mean rotation was proposed based on critical point theory to generalize the effects of rotation on turbulence to arbitrary mean deformations. The model was then incorporated in a code used at Rocketdyne and tested for a backward-facing step and a dump combustor. Preliminary results show promise. Further collaborations on modeling rotating flows will continue between CTR, NASA/Ames, and Rocketdyne.

N. N. Mansour

53-34
N95-21056 / 355
P-17

Center for Turbulence Research
Proceedings of the Summer Program 1994

Homogeneous turbulence subjected to mean flow with elliptic streamlines

By G. A. Blaisdell[1] AND K. Shariff[2]

Direct numerical simulations are performed for homogeneous turbulence with a mean flow having elliptic streamlines. This flow combines the effects of rotation and strain on the turbulence. Qualitative comparisons are made with linear theory for cases with high Rossby number. The nonlinear transfer process is monitored using a generalized skewness. In general, rotation turns off the nonlinear cascade; however, for moderate ellipticities and rotation rates the nonlinear cascade is turned off and then reestablished. Turbulence statistics of interest in turbulence modeling are calculated, including full Reynolds stress budgets.

1. Introduction

1.1. Motivation

There are many important reasons for studying the elliptic streamline flow. This flow contains the effects of both rotation and strain and is therefore similar to the mean flow in a vortex strained in the plane perpendicular to its axis. Such flows provide insight into fundamental vortical interactions within turbulence, and the instability caused by the strain has been proposed as a universal mechanism for energy transfer from large scales to small scales (Pierrehumbert 1986).

A strained vortex also occurs in airplane wakes, in which each wingtip vortex induces a strain field on the other. The strain field can affect the stability of these vortices and thereby their turbulent structure downstream. The ability to understand and predict the turbulent structure of the vortices is important to the wake hazard problem which is of major concern for the safety of commercial aircraft.

Another example of a flow with the combined effects of rotation and strain is the outer core of the earth's interior. The electrically conducting fluid in the outer portion of the earth's core rotates with the earth but is also strained by tidal forces. A large-scale secondary flow results, which has been proposed as the cause of the magnetic field (Malkus & Berry 1988). Additional examples are flow in fluid-filled satellites and in rectangular cavities.

The elliptic streamline flow is also a good test case for turbulence models for rotating flows. It has an added complication beyond that of pure rotation, but it is still a basic flow. The additional strain rate is present in most practical engineering flows and, therefore, is a necessary effect for turbulence models to capture. The behavior of the turbulent statistics shown in section 3 are quite complex, and thus the elliptic streamline flow presents a challenging case for turbulence modelers.

1 Purdue University
2 NASA Ames Research Center

1.2. Background

The linear stability of elliptic streamline flow was studied by Pierrehumbert (1986), Bayly (1986), and Waleffe (1990), who performed inviscid stability analyses using different methods. For circular streamlines (pure rotation) there are no unstable modes, while for elliptic streamlines a band of unstable modes exists in which the growth rate depends on the polar angle of the wavenumber vector. The band of unstable angles increases in width for increasing ellipticity of the streamlines. Also, the growth rate of the unstable modes is independent of the magnitude of the wavenumber vector. Therefore, arbitrarily small three-dimensional fluctuations can be created by an instability of a basic two-dimensional flow. Pierrehumbert suggested that this might be a mechanism for the cascade process in turbulent flows.

The effects of viscosity were studied by Landman & Saffman (1987). The growth rate of the instabilities is modified by viscosity so that the growth rate is no longer independent of the magnitude of the wavenumber vector. They found a high wavenumber cut-off of the instability. However, there is no low wavenumber cut-off, and arbitrarily large scales are unstable. This fact has important implications for doing numerical simulations of this flow, which are discussed below.

An interesting experiment corresponding to elliptic streamline flow was done by Malkus (1989). A tank with moving flexible walls was used to create a flow with elliptic streamlines. He observed a collapse phenomenon in which the two-dimensional flow suddenly breaks down into three-dimensional small-scale motions. Waleffe (1990) studied the stability of the enclosed elliptic flow and suggested the collapse phenomenon is due to nonlinear interactions in which the mean flow is altered. Although the collapse is observed in a confined flow, there is some evidence that a similar phenomenon may occur in one of the homogeneous turbulence simulations discussed below.

Lundgren & Mansour (1991) investigated the stability of a vortex in a rectangular domain. This flow is very similar to the elliptic streamline flow and displays a similar instability. However, their flow has a mean velocity which decays in time, and their flow is inhomogeneous. These two factors introduce additional complicating effects and make gathering turbulence statistics difficult because of the low statistical sample that is available. The elliptic streamline flow and its instability is also related to the instability of a strained, finite-sized vortex with uniform vorticity studied by Widnall *et al.* (1974) and others.

An experiment which was designed to correspond to the homogeneous elliptic streamline flow was performed by Benoit (1992). He investigated grid generated turbulence created by a rotating grid and then passed through a specially designed diffuser with elliptic cross-sections. Benoit also analyzed the flow using linear rapid distortion theory. We have not had a chance to compare his results with those of the current simulations; however, such a comparison is planned for future work.

There has been a considerable amount of work done on the stability of the elliptic streamline flow. However, there has not been any direct numerical simulation of the homogeneous elliptic flow. With the use of direct numerical simulation, the nonlinear development of the flow and the fully turbulent state can be examined.

1.3. Objectives

The objectives of this work are to perform a preliminary investigation of the elliptic streamline flow for the fully turbulent case and to provide statistics for comparison with turbulence models. One of the issues to be investigated is whether the linear instability modes grow to dominate the flow even in the presence of large initial disturbances. Whether this is the case is dependent on the governing parameters. For the elliptic streamline flow the governing parameters are: (1) the ratio of the rotation rate to the strain rate, which gives the aspect ratio of the elliptic streamlines, (2) the ratio of a mean flow time scale, such as the rotation rate, to the turbulence time scale, and (3) the turbulent Reynolds number. One major objective is to study the effect of these various parameters. However, in this preliminary study we have not been able to cover the full parameter space.

Another issue has to do with the long term behavior of the turbulence. Does the turbulence grow continually, eventually decay, reach an asymptotic stationary state, or grow and decay in a periodic fashion? The linear theory would suggest exponential growth. The possibility of an asymptotic stationary state is suggested by the related flow of homogeneous rotating shear flow (Bardina *et al.* 1983, and Speziale & Mac Giolla Mhuiris 1989), in which case there seems to be the possibility of obtaining a state in which the turbulent kinetic energy does not grow or decay. In rotating shear flow the direction of strain is fixed in the rotating frame of reference, while in elliptic streamline flow the direction of strain is fixed in the stationary frame of reference. This difference is very important. One consequence of this difference is that for elliptic streamline flow a fluid element is periodically strained as it rotates around an elliptic streamline. This periodic straining of a fluid element might cause the turbulence to grow and then decay in a periodic fashion.

Turbulence statistics, including full Reynolds stress budgets, have been calculated during each of the simulations. The behavior of these statistics is discussed below; however, a comparison with turbulence models has not been done at this time.

2. Governing equations

Consider homogeneous turbulence with the mean flow

$$U_i = U_{i,j}x_j, \quad U_{i,j} \equiv \begin{pmatrix} 0 & 0 & -\gamma-\epsilon \\ 0 & 0 & 0 \\ \gamma-\epsilon & 0 & 0 \end{pmatrix}, \tag{1}$$

which describes a one-parameter family of streamline patterns in the x-z plane (the other parameter sets the strength of the flow). The case $\gamma = 0$ corresponds to pure strain with two principal directions at $\pm 45°$ relative to the x-axis while $0 < |\gamma| < |\epsilon|$ gives vortical strain dominated flows with hyperbolic streamlines, their asymptotes being shallower or steeper than the pure strain case according as $(\epsilon-\gamma)/(\epsilon+\gamma) < 1$ or > 1. The limit $|\epsilon| = |\gamma|$ is pure shear. The case $\epsilon = 0$ corresponds to pure rotation while $0 < |\epsilon| < |\gamma|$ gives vortical rotation dominated flows with geometrically similar elliptic streamlines with aspect ratio $E \equiv \sqrt{(\gamma+\epsilon)/(\gamma-\epsilon)}$. This case is depicted in Fig. 1.

The code shear_i, developed by Dr. R. S. Rogallo (of Los Altos Hills, Calif.) to run on the Intel parallel computers at NASA Ames for the case of pure shear and employing a subset of the techniques described in Rogallo (1981), was modified to treat the above cases. The xz plane was chosen as the plane of deformation to minimize disruption to the code. The program uses the second-order Runge-Kutta scheme to time-advance the Fourier transformed Navier-Stokes equation (notation will be explained momentarily):

$$\frac{d}{dt}(F\widehat{u}_i) = F\left\{\Pi^{(2)}_{ij}U_{j,m}\widehat{u}_m - i\Pi^{(1)}_{ij}k_m\widehat{u_j u_m}\right\} \tag{2}$$

Due to the use of coordinates that deform with the mean flow, the k_i in Eq. (2) represent time-dependent physical wavenumbers:

$$k_i = k'_j B_{ji}(t), \quad \dot{B}_{ij} = -B_{ik}U_{k,j}, \tag{3}$$

while hats denote the three-dimensional Fourier transform with respect to computational wavenumbers k'_i. Space discretization is implied by the restriction of k'_i to integers $-M/2 \leq k'_i \leq M/2$; homogeneity is realized when there is a sufficiently large range of small wavenumbers with energy tending to zero. The symbol $\Pi^{(n)}_{ij} \equiv \delta_{ij} - nk_ik_j/k^2$ with $n = 1$ is the projector applied to the Navier-Stokes equation to eliminate pressure; a slightly different projector, $\Pi^{(2)}_{ij}$, appears in the linear term due to an additional contribution from the time derivative term in deforming coordinates. The aliasing error concomitant with the pseudo-spectral evaluation of $\widehat{u_j u_m}$ is controlled (but not exactly eliminated) by a combination of phase shifting and spherical truncation in which modes with $k' > 2(M/3)^2$ are discarded upon return to wavenumber space. The viscous integrating factor F, satisfying $(1/F)dF/dt = +\nu k^2(t)$, is obtained analytically. Since in the linearized limit exact time integration of (2) is not possible (or at least not trivial (Waleffe 1990)), the present version of the program does not treat the rapid distortion limit exactly. Rather, the time step is chosen to be the more restrictive one obtained from the mean flow and the non-linear term. For pure shear the flow-field can be re-meshed to prevent extreme distortion of the computational domain. In the elliptic flow, however, a fluid element undergoes time-periodic shearing and straining, and rather than tackle the corresponding re-meshing problem, small enough ellipticities are considered so that the minimum interior angle of the element, $\theta_{\min} = \tan^{-1}\left[2E/(E^2-1)\right]$, does not become too small (for the largest case of $E = 2$ considered, $\theta_{\min} = 53°$).

The code was tested for: (i) The linear inviscid and viscous behavior of a single Fourier mode compared with the results of Landman & Saffman (1987) (ii) Pure rotation (Mansour *et al.* 1991, $Ro = 0.247$, their Fig. 2*a*) (iii) Pure shear (Rogers *et al.* 1986, Case C128U).

3. Simulations and results

One of the objectives of this study is to examine the effect of the relative time scales of the mean flow and the turbulence and the effect of the elliptic streamline

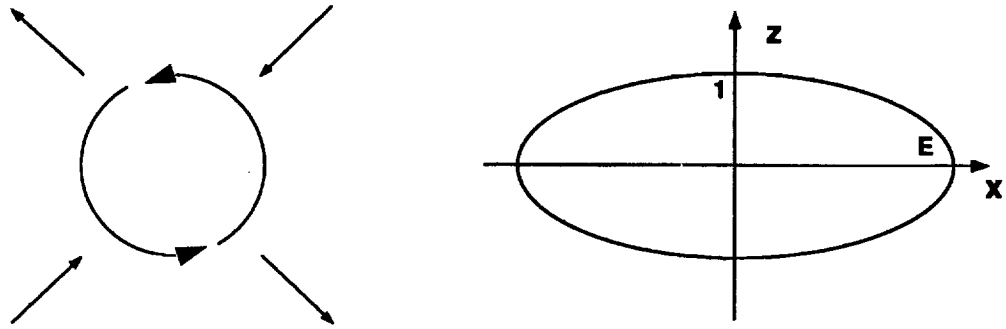

FIGURE 1. (a) Schematic view of combination of rotation and strain. (b) Elliptic streamline. (The direction of the arrows corresponds to $\gamma > 0$ and $\epsilon > 0$.)

Table 1. Initial condition and run parameters for the simulations.

Case	E	Ro	Re_{T_0}	grid	k_p
A	1.1	1.46	51	128^3	18
B	1.1	0.247	51	128^3	18
C	1.1	0.0037	51	128^3	18
D	2.0	0.247	51	128^3	18
D′	2.0	0.247	51	256^3	36

aspect ratio. We were guided in our choice of parameters by the pure rotation DNS of Mansour *et al.* (1991). Following them we define a Rossby number as $Ro = \varepsilon/(\Omega k)$, where ε is the dissipation rate of turbulent kinetic energy per unit mass, $\Omega \equiv \sqrt{\gamma^2 - \epsilon^2}$ is the rotation frequency, and k is the turbulent kinetic energy per unit mass. The period for a fluid element to traverse an elliptical streamline is $T = 2\pi/\Omega$. This is also the period of oscillation for the wavenumber vectors in the linear stability analyses. The Rossby number, Ro, is the ratio of the time scale of the mean flow and the time scale of the turbulence. Mansour *et al.* have considered a range of Rossby numbers. The general effect of increasing rotation rates is to shut off the nonlinear cascade process. We have chosen to use three of their values of Ro: a case with weak rotational effects ($Ro = 1.46$), moderate rotational effects ($Ro = 0.247$), and strong rotational effects ($Ro = 0.0037$). The elliptic streamline flow has the additional parameter of the aspect ratio of the elliptic streamlines, E. We have chosen to use $E = 1.1$ for most of the runs in order to remain close to the case of pure rotation. In one case we use $E = 2.0$ to see the effect of larger aspect ratio. The parameters for the simulations to be presented are shown in table 1.

The initial conditions for the simulations were obtained in the same way as those

of Mansour *et al.* (1991). An initial energy spectrum was specified of the form

$$E(\kappa) = \kappa^4 \exp(-2(\kappa/\kappa_p)^2) \quad , \tag{4}$$

where κ_p is the location of the peak in the spectrum. For most of the runs κ_p was chosen to be 18 and the computational grid was 128^3. The flow field was then evolved as decaying isotropic turbulence until it became fully developed as measured by the velocity derivative skewness obtaining a steady value near -0.5 and the turbulent kinetic energy displaying algebraic decay with a constant decay rate. This developed flow field was then used as initial conditions for the elliptic flow runs. The simulations presented here do not match the Reynolds number of Mansour *et al.* We attempted to do so, but were confronted with the difficulty that, with the elliptic streamline flow, the large scales gain energy and quickly outgrow the computational domain. This problem does not occur for the pure rotation case where the turbulence simply decays. As a result, we found it necessary to change our initial conditions to make the computational domain larger relative to the initial integral scales of the turbulence. Because of the corresponding loss of resolution in the small scales, we reduced the Reynolds number. All of the elliptic flow simulations presented here have an initial turbulent Reynolds number $Re_T = q^4/(\varepsilon\nu) = 51$ ($Re_t = k^2/(\varepsilon\nu) = 12.75$ following the notation of Mansour *et al.*). This compares to the value $Re_T = 109$ ($Re_t = 27.24$) for the 128^3 simulations of Mansour *et al.* With the peak in the initial spectrum pushed to higher wavenumbers, we were able to run the simulations further in time before the turbulence outgrew the computational domain. Simulation D′ is the same as case D except that a 256^3 grid was used and $k_p = 36$ so that the computational domain is twice as large relative to the turbulence length scales. The larger domain allowed the simulation to be carried out further in time and also provided a check on the effect of the domain size on case D.

3.1. Case A

Case A has an initial Rossby number of 1.46, which indicates that the effect of rotation is relatively weak. Since the dominant effect of rotation on the turbulence is to suppress the nonlinear cascade, it is useful to have a measure of the nonlinear transfer of energy from large scales to small scales. Mansour *et al.* (1991) used a generalized skewness defined by

$$S = -\frac{6\sqrt{15}}{7} \frac{\int \kappa^2 T(\kappa)\, d\kappa}{\left(\int \kappa^2 E(\kappa)\, d\kappa\right)^{3/2}} \quad , \tag{5}$$

where κ is the magnitude of the wavenumber vector, $E(\kappa)$ is the three-dimensional energy spectrum, $T(\kappa)$ is the transfer spectrum, and the numerical prefactor is such that for isotropic turbulence $S = -0.5$. The evolution of S for case A is shown in Fig. 2b. S begins near -0.5 since the initial conditions consist of decaying isotropic turbulence. Within one period the skewness falls to below -0.1, indicating that the nonlinear cascade has been suppressed considerably. The reduction in S seems far

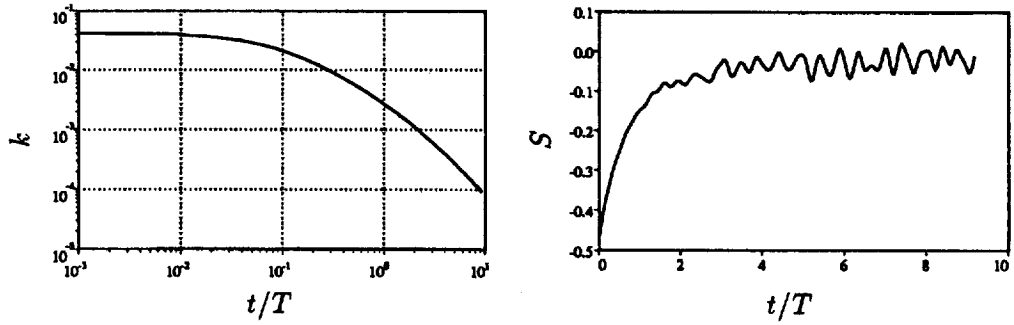

FIGURE 2. (a) Turbulent kinetic energy, k, for case A. (b) Skewness, S, for case A.

greater than that for the corresponding pure rotation case of Mansour *et al.* , for which S is reduced to -0.4. However, the extent of the two simulations is not the same; the final time for the simulation by Mansour *et al.* is $t/T = 0.25$.

Because the rotation rate in case A is relatively low and the ellipticity is small, the production of turbulent kinetic energy is also low. Dissipation dominates production during the course of the simulation so that the turbulence decays, as shown in Fig. 2a. However, since the flow is linearly unstable and the minimum unstable wave length fits within the computational domain, we believe that the turbulence must eventually grow. For this case the growth rates are very low, and so it would take a very long time to observe growth. A period of decay followed by growth is observed in case B.

3.2. Case B

Case B has an initial Rossby number of 0.247. Because of the higher production rate compared to case A, the growth in turbulent kinetic energy is observed within a reasonable period of time. The turbulent kinetic energy history is shown in Fig. 3a. There is a period of decay followed by exponential growth (as indicated by the linear increase on a semilog plot). The skewness for case B is shown in Fig. 3b. The rotation causes S to decrease to -0.2 very quickly; S then slowly decays to near zero. At later times S becomes periodic with an increasing amplitude. The period of oscillation corresponds to half the period, T, for a fluid element to traverse an elliptic streamline; the period of oscillation is also the period of the strain field relative to a frame of reference rotating with a fluid element.

The exponential growth in the turbulent kinetic energy, the suppression of nonlinear processes, and the periodic behavior indicate that the fluctuations are likely dominated by the linear instability modes. The linear analysis of Bayly shows the modes that are unstable lie in a narrow band depending on the polar angle measured from the rotation axis of the wavenumber vector. An angular spectrum, $E(\theta)$, which gives the energy as a function of angle, is shown in Fig. 4 at the final time of simulation B. The spectrum is plotted as a function of $\cos\theta$ so that an isotropic field will give a uniform distribution. The linear theory predicts a small band of unstable modes near $\theta = 2\pi/3$ or $\cos\theta = 1/2$. This is exactly what is seen in Fig. 4. So, for case B the fluctuations are clearly dominated by the linear instability modes.

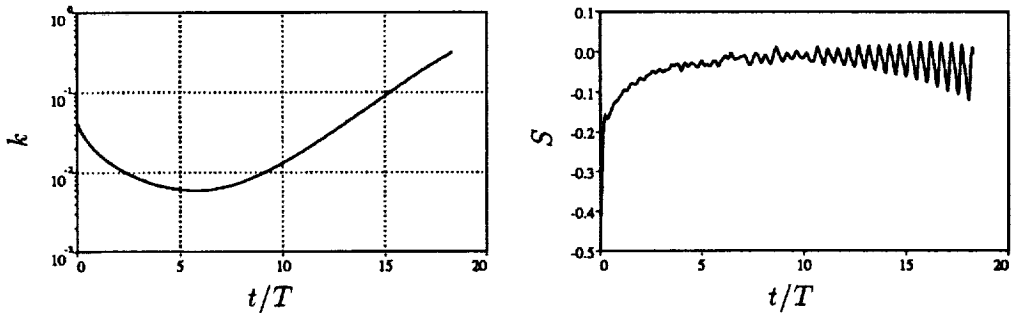

FIGURE 3. (a) Turbulent kinetic energy, k, for case B. (b) Skewness, S, for case B.

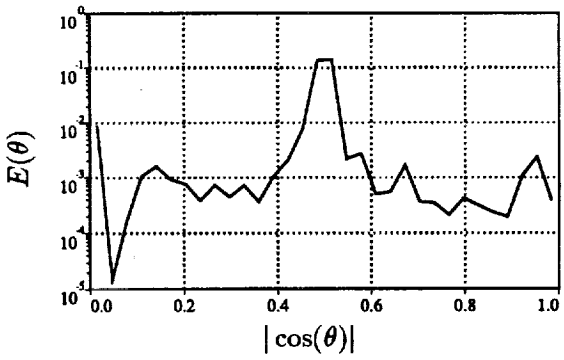

FIGURE 4. Angular energy spectrum, $E(\theta)$, for case B.

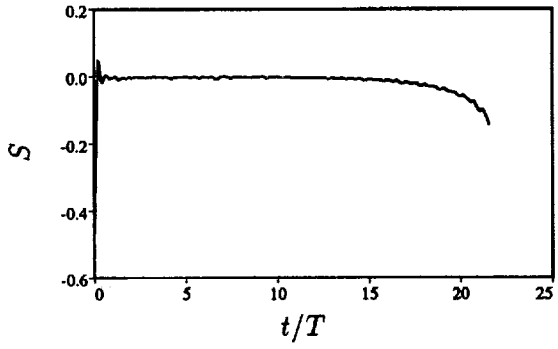

FIGURE 5. Skewness, S, for case C.

Based on the increasing amplitude of the oscillations in S shown in Fig. 3b, one might expect that nonlinear processes would increase and eventually the flow would become fully turbulent. To determine if this is the case would require a much larger computational domain so that the simulation could be carried further in time. Perhaps with a different choice of parameters, such an evolution could be observed within a time that is computationally affordable.

3.3. Case C

Case C has the lowest Rossby number, $Ro = 0.0037$, indicating very strong rotation effects. In the simulations of Mansour *et al.* the nonlinear cascade is almost completely shut off as S is nearly zero. The history of S for case C is shown in Fig. 5. S decays very quickly and remains nearly zero until the last portion of the simulation when the nonlinear processes start becoming more important. The behavior of S is similar to that in case B, and again it would be interesting to be able to continue the simulation to watch the restoration of the nonlinear cascade. The angular spectrum, $E(\theta)$, for case C (not shown) is very similar to that of case B. Therefore, both flows are dominated by the linear instability modes. The evolution of the turbulent kinetic energy for case C (not shown) also indicates exponential growth of the turbulence, however with negligible decay at early times.

3.4. Cases D and D'

Case D was done to see the effects of a larger aspect ratio of the elliptic streamlines. The aspect ratio is $E = 2$ and the initial Rossby number is $Ro = 0.247$, which is the intermediate value of the three considered. Because the large scales grow to fill the computational domain, we checked the adequacy of the domain size by running simulation D', which has a 256^3 grid and a domain size twice as large as that for case D. The results of the two simulations are compared below.

The turbulent kinetic energy for case D grows, but does not seem to grow exponentially. The growth seems to be more algebraic as indicated in Fig. 6a, which shows linear growth on a log-log plot. The exponent for the growth rate is close to 4. The two simulations agree very well, which indicates that the domain size is adequate up to the point where the simulations were terminated.

The skewness for cases D and D' are shown in Fig. 6b, and again they agree very well — the small differences between the simulations are due to differences in the initial, isotropic flow fields. The evolution of S displays some interesting behavior. At early times the rotation suppresses the nonlinear cascade and S is reduced to below -0.2. Then the nonlinear cascade seems to be reestablished as S grows back to -0.4. At later times S displays oscillations of period $T/2$ and seems to be decreasing in magnitude. The presence of the nonlinear cascade indicates that the fluctuations are not dominated by the linear instability modes. This is also seen in the angular spectrum which is presented in Fig. 7. The fluctuations are broad-band, while the linear stability analysis predicts that a limited band of modes are destabilized, although the band of modes is considerably broader for $E = 2.0$ than for $E = 1.1$ as in case B. (The picture presented by the angular spectrum is not completely clear because the spectra computed during the simulations used the physical wavenumber vectors to define the spectra, while the linear theory is based on the computational wavenumber vectors. Therefore, in order to make a valid comparison with the linear theory, the spectra subroutine must be modified and the simulations rerun.)

The behavior of S shown in Fig. 6b at later times brings up some interesting questions. Is the nonlinear cascade process being periodically turned on and off? If so, is this related to the collapse phenomenon observed in the experiments of

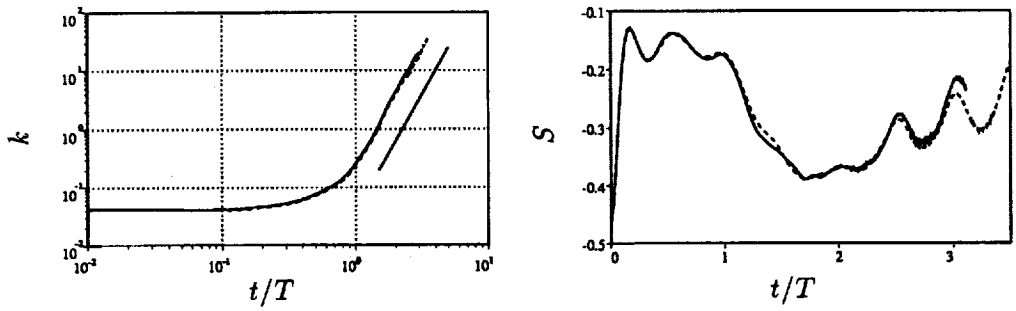

FIGURE 6. (a) Turbulent kinetic energy, k, and (b) skewness, S, for cases D, ——— , and D', ---- . (The line for t^4 is shown for reference.)

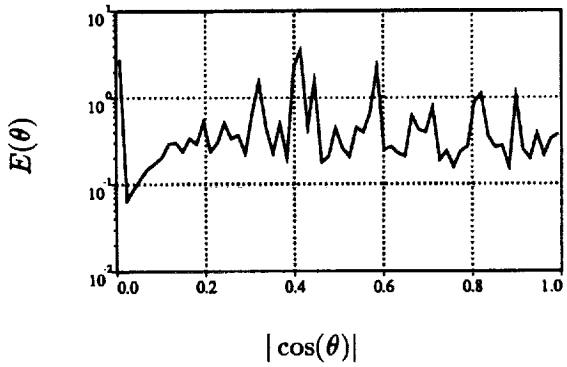

FIGURE 7. Angular energy spectrum, $E(\theta)$, for case D' at the final time of the simulation.

Malkus in which three-dimensional turbulence suddenly appears, or is this a different phenomenon? Does the skewness stay at large values, go back to zero (and then return), or oscillate about some intermediate value?

To be able to answer some of these questions we need to be able to run the simulations further in time. However, the difficulty in doing so is that the large length scales grow in amplitude and eventually dominate the flow so that the computational domain size becomes inadequate. The comparisons shown above between cases D and D' seem to indicate that the domain size for case D is adequate at least up to the time when the simulation was terminated. However, consideration of the radial, three-dimensional energy spectrum shows that even case D' has run out of box size by the end of the simulation. Fig. 8 shows the evolution of $E(\kappa)$ for case D'. The energy in the large scales steadily rises and the peak in the spectrum moves to the low wavenumbers. By the end of the simulation, the peak in the spectrum has run into the low wavenumber limit of the box. Also note that at the final time the high-wavenumber end of the spectrum seems to show some lack of small-scale resolution. The Reynolds number increases greatly during the course of the simulation, and by the end of the simulation the range of length scales is too great to be

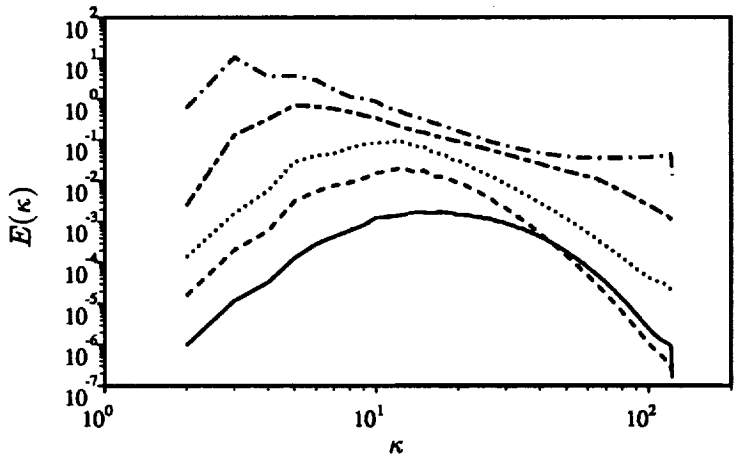

FIGURE 8. Radial energy spectra, $E(\kappa)$, for case D'. ——— , $t/T = 0.0$; ---- , $t/T = 1.02$; ····· , $t/T = 1.52$; —·— , $t/T = 2.31$; —·— , $t/T = 3.50$.

captured using 256^3 grid points. In order to carry the simulations further in time, more grid points are needed. It is feasible to perform 512^3 simulations; however, even this size grid would soon be outgrown. In order to overcome these difficulties, large-eddy simulation (LES) can be used so that high Reynolds numbers can be achieved without fully resolving the small length scales. This will allow more grid points to be used to capture the large length scales. We should also investigate the parameter space further to see if a higher aspect ratio, E, would produce similar behavior in a shorter time.

3.5. Implications for modeling

One of the goals of this study is to provide insight for turbulence modeling of rotating flows. To this end Reynolds stresses and the full Reynolds stress budgets were computed during the course of the simulations. While we have not been able to analyze the behavior of the Reynolds stresses fully, there are some observations we can make. We will discuss results from cases B and D', since the results from these cases are the most interesting.

3.5.1 Case B

The history of the Reynolds shear stress, $R_{13} = \overline{u_1' u_3'}$, is shown in Fig. 9 for case B. This case is dominated by the linear instability modes, and oscillations of period $T/2$ are clearly seen on top of the exponential growth. This is not inconsistent with the Floquet behavior of a single unstable Fourier mode according to linear analysis (Bayly 1986), which predicts that at late times the behavior should be T-periodic but modulated by a growing exponential. The deviation from exponential growth towards the end of the simulation reflects the behavior of other indicators of nonlinearity, namely, skewness (Fig. 3b) and slow pressure-strain (Fig. 10). An interesting point is that whereas the turbulent kinetic energy shown in Fig. 3 is relatively smooth, oscillations appear in the Reynolds stresses, representing inter-component transfer of energy.

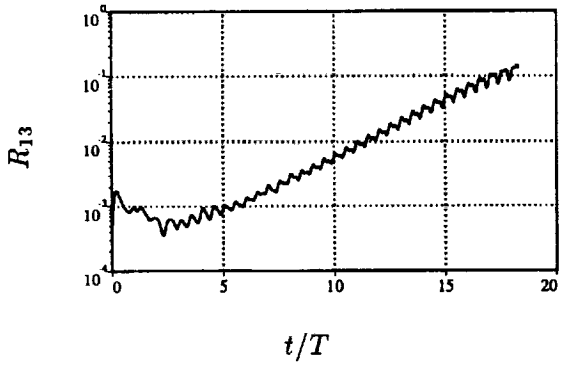

FIGURE 9. History of the Reynolds shear stress, R_{13}, for case B.

The Reynolds stress equations for homogeneous turbulence are (Reynolds 1987)

$$\frac{\overline{D}R_{ij}}{Dt} = P_{ij} + O_{ij} + T_{ij} - D_{ij} \quad , \tag{6}$$

where P_{ij} is the production term, O_{ij} is the kinematic rotation term, T_{ij} is the pressure-strain term, and D_{ij} is the dissipation rate tensor. The pressure-strain tensor is split into two parts, T_{ij}^r the rapid pressure-strain, and T_{ij}^s the slow pressure-strain. The Reynolds stress budgets for case B are shown in Fig. 10 for the 1-3 component. As a check, the sum of all the terms on the right hand side of Eq. (6) are compared to the time derivative of the Reynolds stresses, which was computed separately using the time history of the Reynolds stresses. The two terms compare very well, showing that the budgets are balanced. The dominant terms are the pressure-strain term, T_{ij}, and the kinematic rotation term, O_{ij}: they are of opposite sign and tend to partly cancel. The pressure-strain is dominated by the rapid (linear) part. The production term is important and much larger than the dissipation term, D_{ij}. Since the linear terms — rapid pressure-strain, kinematic rotation, and production — dominate, case B should be well described by the linear analysis (i.e. rapid distortion theory).

In order to get a better understanding of the turbulence structure, it is useful to consider the invariants of the Reynolds stress anisotropy tensor and various other tensor quantities. The Reynolds stress anisotropy tensor is defined as $b_{ij} = R_{ij}/q^2 - 1/3\delta_{ij}$. By definition the trace of b_{ij} is zero. The second and third invariants are $II_b = -\frac{1}{2}b_{ij}b_{ji}$ and $III_b = \frac{1}{3}b_{ij}b_{jk}b_{ki}$. The invariant map (Lumley 1978) for case B is shown in Fig. 11a. All physically realizable turbulence must lie within the triangular-shaped marked region. The left boundary corresponds to flow through an axisymmetric contraction, which would have vortex lines pulled all in one direction; the right boundary corresponds to flow through an axisymmetric expansion, which would flatten vortex lines into pancakes; and the origin corresponds to isotropic flow. From the figure it appears that the state of the turbulence changes periodically as the fluid element revolves around the elliptical streamline.

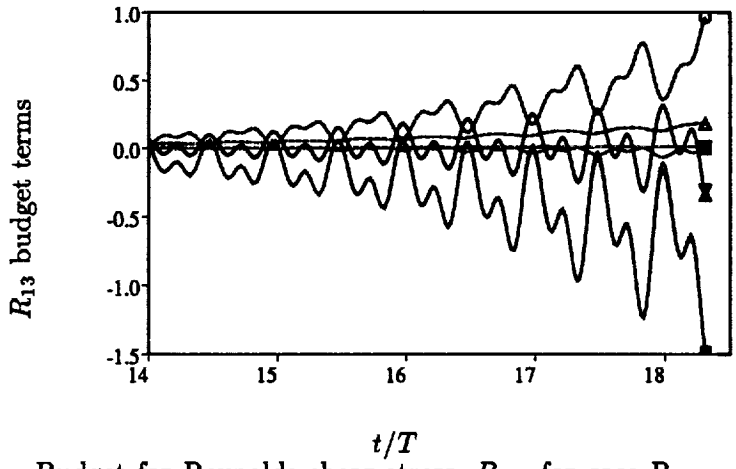

FIGURE 10. Budget for Reynolds shear stress, R_{13}, for case B. —— △ , Sum of all terms on the right hand side; —— ▽ , dR_{ij}/dt; ---- △ , P_{ij}; ---- ▽ , $-D_{ij}$; ---- ○ , O_{ij}; ····· + , T_{ij}; ····· □ , T^s_{ij}; ····· ■ , T^r_{ij}. (Since the total pressure-strain is nearly the rapid part, the symbol, ■ , lies over the + symbol.)

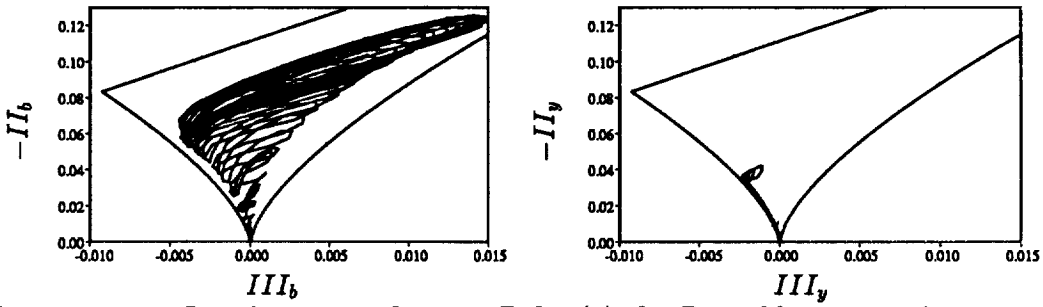

FIGURE 11. Invariant maps for case B for (a) the Reynolds stress anisotropy tensor, and (b) the structure dimensionality anisotropy tensor.

Invariant maps for the dissipation tensor and the vorticity correlation tensor are very similar to those for the Reynolds stress tensor shown in Fig. 11a. Another quantity of interest is the structure dimensionality tensor introduced by Reynolds (1989). For homogeneous flows it is most easily defined in wave space as

$$Y_{ij} = \int \frac{\kappa_i \kappa_j}{\kappa^2} E_{nn}(\vec{\kappa})\, d\vec{\kappa} \quad , \tag{7}$$

where $E_{ij}(\vec{\kappa})$ is the velocity spectrum tensor. The invariant map for the corresponding anisotropy tensor is shown in Fig. 11b, and it displays a much different behavior than for the Reynolds stress tensor. The invariants hug the left boundary and then deviate near the end of the simulation. A simulation not presented here, which had $E = 1.1$, $Ro = 0.116$, and $Re_T = 115$, had the invariants hugging the right boundary of the anisotropy map. So, there does not seem to be a special preference for the left boundary of the invariant map for the elliptic streamline flow. At this

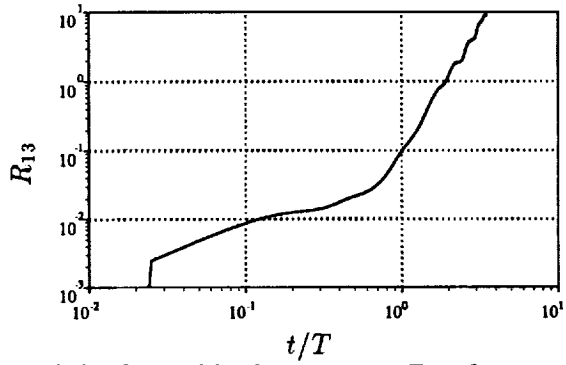

FIGURE 12. History of the Reynolds shear stress, R_{13}, for case D′.

point we are not sure what this behavior implies about the vortical structure of the turbulence.

3.5.2 Case D′

The history of the Reynolds shear stress for case D′ is shown in Fig. 12. It is not as oscillatory as for case B and and has oscillations in slope rather than magnitude. As for case B, the turbulent kinetic energy shown in Fig. 6 does not display the oscillations observed in individual Reynolds stress components. The budget for R_{13} is shown in Fig. 13. For case D′ all the terms in the Reynolds stress equations are important. The linear terms are large, but the nonlinear terms — the slow part of the pressure-strain and the dissipation rate — are significant. This would be a good test case for comparison with predictions from turbulence models.

The invariant maps of the Reynolds stress anisotropy tensor and the structure dimensionality anisotropy tensor are shown in Fig. 14. The invariants of the Reynolds stress tensor do not seem to follow a recognizable pattern, except that near the end of the simulation they oscillate in a region near the left boundary of the invariant map. The invariants of the structure dimensionality tensor remain near the origin. They oscillate once along the left boundary of the invariant map and then oscillate along the right boundary. Again, we are not sure what this behavior implies about the vortical structure of the turbulence.

4. Conclusions

Preliminary calculations of homogeneous turbulence subjected to mean flow with elliptic streamlines have been performed. The cases considered include a series of three runs with a low aspect ratio of the elliptical streamlines and which span a range of Rossby numbers. A fourth case was done with moderate values of aspect ratio and Rossby number; this case shows the most interesting results.

The case with a low aspect ratio and a high Rossby number (low rotation rate) simply decays. The other two low aspect ratio simulations show exponential growth of the turbulent kinetic energy in agreement with the linear theory. These simulations are dominated by linear effects. Examination of the turbulence cascade, using a generalized skewness, shows that the nonlinear transfer is greatly reduced

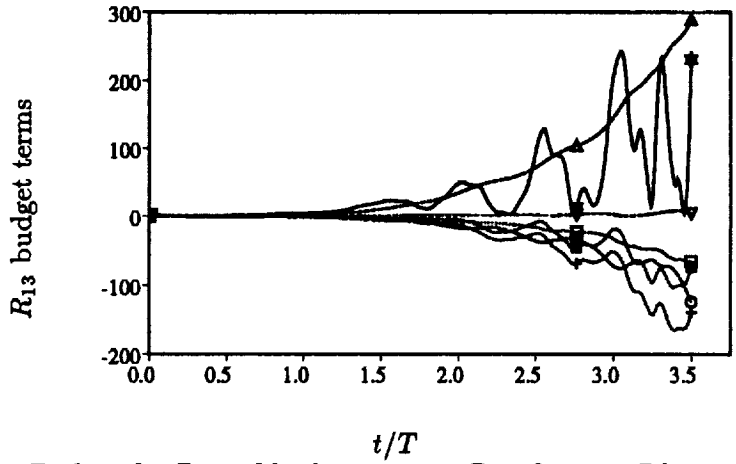

FIGURE 13. Budget for Reynolds shear stress, R_{13}, for case D'. —— △ , Sum of all terms on the right hand side (times ten); —— ▽ , $10dR_{ij}/dt$; ---- △ , P_{ij}; ---- ▽ , $-D_{ij}$; ---- ○ , O_{ij}; ····· + , T_{ij}; ····· □ , T^s_{ij}; ····· ■ , T^r_{ij}. (Note that the first two terms have been enlarged by ten.)

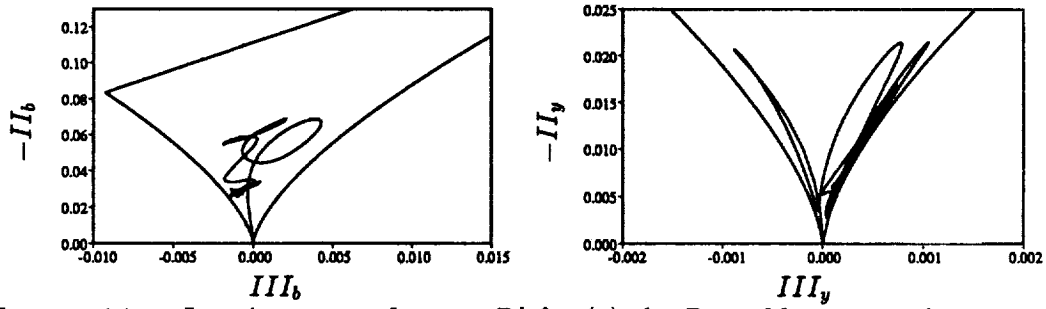

FIGURE 14. Invariant maps for case D' for (a) the Reynolds stress anisotropy tensor, and (b) the structure dimensionality anisotropy tensor.

for these cases. However, in the later stages of the simulations, nonlinear effects begin to grow.

For the case with a moderate aspect ratio and Rossby number, the nonlinear cascade is reduced and then reestablished and finally displays large amplitude oscillations. This behavior may be related to the resonant collapse phenomenon observed in experiments of the elliptic streamline flow. The turbulent kinetic energy for this case shows algebraic rather than the exponential growth predicted by the linear theory.

One difficulty with these simulations is that the large scales grow in energy and eventually dominate the flow. As a consequence, the computational box size becomes inadequate and the simulations must be stopped. Since the long time behavior of the turbulence is of interest, a means of extending the simulations further in time is needed, and this is one of the goals for future work.

The elliptic streamline flow presents a challenging case for turbulence modelers. The Reynolds stresses display complex behavior and they oscillate as they grow.

The Reynolds stresses and their budgets have been computed during the course of each simulation, but they have not been analyzed in detail nor compared to predictions of turbulence models.

The elliptic streamline flow is a very interesting case. It is related to important flows in engineering and geophysical applications, and it displays a wide range of behavior that is yet to be understood. There are many tasks to be done in continuing this work. Further simulations are needed to better map out the parameter space. Upon identifying interesting cases, such as case D in the current work, simulations on larger grids should be done. In order to carry the simulations further in time, large-eddy simulations should be used so that the small length scales do not have to be resolved and more of the computational grid can be used to capture the large length scales. Finally, a detailed analysis of the Reynolds stresses and their budgets, and a comparison with turbulence models is needed.

Acknowledgements

The authors thank Dr. R. S. Rogallo for use of his program, help extended during modification, and numerous other discussions.

REFERENCES

BARDINA, J., FERZIGER, J. H., & REYNOLDS, W. C. 1983 Improved turbulence models based on large-eddy simulation of homogeneous, incompressible turbulent flows. Thermosciences Division Report TF-19, Stanford University, Stanford, California.

BAYLY, B. J. 1986 Three dimensional instability of elliptic flow. *Phys. Rev. Lett.* **57,** 2160–2171.

BENOIT, J.-P. 1992 Etude expérimentale et théorique d'une turbulence homogéne soumise à des effets couplés de rotation et de déformation plane. Ph.D. thesis, L'Ecole Central de Lyon, France.

LANDMAN, M. J. & SAFFMAN, P. G. 1987 The 3-D instability of strained vortices in a viscous fluid. *Phys. Fluids.* **30,** 2339–2342.

LUMLEY, J. L. 1978 Computational modeling of turbulent flows. *Advances in Applied Mechanics.* **18,** 123–173.

LUNDGREN, T. S. & MANSOUR, N. N. 1991 Transition to turbulence in an elliptic vortex. *Annual Research Briefs.* Center for Turbulence Research, NASA Ames/Stanford Univ.

MALKUS, W. V. R. 1989 An experimental study of global instabilities due to the tidal (elliptical) distortion of a rotating elastic cylinder. *Geophys. Astrophys. Fluid Dyn.* **48,** 123–134.

MALKUS, W. V. & BERRY, M. E. 1988 Order and disorder in planetary dynamos. *Summer Study Program in Geophysical Fluid Dynamics*, (eds. W. V. Malkus and M. E. Berry).

MANSOUR, N. N., CAMBON, C. & SPEZIALE, C. G. 1991 Single point modeling of initially isotropic turbulence under uniform rotation. *Annual Research Briefs.* Center for Turbulence Research, NASA Ames/Stanford Univ.

PIERREHUMBERT, R. T. 1986 Universal short-wave instability of two-dimensional eddies in an inviscid fluid. *Phys. Rev. Lett.* **57,** No. 17, 2157–2159.

REYNOLDS, W. C. 1987 Fundamentals of turbulence for turbulence modeling and simulation. *Lecture Notes for Von Karman Institute*, April 1987.

REYNOLDS, W. C. 1989 Effects of rotation on homogeneous turbulence. *10th Australian Fluid Mechanics Conference,* University of Melbourne, Australia, December 1989.

ROGALLO, R. S. 1981 Numerical experiments in homogeneous turbulence. NASA Technical Memorandum 81315.

ROGERS, M.M., MOIN, P. & REYNOLDS, W.C. 1986 The structure and modeling of the hydrodynamic and passive scalar fields in homogeneous turbulent shear flow. Thermosciences Division Report TF-25, Stanford University, Stanford, California.

SPEZIALE, C. G. & MAC GIOLLA MHUIRIS, N. 1989 On the prediction of equilibrium states in homogeneous turbulence. *J. Fluid Mech.* **209,** 591–615.

WALEFFE, F. 1990 The three-dimensional instability of strained vortices. *Phys. Fluids A.* **2,** 76–80.

WIDNALL, S. E., BLISS, D. B., & TSAI, C.-Y. 1974 The instability of short waves on a vortex ring. *J. Fluid Mech.* **66,** 35–47.

C-5

22-34
373
p. 10

Center for Turbulence Research
Proceedings of the Summer Program 1994

N95-21057

On the transition towards slow manifold in shallow-water and 3D Euler equations in a rotating frame

By A. Mahalov[1]

The long-time, asymptotic state of rotating homogeneous shallow-water equations is investigated. Our analysis is based on long-time averaged rotating shallow-water equations describing interactions of large-scale, horizontal, two-dimensional motions with surface inertial-gravity waves field for a shallow, uniformly rotating fluid layer. These equations are obtained in two steps: first by introducing a Poincaré/Kelvin linear propagator directly into classical shallow-water equations, then by averaging. The averaged equations describe interaction of wave fields with large-scale motions on time scales long compared to the time scale $1/f_0$ introduced by rotation ($f_0/2$-angular velocity of background rotation). The present analysis is similar to the one presented by Waleffe (1991) for 3D Euler equations in a rotating frame. However, since three-wave interactions in rotating shallow-water equations are forbidden, the final equations describing the asymptotic state are simplified considerably. Special emphasis is given to a new conservation law found in the asymptotic state and de-coupling of the dynamics of the divergence free part of the velocity field. The possible rising of a de-coupled dynamics in the asymptotic state is also investigated for homogeneous turbulence subjected to a background rotation. In our analysis we use long-time expansion, where the velocity field is decomposed into the 'slow manifold' part (the manifold which is unaffected by the linear 'rapid' effects of rotation or the inertial waves) and a formal 3D disturbance. We derive the physical space version of the long-time averaged equations and consider an invariant, basis-free derivation. This formulation can be used to generalize Waleffe's (1991) helical decomposition to viscous inhomogeneous flows (e.g. problems in cylindrical geometry with no-slip boundary conditions on the cylinder surface and homogeneous in the vertical direction).

1. Introduction

There are many important engineering (e.g. turbomachinery, ship propellers) and geophysical (geophysical turbulence) problems in which rotation significantly modify the turbulence properties of fluid flows. The interest in the effects of rotation is reflected in the large body of theoretical, experimental, and numerical work documenting them (Hopfinger 1989). As the effects are both multi-fold and subtle, the development of models which account for the effects of rotation require an understanding of the processes occurring in these flows. The objective of this work

1 Department of Mathematics, Arizona State University, Tempe, AZ 85287-1804

PAGE 372 INTENTIONALLY
PRECEDING PAGE BLANK NOT FILMED

is to examine the long-time evolution of solutions of shallow-water and 3D Euler equations in a rotating frame. We are especially interested in possible de-coupling of dynamics on slow manifold and in developing new conservation laws valid in the asymptotic state.

The paper is organized as follows. The long-time averaged rotating shallow-water equations are presented in Section 2. Special emphasis is given to a new conservation law found in the asymptotic state and to the de-coupling of dynamics of the divergence free part of the velocity field. Section 3 is devoted to homogeneous turbulence subjected to uniform rotation. In our analysis we use long-time expansion, where the velocity field is decomposed into the 'slow manifold' part (the manifold which is unaffected by the linear 'rapid' effects of rotation or the inertial waves) and a formal 3D disturbance. We derive the physical space version of the long-time averaged equations and consider an invariant, basis-free derivation. This can be useful in generalizations of Waleffe (1991) helical decomposition to viscous inhomogeneous flows (e.g. problems in cylindrical geometry with no-slip boundary conditions on the cylinder surface and homogeneous in the vertical direction). Finally, the possible rising of a de-coupled dynamics of the slow manifold is investigated. This study was motivated by the previous studies of Squires *et al.* (1993) and Cambon *et al.* (1994).

2. Rotating shallow-water equations

It has been long realized that geophysical flows admit motions varying on different time scales. In many situations, the low frequency class contains the majority of energy and is therefore the class of main interest. However, long-time computation of this class of motions using unmodified Eulerian equations is prohibitive due to severe accuracy and time step restrictions (Browning *et al.* 1990). The disparity of time scales leads to problems in the numerical solution of the equations because the Courant number is determined by the fastest time scale and therefore limits the time step which makes explicit solution impractical. In our approach collective contribution to the dynamics made by fast wave motions is accounted for by an averaging procedure. Elimination of "fast" time scales through the averaging procedure leads to equations that more accurately and efficiently describe dynamics on long time scales. These equations are obtained in two steps: first by introducing a Poincaré/Kelvin linear propagator directly into classical shallow-water equations, then by averaging. Averaged equations describe interaction of wave fields with large-scale motions on time scales long compared to a time scale $1/f_0$ introduced by rotation ($f_0/2$-angular velocity of background rotation). These are fully nonlinear equations containing classical quasigeostrophic equation as a completely decoupled subsystem. Two other equations describing departure from quasigeostrophy are coupled to the latter equation. Special emphasis is given to a new conservation law found in the asymptotic state and de-coupling of dynamics of the divergence free part of the velocity field.

The equations for shallow-water are:

$$[\frac{\partial}{\partial t} + \mathbf{U} \cdot \nabla]\mathbf{U} = -g\nabla H + f_0 \mathbf{U} \times e_3, \tag{1}$$

$$\frac{\partial}{\partial t}H = -\nabla \cdot [\mathbf{U}H] \tag{2}$$

where ∇ and $\mathbf{U}$ are two-dimensional and in the (x_1, x_2)-plane, $\mathbf{U}$ is the velocity, g is the reduced acceleration of gravity (a constant), H is a function of x_1, x_2, and t and is the free-surface height of the shallow layer of fluid, $\hat{H}_0$ is a constant and is the mean depth of the layer, e_3 is the unit vector in x_3, and f_0 is the Coriolis parameter. Equations (1) and (2) with boundary conditions describe the full system. The system (1)-(2) could also be thought of as describing a two-dimensional compressible gas, with H being the density. Note that (1) and (2) imply

$$[\frac{\partial}{\partial t} + \mathbf{U} \cdot \nabla]Q = 0 \tag{3}$$

where Q is the potential vorticity

$$Q \equiv \frac{f_0 + \Omega}{H} \tag{4}$$

where Ω is the vorticity. Note that Eqs. (1), (3), and (4) are also a complete description of shallow-water motion. The fast time scale that we average over is $1/f_0$. Here we treat f_0 as constant, though later we will modify it to be a function of x_2 or in polar coordinates a function of r.

2.1 Linear propagator

We have for the linear propagator

$$\frac{\partial \mathbf{U}}{\partial t} = -g\nabla H + f_0 \mathbf{U} \times e_3, \quad \frac{\partial H}{\partial t} = -\hat{H}_0 \nabla \cdot \mathbf{U}. \tag{5}$$

Introducing $D = \nabla \cdot \mathbf{U}$ and $\Omega = curl\ \mathbf{U} \cdot e_3$, we obtain

$$\frac{\partial D}{\partial t} = -g\Delta H + f_0\Omega, \quad \frac{\partial \Omega}{\partial t} = -f_0 D, \quad \frac{\partial H}{\partial t} = -\hat{H}_0 D. \tag{6}$$

In the case of homogeneous flows we use Fourier representation (for simplicity we assume 2π periodicity in x_1 and x_2)

$$D = \sum_k e^{ik\cdot x} D_k, \quad \Omega = \sum_k e^{ik\cdot x}\Omega_k, \quad H = \sum_k e^{ik\cdot x} H_k$$

where $k = (k_1, k_2)$, $x = (x_1, x_2)$. Then in Fourier space Eq. (6) becomes

$$\frac{\partial D_k}{\partial t} = g|k|^2 H_k + f_0\Omega_k, \quad \frac{\partial \Omega_k}{\partial t} = -f_0 D_k, \quad \frac{\partial H_k}{\partial t} = -\hat{H}_0 D_k. \tag{7}$$

We supplement (7) with initial conditions

$$D_k(0) = D_k^0, \quad \Omega_k(0) = \Omega_k^0, \quad H_k(0) = H_k^0. \tag{8}$$

Solutions of the linear propagator Eqs. (7)-(8) are well-known (e.g. Pedlosky 1979); those corresponding to the free surface gravity waves represent the fast time scale. Defining $\phi_k = f_0\sqrt{1+L_R^2|k|^2}$ where $L_R^2 = g\hat{H}_0/f_0^2$ is the Rossby deformation radius, we have

$$\begin{pmatrix} D_k(t) \\ \Omega_k(t) \\ H_k(t) \end{pmatrix} = (\mathbf{A}(k) + \cos(\phi_k t)\mathbf{A}_c(k) + \sin(\phi_k t)\mathbf{A}_s(k)) \begin{pmatrix} D_k^0 \\ \Omega_k^0 \\ H_k^0 \end{pmatrix} \equiv \exp(\mathbf{L}t) \begin{pmatrix} D_k^0 \\ \Omega_k^0 \\ H_k^0 \end{pmatrix}. \tag{9}$$

Here $\mathbf{A}(k)$, $\mathbf{A}_c(k)$ and $\mathbf{A}_s(k)$ are 3×3 matrices defined as follows

$$\mathbf{A}(k) = \frac{1}{\phi_k^2}\begin{pmatrix} 0 & 0 & 0 \\ 0 & g\hat{H}_0|k|^2 & -f_0 g|k|^2 \\ 0 & -\hat{H}_0 f_0 & f_0^2 \end{pmatrix}, \quad \mathbf{A}_c(k) = \frac{1}{\phi_k^2}\begin{pmatrix} \phi_k^2 & 0 & 0 \\ 0 & f_0^2 & f_0 g|k|^2 \\ 0 & \hat{H}_0 f_0 & g\hat{H}_0|k|^2 \end{pmatrix},$$
$$\mathbf{A}_s(k) = \frac{1}{\phi_k}\begin{pmatrix} 0 & f_0 & g|k|^2 \\ -f_0 & 0 & 0 \\ -\hat{H}_0 & 0 & 0 \end{pmatrix}. \tag{10}$$

2.2 The asymptotic limit of rotating homogeneous shallow-water equations

We write classical rotating shallow-water equations (1)-(2) using the variables $D = \nabla\cdot\mathbf{U}$, $\Omega = curl\mathbf{U}\cdot e_3$ and H. Letting $\mathbf{V}^{tr} = (D,\Omega,H)$ (tr- transpose), these equations can be written symbolically in the form

$$\frac{\partial \mathbf{V}}{\partial t} = \mathbf{L}\mathbf{V} + \mathbf{B}(\mathbf{V},\mathbf{V}). \tag{11}$$

Here $\mathbf{L}$ is the linear propagator operator corresponding to Poincaré/Kelvin waves. We introduce this linear propagator directly into nonlinearity using the change of variables $\mathbf{V} = \exp(\mathbf{L}t)\mathbf{v}$ where $\mathbf{v}^{tr} = (d,\omega,h)$ and $\exp(\mathbf{L}t)$ is defined by (9). Equation (11) written in $\mathbf{v}$ variables has the form

$$\frac{\partial \mathbf{v}}{\partial t} = \mathbf{B}(t,\mathbf{v},\mathbf{v}) \tag{12}$$

where

$$\mathbf{B}(t,\mathbf{v},\mathbf{v}) = \exp(-\mathbf{L}t)\mathbf{B}(\exp(\mathbf{L}t)\mathbf{v},\exp(\mathbf{L}t)\mathbf{v}).$$

Equation (12) is explicitly time-dependent with rapidly varying coefficients. Using the standard averaging methods (e.g. Hale 1980), we average over the fast time scale of the gravity waves and obtain

$$\frac{\partial \mathbf{v}}{\partial t} = \tilde{\mathbf{B}}(\mathbf{v},\mathbf{v}),\ \tilde{\mathbf{B}}(\mathbf{v},\mathbf{v}) = \frac{1}{2T}\int_{-T}^{T}\mathbf{B}(s,\mathbf{v},\ \mathbf{v})ds. \tag{13}$$

These equations are exact in the limit $\mu = f_0 T \gg 1$ where μ is a non-dimensional parameter. We present explicit final form of the regularized (long-time averaged) Eqs. (13). The calculation leading to these equations is lengthy but straightforward. Here we present only the final result for periodic case. We use the following notations: m and k are wavevectors so that $m = (m_1, m_2)$, $k = (k_1, k_2)$; $(mke_3) = (m \times k) \cdot e_3 = m_1 k_2 - k_1 m_2$; $k \cdot x = k_1 x_1 + k_2 x_2$ and $m \cdot k = m_1 k_1 + m_2 k_2$; $\phi_k^2 = f_0^2 + g\hat{H}_0 |k|^2$. The regularized (long-time averaged) equations are conveniently written in new variables

$$A = d, \; B = f_0 \omega - g\Delta h, \; C = \hat{H}_0 \omega - f_0 h \tag{14}$$

where Δ is the Laplace operator. Physical interpretation of these variables is as follows. $C/\hat{H}_0$ is quasigeostrophic potential vorticity; $g\Delta h/f_0$ is quasigeostrophic component of vorticity and, therefore, B/f_0 is ageostrophic component of vorticity. In the quasigeostrophic case we have $A = B = 0$. Let

$$A = \sum_n e^{in \cdot x} A_n, \quad B = \sum_n e^{in \cdot x} B_n, \quad C = \sum_n e^{in \cdot x} C_n. \tag{15}$$

We note that three-wave interactions are forbidden since the equation $\pm\phi_k \pm \phi_m = \phi_n$ $(n = k+m)$ has no solutions. Then the final equations describing the asymptotic state are much simpler than in the case of 3D Euler equations considered by Waleffe (1991). We obtain after averaging (Eq. (13) in A, B, C variables)

$$\begin{aligned}
\frac{dA_n}{dt} &= \sum_{k:|k|=|n|} C_{n-k}(\alpha(k, n-k)A_k + \beta(k, n-k)B_k), \\
\frac{dB_n}{dt} &= \sum_{k:|k|=|n|} C_{n-k}(-\phi_n^2 \beta(k, n-k)A_k + \frac{\phi_n^2}{\phi_k^2}\alpha(k, n-k)B_k), \\
\frac{dC_n}{dt} &= \sum_{k:\text{no restriction}} \phi_n^2 \gamma(k, n-k) C_{n-k} C_k.
\end{aligned} \tag{16}$$

Here

$$\alpha(k, m) = \frac{g(mke_3)(2\phi_k^2(m \cdot k) + f_0^2(|k|^2 - |m|^2))}{2|k|^2 \phi_k^2 \phi_m^2},$$

$$\beta(k, m) = \frac{f_0 g(|m|^4 - |k|^4 - \frac{5}{2}|m|^2|k|^2)}{2|k|^2 \phi_k^2 \phi_m^2}, \quad \gamma(k, m) = \frac{g(mke_3)}{\phi_m^2 \phi_{k+m}^2} \tag{17}$$

are geometric parameters. Equations (16) are exact in the limit $\mu = f_0 T \gg 1$. They have property that the third equation is completely decoupled from the first two equations. After the third equation is solved, the first two equations become linear equations in A and B. From the third equation in (16), it can be easily shown that $C(t, x)$ obeys in physical space

$$\frac{\tilde{D}}{\tilde{D}t} C = 0 \tag{18}$$

where $\frac{\tilde{D}}{\tilde{D}t}$ is the advective derivative, based on the velocity $\tilde{\mathbf{v}} = e_3 \times \nabla\tilde{\psi}$ where $\tilde{\psi} \equiv (1 - L_R^2\Delta)^{-1}C/\hat{H}_0$. Note that in the quasigeostrophic limit, $\tilde{\psi}$ is the stream function associated with the quasigeostrophic potential vorticity $C/\hat{H}_0$, and $\tilde{\mathbf{v}}$ is the quasigeostrophic velocity. The above Eq. (18) implies that C and all of its moments are conserved because $\tilde{\mathbf{v}}$ is divergence free (a well-known fact within the context of two-dimensional incompressible turbulence). For a given geostrophic component $C(t,x)$ found from (18), equations for ageostrophic components A and B have the form

$$\begin{aligned}\frac{dA_n}{dt} &= \sum_{k:|k|=|n|} C_{n-k}(\alpha(k,n-k)A_k + \beta(k,n-k)B_k),\\ \frac{dB_n}{dt} &= \sum_{k:|k|=|n|} C_{n-k}(-\phi_n^2\beta(k,n-k)A_k + \frac{\phi_n^2}{\phi_k^2}\alpha(k,n-k)B_k).\end{aligned} \tag{19}$$

It can be easily shown that these equations have a new conservation law

$$M = \sum_n(\phi_n^2|A_n|^2 + |B_n|^2). \tag{20}$$

The conservation of M is proved by direct differentiation of (20), substitution of expressions for dA_n/dt and dB_n/dt from (19) and using properties of the geometric coefficients $\alpha(k,m)$ and $\beta(k,m)$ given by (17). Another approach for determining this conservation law would be to derive the long-time averaged equations from a variational principle. Existence of conserved quantity M allows us to control the size of ageostrophic component in terms of its initial value. One could use this conservation law to examine the Lyapunov stability conditions for the equilibrium solutions of the long-time averaged equations. We note that M is not conserved by the full rotating shallow-water Eqs. (1)-(2).

3. On the asymptotic limit of 3D Euler equations in a rotating frame

In a frame of reference rotating with constant angular velocity $f_0/2$ about the x_3 axis, the inviscid Euler equations have the form

$$\frac{\partial \mathbf{U}}{\partial t} + \mathbf{U}\cdot\nabla\mathbf{U} + f_0\mathbf{J}\mathbf{U} = -\nabla p, \quad \nabla\cdot\mathbf{U} = 0. \tag{21}$$

Here $\mathbf{U} = (U,V,W)$ is the velocity field, p is modified pressure and $\mathbf{J}$ is the rotation matrix ($\mathbf{J}\mathbf{U} = e_3 \times \mathbf{U}$). It is convenient to write (21) in the form

$$\frac{\partial \mathbf{U}}{\partial t} + f_0\mathbf{J}\mathbf{U} = \mathbf{U}\times curl\mathbf{U} - \nabla(p + |\mathbf{U}|^2/2), \quad \nabla\cdot\mathbf{U} = 0. \tag{22}$$

We present a coordinate-free derivation of long-time averaged Euler equations describing dynamics on time scales long compared to the time scale $1/f_0$ introduced by rotation. This can be useful in generalizations of Waleffe (1991) helical decomposition to viscous inhomogeneous flows (e.g. problems in cylindrical geometry with

no-slip boundary conditions on the cylinder surface and homogeneous in the vertical direction).

We define the Leray projection $\mathbf{P}$ (projection on divergence free vector fields). Then Eq. (22) can be written in operator form as follows

$$\frac{d\mathbf{U}}{dt} + f_0(\mathbf{PJ})\mathbf{U} = \mathbf{P}\{\mathbf{U} \times curl\mathbf{U}\}. \tag{23}$$

We introduce a change of variables (canonical, preserving both energy and helicity)

$$\mathbf{U} = \exp(-f_0\mathbf{PJ}t)\mathbf{u}. \tag{24}$$

This transformation is analogous to the van der Pol transformation widely used in the theory of nonlinear oscillators (e.g. Wiggins 1990). Equation (23) written in $\mathbf{u}$-variables now becomes

$$\frac{d\mathbf{u}}{dt} = \exp(f_0\mathbf{PJ}t)\mathbf{P}\{\exp(-f_0\mathbf{PJ}t)\mathbf{u} \times curl(\exp(-f_0\mathbf{PJ}t)\mathbf{u})\}. \tag{25}$$

We note that the operator $\mathbf{PJ}$ has the following representation ($\mathbf{A} = curl^2$ is the Stokes operator)

$$\mathbf{PJ} = -\mathbf{A}^{-1}\frac{\partial}{\partial x_3}curl. \tag{26}$$

This representation in the periodic (homogeneous) case reduces to $\mathbf{PJ}(e^{ik\cdot x}\mathbf{u}_k) = e^{ik\cdot x}\frac{k_3}{|k|^2}k \times \mathbf{u}_k \equiv e^{ik\cdot x}\frac{k_3}{|k|^2}\mathbf{R}(k)\mathbf{u}_k$ where $\mathbf{u}_k$ is the Fourier coefficient corresponding to wavevector $k = (k_1, k_2, k_3)$ and $\mathbf{R}(k)\mathbf{u}_k = k \times \mathbf{u}_k$. The operator $\mathbf{R}(k)$ becomes diagonal in the helical basis described in Waleffe (1991) (Eq. (3) in his paper). In the case of horizontally inhomogeneous flows a more general representation (26) should be used. From (26) we obtain

$$\exp(f_0\mathbf{PJ}t) = \mathbf{C}(t) - \mathbf{A}^{-\frac{1}{2}}\mathbf{S}(t)curl \tag{27}$$

and

$$curl\exp(f_0\mathbf{PJ}t) = \mathbf{C}(t)curl - \mathbf{A}^{\frac{1}{2}}\mathbf{S}(t) \tag{28}$$

where

$$\mathbf{C}(t) = \cosh(f_0t\mathbf{A}^{-\frac{1}{2}}\frac{\partial}{\partial x_3}), \quad \mathbf{S}(t) = \sinh(f_0t\mathbf{A}^{-\frac{1}{2}}\frac{\partial}{\partial x_3}).$$

We note that $\mathbf{C}(t)$ is an even and $\mathbf{S}(t)$ is an odd operator-valued function. Using (27), we have for the nonlinear term in (25)

$$\begin{aligned}\exp(f_0\mathbf{PJ}t)\mathbf{P}\{\mathbf{U} \times curl\mathbf{U}\} = (\mathbf{C}(t) - \mathbf{A}^{-\frac{1}{2}}\mathbf{S}(t)curl)\mathbf{P}\{\mathbf{U} \times curl\mathbf{U}\} = \\ \mathbf{C}(t)\{\mathbf{U} \times curl\mathbf{U}\} - \mathbf{A}^{-\frac{1}{2}}\mathbf{S}(t)[\mathbf{U}, curl\mathbf{U}] - \nabla\mathbf{q}\end{aligned} \tag{29}$$

since $curl(\mathbf{U} \times curl\mathbf{U}) = [\mathbf{U}, curl\mathbf{U}]$. Here $[\ ,\ ]$ is a commutator of two vector fields: $[\mathbf{U}, curl\mathbf{U}] \equiv (\mathbf{U} \cdot \nabla) curl\mathbf{U} - (curl\mathbf{U} \cdot \nabla)\mathbf{U}$; q is a modified pressure. From (24), (27) and (28) we find that

$$\mathbf{U} = \mathbf{C}(t)\mathbf{u} + \mathbf{A}^{-\frac{1}{2}}\mathbf{S}(t) curl\mathbf{u}, \quad curl\mathbf{U} = \mathbf{C}(t) curl\mathbf{u} + \mathbf{A}^{\frac{1}{2}}\mathbf{S}(t)\mathbf{u}.$$

We substitute these expressions in (29). Then equation (25) becomes

$$\frac{\partial \mathbf{u}}{\partial t} = \mathbf{B}(t, \mathbf{u}, \mathbf{u}) - \nabla q, \quad \nabla \cdot \mathbf{u} = 0. \tag{30}$$

Here $\mathbf{B}(t, \mathbf{u}, \mathbf{u})$ is given by

$$\mathbf{B}(t, \mathbf{u}, \mathbf{u}) = \mathbf{C}(t)\{\mathbf{U} \times curl\mathbf{U}\} - \mathbf{A}^{-\frac{1}{2}}\mathbf{S}(t)[\mathbf{U}, curl\mathbf{U}] =$$

$$\mathbf{C}(t)\{\mathbf{C}(t)\mathbf{u} \times \mathbf{C}(t) curl\mathbf{u}\} - \mathbf{A}^{-\frac{1}{2}}\mathbf{S}(t)[\mathbf{C}(t)\mathbf{u}, \mathbf{C}(t) curl\mathbf{u}] +$$

$$\mathbf{C}(t)\{\mathbf{A}^{-\frac{1}{2}}\mathbf{S}(t) curl\mathbf{u} \times \mathbf{A}^{\frac{1}{2}}\mathbf{S}(t)\mathbf{u}\} - \mathbf{A}^{-\frac{1}{2}}\mathbf{S}(t)[\mathbf{A}^{-\frac{1}{2}}\mathbf{S}(t) curl\mathbf{u}, \mathbf{A}^{\frac{1}{2}}\mathbf{S}(t)\mathbf{u}] + \tag{31}$$

$$\mathbf{C}(t)\{\mathbf{C}(t)\mathbf{u} \times \mathbf{A}^{\frac{1}{2}}\mathbf{S}(t)\mathbf{u}\} - \mathbf{A}^{-\frac{1}{2}}\mathbf{S}(t)[\mathbf{C}(t)\mathbf{u}, \mathbf{A}^{\frac{1}{2}}\mathbf{S}(t)\mathbf{u}] +$$

$$\mathbf{C}(t)\{\mathbf{A}^{-\frac{1}{2}}\mathbf{S}(t) curl\mathbf{u} \times \mathbf{C}(t) curl\mathbf{u}\} - \mathbf{A}^{-\frac{1}{2}}\mathbf{S}(t)[\mathbf{A}^{-\frac{1}{2}}\mathbf{S}(t) curl\mathbf{u}, \mathbf{C}(t) curl\mathbf{u}].$$

Separation of "fast" and "slow" oscillations in (31) is equivalent to a search for resonances which is a geometry dependent problem. One immediate simplification is that odd terms make no contribution to the time-averaged equations. Thus averaging of (30)-(31) reduces to averaging of four even terms

$$\begin{aligned} &\mathbf{C}(t)\{\mathbf{C}(t)\mathbf{u} \times \mathbf{C}(t) curl\mathbf{u}\}, \quad \mathbf{C}(t)\{\mathbf{A}^{-\frac{1}{2}}\mathbf{S}(t) curl\mathbf{u} \times \mathbf{A}^{\frac{1}{2}}\mathbf{S}(t)\mathbf{u}\}, \\ &\mathbf{A}^{-\frac{1}{2}}\mathbf{S}(t)[\mathbf{C}(t)\mathbf{u}, \mathbf{A}^{\frac{1}{2}}\mathbf{S}(t)\mathbf{u}], \quad \mathbf{A}^{-\frac{1}{2}}\mathbf{S}(t)[\mathbf{A}^{-\frac{1}{2}}\mathbf{S}(t) curl\mathbf{u}, \mathbf{C}(t) curl\mathbf{u}]. \end{aligned} \tag{32}$$

It is convenient to work in the basis of the Stokes operator $\mathbf{A}$. The operators $\mathbf{C}(t)$ and $\mathbf{S}(t)$ have a block-diagonal form in this basis. Since $\mathbf{C}(t) = \cosh(f_0 t \mathbf{A}^{-\frac{1}{2}} \frac{\partial}{\partial x_3})$ and $\mathbf{S}(t) = \sinh(f_0 t \mathbf{A}^{-\frac{1}{2}} \frac{\partial}{\partial x_3})$, they become simple oscillations in the basis of $\mathbf{A}$. These oscillations have frequencies $f_0 \frac{j_3}{\sqrt{\lambda_j}}$ where λ_j are the eigenvalues of $\mathbf{A}$ and j_3 is axial wavenumber. Then resonances in (32) are given by

$$\pm \frac{k_3}{\sqrt{\lambda_k}} \pm \frac{m_3}{\sqrt{\lambda_m}} = \frac{n_3}{\sqrt{\lambda_n}}.$$

In the case of periodic (homogeneous) flows the helical basis formed by eigenfunctions of the *curl* operator acting in the space of divergence free vector fields is very

useful. The operator $\mathbf{PJ}$ ($\frac{k_3}{|k|^2}\mathbf{R}(k)$ in Fourier space) becomes diagonal in this basis. In this case we have $\lambda_j = |j|$ where $j = (j_1, j_2, j_3)$ is the wavevector. Then averaging of (30) leads to equations studied by Waleffe (1991). In particular, he argued that in the asymptotic state of rotating homogeneous turbulence interactions are restricted to pairs of wavevectors satisfying resonance conditions ($n = k + m$)

$$\pm\frac{k_3}{|k|} \pm \frac{m_3}{|m|} = \frac{n_3}{|n|}. \tag{33}$$

Now we consider homogeneous (periodic in three directions) flows and discuss equations describing the asymptotic limit of 3D Euler equations in a rotating frame. Both computations and experiments have noted an increase in integral length scales along the rotation axis relative to those in non-rotating turbulence. Increase in the integral length scales has been thought to be a prelude to a Taylor-Proudman reorganization to two-dimensional turbulence. It has been also suggested that this process is self-similar (Squires *et al.* 1993). The 'slow manifold' interactions (interactions which are unaffected by the linear 'rapid' effects of rotation or the inertial waves) are obtained in (33) with $k_3 = m_3 = 0$. These interactions are invariant under scalings of k_3, m_3 in a trivial way. It is reasonable to conjecture that at zero Rossby number the only acting triads in the asymptotic state are those which are invariant under the scalings $k_3 \to \xi k_3$, $m_3 \to \eta m_3$ where ξ and η are arbitrary real numbers. This is called the *selection principle for triad interactions in the asymptotic state.* It is inspired by the observations of Squires *et al.* (1993) on self-similar asymptotic states of rotating homogeneous turbulence. One can easily find solutions of the resonant Eq. (33) obeying the selection principle. These are $\{m_3 = 0, |n| = |k|\}$, $\{k_3 = 0, |n| = |m|\}$ and $\{n_3 = 0, |k| = |m|\}$ with the $+, -$ signs chosen appropriately. Since these interactions are unaffected by scalings of the vertical wavenumber, they remain active even at zero Rossby number. It is possible to show that the interactions $\{n_3 = 0, |k| = |m|\}$ make no contribution to the averaged equations. Defining $k_\perp = (k_1, k_2)$ to be the horizontal wavevector perpendicular to the rotation axis, interactions active in the asymptotic state can be written in the form $\{k_3 = m_3 = 0\}$, $\{m_3 = 0, |n_\perp| = |k_\perp|\}$ and $\{k_3 = 0, |n_\perp| = |m_\perp|\}$. The form of these interaction manifolds suggests splitting the velocity field into two parts, each separately related to the horizontal or vertical velocities. We proceed to define splitting by first defining ω to be vertical (in the direction of rotation) component of the vorticity vector. Then we define splitting of the total velocity $\mathbf{u}$ as follows

$$\mathbf{u} = \tilde{\mathbf{v}} + \mathbf{v} \quad \textit{where} \quad \tilde{\mathbf{v}} = e_3 \times \nabla\tilde{\psi}$$

and $\tilde{\psi}$ is related to ω by the equation $-\Delta\tilde{\psi} = \omega$. Applying averaging to the transformed Euler Eq. (30) (we note that only averaging of the even terms given by (32) is required) and using the selection principle, we obtain equations valid in the asymptotic state. Our analysis is similar to the one presented in Section 2.2 where de-coupling of the divergence free part of the total shallow-water velocity

field was rigorously proved (see Eq. (18)). We find that in the asymptotic limit $\omega(t,x)$ obeys in physical space

$$\frac{\tilde{D}}{\tilde{D}t}\omega = 0 \tag{34}$$

where $\frac{\tilde{D}}{\tilde{D}t}$ is the advective derivative, based on the velocity $\tilde{\mathbf{v}} = e_3 \times \nabla\tilde{\psi}$ where $-\Delta\tilde{\psi} = \omega$. This equation should be compared with Eq. (18). Thus we obtain de-coupling (in the asymptotic state) of the dynamics of $\tilde{\mathbf{v}}$ (two-component and horizontally divergence free). It satisfies classical 2D Euler equations (34). The de-coupling which is linked to the $\tilde{\mathbf{v}}$ part of the total velocity can reflect the rise of an inverse energy cascade. Our future plans include confirmation of inverse cascade using the CTR database. Another avenue is to search for new conservation laws in the asymptotic limit of rotating homogeneous 3D Euler equations similar to the one we found for the long-time averaged shallow-water equations (Section 2.2, Eq. (20)). One possible approach for determining new conservation laws would be to derive the long-time averaged Euler equations from a variational principle.

REFERENCES

BROWNING, G. L., HOLLAND, W. R., KREISS, H.-O., & WORLEY, S. J. 1990 An accurate hyperbolic system for approximately hydrostatic and incompressible oceanographic flows. *Dyn. Atm. Oceans.* **14,** 303.

CAMBON C., MANSOUR N. N., & SQUIRES K. D. 1994 Anisotropic structure of homogeneous turbulence subjected to uniform rotation. *Proc. 1994 Summer Program.* Center for Turbulence Research, NASA Ames/Stanford Univ.

HALE, J. K. 1980 *Ordinary Differential Equations.* Krieger Publishing Company.

HOPFINGER, E. J. 1989 Turbulence and vortices in rotating fluids. *Theor. and Appl. Mech.* **125,** 117.

PEDLOSKY, J. 1979 *Geophysical Fluid Dynamics.* Springer-Verlag.

SQUIRES K. D., CHASNOV J. R., MANSOUR N. N., & CAMBON C. 1993 Investigation of the asymptotic state of rotating turbulence using large-eddy simulation. *Annual Research Briefs.* Center for Turbulence Research, NASA Ames/Stanford Univ.

WALEFFE, F. 1991 Non-linear interactions in homogeneous turbulence with and without background rotation. *Annual Research Briefs - 1991.* Center for Turbulence Research, NASA Ames/Stanford Univ.

WIGGINS, S. 1990 *Introduction to Applied Nonlinear Dynamical Systems and Chaos.* Springer-Verlag.

Center for Turbulence Research
Proceedings of the Summer Program 1994

N95-21058

On the asymptotic similarity of rotating homogeneous turbulence

By K. D. Squires[1], J. R. Chasnov[2] AND N. N. Mansour[3]

Asymptotic similarity states at large Reynolds numbers and small Rossby numbers in rotating homogeneous turbulence are investigated using the database obtained from large-eddy simulations of the incompressible Navier-Stokes equations. Previous work has shown that the turbulence kinetic energy and integral length scales are accurately described by simple scaling laws based on the low wavenumber part of the three-dimensional energy spectrum (Squires *et al.* 1994). The primary interest of the present study is to search for spectrum similarity in the asymptotic state. Four independent energy spectra are defined. It is shown that rescaling of these energy spectra in the asymptotic regime will collapse three out of the four spectra. The spectrum which does not collapse is a function only of the vertical wavenumber and corresponds to two-component motions in the plane normal to the rotation axis. Detailed investigation of the cause of this anomalous behavior reveals the existence of a strong reverse cascade of energy from small-to-large scales of the two-dimensional, two-component motions. This feature of the rotating flow is presumably linked to the lack of a complete similarity state, though further study of this issue is required.

1. Introduction

Solid-body rotation of initially isotropic turbulence represents the most basic turbulent flow whose structure is altered by system rotation but without the complicating effects introduced by mean strains or flow inhomogeneities. Squires, Chasnov, Mansour & Cambon (1994) (referred to as SCMC throughout this manuscript) examined the long-time, asymptotic evolution of rotating homogeneous turbulence at large Reynolds numbers and small Rossby numbers. They found that the kinetic energy decay exponent was reduced by approximately a factor of two relative to its value in non-rotating turbulence and was independent of the rotation rate. SCMC also found that the integral length scales undergo power-law growth and that the evolution of both the kinetic energy and length scales in the asymptotic regime is accurately described using simple scaling laws based on the invariants of the low wavenumber part of the initial energy spectrum.

1 The University of Vermont
2 The Hong Kong University of Science and Technology
3 NASA Ames Research Center

The scaling laws of the kinetic energy and integral length scales deduced by SCMC suggest the existence of an asymptotic similarity state in rotating homogeneous turbulence. Since a similarity state permits prediction of the flow evolution using a simple rescaling of the statistics, existence of asymptotic similarity states enables prediction of the ultimate statistical evolution of the flow without detailed knowledge of non-linear transfer processes. Similarity states thus imply a certain universal character to a flow which may ultimately simplify modeling of complex turbulent flows at high Reynolds numbers.

The objective of the present work, therefore, is to search an asymptotic similarity state for the energy spectra. In §2 an overview of the LES database used in this study is summarized. Also presented in §2 is the time development of the kinetic energy power-law exponent, integral length scales, and asymptotic scaling laws obtained from both dimensional analysis and the simulation database. The reader is referred to Squires *et al.* (1993, 1994) for a more complete discussion. In §3 the asymptotic spectrum similarity is analyzed and tested using the LES database.

2. Database overview and scaling laws

2.1 Database overview

The database used in the present study was obtained using large-eddy simulation of the incompressible Navier-Stokes equations in a rotating frame of reference. The use of a large-eddy simulation with zero molecular viscosity ensures that the flows considered are nominally at infinite Reynolds numbers. For purposes of discussion the vertical (x_3) axis is taken along the axis of rotation. The governing equations were solved using the pseudo-spectral method developed by Rogallo (1981). Subgrid-scale motions were parameterized using a spectral-eddy viscosity modified for system rotation (Kraichnan 1976, Chollet & Lesieur 1981, Aupoix 1984). Calculations were performed from isotropic Gaussian initial conditions using an initial energy spectrum of the form

$$E(k,0) = \frac{1}{2} C_s \frac{u_0^2}{k_p} \left(\frac{k}{k_p}\right)^s \exp\left[-\frac{1}{2} s \left(\frac{k}{k_p}\right)^2\right], \tag{1}$$

where C_s is given by

$$C_s = \sqrt{\frac{2}{\pi}} \frac{s^{\frac{1}{2}(s+1)}}{1 \cdot 3 \cdot \ldots \cdot (s-1)} \tag{2}$$

and k_p is the wavenumber at which the initial energy spectrum is maximum. SCMC performed simulations with $s = 2$ and $s = 4$, corresponding to the initial energy spectrum having a low wavenumber form proportional to either k^2 or k^4.

Simulations were performed using resolutions of $128 \times 128 \times 512$ on a computational domain which is four times longer along the rotation axis than in the other directions. This yields an isotropic grip in physical space, but permits the development of large-scale anisotropies without compromising the usefulness of the computational results. The maximum wavenumber in each of the three coordinate

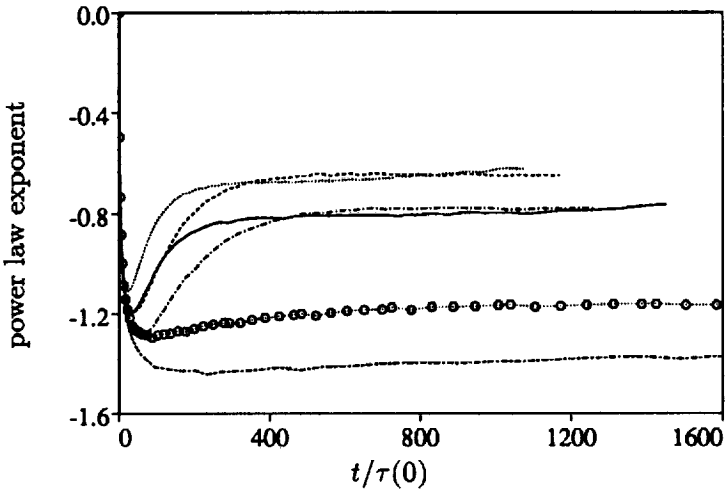

FIGURE 1. Time development of the power-law exponent of $\langle \mathbf{u}^2 \rangle$ in rotating turbulence. k^2 spectrum: o·····o $\Omega = 0$; - - - - $\Omega = 0.5$; ····· $\Omega = 1.0$. k^4 spectrum: —-— $\Omega = 0$; —·— $\Omega = 0.5$; ——— $\Omega = 1.0$.

directions was 95, the initial root-mean-square velocity fluctuation u_0 was 1/2, and the wavenumber at which the initial spectrum was initially maximum, k_p, was 75. For each spectrum type, i.e., low wavenumber part proportional to k^2 or k^4, simulations results are available for three rotation rates, $\Omega = 0$, 0.5, and 1.0. The flows were evolved over a sufficiently long period so that the effects of rotation on the flow dynamics were clearly evident, and the kinetic energy decay and integral length-scale growth approximated power-law forms. This corresponds to an evolution of the flow to low Rossby numbers, where the Rossby number is a measure of the relative strength of inertial forces to Coriolis forces.

2.2 Statistical evolution and scaling laws

The effect of rotation on the evolution of the turbulence kinetic energy ($\langle \mathbf{u}^2 \rangle$) can be illustrated through examination of the power-law exponent, n (in $\langle \mathbf{u}^2 \rangle \propto t^{-n}$, see Fig. 1). In Fig. 1, the time axis is made dimensionless using the eddy turnover time in the initial field

$$\tau(0) = L_u(0)/\langle \mathbf{u}^2 \rangle^{1/2} \tag{3}$$

where $L_u(t)$ is the velocity integral scale at time t defined as

$$L_u(t) = \frac{\pi}{2} \frac{\int_0^\infty k^{-1} E(k,t) dk}{\int_0^\infty E(k,t) dk}. \tag{4}$$

Power-law exponents have been plotted for each initial spectrum type and rotation rate used in the calculations. It is evident from Fig. 1 that following an initial transient the power-law exponent becomes independent of time. Comparison of the power-law exponents for both initial spectrum types demonstrates the reduction

in the decay rate of kinetic energy in rotating turbulence. It is also clear from Fig. 1 that in the asymptotic regime the power-law exponent of the kinetic energy is independent of the rotation rate provided the rotation is non-zero. The value of the exponent depends only on the form of the initial energy spectrum.

It is possible to derive the appropriate asymptotic scalings of $\langle \mathbf{u}^2 \rangle$ for non-rotating turbulence using dimensional analysis (e.g., see Chasnov 1994). For the rotating flow, assuming that non-linear triadic interactions are correlated over a time scale directly proportional to Ω, SCMC showed that the asymptotic scalings for the kinetic energy are

$$\langle \mathbf{u}^2 \rangle \propto B_0^{\frac{2}{5}} t^{-\frac{6}{5}} (\Omega t)^{\frac{3}{5}} \quad (k^2 \text{ spectrum}) \tag{5}$$

$$\langle \mathbf{u}^2 \rangle \propto B_2^{\frac{2}{7}} t^{-\frac{10}{7}} (\Omega t)^{\frac{5}{7}} \quad (k^4 \text{ spectrum}). \tag{6}$$

For the k^2 spectrum B_0 is invariant while for the k^4 initial conditions B_2 is time dependent. However, the time dependence of B_2 is weak relative to the overall turbulence decay. It is assumed invariant for the purposes of developing asymptotic scalings. The scaling laws (5) and (6) predict that in rotating turbulence the kinetic energy decay exponent is reduced by a factor of two, relative to its value in the non-rotating flow. As shown by Fig. 1, simulation results agree with these predictions.

SCMC also examined the development of the integral length scales. These length scales are obtained from integration of the two-point correlation function

$$L_{\alpha\alpha;\beta} = \frac{1}{\langle u_\alpha^2 \rangle} \int \langle u_\alpha(\mathbf{x}) u_\alpha(\mathbf{x} + r\mathbf{e}_\beta) \rangle dr_\beta \,, \tag{7}$$

where $\mathbf{e}_\beta$ is the unit vector in the β direction, and α, $\beta = 1$, 2, or 3. The length scale $L_{\alpha\alpha;\beta}$ measures the correlation between the α velocity components with separation in the β direction. SCMC examined the evolution of five length scales. In the horizontal plane these integral scales are

$$L_{h1} = \frac{1}{2}(L_{11,1} + L_{22,2}), \quad L_{h2} = \frac{1}{2}(L_{11,2} + L_{22,1}), \quad L_{h3} = \frac{1}{2}(L_{33,1} + L_{33,2}). \tag{8}$$

The integral scale L_{h1} measures the horizontal correlation of longitudinal horizontal velocities, L_{h2} the horizontal correlation of lateral horizontal velocities, and L_{h3} the horizontal correlation of vertical velocities. For vertical correlations (along the axis of rotation) there are two independent integral scales

$$L_{v1} = \frac{1}{2}(L_{11,3} + L_{22,3}), \qquad L_{v2} = L_{33,3} \,, \tag{9}$$

where L_{v1} measures the vertical correlation of horizontal velocities and L_{v2} the vertical correlation of vertical velocities.

Shown in Fig. 2 is the time development of the integral scales from SCMC for the highest rotation rate used with each initial condition type. Also shown for reference is the slope corresponding to the asymptotic growth rate in non-rotating isotropic

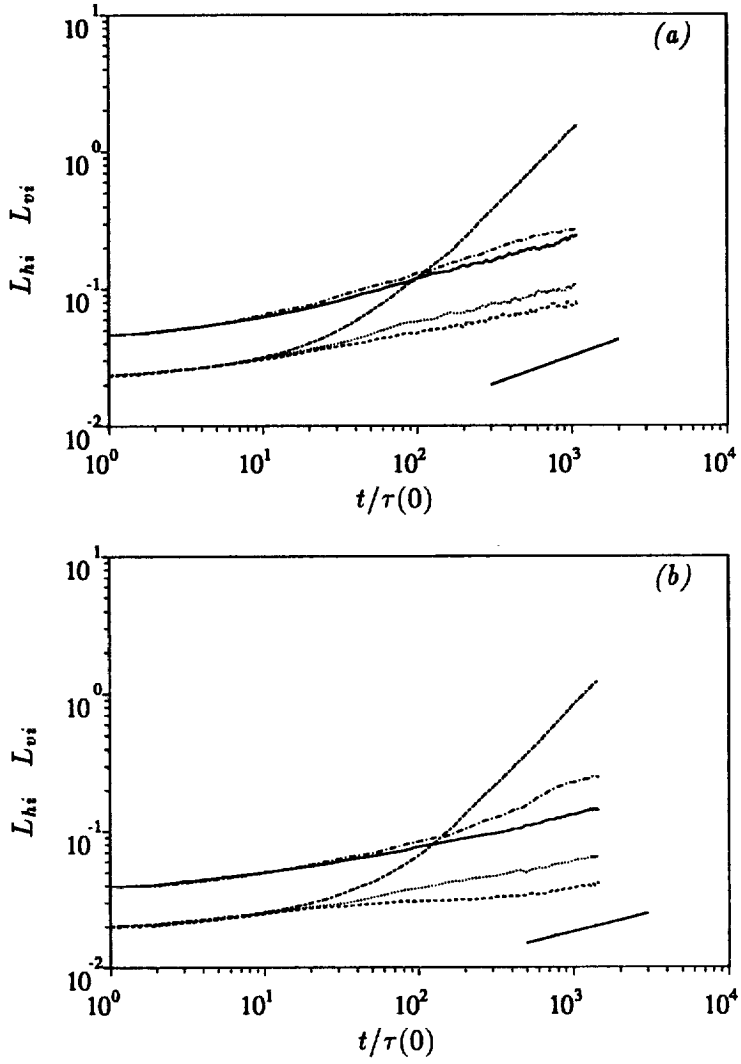

FIGURE 2. Time development of integral length scales in rotating turbulence, $\Omega = 1$. Asymptotic growth rate in non-rotating turbulence also shown in lower portion of figure. —— L_{h1}; ---- L_{h2}; ····· L_{h3}; —·— L_{v1}; —·— L_{v2}. (*a*) k^2 spectrum; (*b*) k^4 spectrum.

turbulence. It is clear from Fig. 2 that L_{v1} grows much more rapidly than all other integral scales. Also, the growth of the other four integral scales appear to be slightly suppressed relative to the non-rotating case. In addition, the simulations provide evidence that all the integral length scales exhibit power-law growth asymptotically and, with the important exception of L_{v1}, the power-law exponents are all the same. Thus, in the horizontal plane there appears to be a single independent length scale, which we denote generically as L_h, whereas there exists two independent length scales in the vertical direction, namely L_{v1} and L_{v2}. SCMC further demonstrated

that the evolution of the integral scales from two simulations of a k^2 spectrum at different rotation rates Ω could be collapsed according to the asymptotic scaling laws

$$L_h \propto B_0^{\frac{1}{5}} t^{\frac{2}{5}} (\Omega t)^{-\frac{1}{5}}, \quad L_{v1} \propto B_0^{\frac{1}{5}} t^{\frac{2}{5}} (\Omega t)^{\frac{3}{5}}, \quad L_{v2} \propto B_0^{\frac{1}{5}} t^{\frac{2}{5}} (\Omega t)^{-\frac{1}{5}}, \tag{10}$$

while for the k^4 spectrum a collapse was achieved using the scaling laws

$$L_h \propto B_2^{\frac{1}{7}} t^{\frac{2}{7}} (\Omega t)^{-\frac{1}{7}}, \quad L_{v1} \propto B_2^{\frac{1}{7}} t^{\frac{2}{7}} (\Omega t)^{\frac{6}{7}}, \quad L_{v2} \propto B_2^{\frac{1}{7}} t^{\frac{2}{7}} (\Omega t)^{-\frac{1}{7}}. \tag{11}$$

3. Asymptotic spectrum similarity

Power-law behavior of both the kinetic energy (Eqs. 5 and 6) and integral length scales (Eqs. 10 and 11) suggest the existence of energy spectra which are asymptotically similar, i.e., the time- and rotation-dependent spectra collapse by appropriately rescaling the wavenumber and spectral density axes. For brevity, we consider here only our results for the k^2 initial conditions. More complete results will be presented in a future publication.

As the first obvious candidate for an asymptotically similar spectrum, we define an axisymmetric energy spectrum as a function of $k_\perp$ and k_3 as

$$\Psi(k_\perp, k_3, t) = \pi k_\perp \langle u_i(\mathbf{k}, t) u_i(\mathbf{k}, t)^* \rangle, \tag{12}$$

where

$$k_\perp = \left(k_1^2 + k_2^2\right)^{\frac{1}{2}} \tag{13}$$

is the horizontal wavenumber perpendicular to the rotation axis, $u_i(\mathbf{k})$ is the Fourier transform of a periodic velocity field $u_i(\mathbf{x})$, * denotes the complex conjugate, and the angular brackets used in (12) denote an average over a horizontal ring in three-dimensional wavespace with center located at a fixed value of k_3. The relationship between the spectrum in (12) and the kinetic energy per unit mass of the fluid is given by

$$\frac{1}{2}\langle \mathbf{u}^2 \rangle = \int_{-\infty}^{\infty} dk_3 \int_0^{\infty} dk_\perp \Psi(k_\perp, k_3, t). \tag{14}$$

An attempt to construct a similarity form directly for the spectrum $\Psi(k_\perp, k_3, t)$ is impeded by the existence of two distinct vertical integral scales in the rotating flow. The choice of an appropriate length scale for rescaling k_3 is thus ambiguous, making it unlikely that the full spectrum $\Psi(k_\perp, k_3, t)$ will be asymptotically similar. We may, however, integrate out the vertical wavenumber from the spectrum defined in (12) to construct an energy spectrum which is a function only of the horizontal wavenumber:

$$\Psi_\perp(k_\perp, t) = \int_{-\infty}^{\infty} dk_3 \Psi(k_\perp, k_3, t). \tag{15}$$

The simulation results have shown that there is only a single horizontal length scale (10) which may be used to scale the horizontal wavenumber $k_\perp$. This allows us to propose the following general form for the similarity state of the spectrum $\Psi_\perp$:

$$\Psi_\perp(k_\perp, t) = \langle \mathbf{u}^2 \rangle L_h \widehat{\Psi}_\perp(L_h k_\perp). \tag{16}$$

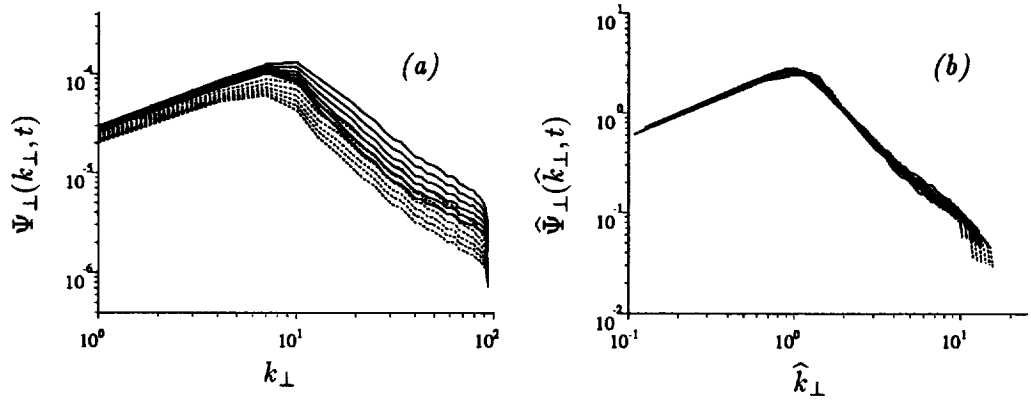

FIGURE 3. Time development of $\Psi_\perp(k_\perp)$. ---- $\Omega = 0.5$; —— $\Omega = 1.0$. (*a*) unscaled; (*b*) scaled.

Making use of the known asymptotic behavior of the kinetic energy (5) and integral scales (10), the similarity state (16) is given explicitly as

$$\Psi_\perp(k_\perp,t) = B_0^{\frac{3}{5}} t^{-\frac{4}{5}} (\Omega t)^{\frac{2}{5}} \widehat{\Psi}_\perp(\widehat{k}_\perp), \qquad \widehat{k}_\perp = B_0^{\frac{1}{5}} t^{\frac{2}{5}} (\Omega t)^{-\frac{1}{5}} k_\perp . \tag{17}$$

Shown in Fig. 3 are the unscaled and scaled spectra $\Psi_\perp(k_\perp,t)$ and $\widehat{\Psi}_\perp(\widehat{k}_\perp,t)$ after the flows have evolved sufficiently to be considered asymptotic in the sense that rotation effects are important (low Rossby numbers) and the statistics follow power-law forms. Spectra from calculations using both non-zero rotation rates have been included in the figures. While the decay with increasing time and the dependence on rotation rate is evident in Fig. 3*a*, the scaled spectra and wavenumbers (17) in Fig. 3*b* show a remarkable collapse, indicating that $\widehat{\Psi}_\perp$ is independent of both time and rotation rate. The results shown in Fig. 3*b* thus confirm the similarity state given by (17). This is a significant result since we have succeeded in reducing the number of independent variables in the problem from four, ($k_\perp$, t, Ω, and B_0), where B_0 represents the effect of initial conditions, to simply one, ($\widehat{k}_\perp$).

We must still confront the difficulty of finding similarity spectra which are functions of the vertical wavenumber k_3. We know from the LES results that two vertical length scales exist, one associated with the horizontal velocities and the other with the vertical velocities. This suggests splitting the energy spectrum into two spectra, each separately related to the horizontal or vertical velocities. A simple splitting, however, does not take into account the constraint imposed by the continuity equation on the flow field. Rather, we proceed to define spectra (Herring 1974) by first projecting the Fourier components of the velocity field onto two unit vectors perpendicular to $\mathbf{k}$ (the velocity component parallel to $\mathbf{k}$ is zero by virtue of the continuity equation):

$$u_i(\mathbf{k}) = \phi_1(\mathbf{k}) e_i^{(1)}(\mathbf{k}) + \phi_2(\mathbf{k}) e_i^{(2)}(\mathbf{k}), \tag{18}$$

where

$$\mathbf{e}^{(1)}(\mathbf{k}) = \frac{\mathbf{k} \times \mathbf{\Omega}}{|\mathbf{k} \times \mathbf{\Omega}|}, \quad \mathbf{e}^{(2)}(\mathbf{k}) = \frac{\mathbf{k} \times \mathbf{e}^{(1)}(\mathbf{k})}{|\mathbf{k} \times \mathbf{e}^{(1)}(\mathbf{k})|}. \tag{19}$$

We note that the field $\phi_1(\mathbf{k})$ consists only of horizontal velocity fluctuations, whereas the field $\phi_2(\mathbf{k})$ contains both horizontal and vertical fluctuations. We then use the scalar fields $\phi_1(\mathbf{k})$ and $\phi_2(\mathbf{k})$ to define energy spectra in analogy to (12):

$$\Psi^{(1)}(k_\perp, k_3, t) = \pi k_\perp \langle \phi_1(\mathbf{k}, t) \phi_1(\mathbf{k}, t)^* \rangle, \tag{20}$$

$$\Psi^{(2)}(k_\perp, k_3, t) = \pi k_\perp \langle \phi_2(\mathbf{k}, t) \phi_2(\mathbf{k}, t)^* \rangle, \tag{21}$$

where we have now separated the energy spectrum into two spectra:

$$\Psi(k_\perp, k_3, t) = \Psi^{(1)}(k_\perp, k_3, t) + \Psi^{(2)}(k_\perp, k_3, t). \tag{22}$$

The significance of this separation can be seen by expressing the integral length scales L_{v1} and L_{v2} of (9) in terms of $\Psi^{(1)}$ and $\Psi^{(2)}$, i.e.,

$$L_{v1} = \frac{\pi}{\langle u_1^2 + u_2^2 \rangle} \int_0^\infty dk_\perp \Psi^{(1)}(k_\perp, 0), \tag{23}$$

and

$$L_{v2} = \frac{\pi}{\langle u_3^2 \rangle} \int_0^\infty dk_\perp \Psi^{(2)}(k_\perp, 0). \tag{24}$$

The LES results show that the horizontal and vertical mean-square velocity fluctuations decay asymptotically with the same power-law form, so that (23) and (24) serve the hopeful purpose of matching the two independent vertical integral scales to the two different spectra.

In analogy to the similarity form given in (16), we now postulate the following general similarity states of the form

$$\Psi^{(1)}(k_\perp, k_3, t) = \langle \phi_1^2 \rangle l_1^h l_1^v \widehat{\Psi}^{(1)}(l_1^h k_\perp, l_1^v k_3), \tag{25a}$$

$$\Psi^{(2)}(k_\perp, k_3, t) = \langle \phi_2^2 \rangle l_2^h l_2^v \widehat{\Psi}^{(2)}(l_2^h k_\perp, l_2^v k_3), \tag{25b}$$

where $\langle \phi_1^2 \rangle$, l_1^h, l_1^v, and $\langle \phi_2^2 \rangle$, l_2^h, l_2^v are the mean-square fluctuations and horizontal and vertical integral scales associated with the $\Psi^{(1)}$ and $\Psi^{(2)}$ spectra, respectively. The relations between the mean-square fluctuations, the integral scales, and the spectra are given for reference by

$$\langle \phi_{1,2}^2 \rangle = \int_{-\infty}^\infty dk_3 \int_0^\infty dk_\perp \Psi^{(1,2)}(k_\perp, k_3, t), \tag{26}$$

and

$$l_{1,2}^v = \frac{\pi}{\langle \phi_{1,2}^2 \rangle} \int_0^\infty dk_\perp \Psi^{(1,2)}(k_\perp, 0, t), \quad l_{1,2}^h = \frac{1}{\langle \phi_{1,2}^2 \rangle} \int_{-\infty}^\infty dk_3 \int_0^\infty \frac{\Psi^{(1,2)}(k_\perp, k_3, t)}{k_\perp}. \tag{27}$$

We have computed the amplitudes and integral scales given by (26) and (27) from the LES database. The mean-square values $\langle\phi_1^2\rangle$ and $\langle\phi_2^2\rangle$ decay asymptotically at the same rate as the total kinetic energy per unit mass as given in (5), and the horizontal integral scales l_1^h and l_2^h and vertical integral scales l_1^v and l_2^v grow asymptotically as L_h (for both horizontal integral scales) and L_{v1} and L_{v2}, respectively, as given by (10).

Although the similarity states proposed in (25) appear to be reasonable, a closer examination reveals a further problem. We recall that the asymptotic form of the energy and integral scales were constructed on the basis of the invariant B_0, related to the form of the energy spectrum near zero wavenumber. Assuming a flow field starting from isotropic initial conditions (as in our simulations), the forms of the spectra $\Psi^{(1)}(k_\perp, k_3, t)$ and $\Psi^{(2)}(k_\perp, k_3, t)$ near $k = 0$ are

$$\begin{aligned}\Psi^{(1)}(k_\perp, k_3, t) &= 2\pi k_\perp (B_0 + O(k)),\\ \Psi^{(2)}(k_\perp, k_3, t) &= 2\pi k_\perp (B_0 + O(k)),\end{aligned} \tag{28}$$

where $O(k)$ represents terms which vanish as $k = (k_\perp^2 + k_3^2)^{1/2} \to 0$ and B_0 is independent of time. Near $k = 0$ the similarity forms of the spectra must necessarily be

$$\widehat{\Phi}^{(1)}(l_1^h k_\perp, l_1^v k_z) \sim 2\pi l_1^h k_\perp, \qquad \widehat{\Phi}^{(2)}(l_2^h k_\perp, l_2^v k_z) \sim 2\pi l_2^h k_\perp; \tag{29}$$

and substituting (28) and (29) into (25) yields

$$B_0 \propto \langle\phi_1^2\rangle (l_1^h)^2 l_1^v, \qquad B_0 \propto \langle\phi_2^2\rangle (l_2^h)^2 l_2^v. \tag{30}$$

Eq. (30) is an important result in that it provides two additional constraints on the allowed form of an asymptotic similarity state based on the invariant B_0. The second constraint of (30) can be seen to be satisfied by the LES results, where

$$\langle\phi_2^2\rangle \propto B_0^{\frac{2}{5}} t^{-\frac{6}{5}} (\Omega t)^{\frac{3}{5}}, \quad l_2^h \propto B_0^{\frac{1}{5}} t^{\frac{2}{5}} (\Omega t)^{-\frac{1}{5}}, \quad l_2^v \propto B_0^{\frac{1}{5}} t^{\frac{2}{5}} (\Omega t)^{-\frac{1}{5}}. \tag{31}$$

However, the first constraint of (30) is widely violated by the LES results due to the rapid growth in the vertical integral scale:

$$\langle\phi_1^2\rangle \propto B_0^{\frac{2}{5}} t^{-\frac{6}{5}} (\Omega t)^{\frac{3}{5}}, \quad l_1^h \propto B_0^{\frac{1}{5}} t^{\frac{2}{5}} (\Omega t)^{-\frac{1}{5}}, \quad l_2^v \propto B_0^{\frac{1}{5}} t^{\frac{2}{5}} (\Omega t)^{\frac{3}{5}}, , \tag{32}$$

so that

$$\langle\phi_1^2\rangle (l_1^h)^2 l_1^v \propto B_0 (\Omega t)^{\frac{4}{5}}.$$

The similarity state in (25a) constructed for $\Phi^{(1)}(k_\perp, k_3, t)$ must thus be in error. However, the similarity state in (25b) constructed for $\Phi^{(2)}(k_\perp, k_3, t)$ may possibly be correct in so far as the constraint given by the second of (30) is satisfied.

To test the correctness of the similarity state for $\Phi^{(2)}(k_\perp, k_3, t)$, we isolate the troublesome k_3 dependence of the spectrum by integrating over $k_\perp$ to obtain the (usual) one-dimensional spectrum

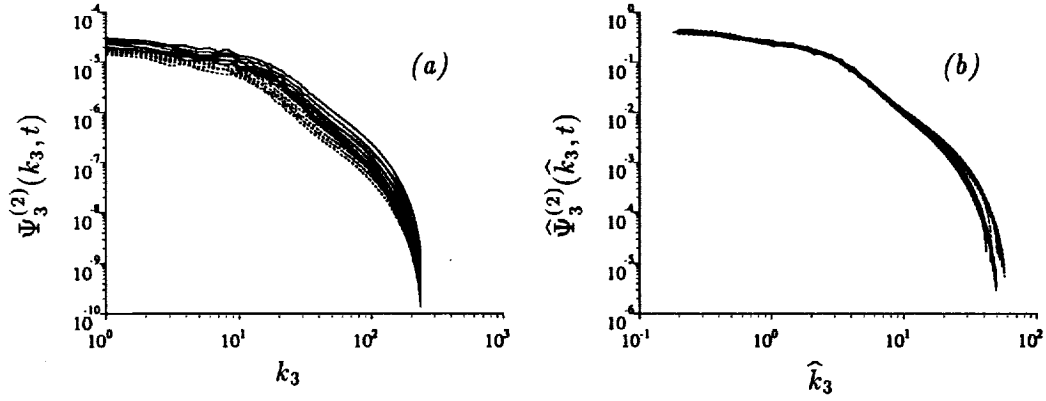

FIGURE 4. Time development of $\Psi_3^{(2)}(k_3)$. ---- $\Omega = 0.5$; —— $\Omega = 1.0$. (*a*) unscaled; (*b*) scaled.

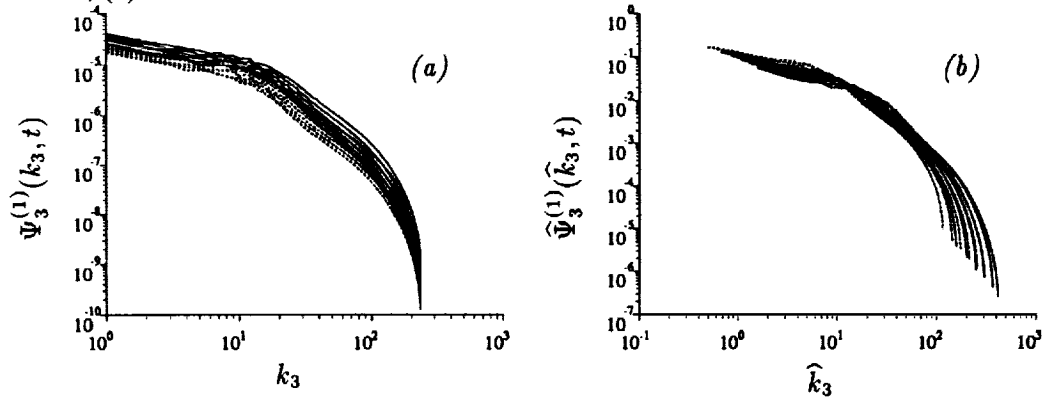

FIGURE 5. Time development of $\Psi_3^{(1)}(k_3)$. ---- $\Omega = 0.5$; —— $\Omega = 1.0$. (*a*) unscaled; (*b*) scaled.

$$\Psi_3^{(2)}(k_3,t) = \int_0^\infty dk_\perp \Psi^{(2)}(k_\perp,k_3,t); \tag{33}$$

and the corresponding similarity state is postulated to be

$$\Psi_3^{(2)}(k_3,t) = \langle\phi_2^2\rangle l_2^v \widehat{\Psi}_\perp(l_2^v k_3), \tag{34}$$

which using (31), may be written explicitly as

$$\Psi_3^{(2)}(k_3,t) = B_0^{\frac{3}{5}} t^{-\frac{4}{5}} (\Omega t)^{\frac{2}{5}} \widehat{\Psi}_3^{(2)}(\widehat{k}_3), \qquad \widehat{k}_3 = B_0^{\frac{1}{5}} t^{\frac{2}{5}} (\Omega t)^{-\frac{1}{5}} k_3 . \tag{35}$$

Shown in Fig. 4 are the unscaled spectra $\Psi_3^{(2)}(k_3,t)$ and the scaled spectra $\widehat{\Psi}_3^{(2)}(\widehat{k}_3,t)$ obtained from (35). As before, results for both non-zero rotation rates are shown in the figure. In Fig. 4*a* the spectra at different times and rotation rates

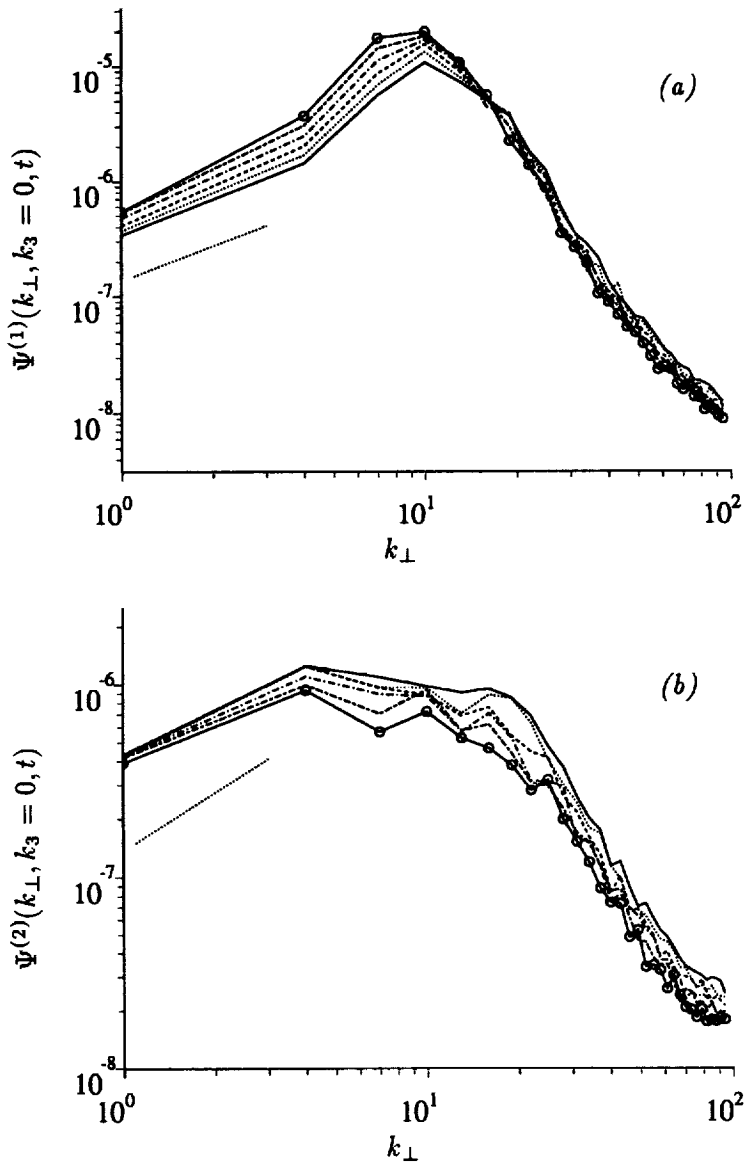

FIGURE 6. Time development of $\Psi^{(1)}(k_\perp, k_3)$ (Fig. 6a) and $\Psi^{(2)}(k_\perp, k_3)$ (Fig 6b) for $k_3 = 0$ and $\Omega = 1.0$. Increasing time is from ——— to o——o ; ····· asymptotic behavior as $k_\perp \to 0$ (Eqn. 29).

are clearly distinguishable whereas in Fig. 4*b* the spectra $\widehat{\Psi}_3^{(2)}(\widehat{k}_3, t)$ for the times plotted and both Ω collapse onto a single curve. Together with the previous results of Fig. 3, we have thus confirmed the complete similarity state of $\Psi^{(2)}(k_\perp, k_3, t)$ given by (25b).

For comparison, the troublesome one-dimensional spectrum $\Psi^{(1)}(k_3, t)$ and the

scaled spectrum corresponding to the assumed similarity form given by (25a) are shown in Fig. 5. As anticipated from the inconsistency of the assumed similarity form with the constraint given by the first of (30), the rescaling shown in Fig. 5*b* does not collapse $\widehat{\Psi}_3^{(1)}(\widehat{k}_3)$ onto a single curve.

Thus we have demonstrated spectral similarity for three out of four spectra, namely $\Psi_\perp^{(1)}(k_\perp, t)$, $\Psi_\perp^{(2)}(k_\perp, t)$, and $\Psi_3^{(2)}(k_3, t)$ are asymptotically similar, whereas $\Psi_3^{(1)}(k_3, t)$ is decidedly not.

Further evidence of the anomalous asymptotic behavior of $\Psi_3^{(1)}$ is provided in Fig. 6. Shown in the figure, for $\Omega = 1.0$, are $\Psi^{(1)}$ (Fig. 6*a*) and $\Psi^{(2)}$ (Fig. 6*b*) as a function of $k_\perp$ for $k_3 = 0$. From (28), the spectra in these figures should follow the asymptotic form $\Psi^{(1,2)}(k_\perp, k_3 = 0, t) \sim 2\pi k_\perp B_0$ as $k_\perp \to 0$. Considering Fig. 6*b*, $\Psi^{(2)}(k_\perp, 0, t)$ decays as one would expect from a decaying three-dimensional turbulence. The energy at larger values of $k_\perp$ decay more rapidly than the energy at smaller values, and consequently the peak of the spectrum systematically moves to lower wavenumbers. The invariance of the form of the spectrum as $k_\perp \to 0$ is respected. The spectrum $\Psi^{(1)}(k_\perp, 0, t)$ shown in Fig. 6*a*, however, behaves much differently. A strong increase in the energy at small values of $k_\perp$ is clearly evident. The invariance of the spectrum as $k_\perp \to 0$ is a rigorous result, yet appears to be irrelevant to the time-development of this spectrum. It is important to note that the spectrum $\Psi^{(1)}(k_\perp, 0, t)$ corresponds to two-dimensional, two-component motions, and what we are observing in Fig. 6*a* is apparently a reverse cascade of energy from small to large scales, well-known within the context of two-dimensional turbulence. The existence of a reverse cascade may be the reason why a similarity state based on the invariance of the low wavenumber coefficient does not develop for the $\Psi^{(1)}$ spectrum. The establishment of a two-dimensional reverse cascade is an important feature of three-dimensional turbulence in a rotating frame, and obviously requires a deeper understanding than we have achieved thus far. Other recent investigations (Bartello *et al.* 1994; Hossain 1994) have also confronted this very question, although from a different perspective than the present work.

Finally, the strong reverse cascade of energy of the two-dimensional, two-component motions has interesting implications as to the asymptotic structural evolution of rotating homogeneous turbulence. The reader is referred to Cambon, Mansour & Squires (1994) (contained in this proceedings) for further discussion of these issues.

Acknowledgments

The authors are grateful to Dr. R. Rogallo and Dr. A. Wray for their assistance with the VECTORAL compiler and homogeneous turbulence code used during the course of this study. Helpful discussions with C. Cambon, A. Mahalov, and W. C. Reynolds are also appreciated. K. D. S. was partially supported for this work by the American Society of Engineering Education.

REFERENCES

AUPOIX, B. 1984 Eddy viscosity subgrid-scale models for homogeneous turbulence. *Proc. of Macroscopic Mod. Turb. Flows, Lecture Notes in Phys.* **230,** 45.

BARTELLO, P., MÉTAIS, O. & LESIEUR, M. 1994 Coherent structures in rotating three-dimensional turbulence. *J. Fluid Mech.* **273,** 1.

CAMBON, C. & JACQUIN, L. 1989 Spectral approach to non-isotropic turbulence subjected to rotation. *J. Fluid Mech.* **202,** 295–317.

CAMBON, C., MANSOUR, N. N. & SQUIRES, K. D. 1994 Anisotropic structure of homogeneous turbulence subjected to uniform rotation. *Proc. of the 1994 Summer Program,* NASA/Stanford Center for Turbulence Research.

CHOLLET, J. P. & LESIEUR, M. 1981 Parameterization of small scales of three-dimensional isotropic turbulence utilizing spectra closures. *J. Atmos. Sci.* **38,** 2747.

CHASNOV, J. R. 1994 Similarity states of passive scalar transport in isotropic turbulence. *Phys. Fluids.* **6,** 1036.

HERRING, J. R. 1974 Approach of axisymmetric turbulence to isotropy. *Phys. Fluids.* **17,** 859.

HOSSAIN, M. 1994 Reduction in the dimensionality of turbulence due to a strong rotation. *Phys. Fluids A.* **6,** 1077.

KRAICHNAN, R. H. 1976 Eddy viscosity in two and three dimensions. *J. Atmos. Sci.* **33,** 1521.

ROGALLO, R. S. 1981 Numerical experiments in homogeneous turbulence. *NASA TM 81315.*

SQUIRES, K. D., CHASNOV, J. R., MANSOUR, N. N. & CAMBON, C. 1993 Investigation of the asymptotic state of rotating turbulence using large-eddy simulation. *Annual Research Briefs,* NASA/Stanford Center for Turbulence Research, 157-170.

SQUIRES, K. D., CHASNOV, J. R., MANSOUR, N. N. & CAMBON, C. 1994 The asymptotic state of rotating homogeneous turbulence at high Reynolds number. *AGARD Conf. Proc. CP-551,* in press.

S24-34
29754
N95-21059
397
P. 24

Center for Turbulence Research
Proceedings of the Summer Program 1994

Anisotropic structure of homogeneous turbulence subjected to uniform rotation

By C. Cambon[1], N. N. Mansour[2] AND K. D. Squires[3]

Large-eddy simulation results are used to investigate the development of anisotropies and the possible transition towards a quasi two-dimensional state in rotating turbulence at high Reynolds number. The present study demonstrates the existence of two transitions that are identified by two Rossby numbers. The first transition marks the onset of anisotropic effects and corresponds to a macro Rossby number Ro^L (based on a longitudinal integral length scale) near unity. A second transition can be defined in terms of a lower bound of a micro-Rossby number Ro^ω also near unity (defined in this work as the ratio of the rms fluctuating vorticity to background vorticity) and corresponds to a continued development of anisotropy but with an increasing emergence of those indicators based on the pure two-dimensional component of the flow, e.g., integral length scales measured along the rotation axis. Investigation of the vorticity structure shows that the second transition is also characterized by an increasing tendency for alignment between the fluctuating vorticity vector and the basic angular velocity vector with a preference for corrotative vorticity.

1. Introduction

Turbulence plays an important role in the performance of many engineering systems where the mean flow is dominated by rotation, technologically relevant examples include the flow in turbomachines as well as reciprocating engines with swirl and tumble. The difficulty in evaluating the performance of these systems is due primarily to their complex nature and to the poor performance of turbulence models used for prediction of the flow fields encountered in these systems. The principal reason for deficiencies in turbulence modeling of rotating flows is in turn related to the fact that mean rotation has an indirect and subtle effect on quantities such as the turbulence kinetic energy and its dissipation rate, i.e., mean rotation does not appear explicitly in the transport equations for either quantity. However, accounting for system rotation is crucial since it alters the nonlinear interactions among turbulent scales. Thus, a better understanding of the effects of system rotation on turbulent flows is needed to properly guide the development of turbulence models.

A flow particularly well suited for increasing our fundamental understanding is rotating homogeneous turbulence since the effect of system rotation can be examined

1 Ecole Centrale de Lyon, France
3 NASA-Ames Research Center
3 The University of Vermont

PRECEDING PAGE BLANK NOT FILMED PAGE 396 INTENTIONALLY

independent of other complicating influences such as mean gradients, body forces (other than the Coriolis force), wall effects, or organized structures. A topic central to studies of rotating homogeneous turbulence is the generation of anisotropy by background rotation and possible transition towards a quasi two-dimensional state. Important in this regard is that it can be shown that the initial breaking of isotropy arises ultimately from nonlinear interactions which are modified by system rotation (Cambon & Jacquin 1989). Thus, the range of Reynolds and Rossby numbers for which anisotropy will develop is not easily predicted. Furthermore, the typical measures used to describe anisotropy, e.g., that of the Reynolds stress and length scales, require a detailed two-point approach which should also include angular dependence of the distribution of the energy density in wave space. It is also important to emphasize that the Taylor-Proudman theorem cannot predict a transition from a three-dimensional to a two-dimensional structure at zero Rossby number, but only shows that the 'slow manifold' (i.e., the manifold which is unaffected by the linear 'rapid' effects of rotation or inertial waves) is the 'two-dimensional manifold' (see Proudman 1916, Cambon, Mansour & Godeferd 1994).

Insight into the development of anisotropic features in rotating turbulence was examined using direct numerical simulation (DNS) and large-eddy simulation (LES) by Bardina, Ferziger & Rogallo (1984). They found that anisotropy is primarily reflected by the integral length scales whereas the Reynolds stress tensor remained quasi-spherical. Bardina *et al.* did not address, however, the underlying anisotropic spectral shape nor the relevant parameter regime for anisotropy development. Several investigators have used both theoretical and experimental approaches (Jacquin, Leuchter & Geoffroy 1989, Cambon & Jacquin 1989, and Jacquin, Leuchter, Cambon & Mathieu 1990) to investigate anisotropic effects in rotating turbulence, including a non-isotropic spectral description by Cambon (1982) which provided further insight into characterizing the key anisotropy indicators and the relevant parameter ranges over which anisotropic effects would develop. These studies showed that the most important indicators are expressed using the integral length scales with vertical (along the basic rotation axis) separation and vertical or horizontal velocity components. These previous works also support the conjecture that anisotropy in rotating turbulence is triggered when a macro-Rossby number Ro^L becomes smaller than unity. An optimal collapse of measurements was obtained by defining Ro^L as

$$Ro^L = \frac{\sqrt{\langle u_3^2 \rangle}}{2\Omega_3 L_{33}^3} \tag{1}$$

where Ω_3 is the angular velocity of the rotating frame (without loss of generality we choose the vertical direction x_3 along the rotation vector and in what follows we shall drop the subscript from the definition, i.e., $\Omega = \Omega_3$), u_i is the velocity fluctuation, and $\langle\rangle$ denotes statistical averaging. The integral length scales are defined using the two-point correlation

$$L_{ij}^n = \frac{\int_0^\infty \langle u_i(\mathbf{x},t) u_j(\mathbf{x}+r\mathbf{n},t)\rangle dr}{\langle u_i(\mathbf{x},t) u_j(\mathbf{x},t)\rangle} \tag{2}$$

where no summation is implied in the above definition and **n** is the unit vector in the direction referred to by the superscript n.

Evidence of a second transition in the development of anisotropic features in rotating turbulence has come mainly from computational approaches, both DNS as well as EDQNM, where high rotation rates are more easily attained than in laboratory experiments (e.g., see Mansour, Cambon & Speziale 1991a,b). The second transition corresponds to the lower limit of an intermediate range of Rossby numbers in which nonlinear, and therefore the non-isotropic, effects of rotation are statistically insignificant. It is conjectured that the second transition occurs when a micro-Rossby number $Ro^\lambda \sim u'/(2\Omega\lambda)$ (based on a Taylor microscale λ) is smaller than 1. For $Ro^\lambda < 1$ non-linear interactions are negligible, e.g., nearly zero derivative skewness, and the flow can be accurately predicted using Rapid Distortion Theory (RDT). It is important to point out that the RDT solution cannot lead to the development of anisotropy, e.g., Speziale *et al.* (1987) have shown that starting with an initially isotropic flow, the flow remains isotropic under very rapid rotation. Mansour *et al.* (1991c) have shown that while rotation will change the anisotropy of the Reynolds stress tensor due to the scrambling effects of rotation, it does not lead to the generation of new anisotropy. It should also be pointed out that one can predict a reduction of the dimensionality, which is part of the anisotropy development (Cambon & Jacquin 1989), of rotating turbulence by consideration of resonant triads selected at very low Rossby number (Waleffe 1991). However, it is not possible to predict the range of Rossby numbers over which the reduction may occur nor the measure of the manifold of resonant triads relative to all possible triads using this approach. Since the Taylor microscale can be defined from different components in anisotropic turbulence, similar to the integral length scales, it is more convenient to mark the second transition using a micro-Rossby number defined in terms of the vorticity

$$Ro^\omega = \frac{\sqrt{\langle \omega_i \omega_i \rangle}}{2\Omega} \tag{3}$$

where $\omega_i = \epsilon_{ijk} u_{k,j}$. Note that Ro^λ and Ro^ω are proportional since $\omega' \sim u'/\lambda$.

Based upon the summary presented above, there exists evidence to support the simple scheme of an intermediate range of Rossby numbers over which anisotropies in rotating turbulence will develop. This range is marked by a macro-Rossby number close to 1 (where the macro-Rossby number is based on "vertical" quantities) for the upper bound and a micro-Rossby close to 1 for the lower bound. The intermediate range of Rossby numbers involves the Reynolds number through the ratio L/λ and is also consistent with the classical use of an 'Oszmidov scale' (Jacquin *et al.* 1989). The Oszmidov scale for rotation can be defined by $Lo = (\epsilon/(2\Omega)^3)^{1/2}$ (see also Zeman 1994) where the Brunt-Wäisälä frequency has been replaced by the basic vorticity 2Ω so that Lo characterizes the smallest scale up to which the rotation is acting. A value of the macro-Rossby number nearly 1 corresponds to an Oszmidov scale close to the integral length scale $Lo = L$, whereas the micro-Rossby number close to unity corresponds to an Oszmidov scale near the Kolmogorov scale $Lo = \eta$. Hence, the intermediate range of Rossby numbers can be linked to the

largest ($L \sim k^{3/2}/\epsilon$) and the smallest length scales ($\eta = (\nu^3/\epsilon)^{1/4}$) having physical relevance in homogeneous turbulence.

While the majority of previous work has provided evidence of two transitions in the development of anisotropy in rotating turbulence, there exists no previous work in which *both* transitions are evident in the same experimental case or computational run. It is difficult in experiments to obtain large enough rotation rates to observe the second transition while previous computations have not had statistical samples large enough to observe the first transition. An additional difficulty associated with DNS is that the Reynolds number range achievable in DNS prohibits a detailed examination of the generation of anisotropy arising from non-linear interactions since molecular viscosity effectively drives the flow to the RDT limit before non-linear effects become significant. Thus, the most viable approach for examining anisotropy development is simulations performed at high Reynolds numbers using large-eddy simulation. Relevant in this regard is the recent LES study by Bartello, Métais and Lesieur (1994). Bartello *et al.* examined the structural evolution of initially isotropic turbulence subjected to uniform system rotation and observed a single transition marking the generation of anisotropy. The transition in their work occurred around $Ro^\omega \sim 1$ (referred to as the second transition above) with significant anisotropy developing only for $Ro^\omega < 1$.

Therefore, the primary motivation of the work presented in this paper has been to provide a detailed examination of the evolution of statistical and structural anisotropy indicators in rotating homogeneous turbulence at high Reynolds numbers. Especially important to this work are simulations of rotating homogeneous flows in which the intermediate range of Rossby numbers is achieved, i.e., $Ro^L < 1$ and $Ro^\omega > 1$ in order to permit observation of all possible transitions. Of further interest in this work is examination of the underlying structure of the vorticity field as anisotropy develops. Evidence exists of a tendency for alignment of the vorticity along the rotation axis with a preference for alignment of corrotative (i.e., parallel or cyclonic) vorticity compared to contrarotative (i.e., antiparallel or anticyclonic) vortices (e.g., see Bartello *et al.* 1994).

An overview of the LES database used in this work is presented in §2, including time development of measures of the anisotropy and examination of the vorticity structure using a joint pdf of the cosine of the angle between the x_3-component of the vorticity vector and background rotation vector with the local micro-Rossby number $\omega_i\omega_i/(2\Omega)$. Discussed in §3 is the anisotropy 'shape', i.e., interpretation of the 'cigar type' of covariance matrices for both the velocity and the vorticity field, using extensively the concepts of 'directional dependence' and 'polarization' (Cambon, Jacquin & Lubrano 1992) or, almost equivalently, those of 'dimensionality' and 'componentality' (Reynolds & Kassinos 1994). The relevance of a classic centrifugal instability for predicting the asymmetry of the vorticity structure in terms of corrotative and contrarotative vortices is discussed, together with a summary of the work from this study, in §4.

2. Database overview and simulation results

2.1. LES database

In this work a pseudo-spectral method was used to integrate the filtered Navier-Stokes equations for an incompressible fluid in a rotating reference frame. The formulation uses an implicit treatment of linear rotation terms which allows exact integration of the rapid distortion equations (Rogallo 1981, Mansour *et al.* 1991a). Subgrid-scale stresses were parameterized using a spectral-eddy viscosity (Kraichnan 1976, Chollet & Lesieur 1981) modified for rotating turbulence (see Cambon, Bertoglio & Jeandel 1981 and Squires, Chasnov, Mansour & Cambon 1994). Use of a subgrid-scale model yields a third relevant Rossby number

$$Ro^{sg} = \sqrt{\frac{E(k_c,t)k_c^3}{8\Omega^2}} \tag{4}$$

referred to as the cut-off Rossby in this manuscript (k_c is the cut-off wavenumber and $E(k,t)$ the classic shell-averaged energy spectrum). Since the molecular viscosity was dropped from the Navier-Stokes equations, the simulations can be considered to represent asymptotically the dynamics at infinite Reynolds number.

The computations were performed using an elongated domain in which the vertical dimension is four times the horizontal length. This geometry and the isotropic initial data were carefully optimized in order to permit the development of the flow without disturbing statistical symmetries. This is especially important in the present work since the initial three-dimensional isotropy is broken only by nonlinear dynamics. Care was also exercised in order to insure that the length scales remain small compared to the size of the computational box. Four datasets were used in the course of this work: the first case (referred to as D0) was obtained at a resolution of $64 \times 64 \times 256$ collocation points and rotation rate of 0.1. Case D0 was used primarily as a means of obtaining preliminary structural results but also permits examination of the effect of resolution. The other cases, referred to as D1, D2, and D3 for computations performed using rotation rates of 0.1, 0.5, and 1.0, respectively, were performed using resolutions of $128 \times 128 \times 512$ collocation points. The reader is referred to Squires, Chasnov, Mansour & Cambon (1993, 1994) for additional details concerning the simulations.

2.2. Statistical evolution

Shown in Fig. 1 are the time histories of the three relevant Rossby numbers Ro^L, Ro^ω, and Ro^{sg} for Cases D0 and D1 (Fig. 1*a*), Case D2 (Fig. 1*b*), and Case D3 (Fig 1*c*). The time axis in Fig. 1 has been made dimensionless by the initial eddy turnover time. It is evident from the figure, especially for Cases D0 and D1, that the initial value of any Rossby number is large enough to ensure that the rotation has an initially weak influence and that there is adequate time for development of triple correlations as in non-rotating turbulence. We find that as in previous DNS and experimental studies, the value of the macro- and the micro-Rossby numbers decrease with time. Eventually, the intermediate range of Rossby numbers, i.e.,

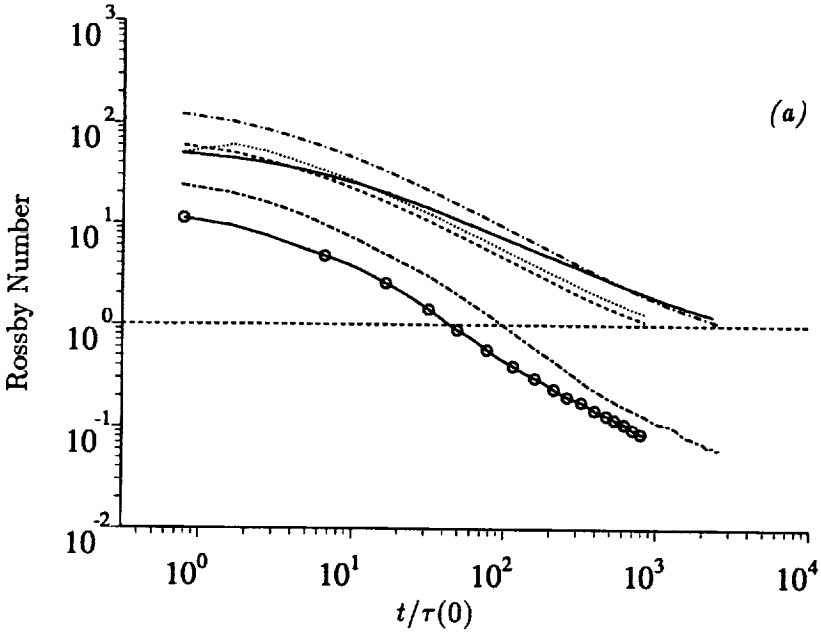

FIGURE 1A. Rossby number development. (*a*) Case D0: ⟜⟜ Ro^L; ---- Ro^ω; ····· Ro^{sg}. Case D1: —-— Ro^L; —·— Ro^ω; —— Ro^{sg}.

$Ro^L < 1$ and $Ro^\omega > 1$, is attained during the simulation. Fig. 1*a* shows that the intermediate range is maintained for more than a decade for Case D1, ending at approximately the final time of the calculation. In addition, the results in Fig. 1 also show the effect of resolution (Cases D0 and D1) as well as a portion of the calculation occurring after the second transition (Cases D2 and D3).

To test the validity of computing statistics using only the large scales in an LES computation, Chasnov (1994) assumed that an inertial range extends towards infinity after the cut-off wavenumber. Chasnov found that this extension of the spectrum yields relatively small corrections to the values of the kinetic energy and the integral length scales as compared to computing these values from the resolved scales. Thus, computing the macro-Rossby number using data from only the resolved scales does not present any theoretical or practical difficulties. Because the smallest scales of motion are not represented in large-eddy simulation, however, the definition of a micro-Rossby deserves additional discussion. It is worth noting that an extension of the spectrum past the cut-off wavenumber to account for the unresolved scales will result in a divergent vorticity field; therefore, this approach cannot be used to define a micro-Rossby number. Thus, in this work the micro-Rossby number shall be defined using the vorticity field from the resolved scales, yielding an effective Ro^ω in the same way as the use of an eddy viscosity in LES yields an effective Reynolds number.

Note that it is also possible to define a pseudo-Reynolds number Re^* based on the resolved scales as the ratio between the macro- and the micro-Rossby numbers in

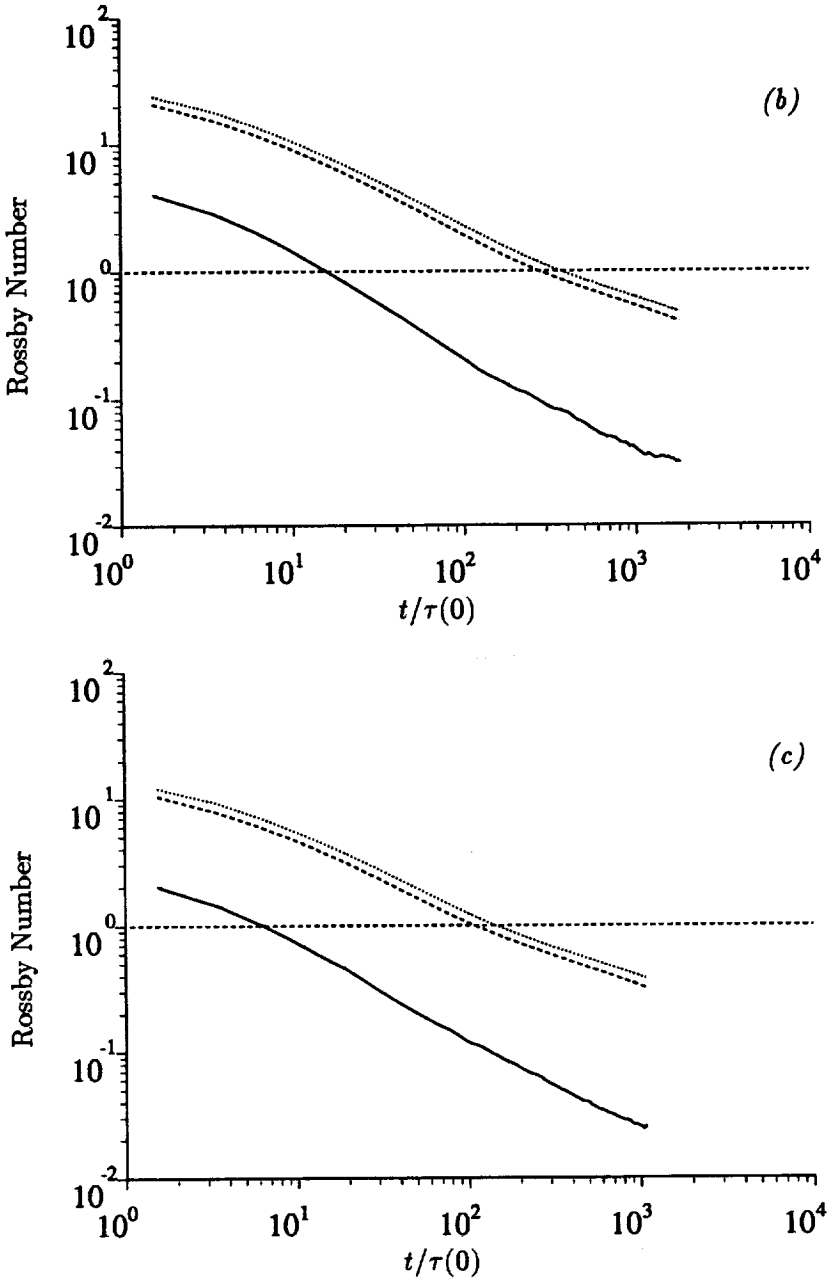

FIGURE 1B - C. Rossby number development. Case D2 (*b*) and Case D3 (*c*): —— Ro^L; ---- Ro^ω; ····· Ro^{sg}.

agreement with the isotropic relationship, i.e., $Re^* = k^2/(\nu\epsilon) = (2/3)(Ro^\omega/Ro^L)^2$. The time development of Re^* is presented in Fig. 2. As opposed to the behavior observed in DNS and experiments, Re^* increases with elapsed time since the integral

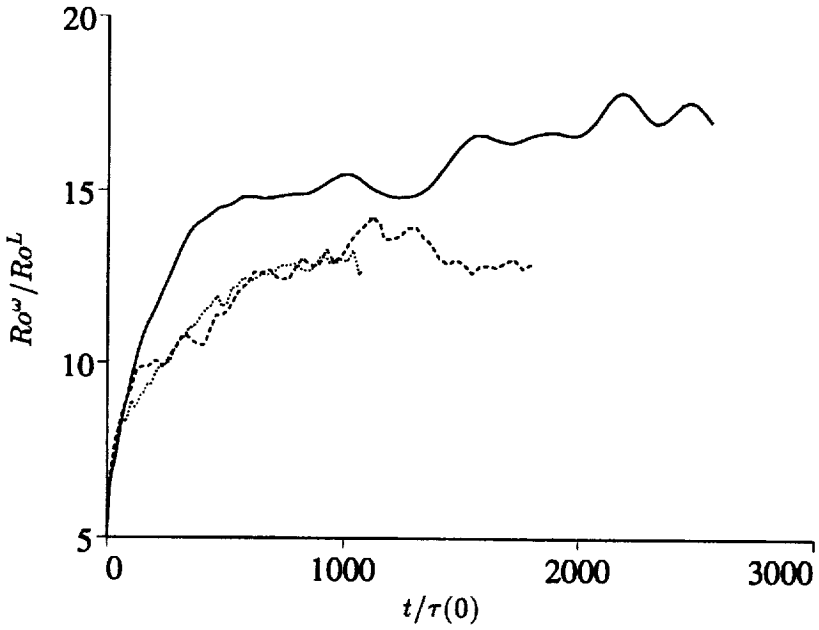

FIGURE 2. Time development of "Reynolds number". —— Case D1; ---- Case D2; ····· Case D3.

length scale continually increases while the resolved Taylor microscale (or $\lambda \propto u'/\omega'$) tends to be blocked by the cut-off scale $2\pi/k_c$. The latter behavior is consistent with the nearly equivalent values of Ro^ω and Ro^{sg}, with the exception of very early times in the development (Fig. 1). Some discrepancies between Cases D0 and D1 shown in Fig. 1*a* illustrate the effect of the resolution: Ro^ω and Ro^{sg} are shown to be nearly equal during the entire time development only at the finer resolutions.

Of the various statistical measures of anisotropy, the measure most widely utilized in previous investigations has been that of the Reynolds stress, i.e., $b_{ij} = R_{ij}/R_{ll} - \delta_{ij}/3$, where $R_{ij} = \langle u_i u_j \rangle$. Note that there is only one component relevant in the semi-axisymmetric configuration created by rotation, $b_{33} = b_{ij}\frac{\Omega_i\Omega_j}{\Omega^2}$, since $b_{11} = b_{22} = -b_{33}/2$ and the off-diagonal components are zero. Fig. 3 shows the evolution of the Reynolds stress anisotropy as a function of time for the three high resolution cases considered. We find a mild positive maximum value of about 0.06 which is consistent with a 'cigar-type' shape (i.e., elongation in one direction) for the Reynolds stress tensor with a ratio of horizontal and vertical principal components $\frac{1}{2}(\langle u_1^2\rangle + \langle u_2^2\rangle)/\langle u_3^2\rangle$ about 0.7-0.8. A very good collapse of the 3 cases (D1, D2, D3) is demonstrated in Fig. 4 in terms of the macro-Rossby number and the anisotropy does indeed appear to be triggered around $Ro^L = 1$. A similar collapse, and further confirmation of the first transition, is found using the vorticity ratio $\frac{1}{2}(\langle \omega_1^2\rangle + \langle \omega_2^2\rangle)/\langle \omega_3^2\rangle$. In order to provide an anisotropy measure for the vorticity in agreement with the one used for the velocity, the component b_{33}^ω of the vorticity

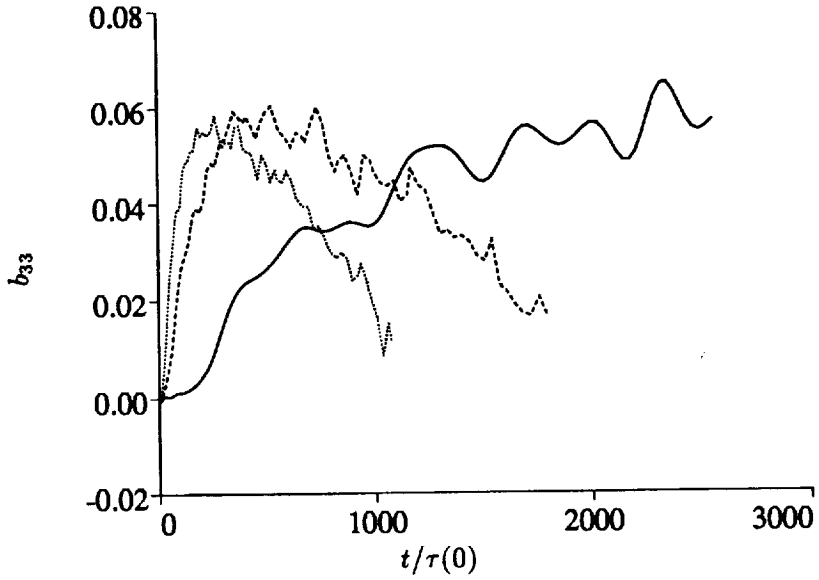

FIGURE 3. Time development of b_{33} component of Reynolds stress anisotropy. —— Case D1; ---- Case D2; ····· Case D3.

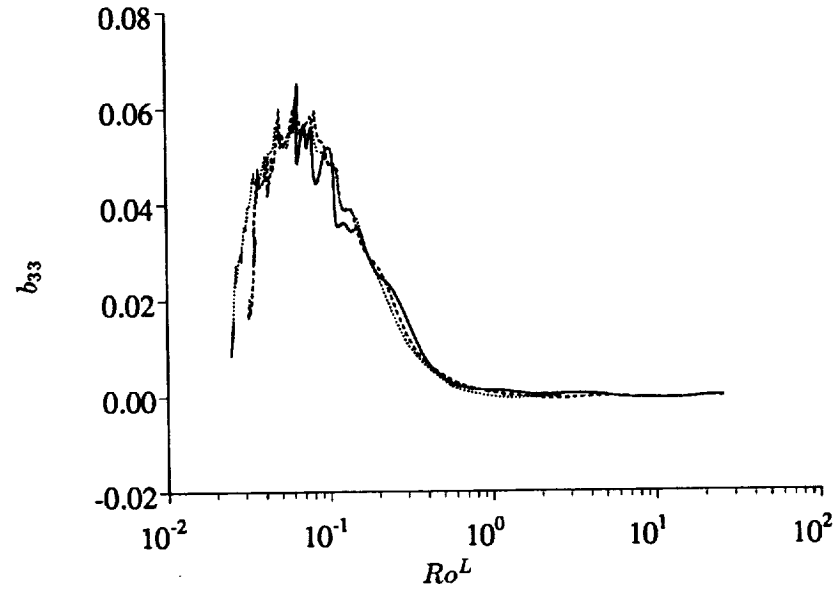

FIGURE 4. Development of b_{33} as a function of the macro Rossby number. —— Case D1; ---- Case D2; ····· Case D3.

deviator

$$b^{\omega}_{ij}\frac{\Omega_i\Omega_j}{\Omega^2} = b^{\omega}_{33} = \frac{\langle\omega_3^2\rangle}{\langle\omega^2\rangle} - \frac{1}{3} \tag{5}$$

is plotted in Fig. 5. We find that the vorticity tensor exhibits the same type of anisotropy shape ('cigar-type') as the Reynolds stress tensor.

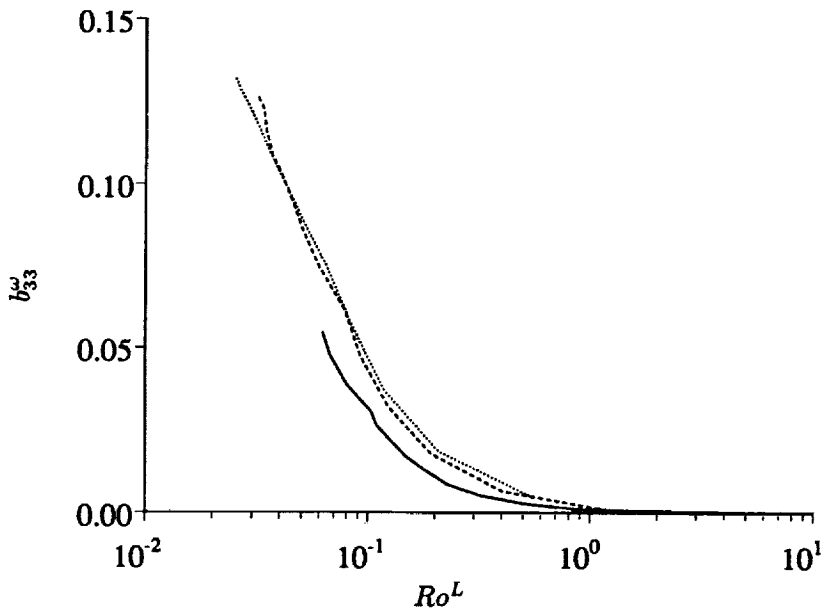

FIGURE 5. Development of vorticity anisotropy b^{ω}_{33} as a function of the macro Rossby number. —— Case D1; ---- Case D2; ····· Case D3.

Similar anisotropy is also found using the most relevant integral length scales, L^3_{33} and $L^3_{11} + L^3_{22} = 2L^3_{11}$ (Fig. 6). An anisotropy measure of the integral length scales can be defined as

$$b^L = \frac{\langle u_1^2\rangle L^3_{11} + \langle u_2^2\rangle L^3_{22}}{\sum_{i=1,3}\langle u_i^2\rangle L^3_{ii}} - \frac{1}{2} \tag{6}$$

based on a true tensor of '2D-energy components' $\mathcal{E}^3_{ij} = \langle u_i u_j\rangle L^3_{ij}$ (Cambon 1990). The quantity b^L is shown in Fig. 7 and is also consistent with the results observed in Figs. 4-6.

Finally, it is interesting to note that the slight plateau exhibited in Fig. 3 and Fig. 4 is consistent with the blocking of nonlinear anisotropic effects previously observed in DNS and EDQNM computations after the second transition $Ro^{\omega} \sim 1$. However, the fact that the anisotropy reflected by the vorticity ratio and the integral length scale ratio continues to increase after the second transition ($Ro^{\omega} < 1$) is surprising and requires further investigation.

2.3. Vorticity structure

The anisotropy reflected by the Reynolds stress tensor and the vorticity correlation tensor has motivated a refined structural analysis. The joint-probability of $\cos\alpha = \omega_3/\omega$ and of the local Rossby number, $\sqrt{\omega_i\omega_i}/2\Omega$, is plotted for different

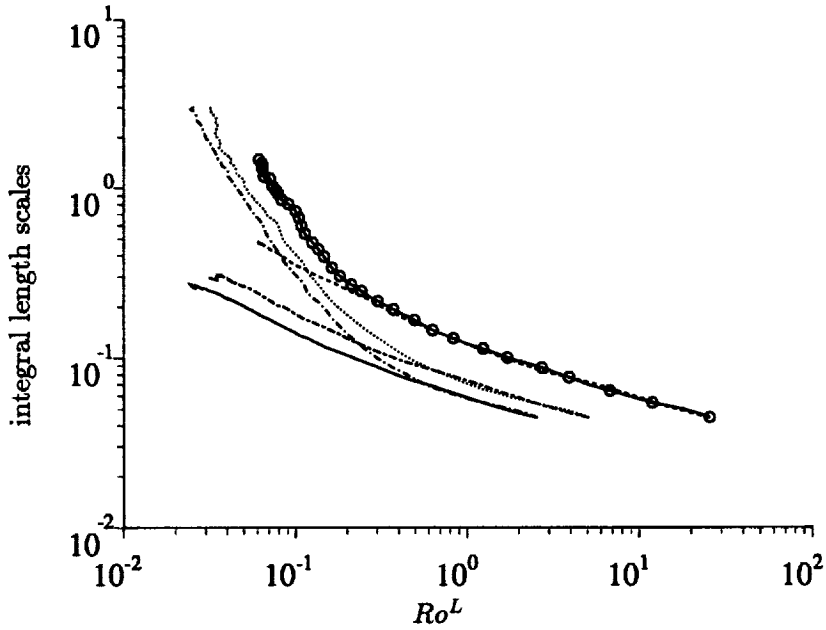

FIGURE 6. Development of integral length scales L_{33}^3 and L_{11}^3 as a function of the macro Rossby number. Case D1: o—o $L_{11}^3 + L_{22}^3$; ---- L_{33}^3. Case D2: ····· $L_{11}^3 + L_{22}^3$; — — L_{33}^3. Case D3: —·— $L_{11}^3 + L_{22}^3$; —— L_{33}^3.

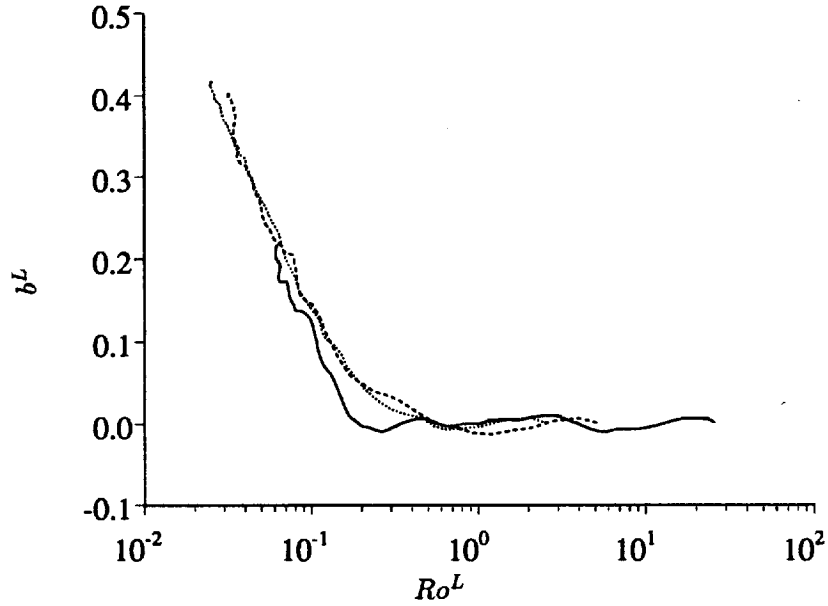

FIGURE 7. Development of length scale anisotropy b^L as a function of the macro Rossby number. —— Case D1; ---- Case D2; ····· Case D3.

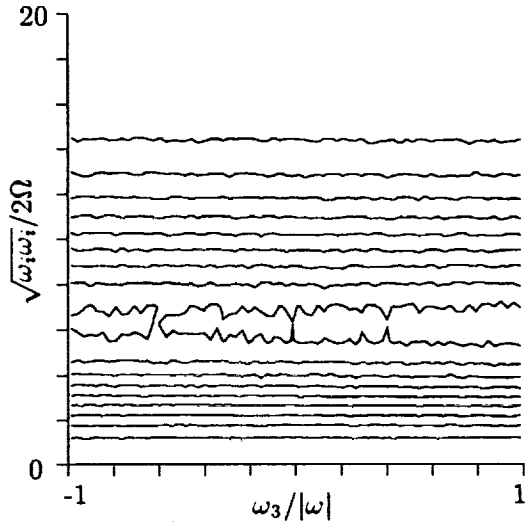

FIGURE 8. Joint pdf of local Rossby number and cosine of the angle between vertical vorticity and vorticity magnitude for Case D2, $t/\tau(0) = 13$. Contour levels drawn between 0 and 8 with an interval of 0.4.

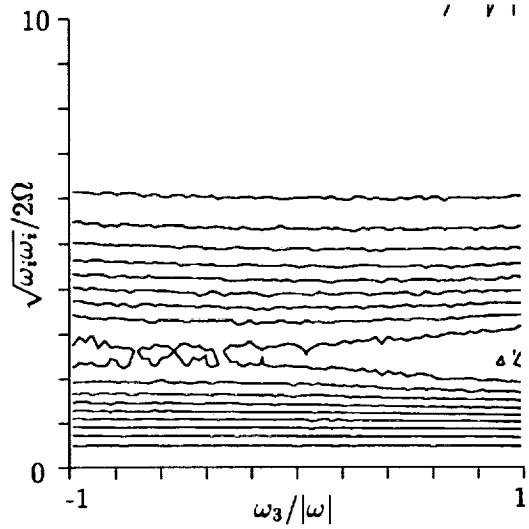

FIGURE 9. Joint pdf of local Rossby number and cosine of the angle between vertical vorticity and vorticity magnitude for Case D2, $t/\tau(0) = 48$. Contour levels drawn between 0 and 8 with an interval of 0.4.

times in Figs. 8 through 11. The x-axis represents binning in terms of the cosine of the angle between the rotation axis and the vorticity vector. Values of the cosine equal to -1 represent contrarotative or antiparallel eddies, values of the cosine equal to 1 represent corrotative or parallel eddies. The use of the cosine of the angle rather than the angle itself ensures equal probability of occurrence in any bin. The

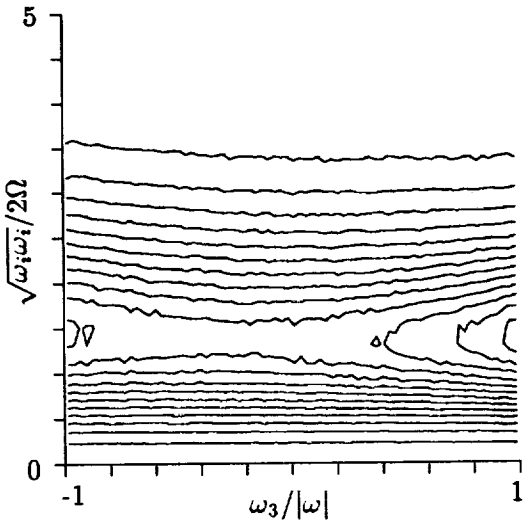

FIGURE 10. Joint pdf of local Rossby number and cosine of the angle between vertical vorticity and vorticity magnitude for Case D2, $t/\tau(0) = 109$. Contour levels drawn between 0 and 8 with an interval of 0.4.

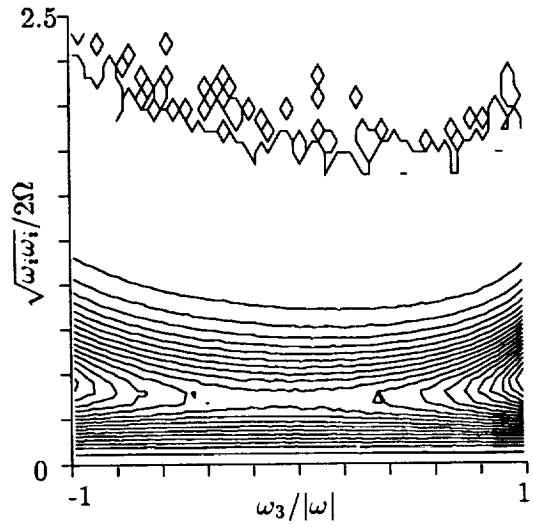

FIGURE 11. Joint pdf of local Rossby number and cosine of the angle between vertical vorticity and vorticity magnitude for Case D2, $t/\tau(0) = 1168$. Contour levels drawn between 0 and 8 with an interval of 0.4.

y-axis represents binning in terms of the local micro-Rossby number, and because Ω is uniform, it is also a measure of the magnitude of the vorticity fluctuation. Fig. 8 corresponds to the beginning of the intermediate range ($Ro^L = 1, Ro^\omega = 8$, see Fig. 1*a*) and the horizontal layering reflects a complete isotropy at a very fine level (statistical equidistribution of the orientation of the vortices). At smaller Ro^ω

ranging from 2 to 1 (Figs. 9 to 11), the distribution shows a distinct tendency for the vortices to be increasingly aligned with the basic rotation axis. The distribution exhibits two peaks near $\cos\alpha = 1$ and $\cos\alpha = -1$ with a preference of corrotative eddies ($\cos\alpha = 1$) clearly exhibited in the distribution. This finding is consistent with that previously observed by Bartello *et al.* (1994) that corotating vorticity tends to become the dominant vorticity in the flow.

3. Interpretation of the anisotropic structure

3.1. Velocity and vorticity fields

The development of anisotropy can be easily argued for most homogeneous flows based upon the type of mean deformation. For instance, the anisotropy created by a distorting duct can be interpreted as follows: in the direction of maximum stretching (chosen as x_3 for sake of discussion), the vorticity is elongated so that the intensity of vortices is reinforced in accordance with conservation of angular momentum and $\langle\omega_3^2\rangle$ becomes dominant with respect to other (horizontal) principal components. In this case the covariance $\langle\omega_i\omega_j\rangle$ assumes a 'cigar type' shape under the influence of the mean strain. Because of the more rapid rotation of the eddy in the plane normal to the axis of stretching, the velocity components orthogonal to the x_3 axis will become larger, creating a 'pancake type' shape for the tensor $\langle u_i u_j\rangle$, i.e., two dominant components relative to a third weak component. The interesting feature of the rotating flow, however, is that ***both*** the single-point covariance matrices of the velocity and vorticity field possess a 'cigar type' shape. This is a very specific feature not observed in other anisotropic flows subjected to mean deformation and in turn motivates a more refined interpretation than can be obtained from Figs. 3-5.

The specific anisotropy created by rotation through non-linear interactions can best be described using a two-point approach, or at least a single-point approach that carries information about both the 'dimensionality' and 'componentality' of the flow. For this purpose it is convenient to utilize spectral variables (e, Z, h) that completely characterize the double correlations at two points for any homogeneous anisotropic field. These three variables are invariants of the flow: the energy, e, the polarization anisotropy, Z, and the helicity, h, and correspond to double correlations of the two components (or helical modes intensities) in the plane normal to the wave vector $\mathbf{k}$ (see Cambon & Jacquin 1989 for a complete discussion). In the semi-axisymmetric configuration created by rotation through nonlinear effects, only e and Z are relevant and they depend only on the wavevector modulus k and on the cosine of the angle between $\mathbf{k}$ and $\mathbf{\Omega}$, i.e., $\cos\theta_k = k_3/k$. It is important to note that e is a three-dimensional energy spectrum ($e \propto \frac{1}{2}\langle\widehat{u}_i^*\widehat{u}_i\rangle$) but is not spherically averaged. Thus, the difference between e and the spherically averaged value, i.e., $e(k, cos\theta_k) - E(k)/(4\pi k^2)$, characterizes a directional anisotropy. The complex scalar Z gives at fixed $\mathbf{k}$ the difference of the two nonzero principal components of $\langle\widehat{u}_i^*\widehat{u}_j\rangle$ as its modulus, $|Z|$, and the orientation of the related principal axes as its argument. Thus, Z characterizes a polarization anisotropy. The transport of these quantities is governed by

$$\left(\frac{\partial}{\partial t} + 2\nu k^2\right) e(k, k_3/k, t) = T^e(k, k_3/k, t) \qquad (7a)$$

and

$$(\frac{\partial}{\partial t} + 2\nu k^2 + 4i\Omega\frac{k_3}{k})\, Z(k, k_3/k, t) = T^z(k, k_3/k, t) \tag{7b}$$

which describes the dynamics in the presence of rotation with an exact separation of contributions from linear (or rapid) terms on the left hand sides and of contributions from nonlinear terms on the right hand sides. The terms T^e and T^z are spectral transfer terms that involve cubic correlations. In an LES calculation T^e and T^z may be replaced by $(T^e - 2\nu_{sg}k^2 e)$ and $(T^z - 2\nu_{sg}k^2 Z)$, so that ν is replaced by ν_{sg} in (7), whereas $T^{(\cdot)}$ denote the resolved transfer terms.

One of the primary advantages of the decomposition into the invariants e and $|Z|$ is that the spectral tensor of double correlations, vorticity as well as velocity, at two points can be expressed in terms of e and Z in a fixed frame of reference. Any single-point tensor obtained by subsequently integrating in wave-space can then be split into a pure (three-dimensional) isotropic contribution (from $E/(4\pi k^2)$), a contribution from the directional anisotropy ($e - E/(4\pi k^2)$), and a contribution from the polarization anisotropy Z. For convenience this splitting is applied to the Reynolds stress tensor,

$$R_{ij} = q^2\left(\frac{\delta_{ij}}{3} + b^e_{ij} + b^z_{ij}\right) \tag{8}$$

and to the tensors introduced by Reynolds & Kassinos (1994), i.e., the dimensionality structure tensor

$$D_{ij} = q^2\left(\frac{\delta_{ij}}{3} - 2b^e_{ij}\right) \tag{9}$$

and the circulicity tensor

$$F_{ij} = q^2\left(\frac{\delta_{ij}}{3} + b^e_{ij} - b^z_{ij}\right). \tag{10}$$

The superscripts e and z in (8)-(10) denote contributions from $e - E/(4\pi k^2)$ and from Z, respectively. The dimensionality tensor

$$D_{ij} = \left\langle \frac{\partial\psi_k}{\partial x_i}\frac{\partial\psi_k}{\partial x_j}\right\rangle \qquad \text{with} \qquad \nabla^2\psi_i = -\omega_i = -\epsilon_{ijk}\frac{\partial u_k}{\partial x_j} \tag{11a}$$

is equivalently defined by

$$D_{ij} = \int 2\frac{k_i k_j}{k^2} e(\mathbf{k}, t)\, d^3\mathbf{k} \tag{11b}$$

and displays the directional dependence of the spectral distribution of energy. It is clear from (9) and (11) that 'directional dependence' and 'dimensionality' are similar concepts. Eq. (8), however, shows that the 'componentality' of the Reynolds stress tensor (denoted by its deviatoric part b_{ij}) results from additive contributions from 'dimensionality' (or 'directivity') b^e_{ij} and from 'polarization' b^z_{ij}. The circulicity tensor $F_{ij} = \langle\psi_{i,k}\psi_{j,k}\rangle$ characterizes the contribution from the largest scales to

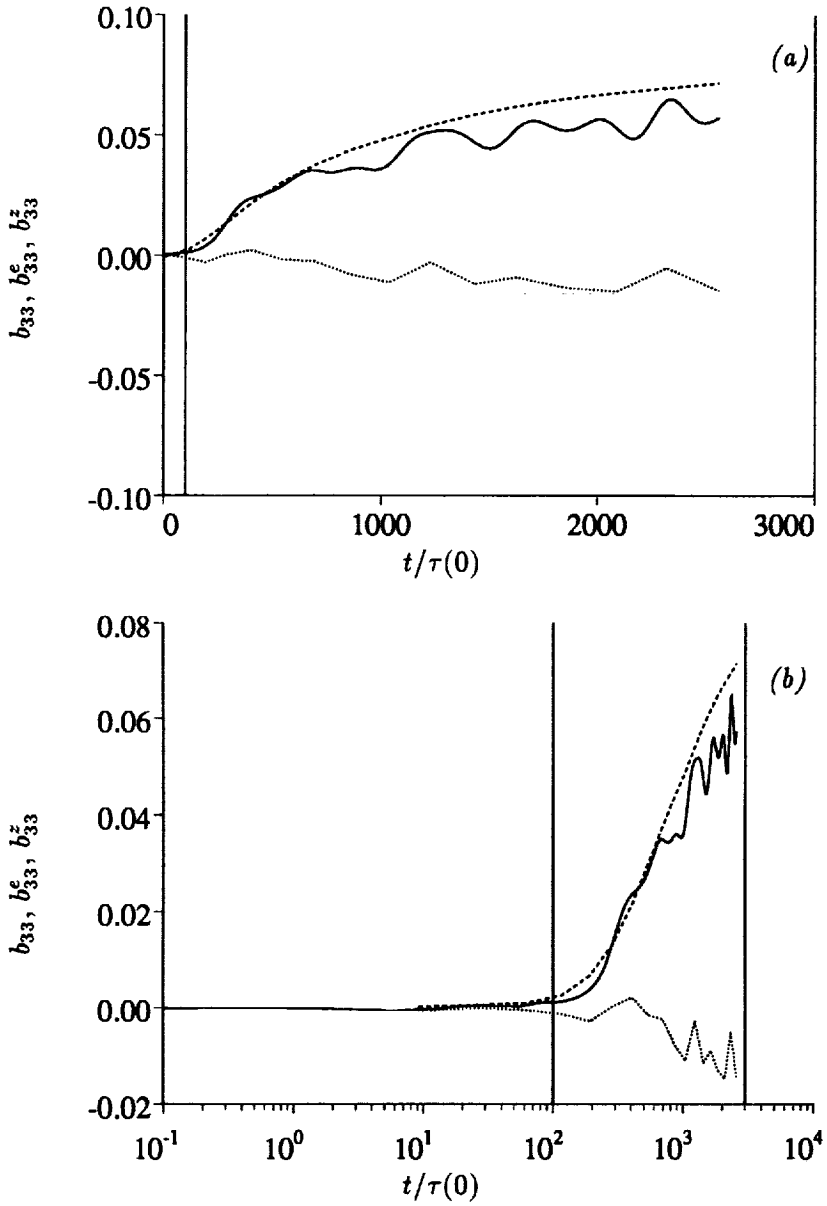

FIGURE 12. Reynolds stress anisotropy for Case D1, intermediate range of Rossby numbers Ro^L and Ro^ω occurring for $100 \leq t/\tau(0) \leq 3000$ (marked by solid vertical lines on figure). —— b_{33}; ---- b_{33}^{ϵ}; ····· b_{33}^{z}.

the vorticity covariance matrix since it is obtained by integrating $\langle \widehat{\omega}_i^* \widehat{\omega}_j \rangle / k^2$ (see Eq. 11a). It is also worth noting that the 'directional dependence' of F_{ij} is exactly the same as that of the Reynolds stress tensor whereas its 'polarization' is exactly the opposite.

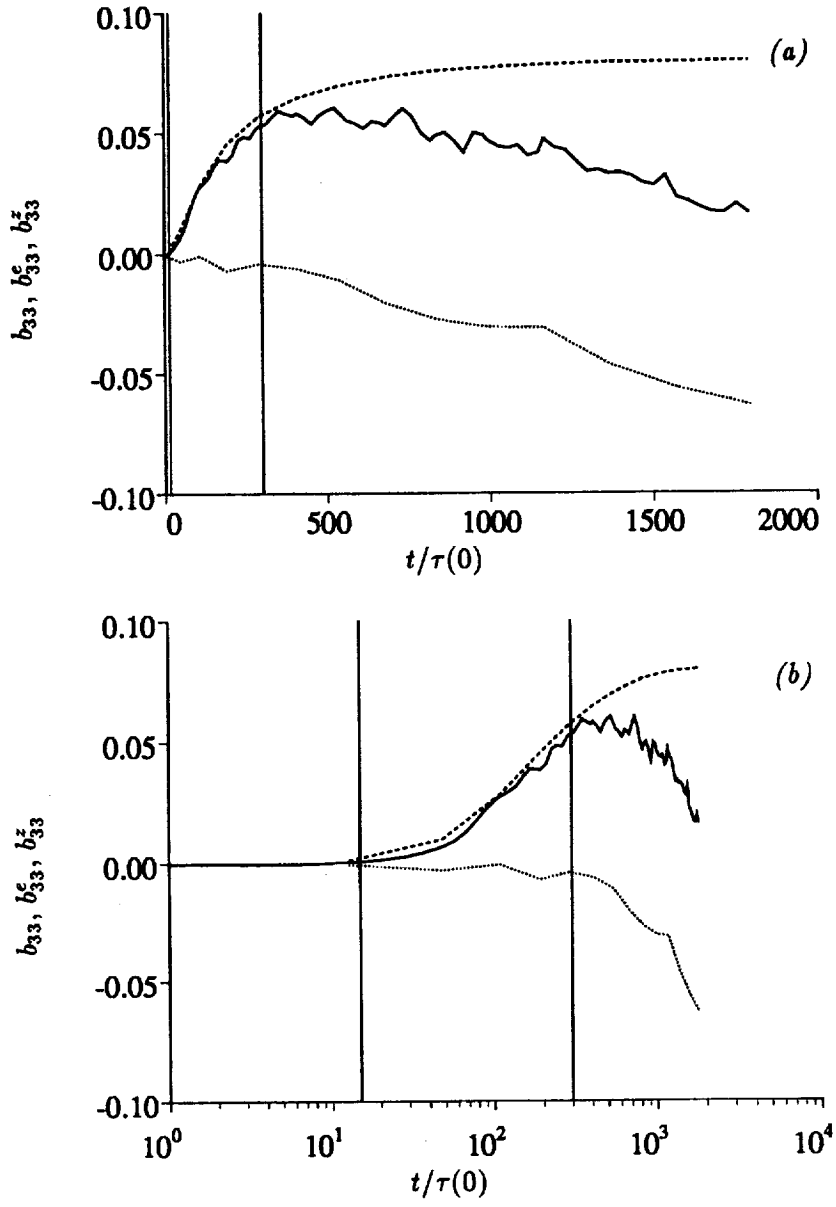

FIGURE 13. Reynolds stress anisotropy for Case D2, intermediate range of Rossby numbers Ro^L and Ro^ω occurring for $15 \leq t/\tau(0) \leq 300$ (marked by solid vertical lines on figure). —— b_{33}; ---- b^e_{33}; ····· b^z_{33}.

Shown in Fig. 12*a* (linear time axis) and Fig. 12*b* (logarithmic time axis) are the relevant anisotropy indicators in semi-axisymmetric turbulence, i.e., b_{33} and components b^e_{33} and b^z_{33}, computed using (8), (9), and (11*b*) for Case D1. The

strong dominance of b_{33}^e relative to b_{33}^z demonstrates that the 'slow' effect of rotation is mainly a 'dimensional' one. This is further supported by the observation that the spectral density of energy tends to concentrate in the wave-plane $k_3 = 0$, i.e., the pure two-dimensional manifold, since a complete concentration at $k_3 = 0$ corresponds to a vanishing of vertical variability in physical space (see Squires *et al.* 1993). If a pure two-dimensional/three-component (2D-3C) state was reached, D_{33}/q^2 would be zero according to (11) so that $b_{33} \sim b_{33}^e$ would be equal to 1/6.

It is also important to remark that the contribution from the 'polarization' indicated by a slightly negative value for b_{33}^z in Fig. 12 is not insignificant. For example, the RDT solution, through scrambling effects by inertial waves, modifies the angle of polarization through a (k_3/k)-dependent angle of rotation $(2\Omega t k_3/k)$ so that the contribution from Z is 'killed off' on average by linear effects and, hence, $b_{33}^z \sim 0$. However, inertial waves cannot affect Z in the slow manifold $k_3 = 0$ where Z is real and the polarization discriminates contributions to vertical velocity components $e + Z$ from contributions to horizontal velocity components $e - Z$. The quantity $e - Z$ at $k_3 = 0$ is precisely the two-dimensional/two-component mode since it contributes only to the horizontal velocity field in the slow (two-dimensional) manifold and $k^2(e - Z)$ contributes only to the vertical vorticity component. Accordingly $e + Z$ at $k_3 = 0$ is the 2D-3C mode in the slow manifold, which only contributes to the vertical velocity component, whereas $k^2(e + Z)$ contributes only to horizontal vorticity components. The dynamics of these two modes of the slow manifold are accounted for in physical space through products of integral length scales and related Reynolds stress components (e.g., Eq. 6) but are weakly reflected by single-point velocity or vorticity correlations obtained by averaging over all angles in spectral space. In any case, examination of contributions from only the slow manifold would indicate that the weak negative value of b_{33}^z may characterize a tendency of the velocity field to be rather horizontal and of the vorticity field to be rather vertical. For the vorticity correlations the 'cigar type' shape created by the 'dimensionality' for the circulicity tensor is slightly increased by polarization (since $b_{33}^e - b_{33}^z > b_{33}^e$) according to (9), whereas the 'cigar type' shape of the Reynolds stress tensor is slightly diminished since $b_{33}^e + b_{33}^z < b_{33}^e$. However, it is important to also note that the 'dimensionality effect' is not balanced by the 'polarization effect'. In addition, the latter effect can be interpreted as a 'componentality effect' but restricted to the slow manifold where inertial waves cannot destroy it.

It is further interesting to examine b_{33} and its contributions from e and Z for Cases D2 and D3. The development shown in Figs. 13 and 14 are consistent with the previous discussion for Fig. 12 but also clearly suggest that the only significant contribution from Z is obtained *after* the second transition in accordance with the location of $Ro^\omega = 1$ (cf. Fig. 1*b* and Fig. 1*c*). The stabilization of b_{33} at early times following the second transition is due to the balanced increase of b_{33}^e and decrease b_{33}^z. For increasing time past the second transition it is also clear from Figs. 13 and 14 that the behavior of b_{33} is driven by the increasingly negative value of b_{33}^z. It is possible that for longer evolution times b_{33} may become negative, indicating a two-dimensional/two-component state of the Reynolds stress tensor. However, it is

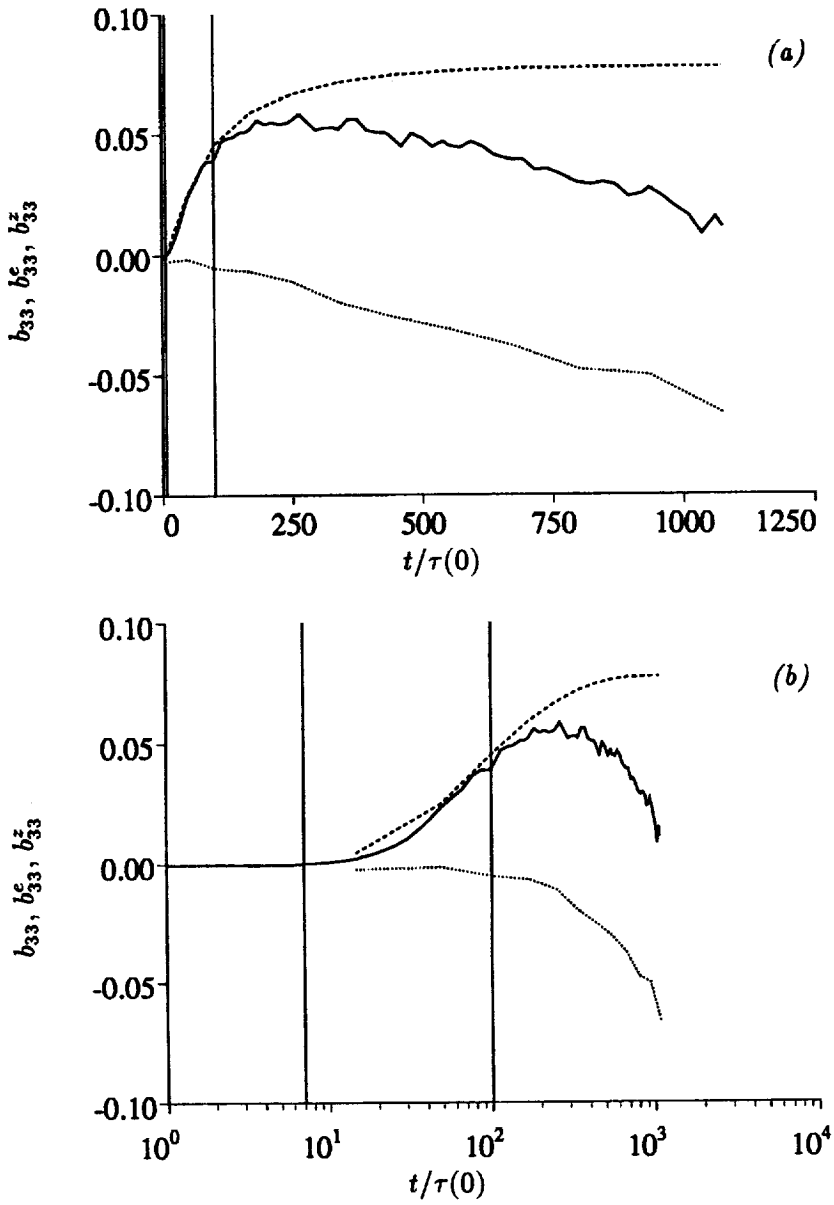

FIGURE 14. Reynolds stress anisotropy for Case D3, intermediate range of Rossby numbers Ro^L and Ro^ω occurring for $7 \leq t/\tau(0) \leq 100$ (marked by solid vertical lines on figure). —— b_{33}; ---- b_{33}^{ϵ}; ····· b_{33}^{z}.

difficult to confirm this tendency even in high resolution LES since the imposition of periodic boundary conditions will have an adverse effect on the overall evolution of the flow.

Finally, the three cases are plotted in Fig. 15 in terms of Ro^L. The collapse of the

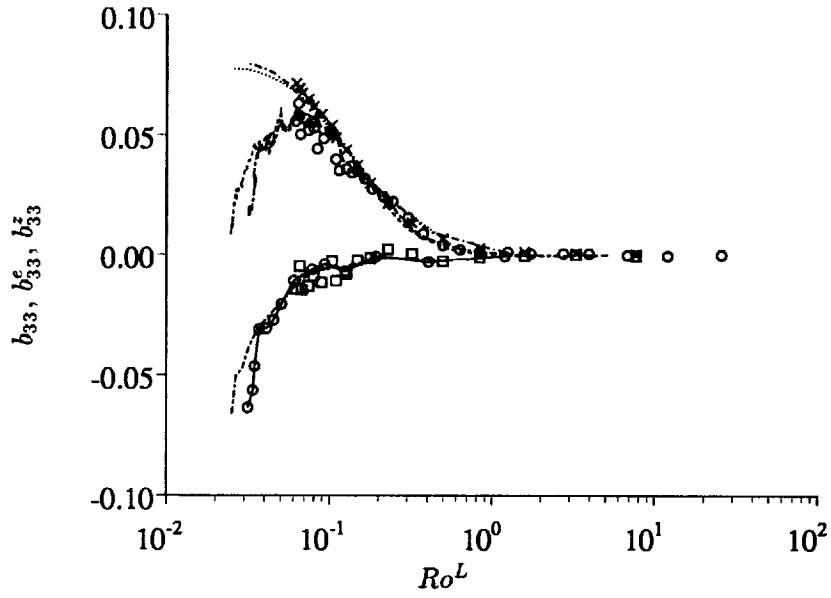

FIGURE 15. Reynolds stress anisotropy as a function of the macro Rossby number. Case D1: o b_{33}; × b^e_{33}; □ b^z_{33}. Case D2: —·— b_{33}; —·— b^e_{33}; o—o b^z_{33}. Case D3: ---- b_{33}; ····· b^e_{33}; —·— b^z_{33}.

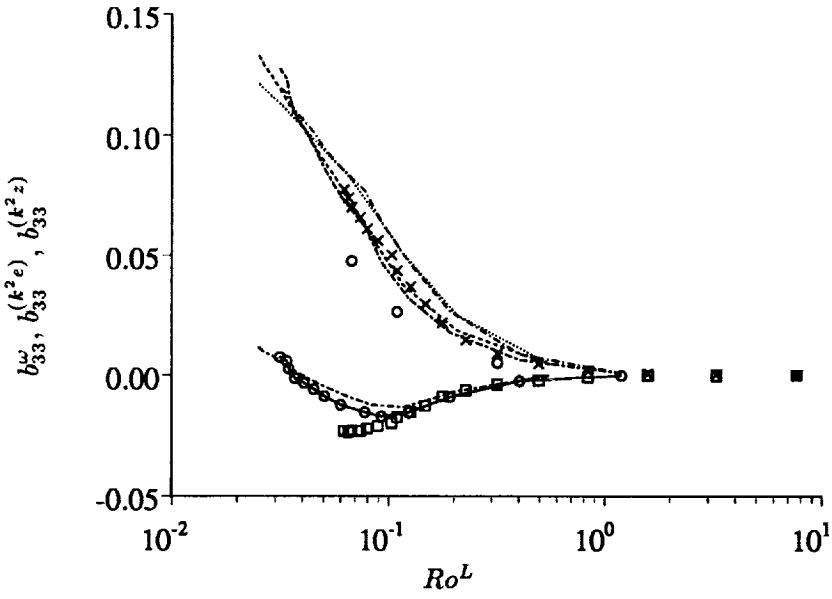

FIGURE 16. Vorticity anisotropy as a function of the macro Rossby number. Case D1: o b^{ω}_{33}; × $b^{(k^2e)}_{33}$; □ $b^{(k^2z)}_{33}$. Case D2: —·— b^{ω}_{33}; —·— $b^{(k^2e)}_{33}$; o—o $b^{(k^2z)}_{33}$. Case D3: ---- b^{ω}_{33}; ····· $b^{(k^2e)}_{33}$; —·— $b^{(k^2z)}_{33}$.

data for the three cases is remarkable and demonstrates that the findings discussed for Case D1 apply to the other two cases as well. Furthermore, the results in Fig. 15 also show that the macro Rossby number is the key parameter determining the state of the turbulence. The onset of anisotropy is clearly indicated for $Ro^L < 1$ while a second transition occurs at approximately $Ro^L < 0.1$ which corresponds to $Ro^\omega < 1$.

Analogous quantities to the anisotropy measures of the velocity field shown in Fig. 15 have been plotted in Fig. 16 for the vorticity field. These quantities were calculated using a k^2 weighting factor so that $b_{33}^{(k^2 e)} - b_{33}^{(k^2 z)}$ yields b_{33}^{ω}, i.e., the anisotropy of the single-point vorticity correlation tensor. The relative role of Z (or polarization) in the development of the anisotropy is weak compared to the contribution due to the role of e (i.e., dimensionality). This is a reflection of the concentration of energy around $k_3 = 0$. As was also observed for the velocity, the collapse of the vorticity anisotropy for the three cases in terms of the macro Rossby number is again remarkable. In this case the first transition is clear while the second is marked by a change in the slope of $b_{33}^{(k^2 z)}$.

Finally, it is again worth noting that the 'cigar-type' shape created by the pure 'dimensionality' effect ($b_{33}^{e} > 0$, $b_{33}^{(k^2 e)} > 0$), has nothing to do with a tendency of the velocity vector or the vorticity vector to be aligned with the rotation vector. The relative concentration of spectral energy at $k_3 = 0$ corresponds to a lack of energy about "vertical" wavenumbers $\mathbf{k}$ (i.e., nearly aligned with the rotation axis). The contribution of these modes at "vertical" wavenumbers is to horizontal velocity or vorticity components since $\hat{\mathbf{u}}$ and $\hat{\omega}$ are normal to $\mathbf{k}$. In other words, $b_{33}^{e} > 0$ (and $b_{33}^{(k^2 e)} > 0$) characterize the lessening of dimensionality in the presence of the incompressibility constraint.

4. Summary

The relevance of two threshold Rossby numbers which delineate anisotropic effects in rotating turbulence has been demonstrated using the database from high-resolution LES at asymptotically high Reynolds numbers. Anisotropy created by background rotation can only be initiated by nonlinear interactions and is triggered when a macro-Rossby number becomes smaller than 1. An excellent collapse of the main anisotropy indicators was demonstrated in terms of the macro-Rossby number.

The second transition corresponding to a micro-Rossby number Ro^ω close to 1 was found in previous experimental, EDQNM, and DNS results as the beginning of the shut-off of the energy cascade indicating that non-isotropic, non-linear effects were frozen. In the LES results used in this study, a second transition is indeed observed for $Ro^\omega < 1$ but represents a reorganization of the anisotropy rather than a stabilization. The description of this complex anisotropic structure has motivated a detailed analysis of the 'dimensionality' and 'polarization' effects of steady system rotation. These effects can be summarized by considering a rectangular domain in spectral space where $|k_3/k|$ is plotted on the vertical axis and k on the horizontal axis (Fig. 17). The domain can be separated horizontally in a narrow band $|k_3/k| < \epsilon_s << 1$ near $k_3 = 0$ (the slow manifold denoted 's') and the remaining

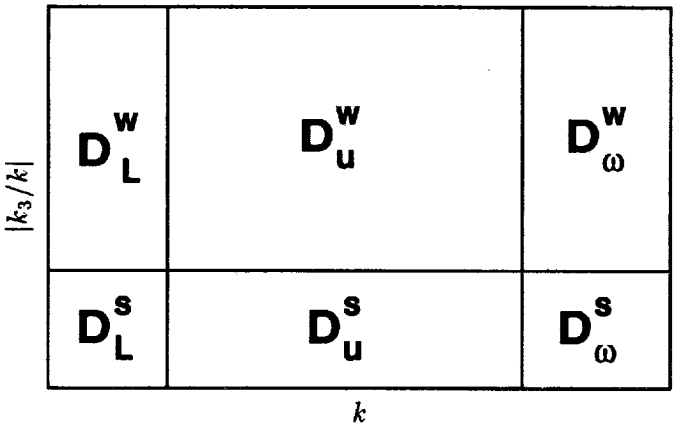

FIGURE 17. Sub-domains in k-space.

upper band (denoted 'w') where the scrambling effect of inertial waves are present. The spectral domain can be further subdivided into three bands of wavenumbers that characterize the largest scales (L), the energetic scales (u), and the vorticity scales (ω). The six sub-domains corresponding to these divisions are denoted as $D_L^w, D_u^w, D_\omega^w, D_L^s, D_u^s, D_\omega^s$ in Fig. 17. The first transition is characterized by the beginning of a lessening of dimensionality and concentration of energy towards the slow manifold in agreement with $b_{33}^e > 0$ (which characterizes an angular drain of energy from D_u^w to D_u^s) and $b^{(k^2e)} > 0$ (which characterizes an angular drain of energy from D_ω^w to D_ω^s). Polarization, or componentality, only affects the slow manifold and is reflected by $b^L > 0$ (which characterizes D_L^s). When the Rossby number is in the intermediate range ($Ro^L < 1$ and $Ro^\omega > 1$), the polarization indicators b_{33}^z and $b_{33}^{(k^2z)}$ remain weak so that the global anisotropy reflected by b_{33} and b_{33}^ω is an almost pure dimensional effect. After the second transition, the polarization effect in the slow manifold seems to emerge not only in D_L^s, but also in D_u^s through $b_{33}^z < 0$ so that $b_{33} = b_{33}^e + b_{33}^z$ results from opposite 'dimensional' and 'polarization' effects. Nevertheless, the vorticity anisotropy $b_{33}^\omega = b_{33}^{(k^2e)} - b_{33}^{(k^2z)}$ continues to be essentially due to the dimensional contribution $b_{33}^{(k^2e)}$. Such a pattern may correspond to opposite values of the polarization anisotropy in the domains D_L^s ($Z < 0 \rightarrow b^L > 0$), D_u^s ($Z < 0 \rightarrow b_{33}^z > 0$) and D_ω^s ($Z > 0$).

An analysis of the vorticity structure was performed by means of a joint-pdf representation of the $\cos\alpha = \omega_3/\omega$ and the local Rossby number $\sqrt{\omega_i\omega_i}/(2\Omega)$. The second transition ($Ro^\omega \sim 1$) is shown to be characterized by a tendency of the vortices to be aligned with the basic rotation vector with an increasing dominance of corrotative eddies. This last result could be explained by a classical Bradshaw-Richardson stability criterion (Bradshaw 1969), also consistent with Rayleigh centrifugal criterion, at least for values close to zero absolute vorticity $\omega_i + 2\Omega_i = 0$ or zero tilting vorticity $\frac{1}{2}\omega_i + 2\Omega_i$, as discussed by Cambon *et al.* (1994a). These results for the vorticity structure are also in qualitative agreement with those of Bartello *et al.* (1994). However, in the present study this is a side effect and not the main source

of the anisotropy. The fact that the maximum value of $\omega_3/(2\Omega)$ is nearly the same as Ro^ω is consistent with the fact that the componentality effect (with corresponds to a polarization effect in the slow manifold) has a relatively weak effect on the structure of the vorticity field. Statistically, the 'cigar type' shape of the vorticity correlations tensor mainly reflects the pure dimensional effect.

It should also be noted that anisotropic trends would be blocked for $Ro^\omega < 1$, except for quantities only dependent on the slow manifold (e.g., b^L), in accordance with a shut-off of the energy cascade if viscous effects were present in the simulations. The reorganization of the anisotropy (especially as reflected by b^z_{33} in the Reynolds stress as well as in the circulicity tensor) after the second transition is only allowed in the absence of dissipation.

REFERENCES

BARDINA, J., FERZIGER, J. H. & ROGALLO, R. S. 1985 Effect of rotation on isotropic turbulence: computation and modeling. *J. Fluid Mech.* **154,** 321-336.

BARTELLO, P., MÉTAIS, O. & LESIEUR, M. 1994 Coherent structures in rotating three-dimensional turbulence. *J. Fluid Mech.* **273,** 1.

BRADSHAW, P. 1969 The analogy between streamline curvature and buoyancy in turbulent shear flow. *J. Fluid Mech.* **36,** 177-191.

CAMBON, C. 1982 Étude spectrale d'un champ turbulent incompressible soumis à des effets couplés de déformation et de rotation imposés extérieurement. *Thèse de doctorat d'état, Université Claude Bernard-Lyon I.*

CAMBON, C. 1990 Single and two point modeling of homogeneous turbulence. *Annual Research Briefs,* NASA/Stanford Center for Turbulence Research, 23-38.

CAMBON, C., BERTOGLIO, J. P. & JEANDEL, D. 1981 Spectral closure of homogeneous turbulence. *AFOSR-Stanford Conf. on Complex Turb. Flows.*

CAMBON, C. & JACQUIN, L. 1989 Spectral approach to non-isotropic turbulence subjected to rotation. *J. Fluid Mech.* **202,** 295-317.

CAMBON, C., JACQUIN, L. & LUBRANO, J. L. 1992 Toward a new Reynolds stress model for rotating turbulent flows. *Phys. Fluids A.* **4,** (4), 812-824.

CAMBON C., BENOIT, J. P., SHAO, L., & JACQUIN, L. 1994a Stability analysis and large-eddy simulation of rotating turbulence with organized eddies. *J. Fluid Mech.* **278,** 1-27.

CAMBON, C., MANSOUR, N. N. & GODEFERD, F. S. 1994b The energy transfer in rotating turbulence. In preparation.

CHASNOV, J. 1994 Similarity states of passive scalar transport in isotropic turbulence. *Phys. Fluids.* **6**(2), 1036-1051.

CHOLLET, J. P. & LESIEUR, M. 1981 Parametrization of small scales of three-dimensional isotropic turbulence utilizing spectral closures.. *J. Atmos. Sci.* **38,** 2747-2757.

JACQUIN, L., LEUCHTER, O., CAMBON, C., & MATHIEU, J. 1990 Homogeneous turbulence in the presence of rotation. *J. Fluid Mech.* **220,** 1-52.

JACQUIN, L., LEUCHTER, O. & GEOFFROY, P. 1989 Experimental study of homogeneous turbulence in the presence of rotation. *6th symposium on Turbulent Shear FLows.* Springer Verlag, Heidelberg.

KRAICHNAN, R. H. 1976 Eddy viscosity in two and three dimensions. *J. Atmos. Sci.* **33,** 1521-1536.

MANSOUR, N. N., CAMBON, C. & SPEZIALE C. G. 1991a Theoretical and computational study of rotating isotropic turbulence. *Studies in Turbulence,* ed. by T. B. Gatski, S. Sarkar and C. G. Speziale, Springer Verlag, New-York.

MANSOUR, N. N., CAMBON, C. & SPEZIALE C. G. 1991b Single point modeling of initially isotropic turbulence under uniform rotation.. *Annual Research Briefs,* NASA/Stanford Center for Turbulence Research, 159-168.

MANSOUR, N. N., SHIH, T.-H. & REYNOLDS, W. C. 1991c The effects of rotation on initially anisotropic homogeneous flows. *Phys. Fluids A.* **3,** (10), 2421-2425.

PROUDMAN, J. 1916 On the motion of solids in a liquid possessing vorticity. *Proc. R. Soc. London, A.* **92,** 408.

REYNOLDS, W. C., & KASSINOS, S. 1994 A one-point model for the evolution of the Reynolds stress and structure tensors in rapidly deformed homogeneous turbulence. *Osborne Reynolds Centenary Symposium,* UMIST Manchester, United Kingdom, May 1994.

ROGALLO, R. S. 1981 Numerical experiments in homogeneous turbulence. NASA Technical Memorandum 81315.

SPEZIALE, C. G., MANSOUR, N. N., & ROGALLO, R. S. 1987 Decay of turbulence in a rapidly rotating frame. *Proc. 1987 Summer Program,* NASA/Stanford Center for Turbulence Research, Report CTR-S87, 205-212.

SQUIRES, K. D., CHASNOV, J. R., MANSOUR, N. N. & CAMBON, C. 1993 Investigation of the asymptotic state of rotating turbulence using large-eddy simulation. *Annual Research Briefs,* NASA/Stanford Center for Turbulence Research, 157-170.

SQUIRES, K. D., CHASNOV, J. R., MANSOUR, N. N. & CAMBON, C. 1994 The asymptotic state of rotating homogeneous turbulence at high Reynolds number. *AGARD Conf. Proc. CP-551,* in press.

WALEFFE, F. 1991 Non-linear interactions in homogeneous turbulence with and without background rotation. *Annual Research Briefs,* Center for Turbulence Research, NASA Ames/Stanford University, 31-43.

ZEMAN, O. 1994 A note on the spectra and decay of rotating homogeneous turbulence. To appear in *Phys. Fluids.*

20034
39755 421
N95-21060 -12

Center for Turbulence Research
Proceedings of the Summer Program 1994

Single point modeling of rotating turbulent flows

By A. H. Hadid[1], N. N. Mansour[2] AND O. Zeman[3]

A model for the effects of rotation on turbulence is proposed and tested. These effects which influence mainly the rate of turbulence decay are modeled in a modified turbulent energy dissipation rate equation that has explicit dependence on the mean rotation rate. An appropriate definition of the rotation rate derived from critical point theory and based on the invariants of the deformation tensor is proposed. The modeled dissipation rate equation is numerically well behaved and can be used in conjunction with any level of turbulence closure. The model is applied to the two-equation k-ϵ turbulence model and is used to compute separated flows in a backward-facing step and an axisymmetric swirling coaxial jets into a sudden expansion. In general, the rotation modified dissipation rate model show some improvements over the standard k-ϵ model.

1. Motivation and objectives

The ability to accurately model the effects of rotation on turbulence has a wide variety of important applications in rotating machinery and combustion devices. Many turbulent flows of engineering importance involve combinations of rotational and irrotational strains. However, turbulence models of the eddy viscosity type are oblivious to the presence of rotational strains since they depend only on the mean velocity gradients through their symmetric part (i.e. the mean rate of strain tensor). The rotation rate, for example, does not explicitly enter the equations for the turbulent kinetic energy and its dissipation rate, yet evidence from experiments (Wigeland and Nagib 1978, Jacquin et al. 1990) and from direct numerical simulation (Bardina *et al.* 1985, Speziale *et al.* 1987, Mansour *et al.* 1991) show that the decay rate of turbulence is reduced by the presence of rotation.

The effects of rotation on turbulence are known to be subtle. They are manifested through changes in the spectrum of the turbulence caused by nonlinear interactions. For initially isotropic turbulence, rotation inhibits the cascade of energy from large to small scales. Zeman (1994) proposed a modified energy spectrum that takes into account the effects of rotation at high Reynolds number by introducing a rotation wavenumber, $k_\Omega = \sqrt{\Omega^3/\epsilon}$, below which rotation effects on spectral transfer are important. Much of the application work in simulating rotating flows have been conducted using varieties of eddy viscosity models (k-ϵ or k-l) and second order closure models with modified dissipation rate transport equation to account for

1 Rocketdyne Division/Rockwell International
2 NASA/Ames Research Center
2 Center for Turbulence Research

rotational effects. However, most of these models fail to predict the asymptotic behavior of the turbulence decay rate in the limits of large rotation rate. The objectives of this work are to model the effects of rotation using single-point two equation models and to offer an appropriate definition of the mean rotation rate that is consistent with the fact that spin is the main cause of reduction in the dissipation rate.

2. Accomplishments

For incompressible viscous flow with constant properties, the modeled transport equations for the turbulent kinetic energy, k, and its dissipation rate, ϵ, that are widely used for engineering applications take the form;

$$k_{,t} + U_j k_{,j} = D_k + P_k - \epsilon \tag{1}$$

$$\epsilon_{,t} + U_j \epsilon_{,j} = D_\epsilon + P_\epsilon - \Phi_\epsilon \tag{2}$$

where D_k and D_ϵ are the diffusion terms for k and ϵ respectively and are modeled as

$$D_k = \left[\left(\nu + \frac{\nu_t}{\sigma_k}\right) k_{,j}\right]_{,j}, \qquad D_\epsilon = \left[\left(\nu + \frac{\nu_t}{\sigma_\epsilon}\right) \epsilon_{,j}\right]_{,j},$$

where ν is the laminar viscosity and ν_t is the eddy viscosity $= C_\mu k^2/\epsilon$. σ_k and σ_ϵ are the ratio of Prandtl to Schmidt numbers and are taken as constants. P_k is the production term for k given as $P_k = -\overline{u_i' u_j'} U_{i,j}$, where $\overline{u_i' u_j'}$ is the Reynolds stress term and U_i is the mean velocity in the i-direction.

Assuming that the production of the dissipation rate P_ϵ is proportional to the production of turbulent kinetic energy P_k, i.e $P_\epsilon \sim P_k/T$ where T is the turbulent time scale given by $T = k/\epsilon$. Similarly assume that the destruction rate of dissipation rate Φ_ϵ is proportional to the turbulent energy dissipation rate term, i.e. $\Phi_\epsilon \sim \epsilon/T$. The modeled form of the dissipation rate equation becomes

$$\epsilon_{,t} + U_j \epsilon_{,j} = D_\epsilon + C_1 \frac{\epsilon}{k} P_k - C_2 \frac{\epsilon^2}{k} \tag{3}$$

Due to the symmetry of the Reynolds stress tensor $\overline{u_i' u_j'}$, the kinetic energy production term can be written as $P_k = -\overline{u_i' u_j'} S_{ij}$, where $S_{ij} = (U_{i,j} + U_{j,i})/2$ is the mean rate of strain tensor. Therefor it can be seen that the standard dissipation rate, eq. (3), has no explicit dependence on the mean rotation tensor $\Omega_{ij} = (U_{i,j} - U_{j,i})/2$. It follows that the commonly used modeled dissipation rate equation can only be affected indirectly by rotational strains through the changes that they induce in the Reynolds stress tensor.

In order to sensitize the dissipation rate equation to rotational effects, consider the simple case of isotropic turbulence in a rotating frame. In this case, an initially decaying isotropic turbulence is described by;

$$k_{,t} = -\epsilon \tag{4}$$

$$\epsilon_{,t} = -C_2 \frac{\epsilon^2}{k} \tag{5}$$

Equations (4) and (5) do not distiguish the difference between isotropic turbulence in a rotating frame and in an inertial frame. Models that have a non zero rotational correction have been proposed by Bardina *et al.* (1985), for example, for rotating isotropic turbulence where eq. (5) takes the form

$$\epsilon_{,t} = -C_2 \frac{\epsilon^2}{k} - C_3 \Omega \epsilon \tag{6}$$

with $C_2 = 1.83$ and $C_3 = 0.15$.

The above model is able only to accurately predict the reduction in the decay rate of the turbulent kinetic energy in rotating isotropic turbulence for weak to moderate rotation rates where the effects are small. However, for sufficiently high rotation rates and long enough time, the model drastically underpredicts the decay rate of the turbulent kinetic energy.

Hanjallic and Launder (1980) proposed a model for which the ϵ-transport equation in rotating isotropic turbulence takes the form

$$\epsilon_{,t} = -C_2 \frac{\epsilon^2}{k} - C_3 \Omega^2 k \tag{7}$$

where $C_2 = 1.92$ and $C_3 = 0.27$.

This model predicts unphysical behavior of negative dissipation rate at high rotation rates, thus violating the realizability constraint. Other modifications to the dissipation rate transport equation have been proposed to account for rotational strains, e.g Raj (1975) and Pope (1978). Again they fail in one way or another to account accurately for the rotational effects.

3. Proposed model

In the present work a new model is proposed that accounts for rotational effects and correctly predicts the asymptotic behavior at zero to inifinte rotation rates. Consider the dissipation rate equation in rotating isotropic turbulence

$$\epsilon_{,t} = -\left(1.7 + \frac{5}{6} \frac{\alpha^2}{\alpha^2 + 1}\right) \frac{\epsilon^2}{k} \tag{8}$$

with

$$\alpha = 0.35 Ro^{-1} \tag{9}$$

where Ro is the Rossby number defined as $Ro^{-1} = \Omega k/\epsilon$. For $\Omega >> 1$, $C_2 = 2.5$, which gives a power law exponent $n = 0.6$ (in $k \sim t^{-n}$) maching the power law proposed by Squires *et al.* (1993) for the asymptotic state of rotating homogeneous turbulence at high Reynolds numbers.

The experminental data of Jacquin *et al.* (1990) are used to test the proposed model. Their experiments consisted of measuring the velocity field and characteristic quantities characterizing the fluctuating field downstream of a rotating cylinder

containing a honycomb structure and a turbulence producing grid. The coupled differential equations for k and ϵ describing the effects of rotation on an initially isotropic turbulence can be written as

$$k_{,t} = -\epsilon \tag{10}$$

$$\epsilon_{,t} = -\left(C_2 + C_3 \frac{\alpha^2}{\alpha^2 + 1}\right) \frac{\epsilon^2}{k} \tag{11}$$

These equations were solved numerically using a fourth-order Runge-Kutta integration scheme. The model predictions (with $C_2 = 1.7$ and $C_3 = 5/6$) are compared with the experimental data of Jacquin *et al.* (1990) as shown in Fig. 1a. The model predicts well the evolution of turbulent kinetic energy and its decay rate for a wide range of rotation rates. We have also tested the model for the three Reynolds numbers measured by Jacquin *et al.* (1990), and found similar agreement of the model predictions with the data. We should point out at this point that the value $C_2 = 1.7$, proposed here for zero rotation rate, is lower than the value conventionally used in k-ϵ modeling. We find that with the conventional value of $C_2 = 1.92$ (and $C_3 = 3/5$) the model fails to predict the experimental data (see Fig. 1b)

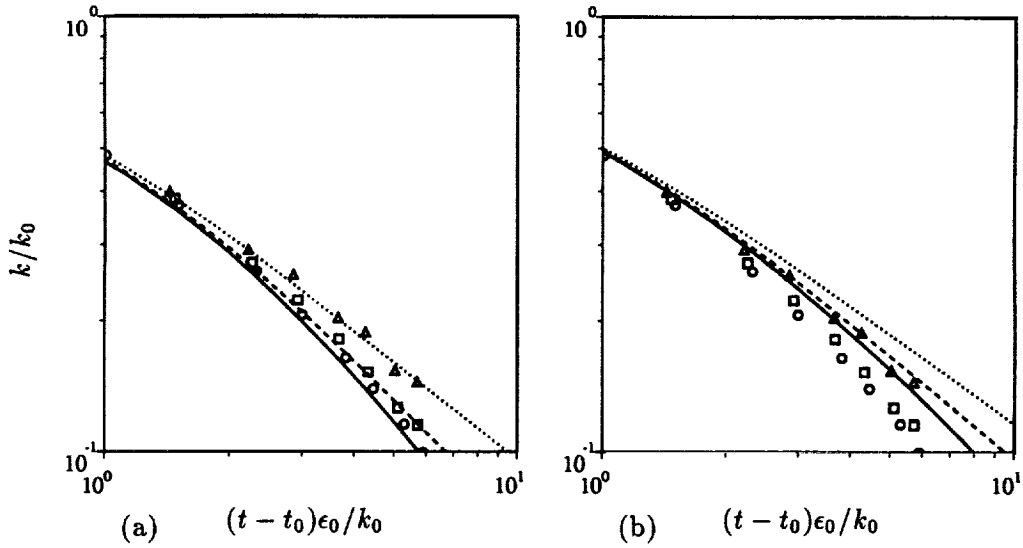

FIGURE 1. Decay of turbulent kinetic energy. Symbols are the data of Jacquin *et al.* (1990), lines are the model predictions. o & —— $\Omega = 62.8$ (rad/s), □ & ---- $\Omega = 31.4$ (rad/s), △ & ····· $\Omega = 15.7$. (a) Model predictions with $C_2 = 1.7$ and $C_3 = 5/6$; (b) Model predictions with $C_2 = 1.92$ and $C_3 = 3/5$.

4. Rotation Rate For General Flows

In order to test the rotational correction proposed in eq. (8) to the dissipation rate equation for general flows where the rotation rate is a function of position and

in the presence of mean strains, the question arises as to what is the appropriate definition of the rotation rate, Ω?

In most previous studies, the rotation rate or the mean vorticity Ω was replaced by $\sqrt{\Omega_{ij}\Omega_{ij}/2}$, where $\Omega_{ij} = (U_{i,j} - U_{j,i})/2$ is the rotation rate tensor of the mean flow. However, such definition does not distinguish between a vortex sheet and a vortex. A definition of a vortex or a region of vorticity (with spin) was given by Chong *et al.* (1990) -using the arguments of the critical point theory and the invariants of the deformation tensor- as a region in space where the vorticity is sufficiently strong to cause the rate of strain tensor to be dominated by the rotation tensor, i.e. the rate of deformation tensor has complex eigenvalues. This definition satisfies the principle of frame invariance since it depends only on the properties of the deformation tensor. We shall use it because the reduction in the dissipation rate is due mainly to the spin that the mean imposes on the turbulence. Consider the matrix D_{ij} of the elements of the deformation tensor,

$$D_{ij} = U_{i,j} \tag{12}$$

which can be split to

$$D_{ij} = S_{ij} + \Omega_{ij} \tag{13}$$

The complex eigenvalues of D_{ij} are found by solving the characteristic equation $|D_{ij} - \lambda\delta_{ij}| = 0$, where the λ's are the eigenvalues of D_{ij}. For a 3×3 matrix, λ can be found from the solution of

$$\lambda^3 + P\lambda^2 + Q\lambda + R = 0 \tag{14}$$

where P, Q and R are the matrix invariants and are given by

$$P = -U_{i,i} \tag{15}$$

$$Q = \frac{1}{2}(P^2 - S_{ij}S_{ji} - \Omega_{ij}\Omega_{ji}) \tag{16}$$

$$R = \frac{1}{3}\left(-P^3 + 3PQ - S_{ij}S_{jk}S_{ki} - 3\Omega_{ij}\Omega_{jk}S_{ki}\right) \tag{17}$$

For an incompressible flow $P = 0$ from continuity and the characteristic equation becomes

$$\lambda^3 + Q\lambda + R = 0 \tag{18}$$

Now if

$$A = \left[-\frac{R}{2} + \sqrt{\left(\frac{R^2}{4} + \frac{Q^3}{27}\right)}\right]^{1/3}$$

and,

$$B = \left[-\frac{R}{2} - \sqrt{\left(\frac{R^2}{4} + \frac{Q^3}{27}\right)}\right]^{1/3}$$

then the three roots of λ are;

$$\left[A+B, -\frac{A+B}{2}+\mathrm{i}\frac{A-B}{2}\sqrt{3}, -\frac{A+B}{2}-\mathrm{i}\frac{A-B}{2}\sqrt{3}\right]$$

That is λ can have:

(i) all real roots which are distinct when

$$[(Q/3)^3+(R/2)^2] < 0,$$

or

(ii) all real roots where at least two roots are equal when

$$[(Q/3)^3+(R/2)^2] = 0,$$

or

(iii) one real root and a pair of complex conjugate roots when

$$[(Q/3)^3+(R/2)^2] > 0.$$

We shall follow Chong *et al.* (1990) and define the rotation rate

$$\Omega = \Im(\lambda) = \frac{\sqrt{3}}{2}(A-B), \quad \text{when } [(Q/3)^3+(R/2)^2] > 0, \tag{19}$$

$\Omega = 0$ otherwise. It is important to note that for two dimensional Cartesian flows, the rotation rate defined by Eq. (19) reduces to $\Omega = \sqrt{|Q|}$, when Q, the determinant of the deformation tensor matrix, is negative. For pure shear the definition, eq. (19) yields $\Omega = 0$. Conventional models that are calibrated for shear flows, need not be recalibrated when corrections based on Ω are added to the model.

5. Numerical Procedure

For a two-dimensional, incompressible and steady turbulent flow, the Reynolds averaged momentum, continuity, turbulent kinetic energy and dissipation rate equations can be written in the generalized form;

$$\frac{\partial}{\partial x}(\rho U\Phi)+\frac{1}{r}\frac{\partial}{\partial y}(\rho r V\Phi) = \frac{\partial}{\partial x}\left(\Gamma_{\Phi_x}\frac{\partial\Phi}{\partial x}\right)+\frac{1}{r}\frac{\partial}{\partial y}\left(r\Gamma_{\Phi_r}\frac{\partial\Phi}{\partial y}\right)+S_\Phi \tag{20}$$

Where $r = 1$ for Cartesian two-dimensional flow, and $y = r$ for two-dimensional axisymmetric flow. Table 1 gives a summary of the terms in eq. (20) for the dependent variables solved in the code.

Φ	Γ_{Φ_x}	Γ_{Φ_r}	S_Φ
1	0.	0.	0.
U	$2\mu_e$	μ_e	$-\partial P/\partial x + 1/r\partial(\mu_e r\partial V/\partial x)/\partial y$
V	μ_e	$2\mu_e$	$-\partial P/\partial y + \partial(\mu_e \partial U/\partial y)/\partial y$
W	μ_e	μ_e	$-\rho VW/r - W/r^2\partial(r\mu_e)/\partial r$
k	$\mu + \mu_t/\sigma_k$	$\mu + \mu_t/\sigma_k$	$P_k - \rho\epsilon$
ϵ	$\mu + \mu_t/\sigma_\epsilon$	$\mu + \mu_t/\sigma_k$	$C_1 P_k \epsilon/k - C_2\rho\epsilon^2/k$

Table 1. Summary of the governing equations. ρ is the density, Γ_{Φ_x} and Γ_{Φ_r} are the exchange coefficients in the axial and radial directions respectively, S_Φ is the source term for the variable Φ. In the table, μ_e is the effective viscosity given as $\mu_e = \mu + \mu_t$, where μ is the laminar viscosity and μ_t is the turbulent viscosity, $\mu_t = C_\mu \rho k^2/\epsilon$.

In the standard k-ϵ turbulence model the constants C_μ, C_1, C_2, σ_k and σ_ϵ have the values 0.09, 1.44, 1.92, 1.0 and 1.0 respectively.

In the rotation modified k-ϵ turbulence model, only C_2 takes the form given by eq. (11) i.e, $C_2 = 1.7 + (5/6)\alpha^2/(\alpha^2 + 1)$.

The governing transport eq. (20) is solved using the primitive variables on a nonstaggered mesh and converted into a system of algebraic equations by integrating over control volumes defined around each grid point. The SIMPLE pressure-correction scheme (Patankar 1980) is used to couple the pressure and velocities and the resulting algebraic equations are solved iteratively. The convective terms are differenced using a second-order upwind scheme while the diffusion terms are approximated by a central differencing scheme.The physical domain is discretized using a non-uniform mesh where grid points are clustered close to the walls.

6. Model Application

The performance of the present model for complicated recirculating flows is demonstrated through calculations and comparisons with the experimental data of Driver & Seegmiller (1985) for backward-facing step flows and with the experiments of Roback & Johnson (1983) for a confined swirling coaxial jets into a sudden expansion.

Figure 2, shows the streamlines for the backward-facing step using the rotation modified k-ϵ turbulence model. The calculations were performed on a 100x40 grid points. The computational domain had a length of $50H$ (H is the step height) and a width of $9H$. The experimental data were used to specify the inflow conditions for a channel flow calculation where the fully developed profiles at the channel exit were used as the inlet conditions for the backward-facing step calculations. Fully developed flow conditions were imposed at the outflow boundary. The standard wall function approach (Launder & Spalding 1974) was used to bridge the viscous sublayer near the wall.

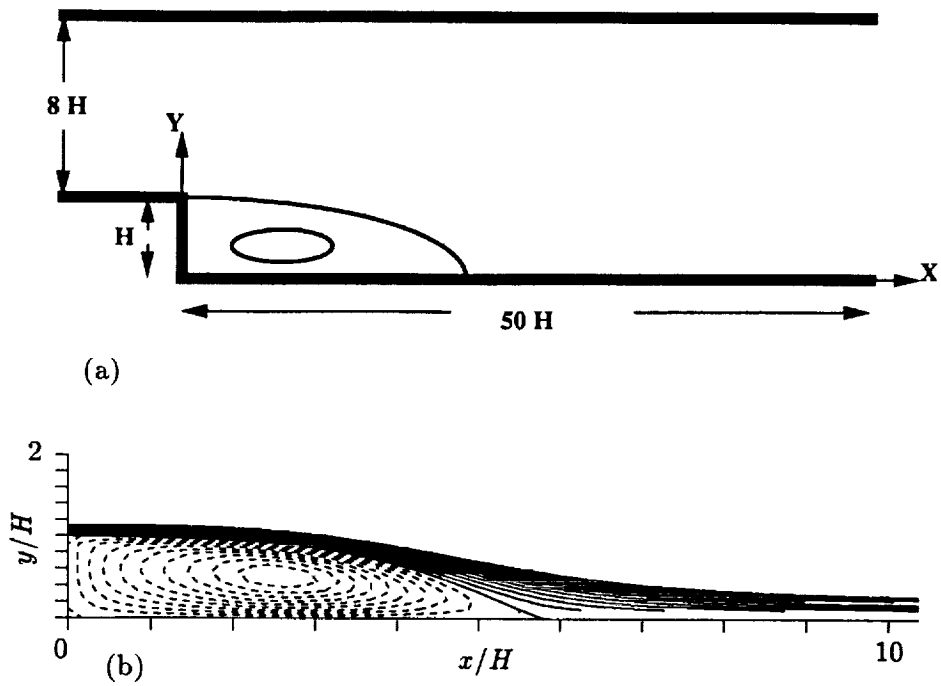

FIGURE 2. Backward-facing step geometry and stream-function contours. The contour levels were set between (-0.1 and 0.1) with an increment level = 0.01. ---- negative values, —— positive values.

The computed reattachment lengths were $5.50H$ using the standard k-ϵ turbulence model and $6.22H$ for the rotation modified k-ϵ turbulence model. The modified k-ϵ model prediction is closer to the experimental value of $6.10H$. While these results are encouraging, they are mainly due to the fact that we have changed the value of C_2 for the non-rotating case. In general, a change in the value of C_2 will result in poor predictions of the mean profiles. The mean velocity profile at three locations downstream are shown on Fig. 3, while the turbulent stress profiles at $X/H = 4$ are shown on Fig. 4. All the quantities were normalized by the step height (H) and the experimental reference free-stream velocity (U_{ref}). It can be seen that the overall performance of the rotation modified dissipation rate equation is better than the standard k-ϵ model especially in the recirculation region (Figs. 3a, and 4). Some improvements are also obtained in the recovery region using the modified k-ϵ model. Figure 5 shows the contours of the effective rotation rate used as defined by Eq. (19).

For the 2D/axisymmetric swirling flow computations, the expressions for the invariants Q and R (Eqs. (16) & (17) respectively) are expanded and Eq. (19) is used to obtain the values of Ω. The model was used to predict the mean profiles for a confined double concentric jets with a swirling outer jet flow into a sudden expansion (Roback & Johnson, 1983, see Fig. 6). Measurements are available for the mean

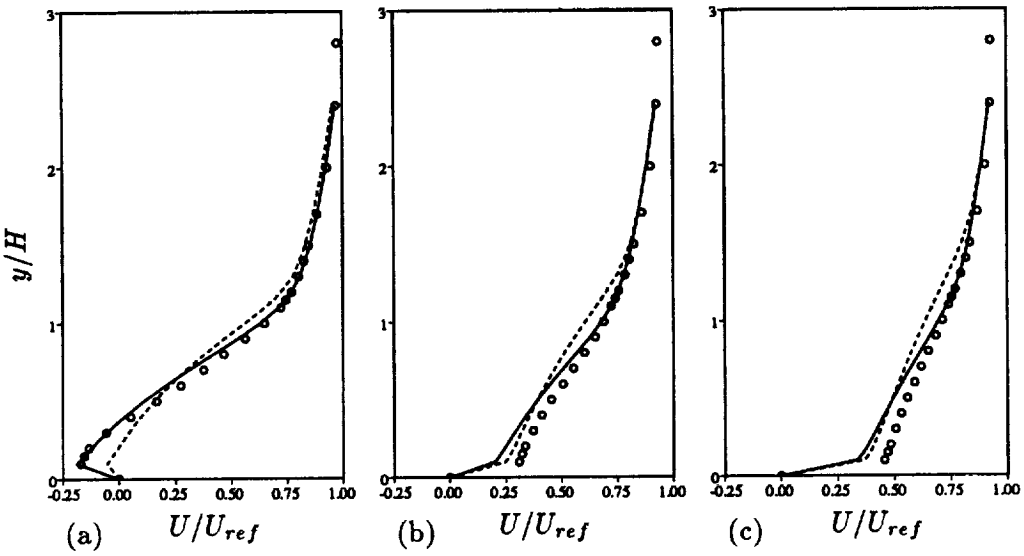

FIGURE 3. Mean axial velocity profiles at different axial locations. o data (Driver & Seegmiller, 1985); —— modified k-ϵ model; ---- standard k-ϵ model. (a) $X/H = 4$, (b) $X/H = 8$, (c) $X/H = 12$.

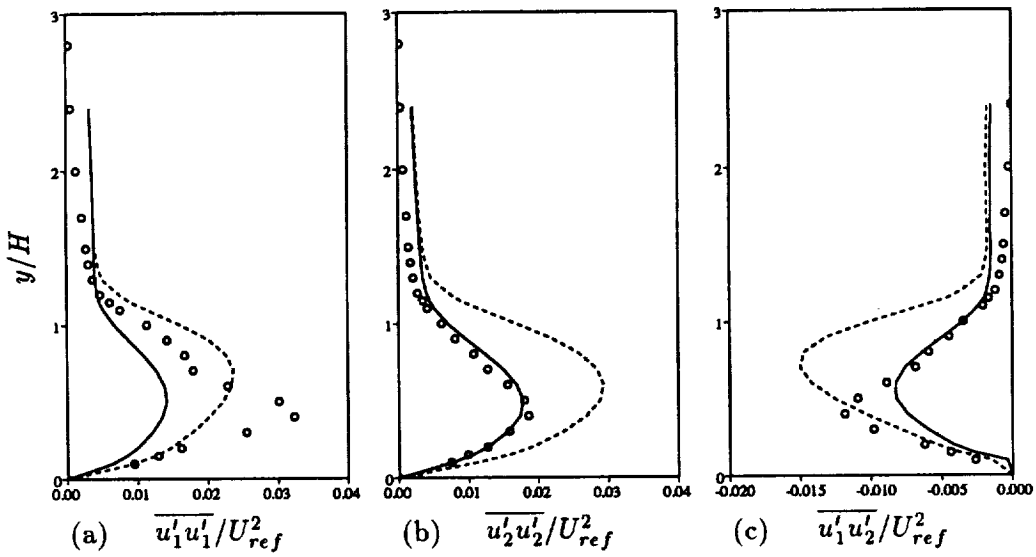

FIGURE 4. Turbulent stress profiles at $X/H = 4$. o data (Driver & Seegmiller, 1985); —— modified k-ϵ model; ---- standard k-ϵ model. (a) $\overline{u_1'u_1'}/U_{ref}^2$, (b) $\overline{u_2'u_2'}/U_{ref}^2$, (c) $\overline{u_1'u_2'}/U_{ref}^2$.

velocity profiles and velocity fluctuations downstream of the expansion. Simulations with a coarse nonuniform grid of 30×20 mesh points were made. However, there is some uncertainty about the inlet conditions to be used since the first velocity

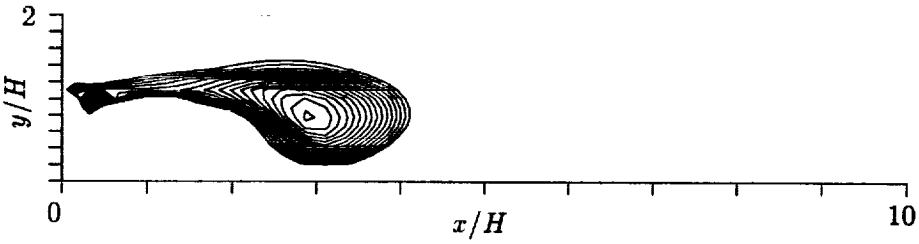

FIGURE 5. Contours of the effective rotation rate, Ω. Contour levels were set between (0.1,1.0) with an increment level = .01. are

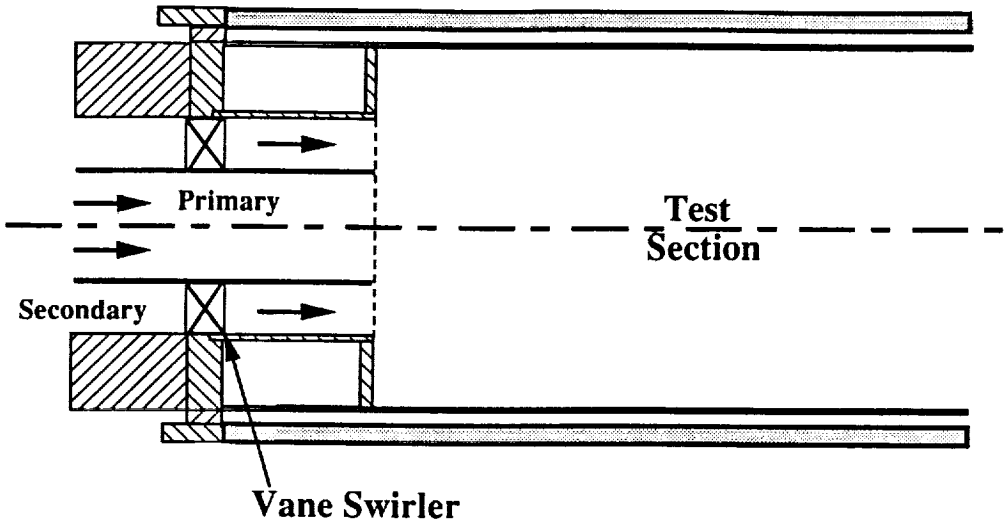

FIGURE 6. Roback & Johnson's swirling coaxial jets discharging into an expanded duct.

profiles measured were 5mm downstream of the expansion.

To predict this flow, the measured profiles at 5mm were adjusted near the edges and were used as inlet conditions at the expansion plane. Preliminary results obtained with the coarse mesh indicate similar trends as the experiment. Figure 7 shows the streamline contours using the standard and the modified k-ϵ turbulence models. The figure shows that a closed internal recirculation zone forms at the center with an additional zone at the corners downstream of the step. This causes a flow diversion outwards with high gradients between these regions. Figure 8 shows the axial and tangential velocity profiles at 25 mm downstream of the expansion using the standard and the modified k-ϵ turbulence models. Results in this case indicate little or no improvements offered using the modified k-ϵ model over the standard k-ϵ model. Finer mesh may improve the results but the uncertainties in the inlet boundary conditions raise the question about the adequacy of using this experiment for validation purposes.

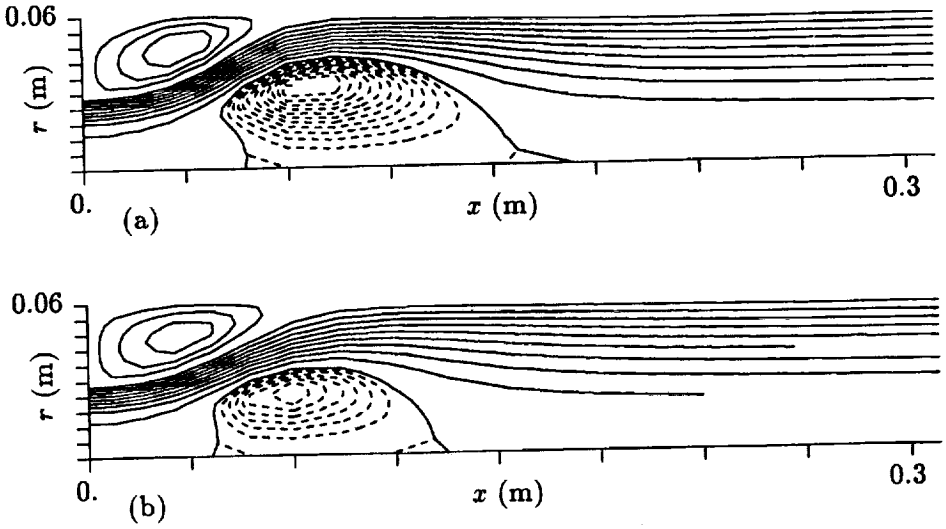

FIGURE 7. Swirling coaxial jets discharging into an expanded duct. Stream-function contour. ---- levels were set between (-0.15,0.) with an increment level = 0.01, —— levels were set between (0.,0.7) with an increment level = 0.05. (a) Standard k-ϵ model, (b) Modified k-ϵ model.

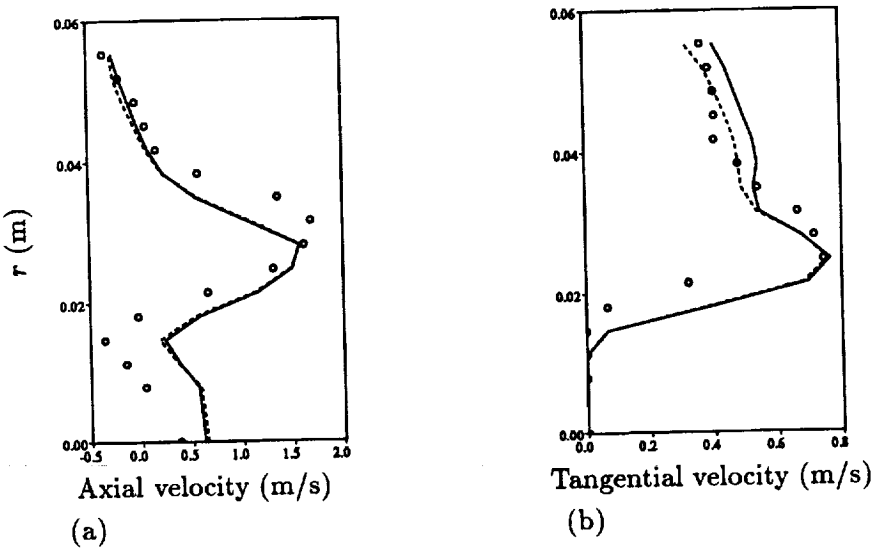

FIGURE 8. Velocity profiles at X = 25 mm. o data (Roback & Johnson, 1983); —— modified k-ϵ model; ---- standard k-ϵ model. (a) Axial Velocity, (b) Tangential velocity.

7. Conclusions

A new simple model for the turbulent energy dissipation rate equation has been proposed to account for the rotational effects on turbulence. A frame invariant

definition of the rotation rate proposed by Chong *et al.* (1990) based on the critical point theory was used. The model can be used in conjunction with any level of turbulence closure. It was applied to the two-equation k-ϵ turbulence model and was tested for separted flows in a backward-facing step and for axisymmetric swirling jet into a sudden expansion. The model is numerically stable and showed improvements over the standard k-ϵ turbulence model. It is important to point out that the present study was carried out to roughly evaluate the model, but that a systematic recalibration of the constants in the k-ϵ model is needed before going any further with the proposed model.

The authors would like to acknowledge many discussions with Dr. K. Shariff regarding proper definition of the rotation rate.

REFERENCES

BARDINA, J., FERZIGER, J. & ROGALLO, R. 1985 Effects of Rotation on Isotropic Turbulence: Computation and Modeling. *J. Fluid Mech.* **154,** 321-336.

DRIVER, D. & SEEGMILLER, H. 1985 Features of a Reattaching Turbulent Shear Layer in Divergent Channel Flow. *AIAA Journal.* **23,** 163-171.

HANJALIC, K. & LAUNDER, B. 1980 Sensitizing the Dissipation Equation to Irrotational Strains. *ASME J. Fluids Eng.* **102,** 34-40.

JACQUIN, L., LEUCHTER, O., CAMBON, C. & MATHIEU J. 1990 Homogenous Turbulence in the Presence of Rotation. *J. Fluid Mech.* **220,** 1-52.

LAUNDER, B. & SPALDING, D. 1974 The Numerical Computation of Turbulent Flows. *Comput. Methods Appl. Mech. and Engg.* **3,** 269-289.

MANSOUR, N. N., CAMBON, C. & SPEZIALE C. G. 1991 Theoretical and computational study of rotating isotropic turbulence. *Studies in Turbulence,* ed. by T. B. Gatski, S. Sarkar and C. G. Speziale, Springer Verlag, New-York.

CHONG, M. S., PERRY, A. E. & CANTWELL, B. J. 1990 A General Classification of Three-dimensional Flow Fields. *Phys. Fluids A.* **2,** (5), 765-777.

ROBACK, R. & JOHNSON, B. 1983 Mass and Momentum Turbulent Transport Experiment With Confined Swirling Co-Axial Jets. *NASA CR-168252.*

SPEZIALE, C., MANSOUR, N. & ROGALLO, R. 1987 The Decay of Isotropic Turbulence in a Rapidlly Rotating Frame. *Proceedings of the 1987 Summer Program,*CTR, NASA Ames/Stanford University.

SQUIRES, K., CHASNOV, J., MANSOUR, N. & CAMBON, C. 1993 Investigation of the Asymptotic State of Rotating Turbulence Using LES. *Annual Research Briefs - 1990,* CTR, NASA Ames/Stanford University.

WIGELAND, R. & NAGIB, H. 1978 Grid-Generated Turbulence With and Without Rotation About the Streamwise Direction. *IIT Fluids and Heat Transfer Report, R78-1,* Illinois Institute of Technology.

ZEMAN, O. 1994 A Note on the Spectra and Decay of Rotating Homogeneous Turbulence. *Phys. Fluids.* **6,** 3221-3223.